R-6199

RECEIVED
AUG 16 1965
RPL-62-24.2

INVESTIGATION OF COOLING PROBLEMS AT HIGH CHAMBER PRESSURES

FINAL REPORT

FOR PERIOD: 1 JULY 1963
TO 31 MARCH 1965

N65 32758
(ACCESSION NUMBER)
(THRU)
140
(PAGES)
1
(CODE)
CR 64530
(NASA CR OR TMX OR AD NUMBER)
28
(CATEGORY)
FACILITY FORM 602

ROCKETDYNE
A DIVISION OF NORTH AMERICAN AVIATION, INC.
6633 CANOGA AVE., CANOGA PARK, CALIFORNIA

CONTRACT NO. NAS 8-4011

GPO PRICE $ _____

CSFTI PRICE(S) $ _____

Hard copy (HC) 7.40

Microfiche (MF) 2.50

ff 653 July 65

MAY 1965

PREPARED FOR

PROPULSION AND VEHICLE ENGINEERING DIVISION
GEORGE C. MARSHALL SPACE FLIGHT CENTER
HUNTSVILLE, ALABAMA

ROCKETDYNE
A DIVISION OF NORTH AMERICAN AVIATION, INC.
6633 CANOGA AVENUE, CANOGA PARK, CALIFORNIA

R-6199 10

INVESTIGATION OF COOLING PROBLEMS AT HIGH CHAMBER PRESSURES

FINAL REPORT

Contract No. NAS8-4011

National Aeronautics and Space Administration
George C. Marshall Space Flight Center
Huntsville, Alabama

PREPARED BY

Research and Advanced Projects Departments

APPROVED BY

R. J. Thompson Jr.

R. J. Thompson, Jr.
Vice President and Director, Research

NO. OF PAGES 423 & xx **REVISIONS** DATE July 1965

DATE	REV. BY	PAGES AFFECTED	REMARKS

FOREWORD

Rocketdyne, a Division of North American Aviation, Inc., has prepared this final report which documents in detail all of the work performed in fulfillment of the program "Investigation of Cooling Problems at High Chamber Pressures" during the period from 1 July 1963 to 31 March 1965 as sponsored by the National Aeronautics and Space Administration under Contract No. NAS8-4011. The work was performed by the Heat Transfer and Fluid Dynamics Unit of the Research Department and the Aerothermodynamics Unit of the Advanced Projects Department. The program was administered by Messrs. Henry Burlage and Jack Suddreth of NASA Headquarters. Mr. Max Nein of NASA Marshall Space Flight Center was the technical monitor.

ACKNOWLEDGMENT

This report was prepared by W. S. Hines, F. W. Hoehn, W. S. Miller, A. S. Okuda, and J. D. Seader of the Research Department, and W. R. Wagner of the Advanced Projects Department. The Program Manager was R. B. Lawhead and the Project Engineer was J. D. Seader.

ABSTRACT

32758

Analytical and experimental results are presented of a continuation of the investigation to develop the engineering data and technology required to design cooling systems for liquid propellant rocket engines operating at chamber pressures from 1500 to 5000 psia and thrust levels up to 6 million pounds using liquid oxygen/hydrocarbon and liquid oxygen/liquid hydrogen as propellants.

author

CONTENTS

Foreword iii
Acknowledgment iii
Abstract v
Summary 1
Analytical Studies 1
Experimental Studies 6
Introduction 11
Analytical Studies 13
General Design Factors 15
Gas-Side Heat Transfer 15
Pressure Gradient Effects 15
Combustion Chamber Initial Momentum Thickness 34
Wall Curvature Effects 36
Surface Roughness Effects 48
Injector Effects 50
Discontinuous Wall Surfaces 52
Coolant-Side Heat Transfer 55
Hydrogen in the Critical Temperature Region 55
Tube Flow Curvature Effects 56
Tube Surface Roughness Effects 66
Generalization of Heat Transfer Correlations 68
Gas-Side Heat Transfer Coefficient Variations 68
Chamber Pressure Variation Effects 69
Other Chamber Geometries 70
Regenerative Coolant Pressure Drop Scaling 72
Film-Cooling Scaling 77
Radiation-Cooling Scaling 78
Transpiration Scaling 81
Ablative Scaling 81

Gaseous Film-Cooling Theory 81
Mixing Approach to Film-Cooling Theory 83
Film-Cooling Equation Development 107
Liquid Film-Coolant Surface Stability 113
Thermal Stress Studies 121
Tangential Thermal Stress Plasticity Onset 121
Longitudinal Thermal Buckling 133
Combined Thermal Stress Conditions 149
Life-Cycling Capability 153
Performance Loss Considerations 163
Engine Performance 163
Performance Loss With Film Cooling 170
Dump-Cooling Performance Degradation 184
Turbine Exhaust Gas Cooling 189
Film Cooling 189
Design Considerations 195
Combined Turbine Gas and Regenerative Cooling 195
Dump Cooling 197
Combined Cooling Methods 205
Film-Regenerative Cooling 205
Combined Film-Ablative Cooling 212
Film-Radiation Cooling 213
Conventional Engine Design Layouts 215
LO_2/LH_2 Engine 215
LO_2/RP-1 Engine 222
Advanced Chamber Design 225
Advanced Nozzle Considerations 225
Chamber Contours 226
Heat Transfer Coefficients 231
Cooling Studies 231
LO_2/LH_2 Propellant System 233

LO_2/RP-1 Propellant System 247
Film Cooling 256
Advanced Chamber Design Layouts 258
Novel Cooling Methods 263
Contact Resistance Liner 263
Film Cooling With Spiral Tangential Injection 268
FLOX Substitution 271
Effect on Chamber Heat Flux 271
Effect of Gas-Side Carbon Deposition 276
Mixture Ratio Shift Effects 279
Conclusions 287
Experimental Studies 289
Test Hardware 291
Tube Bundle Combustion Chamber 291
Machined-Passage Thrust Chamber 294
Supplemental Cooling Injection Systems 309
Supporting Test Equipment 323
Propellant Flow Systems 323
Sequence Control System 328
Instrumentation 330
Experimental Test Results 333
Cold-Flow Studies 333
Calorimetric Test Firings 336
Test No. 001 338
Test No. 002 338
Test No. 003 340
Test No. 004 340
Test No. 005 340
Test No. 006 341
Test No. 007 341

Supplemental Cooling Test Firings 341
Test No. 008—Transpiration Cooled 342
Test No. 009—Transpiration Cooled 343
Test No. 010—Slot Injection, Film Cooled 344
Test No. 011—Slot Injection, Film Cooled 344
Test No. 012—Radial Hole Injection, Film Cooled 345
Test No. 013—Slot Injection, Film Cooled 345
Experimental Data Analysis 353
Calorimetric Results 353
Supplemental Cooling Results 364
Combustion Chamber and Flow Development Section Heat Flux . . 386
Conclusions 386
Thermal Buckling Experiments 389
Experimental Apparatus 390
Experimental Procedure 395
Results 396
Types of Failure 396
Effect of Cycling 399
Strain at Failure 401
Conclusions 407
Nomenclature 409
References 417

ILLUSTRATIONS

1. Comparison of Laminar and Turbulent Boundary Layer Velocity Profiles 22
2. Comparison of Skin Friction Theory with Experimental Data 27
3. Typical Velocity Profile Exponent Variation for LO_2/RP-1 Engines 33
4. Illustration of Curvature Effects 37
5. Velocity Distributions in a Curved Two-Dimensional Channel 42
6. Turbulent Boundary Layer Velocity Profile Exponent . . . 43
7. Multichamber Nozzle Flow Impingement 53
8. Variation of Specific Heat of Para-Hydrogen With Pressure 57
9. Liquid Hydrogen Heat Transfer Data for Pressures > 1500 psia 58
10. Critical Curvature Ratio for 10-Percent Overall Friction Coefficient Increase-Pipe Flow 61
11. Available Curved-Tube Data for Heat Transfer Coefficient Ratio 63
12. Peak Heat Flux Ratio Dependence on Number of Thrust Chamber Elements 71
13. Maximum Allowable Chamber Pressure for Multi-Element Thrust Design With Regenerative Cooling 73
14. Film-Coolant Ratio Dependence on Number of Thrust Chamber Elements 79
15. a. Possible Film-Cooling Injection Methods for Single-Wall Chambers 84
    b. Possible Film-Cooling Injection Methods for Single-Wall Chambers 85

16. a. Possible Film-Cooling Methods for Tube-Wall Chambers 87
b. Possible Film-Cooling Methods for Tube-Wall Chambers 88
17. Mixing Profiles for Two Free Jets at Various Velocities, Two-Dimensional Solution 91
18. Conduction Analogy for Film-Cooling Velocity Profile . . 92
19. Comparison of Velocity Development on Film-Cooled Surface 94
20. a. Comparison of Film-Coolant Mixing Velocity Profiles 95
b. Comparison of Film-Coolant Mixing Velocity Profiles 96
c. Comparison of Film-Coolant Mixing Velocity Profiles 97
21. Velocity Profiles in Mixing Region (Zero Shear at Wall and Constant Properties) 98
22. Velocity Profiles in Mixing Region (Zero Shear at Wall and Constant Properties) 99
23. Three Regions of Velocity and Temperature Profile Development 103
24. Location of Point of Wall Temperature Rise from Coolant Temperature Value 105
25. Typical Trend of Experimental Data for Film Cooling . . . 108
26. Schematic of Analytical Model for Film-Coolant Stability 114
27. Onset of Plasticity at Tube Wall Outer Surface 123
28. Onset of Plasticity on Tube Wall Inner Surface 124
29. Tangential Thermal Stress Distribution 126
30. Nonlinear Plastic Stress Solution for 347 Stainless Steel Tube with 0.010-inch Wall 129

31. Stress-Strain Diagram for Inconel-X 131
32. Imposed Stress and Strain in Inconel-X Tube Wall with Assumed Linear Temperature Distribution 132
33. Degree of Plasticity for 0.010-inch Inconel-X 134
34. Buckling Behavior Under Thermal Loading 136
35. Chamber Showing Longitudinal Thermal Buckling 137
36. Buckling of Circular Columns and Tubes (based on elastic theory) 138
37. Analytical Critical Buckling Temperature Difference . . . 141
38. Critical Strain at Buckling Onset vs Tube Diameter-to-Thickness Ratio (Data of Lee, Ref. 51) 142
39. Typical Inelastic-Elastic Buckling Diagram (Data of Shanley, Ref. 47) 145
40. Correlation of Inelastic Wavelength Parameter with Diameter-to-Thickness Ratio (Data from Ref. 51, Inelastic Buckling) 146
41. Maximum Tube Thickness-to-Radius Ratio Relationship With Thermal Buckling 148
42. Design Solution for Combined Pressure and Thermal Stress. . 150
43. Example of Thermal Stress Cycling in the Plastic Range . . 155
44. Cyclic Life Parameter for Longitudinal Stresses 159
45. Cyclic Life Parameter for Tangential Stresses 161
46. Short-Term Fatigue of Materials Under Room-Temperature Cycling Conditions (Data Ref.: NASA TND 1574) 162
47. Engine Specific Impulse Comparison for Regeneratively Cooled LO_2/LH_2 Engines 167
48. Engine Specific Impulse Comparison for Partially Film-Cooled LO_2/LH_2 Engines 168
49. Engine Specific Impulse Comparison for Partially Film-Cooled LO_2/RP-1 Engines 169

50. LO_2/RP-1 Film-Cooling Performance Loss 172
51. LO_2/LH_2 Film-Cooling Performance Loss 173
52. Effect of LO_2/RP-1 Mainstream Mixture Ratio Shift on Percent of Film Coolant for Nominal MR = 2.35 174
53. Effect of LO_2/LH_2 Mainstream Mixture Ratio Shift on Percent of Film Coolant at Nominal MR = 5.0 175
54. Effect of Mixture Ratio Variation on Performance With Film Cooling 178
55. Loss in Specific Impulse with Film Cooling for LO_2/LH_2 (Based on 100-percent mixing) 180
56. Loss in Specific Impulse with Film Cooling for LO_2/RP-1 . . 181
57. Typical Schematic of Advanced Nozzle High D_p/D_t Design with Film and Combined Turbine Gas Cooling 196
58. Coolant Velocity and Static Pressure Distribution for Turbine Gas Dump-Cooling Design 199
59. Coolant and Wall Temperatures for Dump-Cooling Design Employing Turbine Exhaust Gases 200
60. Typical Overboard Cooling Method for High Area Ratio . . 202
61. Approximate Combined Film-Regenerative Cooling Flow Requirement Diagram 208
62. Ratio of Film-Coolant Requirements vs Heat Flux Ratio . . 209
63. LO_2/LH_2 Conventional Engine Layout for 3000-psia Chamber Pressure 217
64. LO_2/RP-1 Conventional Engine Layout for 2500-psia Chamber Pressure 218
65. Annular Combustor Design, Reverse-Flow Nozzle 229
66. Annular Combustor Design, Reverse-Flow Nozzle 230
67. Advanced Nozzle Heat Transfer Coefficient Distribution . . 234
68. Advanced Nozzle Heat Transfer Coefficient Distribution . . 235

69. Regenerative Design Limits for the Combustion Zone of an Annular Design Using LO_2/LH_2 241
70. Typical Advanced Nozzle Design Configuration with Annular Combustion Chamber for LO_2/LH_2 Propellants . . . 243
71. Throat Heat Flux for LO_2/RP-1 Propellants, Advanced Nozzle Design 248
72. Regenerative Design Upper Chamber Pressure Limits for Combustion Zone of an Annular Nozzle Design Using LO_2-RP-1 Propellants 250
73. Regenerative Design Limits for the Combustion Zone of an Annular Design Using LO_2/RP-1 Propellants 252
74. LO_2/LH_2 Advanced Engine Design Layout for 3000-psia Chamber Pressure and D_p/D_t = 3.5, Thrust=6 million pounds. . 259
75. LO_2/LH_2 Advanced Engine Design Layout for 3000-psia Chamber Pressure and D_p/D_t=5.0, Thrust=6 million pounds.. . 260
76. Novel Cooling Methods 266
77. Effect Upon Heat Transfer Rate of Varying Gas-Side Surface Temperature with RP-1 Fuel 278
78. Regenerative-Cooling Upper Limit Change with Heat Flux Change 280
79. Tube Bundle Combustion Chamber on Mandrel 292
80. Machined-Passage Thrust Chamber Assembly 295
81. Machined-Passage Thrust Chamber Assembly 296
82. Transpiration-Cooled Coaxial Injector Assembly 298
83. Transpiration-Cooled Coaxial Injector 299
84. Machined-Passage Combustion Chamber Assembly 300
85. View of Machined-Passage Combustion Chamber Before Brazing of Manifold Covers (Injector End) 301
86. View of Machined-Passage Combustion Chamber Before Brazing of Manifold Covers (2-D End) 302

87. Machined-Passage 2-D Flow Development Section 304
88. Machined-Passage 2-D Flow Development Section 305
89. Nozzle Heat Flux Distribution as a Function of Chamber Pressure 307
90. Minimum Required Water Coolant Velocities as a Function of Chamber Pressure in the Nozzle 308
91. Machined-Passage Nozzle Spacer Bar and Sideplate Limit . . 310
92. Machined-Passage Nozzle Sideplate 311
93. Machined-Passage Nozzle Outer Sideplate 312
94. Machined-Passage Nozzle Assembly 313
95. Transpiration-Cooling Section 314
96. Film-Cooling Section With Continuous-Slot Tangential Injection 315
97. Film-Cooling Section With Radial-Hole Injection 316
98. Overall View of Typical Supplemental Cooling Section . . 317
99. Enlarged Views of Supplemental Cooling Sections 318
100. Experimental Flow System for Motor Firings 324
101. High Pressure Test Stand Facility 325
102. High Pressure Hydrogen Supply System 326
103. Typical Firing Sequence with Film Cooling 329
104. Typical Nozzle Water Coolant Temperature Rise Curve for Calorimetric Test Firing, Test No. 006, Station 4 331
105. Typical Nozzle Water Coolant Temperature Rise for Test Firing with Supplement Cooling, Test No. 010, Station 4 . . 332
106. Water Flow Test with Transpiration-Cooled Coaxial Injector 334
107. Oxidizer-Side Injector Δ P Results 335
108. Transient Thermopile MV Output at Station 4 for Test No. 001 339

109. Hardware Damage, Posttest 013 347
110. Hardware Damage, Posttest 013 348
111. Coaxial Jet Injector Damage, Posttest 013 349
112. Oscillograph Record of Test No. 013 350
113. Nozzle Heat Flux Distribution for Test No. 002 354
114. Nozzle Heat Flux Distribution for Test No. 003 355
115. Nozzle Heat Flux Distribution for Test No. 004 356
116. Nozzle Heat Flux Distribution for Test No. 005 357
117. Nozzle Heat Flux Distribution for Test No. 006 358
118. Nozzle Heat Flux Distribution for Test No. 007 359
119. Calorimetric Nozzle Heat Flux at Station 1 365
120. Calorimetric Nozzle Heat Flux at Station 3 366
121. Calorimetric Nozzle Heat Flux at Station 4 367
122. Calorimetric Nozzle Heat Flux at Station 5 368
123. Calorimetric Nozzle Heat Flux at Station 6 369
124. Effect of Chamber Pressure on Heat Flux 370
125. Relative Effectiveness of the Supplemental Cooling Method 372
126. Transpiration-Cooling Efficiency, Test No. 008 374
127. Film-Cooling Efficiency with Continuous-Slot Tangential Injection, Test No. 010 375
128. Film-Cooling Efficiency with Continuous-Slot Tangential Injection, Test No. 011 376
129. Film-Cooling Efficiency with Radial-Hole Injection, Test No. 012 377
130. Variation of T^+ for Adiabatic Wall Conditions 384
131. Variation of T^+ with 50 Percent of Total Heat Flux Absorbed by Regenerative Cooling 385
132. Effect of Partial Regenerative Cooling on Film Cooling Efficiency 387

133. Schematic of Thermal Buckling Test Apparatus 391
134. Thermal Buckling Test Apparatus 392
135. Schematic of Test Section 393
136. Single-Tube Test Section 394
137. Ripple-Type Failure 397
138. Diamond-Type Failure 398
139. Multiple Tube Failure 400
140. Linearized Test Section Temperature Profiles Prior to Failure 402
141. Comparison of Linearized and Heat Generation Temperature Profiles for Test No. 1 404
142. Effect of Tube Diameter to Wall Thickness Ratio on Strain at Failure 405

TABLES

1. Comparative Wall Skin Friction in Throat Region at High Chamber Pressures for LO_2/LH_2 Engines 34
2. Comparison of Film-Cooling Injection Methods for Single Wall Designs 86
3. Comparison of Film-Cooling Theories 112
4. Stability Regimes for Film-Coolant Adherence 119
5. LO_2/LH_2 Turbine-Exhaust-Gas Cooling Requirements for Advanced Nozzle Designs With $D_p/D_t = 3.5$ 191
6. LO_2/LH_2 Turbine-Exhaust-Gas Cooling Requirements for Advanced Nozzle Designs With $D_p/D_t = 7.0$ 192
7. LO_2/RP-1 Turbine-Exhaust-Gas Cooling Requirements for Advanced Nozzle Designs With $D_p/D_t = 3.5$ 193
8. LO_2/RP-1 Turbine-Exhaust-Gas Cooling Requirements for Advanced Nozzle Designs With $D_p/D_t = 7.0$ 194
9. Comparison of Turbine Exhaust Gas Cooling By Dump- and Film-Cooling Methods 198
10. Typical Nominal Performance Parameters-Bell Chamber Design . 216
11. Advanced Nozzle Contours 227
12. Advanced Nozzle Dimensions 228
13. Summary of Heat Transfer Values for Annular Nozzle Designs . 232
14. Approximate Coolant Tube Number Requirements for Advanced Nozzle Designs Based Upon Cooling Requirements for a Single Up-Pass Design With LO_2/LH_2 Propellants 237
15. Supersonic Region Film-Cooled Length Required for Advanced Nozzle Designs With LO_2/LH_2 Propellants 238
16. Summary of Approximate Film Cooling Requirements for an Annular Combustor With $D_p/D_t = 3.5$ at a Maximum Wall Temperature of 2000 R With LO_2/LH_2 Propellants 244

17. Minimum Supersonic Region Film-Cooled Lengths for Nozzle Skirt With Film-Cooling Augmentation, Advanced Nozzles With LO_2/RP-1 253
18. Approximate Coolant Tube Number Requirements for Advanced Nozzle Designs Based Upon Regenerative Cooling With a Single Up-Pass Design With LO_2/RP-1 Propellants 255
19. Heat Flux Reductions With Contact Resistance Liners . . . 264
20. Performance Comparison of F_2/O_2 With O_2 Oxidizer 272
21. FLOX/Hydrogen Combustion Gas Physical Properties and Chamber Parameters 273
22. FLOX/RP-1 Combustion Gas Physical Properties and Chamber Parameters 274
23. Experimental Program Test Results 337
24. Supplemental Cooling Efficiencies 378
25. Thermal Buckling Test Sections 395
26. Strain at Failure for Thermal Buckling Experiments 403

SUMMARY

Analytical and experimental studies were conducted to continue the development of engineering data and technology required to design cooling systems for liquid propellant rocket engines operating at chamber pressures from 1500 to 5000 psia at thrust levels up to 6 million pounds using liquid oxygen/hydrocarbon (e.g., RP-1) and liquid oxygen/liquid hydrogen as propellants.

ANALYTICAL STUDIES

The analytical studies performed during the follow-on to Contract NAS8-4011 were based upon the cooling methods which were shown during the initial contract period (Ref. 1) to be the most advantageous for high-chamber-pressure, high-thrust chamber designs using the above stated propellant systems. The previous analytical studies resulted in the development of preliminary procedures for the synthesis of actual thrust chamber designs utilizing advanced cooling methods. The results of the experimental studies conducted during the follow-on program, as described below, provided verification of the application of these procedures and were, in part, incorporated into the analytical studies. The major emphasis was placed on the LO_2/LH_2 propellant system.

Analytical studies during the follow-on program were directed primarily toward the actual evaluation of mass-transfer-cooled designs and combined mass-transfer and regeneratively cooled designs because these cooling approaches offered potential suitability from performance, pressure drop, weight, and manufacturing standpoints. Since other methods offer advantages at high expansion area ratio (e.g., dump and radiation cooling), these methods were considered in applicable regions.

Advanced thrust chamber nozzle designs of the expansion-deflection, horizontal flow, and plug types offer advantages from a performance and nozzle length-saving viewpoint. These nozzle types, however, experience higher heat transfer rates due to varying degrees of turning imposed on the combustion gas. Advanced combustion chambers such as the toroidal design offer increased packaging, weight, and length advantages. However, they also have a somewhat higher heat transfer rate imposed. Studies were made to optimize cooling system designs for these advanced nozzles as well as conventional nozzles.

Gas-side heat transfer coefficient approaches were examined for use in conventional and advanced nozzles. It was determined that the boundary layer approach using finite increment integration solutions represented the most accurate design approaches. A new calculational procedure was developed based on an empirical fit of variable pressure gradient turbulent skin friction coefficient data. The effect of a large favorable pressure gradient was found to increase the local gas-side heat transfer coefficient.

Another gas-side heat transfer factor examined was that of initial boundary layer thickness and the growth of the boundary layer in the combustion zone. Turbulence effects and local mixture ratio variations were shown to strongly influence the heat rates near the injector face. Gas-side surface roughness and wall curvature effects were shown to change the level of heat input especially in the throat region where high local Reynolds numbers exist.

Discontinuous wall surface conditions were examined for engine designs such as those employing multiple thrust chambers truncated to a small expansion ratio and clustered about an advanced nozzle configuration.

For these designs, it was shown that the heat transfer rate at the nozzle impingement point was not controlling so long as the impingement angle and pressure were minimized.

For regeneratively cooled designs, the coolant-side heat transfer coefficient prediction method was improved by definition of the critical temperature region effect on hydrogen cooling at high pressures and by improved correlations of experimental data for surface roughness effects at high Reynolds numbers. Preliminary data on tube curvature effects in the throat region show significant increases in the coolant-side convective coefficient. The effects of these latter factors can increase the regenerative-cooling feasibility limit and bring it closer to the wall heat conduction limit.

The film-cooling approach for handling high heat fluxes has considerable merit due to a relatively low-coolant-flow requirement for the large thrust levels examined, a minimum requirement for manufacturing, and a maximum in terms of performance reliability. An intensive examination of the presently available analytical approaches, development of new approaches, and the specification for the gathering of new, more applicable data was, therefore, justified. An analytical film-cooling model based upon differing velocity stream mixing was developed which compared favorably to existing analytical models. It was seen that the wall temperature and effective film-cooling utilization efficiency was found to improve as the coolant velocity was increased to approach the gas velocity. Different design approaches were investigated for film-cooling injection methods. It was determined that the best approaches employ coaxial tangential injection with a louver-type construction.

Scaling parameters were developed to scale the present and previous contract results to other thrust chamber pressure and area ratio conditions for the basic cooling methods. The principal parameter affecting coolant design factors was shown to be the chamber pressure, with influences of other variables such as thrust, occurring when a wide variation from the design point was examined. Lower chamber pressure feasibility limits were indicated for multichamber configurations.

Previous studies showed that the thin-wall tubes in a high-chamber-pressure, regeneratively cooled design would be subject to thermal buckling and a short operational life due to the inelastic thermal stress conditions. Elastic and inelastic regimes of thermal buckling were considered. Comparisons were made of the wall plasticity onset point and graphical plastic-elastic strain approaches for longitudinal and tangential strain conditions were developed. The importance of utilizing coolant jacket tubes of small diameter-to-thickness ratio was indicated.

Life-cycling capability was compared for various materials using nondimensional rating parameters for life. It was shown that materials with a good ductility and small thermal expansion showed a good life capability. Wall temperature increases showed a trend toward a rapid deterioration in life-cycling capability. Stainless-steel materials were indicated to be superior over the Inconel family at high temperatures.

Performance losses associated with cooling were reviewed for high-chamber-pressure conditions. It was shown that for a conventional gas generator cycle condition, the increasing pump power requirements and losses negated the pressure-derived performance gain at higher and higher pressure. With regenerative designs, the cooling jacket pressure loss was shown to become prohibitive at higher pressures. Performance losses

with film cooling were compared based on various degrees of mixing and interchange of heat transfer between the coolant and mainstream. Liquid oxygen/liquid hydrogen film-cooled designs were described as having the lowest performance loss because of the relatively small coolant flow required and because of a low coolant molecular weight when using hydrogen. Equations for dump-cooling losses were formulated and programmed. Sample cases showed small percentage losses when hydrogen was used as a dump coolant.

Turbine exhaust gas cooling was found to be an excellent method for high-thrust designs at high area ratios because the flowrate required was found to be within the available flow percentage. The advanced nozzle designs showed this cooling method to be particularly attractive in the high expansion sections. Film and dump cooling with the turbine exhaust gas were investigated with the former proving to be the most advantageous from a heat transfer standpoint because it results in wall surface temperatures several hundred degrees lower and, consequently, provides a greater stress and reliability margin.

The combined cooling methods (regenerative-film, film-ablative, and film-radiative) can be used to advantage. For high heat flux conditions, the combined film and regenerative method appears attractive up to at least 5000-psia pressure if optimization is made with respect to coolant-side pressure drop and film-coolant performance loss.

To visualize the incorporation of the more advantageous cooling methods, design layouts of advanced and conventional nozzle designs were made. Film cooling, regenerative cooling, and combined film-regenerative cooling were used for the high heat flux regions, with turbine exhaust gas used in the high area ratio portion of the nozzles. Pump size relative to the chamber size and incorporation of the turbopumps into the advanced nozzle configurations appeared to be the paramount design problem area. Thus, increased pump speeds with decreased size, and the use of clustered pump units of small individual size are indicated.

Advanced nozzles were shown to have approximately the same upper limits in chamber pressure operation with somewhat higher throat heat fluxes dependent on the throat curvature, combustion zone length and pressure gradient. With advanced nozzle configurations, combustion zone heat transfer rates could be substantially reduced over the conventional designs by the allowance of high contraction ratio conditions.

Novel cooling methods including the use of a contact resistance liner of refractory material for wall heat flux reductions were briefly examined. This method can be effective if a reasonably close control of design parameters can be achieved.

Substitution of FLOX for increased performance was examined from a heat transfer standpoint. Heat fluxes were found to be within 10 percent of the LOX values for fluorine concentrations to 70 percent. Existing data indicate that the gas-side carbon layer in a FLOX/RP-1 system is as effective as it is for LOX/RP-1 for the lower range of fluorine concentrations.

EXPERIMENTAL STUDIES

The experimental studies performed during the follow-on to Contract NAS8-4011 were directed toward the measurement of gas-side heat transfer with and without supplementary mass transfer cooling at the high heat flux conditions of high-chamber-pressure engines, and to a study of inelastic thermal buckling of coolant tubes at high temperatures.

The gas-side heat transfer measurements were made under steady-state conditions with a small two-dimensional copper motor having a throat area of 0.50 in.^{2}. Initially, a copper tube bundle construction was designed to permit the highest possible heat flux conditions using

coolant water flowing inside the tube walls. However, because of considerable difficulties in obtaining adequate seals, this design was discarded in favor of a drilled-passage design which permitted the attainment of adequate, but somewhat lower, heat flux levels.

The motor consisted of a 2.25-inch-diameter transpiration-cooled coaxial jet injector, a 3-inch-long combustion chamber in which the flow cross section was converted from circular to rectangular, a 4.42-inch-long rectangular flow development section to establish a relatively smooth gas flow, and a two-dimensional nozzle with a 4:1 contraction ratio and a 2:1 expansion ratio. The motor was sufficiently instrumented to permit the measurement of characteristic velocity efficiency and local heat flux at a number of stations, with particular emphasis on the nozzle entrance and throat regions. The local heat flux values were determined by the calorimetric method based on measurements of water-coolant flow-rate and temperature rise. All firings were conducted with LO_2/GH_2. The mixture ratio varied from 3.5 to 5.5. In general, about 2 seconds of mainstage operation were required to achieve steady-state conditions.

The first seven firing tests were conducted without supplementary mass transfer cooling to determine base values of the local gas-side heat flux distribution. The chamber pressure was varied from about 500 to 800 psia. Throat heat fluxes as high as 33.2 Btu/in.^{2}-sec were measured. This value corresponds to large-engine operation to chamber pressures of about 1750 psia, the approximate limit of chamber pressure feasibility for complete regenerative cooling. Under these conditions, the estimated gas-side copper wall temperature at the throat was as high as about 1300 F. No throat erosion was detected for these extreme conditions. Tube wall designs for large advanced chambers using small-diameter copper tubing are currently being considered. A prelimariny analytical study indicated that long-life low-wall-temperature (700 F) designs may be able to be developed with comparatively thick-wall copper tubing because of its extremely high thermal conductivity. However, severe stress limitations

with copper preliminarily indicated application only in advanced nozzle configurations where small, nearly circular tube cross sections are required.

After correcting for combustion characteristic velocity efficiency, which ranged from 93.6 to 96.6 percent, the measured local heat fluxes were compared to values predicted by the simplified Bartz equation using a film reference temperature and neglecting any effects of recombination or radiative transfer. In general, the measured values at the nozzle entrance and throat regions were in excellent agreement with the Bartz equation with average deviations of about 9 and 7 percent, respectively.

Slight intermittent chugging was observed during some of the firings due to a lower-than-desirable injector pressure drop-to-chamber pressure ratio. The chugging was generally of low-pressure amplitude and frequency such that the heat transfer results should not have been affected.

The effect of supplementary mass transfer cooling was investigated by inserting various 1/2-inch-thick injector sections between the flow development section and the nozzle section. In all cases, GH_2 was the injected coolant. Included were film cooling with continuous-slot tangential injection, film cooling with radial-hole injection, and transpiration cooling. The continuous-slot, film-cooling injector utilized a 0.030-inch slot gap with closely spaced vanes to obtain uniform film-coolant injection velocity. The radial-hole, film-cooling injector utilized a single row of 0.062-inch-diameter, equally spaced holes having a total injection area equal to that of the slotted injector. The transpiration injector was constructed of 0.082-inch-thick Rigimesh, which was fabricated for a specified 20-psi pressure drop with a 300-scfm/ft^2 air flow when exhausting to the atmosphere. The injected film coolant was metered and controlled by a sonic flow restrictor independent of the chamber pressure.

Five firings were conducted with supplementary mass transfer cooling. Chamber pressure ranged from about 570 to 830 psia. During an attempted firing at a chamber pressure of 1000 psia, a detonation occurred in the hydrogen manifold causing separation of one of the coolant discharge lines from the chamber and subsequent coolant-water flow unbalance, localized overheating, and eventual failure of the copper chamber.

For the mass-transfer-cooled tests, the reduction in heat flux to the water coolant was measured, and the chamber wall temperatures were calculated by the procedures described. The film-cooling efficiencies were then determined based on the relations derived in Ref. 1.

The results indicate that the more difficult fabrication procedure required for the continuous-slot tangential film-coolant injection technique is warranted because significantly higher film-coolant efficiencies were obtained as compared to radial-hole or transpiration injection. The efficiencies obtained with the tangential injection method were as high as about 60 percent at the throat, which was considerably higher than the 25 percent predicted from correlations based on adiabatic wall conditions. Analytical examination of the boundary layer equations indicated that such an increase in film-coolant efficiency is to be expected when a portion of the total gas-side flux must be carried across the laminar layer next to the wall. Thus, the combined use of film and regenerative cooling is particularly attractive for chamber designs at chamber pressures beyond the feasibility limits of complete regenerative cooling.

Inelastic thermal buckling tests were conducted with 0.50-inch OD stainless steel tubes of varying wall thickness. The tubes were preloaded to an initial stress and then strained to failure by electrical heating.

Ripple-type buckling failures were obtained with single tubes of 0.010-inch wall thickness or greater at maximum temperatures of 1400 to 1500 F. For a thinner-walled tube, individual buckling waves were obtained at a maximum temperature of only about 800 F. A test with a three-tube brazed configuration indicated that much higher buckling strains and corresponding maximum temperatures are possible for the multiple-tube arrangement of thrust chambers. The use of relatively small tubes with a minimum wall thickness of about 0.010 inch appears feasible for high-chamber-pressure designs despite operation in the inelastic region if adequate cooling is provided to maintain the gas-side wall temperatures below certain limiting values. For stainless steel, temperatures as high as 1600 F appear to be feasible.

INTRODUCTION

On 9 April 1962, a program entitled "Investigation of Cooling Problems at High Chamber Pressures" was initiated by Rocketdyne under Contract No. NAS8-4011. The object of this investigation was to develop the engineering data and technology required to design cooling systems for liquid propellant rocket engines operating at chamber pressures from 1500 to 5000 psia at thrust levels up to 6 million pounds using liquid oxygen/hydrocarbon and liquid oxygen/liquid hydrogen as propellants. The critical cooling problems were to be determined, and solutions to these problems were to be developed.

During the period from 9 April 1962 to 8 January 1963, reported in Ref. 1, Rocketdyne conducted analytical and experimental studies on the applicability of regenerative cooling at high chamber pressures. Because of the high heat flux conditions at high chamber pressures, an excessive coolant-side pressure drop was encountered which indicated definite chamber pressure feasibility limits for regenerative cooling. Accordingly, preliminary analytical studies were made to determine the applicability of other methods such as film, transpiration, and ablation cooling. Some of the alternate cooling methods showed considerable promise of feasibility to 5000-psia chamber pressure when used either to supplement regenerative cooling or to provide the sole cooling technique.

On 1 July 1963, a follow-on program was initiated by Rocketdyne to continue the investigation of cooling problems at high chamber pressures. The main purpose of the follow-on program was to conduct analytical and experimental studies to determine the most feasible solution to the

chamber cooling problem for any set of engine design conditions within the above stated ranges of pressure and thrust level. To be included were advanced as well as conventional engine configurations, and utilization of two or more simultaneous cooling methods. This report presents in detail the results of the analytical and experimental studies conducted during the follow-on program.

ANALYTICAL STUDIES

The main objectives of the analytical studies were to develop a better understanding of the most promising supplementary chamber cooling methods and to investigate the best means of utilizing these methods in typical high chamber pressure engine designs. The following sections present the results of these studies. First, general heat transfer design factors are discussed including a new theory for determining the gas-side heat transfer coefficient which is particularly useful for advanced engine configurations, an improved method for estimating coolant-side heat transfer for hydrogen, a new film-cooling theory based on a detailed fluid dynamic model, generalized heat transfer correlations for rapid scaling including determination of multichamber effects, thermal stress influences at high chamber pressure for tubular wall construction, and engine performance losses associated with various cooling methods. Then the use of turbine exhaust gas for film and dump cooling is examined. The applicable ranges of combined cooling methods are next determined with particular emphasis on film-regenerative. Typical engine design layouts are presented for conventional and advanced configurations. Some novel cooling methods are briefly considered. Lastly, the effects of FLOX substitution are predicted.

GENERAL DESIGN FACTORS

The general design factors were developed in such a manner as to provide a qualitative insight into the importance of certain parameters in affecting the heat input or heat rejection capability or efficiency of a thrust chamber as well as quantitative computational procedures. The general design factors to be discussed here include gas-side heat transfer, coolant-side heat transfer in regeneratively cooled engines, film-cooling theory, generalization of heat transfer correlations and scaling of results, thermal stress considerations, and cooling performance losses.

GAS-SIDE HEAT TRANSFER

The level of the gas-side heat flux input strongly dictates the choice of cooling method; i.e., film,ablative, regenerative, etc. Existing methods of estimating the gas-side heat flux were summarized in Ref. 1. The ensuing discussion will develop the effects of pressure gradients, surface roughness, and wall curvature which are not adequately included in the existing methods. Additionally, the effect of nonuniform combustion and flow development will be qualitatively covered.

Pressure Gradient Effects

A review of the current methods available from Bartz, et al. (Ref. 2), Tromblay (Ref. 3), and Mayer (Ref. 4) for the evaluation of the gas-side heat transfer coefficient from boundary layer theory indicated that these approaches may be invalid when applied to advanced nozzles, particularly at high pressures. The principal deficiencies appear to be in the pressure

gradient effects on the wall skin friction and, correspondingly, the effects of wall curvature and pressure gradient on the alteration of the boundary layer velocity profile exponent, which has a value of seven for a normal flat plate. Therefore, a revised approach for evaluating the gas-side heat transfer coefficient was developed as described below.

If the effective boundary layer energy thickness (φ) is assumed to be equal to the momentum boundary layer thickness (θ) then a consideration need only be made of the momentum equation (resulting from a similarity of the momentum and energy equations) in the analysis of boundary layer problems associated with thrust chamber heat transfer. The allowance of this reasonable simplification contributes considerably toward the expeditious solution of this class of boundary layer problems. The effect of the above assumption upon the heat transfer coefficient value may be determined in terms of the Stanton number by using a simplified form of the modified Reynolds analogy:

$$\frac{St}{(Pr)^{-2/3}} = \frac{Nu}{Re\ Pr^{1/3}} = \frac{C_f}{2} \qquad (1)$$

The following discussion presents a new technique for determining $C_f/2$ (and thus h_g) under conditions of strong pressure gradients.

A scrutiny of the skin friction coefficient equation yields the important variables for consideration:

$$\left(\frac{C_f}{2}\right) = \frac{\alpha\,(H, \gamma)}{(Re)^{1/\gamma}} \qquad (2)$$

where the shape factor (H) is a measure of the pressure gradient and γ is a variable which depends on the pressure gradient.

In actuality, the dependence of the skin friction coefficient upon Reynolds number is small ($\gamma > 4$) for normal turbulent flow.

The highest level of sophistication available for heat transfer is to base the skin friction coefficient on the energy thickness, φ. However, an evaluation of the Reynolds number based on the momentum thickness is only slightly in error. For reasonable Reynolds numbers ($Re_\theta > 1000$) and a γ value of 4 to 7, a typical 20-percent discrepancy in momentum and energy thickness values appears as a negligible change in the skin friction coefficient. Thus:

$$\left(\frac{C_f}{2}\right) = \frac{\alpha\,(H,\,\gamma)}{(Re)_\varphi^{\,1/\gamma}} \approx \frac{\alpha\,(H,\,\gamma)}{(Re)_\theta^{\,1/\gamma}} \tag{3}$$

It is further assumed that the use of skin friction data taken under adiabatic conditions is applicable to heat transfer conditions (with appropriate temperature-dependent property corrections).

The axisymmetric integral momentum equation in the compressible form is:

$$\left(\frac{d\theta}{ds}\right) + \theta\,\frac{2 + H - Ma^2}{Ma\,\left(1+\frac{\gamma-1}{2}\,Ma^2\right)}\left(\frac{d\,Ma}{ds}\right) + \left(\frac{\theta}{R}\right)\left(\frac{dR}{ds}\right) = \frac{C_f}{2} \tag{4}$$

The growth of the momentum thickness proceeds at a rate dependent upon the skin friction coefficient, the radius change, the Mach number, and velocity gradient. An integration of this equation for the momentum thickness may be made by a finite difference technique using available values of the parameters with an assumed initial momentum thickness at the injector face. Consideration need only be given to a specification of the shape factor (H) and the exponent (γ).

The normally assumed value of $\gamma = 4$ for compressible flow can deviate considerably from the actual value for a given situation. In reality, the value of γ is dependent upon Reynolds number, Mach number, pressure gradient, and surface roughness.

From incompressible flow data, Ref. 5 indicates ranges of momentum thickness Reynolds number where γ has a specific value. These values, however, are for flat-plate data without pressure gradient. However, as will be surmised presently, because of a relationship between γ and $\overline{H}$ and the relationship between the compressible shape factor (H) and incompressible value ($\overline{H}$), it is expected that $\alpha(\gamma)$ can replace $\alpha(\gamma, \overline{H}, Ma)$ provided the velocity profile exponent is known for the condition of pressure gradient and Mach number.

Laminar Flow. Investigations of the skin friction coefficient for laminar flow allow insight into the turbulent case.

The skin friction coefficient for laminar flow from a Pohlhausen velocity distribution with an arbitrary pressure gradient may be written as:

$$\left(\frac{C_f}{2}\right) = \frac{\left(2 + \frac{1}{6}\Lambda\right)\left(\frac{37}{315} - \frac{\Lambda}{945} - \frac{\Lambda^2}{9072}\right)}{(R_\theta)_\theta^{1.0}} \quad \text{(laminar)} \qquad (5)$$

The effect of Mach number on C_f is found to be negligible provided proper reference temperature conditions are used. For the laminar case, some shift in the value of the Reynolds number exponent from one is expected because of compressibility. However, to a good approximation, correction for the skin friction coefficient may be accomplished by a proper reference condition for Reynolds number evaluation resulting from temperature, density, and viscosity effects.

The shape factor $(\bar{H}_L)$ for laminar flow in terms of an arbitrary pressure gradient becomes:

$$\bar{H}_L \equiv \left(\frac{\delta^*}{\theta}\right) = \left[\frac{3/10 - \Lambda/120}{\frac{37}{315} - \frac{\Lambda}{945} - \frac{\Lambda^2}{9072}}\right] \tag{6}$$

The corresponding values of $\bar{H}_L$ for a range of pressure gradient conditions are:

$\Lambda = 12$,	$\bar{H}_L = 2.18$	limit of theory for positive pressure gradient
$\Lambda = 7.052$,	$\bar{H}_L = 2.21$	stagnation point
$\Lambda = 0$,	$\bar{H}_L = 2.61$	flat plate
$\Lambda = -12$,	$\bar{H}_L = 3.50$	separation

Thus, the range for $\bar{H}_L$ in attached flow is restricted to $2.18 < \bar{H}_L < 3.50$ (laminar).

A more sophisticated split-level laminar boundary layer solution for handling strong, favorable, or adverse pressure gradients is provided by Launder(Ref. 6).

<u>Turbulent Incompressible Flow</u>. For turbulent flow, a relationship between the value of the power law velocity exponent (n), and the boundary layer shape factor $(\bar{H})$ is given by Ref. 7.

$$n = \frac{2}{\bar{H} - 1} \tag{7}$$

For turbulent incompressible flow, values may be prescribed for $\bar{H}$ from known values of n as:

$\bar{H}$	= 1.0	,	$n = \infty$	infinite positive pressure gradient
$\bar{H}$	= 1.3	,	$n = 6.7$	flat plate
$\bar{H}$	= 2.8	,	$n = 1.1$	separation

Experimentors have attempted to force the turbulent incompressible skin friction coefficient values to fit the form:

$$\frac{C_f}{2} = \frac{f(\bar{H})}{(Re_\theta)^a} \tag{8}$$

with an assumption of a constant value of "a" over the range in pressure gradient examined. The values of "a" and $f(\bar{H})$ were found to be intimately interdependent for turbulent flow as a result of the hypothesized validity of:

$$n = \left(\frac{2}{\bar{H} - 1}\right) = f(\gamma) \tag{9}$$

As a result, the skin friction coefficient form should become rather

$$\frac{C_f}{2} = \frac{f(a)}{Re_\theta^{\,a}} \tag{10}$$

In terms of γ, the equivalent relationship is:

$$\frac{C_f}{2} = \frac{\alpha(\gamma)}{(Re_\theta)^{1/\gamma}} \tag{11}$$

The relationship of $\alpha(\gamma)$ to $\bar{H}$ as derived from varying Reynolds number, zero pressure gradient data in the literature should, as a consequence, be valid under all pressure gradient conditions, providing the power law velocity profile exponent is known, i.e.:

$$\alpha(\gamma) = f_1(n) = f_2(\bar{H}) \tag{12}$$

A fit of the available data values for $\alpha(\gamma)$ in terms of $\bar{H}$ resulted in the expression:

$$\alpha(\gamma) = 0.0023\,(\bar{H})^{6.62} \tag{13}$$

Numerous data point values of shear stress and a simultaneous measurement of boundary layer velocity profile exponent under adverse pressure gradient or large favorable pressure gradients have not been obtained for turbulent flow, and hence, the values for $\alpha(\gamma)$ at $\gamma = 1$ and $\gamma = \infty$ as given by Eq. 13 represent extrapolations from the limited available data.

<u>Relationship Between γ and n</u>. With the above development of an expression for $\alpha(\gamma)$ for use in Eq. 11, a relationship between γ and n is next derived.

Figure 1 is a comparison of velocity profile curves for various pressure gradients. For the laminar case, where $\gamma = 1$, the following velocity distribution equation applies:

$$\frac{U}{U_\infty} = 2\left(\frac{y}{\delta}\right)^1 - 2\left(\frac{y}{\delta}\right)^3 + \left(\frac{y}{\delta}\right)^4 \quad \text{(Polhausen distribution) for laminar flow} \tag{14}$$

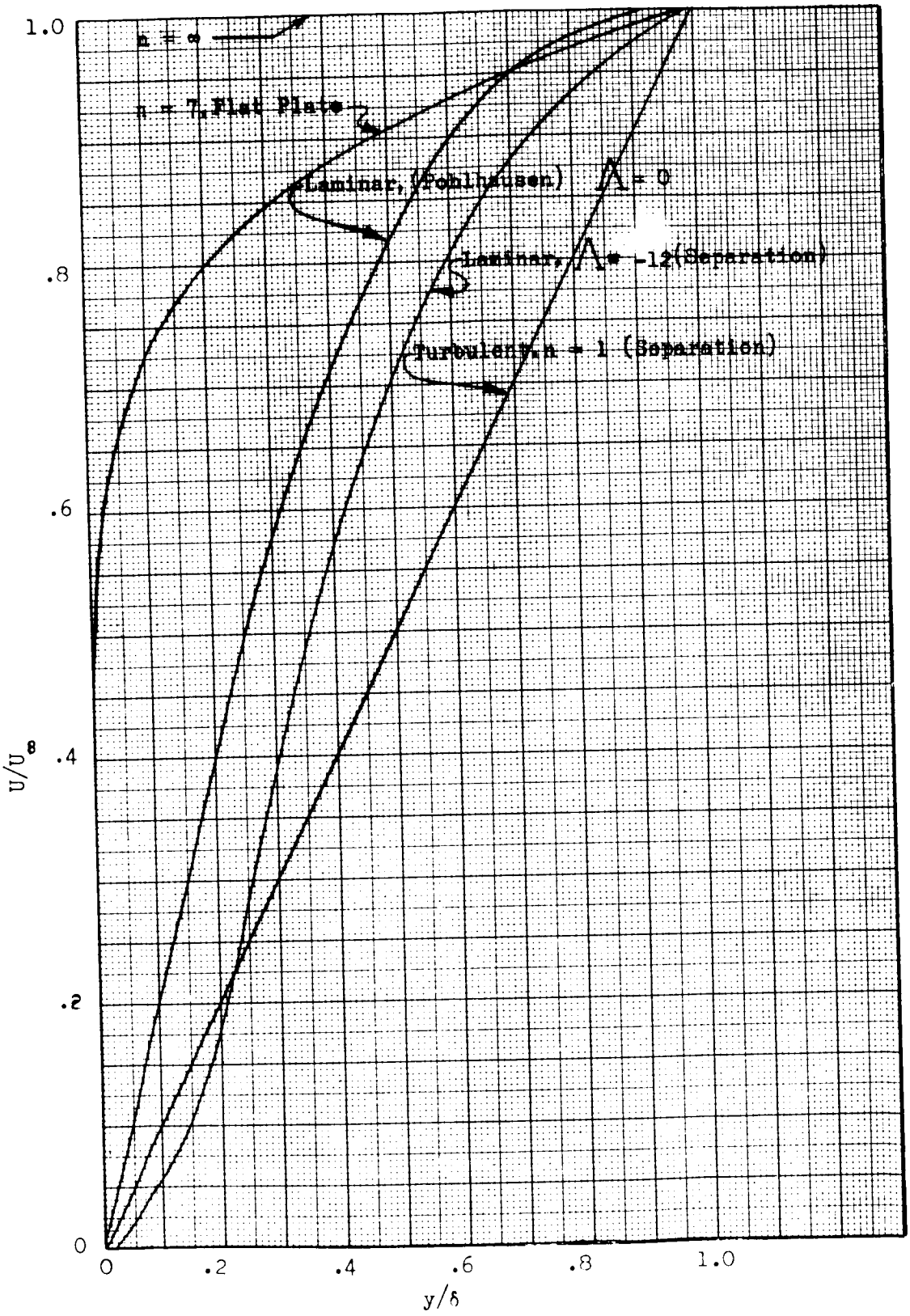

Figure 1. Comparison of Laminar and Turbulent Boundary Layer Velocity Profiles

This reduces to the following expression near the wall where the principal effect of shear stress occurs:

$$\frac{U}{U_\infty} = 2 \left(\frac{y}{\delta}\right)^{1.0} \tag{15}$$

Therefore, the corresponding value of n is 1.

This may be compared to an assumed turbulent case with n = 1.0:

$$\frac{U}{U_\infty} = \left(\frac{y}{\delta}\right)^{1/n} = \left(\frac{y}{\delta}\right)^{1.0}_{n=1} \quad \text{(turbulent flow)} \tag{16}$$

Thus, if the turbulent core (n = 1) were to be assumed to approach the wall (without a laminar sublayer), the predicted laminar wall shear stress is twice that of the turbulent case for the same boundary layer thickness.

From turbulent flat plate data with zero pressure gradient, n = 7 and $\gamma = 4$. As a result of the above, two points for determining a relationship between n and γ have been established, namely:

$n = 7$, $\gamma = 4$	turbulent flow, zero pressure gradient	
$n = 1$, $\gamma = 1$	laminar flow, zero pressure gradient (assumed to also hold for turbulent flow with an adverse pressure gradient)	

An attempt will now be made to determine the validity and relationship of n to γ for arbitrary values of n.

The method of Ref. 7 for turbulent pipe flow may be used. Assume the boundary layer considerations also remain the same for any surface flow. The shear stress at the wall converted to a momentum thickness basis becomes:

$$\frac{\tau_o}{\rho \bar{U}^2} = \frac{K}{(Re_\theta)^{1/\gamma}} \tag{17}$$

or

$$\tau_o = K \rho \bar{U}^{(2-1/\gamma)} (\nu)^{1/\gamma} (\theta)^{-1/\gamma} \tag{18}$$

In terms of an equivalent friction velocity (v^*), the shear stress becomes:

$$\tau_o = \rho (v^*)^2 \tag{19}$$

The combination of Eq. and results in:

$$\left(\frac{\bar{U}}{v^*}\right) \propto \left(\frac{v^* \theta}{\nu}\right)^{\{1/\gamma(2-1/\gamma)\}} \tag{20}$$

An integration may be performed to derive the maximum velocity (U_{max}) in terms of the average velocity ($\bar{U}$) as $\bar{U}/U_{max}$ = constant for a given n.

The velocity ratio may be now assumed as:

$$\left(\frac{v^*}{U_{max}}\right) \propto \left(\frac{v^* \theta}{\nu}\right)^{-1/\gamma(2-1/\gamma)} \tag{21}$$

It now becomes reasonable to assume that the above type equation is valid for any distance in the boundary layer less than the momentum thickness as:

$$\frac{U}{v^*} \propto \left(\frac{y}{\theta}\right)^{1/\gamma(2-1/\gamma)} \tag{22}$$

Since the validity of the power law results in:

$$\left(\frac{\theta}{\delta}\right) = f(n) \tag{23}$$

the above equation may be reduced to:

$$\left(\frac{U}{v^*}\right) \propto \left(\frac{y}{\delta}\right)^{1/\gamma(2-1/\gamma)} \tag{24}$$

It is seen in this case that the friction velocity becomes the reference velocity condition for the velocity profile. The variation of the velocity profile exponent (n) and the friction factor exponent (γ) may now be written by equating velocity profile exponents to give:

$$\frac{1}{\gamma(2-1/\gamma)} = \frac{1}{n} \tag{25}$$

or

$$n = (2\gamma - 1) \tag{26}$$

This analytical equation results in comparative values to the previously discussed experimental values as seen in the table below.

n	γ From Eq. 26	γ Experimental
∞	∞	-
11	6	-
9	5	-
7	4	4
5	3	-
3	2	-
1	1	1

Expression for C_f. On the assumption of the correctness of the above development, the value of $\alpha(\gamma)$ from Eq. 13 may be rearranged in terms of n as

$$\alpha(\gamma) = 0.0023\,(\bar{H})^{6.62} = 0.0023\,(1+\frac{2}{n})^{6.62}$$

$$= 0.0023\left[1 + 2/(2\gamma-1)\right] \qquad (27)$$

The general skin friction coefficient relationship may be finally written as:

$$\left(\frac{C_f}{2}\right) = \frac{0.0023\,(1 + 2/n)^{6.62}}{(Re_\theta)^{2/(n+1)}} \qquad (28)$$

This relation is plotted in Fig. 2 and compared to existing data. The fit of $\alpha(n)$ at extremely high and adverse pressure gradient conditions should be modified as better data become available. The agreement shown in Fig. 2 is, however, justification enough for the present usage of the above equation for C_f.

The value of C_f in Eq. 28 is seen to be dependent upon the stipulation of the n value. Additional data must be obtained to determine the dependence of n on such factors as the pressure gradient, Reynolds number, surface roughness, etc. For a zero pressure gradient, Ref. 5 presents the following approximate magnitude of the Reynolds number influence:

Re_θ	γ
100 to 5,000	4
500 to 50,000	5
3,000 to 600,000	6
10,000 to 10^7	7

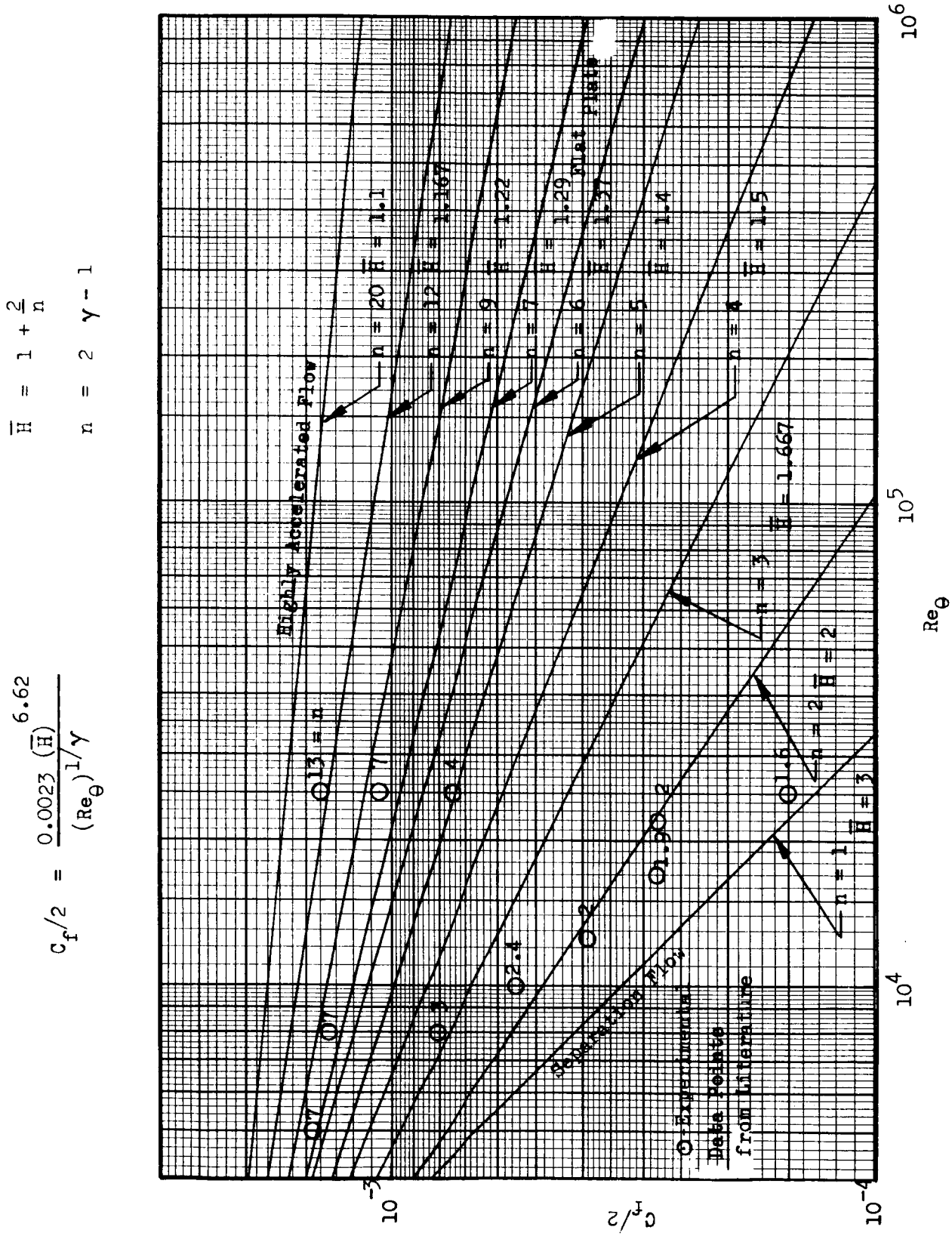

Figure 2. Comparison of Skin Friction Theory with Experimental Data

Computational Procedure. In the previous section, a relationship for the skin friction coefficient was developed. It, in turn, is related to the gas-side heat transfer coefficient by Eq. 1. The computation of the skin friction coefficient at any axial location in the nozzle cannot be determined directly because knowledge of the momentum boundary layer thickness and the velocity profile exponent (n) is needed. Thus, a step-by-step boundary-layer-type solution was required, and accordingly, a computer program was written to make numerical calculations. The general approach was as follows.

The velocity profile exponent (n) for varying pressure gradient conditions cannot be stipulated by the integral momentum or energy equation solutions. For this effect, a semiempirical-analytical incompressible form of Truckenbrodt (Ref. 8) was employed. This combined momentum-energy equation is an open integral type as follows:

$$\theta \frac{\partial H_E}{\partial s} = (\bar{H}-1)(H_E)\left(\frac{\theta}{U}\right)\left(\frac{dU}{ds}\right) + \frac{2(d+t)}{\rho U^3} - (H_E)\left(\frac{C_f}{2}\right) \tag{29}$$

The energy thickness shape factor (H_E) from the energy equation solution employed by Weighardt (Ref. 9) was used in the semiempirical form:

$$H_E = \frac{1.269\,\bar{H}}{\bar{H} - .379} \tag{30}$$

The turbulent dissipation function was derived from the data of Rotta (Ref. 10) for a variable shape factor ($\bar{H}$) as:

$$\frac{d+t}{\rho U^3} = \frac{0.00529}{Re_\theta^{\,[1/(4.9+\bar{H})]}} \tag{31}$$

The compressible shape factor (H) for use in Eq. 4 was developed by using a modified relationship of the form used by Bartz (Ref. 2) for a constant profile exponent, but using the variable profile exponent. For a thermal boundary layer thickness approximately equal to the velocity thickness:

$$H = \frac{\delta^*}{\theta} = \frac{\left(\frac{1}{n}\right)\left(\frac{T_w}{T_\infty}\right) - \int_0^1 \frac{S^n}{1 + bS - cS^2}\, dS}{\int_0^1 \frac{S^n\,(1 - S)\, dS}{1 + bS - cS^2}} \tag{32}$$

where

$$b = \left(\frac{T_o}{T_w} - 1\right) \tag{33}$$

$$c = \left(\frac{\varkappa - 1}{2}\right)\left(\frac{T_\infty}{T_w}\right) Ma^2 \tag{34}$$

The open form finite difference integration of Eq. 29 together with the integral momentum equation (Eq. 4) allowed the solution of θ and $\overline{H}$ as a function of nozzle surface distance. The latter was transformed into the incompressible velocity profile exponent (n) by Eq. 7 . From the computed values of θ and n, Eq. 28 was then used to determine C_f and, subsequently, h_g.

Variable Property Effects. The above discussion was based essentially on constant physical properties. Because of the large temperature gradients in rocket nozzle boundary layers, it was necessary to account for temperature-dependent physical properties. This was accomplished by using the reference temperature technique as follows:

$$\left(\frac{C_f}{2}\right)_r = \frac{\tau_w}{\rho_r\, U^2_\infty} = \frac{\tau_w}{\rho_\infty\, U^2_\infty}\left(\frac{\rho_\infty}{\rho_r}\right) = \left(\frac{C_f}{2}\right)_\infty\left(\frac{T_r}{T_\infty}\right) \tag{35}$$

The reference temperature skin friction coefficient may be written as:

$$\left(\frac{C_f}{2}\right)_r = \frac{\alpha(\gamma)}{\left(\frac{\rho_r \theta U_\infty}{\mu_r}\right)^{1/\gamma}} \tag{36}$$

Thus, for an evaluation of the mass velocity at the free-stream conditions and the gas viscosity at the stagnation value for an arbitrary reference temperature (T_r):

$$\left(\frac{C_f}{2}\right)_\infty = \frac{\alpha(\gamma)}{\left(\frac{\rho_\infty U_\infty \theta}{\mu_{o,\infty}}\right)^{1/\gamma}} \left(\frac{T_\infty}{T_r}\right)\left(\frac{\rho_\infty}{\rho_r}\right)^{1/\gamma} \left(\frac{\mu_r}{\mu_{o,\infty}}\right)^{1/\gamma} \tag{37}$$

Assuming

$$\mu \propto T^{\omega} \tag{38}$$

$$\rho \propto T^{-1} \tag{39}$$

and the usual isentropic relationship:

$$\frac{T_\infty}{T_{o,\infty}} = \frac{1}{1 + \frac{\varkappa-1}{2} Ma^2} \tag{40}$$

The skin friction consequently may be written for an arbitrary reference temperature and varying exponents as:

$$\frac{C_f}{2} = \frac{\alpha(\gamma)}{\left(\frac{\rho_\infty V_\infty \theta}{\mu_{o,\infty}}\right)^{1/\gamma}} \left(\frac{T_{o,\infty}}{T_r}\right)^{1-1/\gamma-\omega/\gamma} \left[\frac{1}{1 + \frac{\varkappa-1}{2} Ma^2}\right]^{1-1/\gamma} \tag{41}$$

where

$$\gamma = \left(\frac{n+1}{2}\right) \tag{42}$$

and as previously derived

$$\alpha(\gamma) = 0.0023\,(\bar{H})^{6.62} = 0.0023\left(1 + \frac{2}{2\,\gamma-1}\right)^{6.62} \tag{43}$$

The reference temperature (T_r) for the evaluation of the skin friction coefficient is not presently well defined. Some experimental data for skin friction coefficients indicate that the proper reference for conditions of heat transfer to a cold wall appears to be best fitted with the reference condition as the adiabatic value. Eckert (Ref. 11) and Johnson and Rubesin (Ref. 12), however, present a more logical average for the reference temperature in terms of the static temperature, stagnation temperature, and wall temperature. A convenient form for handling any reference temperature condition is as follows:

$$T_r = C_1\,T_{aw} + C_2\,T_\infty + C_3\,T_w, \quad 0 \le C_1,\ C_2,\ C_3 \le 1.0 \tag{44}$$

where the reference value is between the adiabatic wall value and the wall temperature value. This latter approach would appear to allow all reference values until more data become available. The Eckert reference form appears to be the most reasonable, however, for present use. The table below illustrates the values for the comparative methods. The above equation was programmed into the gas-side heat transfer coefficient computer program.

Reference Value	C_1	C_2	C_3
Eckert	0.22	0.28	0.50
Johnson and Rubesin	0	0.42	0.58
Wall Value	0	0	1.0
Wall-Adiabatic Wall Mean	0.5	0	0.5
Adiabatic Wall	1.0	0	0

Typical Calculation Examples. The previously discussed procedure for determining the gas-side heat transfer coefficient with the pressure gradient accounted for in terms of a variable velocity profile exponent (n) was used in a number of design calculations.

Analytical results for a typical LO_2/RP-1 design case at a 1500-psia chamber pressure are shown in Fig. 3. It is seen that the velocity profile exponent varies from 8 in the combustion zone to above 15 (set as an arbitrary maximum for computer convergence considerations) in the throat region and then diminishes to a value of 9 at the nozzle exit plane. The flat-plate low-momentum Reynolds number value of 7 is shown for comparison.

These results illustrate that an increased wall shear stress and, consequently, an increased heat transfer rate over that predicted by conventional wall shear stress relationships can be anticipated at high-momentum Reynolds numbers (at high chamber pressures) as the result of a markedly increased velocity profile exponent particularly in the throat region. Some typical calculated values of $C_f/2$ are given in Table 1 for LO_2/LH_2 propellants.

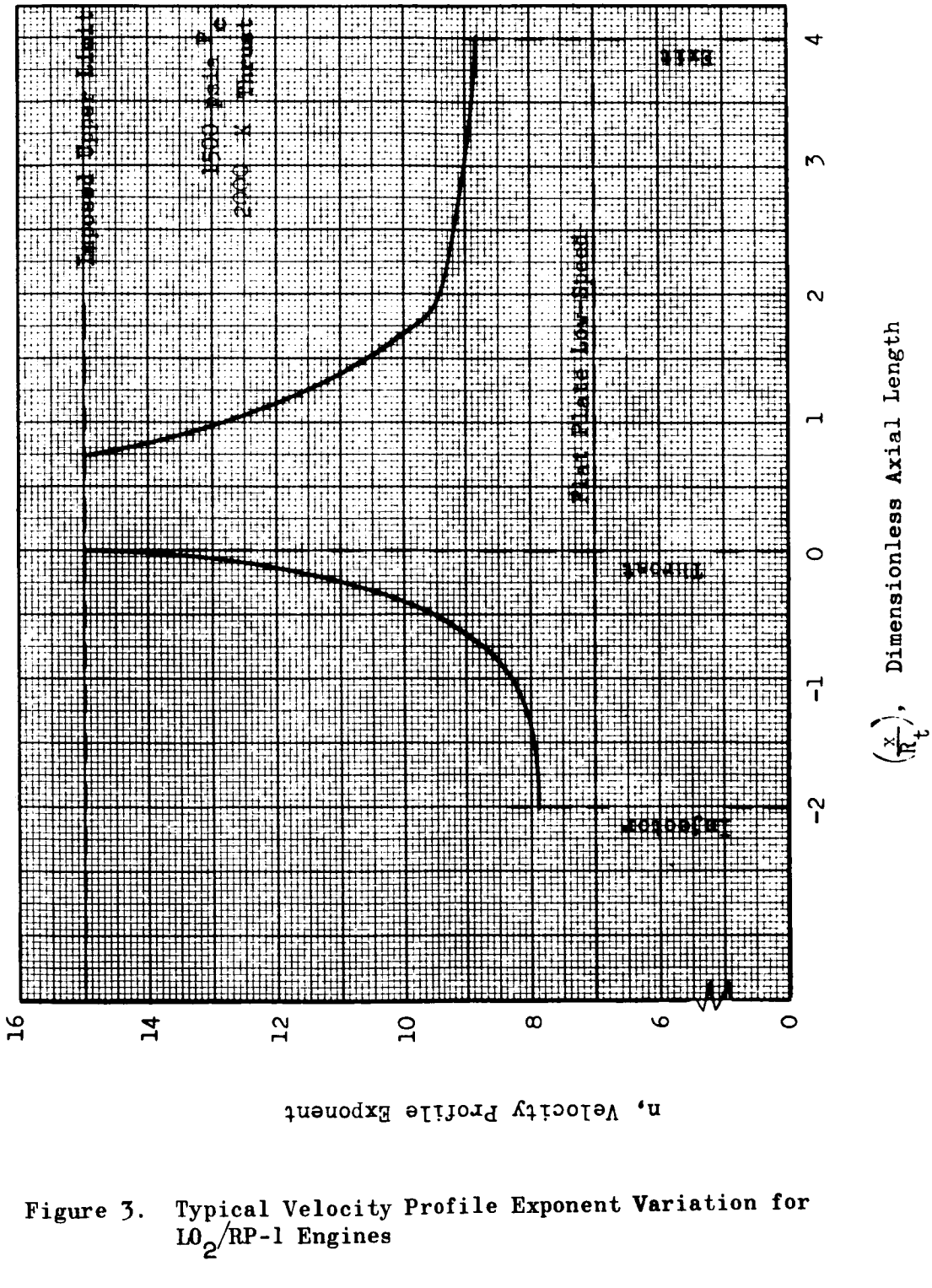

Figure 3. Typical Velocity Profile Exponent Variation for LO_2/RP-1 Engines

TABLE 1

COMPARATIVE WALL SKIN FRICTION IN THROAT REGION AT HIGH CHAMBER PRESSURES FOR LO_2/LH_2 ENGINES

n	$(C_f/2)$ Chamber Pressure, psia		
	1500	3000	5000
7	0.0010	0.00095	0.00085
11	0.0014	0.0013	0.0012
15	0.0016	0.0015	0.0014

Further experimental work on shear stress values with high pressure gradients at high momentum thickness Reynolds numbers would be desirable to substantiate the analytical predictions.

Combustion Chamber Initial Momentum Thickness

To perform an integration of the momentum equation for the evaluation of the axial variation of the heat transfer coefficient, a specification of the initial momentum thickness at the injector face is necessary. The selection of an initial momentum thickness of zero would lead to an unreasonably high heat transfer coefficient in the combustion zone adjacent to the injector face and a somewhat high value in the throat vicinity.

A more reasonable value is the prescription of a minimum thickness prescribed by a laminar stagnation point value as:

$$\theta_o = \left[\frac{K_o \mu}{\rho \left(\frac{\partial U}{\partial s}\right)_o} \right]^{1/2} \qquad \text{(stagnation value)} \qquad (45)$$

For an assumed two-dimensional surface, $K_o = 0.077$. The gas velocity gradient $(\partial U/\partial s)_o$ away from the injector face was developed by assumptions of the 90-percent length to completion of the combustion process. Typical values for this completion length are 12 inches for $LO_2/RP\text{-}1$ and 6 inches for LO_2/LH_2. At these respective lengths, the velocity was considered to be at 90 percent of the predicted isentropic velocity.

Combustion velocity increases were assumed to be given by the form:

$$U = a\, s^n \qquad (46)$$

and, therefore

$$\frac{\partial U}{\partial s} = a\, n\, s^{n-1} \qquad (47)$$

To yield a finite value at the injector face for the velocity gradient, n was chosen as unity with the result:

$$\left(\frac{\partial U}{\partial s}\right)_{s=0} = a \qquad (n=1) \qquad (48)$$

Where the value of "a" is dependent upon propellant and contraction ratio conditions. The values of assumed initial momentum thicknesses (θ_o) are listed in a later section on actual design cases.

Wall Curvature Effects

The study undertaken for the examination of wall curvature effects was divided into the principal areas of heat transfer rate change on the gas-side surface and the change in the coolant-side heat transfer coefficient. The curvature effect particularly in the throat region of a rocket engine can increase the coolant-side heat transfer coefficient by a factor of about 2, and can also cause changes to the gas-side heat transfer input from the combustion gas. Typical qualitative effects are shown in Fig. 4 .

Empirical and analytical work has been limited to laminar-flow cases or isolated cases of turbulent flow. Lack of specific design information at high Reynolds numbers, where a much-reduced coolant pressure drop or flow requirement may be possible, is brought about by the complexity of the turbulent-flow case as well as an apparent lack of interest in other industries toward the curved-flow heat transfer problem. A review of available heat transfer and pressure drop literature was performed with the subsequent development of the key parameters affecting the curvature effect upon heat transfer.

Potential Flow Profile. An examination was first made of the nature of the potential flow velocity profile in a two-dimensional channel. As postulated by Rayleigh (Ref. 13), the curved-flow velocity distribution can consist of an irrotational or centrifugal component and a rotational vorticity component as described by the relationship:

$$u = \underbrace{\zeta r}_{\text{vorticity}} + \underbrace{Br^{-1}}_{\text{centrifugal}} \tag{49}$$

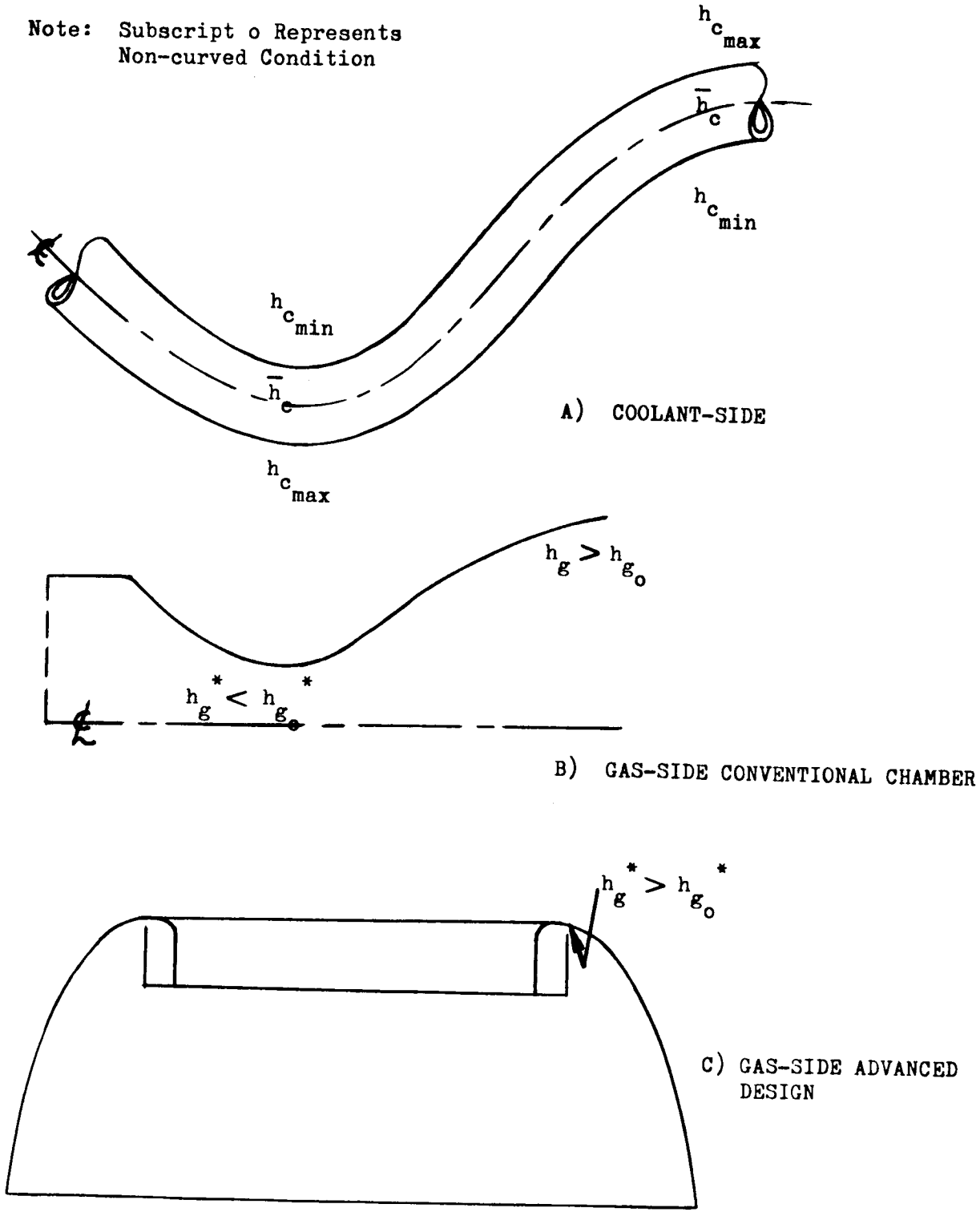

Figure 4. Illustration of Curvature Effects

Experience shows that a purely irrotational flow becomes unstable, and the effect of viscosity causes a conversion into a rotational flow initiating at the inner radius. With the establishment of a rotational flow, no change in velocity profile is observed. According to Kassner (Ref. 14), the conversion of irrotational to rotational flow takes place with the velocity on the outer boundary increasing by the relationship:

$$(u_o)_{rot} = 2(u_o)_{irr} \left(\frac{r_o^2}{r_o^2 - r_i^2} \right) \tag{50}$$

where the subscripts i and o denote the inner and outer radii, respectively.

The classical centrifugal flow problem yields a decreasing circular velocity component with increasing radius. However, as illustrated by Eq. 49 and 50, a rotational flow contribution tends to increase the velocity component at the outer radius. Recent experimental heat transfer work for spiral-twisted tapes within tubes (Ref. 15) shows the velocity distribution to be similar to the vorticity-based component (ζ r); i.e., the velocity increases as the radius increases. However, study in a two-dimensional, large-depth curved channel by Eskinaze and Yeh (Ref. 16) shows the potential distribution to be the form indicated by the latter component (B/r) with the potential velocity diminishing at the outward radius. As a result, a definition of the degree of rotationality in the flow is needed.

A development of the curved-flow velocity distribution compared to the straight flow or average velocity can be accomplished by considering the velocity profile family:

$$u_r = B/r^n \tag{51}$$

where n = 1 and -1 for the centrifugal and vorticity components, respectively. The ratio of the curved to average velocity was developed by integration as:

$u_r/\bar{u}$	n
$\frac{3}{2}\left[\frac{r_o^2 - r_i^2}{r_o^3 - r_i^3}\right] r$	-1
(1)	0
$\frac{1}{2}\left[\frac{r_o^2 - r_i^2}{2\,(r_o - r_i)}\right]\frac{1}{r}$	1

Curved-Flow Shear-Stress Relations. The foregoing discussion developed the behavior of the core of the flow. It is also necessary to develop the relationship of the shear stress with velocity and velocity gradient.

For a curved laminar flow, the shear stress may be expressed as:

$$\tau_L = \mu\left(\frac{\partial u}{\partial r} - \frac{u}{r}\right) \qquad \text{(laminar)} \qquad (52)$$

Similarly, for a curved turbulent flow, the relationship becomes:

$$\tau_T = \rho\,\epsilon\left(\frac{\partial u}{\partial r} - \frac{u}{r}\right) \qquad \text{(Prandtl-turbulent)} \qquad (53)$$

The mixing length theory of von Karman, as developed for curved flow, becomes:

$$\tau_T = \rho \ell^2 \left(\frac{\partial u}{\partial r} - \frac{u}{r}\right)^2 \qquad \text{(von Karman-turbulent)} \qquad (54)$$

For a flow without curvature:

$$\tau_T = \rho \epsilon \frac{\partial u}{\partial r} \qquad (55)$$

The evaluation of the zero shear point in the flow for Eq. 53 through 55 becomes:

$$\frac{\partial u}{\partial r} = c \left(\frac{u}{r}\right) \qquad (56)$$

where c = 0 for a noncurved flow, and c = 1.0 for a curved flow. The experimental data of Wattendorf (Ref. 17) for a two-dimensional channel of large depth resulted in:

$$c \approx 1/2 \text{ to } 2/3 \qquad (57)$$

which is in fair agreement with theory.

The neutral shear point radius for a curved flow can be seen to shift toward the inner radius as the degree of curvature is increased. In terms of a neutral shear point radius (r_n), the ratio of shear of the outer wall to inner wall becomes (Ref. 16):

$$\left(\frac{r_n - r_i}{r_o - r_i}\right) = \left(\sqrt{\frac{\tau_o/\tau_i - 1}{\tau_o/\tau_i - (r_i/r_o)^2}} - 1\right) \Big/ \left(\frac{r_o}{r_i} - 1\right) \qquad (58)$$

Shear stress distributions within the laminar sublayer ($0 \leq Re^* \leq 30$) were found to be undisturbed (Ref. 17). However, in the adjacent turbulent core region, the velocity profile exponent (n), was found to increase on the outer wall and decrease on the inner wall. Figure 5 illustrates a typical velocity distribution for a curved two-dimensional channel flow. Figure 6 shows the velocity profile exponent as a function of the dimensionless curvature parameter.

$$\frac{\rho\, r_c \sqrt{\tau_o/\rho}}{\mu} = \frac{\rho\, r_c\, u^*}{\mu} \tag{59}$$

A curvature Reynolds number may be defined from the above as:

$$Re_c^* = \frac{\rho\, r_c\, u^*}{\mu} \tag{60}$$

which may be rewritten in terms of Re* as:

$$Re_c^* = Re^* \left(\frac{r_c}{y}\right) \tag{61}$$

From Fig. 6, the velocity profile exponent (n) may be written in terms of the latter dimensionless groupings as

$$n = f\left(Re^*, \frac{r_c}{y}\right) \tag{62}$$

Figure 6 becomes useful for the definition of the critical condition for a two-dimensional flow where curvature becomes important. If a fixed shift in velocity profile exponent from a nominal uncurved value (low turbulent Re, $n \approx 7$) is chosen, then this critical condition is given by:

$$\frac{1}{Re_c^*} = K \tag{63}$$

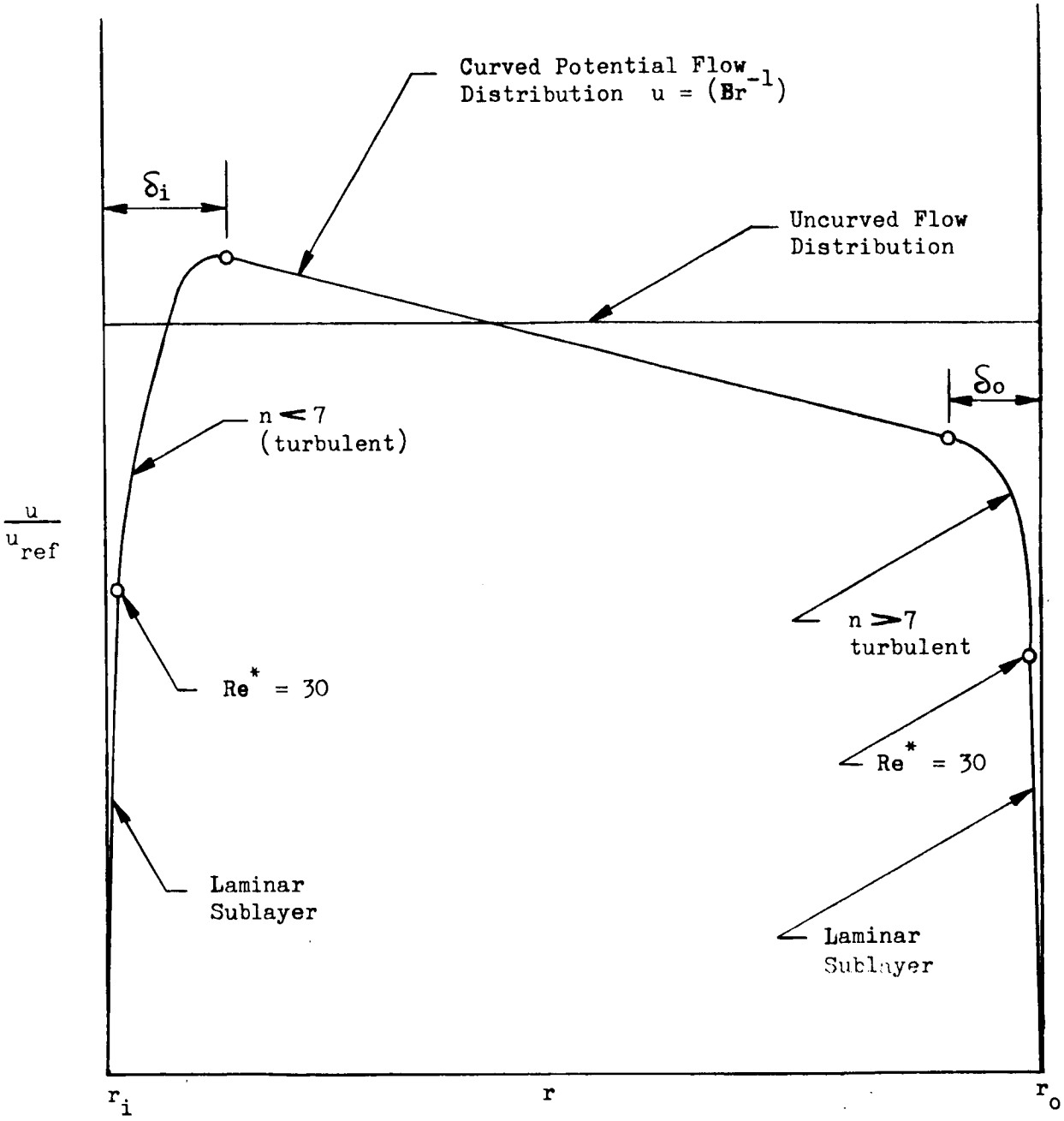

Figure 5. Velocity Distributions in a Curved Two-Dimensional Channel

FORM 608-B-13 NEW 11-62

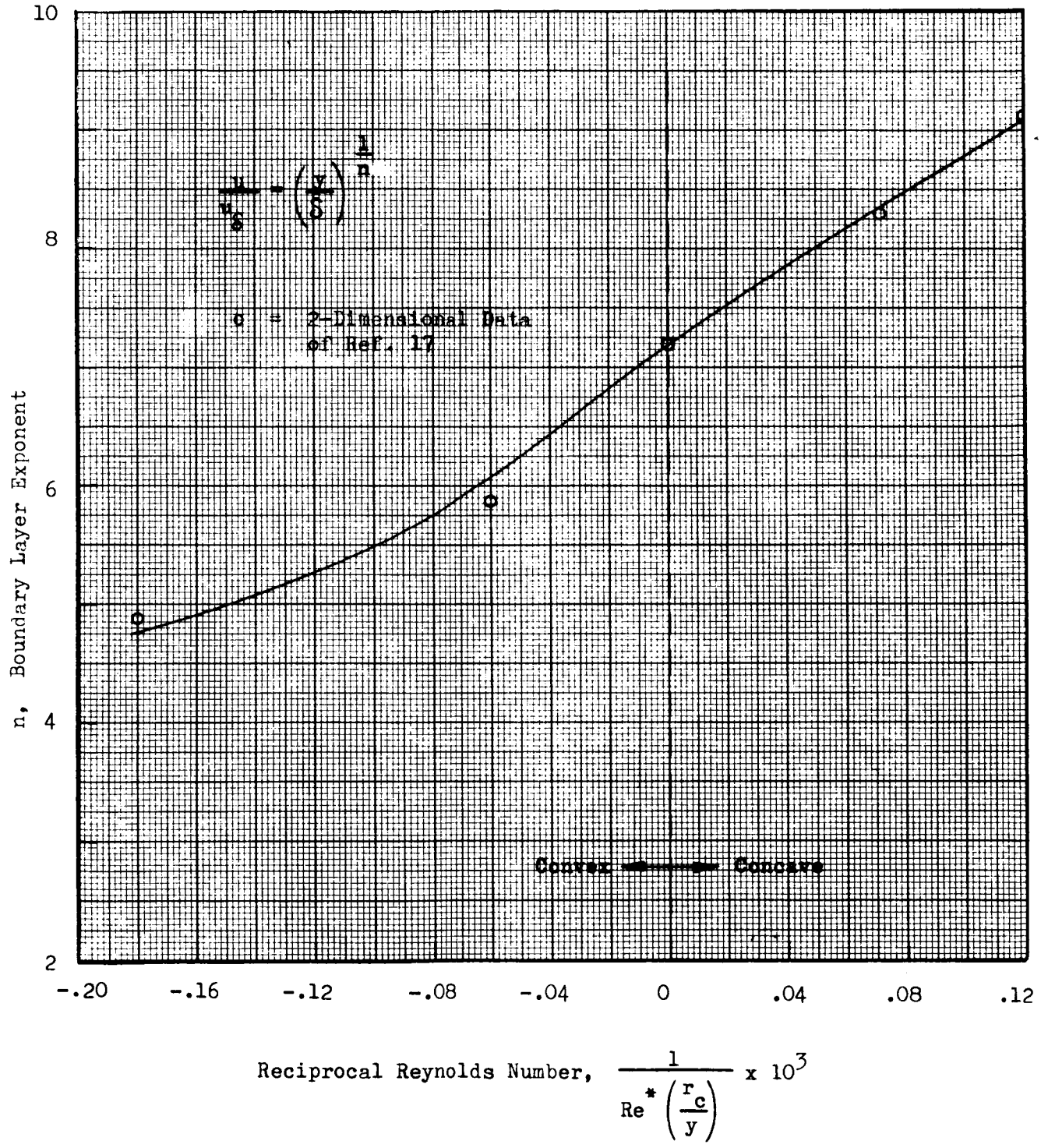

Figure 6. Turbulent Boundary Layer Velocity Profile Exponent

which becomes:

$$\frac{\rho\, r_c\, u_\infty}{\mu} = \frac{1}{K\sqrt{C_f/2}} \tag{64}$$

For a turbulent flow, the skin friction becomes a relatively weak function of surface length or momentum thickness Reynolds number; e.g.,

$$C_f/2 = \alpha\, Re_\theta^{-0.25} \tag{65}$$

Therefore,

$$\left(\frac{r_c}{\theta}\right)_{crit} \leq K'\, Re_\theta^{-0.875} \tag{66}$$

When Eq. 66 is put in terms of a tube curvature-to-radius ratio, the same behavior is shown with increasing Reynolds number. For a circular tube, this behavior may be unrealistic because meager data indicate a Reynolds number effect is not always apparent. It may be surmised that the secondary flow generation in a curved circular tube is probably the principal effect. This is discussed in a subsequent section.

The effect of the alteration in turbulent shear stress profile combined with the potential-flow alteration effect allows the evaluation of wall shear levels for curved two-dimensional flow. By assuming the validity of the Reynolds analogy, the corresponding heat transfer coefficients may be generated. Experimental two-dimensional curved wall local heat transfer data under a high Reynolds number condition are, however, very sorely needed to confirm the predictions.

Predicted Curvature Effect. Determination of the extent of the gas-side heat transfer coefficient change for turbulent flow with the sharp surface curvatures obtained with advanced nozzle designs was examined. Indications from the above analysis as well as experimental evidence and existing theoretical laminar flow analyses are that the heat transfer coefficient for a curved surface relative to a noncurved surface value becomes a function of the radius of curvature to momentum thickness as:

$$\frac{h_c}{h_f} = f\left(Re_\theta, \frac{r_c}{\theta}\right) \tag{67}$$

The dimensionless parameter developed for the effects of the curvature on the friction factor (and by analogy, the heat transfer) in a tube is the Dean number (Ref. 7):

$$De = 1/2\ (Re_D)\ (R/r_c)^2 \tag{68}$$

In terms of the momentum thickness of the boundary layer in a tube, this parameter may be rearranged to:

$$De = (Re_\theta)\ (\theta/r_c)^2\ (R/\theta)^3 \tag{69}$$

The momentum thickness in the velocity boundary layer is defined as:

$$\theta = \int_0^R \frac{U}{U_\infty}\left(1 - \frac{U}{U_\infty}\right) dy \tag{70}$$

If the assumption of a power law profile through the boundary layer is made, i.e.:

$$\frac{U}{U_\infty} = \left(\frac{y}{r}\right)^{1/n} \qquad \text{(tube)} \tag{71}$$

then integration of Eq. 70 gives:

$$\frac{\theta}{R} = \left(\frac{n}{n+1} - \frac{n}{n+2}\right) \tag{72}$$

Combining Eq. 69 and 72 gives the following translation of the parameter given by Eq. 68:

$$De = 1/2\ (Re_D)\left(\frac{R}{r_c}\right)^2 = \frac{Re_\theta\left(\frac{\theta}{r_c}\right)^2}{\left(\frac{n}{n+1} - \frac{n}{n+2}\right)^3} \tag{73}$$

Thus, Eq. 73 confirms the postulate above; namely, that the parameters of importance are Re_θ and r_c/θ. The value of n for tube flow is approximately 7, increasing somewhat at higher Reynolds numbers. As a result, the Dean number based on the momentum thickness is:

$$De_\theta = 1085\ (Re_\theta)\left(\frac{\theta}{r_c}\right)^2 \qquad (n = 7) \tag{74}$$

The premise of a normal velocity distribution in a curved-surface boundary layer is, however, uncertain because the centrifugal forces would tend to alter the velocity profile as shown previously. The relative effects of centrifugal forces as compared to the secondary flow effects is also unknown in the translation of the curved-tube analysis to the curved-surface case. Nevertheless, calculations for the curved-surface case based on available curved-tube results should give reasonably good approximations. Accordingly, turbulent relationships for curved-surface skin friction coefficients based on tube-flow correlations become:

$$\frac{\bar{f}_c}{\bar{f}_o} = (2\ De)^{0.05} \qquad \text{(Ito, Ref. 19)} \tag{75}$$

or

$$\frac{\bar{f}_c}{\bar{f}_o} = 1 + 0.075\,(2\,De)^{0.25} \qquad \text{(White, Ref. 20)} \qquad (76)$$

For advanced annular nozzle designs, an estimate of the curvature parameter based on Eq. 75 and 76 is given in the table below. Under the premise of the applicability of the equations and the analogy to heat transfer, a significant effect on the gas-side heat transfer coefficient may be expected.

Case	Propellant	Chamber Pressure, psia	$Re_\theta \left(\frac{\theta}{r_c}\right)^2$	$\frac{\text{(White)}}{\bar{f}/\bar{f}_o}$	$\frac{\text{(Ito)}}{\bar{f}/\bar{f}_o}$
1	H_2-O_2	1500	0.63	1.5	1.5
2	H_2-O_2	3000	1.6	1.6	1.5
3	H_2-O_2	5000	4.3	1.7	1.6
4	O_2-RP-1	1500	0.95	1.5	1.5
5	O_2-RP-1	3000	2.3	1.6	1.5
6	O_2-RP-1	5000	5.7	1.8	1.6

Assumptions: $r_c = 2\,\delta_T$, F = 2 million pounds

Available data at Rocketdyne for advanced nozzle designs indicate high heat flux values in the turning region. However, the effects of the curvature have not been divorced from the smaller momentum thickness for these test comparisons.

In conclusion, the evaluation of the velocity exponent through the boundary layer can only be accomplished by experimental means. Consequently, the values of wall shear as a function of curvature and Reynolds number can be derived only by empirical means such as those just shown. In addition to the local wall shear stress change with curvature, a shift in the mass velocity distribution in the main core flow can be anticipated. The overall combined effect on the ratio of heat transfer coefficients for a curved surface to a flat surface is then:

$$\left(\frac{h_c}{h_f}\right) \cong \left(\frac{\rho_c \; V_c}{\rho_f \; V_f}\right) \quad \frac{(\tau_o)_c}{(\tau_o)_f} \tag{77}$$

Rocketdyne's computer program for the axially symmetric flow in conventional and advanced nozzles was found to provide for radial variations in momentum in the design analyses by the method of characteristics. In the high heat flux region of the throat where the wall curvature is greatest, the effect is in the change of the wall Mach number to a higher value. In heat transfer analyses, as a consequence, the only remaining comparatively unknown factor for the gas-side film coefficient calculation is the variation in wall shear stress with curvature.

Surface Roughness Effects

Most recently (Ref. 21), surface roughness effects on convective heat transfer have been correlated in terms of a dimensionless roughness parameter (ϵ^*) defined by the expression:

$$\epsilon^* = \left(\frac{\rho V \epsilon}{\mu}\right) \quad \left(\frac{C_f}{2}\right)^{1/2} \tag{78}$$

In terms of a curved surface, the momentum thickness Reynolds number (Re_θ) becomes the defining parameter for the skin friction coefficient (C_f). Hence, the value of ϵ^* may be rewritten in the dimensionless form:

$$\epsilon^* = (Re_\theta) \left(\frac{C_f}{2}\right) \left(\frac{\epsilon}{\theta}\right) \tag{79}$$

Consequently, an estimate may be made of the roughness effects on the gas-side heat transfer coefficient from stipulation of the ϵ^* parameter using the criteria presented by Dipprey based on tube flow results:

$\epsilon^* < 3$ smooth

$3 < \epsilon^* < 70$ transition

$\epsilon^* > 70$ fully rough

The following table lists the calculated values of ϵ^* for an assumed gas-side surface roughness of ~ 40 microinches for several engines covering the pressure range of interest. It may be concluded that roughness effects appear to be negligible because ϵ^* is on the order of only 3 or less.

Case	Propellant	Chamber Pressure, psia	ϵ^*
1	H_2-O_2	1500	0.54
2	H_2-O_2	3000	1.6
3	H_2-O_2	5000	3.5
4	O_2-RP-1	1500	0.71
5	O_2-RP-1	3000	1.3
6	O_2-RP-1	5000	2.3

Injector Effects

A strong influencing factor in the heat transfer rate to the combustion zone wall and to some extent the throat region, is the radial and circumferential uniformity of the injector pattern. In large-thrust engines in the 1.5- to 6-million-pound category, the nonuniformity becomes less because of a larger number of injector elements in proportion to the chamber circumference. Injector effects may be categorized into several areas delineated as follows:

1. Turbulence effects
2. Mixture ratio effects
3. Boundary layer initial thickness
4. Combustion rate variations

Turbulence effects are particularly upsetting to the boundary layer profile in its early stages of formation and can contribute to large increased rates near the injector face. Under high degrees of turbulence, an early transition from a laminar to a turbulent boundary layer occurs which at the low Reynolds number results in a high wall shear stress.

Peripheral mixture ratio effects cause a local variation in combustion rate and an altered temperature condition. Generally, a low-mixture-ratio, fuel-rich condition is provided at the outer wall to reduce the effective adiabatic wall temperature and to prevent catastrophic oxidation of the wall surface. With an overly fuel-rich condition,combustion completion is prevented near the injector and until mixing of the fuel-rich outer region with the main core gases is achieved, the outer injector zone remains at a low enthalpy condition.

A small initial boundary layer thickness is undesirable because it results in a high local skin friction coefficient. It was pointed out in a previous section that gas velocity gradient (dU/ds) changes are principally responsible for variations in initial boundary layer thickness with a high gas velocity generation condition resulting in a small initial boundary layer thickness.

Injectors which initiate a high rate of combustion completeness and exhibit a high performance are detrimental to the heat transfer conditions from three standpoints.

1. With a high-performance design, a small initial boundary layer thickness is formed because of a high gas velocity gradient away from the injector face.
2. A higher gas mass velocity is achieved in a region of the formative portion of the boundary layer where the wall skin friction is high because a greater degree of combustion completeness is achieved in a shorter length.
3. An injector with high performance is more likely to have an adiabatic wall temperature closer to the theoretical value as a result of the absorption of the unburned low enthalpy products into the combustion process and also because such high-performance injectors are more likely to have a more optimum mixture ratio at the injector outer periphery.

The injector nonuniformity effects may be seen directly translatable into the governing heat transfer equation as:

$$h \propto \frac{(\rho_\infty U_\infty)^a \, (H_{aw} - H_a)}{(\theta)^b} \tag{80}$$

where:

$$a \approx 0.8, \quad b \approx 0.2$$

The qualitative effect of the injector nonuniformities may be seen in the tabular comparison below:

Injector Variable	Value of Affected Parameter			
	θ_o	h_g	T_{aw}	Wall Oxidation
High Turbulence	small	high	--	--
Low Mixture Ratio	large	small	low	none
High Mixture Ratio	small	high	high	great
High Performance	small	high	high	--
Small Combustion Chamber	small	high	--	--
Contraction Ratio				

Discontinuous Wall Surfaces

For large-engine designs, the modular concepts of individual combustors clustered around a nozzle shroud or a combustion zone with an attachable skirt appear advantageous. From a heat transfer standpoint, the effect of the resulting discontinuity of the flow requires examination.

Discontinuity in the flow or wall surface can occur normal to or parallel to the flow. In the circumferential direction, module boundaries occur as shown in Fig. 7. The juncture of these flow boundaries on the nozzle surface poses an impingement problem which for a supersonic flow is

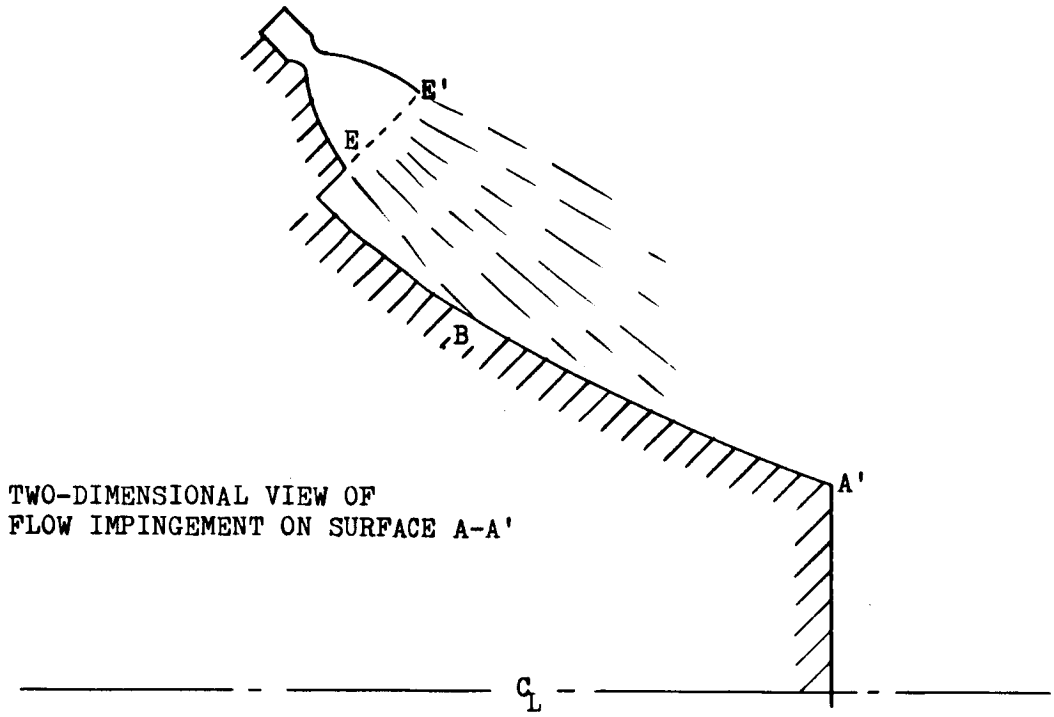

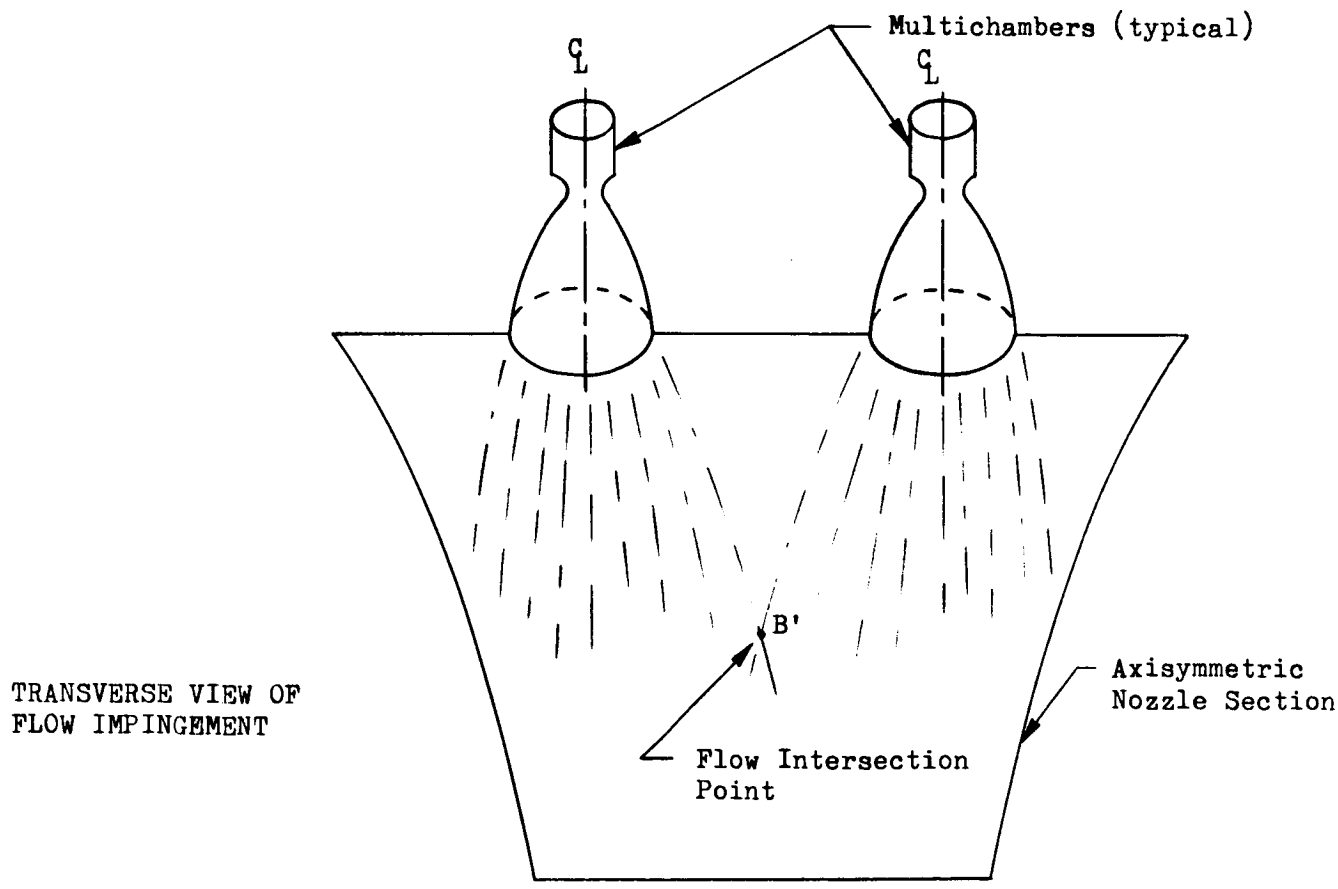

Figure 7. Multichamber Nozzle Flow Impingement

accompanied by a shock condition and disturbance of the boundary layer. In the flow direction, as illustrated in Fig. 7, an impingement occurs when the flow from the multichamber or combustor exit plane (E-E′) impinges at point B on surface A-A′. In this flow, a high-pressure point occurs as a result of the impingement and accompanying shock. The resulting disturbance to the boundary layer increases heat flux conditions locally.

Results of the heat transfer study conducted under Contract NAS8-4000 (Ref. 22) were used for the current study. In this previous study, three vernier 500-pound-thrust motors were fired with different circumferential spacing with O_2/RP-1 and O_2/alcohol propellants. Chamber pressure was approximately 350 psia with the multichambers truncated to an exit area ratio of $\epsilon = 2.0$. Impingement angles measured from the chamber centerline were varied to the most severe condition at a 31-degree angle. It was determined that the most severe impingement heating condition was that indicated at point B in Fig. 7 as a result of the higher measured wall pressures. In the transverse direction, the pressure was diminished to a lower value dependent upon the chamber-to-chamber spacing.

Relationships were developed which indicated the convective film coefficient could be proportioned as:

$$(h_g)_{max} \propto (P)_{max}^{1.0} \tag{81}$$

and for a given impingement surface angle:

$$\frac{P_{max}}{P_c} = \text{constant} \tag{82}$$

As a result, the variation with chamber pressure could be expressed as:

$$h_{g_{max}} \propto P_c^{1.0} \tag{83}$$

at the impingement area.

In general, the experimental results showed that if the impingement occurs from a stream which has a Mach number above 2, the impingement heat transfer rates will not be severe, even for large downstep discontinuities. In all practical multichamber designs proposed, expansion with a partial nozzle is planned. Accordingly, the local heat transfer rate will be higher than for a noninterrupted flow. However, the maximum rate will, in all cases, be much lower than the throat maximum value. As a result, a design will not become limited because of this effect.

COOLANT-SIDE HEAT TRANSFER

The preceding section reviewed pertinent factors controlling the gas-side heat transfer coefficient for high-pressure designs. The following section discusses the comparatively unknown areas concerning the coolant-side heat transfer in a regeneratively-cooled motor design. Included are bulk temperature, roughness, and curvature effects. In particular, a new equation is presented for estimating the convective heat transfer to liquid hydrogen coolant.

Hydrogen in the Critical Temperature Region

In Ref. 1, the following equation was developed for predicting the convective heat transfer coefficient to supercritical pressure liquid hydrogen flowing in coolant tube passages.

$$Nu_b = 0.025\ Re_b^{0.8}\ Pr_b^{0.4}\left(\frac{T_w}{T_b}\right)^{-0.55}\ \varphi_1\ \varphi_2\ \varphi_3\ \varphi_4 \qquad (84)$$

The factor, φ_1 was introduced to account for the effect of bulk temperature in the critical temperature region from about 50 to 120 R. In general, based on existing data (Ref. 23) at pressures below 600 psia, φ_1 was found to be as low as 0.38 at a bulk temperature of 60 R. In essence, this factor helped account for drastic variations in the physical properties of hydrogen in the critical temperature region which were not completely accounted for by the $(T_w/T_b)^{-0.55}$ term.

At the high pressures (> 1500 psia) of interest in this study, however, hydrogen is sufficiently supercritical that such drastic variations in the physical properties with temperature no longer occur. This is typified in Fig. 8 where the specific heat is shown for pressures of 400 and 2000 psia. Therefore, the need for the φ_1 factor was questioned. Fortunately, a new set of experimental liquid hydrogen heat transfer data for pressures as high as 2500 psia were recently reported (Ref. 24). These data for the region from 1500 to 2500 psia are plotted according to Eq. 84 in Fig. 9 . As shown, an adequate and conservative correlation is obtained without the use of a φ_1 factor. Accordingly, for high chamber pressure applications (P_c > 1500 psia), Eq. 84 is recommended with φ_1 = 1.0. For the entire supercritical pressure range.(coolant pressure >188 psia) an alternate correlation is given in Ref. 71.

Tube Flow Curvature Effects

The effect of tube curvature on coolant-side heat transfer was not considered in Ref. 1. It differs from the results of a two-dimensional channel of infinite depth as discussed above in that the generation of

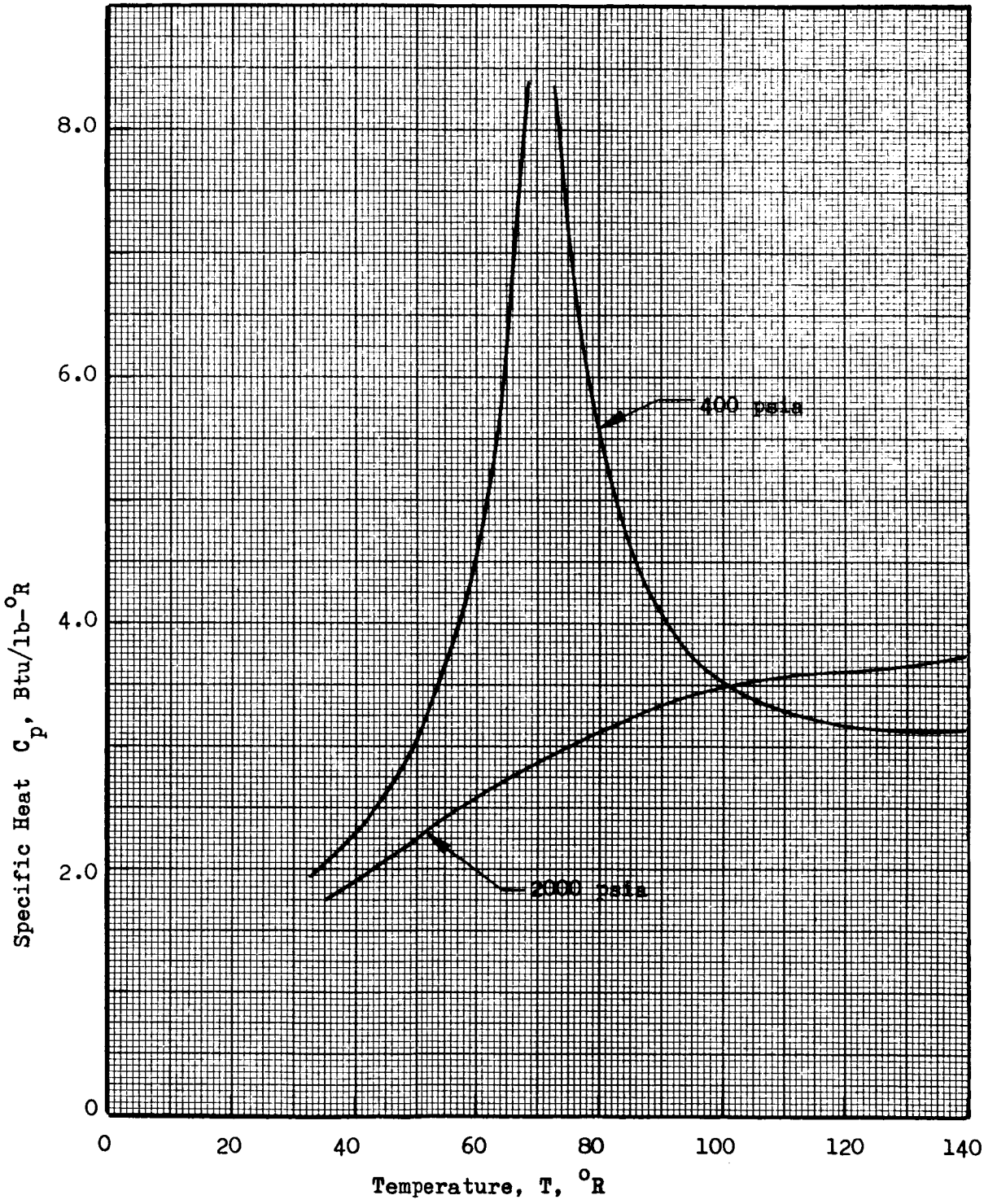

Figure 8. Variation of Specific Heat of Para-Hydrogen With Pressure

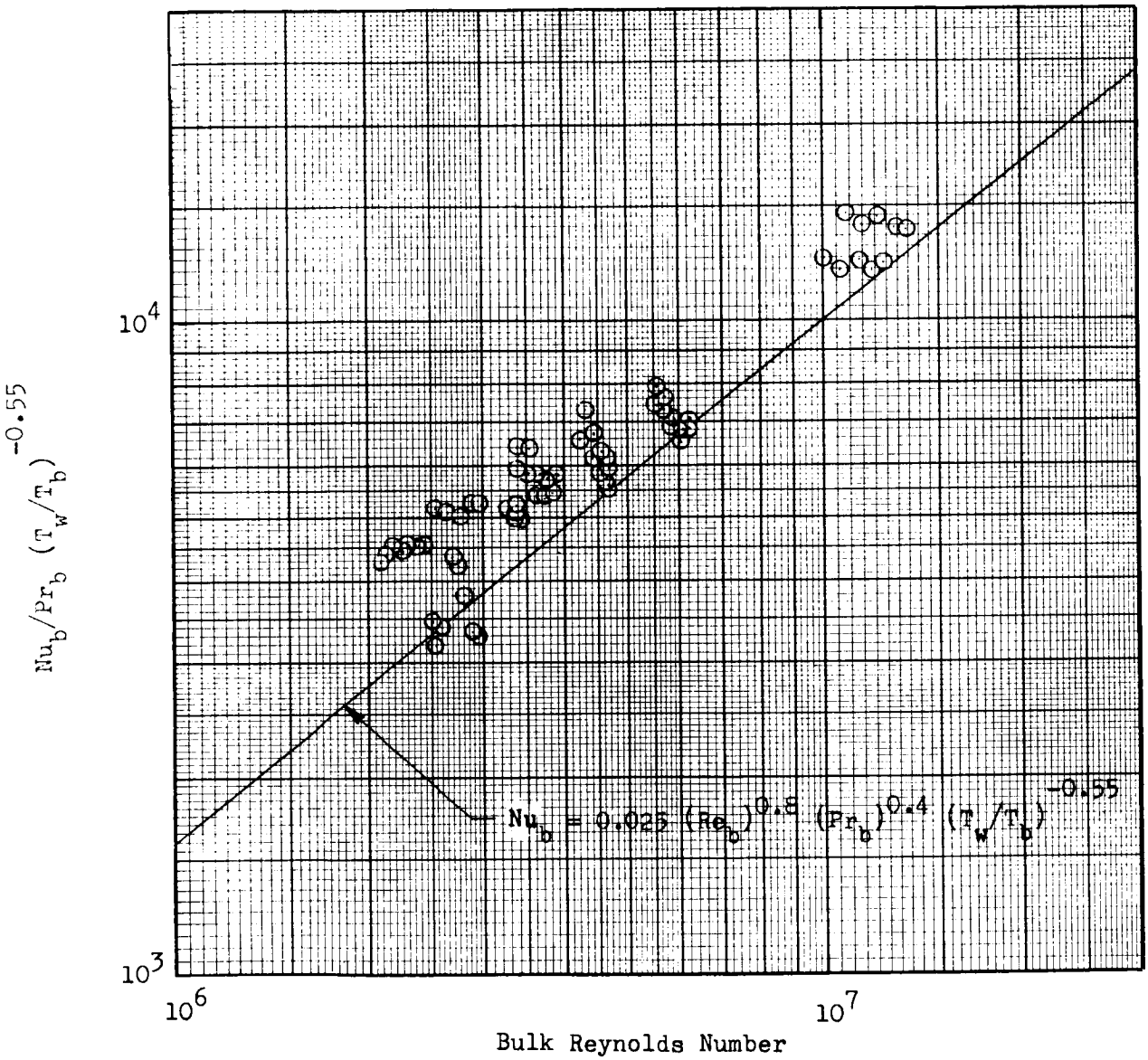

Figure 9. Liquid Hydrogen Heat Transfer Data for Pressures > 1500 psia

secondary flows for the coolant tube provides an additional mechanism for shear and heat transfer. The complexity of the turbulent case for the analytical definition of the wall shear and heat transfer coefficient has led to the extensive use of empiricism. From the laminar situation which can be exactly solved, the dimensionless groupings of Reynolds number and characteristic dimension become correlating parameters. For the three cases of tube flow, curved-plate flow, and curved-plate flow with a pressure gradient, the geometric and Reynolds number parameters are as given in the table below:

Case	Flow Reynolds Number	Dimension Parameter
Curved-Tube Flow	$(Re)_D$	(r_c/R)
Curved Surface	$(Re)_s$	(r_c/s)
Curved Surface With Pressure Gradient	$(Re)_\theta$	(r_c/θ)

The effect of the surface curvature upon friction factors has been investigated analytically by Dean (Ref. 18) and Adler (Ref. 25) for laminar flow in tubes. For turbulent flow in curved pipes, the empirical average friction relationships developed are of the general form (Ref. 19 and 20):

$$\frac{\bar{f}_c}{\bar{f}_o} = K_1 + K_2 \left[Re_D \left(\frac{R}{r_c} \right)^2 \right]^b = K_1 + K_2 \, (2 \, De)^b \qquad (85)$$

The exponent (b) on the Reynolds number varies from 0.05 to 0.25 for the turbulent case as compared to 0.36 to 0.50 for the laminar case. Similarly, the exponent on the curvature ratio (R/r_c) varies from 0.1 to 0.5 for the turbulent case as compared to 0.18 to 0.25 for the laminar

condition. As a result, it is apparently indicated that the curvature effect of Reynolds number increases becomes less important at high Reynolds numbers. However, the effect of curvature is seen to be of equal or greater influence at the higher Reynolds numbers.

Figure 10 shows the tube curvature-to-radius ratio vs Reynolds number for a 10-percent increase in average friction factor coefficient. As shown, curvature effects for a tube become increasingly important as the Reynolds number is increased.

Experimental work on average heat transfer coefficients in coils shows that the ratio of curved tube-to-straight tube coefficients may be empirically expressed by:

$$\frac{\bar{h}_c}{\bar{h}_o} = 1 + 3.5\left(\frac{R}{r_c}\right) \qquad \text{Jeschke (Ref. 26)} \qquad (86)$$

$$\frac{\bar{h}_c}{\bar{h}_o} = 1 + 3.54\left(\frac{R}{r_c}\right) \qquad \text{Russian Work} \qquad (87)$$

No Reynolds number effect was presented for the above work principally because of the small variations of this parameter during testing. More recently, Seban and McLaughlin (Ref. 27) have shown that the increase in the average heat transfer coefficient as a result of curvature is related to the corresponding increase in the friction factor by the momentum analogy. Thus, based on Ito's (Ref. 19) equation:

$$\frac{\bar{h}_c}{\bar{h}_o} = \frac{\bar{f}_c}{\bar{f}_o} = (2\ De)^{0.05} \qquad (88)$$

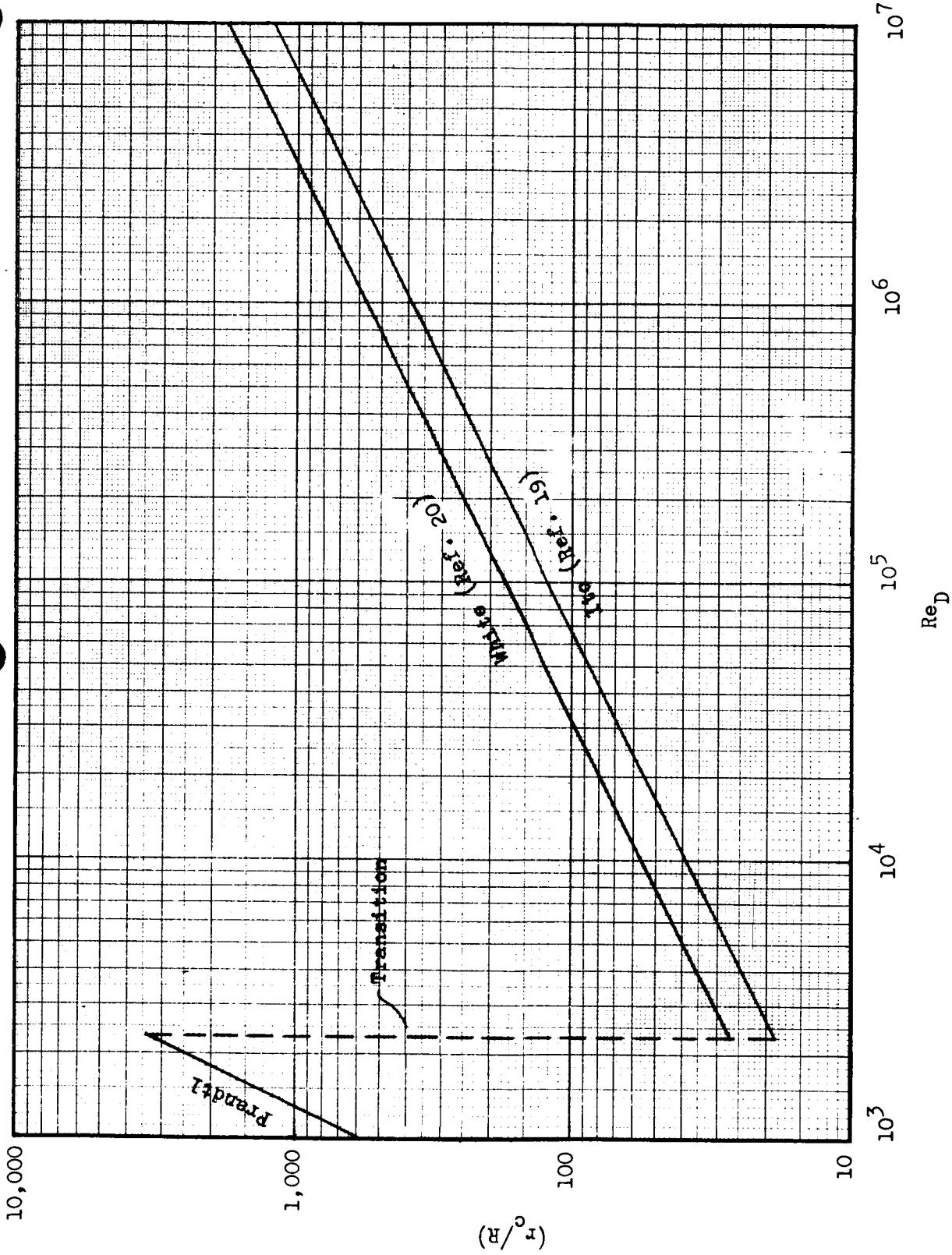

Figure 10. Critical Curvature Ratio for 10-Percent Overall Friction Coefficient Increase-Pipe Flow

For curved-tube flow conditions in a rocket engine, it is of interest to know the curvature arc angle necessary for the development of a fully curved flow situation and the ratio of the concave curved surface to uncurved heat transfer coefficients. Available local wall data for the concave-to-convex heat transfer coefficient are shown in Fig. 11. Ratios of up to 4 have been observed. Comparison with turbulent flow straight-tube data shows the convex surface to have a heat transfer coefficient usually about as high as that for an uncurved tube, a contradiction of the two-dimensional theory and apparently a result of secondary flow generation and higher local wall velocities. As a result of this approximation, the concave surface coefficient may be expressed as:

$$\left(\frac{h_{concave}}{\bar{h}_o}\right) \approx \left(\frac{h_{concave}}{h_{convex}}\right) \tag{89}$$

The ratio of the minimum and maximum heat transfer coefficients to the average value is not yet quantitatively defined.

Work on two-dimensional channels by Eskinazi and Yeh (Ref. 16) shows a fully developed velocity profile to exist after a 108-degree angle of curved section. For the curved-tube flow condition, however, the arc length for flow development is uncertain, but heat transfer data obtained with N_2O_4 (Ref. 28) indicate that an appreciable value of the heat transfer coefficient ratio given by Eq.89 is obtained within about 30 degrees.

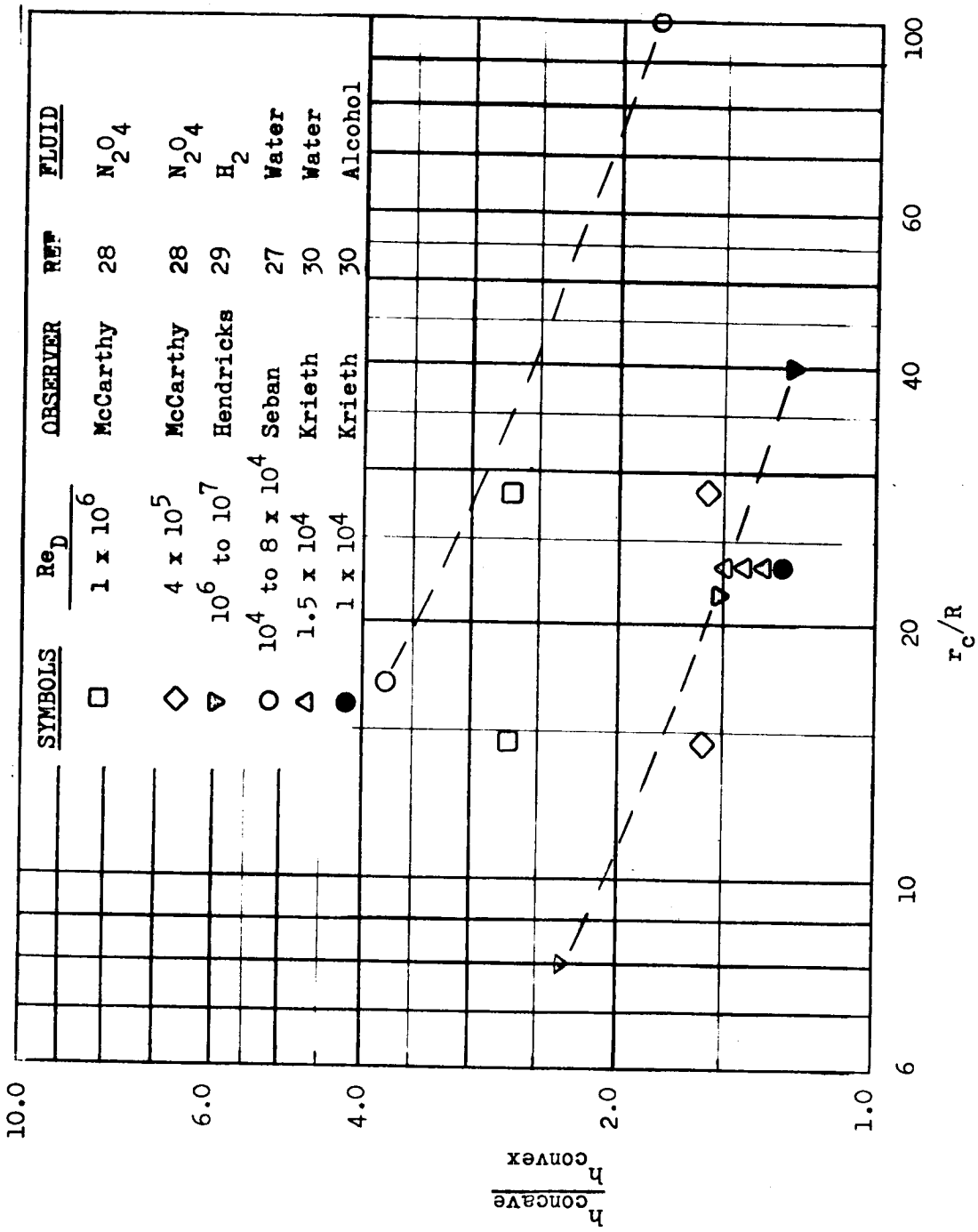

Figure 11. Available Curved-Tube Data for Heat Transfer Coefficient Ratio

I 608-8-13 NEW 11-62

Local wall shear measurements were performed by Wattendorf (Ref. 17) on two-dimensional channels with the resultant values (Re_D= 25,000) based on an average velocity as:

$$\tau_{concave}/\tau_{convex} = 1.784 \text{ for } r_i/r_o = 0.9$$

$$\tau_{concave}/\tau_{convex} = 1.49 \text{ for } r_i/r_o = 0.8$$

If the mean channel curvature radius is expressed by:

$$\bar{r}_c = \frac{r_i + r_o}{2} \tag{90}$$

and the effective width (d_t) as:

$$d_t = r_o - r_i \tag{91}$$

then in terms of the $\bar{d}_c/d_t$ ratio, the wall shear values become:

$$\frac{\tau_{concave}}{\tau_{convex}} = 1.784 \text{ for } \frac{\bar{d}_c}{d_t} = 19$$

$$\frac{\tau_{concave}}{\tau_{convex}} = 1.49 \text{ for } \frac{\bar{d}_c}{d_t} = 9$$

Assuming the validity of the above-mentioned shear-heat transfer analogy, the shear ratio should conform to the behavior of the heat transfer coefficient ratio. Instead, an opposite trend is indicated by Wattendorf's

data. The answer would appear to be that the absolute value of the curvature as well as the width-to-curvature ratio are important geometric nondimensional parameters for curved flows. In conclusion, it appears necessary, as a result, to correlate future curvature work with the following scaling parameters:

$$(Re)_c = \frac{\rho U r_c}{\mu} \quad , \quad \text{curvature Reynolds number} \qquad (92)$$

$$(Re)_\delta = \frac{\rho U \delta}{\mu} \quad , \quad \text{flow Reynolds number} \qquad (93)$$

$$(r_c/\delta) \quad , \quad \text{dimension parameter}$$

where δ is the appropriate characteristic surface length, channel width or tube diameter.

The effect of enhancement of the coolant-side heat transfer coefficient at the rocket engine throat by the curvature effect on the concave side will contribute to a lowered wall temperature or a reduced coolant pressure drop in a regeneratively cooled engine. Correspondingly, the effect of curvature on the gas-side coefficient at the throat region is in the direction of a slightly reduced value. At other locations in the motor, the situation is reversed, particularly in the subsonic convergent region and supersonic divergent region (particularly with advanced nozzle surfaces as shown in Fig. 4). The measurement of local heat transfer coefficients with high Reynolds number curved flows will bring about a greater understanding of the complex problems.

The effect of the increased coolant-side heat transfer coefficient may permit an increase in the regenerative cooling limits toward the heat conduction limit as previously discussed in Ref. 1.

Tube Surface Roughness Effects

An extensive review of the recent work of Dipprey and Sabersky (Ref. 21) was conducted to compare the roughness effects on the heat transfer coefficient based on their data to those obtained and reported in Ref. 1 for hydrogen in roughened tubes.

Dipprey analytically defined a general roughness form for the Stanton number in terms of the rough surface skin friction coefficient (f/2) by the analogy technique to give:

$$St = \frac{(C_f/2)}{1 + \left(\frac{f}{2}\right)^{1/2} \left[g(\epsilon^*, Pr) - 9.48 \right]} \tag{94}$$

where ϵ^* is a dimensionless roughness parameter given previously by Eq. 78.

Dipprey determined the parameter $g(\epsilon^*, Pr)$ from experimental data for water flowing in tubes covering a range of Prandtl number from about 1.20 to 6.0.

The experimental hydrogen data reported in Ref. 1 were compared to Dipprey and Sabersky's general correlation. A better fit of the data was obtained by modifying Eq. 94 to give:

$$St\ (T_w/T_b)^{0.55} = \frac{(f/2)}{0.92 + (f/2)^{1/2}\ [g(\epsilon^*, Pr) - 8.48]} \tag{95}$$

The function $g(\epsilon^*, Pr)$ for an approximately constant Prandtl number of 0.7 (typical of hydrogen) was determined to be:

$$g(\epsilon^*, Pr) = 4.5 + 0.57\ (\epsilon^*)^{3/4}\ ,\ 0 \le \epsilon^* \le 7 \tag{96}$$

$$g(\epsilon^*, Pr) = 4.7\ (\epsilon^*)^{0.2}\ ,\ \epsilon^* \ge 7 \tag{97}$$

Therefore, it is now recommended that the following more-general and less-restricted equation for the roughness factor (φ_4) given in Ref. 1 for convective heat transfer to hydrogen coolant be used:

$$\varphi_4 = \frac{32.4\ (f/2)\ Re_b^{0.2}\ Pr_b^{0.6}}{0.92 + (f/2)^{1/2}\ [g(\epsilon^*, Pr) - 8.48]} \tag{98}$$

where $g(\epsilon^*, Pr)$ is given by Eq. 96 and 97. Values of φ_2 and φ_3 (Eq. 84) are unchanged from the recommendations of Ref. 1.

GENERALIZATION OF HEAT TRANSFER CORRELATIONS

The extension of fixed-point design results from the nominal design points to different thrust levels, chamber pressures, mixture ratios, combustion zone lengths, etc., is useful because differing design conditions may then be quickly examined.

Gas-Side Heat Transfer Coefficient Variations

Gas-side heat transfer coefficient scaling may be developed from the modified Reynolds analogy:

$$\frac{St}{Pr^{-2/3}} = \frac{h_g}{\rho U C_p Pr^{-2/3}} = \left(\frac{K}{Re^a}\right) = \frac{K}{\left(\frac{\rho U \delta}{\mu}\right)^a} \tag{99}$$

Thus, for a constant chamber pressure and propellant combination, geometric changes may be scaled as:

$$h_g \propto \left(\frac{1}{\delta}\right)^a \tag{100}$$

where δ represents the characteristic boundary layer thickness with exponent"a." Extension of the above result to other design configurations may be made by considering that the Reynolds number is based upon surface length. If the boundary layer history in terms of an average pressure gradient to the point of measurement is approximately the same, then:

$\delta \propto x$ and for $a = 0.2$:

$$h_g \propto (1/x^{0.2}) \tag{101}$$

In terms of relative heat fluxes, this may be expressed as:

$$\frac{(q/A)_2}{(q/A)_1} = \left(\frac{x_1}{x_2}\right)^{0.2} = \left(\frac{Re_{x_1}}{Re_{x_2}}\right)^{0.2} \tag{102}$$

for a fixed gas dynamic area ratio location and a constant $(T_{aw} - T_{wg})$.

Film coefficient and heat flux variations with changes in gas temperatures and transport properties were previously developed and may be put into nondimensional form as:

$$\frac{h_{g_2}}{h_{g_1}} = \left(\frac{\mu_2}{\mu_1}\right)^{0.2} \left(\frac{C_{p_2}}{C_{p_1}}\right)^{1.0} \left(\frac{C_1^*}{C_2^*}\right)^{0.8} \left(\frac{Pr_1}{Pr_2}\right)^{2/3} \tag{103}$$

$$\frac{(q/A)_2}{(q/A)_1} = \left(\frac{h_{g_2}}{h_{g_1}}\right)\left(\frac{T_{aw_2} - T_{wg_2}}{T_{aw_1} - T_{wg_1}}\right) \tag{104}$$

<u>Chamber Pressure Variation Effects</u>

Heat transfer coefficient variations with mass velocity may also be developed from Eq. 99. The result is:

$$h_g \propto G^{1-a} \tag{105}$$

For a fixed geometry, the variation of mass velocity is linear with chamber pressure.

$$h_g \propto (P_c)^{1-a} \tag{106}$$

At nominal Reynolds numbers, the value of "a" is 0.2. At extremely high Reynolds numbers or turbulence conditions:

$$a \rightarrow 0$$

and

$$h_g \propto P_c^{1.0} \tag{107}$$

Considering the moderate Reynolds number case:

$$\frac{(q/A)_2}{(q/A)_1} = \left(\frac{P_{c_2}}{P_{c_1}}\right)^{0.8} \tag{108}$$

Other Chamber Geometries

Different chamber geometries may be quickly considered in an approximate manner by using the relation expressed by Eq. 102. With a multichamber design, the peak heat flux may be compared for several cases. If N represents the number of chambers composing the total thrust, these cases are:

1. Constant combustion zone length and contraction ratio
2. Constant L* with contraction ratio proportional to $N^{1/4}$
3. Constant combustion zone L/D* (this is equivalent to a constant L* with contraction ratio proportional to $N^{1/2}$)

The relative maximum heat flux for the multichamber design (N > 1) as compared to the single chamber (N = 1) is shown in Fig. 12 for each of the above three cases. Peak heat flux is seen to be as much as 40 percent greater for a 32-thrust-element design.

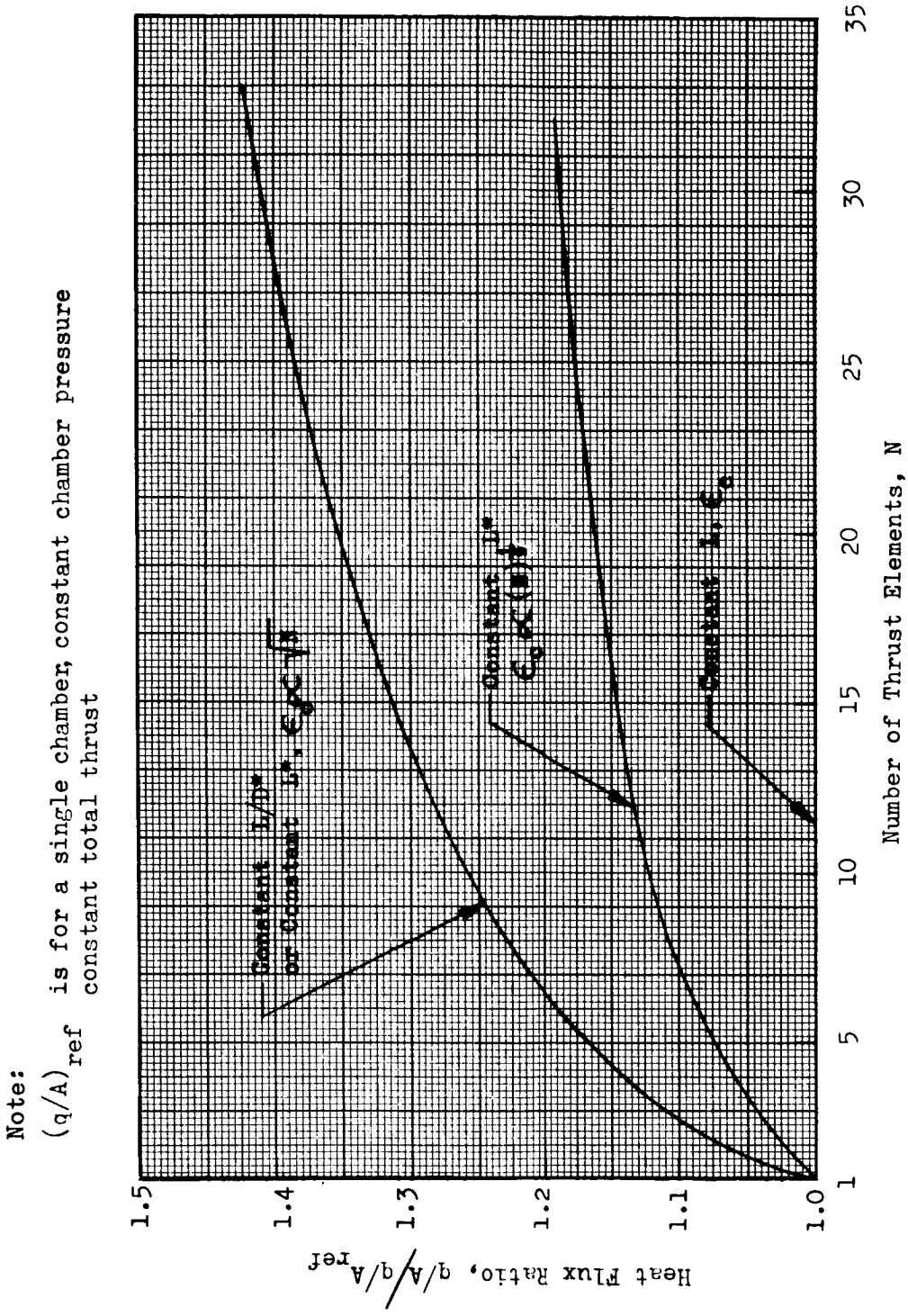

Figure 12. Peak Heat Flux Ratio Dependence on Number of Thrust Chamber Elements

For a regeneratively cooled design, the limiting pressure drop becomes directly related to the average heat flux. A case for a fixed allowable maximum heat flux may be used to define chamber pressure limits for a multichamber by using Eq. 108. This assumes that:

$$\frac{(q/A)_{peak}}{(q/A)_{average}} = \text{constant} \tag{109}$$

As a result, Fig. 12 may be used to derive Fig. 13. Based on the validity of the above premises, Fig. 13 shows that a maximum of a 35-percent reduction in an allowable maximum chamber pressure for regenerative cooling can occur for a 32-thrust-element design. As an example of the use of Fig. 13, a 6-million-pound-thrust O_2/H_2 design with an upper limiting chamber pressure of 2000 psia for complete regenerative cooling of a single chamber may be considered. For a 32-element case, a reduction in allowable chamber pressure to 1300 psia is indicated for the most severe case.

Regenerative Coolant Pressure Drop Scaling

Incompressible Flow. For the scaling of liquid coolant such as RP-1, the heat transfer coefficient in Stanton number form at high velocities is given by:

$$St = \frac{h_c}{G\,C_p} = \frac{0.005}{Re^{0.05}\,Pr^{0.6}} \tag{110}$$

Thus, a good approximation is:

$$h_c \propto G \tag{111}$$

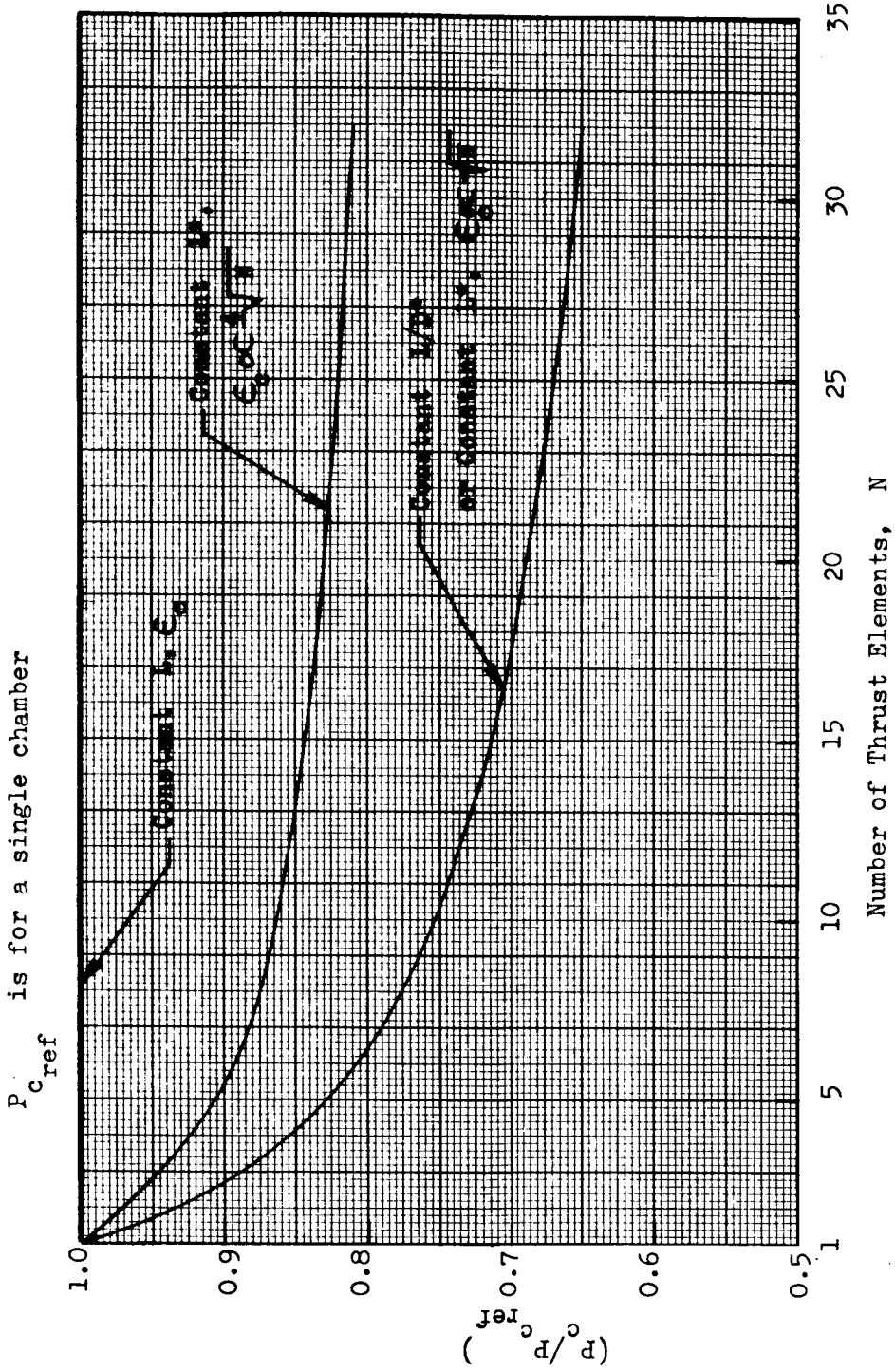

Figure 13. Maximum Allowable Chamber Pressure for Multi-Element Thrust Design With Regenerative Cooling

If the limiting coolant-side wall temperature is sufficiently higher than the coolant bulk temperature, then:

$$q/A \propto G \tag{112}$$

For an incompressible flow considering only tube frictional losses

$$\Delta P = 4 \frac{f\bar{L}}{D} \frac{G^2}{2 g_c \rho} \tag{113}$$

If Eq. 112 and 113 are combined:

$$\Delta P \propto \left(\frac{f\bar{L}}{D}\right) (q/A)^2 \tag{114}$$

For round tubes with geometrically similar chambers, the coolant mass velocity is related to the throat radius and tube diameter by:

$$G \propto \frac{1}{R^* D} \tag{115}$$

Considering a multichamber application with N chambers:

$$R^* \propto 1/\sqrt{N} \tag{116}$$

Therefore,

$$D \propto \sqrt{N/G} \tag{117}$$

With geometrically similar chambers, the effective coolant tube length $(\bar{L})$ is related to the number of chambers by:

$$\bar{L} \propto \frac{1}{\sqrt{N}} \tag{118}$$

Combining Eq.113, 117 and 118, the pressure drop for a constant friction coefficient becomes:

$$\frac{\Delta P_2}{\Delta P_1} = \left[\frac{q/A_2}{q/A_1}\right]^{3.0} \frac{1}{N} \tag{119}$$

It is seen that an extreme sensitivity to the chamber heat flux occurs. If the chamber tube average $(f\sqrt{L}/D)$ ratio remains unchanged, it is seen that from Eq. 114 that:

$$\frac{\Delta P_2}{\Delta P_1} = \left(\frac{q/A_2}{q/A_1}\right)^{2.0} \tag{120}$$

For a constant number of noncircular tubes of elongated cross section with geometrically similar chambers:

$$\frac{\Delta P_2}{\Delta P_1} = \left(\frac{q/A_2}{q/A_1}\right)^{2.0} \frac{1}{\sqrt{N}} \tag{121}$$

For the case of a constant-length chamber tube with circular cross section:

$$\frac{\Delta P_2}{\Delta P_1} = \left(\frac{q/A_2}{q/A_1}\right)^{3.0} \frac{1}{\sqrt{N}} \tag{122}$$

For the case of a constant length with a high aspect ratio tube cross section:

$$\frac{\Delta P_2}{\Delta P_1} = \left(\frac{q/A_2}{q/A_1}\right)^{2.0} \tag{123}$$

Compressible Flow. The compressible-flow case, such as with hydrogen, may quickly be examined by considering geometrically similar chambers and nonsimilar chambers with a coolant density change reflected into the bulk temperature rise. For a high Reynolds number condition and invariant coolant properties, the relations become:

$$\rho \propto \left(\frac{1}{q/A}\right) \qquad \left\{ \begin{array}{l} \text{Geometrically similar, i.e.,} \\ \frac{\bar{L}}{R^*}, \frac{y}{R^*} = \text{constant} \end{array} \right\} \tag{124}$$

$$\rho \propto \frac{1}{(q/A)\sqrt{N}} \qquad \left\{ \begin{array}{l} \text{Nonsimilar, i.e.,} \\ \bar{L} = \text{constant or } y = \text{constant} \end{array} \right\} \tag{125}$$

The incompressible-flow results can be modified by recalling that:

$$\Delta P \propto \left(\frac{1}{\rho}\right) \tag{126}$$

For hydrogen coolant, Eq. 110 for defining the coolant heat transfer coefficient requires the following additional factor:

$$St \propto \left(\frac{T_b}{T_w}\right)^{0.55} \tag{127}$$

Since improvement in a film coefficient is noted with an increased bulk-to-wall temperature ratio approaching a value of 1, the decreased density effect is offset in a direction similar to that previously discussed for mixture ratio changes.

It can be concluded that small increases in heat flux are reflected into strongly increased pressure drops. For designs with a multiple number of chambers composing the total integrated thrust, smaller or higher pressure drops may result, dependent upon the geometric scaling of the

constituent chambers. It is apparent that a number of simplifications were required to allow the above relatively simple comparisons. Exact scaling may only be performed with actual computer design cases.

Film-Cooling Scaling

The scaling of film-cooling relationships is dependent upon the dimensionless temperature grouping (ψ_1) and the ratio of heat input to heat absorption capability of the propellant (ψ_2) where:

$$\psi_1 = \frac{T_{aw} - T_{wg}}{T_{aw} - T_{fc}} \tag{128}$$

$$\psi_2 = \frac{h_g A_s}{\dot{W}_{fc} C_p \eta} \tag{129}$$

For a constant wall surface temperature and a fixed propellant combination the value of ψ_1 is constant. From the expression for ψ_2:

$$\frac{\dot{W}_{fc}}{\dot{W}_g} \propto \frac{h_g A_s}{\dot{W}_g} \tag{130}$$

with

$$h_g \propto \frac{\dot{W}_g}{Re^{0.2} A_g} \tag{131}$$

Therefore,

$$\lambda = \frac{\dot{W}_{fc}}{\dot{W}_g} \propto \left(\frac{A_s}{A_g}\right)\left(\frac{1}{Re^{0.2}}\right) \tag{132}$$

For cylindrical film-cooled elements such as the combustor or for conical surfaces of fixed angle:

$$\frac{A_s}{A_g} = \frac{4\bar{L}}{\bar{D}} \tag{133}$$

Therefore,

$$\frac{\lambda_2}{\lambda_1} = \frac{(\bar{L}/\bar{D})_2}{(\bar{L}/\bar{D})_1} \left(\frac{Re_1}{Re_2}\right)^{0.2} \tag{134}$$

Several cases of application of Eq.134 may be considered. These are:

1. Constant combustion zone length and contraction ratio
2. Constant y/R^* at a given x/R^* (i.e., scalable combustion zone)

For case 1, $\lambda \propto N^{0.5}$, while for case 2, $\lambda \propto N^{0.1}$. The results are plotted in Fig. 14. It is apparent that if a film-cooled multichamber configuration is to be used, a dimensionally scalable combustion zone is required to maintain the film-coolant flow percentage at a value approaching that of a single-thrust-element chamber.

Radiation-Cooling Scaling

This cooling method is readily amenable to scaling. With the assumption of a small wall resistance:

$$\sigma \epsilon' F T_w^4 = h_g (T_{aw} - T_w) \tag{135}$$

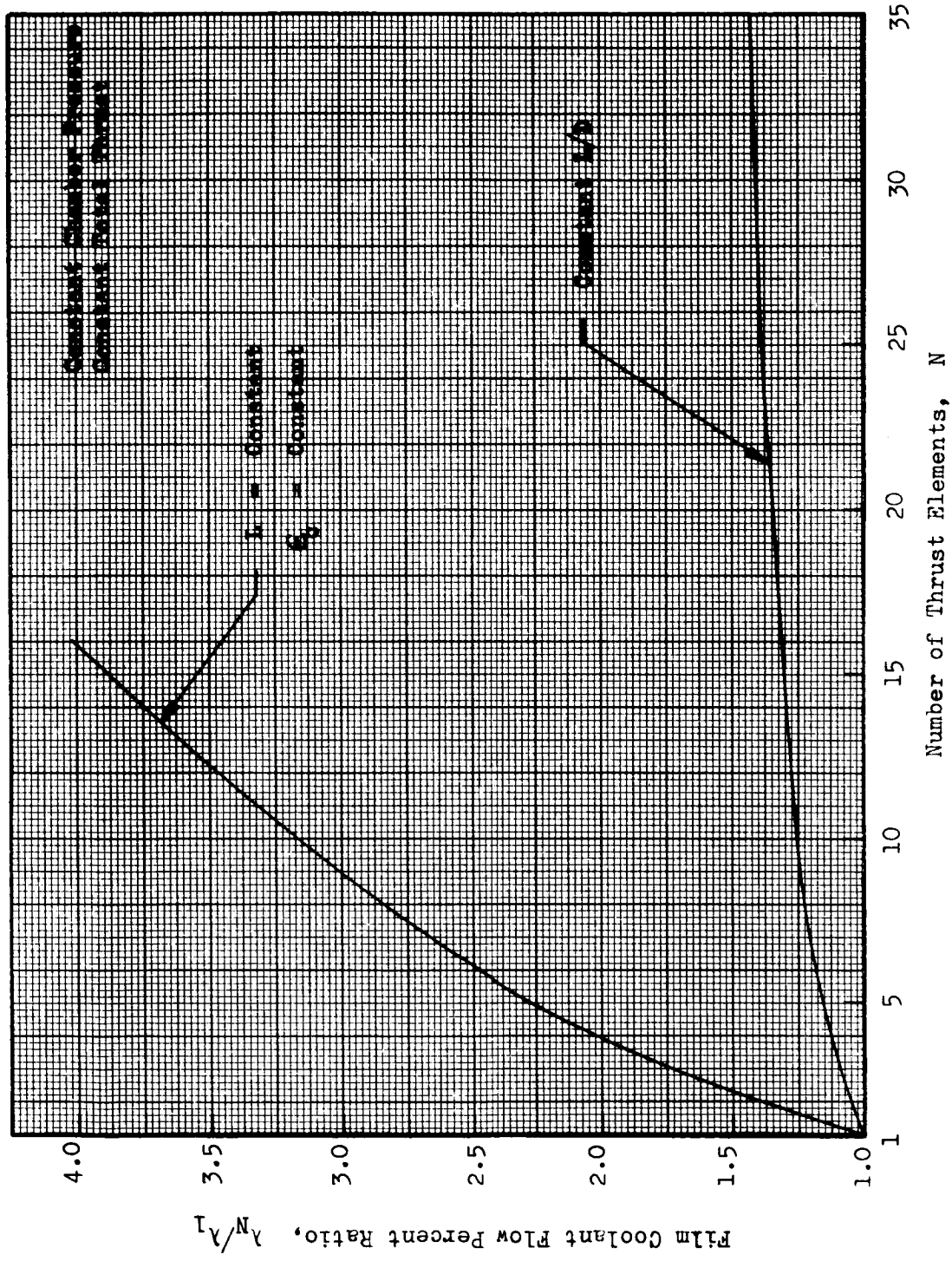

Figure 14. Film-Coolant Ratio Dependence on Number of Thrust Chamber Elements.

Within reasonable scaling limits, T_w may be considered constant relative to the change in T_w^4. As a result, for a constant stagnation temperature:

$$T_w \propto h_g^{1/4} \tag{136}$$

Expressing the gas-side film coefficient as:

$$h_g \propto (P_c/Re^{0.2}\ \epsilon) \tag{137}$$

$$\frac{T_{w_2}}{T_{w_1}} = \left(\frac{P_{c_2}}{P_{c_1}}\right)^{1/4} \left(\frac{\epsilon_1}{\epsilon_2}\right)^{1/4} \left(\frac{Re_1}{Re_2}\right)^{0.05} \tag{138}$$

It is seen that the radiating wall temperature is sensitive to the area ratio and chamber pressure only to the 1/4 power and the Reynolds number to the 0.05 power. Thus, small changes in thrust, chamber pressure, or gas dynamic area ratio show little effect on the wall temperature.

For a fixed maximum wall temperature, the constraint on minimum allowable area ratio becomes:

$$\left(\frac{\epsilon_2}{\epsilon_1}\right) = \left(\frac{P_{c_2}}{P_{c_1}}\right)^{1.0} \left(\frac{Re_1}{Re_2}\right)^{0.2}, \text{ (fixed } T_w) \tag{139}$$

The strongest dependences are shown to be the area ratio and chamber pressure variations.

Transpiration Scaling

Since the transpiration process is quite analogous to the film-cooling method, the scaling procedure for the latter becomes satisfactory.

Ablative Scaling

Since the charring rate at all positions along the exit nozzle length (except at very high area ratio) are little affected by the gas-side film coefficient in high-pressure engines, the use of scaling rules for the evaluation of thickness requirement changes are not required. For time variations (τ), an ablative thickness variation (Δy) may be roughly scaled as:

$$\frac{\Delta y_1}{\Delta y_2} = \frac{\sqrt{\tau_1}}{\sqrt{\tau_2}} \tag{140}$$

GASEOUS FILM-COOLING THEORY

In Ref. 1, one of the more-attractive cooling methods that appeared to have considerable merit for high-pressure, high-thrust designs was the film-cooling method. With a view toward improving the existing analytical approaches, development of new insight into the important film-cooling parameters was continued.

The work of Hatch and Papell (Ref. 31) and Papell and Trout (Ref. 32) as reviewed in Ref. 1 indicated that the gaseous film-cooling process could be represented by an equative balance between the heat input to the film coolant defined by a heat transfer coefficient assuming no interaction effects between the coolant and the mainstream gas, and the film-coolant temperature rise defined by a sensible heat absorption.

An empirical correction factor derived by Papell, et al. was an attempt to account for the mainstream velocity-to-film coolant velocity ratio as causing the apparent shear level and heat transfer input to the film coolant to be higher than predicted. The revision of this assumption to provide a correction in terms of the loss of coolant into the gas stream as a function of the relative mainstream and coolant momentum values was made in Ref. 1. It is now apparent that two processes come into play in reducing the film-coolant effectiveness from the ideal value. The first of these is the reduction in shear level between the film coolant and mainstream gas which can be accomplished by the equalizing of the two velocities. The second is a process wherein the film-coolant layer is dispersed into the mainstream gas by mechanical mixing and diffusive processes. The effect of an increasing film-coolant velocity or momentum is to reduce the shear value and, consequently, to improve the efficiency of the process. Similarly, undesirable diffusive mixing is reduced by a small relative velocity. Initial loss of film coolant in the mainstream gas appears to be governed by the inlet velocity of the film coolant; i.e., a higher coolant velocity contributes to a higher initial loss into the mainstream. Sufficient experimental evidence is not available to separate the two effects.

The mechanical mixing of the two streams is to a great extent dependent upon the means of injection. It may be assumed, as substantiated by experimental data, that tangential injection provides the smallest loss resulting from mechanical mixing. The efficiency of the film-cooling process can be changed markedly by the injection method. The most feasible design of a wall-film-coolant injection "slot" is in reality not a slot but a row of normal orifices along the chamber wall periphery with a guiding cover surface to provide circumferential coolant dispersion as well as guidance in the tangential direction. Several methods

of coolant injection are shown in Fig. 15. Advantages and disadvantages of each of the methods are listed in Table 2. Method F in Fig. 15 appears to be the best injection method with consideration given to pressure drop control, circumferential variation, cooling efficiency, fabrication difficulty, close tolerances, and structural integrity for sheet wall surfaces.

Figure 16 presents an analogous picture for film cooling with a tubular wall construction. The most advantageous techniques would employ a tangentially directed film coolant either with a cover plate over radial holes drilled on the tube surface or from a manifold or tube splice point such as at the injector face location. Investigation of the most optimum technique would have to be made after a comprehensive design and experimental study.

Mixing Approach to Film-Cooling Theory

Since it is recognized that one of the controlling influences in the rate of film-coolant heat absorption is the shear level, an approach to the analytical development of a description of the process was made by the assumption of a turbulent mixing velocity profile with a variable boundary velocity and a similarity in velocity and temperature profiles such as usually exists with a unity Prandtl number and small pressure gradients.

The relationship derived by Hatch and Papell (Ref. 31) and subsequently modified in Ref. 1 becomes:

$$\frac{T_{aw} - T_{c_2}}{T_{aw} - T_{c_1}} = e^{-\left(\frac{h_g \, z \, x}{\eta_f \, \dot{W}_c \, c_{p_c}}\right)} \tag{141}$$

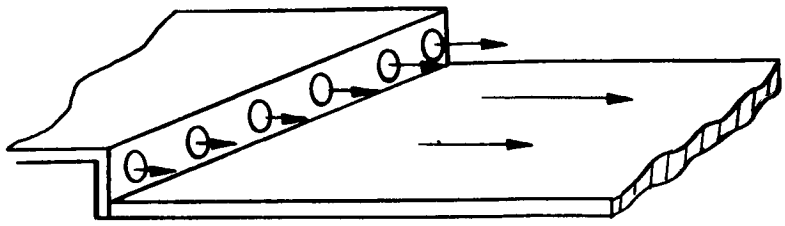

A. Back-Step Tangential Injection

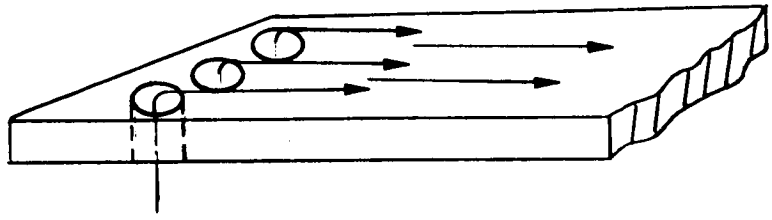

B. Radial Injection

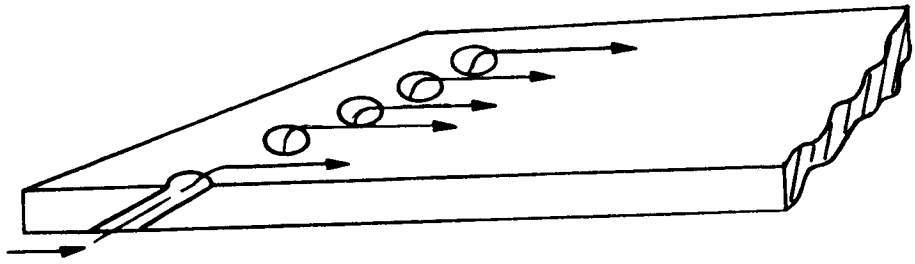

C. Angled Injection

Figure 15a. Possible Film-Cooling Injection Methods for Single-Wall Chambers

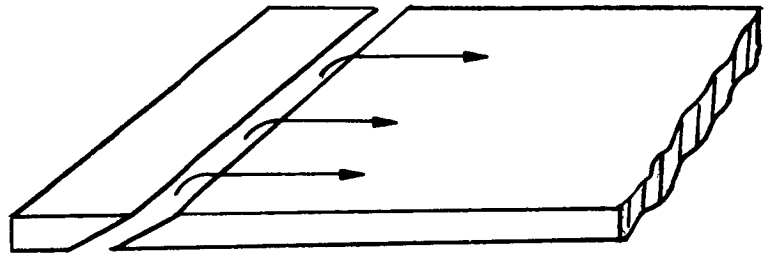

D. Angled Slot Injection

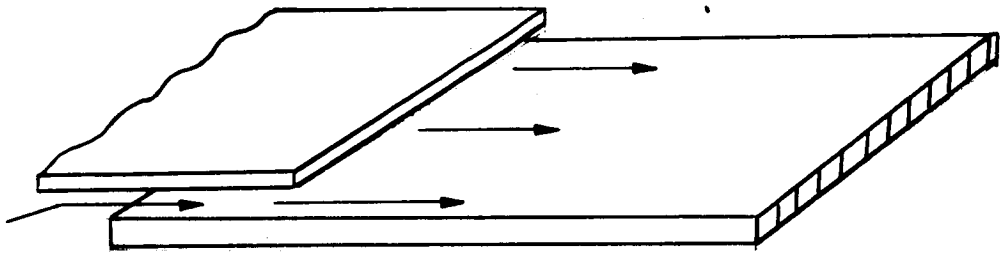

E. Shingle Construction

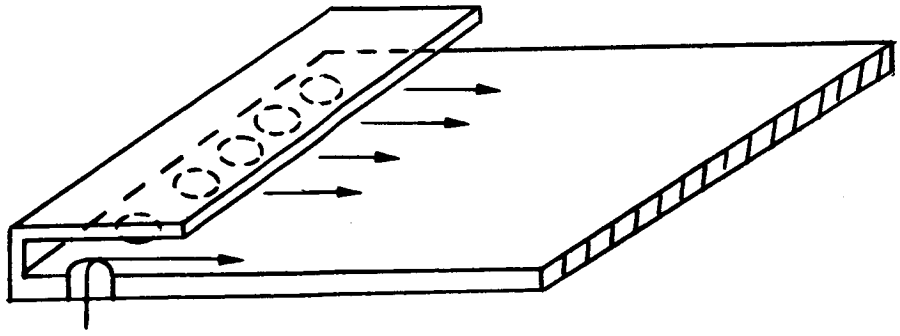

F. Tangential Injection from Covered Radial Holes

Figure 15b. Possible Film-Cooling Injection Methods for Single-Wall Chambers

TABLE 2

COMPARISON OF FILM-COOLING INJECTION METHODS
FOR SINGLE WALL DESIGNS

Method (Fig. 15)	A	B	C	D	E	F
Pressure Drop Control	X	X	X	M	0	X
Circumferential Variation	0	0	0	X	X	X
Cooling Efficiency	M	0	0	0	X	X
Fabrication	X	X	X	0	0	X
Tolerances	X	X	X	0	0	M
Structural Integrity	X	X	X	0	0	M

X good
M moderate
0 poor

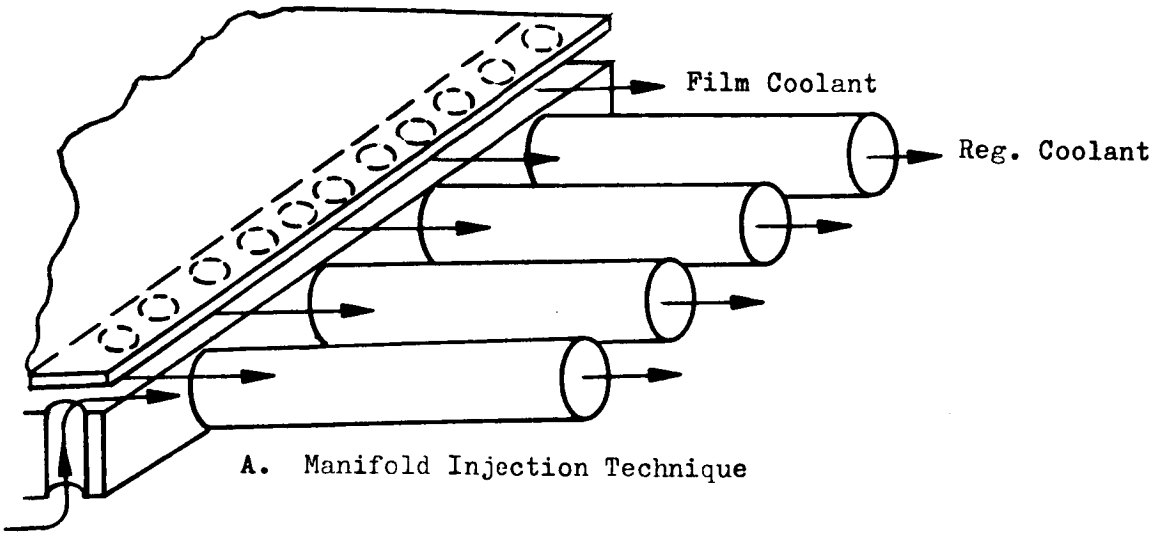

A. Manifold Injection Technique

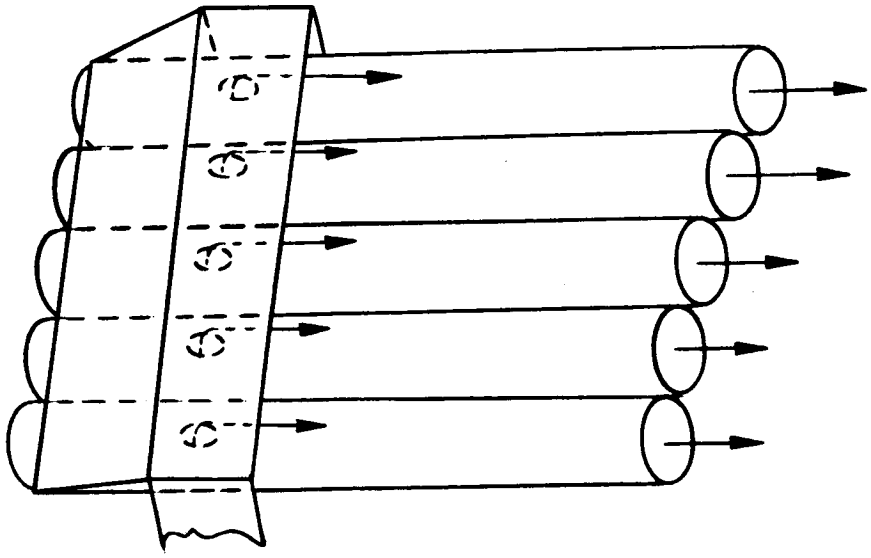

B. Drilled Tube with Cover Plate

Figure 16a. Possible Film-Cooling Methods for Tube-Wall Chambers

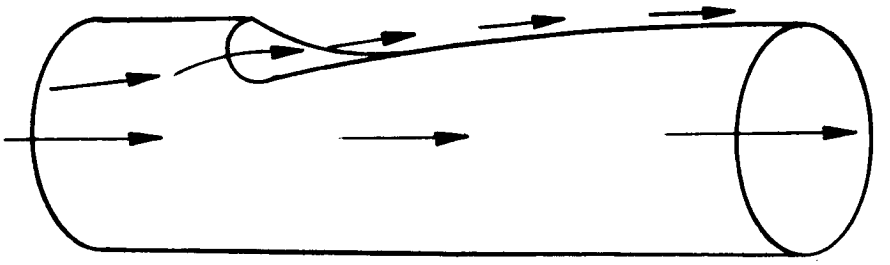

C. Tangentially-Directed Drilled Tube

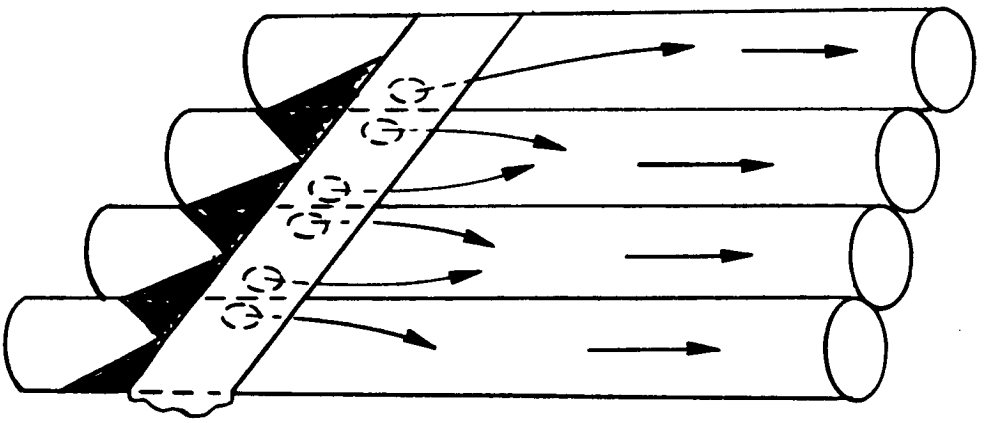

D. Crevice Film Coolant Holes with Cover Band

Figure 16b. Possible Film-Cooling Methods for Tube-Wall Chambers

FORM 608-B-13 NEW 11-62

In differential form, the coolant rise becomes:

$$\frac{dT_c}{dx} = \frac{z\ \rho_g\ V_g}{\dot{W}_c}\left(\frac{C_{pg}}{C_{pc}}\right)\left(\frac{T_{aw} - T_c}{Pr^{2/3}}\right)\left(\frac{0.026}{\eta_f\ Re^{0.2}}\right) \tag{142}$$

where

$$h_g = \frac{0.026\ C_{pg}\ \left(\rho_g\ V_g\right)}{Re^{0.2}\ Pr^{2/3}} \tag{143}$$

with the wall assumed in equilibrium with the adjacent coolant layer and no temperature gradient across the film-coolant layer.

A comparative form for the most severe mixing process in terms of shear level or energy transfer is the assumption of a turbulent free jet mixing process. The consideration of a Goertler-type mixing profile in the region between the film coolant and mainstream gases resulted in the development of a dimensionless velocity profile for the limiting case where the mainstream gas velocity is much greater than the film-coolant velocity, and for the case where the coolant velocity is significant. Both of these cases involved the assumption of an infinite film-coolant depth. For a mainstream gas velocity (V_g) and a film-coolant velocity (V_c), the velocity (U) in the mixing region is given by:

$$\zeta = \frac{U}{V_g} = 1/2\ \left[1 + \text{erf}\ \eta\right],\ \text{for}\ \left(\frac{V_c}{V_g}\right) \approx 0 \tag{144}$$

$$\zeta = \frac{U}{V_g} = \frac{1 + a}{2}\ \left[1 + \left(\frac{1 - a}{1 + a}\right)\text{erf}\ \eta\right],\ \text{for}\ \left(\frac{V_c}{V_g}\right) > 0 \tag{145}$$

where the quantity "a" represents the coolant to mainstream velocity ratio (V_c/V_g) and the quantity (η) is a mixing parameter discussed below. A comparison of these velocity profiles is shown in Fig. 17.

Further study of the velocity profile development indicated that the finite film-coolant depth case could be developed from an analogy with a multilayer heat conduction equation as given by Carslaw and Jaeger (Ref. 33). Figure 18 compares the analogy for the heat transfer and flow cases. The assumption made is that the initially uniform temperature profiles are analogous to the initially uniform velocity profiles and that the analogy may be made with temperature and velocity and with the conduction and mixing parameters.

The error function solution for the heat conduction case may be written as:

$$T - T_o = \frac{T_\infty - T_o}{2} \left[\operatorname{erfc}\left(\frac{\delta' - y}{2\sqrt{\alpha_T \tau}} \right) + \operatorname{erfc}\left(\frac{\delta' + y}{2\sqrt{\alpha_T \tau}} \right) \right] \quad (146)$$

By a lengthy transformation, the equation above may be reduced to:

$$\frac{T - T_o}{T_\infty} = 1 + \frac{\left(1 - \frac{T_1}{T_\infty}\right)}{2} \left[\operatorname{erf}\left(\frac{y}{2\sqrt{\alpha_T \tau}} \right) - \operatorname{erf}\left(\frac{y + \delta'}{2\sqrt{\alpha_T \tau}} \right) \right] \quad (147)$$

By analogy, the general solution for the flow case may be derived as:

$$\zeta = \frac{U}{V_g} = 1 + \left(\frac{1 - a}{2} \right) \left[\operatorname{erf} \eta + \operatorname{erf} \eta_P \right] \quad (148)$$

where by definition:

$$\eta = \varphi \, Re^{\alpha} \left(\frac{y}{x} \right) \quad (149)$$

$$\eta_P = \eta + \varphi \, Re^{\alpha} \left(\frac{2\,\delta}{x} \right) \quad (150)$$

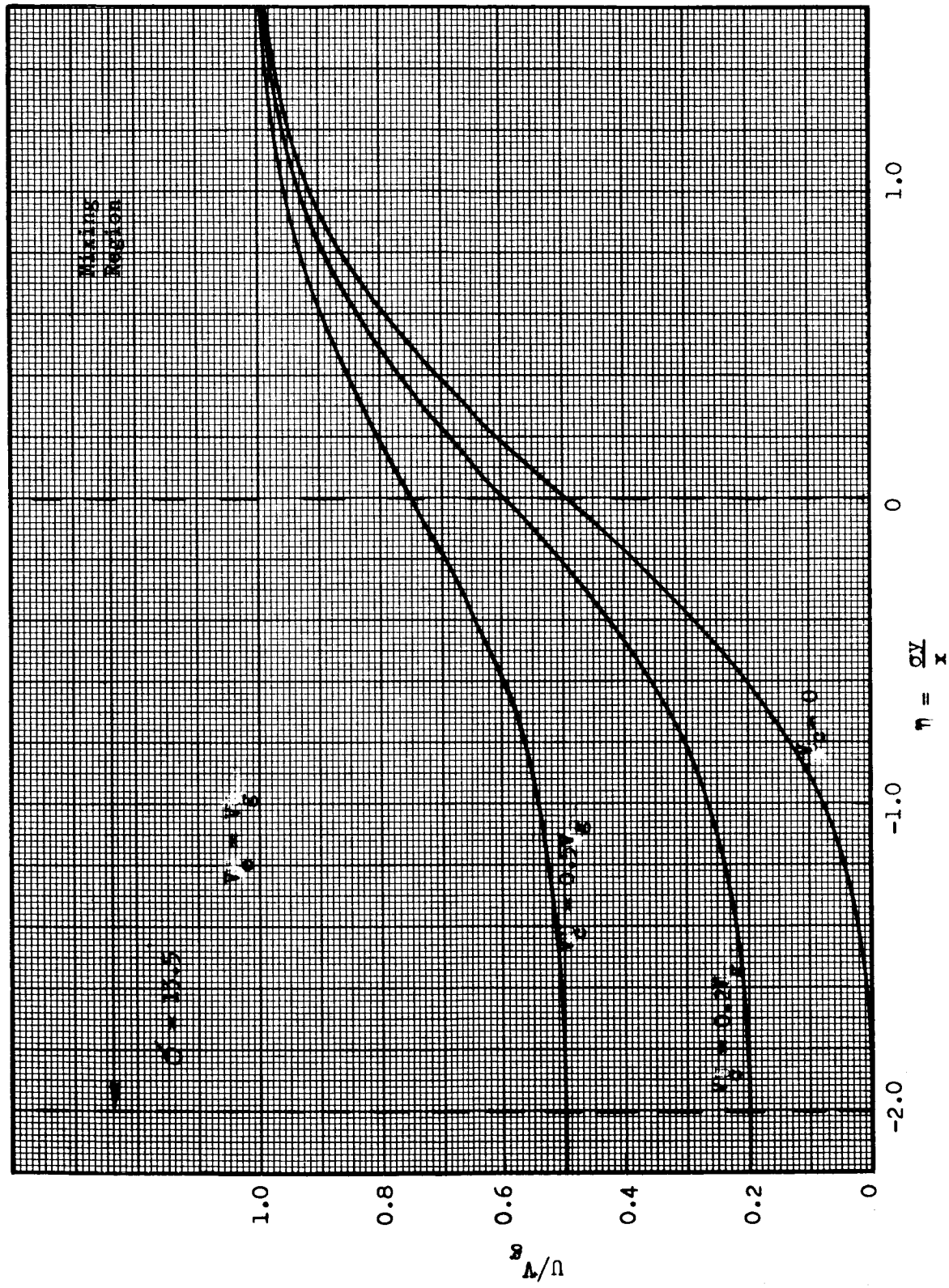

Figure 17. Mixing Profiles for Two Free Jets at Various Velocities, Two-Dimensional Solution

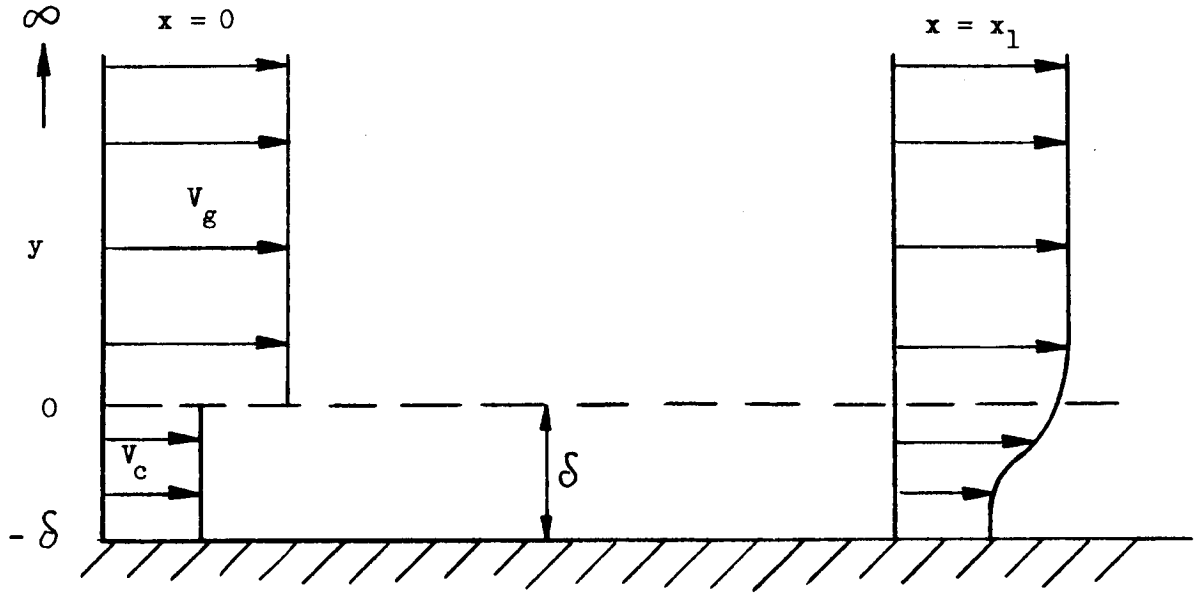

FINITE DEPTH CASE FOR FILM COOLING

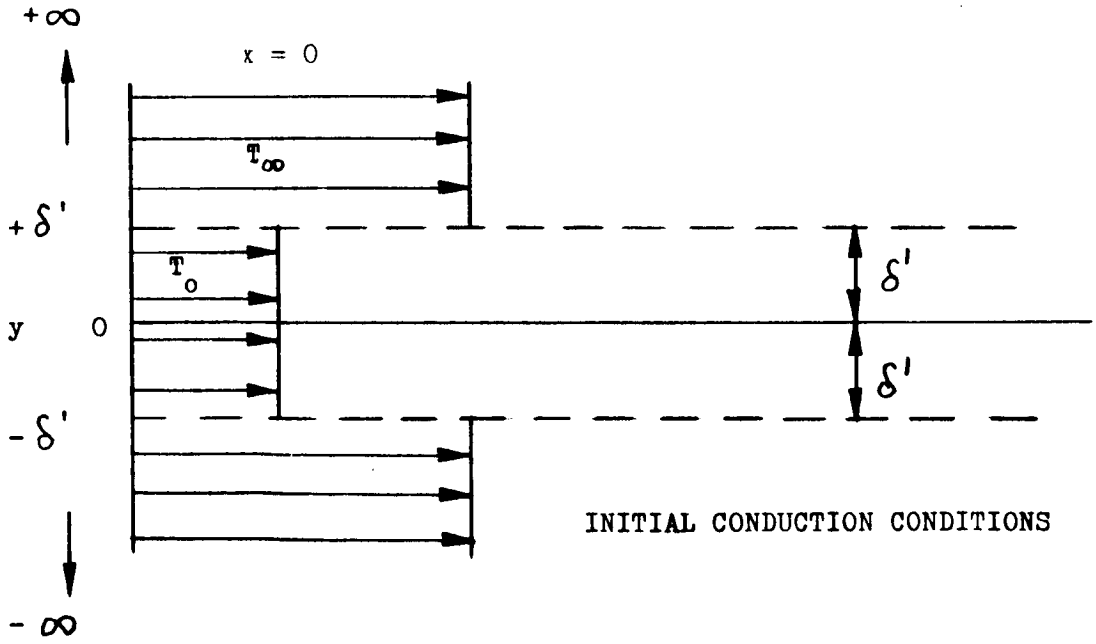

Figure 18. Conduction Analogy for Film-Cooling Velocity Profile

FORM 608-B-13 NEW 11-62

Thus,

$$\zeta = \frac{U}{V_g} = 1 + \left(\frac{1-a}{2}\right)\left\{\mathrm{erf}\left[\varphi\, \mathrm{Re}^{\alpha}\left(\frac{y}{x}\right)\right] - \mathrm{erf}\left[\varphi\, \mathrm{Re}^{\alpha}\left(\frac{y+2\delta}{x}\right)\right]\right\} \quad (151)$$

The velocity at the wall where $y = -\delta$ is obtained from Eq. 151 as:

$$\zeta_w = \frac{U_w}{V_g} = 1 - (1 - a)\left\{\mathrm{erf}\left[\varphi\, \mathrm{Re}^{\alpha}\left(\frac{\delta}{x}\right)\right]\right\} \quad (152)$$

A comparison can be made between the three cases given by Eq. 144, 145, and 148. Equation 148 accounts for the finite depth effect of the film coolant. However, the shear at the wall which plays a significant part in the overall velocity distribution for representative shallow film-coolant depths is not included so that the velocity at the wall is finite rather than zero. The axial development of a typical film-coolant profile is shown in Fig. 19.

Cases 1 through 3 (Fig. 20a, b and c) illustrate the behavior of the velocity profile and the mixing region width progression for the finite and infinite depth film-coolant cases. The cases with the inclusion of the wall shear are not provided.

Typical digital computer velocity profile solutions for the finite-depth cases without wall shear are illustrated in Fig. 21 and 22 for coolant-to-mainstream velocity ratios of 0.2 and 0.8, respectively. Curves are included for three axial locations downstream of the point of film-coolant injection. It is seen that with the velocity ratio, film-cooled depth, and mixing parameter function chosen, a velocity increase at the wall is achieved within a 10-inch length. Hence, the effect of wall shear becomes significant with increased length, as would be expected.

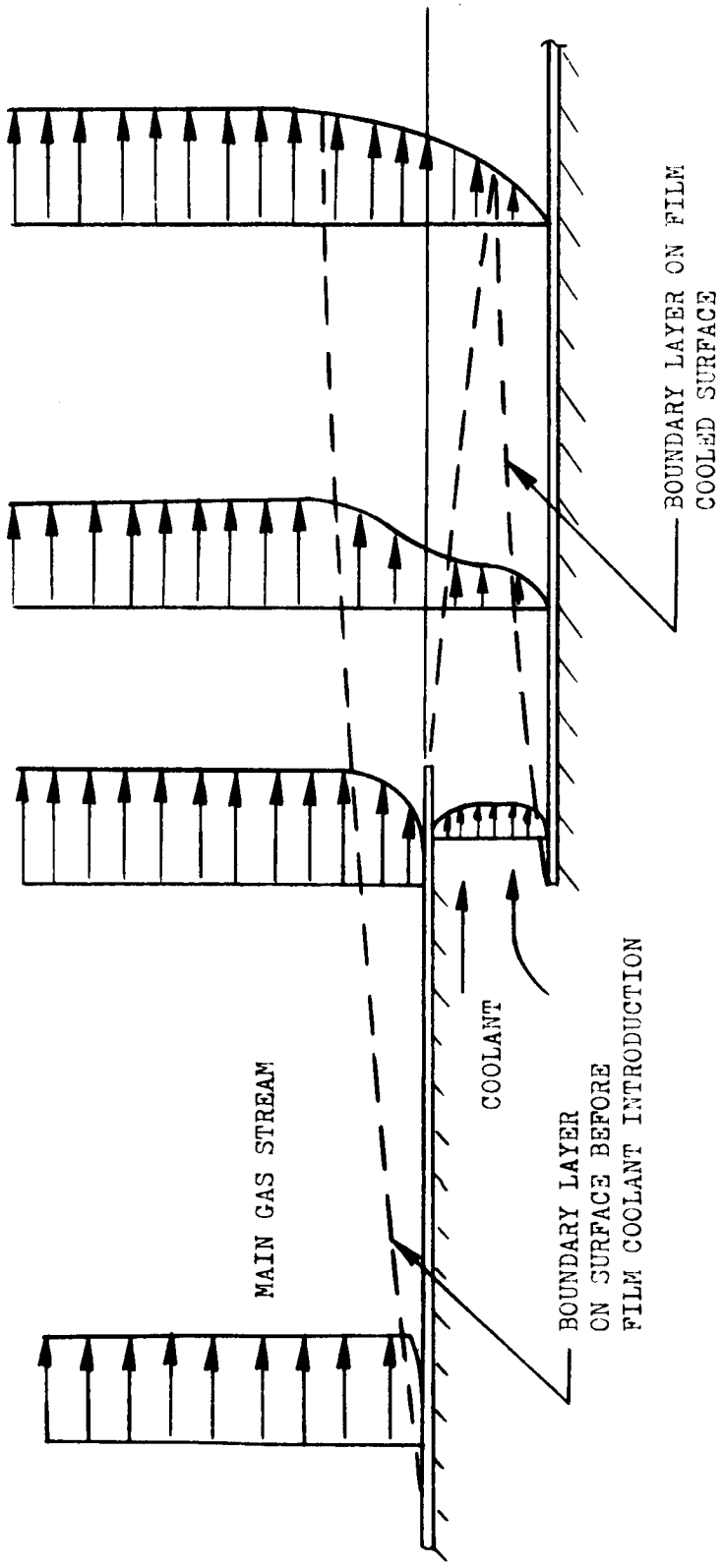

Figure 19. Comparison of Velocity Development on Film-Cooled Surface.

608-B-13 NEW 11-62

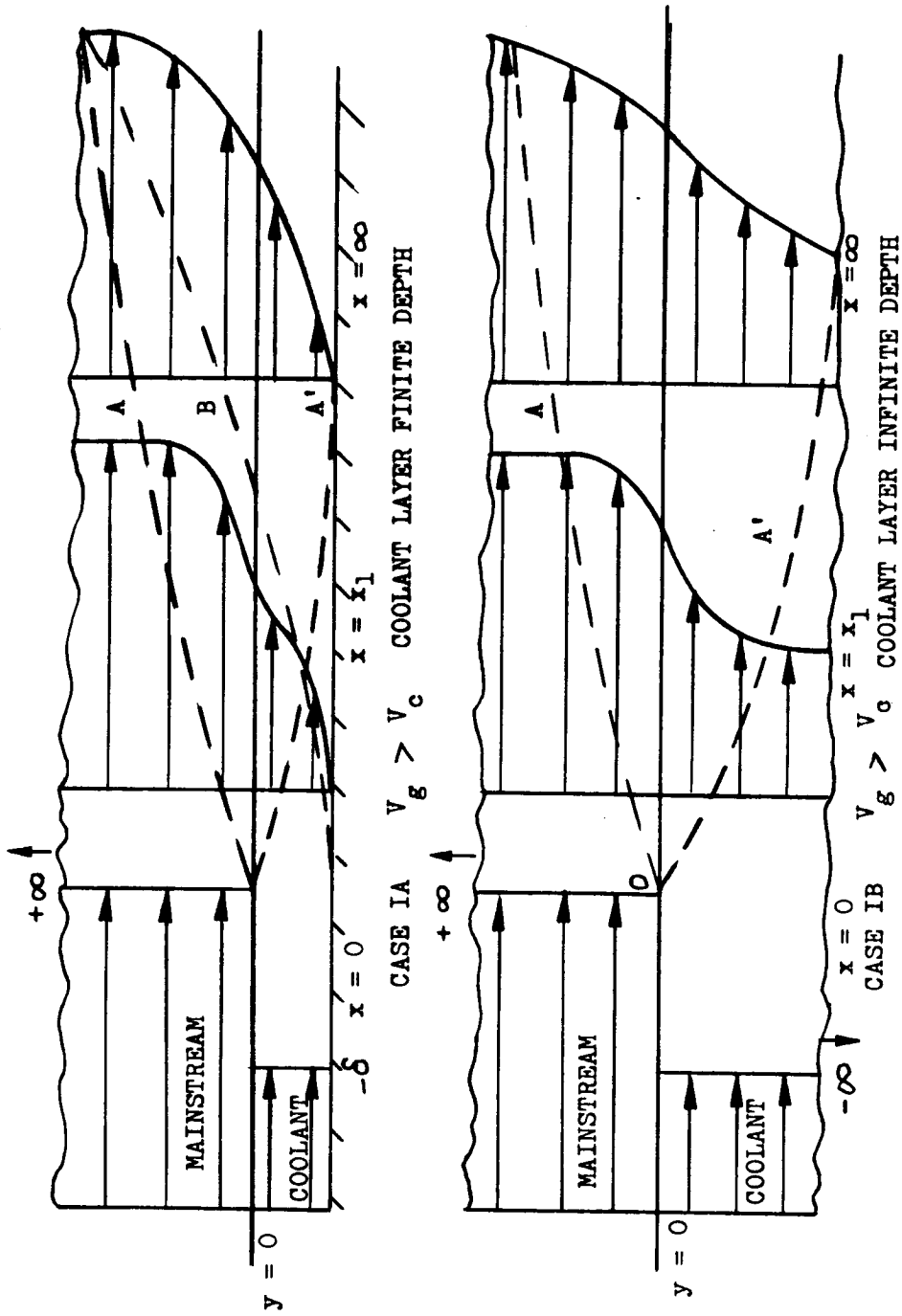

Figure 20a. Comparison of Film-Coolant Mixing Velocity Profiles

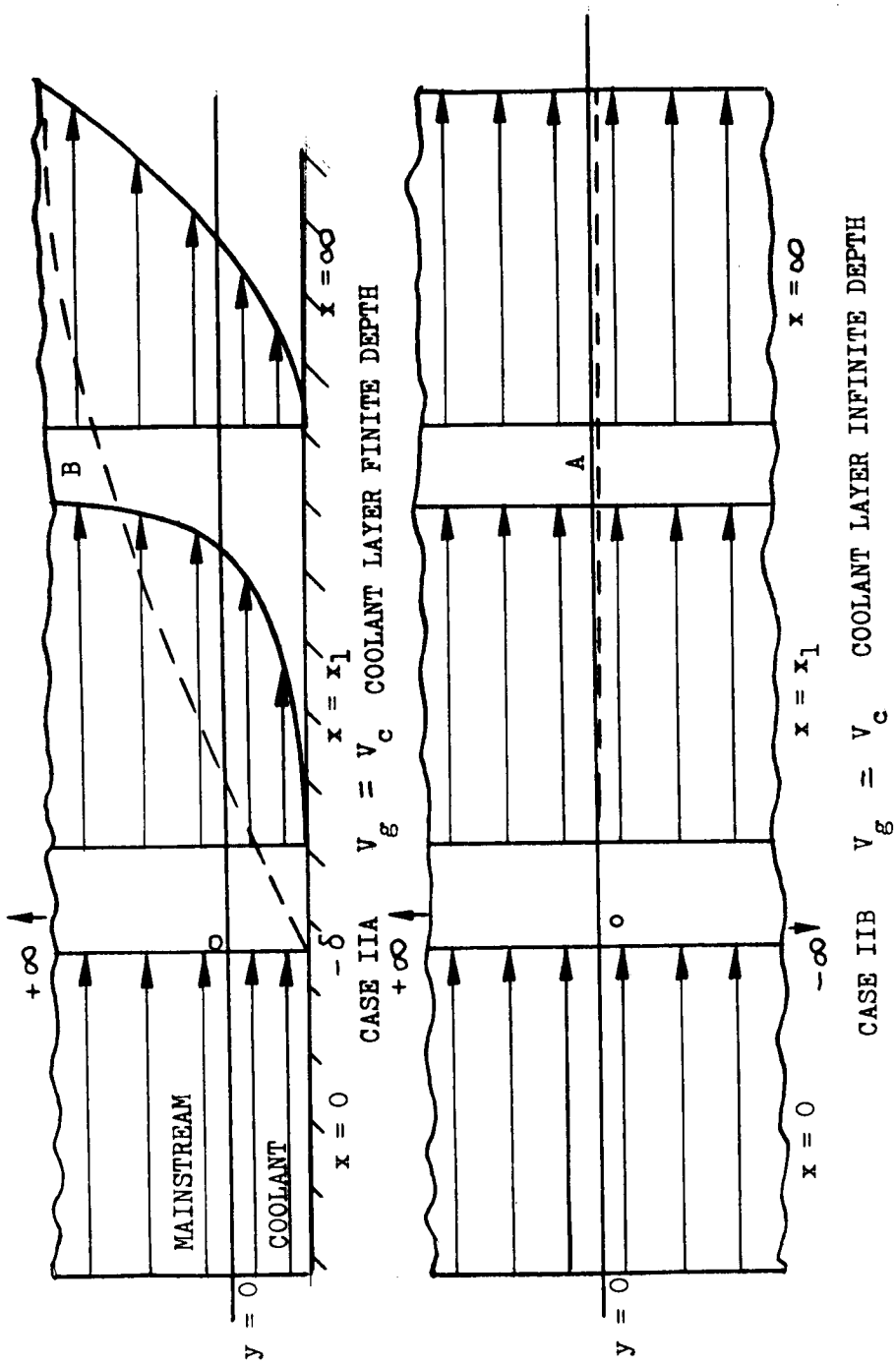

Figure 20b. Comparison of Film-Coolant Mixing Velocity Profiles

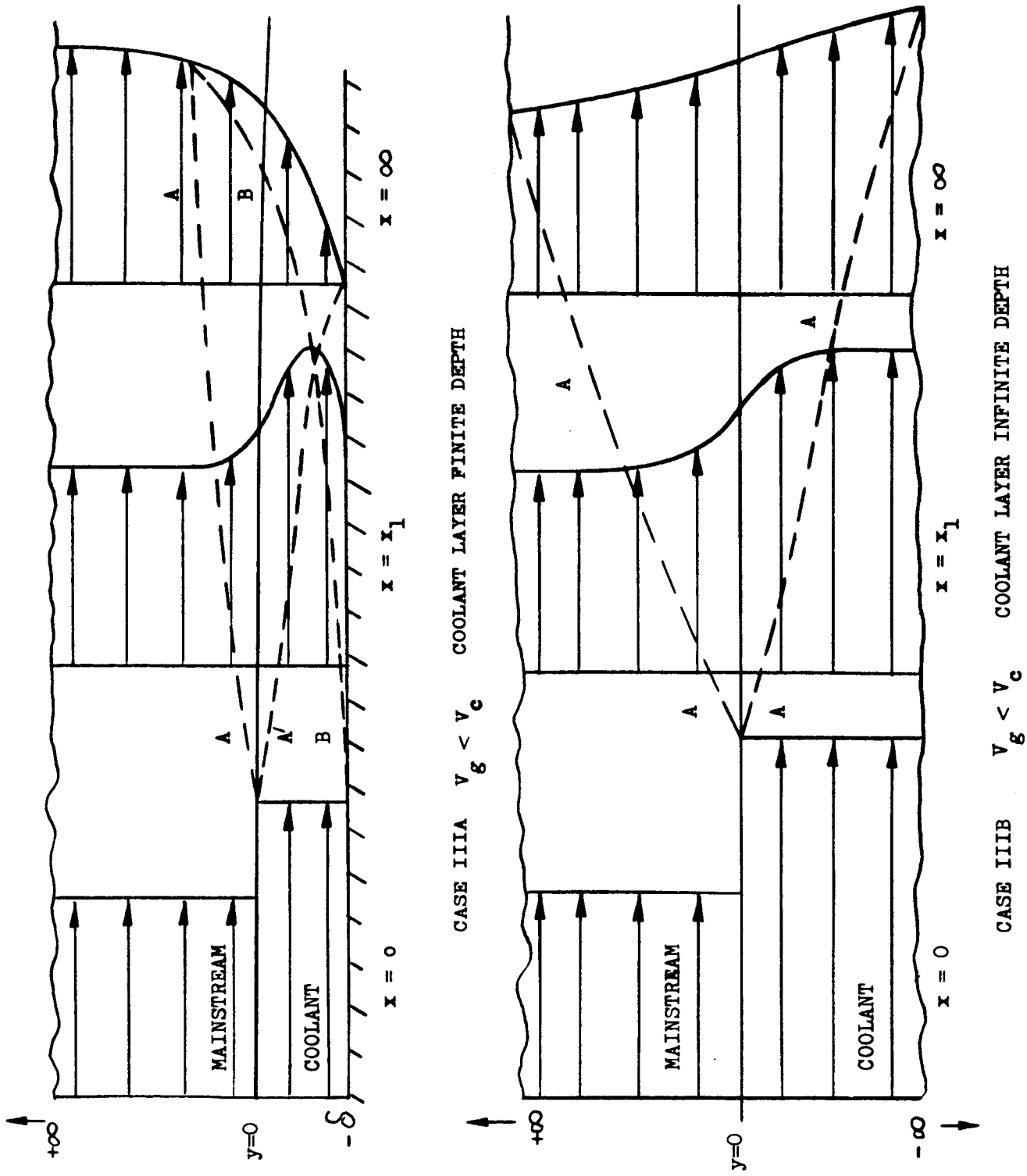

Figure 20c. Comparison of Film-Coolant Mixing Velocity Profiles

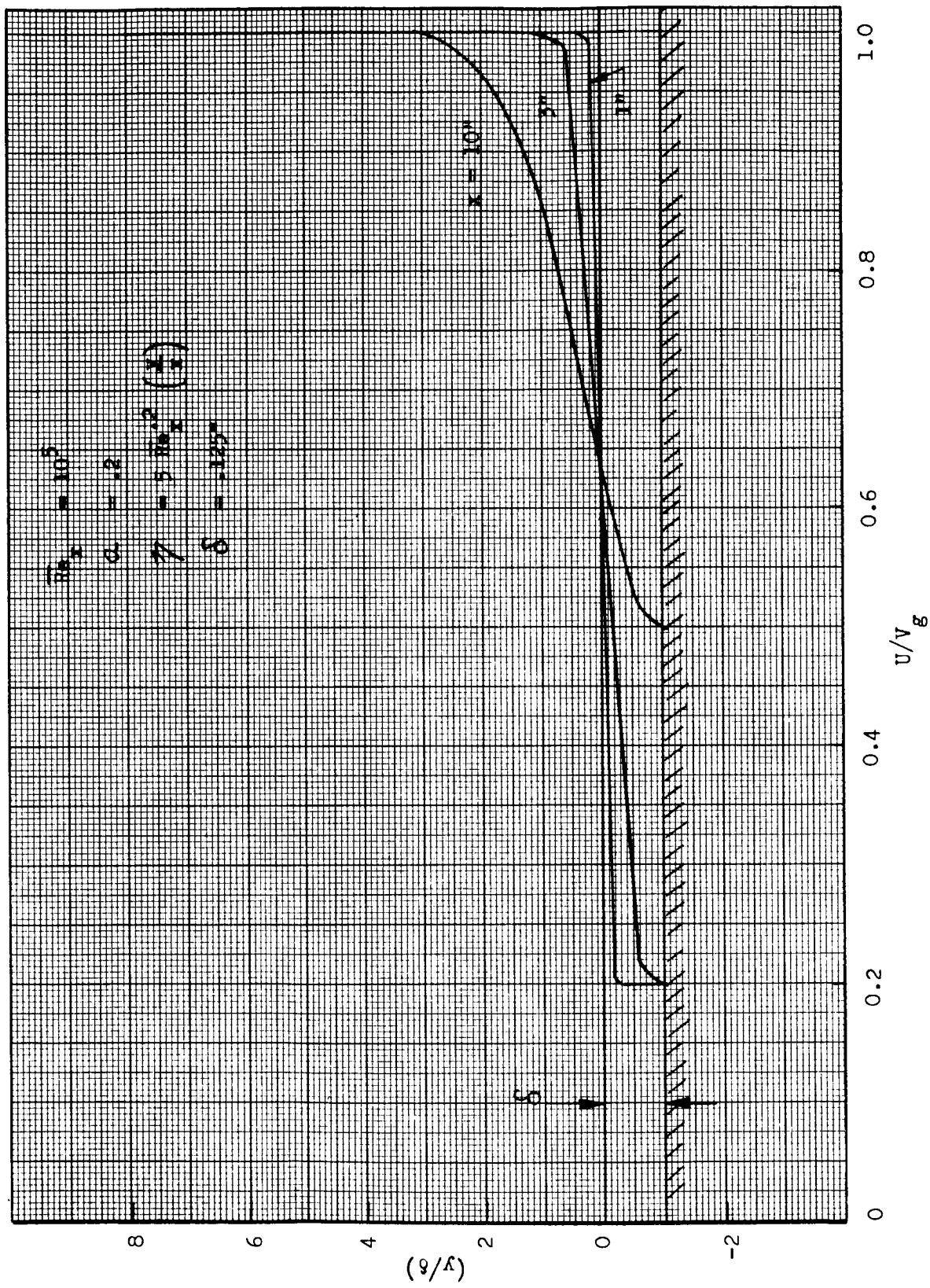

Figure 21. Velocity Profiles in Mixing Region (Zero Shear at Wall and Constant Properties)

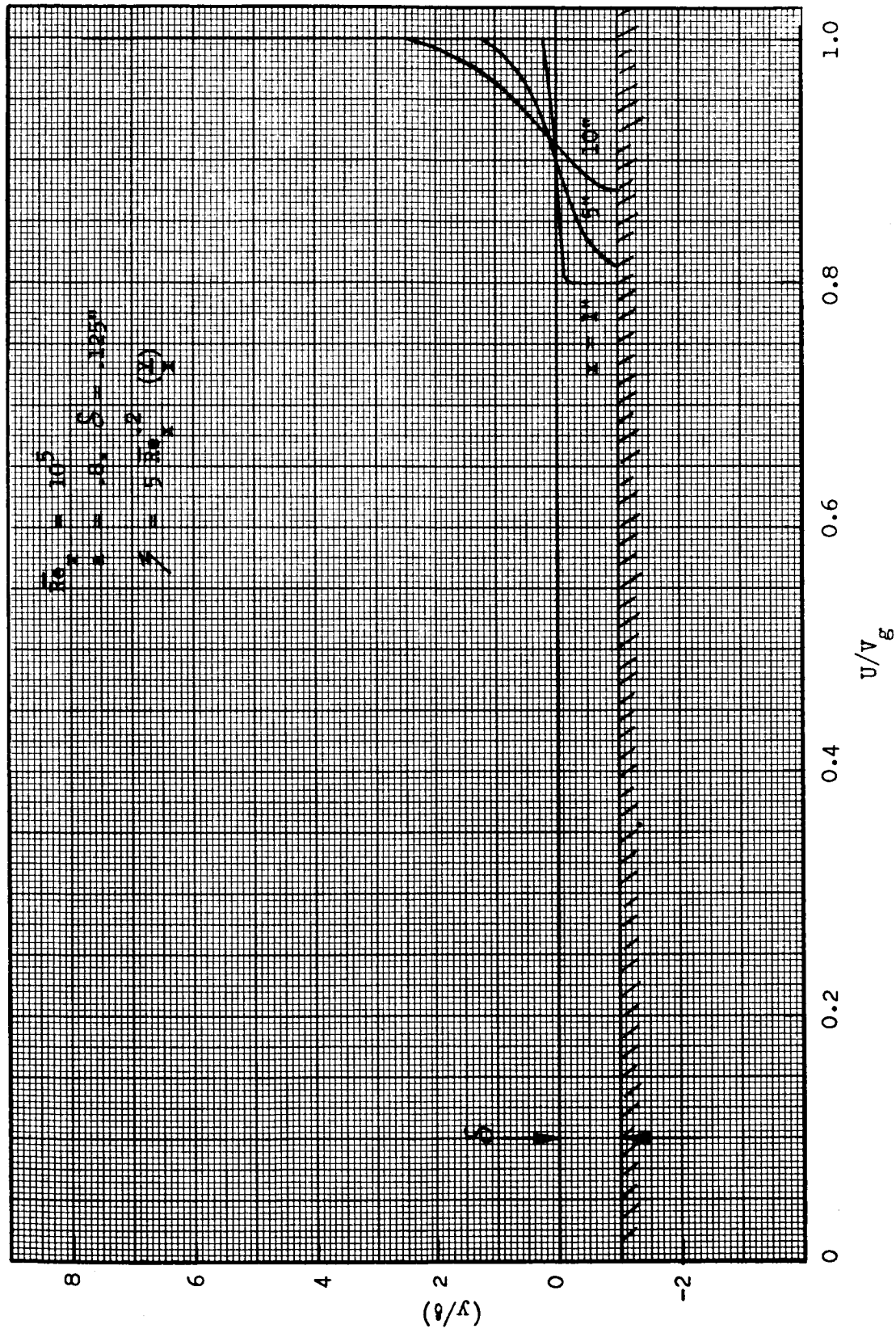

Figure 22. Velocity Profiles in Mixing Region (Zero Shear at Wall and Constant Properties)

However, temperature at the wall will, accordingly, lag the film-coolant surface temperature depending on the film thickness. Unfortunately, the remaining case, i.e., with combined wall shear and coolant-mainstream mixing, becomes complex and presently no closed-form analytical solution is apparent.

Review of the work of Abramovich (Ref. 34) on bounded jets indicated preference for a series solution of the velocity profile formation in the form:

$$\zeta = f\left(\sum_{n=o}^{\infty} C_n \eta^n\right) \qquad \text{(Abramovich)} \qquad (153)$$

This series was truncated and fitted with experimental data. Agreement with the error function solution used in the current development was good.

$$\zeta = f(\text{erf } \eta) \qquad (154)$$

<u>Mixing Parameter</u>. The mixing parameter (η) as defined generally by Eq.149 may be derived from a consideration of available solutions for laminar and turbulent flow. For mixing width and boundary layer development in laminar flow, the value of η becomes:

$$\eta_L = 1/2 \text{ Re}^{0.5} \left(\frac{y}{x}\right) \qquad (155)$$

Similarly, in free jet mixing:

$$\eta_F = 13.5 \left(\frac{y}{x}\right) \qquad (156)$$

Boundary layer growth with a highly turbulent mainstream may be expressed in a form similar to Eq.156.

The growth of a turbulent boundary layer may be similarly used to yield the relationship:

$$\eta_T = C\ Re^{0.2} \left(\frac{y}{x}\right) \tag{157}$$

where approximate limits of C are

$$3.0 < C < 8.3$$

with the lower limit derived from boundary layer growth on a flat plate and the upper limit from pipe entrance flow development.

All of the above relationships may be expressed in the general form:

$$\eta = \varphi\ Re^{\alpha} \left(\frac{y}{x}\right) \tag{158}$$

The limits may be consequently specified in the form for a low film-coolant velocity as:

$$1/2 \leq \varphi \leq 13.5, \quad \varphi\ Re^{\alpha} > 13.5$$

$$1/2 \geq \alpha \geq 0$$

where for the turbulent case

$$\varphi \approx 5.0, \quad \alpha \approx 0.2$$

The experimental data of Seban (Ref. 35) support the value of $\varphi \, Re^{\alpha}$ for free jet mixing as:

$$\varphi \, Re^{\alpha} = \left(\frac{12}{1 - a} \right) \tag{159}$$

which approaches 12 for a small coolant velocity.

A further review of the experimental data of Seban resulted in the values:

a	φN_{Re}^{α} Ref. 35	φN_{Re}^{α} Eq. 159
0	13.5	12.0
0.2	14.7	15.0
0.36	16.4	18.8
0.6	27.9	30.0

It is seen that a good agreement between the calculated results occurs.

Region 1 Behavior (Fig. 23). Penetration of the mainstream velocity profile to the wall surface through the film-coolant layer in the region just downstream of coolant injection (Region 1) was determined from the wall velocity solution previously given as Eq. 152 by assuming wall velocity rises of 1 and 5 percent above the coolant velocity value. The comparative calculated and experimental distances for the mainstream profile penetration are as follows:

a	$(x/\delta)_{calc}$ at 5 percent	$(x/\delta)_{calc.}$ at 1 percent	$(x/\delta)_{exper.}$
0	6.6	6.6	5
0.2	8.49	8.43	---
0.4	13.3	11.85	14
0.6	23.8	18.8	25
0.8	66.2	43.2	30
0.9	224.6	103	---

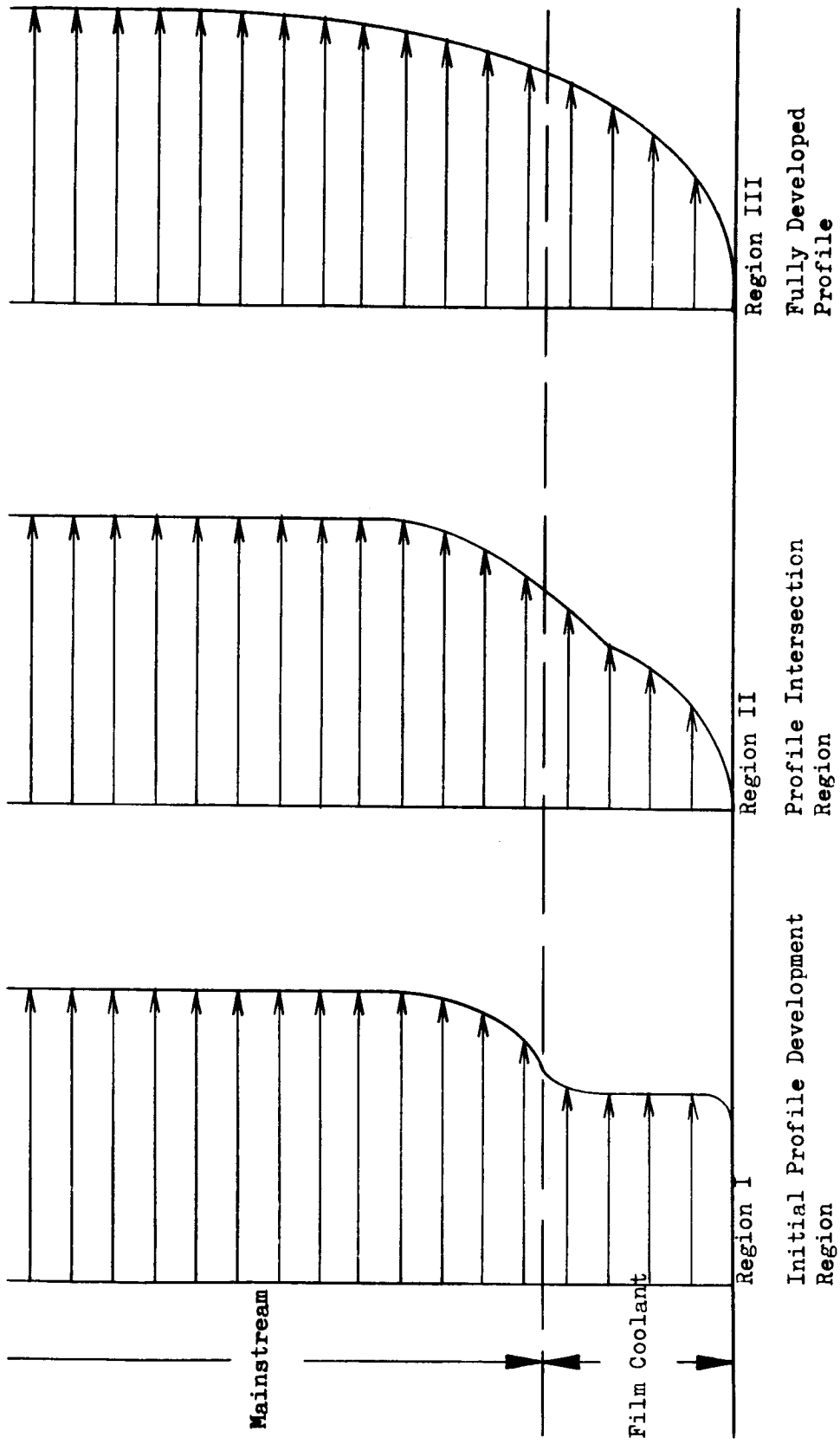

Figure 23. Three Regions of Velocity and Temperature Profile Development

The effect of coolant-to-mainstream velocity ratio (a), may be examined to determine the effects of the slot height change in the actual case upon the point of initial temperature rise of the wall surface.

The initial first approximation assumption may be made that the coolant weight flowrate required to cool a given surface area is independent of the velocity ratio. Then:

$$\dot{W}_c = \rho_c V_c \delta z = \text{constant} \tag{160}$$

For a constant mainstream temperature, pressure and constant coolant density:

$$V_c/V_g (\delta/x) = K/x \tag{161}$$

Utilizing the relationships in the previous table, the solution indicated in Fig. 24 results. The closest axial point of wall temperature rise from the coolant injection temperature will occur at:

$$V_c/V_g = 0.45 , \quad (\delta V_c/V_g) = \text{constant}$$

The choice of a constant film-coolant depth indicates an increase in the distance to the point of wall temperature rise with film-coolant depth. For this case, the minimum distance occurs at:

$$V_c/V_g = 0 , \quad (\delta = \text{constant})$$

For either this case or the previous case examined, the wall temperature rise is delayed as $V_c/V_g \rightarrow 1.0$.

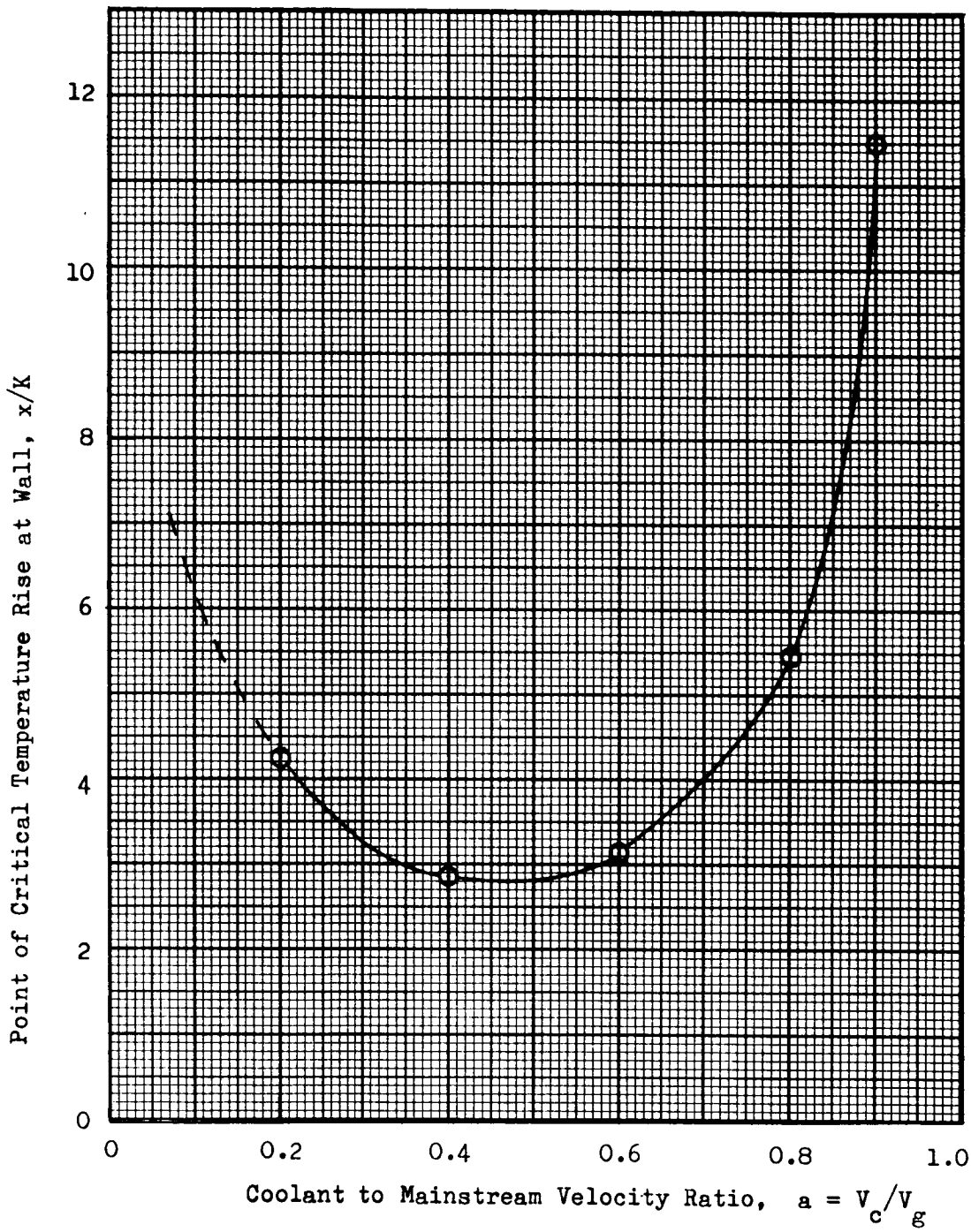

Figure 24. Location of Point of Wall Temperature Rise from Coolant Temperature Value

The combined effect of the penetration of the film-coolant region by the mainstream velocity and the wall shear resulting in the growth of a wall surface boundary layer may be expressed at the point of intersection of the two profiles as:

$$\delta_M + \delta_{BL} = \delta = \frac{x}{\varphi_M \, (Re_x{}^{\alpha})_M} + \frac{x}{\varphi_{BL} \, (Re_x{}^{\alpha})_{BL}} \tag{162}$$

For a laminar boundary layer growth on the wall surface, this results in

$$\delta/x = \frac{4.8}{(Re_x)^{0.5}} + \left(\frac{1 - a}{12}\right), \qquad \text{laminar} \tag{163}$$

and similarly for a turbulent boundary layer growth

$$\delta/x = \frac{0.2}{(Re_x)^{0.2}} + \left(\frac{1 - a}{12}\right), \qquad \text{turbulent} \tag{164}$$

For reasonable levels of length Reynolds number, it will be seen that the width of the mainstream-to-film coolant mixing zone increases much more rapidly than the growth of the boundary layer.

As a result, the case where the wall shear effects are neglected is justifiable providing the wall temperature has not risen significantly above the initial coolant temperature. In nondimensional form, this may be expressed as:

$$\frac{T_g - T_w}{T_g - T_c} \rightarrow 1.0$$

The wall temperature for a rocket motor design case would not achieve an absolute temperature much higher than 25 percent of the mainstream temperature because of wall material limitations. As a result, it may be anticipated that the regions of initial velocity and temperature profile formation can become an important fraction of the total film-cooled length as shown in Fig. 23 and 25.

Evaluation of the summary work of Hartnett, et al. (Ref. 35) indicates a considerable scatter in the available data in the region of main importance, namely:

$$1.0 \geq \frac{T_g - T_w}{T_g - T_c} \geq 0.75$$

which corresponds to:

$$\left(\frac{\rho_g V_g}{\rho_c V_c}\right)\left(\frac{x}{\delta}\right) \leq 50 \tag{165}$$

Film-Cooling Equation Development

Assuming similar transport properties for the film coolant and the mainstream, the velocity-temperature distribution may be expressed as

$$\frac{U - V_g}{V_c - V_g} = \left(\frac{T - T_\infty}{T_c - T_\infty}\right) \tag{166}$$

However, further review of this approach indicates that the film-coolant velocity profile and temperature profile may not have this exact similarity of form, i.e., $n \neq 1$ in the relationship:

$$\frac{U - V_g}{V_c - V_g} = \left(\frac{T - T_\infty}{T_c - T_\infty}\right)^n \tag{167}$$

especially near the wall surface where the velocity actually approaches zero due to wall shear.

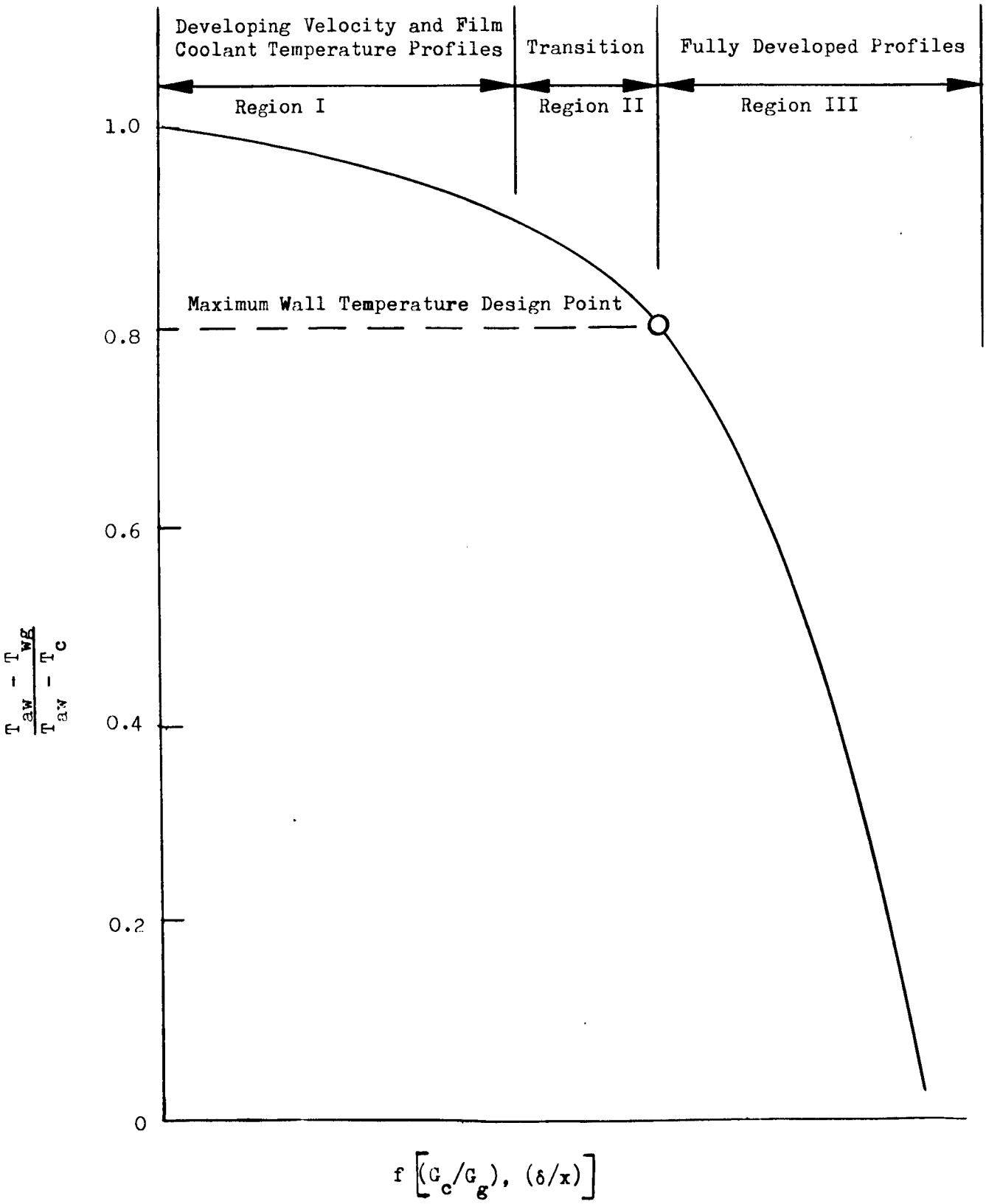

Figure 25. Typical Trend of Experimental Data for Film Cooling

The assumption of the asymptotic velocity profile solution used presently, i.e., with the use of a solution without wall shear, allows a compatibility with the temperature profile requirement which has a similar form to the assumed no wall shear case.

The analysis proposed below results in a solution for the average coolant temperature axial gradient $(\partial \bar{T}_c / \partial x)$. It will be assumed that the wall temperature gradient follows the same form, i.e.,

$$\frac{\partial T_w}{\partial x} = \frac{\partial \bar{T}_c}{\partial x} \tag{168}$$

The lag of the wall temperature rise from the coolant entrance and the extent of exactness of the relationship above requires experimental confirmation under temperature, flow, and heat transfer rate conditions at a level appropriate to rocket engine conditions.

Employing the relationships:

$$\zeta = \frac{U}{V_g} \quad , \quad a = \frac{V_c}{V_g} \quad , \quad \Lambda = \left(\frac{T}{T_\infty}\right) \tag{169}$$

and Eq. 166, the expression for Λ becomes:

$$\Lambda = \left(1 - \frac{T_c}{T_\infty}\right)\left(\frac{\zeta - a}{1 - a}\right) + \frac{T_c}{T_\infty} \tag{170}$$

With assumptions of constant pressure mixing and the perfect gas law, as well as a low Mach number, the energy transport can be written (Ref. 7) per unit width from the energy integral as:

$$q = z \int_{y = y_1}^{y = y_2} \rho U C_p \left(T_{aw} - T\right) dy \tag{171}$$

This equation may be transformed by the method of Korst (Ref. 36) to:

$$q = \rho_\infty V_g C_p T_\infty z \int_{y = y_o}^{y = y_1} \frac{\zeta(1 - Ca^2)(1 - \Lambda)}{\Lambda - Ca^2 \zeta^2} dy \tag{172}$$

From Eq. 158:

$$\frac{d\eta}{dy} = \frac{\varphi Re^\alpha}{x} \tag{173}$$

Combination of Eq. 171, 172, and 173 gives:

$$q = \frac{\rho_\infty V_g C_p T_\infty x z}{Re^\alpha} \left(1 - \frac{T_c}{T_\infty}\right) \psi_M' \tag{174}$$

where:

$$\psi_M' = \frac{1 - Ca^2}{\varphi (1 - a)} \int_{\eta = \eta_o}^{\eta = \infty} \frac{\zeta (1 - \zeta)}{\Lambda - Ca^2 \zeta} d\eta \tag{175}$$

The differential bulk temperature rise of the film coolant is given by:

$$dq = \dot{W}_c C_{p_c} dT_c \tag{176}$$

The final form of the film-cooling equation is:

$$\frac{dT_c}{dx} = \frac{\rho_\infty V_g C_p (T_\infty - T_c) z}{\dot{W}_c C_{p_c} Re^\alpha} \psi'_M \tag{177}$$

The comparable modified form of Eq.177 as originally developed by Hatch and Papell (Ref. 31) and modified in Ref. 1 is:

$$\psi_F' = \frac{0.026}{\eta_f} \quad \text{with } \alpha = 0.2 \tag{178}$$

where the value of η_f was experimentally found to be a function of coolant-to-mainstream velocity ratio. This is substantiated by Eq. 175.

The values of η_f for film cooling can be evaluated from Ref. 31 for variable velocity ratios as:

$$\eta_f = \frac{\varphi}{1 + 0.4 \tan^{-1}\left(\frac{V_g}{V_c} - 1\right)} \tag{179}$$

and from a review of Ref. 31 by Ref. 1 as

$$\eta_f = A + (1-A)\, e^{\left(-B \frac{C_{p_c} G_c}{C_{p_g} G_g}\right)} \tag{180}$$

The actual data were found to vary from values of:

$$0.2 < \eta_f < 1.0$$

Table 3 compares calculated values of ψ_M' from the new mixing approach with ψ_F' which was previously developed from the film-coefficient approach. An arbitrary value of η_f equal to 25 percent was assumed. In general, it is seen that the new approach predicts higher values for a number of conditions. The behavior of the mixing solution indicates a shallow cooling flow requirement peak at an intermediate value of V_c/V_g and a diminishment to zero at $V_c/V_g = 1.0$. This trend is illustrated by the empirical relationship in Eq.180, i.e., an improvement in cooling efficiency or reduction in effective energy transfer level as the two velocities become more nearly equal.

TABLE 3

COMPARISON OF FILM-COOLING THEORIES

V_c/V_g	T_c/T_∞	ψ_M'	ψ_F'
0.2	0.2	0.16	0.10
0.2	0.1	0.18	0.10
0.2	0.05	0.19	0.10
0.5	0.1	0.24	0.10
0	0.1	0.14	0.10
0.8	0.1	0.30	0.10
0.9	0.1	0.32	0.10
0.3	0.1	0.20	0.10

Conditions

$Re = 10^6$ $\delta/x = 0.001$

$\alpha = 0.2$ $Ca = 0$

$\varphi = 5.0$ $\eta_f = 0.25$

LIQUID FILM-COOLANT SURFACE STABILITY

The stability of small disturbances on liquid film surfaces was investigated analytically. With injection of a liquid film coolant such as RP-1 into a film-cooled engine at higher chamber pressure, it can be expected that if the relative film coolant to gas mass velocity is small, a film-cooled length will be established where the coolant layer adheres to the surface with diffusion-controlled mixing of the two streams. As the relative shear level is increased between the coolant flow and the gas stream by increased relative velocity, the film-coolant surface will no longer maintain its ideal streamline flow condition but will exhibit an exponentially increasing surface instability to the point of breakaway of the film-coolant layer from the wall surface and subsequent loss in film-cooling benefit. The relative shear mixing of the film coolant with the main gas stream, as well as the film surface breakaway point become two dominant design considerations in the specification of the film-coolant flow requirements per injection slot and in the specification of the point for downstream location of the next slot. Figure 26 illustrates the proposed behavior for a liquid film coolant on a wall surface to the point of breakaway.

An initial analysis was performed assuming a slow-speed flow. The higher velocity condition is considerably more complex. An oscillation potential for the common boundary at the liquid-gas interface (y = 0) is written as:

$$\varphi = C_o \left[\cosh K (y + h)\right] (\cos Kx)\, e^{i \sigma t}, \quad -h<y<o \tag{181}$$

$$\varphi' = C_1\, e^{-Ky} (\cos Kx)\, e^{i \sigma t}, \quad o < y < \infty \tag{182}$$

according to the technique of Lamb (Ref. 37). A surface periodic wavelength of λ is related to K as:

$$K = \frac{2\pi}{\lambda} \tag{183}$$

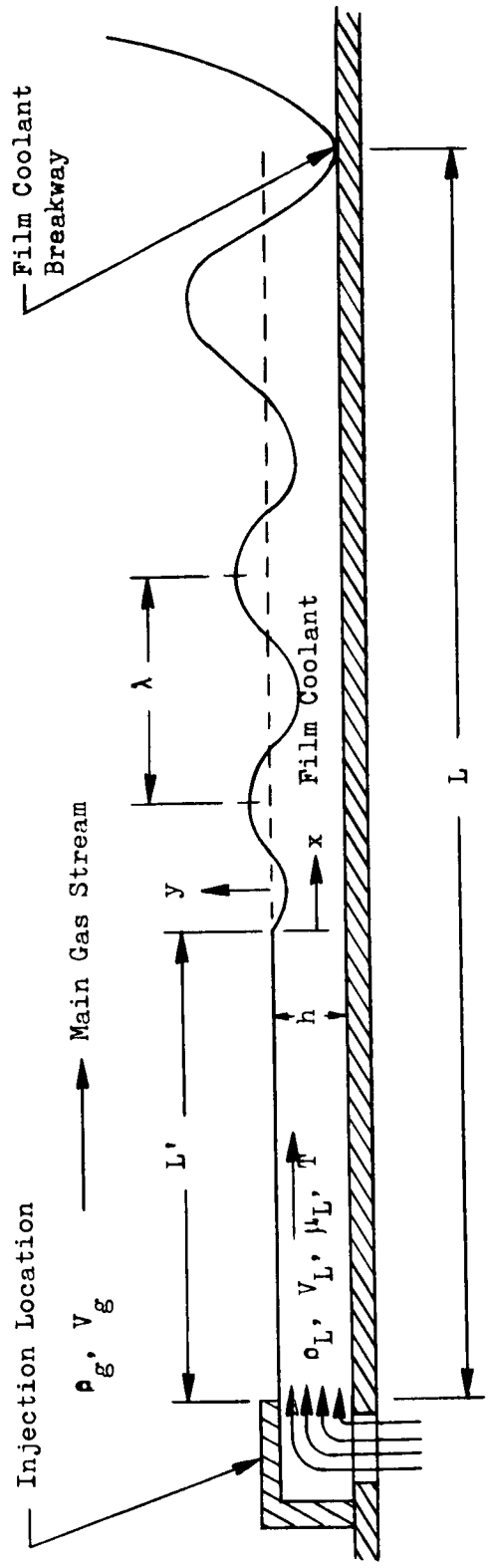

Figure 26. Schematic of Analytical Model for Film-Coolant Stability

An equation for the disturbed surface (η) may be written as:

$$\eta = a (\cos Kx) e^{i \sigma t} \tag{184}$$

For values of σ of 0, a neutrally stable condition exists. For imaginary values of σ, i.e., $i\sigma$, a real value is obtained and the surface disturbance will grow exponentially with time.

Using a balance for the pressure, aerodynamic, viscous and surface tension forces, Wagner (Ref. 38 and 39) has shown that the exponential breakup factor (σ) may be composed of stabilizing and destabilizing factors as:

$$\sigma^2 + \sum_{i \text{ forces}} (\sigma^2)\, i = 0 \qquad \sigma_i^{\,2} = \sigma_1^{\,2} + \sigma_2^2 + \ldots\ \sigma_n^2 \tag{185}$$

For negligible graviational effects and a gas density small compared to the liquid density, Eq. 185 becomes:

$$\sigma^2 + \frac{4\,\mu_L\,\varphi\,\sigma\,K^2}{\rho_L} + \frac{2\,K\,\sigma\,(\rho_L\,V_L - \rho_g\,V_g)}{\rho_L} - \frac{K^2(\rho_L\,V_L^2 - \rho_g\,V_g^{\,2}}{\rho_L} + \frac{TK^3}{\rho_L} = 0 \tag{186}$$

(viscous forces) + (aerodynamic forces) + (surface tension forces) = 0

which is of the form

$$a\,\sigma^2 + b\,\sigma + c = 0 \tag{187}$$

For an instability to occur:

$$(b^2 - 4ac) < 0 \tag{188}$$

This condition will produce imaginary values of σ and, hence, a surface breakup. The relationship for a disturbance growth becomes:

$$b^2-4ac = \left[\frac{4\,\mu_L\,\varphi\,K^2}{\rho_L} + \frac{2K\,(\rho_L\,V_L-\rho_g V_g)}{\rho_L}\right]^2 - 4\left[TK^3 - \frac{K^2(\rho_L\,V_L^2-V_g^2\,\rho_g)}{\rho_L}\right] \leq 0 \tag{189}$$

Defining the following:

$$\psi = K\,h \tag{190}$$

$$We_g = \frac{\rho_g\,V_g^2\,h}{T} \qquad We_L = \frac{\rho_L\,U_L^2\,h}{T} \tag{191, 192}$$

$$Re_g = \frac{\rho_g\,V_g\,h}{\mu_g} \qquad Re_L = \frac{\rho_L\,V_L\,h}{\mu_L} \tag{193, 194}$$

Equation 189 subsequently becomes, in a nondimensional form for slow motion:

$$\frac{2\,\varphi\,\psi}{Re_L} + \left[1 - \left(\frac{Re_g}{Re_L}\right)\left(\frac{\mu_g}{\mu_L}\right)\right]^2 - \left[\frac{\psi}{We_L} - \left(1 - \frac{We_g}{We_L}\right)\right] \leq 0 \quad \text{(unstable)} \tag{195}$$

It is seen that for slow motion, the nondimensional groupings of importance become:

$$\frac{\psi}{Re_L}, \quad \frac{\psi}{We_L}, \quad \frac{We_g}{We_L}, \quad \frac{Re_g}{Re_L}\left(\frac{\mu_g}{\mu_L}\right)$$

For a finite depth case ($K\,h < \infty$), i.e., with $\tanh\,(\psi) < 1$, the nondimensional groupings may be derived as:

$$\frac{\psi}{Re_L\,\tanh\,\psi}, \quad \frac{\psi}{We_L\,\tanh\,\psi}, \quad \frac{We_g}{We_L\,\tanh\,\psi}$$

$$\left(\frac{Re_g}{Re_L}\right)\left(\frac{\mu_g}{\mu_L}\right)\left(\frac{1}{\tanh\,\psi}\right)$$

It may be hypothesized that these parameters remain the important dimensionless groupings for high-speed flow with a shift of relative importance from one to another as the flow velocities are increased. An analytical approach to the high-speed flow stability case would be extremely difficult. Consequently, experimental work with the use of the above parameters for correlation should provide a more practical approach.

The stability of a liquid surface has been examined experimentally by Kinney, et al. (Ref. 40), Graham (Ref. 41), and Sellers (Ref. 42). They developed an inter-relationship between the established coolant film condition and the mainstream Reynolds number based on a friction velocity. Employing a coolant film thickness Reynolds number,

$$Re_L = \left(\frac{\rho_L V_L h}{\mu_L} \right) \tag{196}$$

regimes may be established wherein laminar, transition, turbulent and unstable flow conditions are present. The related friction velocity mainstream Reynolds number may be defined as:

$$Re_g^* = \left(\frac{\rho_g V_g^* h}{\mu_g} \right) \tag{197}$$

The relationship of the two parameters may be expressed as:

$$Re_L = f\,(Re_g^*) \tag{198}$$

Although surface tension effects were observed in these experiments, no attempts were made to provide for the inclusion of a Weber number effect on the film surface stability as would be predicted analytically.

The liquid Reynolds number values observed to result in transition to turbulent flow and also instability are tabulated in Table 4. The effectiveness of the film has been found to gradually diminish with an increased Reynolds number (Re_L) to a value of approximately 400. At conditions much in excess of this value, the flow was seen to rapidly disperse into the mainstream with a corresponding diminishment of heat transfer effectiveness.

The use of the critical film-depth Reynolds number for description of the allowable injection quantity and, consequently, the length between film-coolant injection points is appropriate to film-cooled designs where subcritical pressure operation occurs. Under these conditions, the film coolant experiences a sensible heat absorption to the vaporization point followed by vaporization at constant temperature and diminishment of the film thickness. At supercritical pressures, the behavior of the "fluid" coolant will be such that a continuous change in properties will occur. A coolant such as RP-1 will be subject to cracking and decomposition as the film coolant increases in temperature. If the behavior of the RP-1 film coolant is such that it acts analogously to a liquid layer with sensible heat absorption rather than a gas for a portion of the film-cooled length, the stability length may be established on a similar basis to that previously suggested.

The critical film-depth Reynolds number may be expressed in the form:

$$\left(Re_L\right)_{critical} = \left(\frac{G_c\ h}{\mu_L}\right)_{critical} \tag{199}$$

TABLE 4

STABILITY REGIMES FOR FILM-COOLANT ADHERENCE

Re_L	Re_g^*	Regime	Stable
< 60	< 12	Laminar	Yes
160 to 200	12 to 21	Transition	Yes
360	37	Turbulent	Yes
> 360	> 37	Turbulent	No

Data points from Ref. 40

Substitution of this equation into the modified film-cooling equation form gives the following relationship for the film-cooled length:

$$\left(\frac{T_{aw} - T_w}{T_{aw} - T_c}\right) = e^{-(h_g\, h)/(\eta_f\, C_{p_c}\, \mu_L\, Re_{crit})} \tag{200}$$

With a further substitution of a critical Reynolds number value of 400,

$$\left(\frac{T_{aw} - T_w}{T_{aw} - T_c}\right) = e^{-(0.0025\, h_g\, h)/(\eta_f\, C_{p_c}\, \mu_{crit})} \tag{201}$$

The variation of the film-viscosity value is quite significant from the "liquid" state to an elevated temperature at supercritical pressure. Since a reduced viscosity corresponds to a decreased allowable film-cooled length according to Eq. 201, a good knowledge of the viscosity to the critical instability point is necessary.

Whether or not the behavior of the RP-1 film coolant at supercritical pressure and proposed operating temperatures is treated from a flow stability standpoint analogously to the subcritical liquid layer case or as a mixing process similar to the proposed gaseous film-cooling approach, property values including effective heat capacity and viscosity are required. The treatment of the RP-1 coolant as a gaseous coolant should be considered because the elevated temperature condition and expected decomposition of the coolant would appear to warrant it.

THERMAL STRESS STUDIES

Previous studies (Ref. 1, 43, and 44) have shown that the thin-walled tubes of a regeneratively cooled thrust chamber operating at high temperatures are subject to inelastic thermal buckling and to a short cyclic operating life due to tube wall plasticity introduced by large thermal gradients. During the study reported here, the criteria for plasticity onset on the outer and inner walls were examined in terms of the imposed heat flux and internal pressure. The elastic buckling equations were assumed to provide nondimensional buckling parameters suitable for inelastic studies. Comparisons were then made with available buckling data and equations for confirmation of parameter influence. Fatigue life comparisons of materials under elevated temperature were analytically examined and the comparative effect of longitudinal and tangential stresses explored.

Tangential Thermal Stress Plasticity Onset

A limitation in the degree of regenerative cooling which may be tolerated in a combined film-regeneratively cooled design, as described in Ref. 1 is the plastic thermal stress condition induced in the wall surface due to the wall thermal gradient. In an actual design, the coolant velocity condition for the regenerative portion of the heat load absorption may well be defined by the allowable wall plasticity induced, as well as by the coolant pressure drop.

A refined evaluation for the onset of plasticity in tubular structures was presented by Bland (Ref. 45) in terms of an equation describing the yield criterion for a tangential thermal stress. The equations developed

by Bland have been used for the specification of two plastic thermal stress onset cases where: (1) the plasticity onset occurs at the outer radius or heated surface, and (2) the coolant sidewall surface yields first. The stability equation governing the behavior may be put in terms of the nondimensional pressure parameter (δ_1) comparing the difference in outer surface (q), and inner surface (p), applied pressure relative to the yield stress (σ). A second nondimensional parameter (δ_2) relates the thermal strain to an allowable strain. The third (δ_3) is a relationship between the outer and inner tube radii.

$$\delta_1 = (p - q)/\sigma \tag{202}$$

$$\delta_2 = \frac{E\,\alpha\,(T_b - T_a)}{2(1 - \mu)\,\sigma\,\ln_e\,(r_b/r_a)} \tag{203}$$

$$\delta_3 = (r_b/r_a) \tag{204}$$

For plasticity commencement at the outer compressive surface:

$$\delta_1 = -1/2\ (\delta_2 - 1)\,(1 - \delta_3^2) + \delta_2\,\ln_e\,(1/\delta_3) \tag{205}$$

Similarly, for plasticity commencement at the inner wall surface in tension:

$$\delta_1 = 1/2\ (1 - 1/\delta_3^2) - \delta_2\left[\ln_e\,\delta_3 - 1/2\left(1 - 1/\delta_3^2\right)\right] \tag{206}$$

The solution to these equations was programmed on the digital computer for definition of the pressure and thermal gradient required for plasticity commencement. The results of the digital computer program are shown in Fig. 27 and 28. For a given yield stress, pressure condition,

$$\delta_1 = \left(\frac{p - q}{\sigma}\right) \qquad \delta_2 = \frac{E\alpha\,(T_b - T_a)}{2\,(1 - \mu)\sigma\,\ln_e\left(\frac{r_b}{r_a}\right)}$$

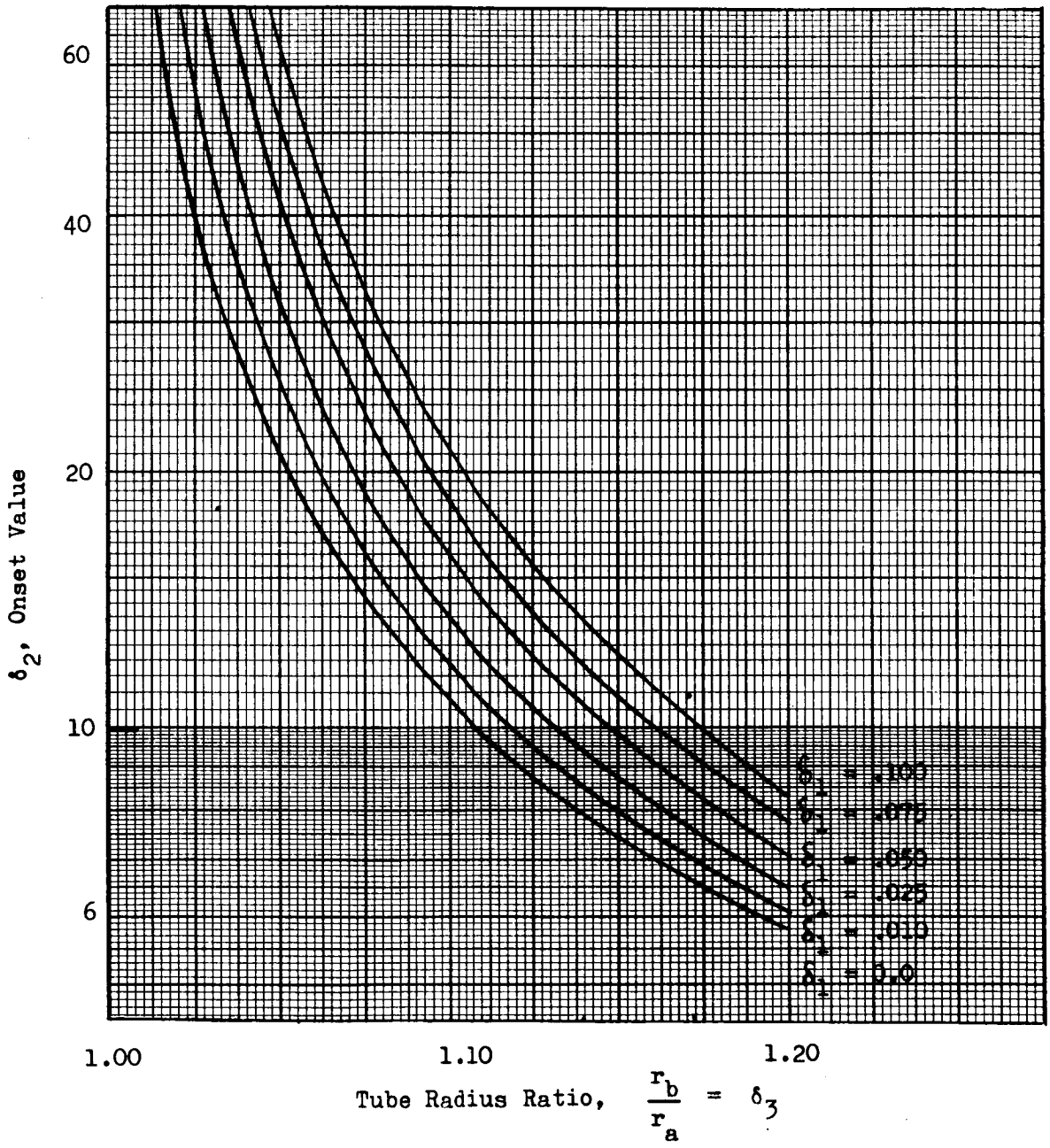

Figure 27. Onset of Plasticity at Tube Wall Outer Surface

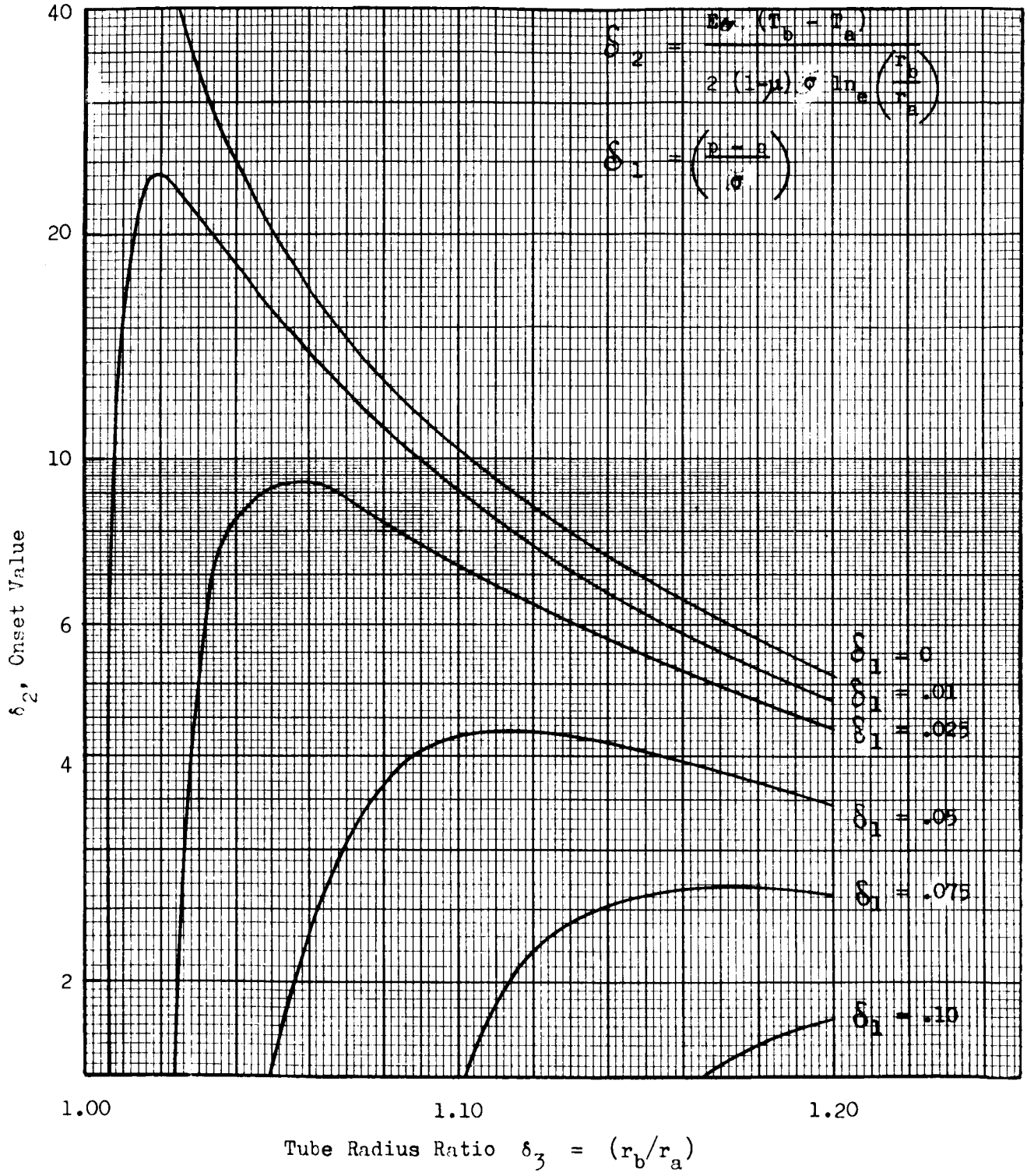

Figure 28. Onset of Plasticity on Tube Wall Inner Surface

and tube radius ratio, the plasticity will occur first on the inner wall and will be followed under high-loading conditions by plasticity at the heated surface. Under actual engine firing conditions, the yield stress at the outer surface will be at a reduced condition due to elevated temperature and, as a result, yielding will occur first at the outer surface. It is seen in Fig. 27 that an increased internal tube pressure will be somewhat beneficial in reducing the tendency toward plasticity at the outer surface since an increased internal pressure contributes to a tensile stress at the outer wall surface (r_b), whereas the thermal stress induces a compressive loading.

Figure 29 shows the behavior of the tube wall under the combined pressure and thermal stress condition. Under high thermal gradient conditions, an inner core of material exists where the stress condition is elastic. At the outer and inner wall surfaces, however, the material will be in a plastic state.

The nondimensional strain parameter (δ_2) given by Eq. 203 may be translated into an equivalent heat flux by consideration of the radial heat conduction equation.

$$q/A_b = \frac{k \Delta T}{r_b \ln_e \left(\frac{r_b}{r_a}\right)} \tag{207}$$

Combining Eq. 203 and Eq. 207 yields:

$$\delta_2 = \frac{E \alpha (q/A_b) r_b}{2 (1 - \mu) \sigma k} \tag{208}$$

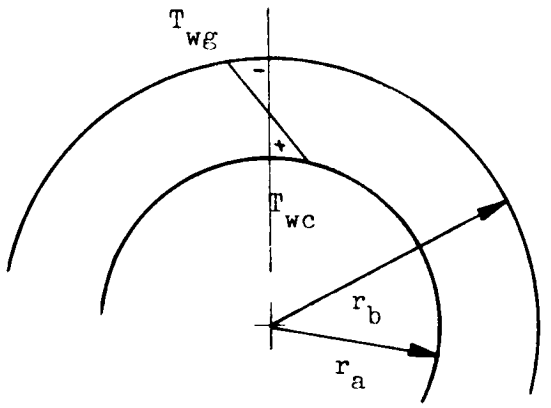

$\Delta T < \Delta T$ critical
(elastic condition)

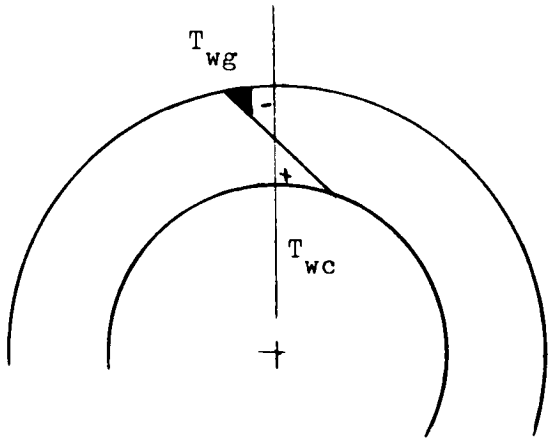

$\Delta T > \Delta T$ critical
(plastic outside surface)

Note: Shading indicates plastic condition

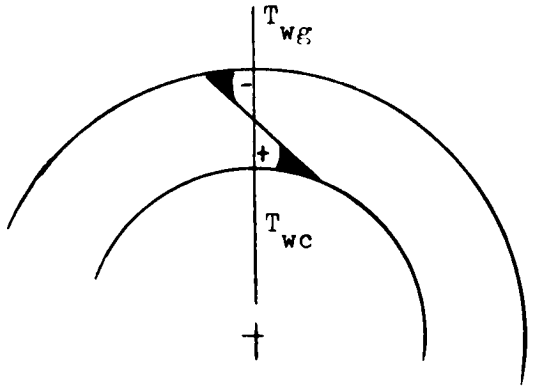

$\Delta T \gg \Delta T$ critical
(plastic outer and inner surface)

Figure 29. Tangential Thermal Stress Distribution

The alleviation of the tangential thermal stress severity, if the heat flux conditions cannot be reduced below yield conditions, becomes imperative because the degree of plasticity defines the cyclic operating life. Since the internal pressure stress condition acts to provide a tensile stress on the outward surface, whereas the thermal stress provides an opposite effect, an augmentation of the pressure stress effect may be a reduction in tube radius. Under combined pressure and thermal loading, the severe compressive tangential thermal stress may be partially or totally compensated by flattening the tube crown. The applied internal pressure provides a moment resulting from the tendency of the tube to assume a circular shape. As the tube achieves the operating temperature conditions under applied heat flux, the accompanying effective thermal stress is consequently reduced.

The complex biaxial thermal and pressure stress picture under near-plastic and plastic conditions requires careful scrutiny if the tubular-wall concept is to be used for the combined film-regenerative cooling method for LO_2/RP-1 propellants in particular.

From the plasticity onset criteria in cylindrical tubes with uniform heating and uniform properties just examined, the heat fluxes imposed at high chamber pressure can be seen to result in considerable yielding of the wall material. As mentioned above, the complex nonlinear equations given by Bland (Ref. 45) for stress distribution in the tangential and radial directions were programmed for digital computer evaluation of nonlinear plastic wall conditions assuming small longitudinal tube stresses. The complexity of the solution by Bland did not allow ready conversion to account for temperature-dependent material properties. Furthermore, the solution assumes plasticity to commence at the inner wall surface and to progress to the outer surface.

Figure 30 shows the computer results for a 0.107-inch-OD x 0.010-inch-wall 347 stainless-steel tube for a heat flux of 21.5 Btu/in.^{2}-sec. The radial stress (σ_r) is small compared with the tangential stress (σ_t) which is much above the yield point on the inner wall (radius = 0.0435 in.) The predicted compressive stress at the outside wall is above the yield point. Thus, a plastic region is predicted at both surfaces. When yielding occurs, the neutral stress point moves to the direction of the unyielded portion of the wall. It is shown below that when yielding occurs at both surfaces, the neutral stress point shifts toward the portion of the wall with the least amount of yielded material.

As a result of the small radial stresses due to the relatively thin wall relative to the tube radius that occurs for a high chamber pressure design, the Tresca yield criterion for a case of small longitudinal stress becomes:

$$\sigma_t - \sigma_r = \sigma_y \qquad (\sigma_t > \sigma_z > \sigma_r) \tag{209}$$

which reduces to:

$$\sigma_t \approx \sigma_y \tag{210}$$

and the one-dimensional case without curvature may be examined, such that inelastic effects can be considered at the inner and outer walls. A graphical approach for visualization of the degree of plasticity, the strain, and the stresses induced was used. This approach was the most practical for the study undertaken; however, the technique is readily amenable to digital computer solution. No distortion of the tube cross section was considered. In the actual situation, distortion of the tube

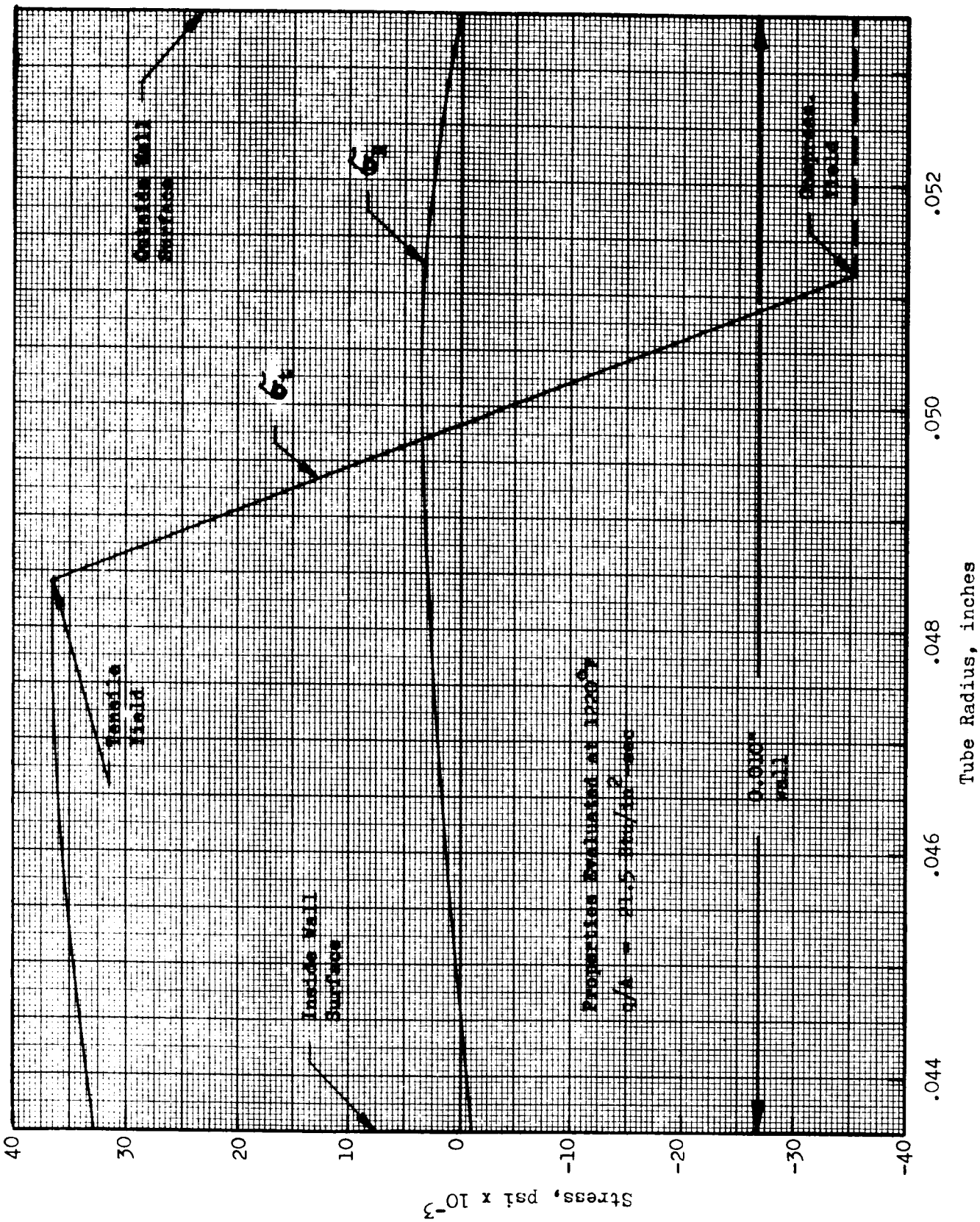

Figure 30. Nonlinear Plastic Stress Solution for 347 Stainless Steel Tube with 0.010-inch Wall

crown curvature to relieve tube stresses will occur; thus, the analytically computed stress conditions are higher than actual. The distortion of the tube crown is dependent upon the tube thickness-to-diameter ratio (t/D).

For the calculations, a constant thermal coefficient of expansion and constant thermal conductivity were used. However, a graphical method does allow variation of these properties if desired. It was assumed that superposition of strains could be used; thus, tensile pressure strain was added to linear thermal strain. The pressure strain (ϵ_p) derived from the internal and external pressure stresses was set for the study examples at 50 percent of ambient yield value. Figure 31 shows the elastic-plastic stress-strain relation used for the case of Inconel-X. From the wall-temperature distribution defined by the heat flux and cooling conditions and stress-strain relations for various temperatures, an appropriate distribution of the yield and ultimate stresses was developed.

Figure 32 illustrates the component stress, strain, and temperature distributions for a high-heat-flux condition of 25.9 Btu/in.^{2}-sec. Other conditions of heat flux were studied up to the heat conduction limit of the 0.010-inch-wall-thickness Inconel-X material with an imposed temperature limit of 1570 F. The shaded areas in Fig. 32 represent plastic regions imposed in the wall. The approach of the plastic region to the ultimate stress line is indicative of approach to failure. For this study, the ultimate stress was chosen as the 1.5-percent strain point. As heat flux is increased to the maximum allowable for wall heat conduction, the percentage of plasticity in the wall and the maximum plastic strain were both found to increase. The largest plasticity for the typical examples chosen occurs at the inner wall due to the added internal pressure stress. For zero internal pressure stress, the greatest plasticity

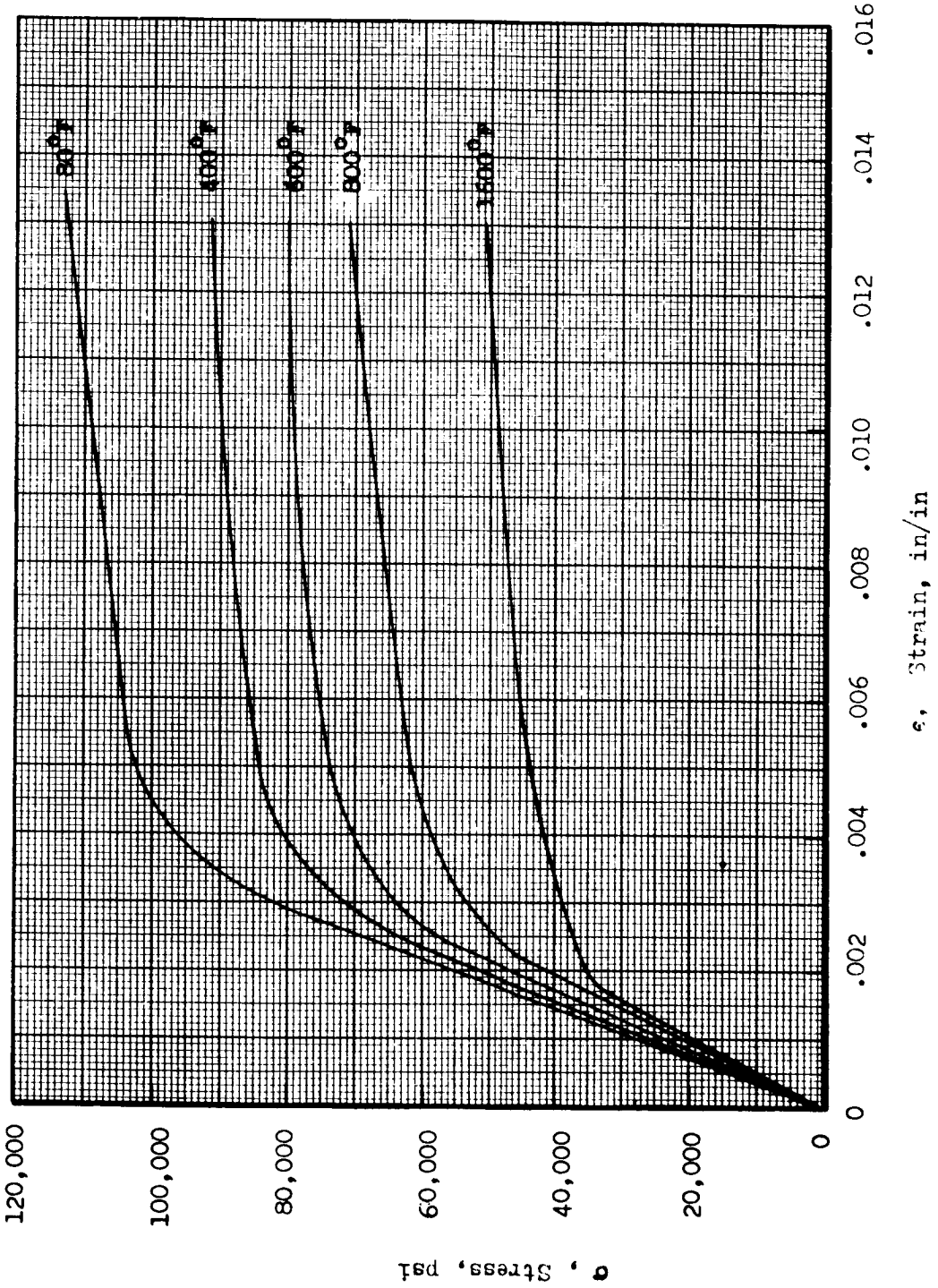

Figure 31. Stress-Strain Diagram for Inconel-X

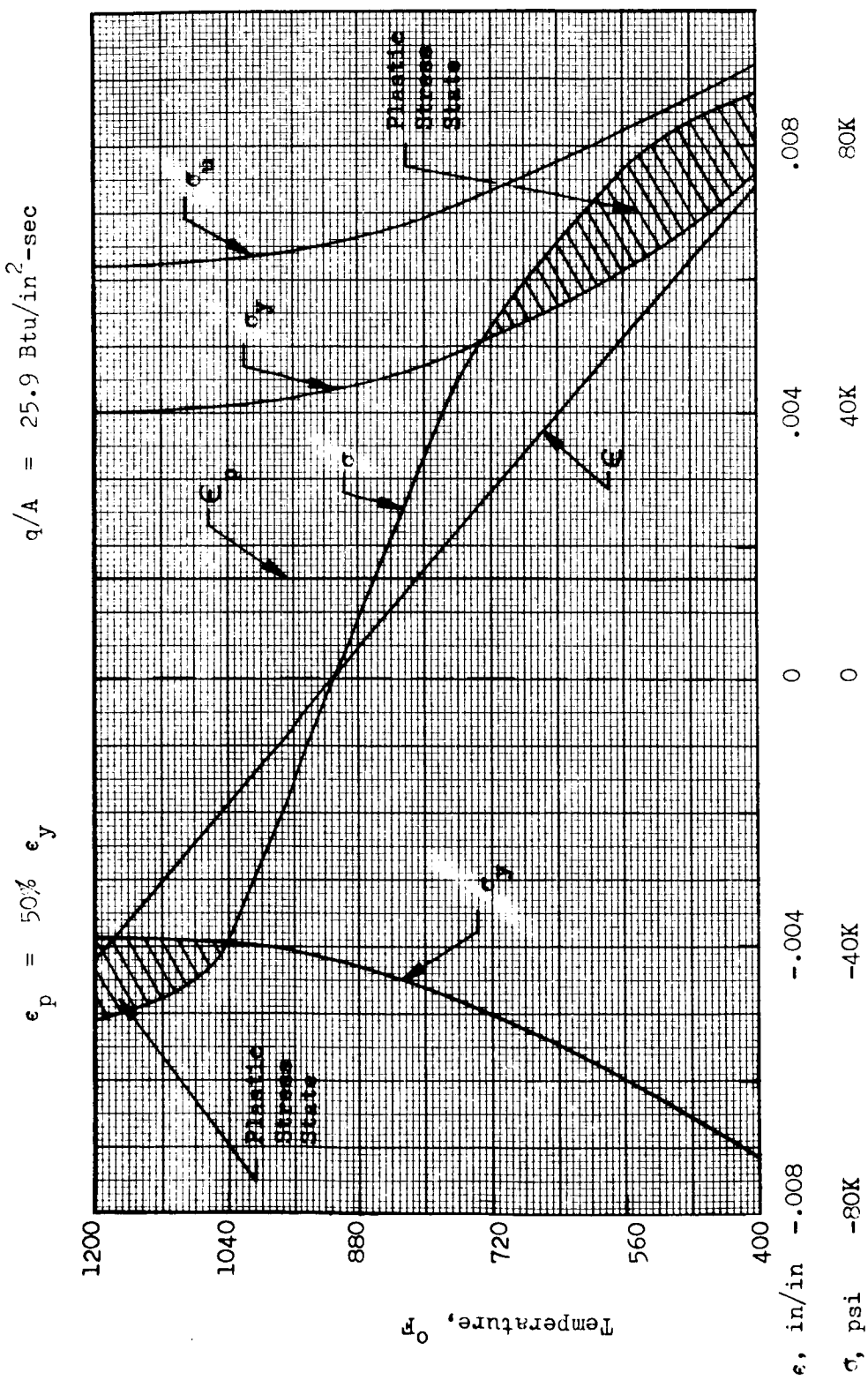

Figure 32. Imposed Stress and Strain in Inconel-X Tube Wall with Assumed Linear Temperature Distribution

occurs at the outer wall (compression) due to a lower yield point at the higher temperature. For an appropriate tube internal pressure condition, an equal amount of plasticity may be introduced in both tube surfaces.

Figure 33 shows the percentage of the wall in the plastic region based on thickness as a function of heat flux. An asymptotic increase to the wall conduction limit is noted. Thus, a large degree of plasticity must be tolerated if heat fluxes of 20 to 40 Btu/in.^{2}-sec are to be transferred through a tube wall.

Longitudinal Thermal Buckling

The nonuniformity of heating around the thrust chamber tube periphery due to the applied heat flux on only a portion of the tube circumference results in a tendency for growth of the heated surface relative to the unheated back side (Ref. 1). Restrained growth of the heated surface will result in buckling of the heated surface and a corresponding transverse crack failure of the tube depending upon the maximum applied temperature differential.

Elastic Case. The behavior of thermal buckling may be developed first by assuming that the applied longitudinal thermal buckling load is large in comparison with the other applied loads. Such a consideration provides for a considerable simplification in the governing equations. The complex elastic buckling equations developed by Flugge (Ref. 46) for axial compression were put into the appropriate nondimensional parameters:

$$\text{Buckling} = f\left(\frac{\lambda}{D}, \frac{\sigma(1-\mu^2)}{E}, \frac{D}{t}, m\right) \qquad (211)$$

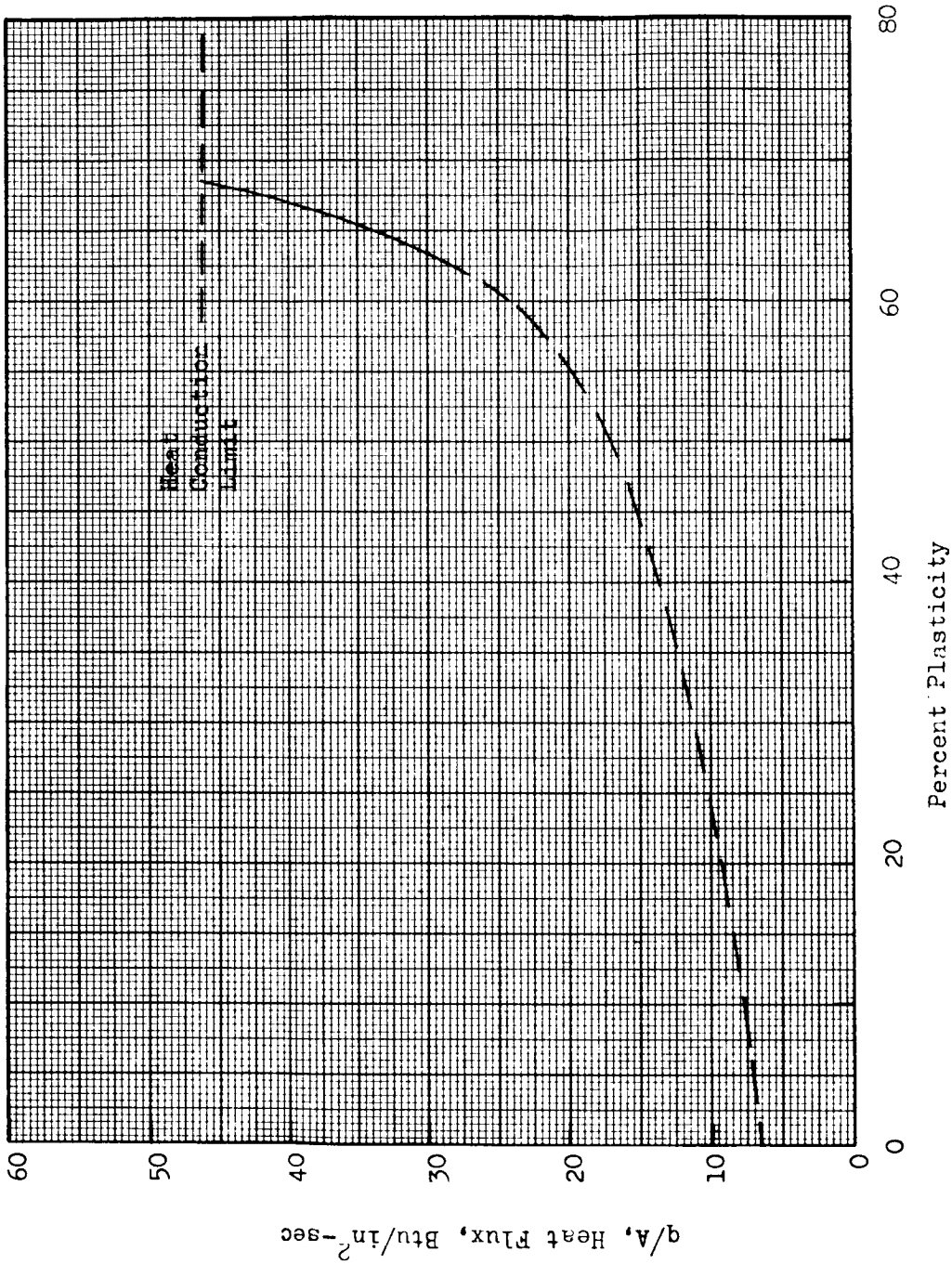

Figure 33. Degree of Plasticity for 0.010-inch Inconel-X

The first parameter represents the buckling wavelength-to-tube diameter ratio. The second describes the applied buckling "strain." The third represents the tube characteristic diameter-to-tube thickness ratio, where for thick-wall tubes, the representative diameter becomes the mean between the inner and outer value. The value (m) represents the number of buckling waves around the tube circumference as shown in Fig. 34. For thin walls and elastic behavior, buckling is such that the m-value tends toward an increased integer value. As illustrated in Fig. 34, fixed nodal points are provided between adjacent tubes at the contact points with an induced thermal buckling. Figure 35 shows a typical thermal buckling failure encountered during engine operation.

Figure 36 shows the solution of the buckling equations in terms of the above nondimensional parameters. For a tube of given diameter-to-thickness ratio, it is seen that the effects of a decreased buckling longitudinal wavelength and an increased number of nodal points around the tube circumference result in a slightly greater allowable strain at the failure point. For a decreased tube diameter-to-thickness ratio, the buckling strain at failure is significantly increased.

As a result, it is seen that for a chamber pressure design employing a tubular wall construction, a small tube diameter-to-thickness ratio is imperative. With a tubular design consisting of a brazed tube bundle, the longitudinal support provided by adjacent tubes and the braze filleting which reduces the effective exposed tube crown, increases the m value and decreases the longitudinal wavelength value.

Inelastic Case. The inelastic local buckling which occurs under high thermal stress conditions can be effectively treated by employment of a "buckling strain" concept due to the nonlinear behavior of the stress-

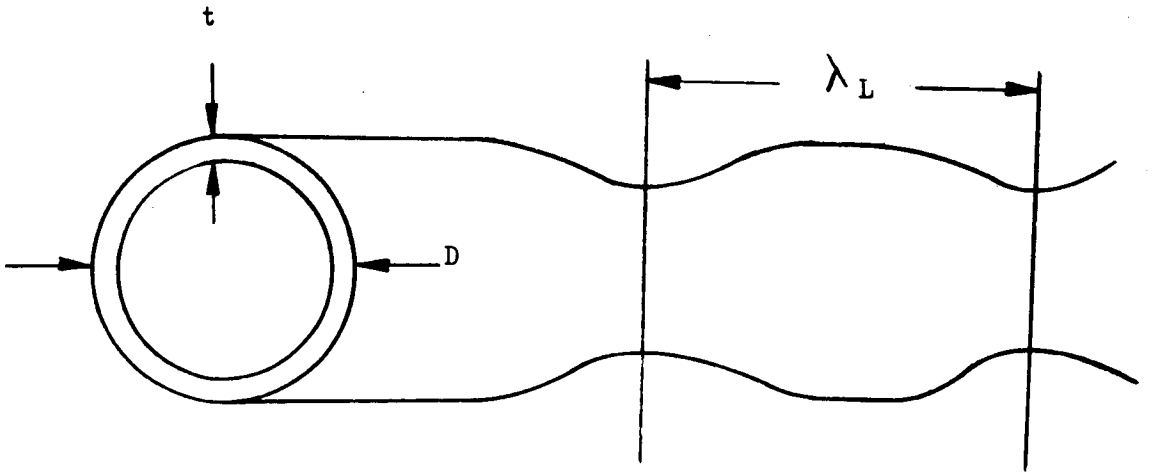

Ideal Longitudinal Buckling (m = 0)

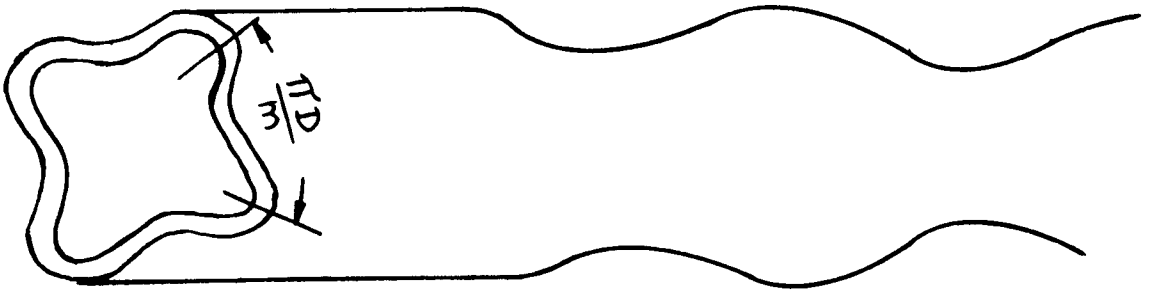

Ideal Longitudinal Buckling (m > 0)

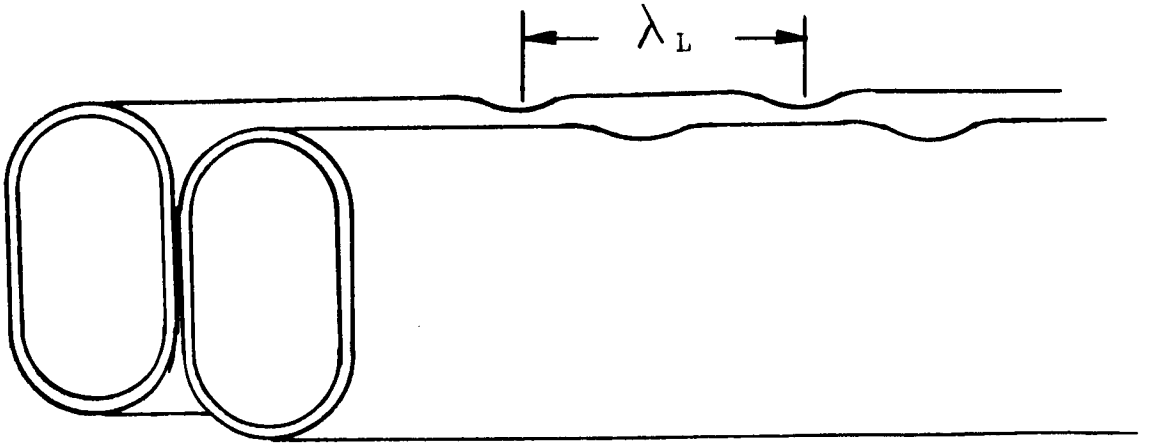

Actual Thrust Chamber Buckling

Figure 34. Buckling Behavior Under Thermal Loading

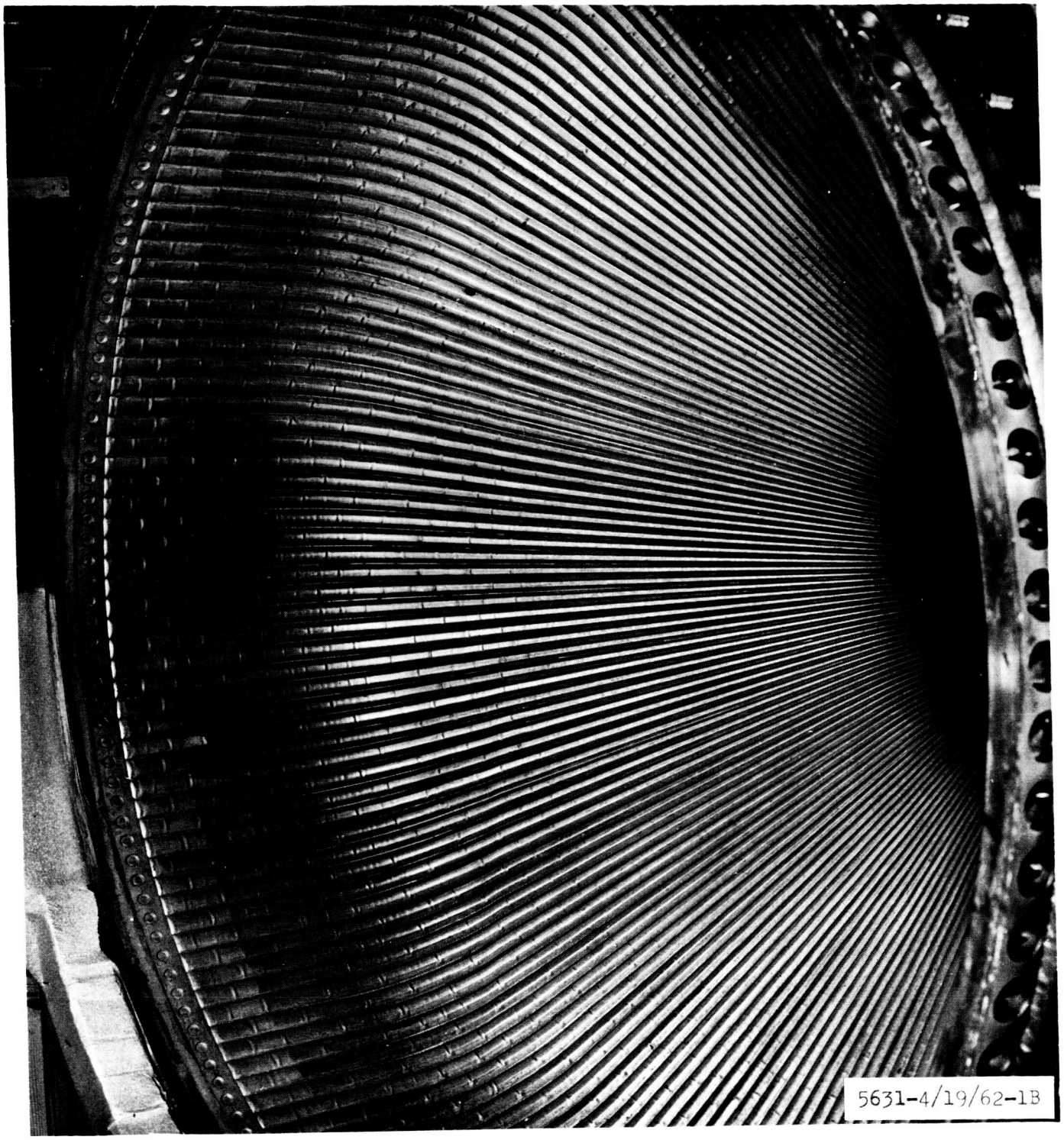

Figure 35. Chamber Showing Longitudinal Thermal Buckling

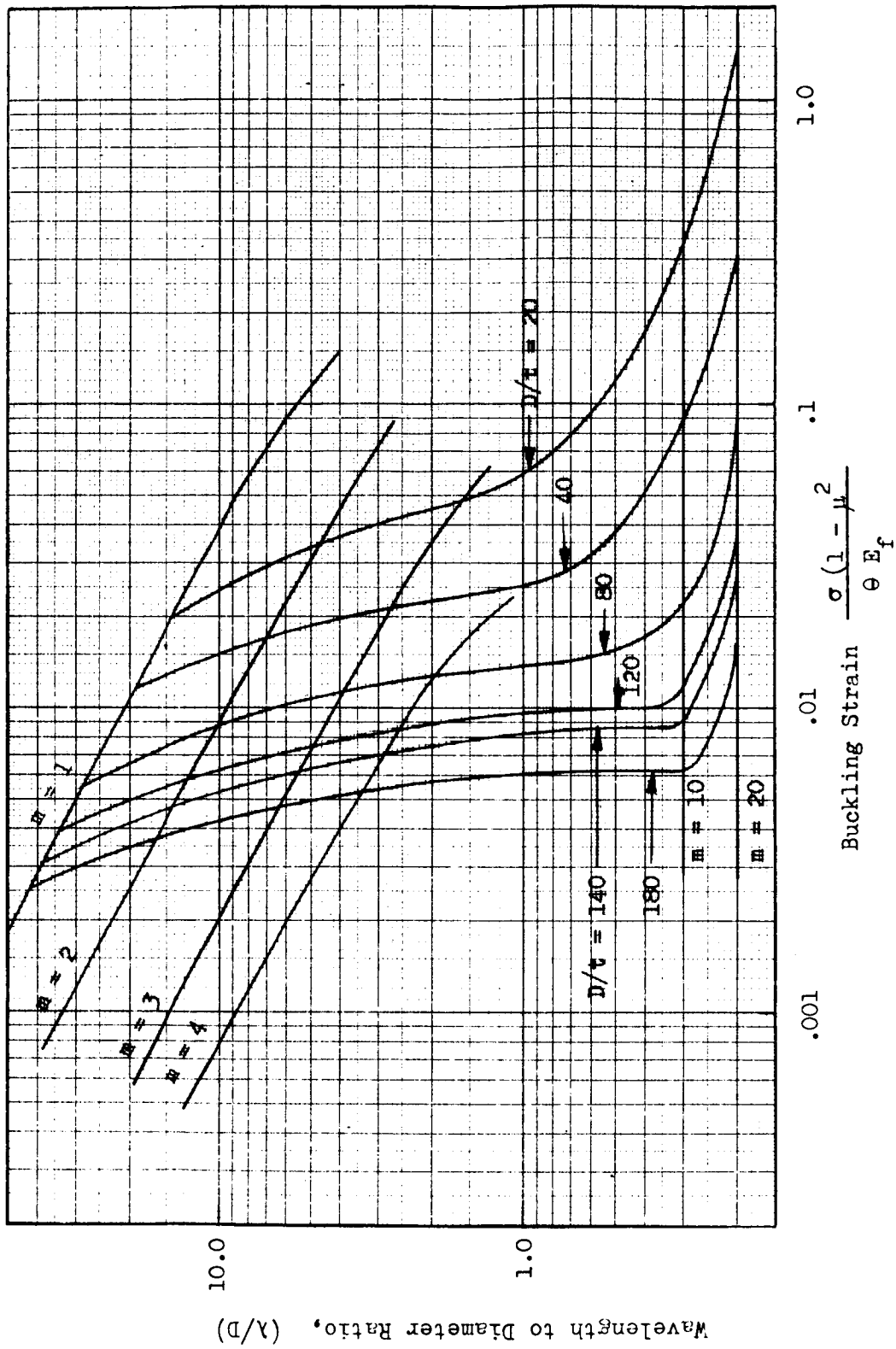

Figure 36. Buckling of Circular Columns and Tubes (based on elastic theory)

strain relationship under high degrees of loading. As discussed by Shanley (Ref. 47), in the inelastic regime, the effective modulus of elasticity becomes the geometrical mean between the tangent and elastic moduli as:

$$E_f = (EE_t)^{1/2} \tag{212}$$

Similarly, the buckling onset is promoted by surface imperfections which can result in a buckling onset of 40 to 65 percent (Ref. 48) of the theoretical value. As a direct result, the nondimensional strain parameter from the elastic case may be written for the inelastic case as:

$$\frac{\sigma\ (1 - \mu^2)}{\theta\ E_f} \tag{213}$$

If the thermal strain:

$$\epsilon_T = \alpha\ \Delta T \tag{214}$$

is related to the effective buckling strain, i.e.,

$$\epsilon_T = \alpha\ \Delta T \propto \sigma\ (1 - \mu^2)/(E_f\ \theta) \tag{215}$$

then the parameters controlling the buckling of the tube may be written in the grouping:

$$\text{Buckling} = f\ \left(\frac{\lambda}{D}\ ,\ \frac{\alpha\ \Delta T}{\theta}\ ,\ \frac{D}{t}\ ,\ m\right) \tag{216}$$

with the effective value of θ under elevated temperature conditions where material properties vary significantly to be experimentally determined for candidate materials. A study of the effects of ductility and material

properties under elevated temperature conditions at the onset point, as well as for the cyclic life of a tube under near-failure cyclic thermal loading is indicated.

A comparison of two typical predicted analytical buckling temperature difference values vs tube diameter-to-thickness ratio is shown in Fig. 37. It is evident that for a given tube width or diameter (D), the circular tube crown is less subject to thermal longitudinal buckling. As a result, the crown flattening proposed to alleviate tangential thermal stress severity is not beneficial for prevention of longitudinal buckling. The temperature gradient values predicted in Fig. 37 lack experimental substantiation and should be used for qualitative comparison only.

Experimental Work. A literature review of recent analytical and experimental inelastic tube buckling data (Ref. 49 through 52) indicated little available data for elevated temperature conditions with either the stainless-steel or Inconel families of materials. The evaluation of the allowable tube wall thickness-to-radius ratio and maximum-allowable temperature for combined film-and-regenerative, regenerative, and dump-cooled skirt designs is necessary for an optimum cooling arrangement. It has been assumed that the inelastic thermal buckling condition can be described in terms of the same principal parameters; as for the elastic case, however, the available data are sparse. The work of Lee (Ref. 51) for inelastic buckling of ambient-temperature aluminum cylinders appears to provide a correlation which can be written in terms of the total strain to the failure point.

Figure 38 illustrates the aluminum data plotted as a function of variables (D/t) and total strain (ϵ) i.e.,

$$\epsilon_{crit} \propto \left(\frac{t}{D}\right) \tag{217}$$

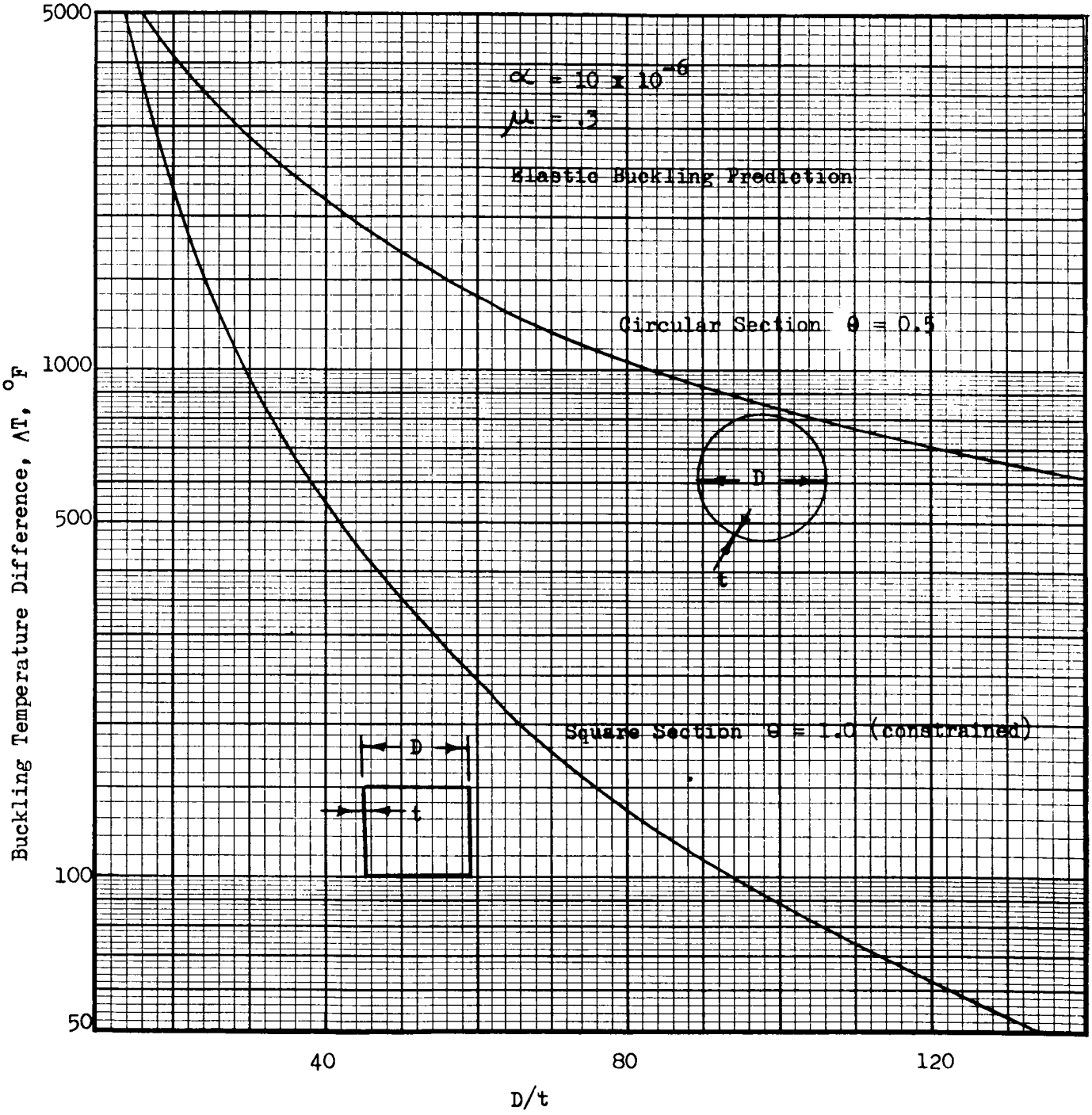

Figure 37. Analytical Critical Buckling Temperature Difference

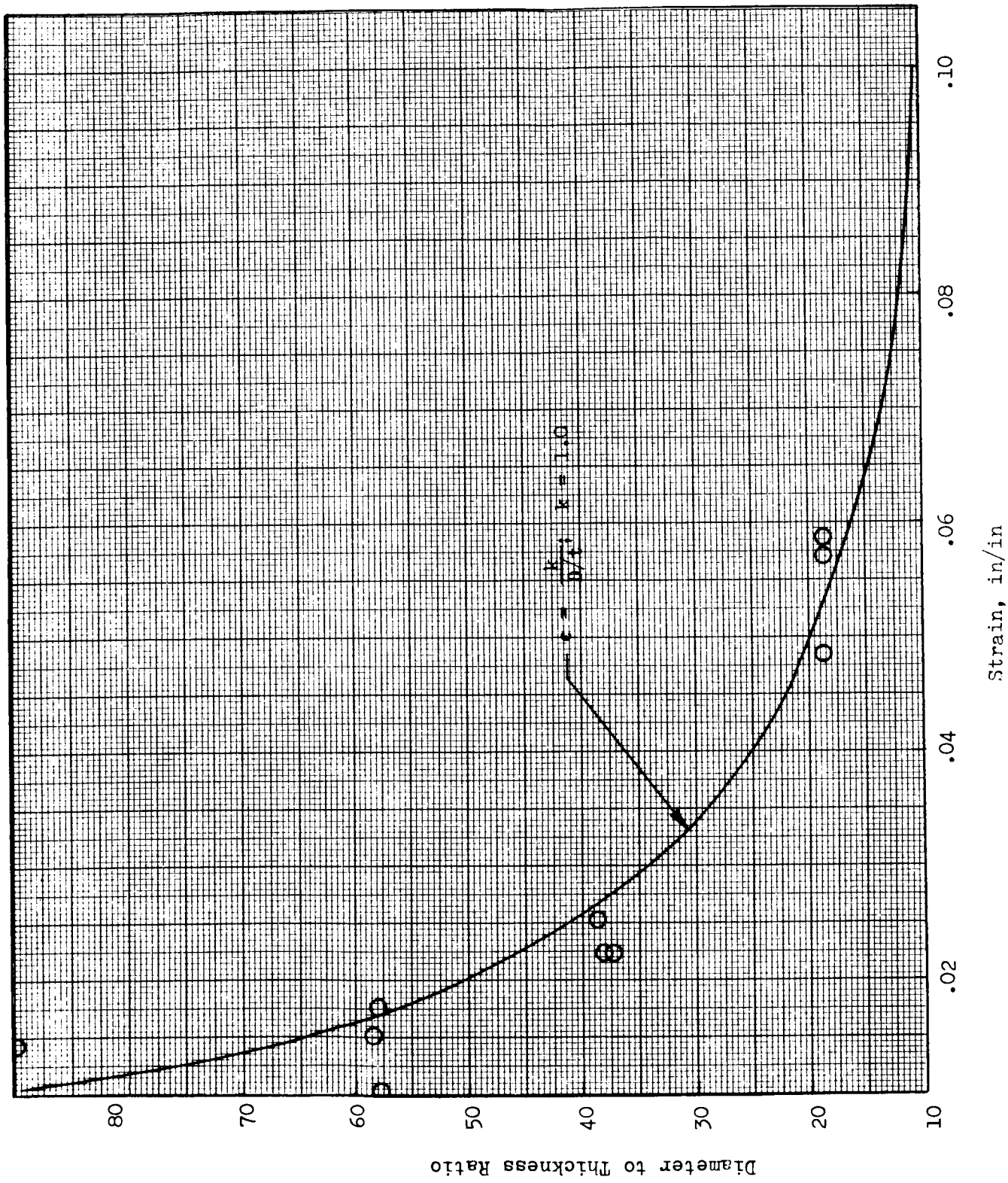

Figure 38. Critical Strain at Buckling Onset vs Tube Diameter-to-Thickness Ratio (Data of Lee, Ref. 51)

Since under thermal environments with constrained conditions the wall temperature rise can be directly translatable to a longitudinal strain, the correlation of data obtained for thrust chamber tube materials should grossly fit a similar relationship including provision for property changes with temperature.

Analytical Work. The local inelastic thermal buckling which can occur on a tube crown under high operating temperature conditions was investigated by analogy with the axial compression case. The criticality equations developed by von Karman (Ref. 53), Shanley (Ref. 47), and Batterman (Ref. 54) were compared.

$$\sigma_{crit} = \frac{4\,E\,E_t\,(t/R)}{[\sqrt{E} + \sqrt{E_t}^{\,2}][3(1-\mu^2)]^{1/2}} \qquad \text{(von Karman)} \quad (218)$$

$$\sigma_{crit} = \frac{\sqrt{E_T E}\,(\frac{t}{R})}{[3\,(1-\mu^2)]^{1/2}} \qquad \text{(Shanley)} \quad (219)$$

$$\sigma_{crit} = \frac{\sqrt{E_t E}\,(\frac{t}{R})}{[3\,(1.25-\mu)]^{1/2}} \qquad \text{(Batterman)} \quad (220)$$

By defining an inelastic behavior parameter for the plastic region

$$\eta = \frac{E_T}{E} \qquad (221)$$

$$\frac{\sigma_{crit}}{E} = \frac{f\,(\eta)\,\frac{t}{R}}{[3\,(1-\mu^2)]^{1/2}}$$

where

$$f(\eta) = \frac{4\eta}{(1+\eta)^2} \qquad \text{(von Karman)} \qquad (223)$$

$$f(\eta) = \eta^{1/2} \qquad \text{(Shanley and Batterman)} \qquad (224)$$

A maximum discrepancy of 25 percent occurs between Eq. 223 and 224.

From the data of Shanley (Ref. 47), a convenient inelastic-elastic buckling diagram approach was developed to visualize buckling onset in terms of the strain parameter (σ_c/E) and t/R ratio as shown in Fig. 39. Safe and unsafe areas for inelastic and elastic buckling are shown. Failure at higher tube thickness-to-radius ratios is indicative of a greater degree of inelastic behavior. Experimentally derived curves at varying temperatures for the commonly used tube materials can be of considerable advantage to the designer.

Critical Wavelength. Data correlating the buckling critical wavelength for the inelastic case derived from the data of Lee (Ref. 51) are shown in Fig. 40, in terms of the wavelength-to-tube diameter ratio. Such a relationship definition is required for the solution of the analytical equations defining critical strain at buckling onset. For the

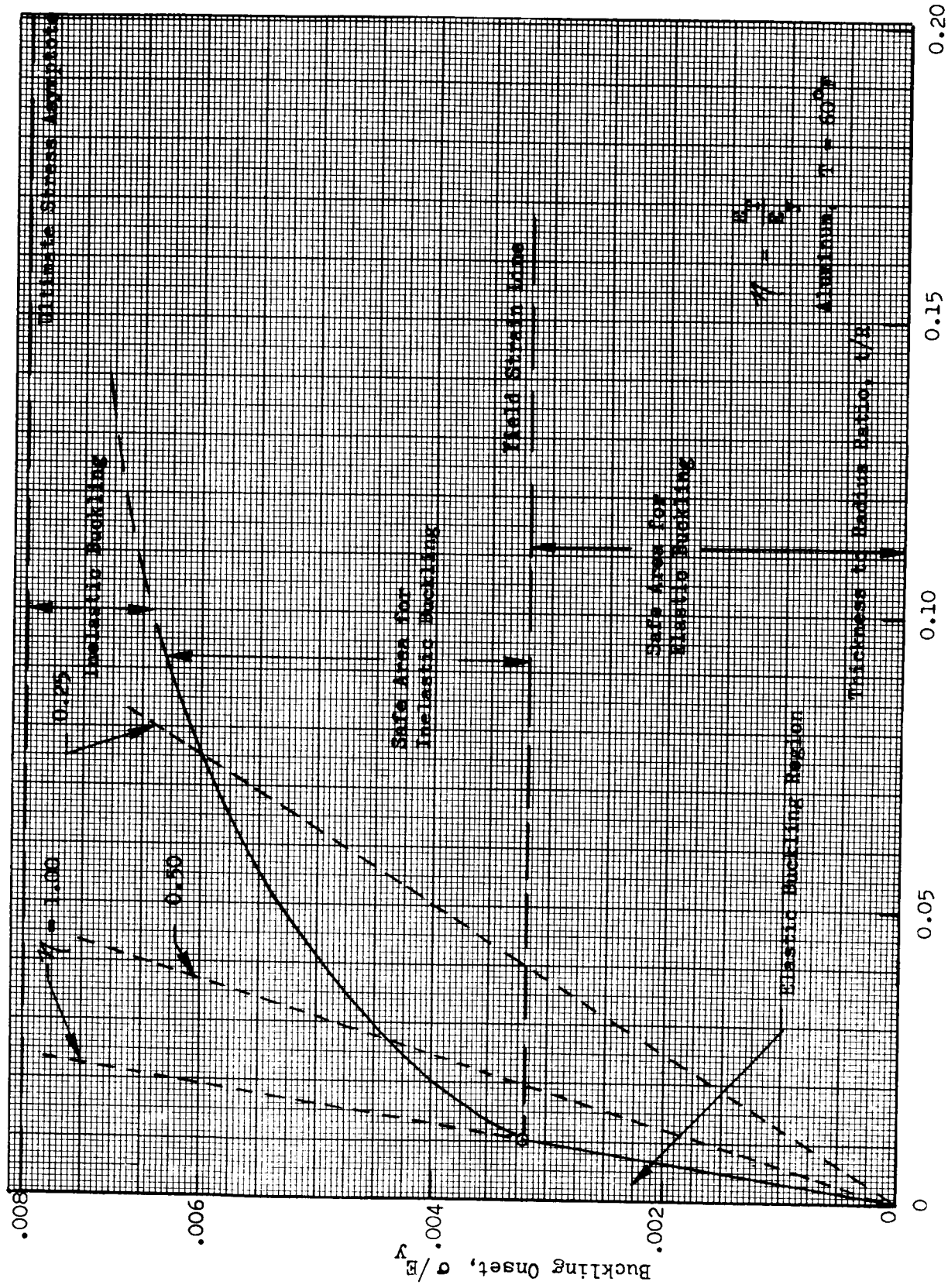

Figure 39. Typical Inelastic-Elastic Buckling Diagram (Data of Shanley, Ref. 47)

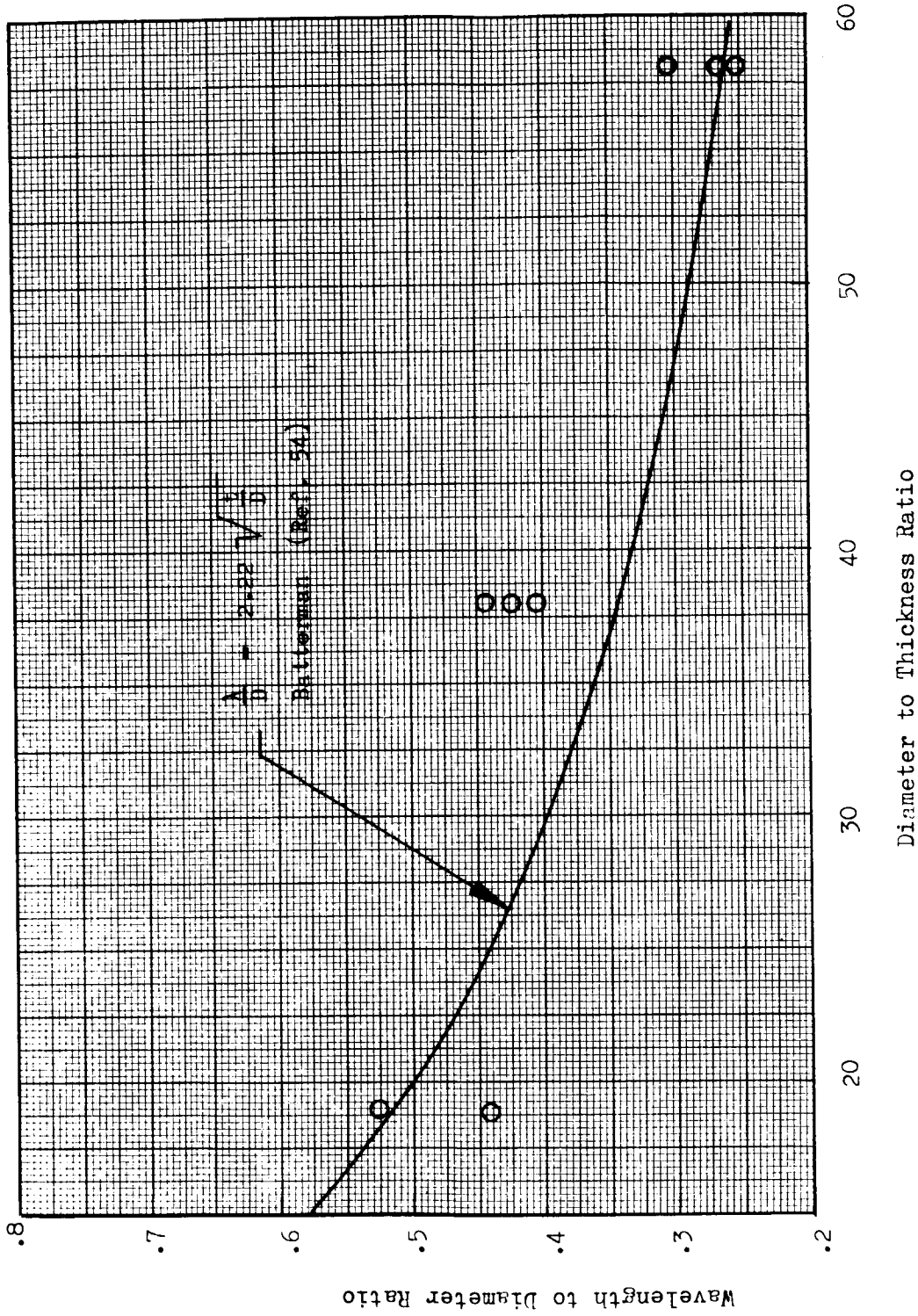

Figure 40. Correlation of Inelastic Wavelength Parameter with Diameter-to-Thickness Ratio (Data from Ref. 51, Inelastic Buckling)

particular inelastic experimental data shown, the trend is toward an increased buckling wavelength-to-diameter ratio with an increased tube diameter-to-thickness ratio. From Fig. 40, it is seen that the buckling wavelengths are small, being from 0.3 to 0.5 of the diameter dimension. Close agreement is seen with a recent analytical approach of Batterman (Ref. 54) considering an outward tube inelastic buckling case. He showed that the inelastic buckling wavelength can be written in terms of the tube thickness-to-diameter ratio as:

$$\left(\frac{\lambda}{D}\right) = \frac{\sqrt{2}\,\pi}{C} \sqrt{\left(\frac{t}{D}\right)} \tag{225}$$

where C is a weak function of the elastic-to-tangent modulus ratio with a value:

$$1.75 \leq C \leq 2.0$$

(over a range of buckling from a tangent modulus equal to the elastic modulus to 1/9 of its value). It can be assumed that an outward buckling behavior will be obtained due to the higher loading condition required for an inward buckle and due to the internal pressure condition in a rocket motor thrust chamber tube.

Figure 41 shows the typical strain diagram approach which may be used for different materials to determine an optimum t/R ratio for a given maximum wall temperature. The simultaneous solution of the thermal

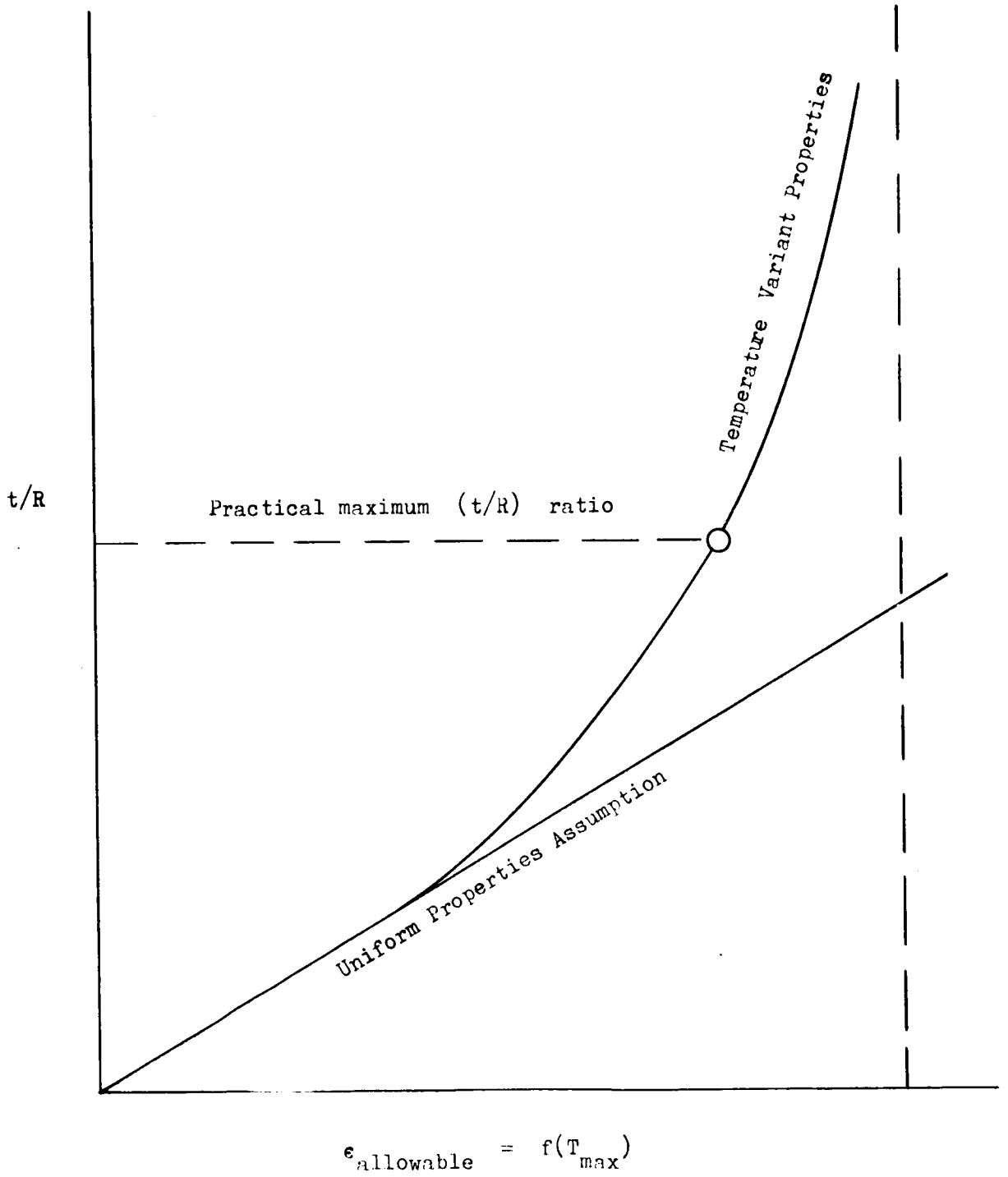

Figure 41. Maximum Tube Thickness-to-Radius Ratio Relationship With Thermal Buckling

stress requirement and that indicated for tube pressure stress is indicated in Fig. 42. For a wall thickness consistent with operating heat flux (for either regenerative, dump, or combined regenerative-film designs) and wall temperature, a tube (t/R) ratio for a particular material can be based to a first approximation by the intersection shown in Fig. 42. However, material capabilities must be individually examined if the upper limits of this concept in terms of wall temperature are to be explored for design study purposes.

Combined Thermal Stress Conditions

The development of tube thermal-stress-derived fatigue cracks in regeneratively cooled chambers is one of the limiting considerations in determination of thrust chamber life. Study to improve the present 2000- to 5000-second life of thrust chamber tubes is even more necessary at high chamber pressure, high heat flux, and high temperature conditions. Previous discussion graphically provided the amount of plasticity introduced in a tube wall as well as the parameters affecting fatigue life. The approach taken was one of individual examination of the tangential and longitudinal plastic stresses. In reality, both stresses occur simultaneously, and the actual effective plastic strain may be expressed by the strain deformation theory for the summation of longitudinal and tangential plastic stresses as:

$$\epsilon_{effective} = \frac{2}{\sqrt{3}} \left[\epsilon_L^{\,2} + \epsilon_L \, \epsilon_T + \epsilon_T^{\,2}\right]^{1/2} \tag{226}$$

It may be seen that if one of the component stresses becomes much greater than the other, an individual examination is valid.

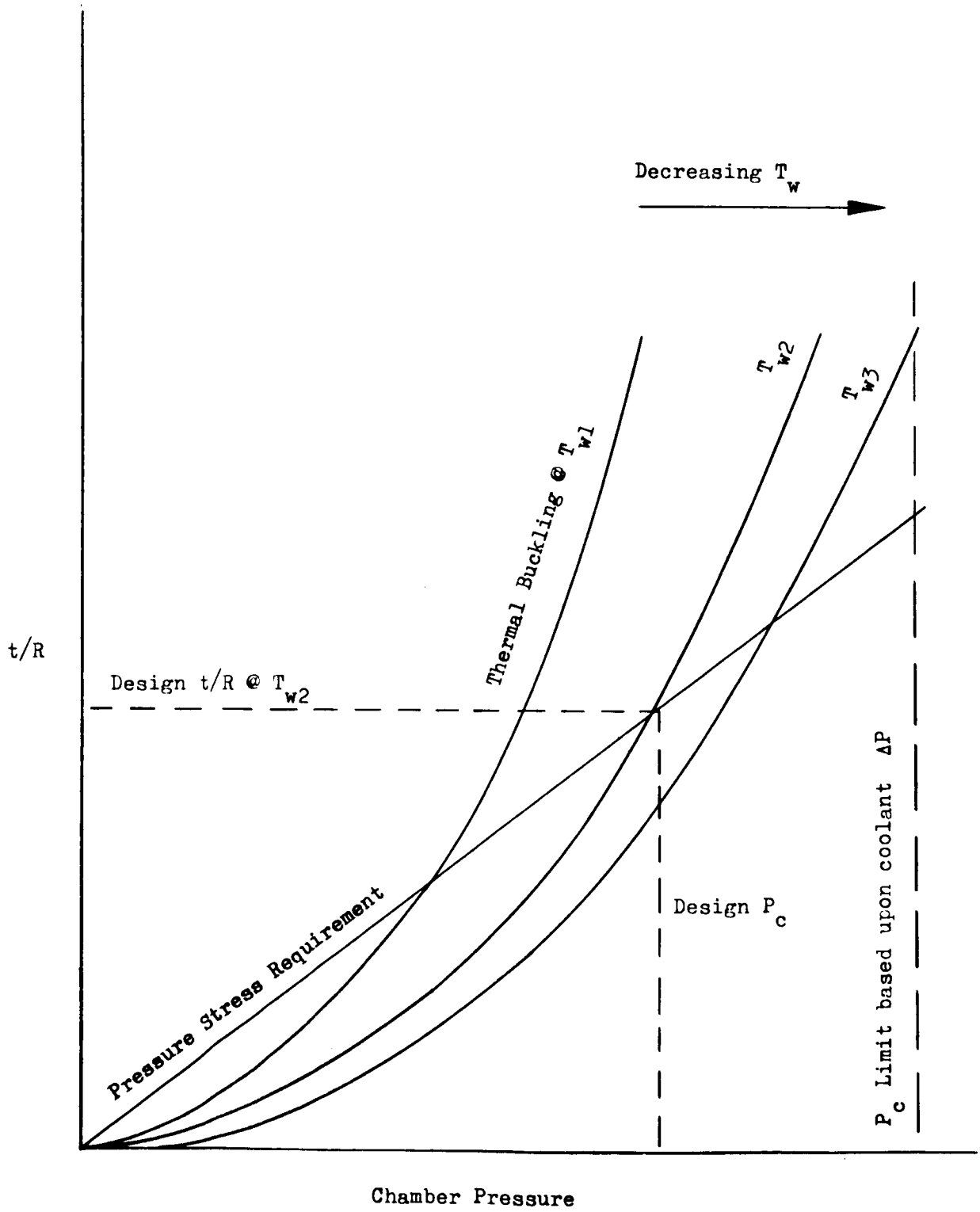

Figure 42. Design Solution for Combined Pressure and Thermal Stress

The ratios of longitudinal to tangential thermal strains are:

$$\varphi_{LT} = \frac{\epsilon_L}{\epsilon_T} = \frac{2k\,(T_{wg} - T_c)}{(q/A)\,(t)} \qquad \text{(gas side)} \qquad (227)$$

$$\varphi_{LT}' = \frac{\epsilon_L'}{\epsilon_T'} = \frac{2k\,(T_{wc} - T_c)}{(q/A)(t)} \qquad \text{(coolant side)} \qquad (228)$$

For a pressure stress smaller than the yield value, these equations may be reduced to:

$$\varphi_{LT} = \frac{2\,[1 - (T_c/T_{wg})]}{1 - (T_{wc}/T_{wg})} \quad \text{and} \quad \varphi_{LT}' \; \frac{2\,[1 - (T_c/T_{wc})]}{T_{wg}/T_{wc} - 1} \qquad (229)\ (230)$$

Setting φ_{LT} and φ_{LT}' equal to 1, which would represent an equivalence of longitudinal and tangential thermal stresses, there results:

$$\frac{T_{wc}}{T_{wg}} = \left[\frac{2\,T_c}{T_{wg}} - 1\right]_{\varphi_{LT} = 1} \quad \text{and} \quad \frac{T_{wg}}{T_{wc}} = \left[3 - 2\,\frac{T_c}{T_{wc}}\right]_{\varphi_{LT}' = 1} \qquad (231)\ (232)$$

Considering $\varphi_{LT} = 1$, for $(T_c/T_{wg}) < 0.5$, an unreal condition occurs. For $0.5 < T_c/T_{wg} < 1.0$, the ratio $T_{wc}/T_{wg} > 1$, which is also an unreal circumstance. For $\varphi_{LT}' = 1$, a similar failure for solution results. Because φ_{LT} and φ_{LT}' must be greater than 1, it is resultantly concluded that the longitudinal stress is always the more severe.

The percentage of plasticity introduced into a cross section may be considered as a rating parameter. It is also indicative of the maximum plastic strain. For the tangential component, the fraction which remains in an elastic condition $(\varphi_{\epsilon T})$ may be developed as

$$\varphi_{\epsilon T} = \frac{2\,\bar{\epsilon}_y\,(1 - \mu)\,k}{\alpha\,(q/A)\,(t)} \qquad (233)$$

with the plastic fraction

$$\varphi_{PT} = (1 - \varphi_{\epsilon T}) \tag{234}$$

Similarly, the maximum and minimum wall surface strain-to-yield strain ratio for the tangential stresses may be derived in terms of the elastic fraction as:

$$\varphi_{max_T} = \frac{1}{\varphi_{\epsilon_T}} + \frac{\epsilon_p}{\epsilon_y} \qquad \text{(coolant-side wall surface)} \tag{235}$$

$$\varphi_{min_T} = \frac{1}{\varphi_{\epsilon_T}} - \frac{\epsilon_p}{\epsilon_y} \qquad \text{(gas-side wall surface)} \tag{236}$$

The effect of internal tube pressure increases is thus shown to aggravate the coolant-side wall surface condition but to aid the gas-side surface stress condition.

For the longitudinal direction, the maximum and minimum surface strains relative to the yield become:

$$\varphi_{max_L} = \frac{\alpha\,(T_{wg} - T_c)}{\epsilon_y\,(1 - \mu)} \qquad \text{(gas-side surface)} \tag{237}$$

$$\varphi_{min_L} = \frac{\alpha\,(T_{wc} - T_c)}{\epsilon_y\,(1 - \mu)} \qquad \text{(coolant-side wall surface)} \tag{238}$$

Since it was shown that the longitudinal strain throughout the tube crown is always higher than the tangential strain if any portion of the tube in the tangential direction has yielded, the entire longitudinal direction component is plastic. As a result, it appears the heat flux effects can be considered small compared to changes made in the tube crown operating temperature, in defining tube cyclic life.

Life-Cycling Capability

The previous discussion has developed steady-state conditions for thermal stresses for the first heating cycle assuming an unstressed initial state. The life cycling capability is linked with both the maximum strain imposed and the percentage of plasticity in the tube cross section, i.e.,

$$N = f\left(\epsilon_{PP}, \frac{1}{x} \int_0^x \epsilon_{PP}\, dx\right) \tag{239}$$

The steady-state condition will induce the maximum thermal stress because it represents the maximum wall ΔT. In terms of the material capability, as discussed below, the ductility change with temperature may result in maximum damage during engine start. Engine shutdown results in pressure and thermal strain reduction from the steady-state value to ambient conditions.

Transient temperature times for stabilization of wall temperature under a step function heat input may be expressed (for a wall of good thermal conductivity) as:

$$\tau = \frac{t\, \rho\, C_p\, (\overline{T}_w - T_i)}{(q/A)} \tag{240}$$

For a 0.010-inch-thick 347 stainless steel wall at a 1000 F average wall temperature under a 30 Btu/in.^{2}-sec heat input rate, a wall transient period of 10 milliseconds is indicated. Hence, in high-chamber-pressure designs, it will be seen that the wall temperature responds almost simultaneously to the chamber pressure rise.

During the achievement of steady-state temperatures, it is apparent that at high heat fluxes, the wall is forced into a plastic state. Upon shutdown, as the strain is removed, the applied stress will reverse in sign from tensile to compressive. Depending upon the material cold-working behavior and the cyclic temperature difference, the wall may yield at a lower temperature point on shutdown. This principle is illustrated in Fig. 43. At point 1, strain is applied in the elastic region at the initial temperature condition. The temperature is above ambient and the elastic modulus is reduced at point 2. At point 3, the stress is plastic and wall temperature continues to rise. The strain reaches its final value at the maximum temperature at point 4. It is not known whether the stress value at point 3 is above that at point 4; however, the path followed appears reasonable. Upon unloading, point 5 is reached by elastic unloading with the modulus of elasticity changing with temperature. At point 6, ambient temperature is achieved, corresponding to a reversed stress in the wall. If the unloading process is elastic to point 6, and subsequent reloading does not result in further plastic flow, a stable stress cycle is established. If not, subsequent behavior on loading will reach point 7 on the second cycle, point 9 on the third, etc., until failure due to excessive plastic strain occurs. A history of the material is necessary to map the behavior during the process described.

For this study, a review of available life cycling data under short-term conditions was reviewed. References 55 and 56 contain some data at room temperature. Reference 57 contains some high-temperature 347 stainless steel data for small cyclic life.

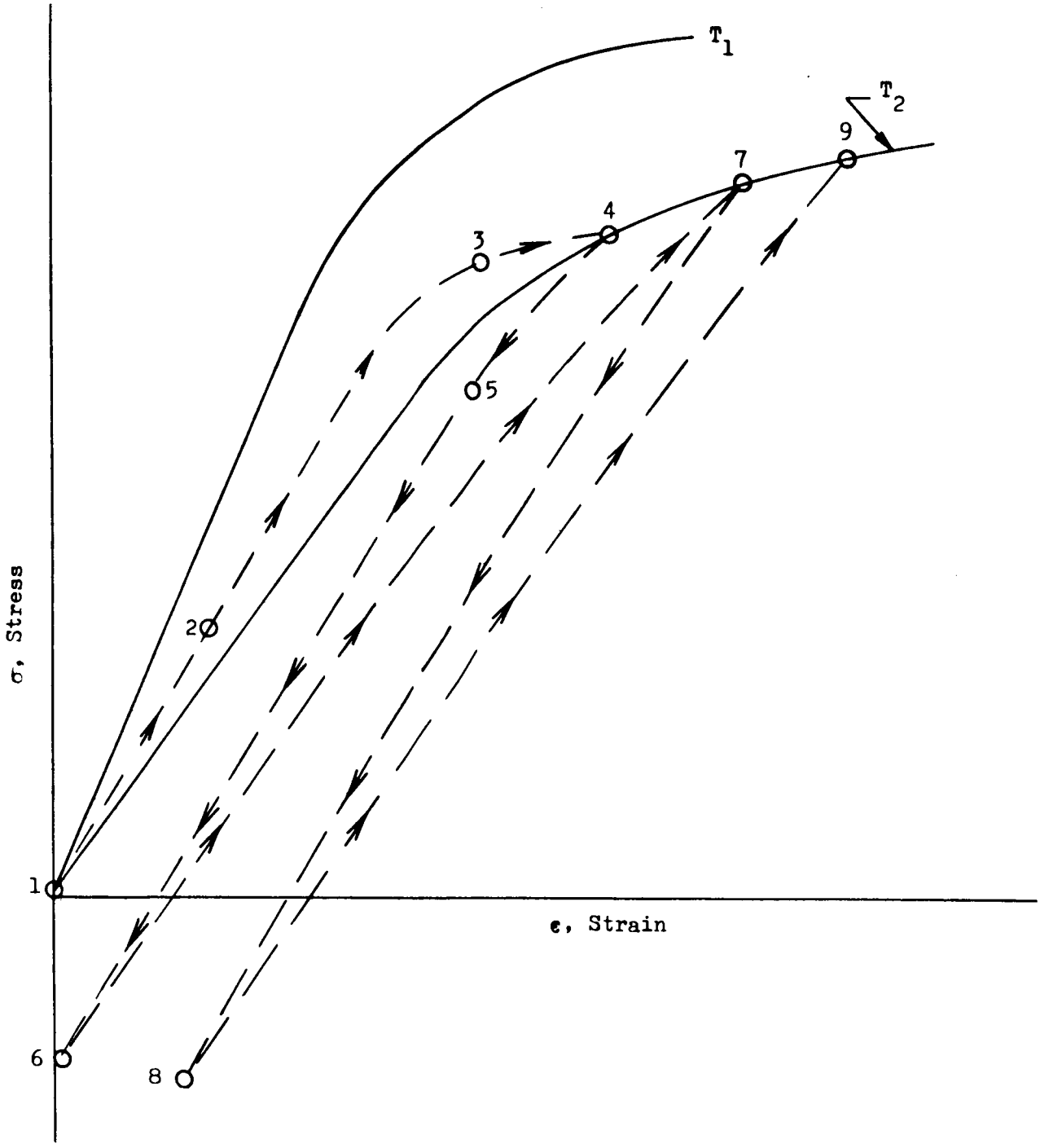

Figure 43. Example of Thermal Stress Cycling in the Plastic Range

The behavior of fatigue either at the short term (< 100 cycles) or at the endurance limit (10^6 cycles) appears to be satisfactorily correlated by the summation of a contribution of the plastic strain ϵ_{PP} (short term) and the elastic strain ϵ_e (long term) as:

$$\Delta \epsilon = \epsilon_{PP} + \epsilon_e \tag{241}$$

In terms of the number of cycles (N_f) to failure, the total strain (Ref. 43) may be written as:

$$\Delta \epsilon = C_1 (N_f)^{C_2} + \frac{C_3}{E} (N_f)^{C_4} \tag{242}$$

The constants are given as:

$$C_1 = 0.75\ D \tag{243}$$

$$C_2 = -1/2 \tag{244}$$

$$C_3 = 2\ \sigma_f \left[(1/4) \log (\sigma_f/\sigma_e)/\log 4N_f \right] \tag{245}$$

$$C_4 = \frac{(-1/2) \log (\sigma_f/\sigma_e)}{\log (4 \times 10^6)} \tag{246}$$

Alternatively, Ref. 44 writes the fatigue behavior in terms of the plastic and elastic contributions as:

$$\Delta \epsilon = \frac{\epsilon_r}{4\ (N_f)^{1/2}} + \frac{\sigma_e}{E} \tag{247}$$

$$\epsilon_r = \ln \left[\frac{100}{100 - \%\ RA} \right] \tag{248}$$

Under high plastic loading conditions, it is seen that the material life becomes directly dependent upon the material ductility and varies inversely as the square of the strain.

Under constrained thermal loading conditions starting from a reference temperature (T_i) the strain may be written as:

$$\epsilon_T = \frac{\alpha (T_f - T_i)}{(1 - \mu)} \tag{249}$$

With large plasticity conditions, the plastic strain may be assumed equal to the total strain as:

$$\Delta \epsilon \approx \epsilon_P \approx \epsilon_T \tag{250}$$

For the chamber tube longitudinal thermal stress, assuming short-term life and thus, the dominance of the first term of Eq. 241, the thermal fatigue rating parameter for materials may be developed by combining Eq. 242, 249, and 250 to give:

$$N_L = \left[\frac{C_L \, D \, (1 - \mu)}{\alpha (T_f - T_i)} \right]^2 \tag{251}$$

where C_L would represent an empirical constant. Thus, the plastic-region cycling capability becomes dependent on the square of the ductility. Additionally, an increase in temperature results in a reduction in operating life by the square.

Material ductility is dependent upon a number of factors, some of which are:

1. Cold working and fabrication
2. Hot working and annealing
3. Alloying
4. Tempering

Thus, if large plastic flow is imposed, a low-ductility, high-strength material would be undesirable. Equation 251 may be used as a fatigue parameter for the comparative life of materials with longitudinal loading because it considers temperature difference to be independent of wall thermal conductivity.

The life behavior for a fixed heat flux, which is more appropriate to the life behavior in the tangential direction, may be similarly developed as:

$$N_t = \left[\frac{2\ C_t\ k\ D\ (1 - \mu)}{\alpha t\ (q/A)}\right]^2 \qquad (252)$$

For a fixed heat flux and minimum wall thickness, the life capability is dependent upon the ductility, thermal conductivity and thermal coefficient of expansion.

Figure 44 compares the relative life behavior of common tube materials with temperature for the longitudinal stress condition. It is seen that a rapid diminishment in life occurs with wall temperature increases. Ductile materials such as 347 stainless steel, copper, and nickel

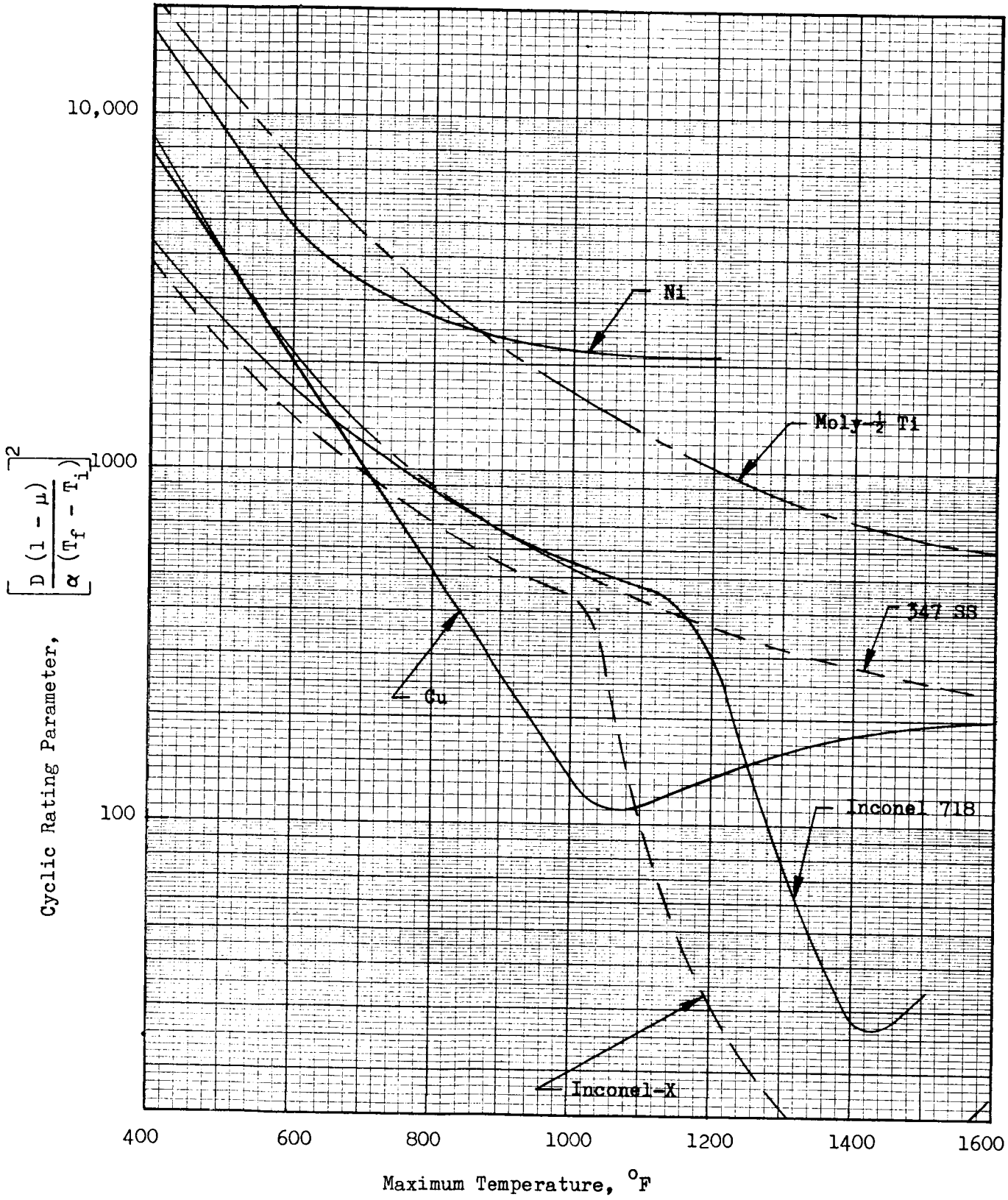

Figure 44. Cyclic Life Parameter for Longitudinal Stresses

are superior at high temperatures. From the published data, the annealed molybdenum-1/2 Ti appears desirable both from a high ductility and low thermal coefficient of expansion. In contrast, at the high temperatures, the nickel alloys have a "hot shortness" or ductility reduction at 1200 to 1400 F. The material life at these temperatures is predicted to be much shorter.

Figure 45 expresses the comparison of the cyclic life parameters for the tangential stress condition for a fixed heat flux and wall thickness. The superior ductility and thermal conductivity of copper, nickel, and annealed molybdenum-1/2 Ti, as well as a low thermal coefficient of expansion for the latter, results in a long life capability. In contrast, 347 stainless steel shows a reduced life due to low thermal conductivity and higher wall temperatures. As in the discussion above, the Inconel family shows poor life capability at the 1200 to 1400 F range for the tangential thermal stresses.

The effect of yield strength upon material life is important because it may dictate a wall thickness above the minimum value for pressure stresses. The general relationship of decreased ductility with an increased strength is an important factor to examine. If the wall thickness is maintained at a minimum value from a manufacturing standpoint and tube-radius distortion without yielding is not a consideration, material strength from a plastic thermal stress standpoint would not appear to be a major factor.

Figure 46 illustrates short-term inelastic fatigue data points for 304 and 310 stainless steels and Inconel-X. The life cycling is seen to vary from the $C_2 = -1/2$ exponent as expressed in Eq. 242. For 310 stainless steel, 304 stainless steel, and Inconel-X, the values of C_2 are -0.684, -0.562, and -0.215, respectively. Further data are required in this low-cyclic-life range under varying temperature conditions for the candidate materials in question.

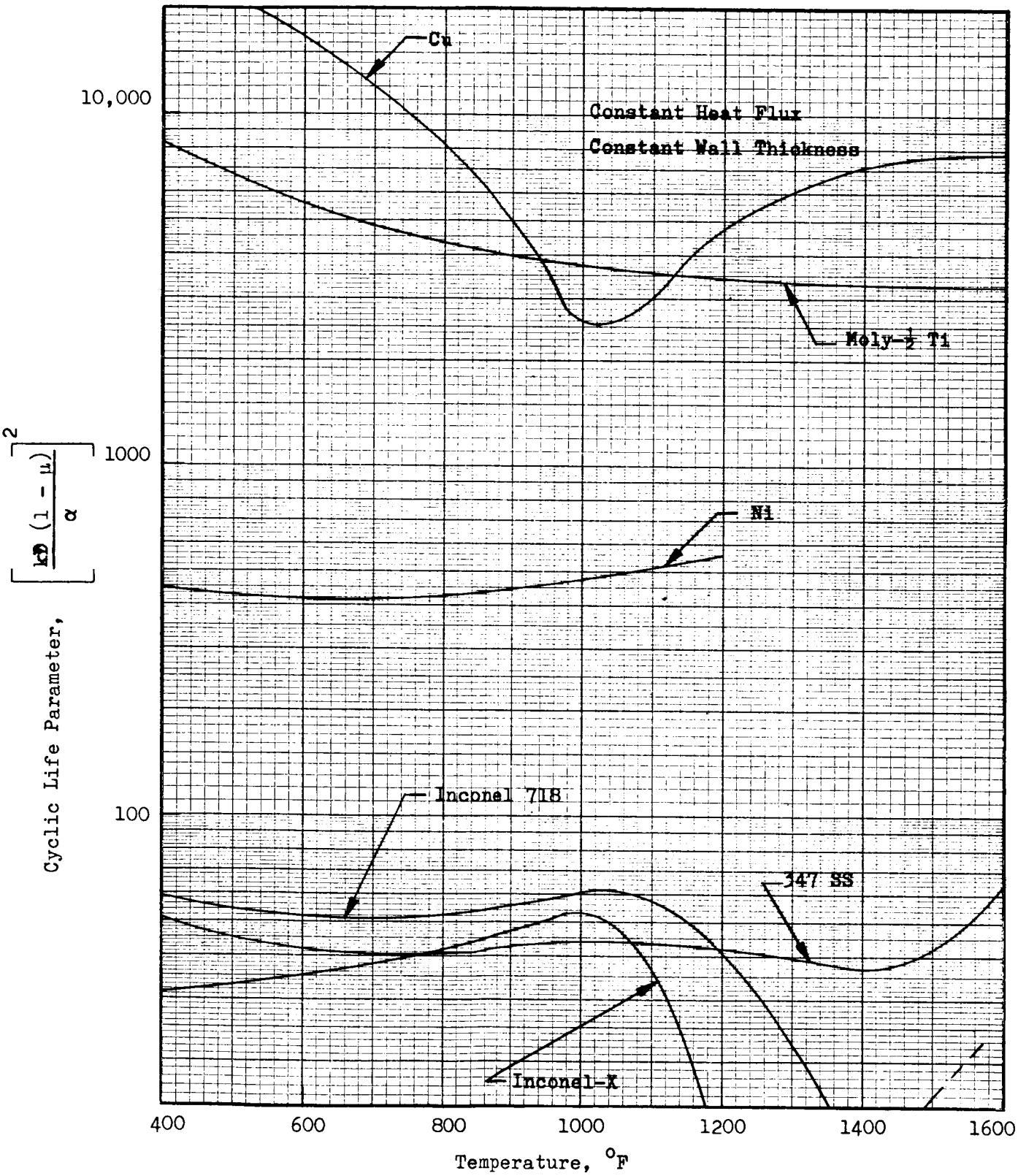

Figure 45. Cyclic Life Parameter for Tangential Stresses

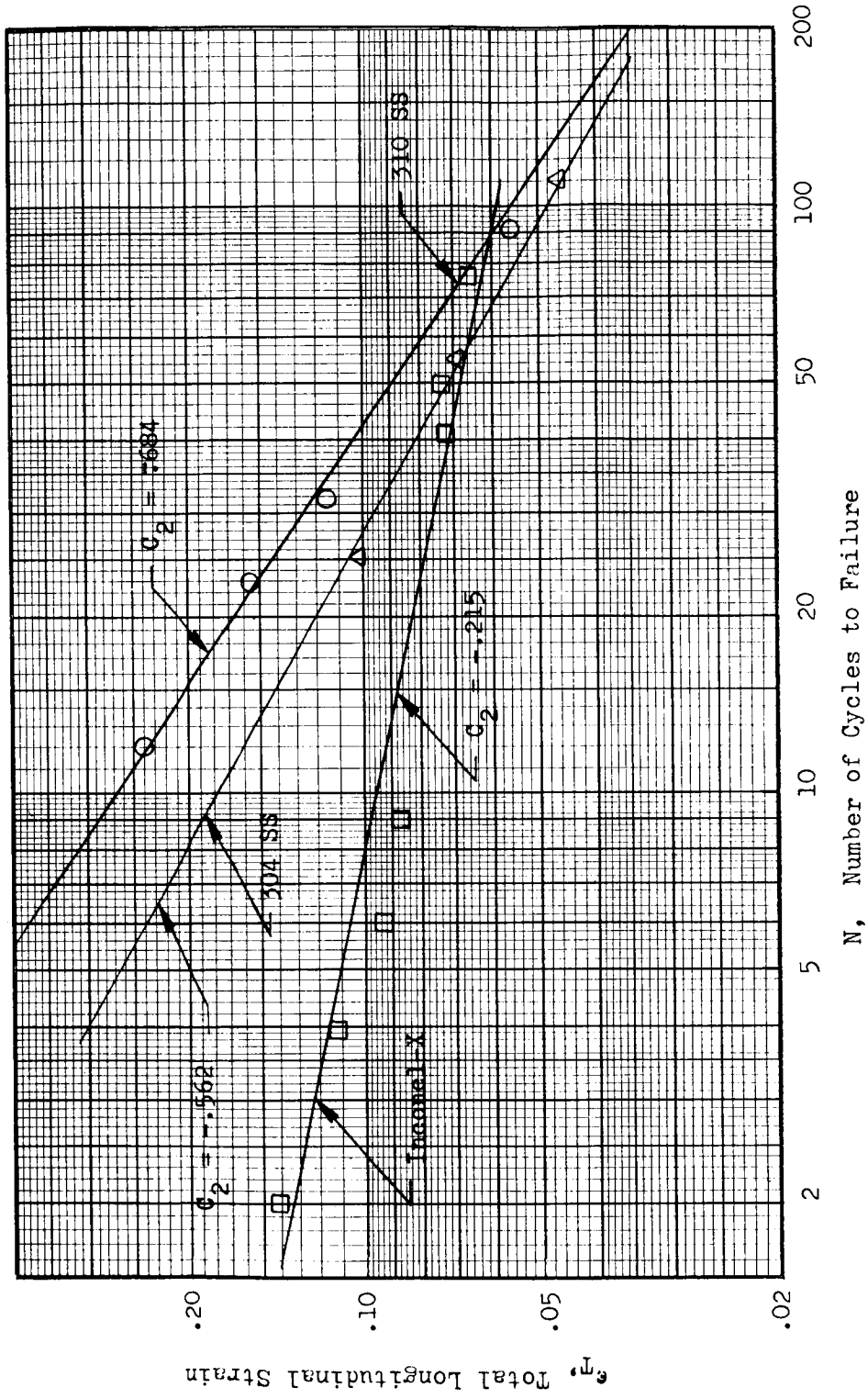

Figure 46. Short-Term Fatigue of Materials Under Room-Temperature Cycling Conditions (Data Ref.: NASA TND 1574)

PERFORMANCE LOSS CONSIDERATIONS

The choice of an appropriate cooling method for a high-pressure, large-thrust engine is to a large extent dictated by the performance loss associated with the cooling technique. In designs where thrust chamber weight and engine specific impulse are not so critical, the choice is not clear. Neglecting the weight comparison, it may be seen that for a regeneratively cooled design, the performance loss would be that associated with pumping pressure losses and consequent turbine exhaust performance recovery efficiencies. For regenerative-topping-cycling systems, because the turbine exhaust losses are essentially recovered at thrust chamber specific impulse values, a cooling performance degradation consideration is not required.

For mass transfer-cooled designs, such as those employing film or transpiration cooling, the combustion of the coolant at high pressure and optimum mixture ratio is mandatory. Hence, promotion of rapid burning of the coolant after utilization is of prime importance.

The following section will discuss analytical approaches to the performance for film and transpiration cooling, regenerative, and dump-cooling methods.

Engine Performance

As a consequence of the completion of the specification of the specific impulse values of the two propellant combinations and the determination of the film-cooling requirements and pump outlet pressures required for regenerative and film cooling as reported in Ref. 1, an analysis of the

theoretical impulse gains at high chamber pressure was undertaken. This was conducted to evaluate the specific impulse response to the cooling method.

A review of the results of the High-Pressure Pumping Technology study (Contract NAS8-4010) indicated the flows required for the turbine as a function of chamber pressure. A development of the turbine τ_T values (percent of mainstage flow) were determined as a function of chamber pressure in the following linear form:

$$\tau_T = C_1 + C_2 P_c \tag{253}$$

Similarly, from an assumption of a completely film-cooled combustion zone, the film coolant requirements were fitted to the following linear form:

$$\tau_{FC} = C_3 + C_4 P_c \tag{254}$$

For a completely regeneratively cooled design, the value of τ_{FC} is zero.

Specific impulse gains over a range in chamber pressures and expansion ratios were put in a linearized form to a good approximation as:

$$(I_s/I_{s_{Ref}}) = 1 + \alpha \left(\frac{P_c - P_{c_{Ref}}}{P_{c_{Ref}}} \right)_{\epsilon = \text{constant}} \tag{255}$$

$$(I_s/I_{s_{Ref}}) = 1 + \beta \left(\frac{\epsilon - \epsilon_{Ref}}{\epsilon_{Ref}} \right)_{P_c = \text{constant}} \tag{256}$$

For the reference case, a chamber pressure of 1500 psia and an expansion ratio of 20 were assumed.

Turbine exhaust gases were assumed to be expanded through an equivalent area ratio of 3 at altitude with an assumed gas generator engine cycle. In the analysis, the principal specific impulse losses at higher chamber pressure are directly attributable to the turbine losses and film-cooling losses. If other methods were to be used to regain the loss assumed here, higher performance would result.

Based on the known turbine exhaust gas properties, values of specific impulse derived relative to the thrust chamber values were:

$$\frac{I_{s_T}}{I_{s_C}} = 0.366 \qquad (LO_2/RP\text{-}1)$$

$$\frac{I_{s_T}}{I_{s_C}} = 0.537 \qquad (LO_2/LH_2)$$

The resulting relationship for the overall performance ratio derived in terms of the flows, specific impulse values, and recovery efficiencies becomes:

$$\varphi_P = \frac{I_{s_C}\left[\varphi_4\,(1 - \tau_T - \tau_{FC}) + \tau_T\,\varphi_1\left(\frac{I_{s_T}}{I_{s_C}}\right) + \tau_{FC}\,\varphi_2\right]}{\varphi_3\,I_{s_{Ref}}} \qquad (257)$$

A thrust chamber base value of 100 percent of frozen specific impulse efficiency was assumed.

Typical results of the performance analysis may be reviewed in Fig. 47, 48, and 49 for chamber pressures to 5000 psia and nozzle expansion ratio values to $\epsilon = 60$.

Figure 47 is for regeneratively cooled LO_2/LH_2 engines. As shown, the effect of chamber pressure is to degrade the specific impulse performance for a constant expansion ratio resulting from increasing turbine exhaust gas losses at a higher chamber pressure. More representative cases are the maintenance of a constant engine performance or a constant maximum diameter. The results indicate that a greater expansion area ratio is required for a constant or increasing performance with chamber pressure.

Figure 48 illustrates a film-cooled LO_2/LH_2 case with an assumed partial loss (φ_2 = 50 percent) in the recovery of the specific impulse from the film coolant. If total recovery of the performance from the hydrogen film coolant is assumed because of its low molecular weight, the performance would be similar to that for a regeneratively cooled refractory metal chamber. The specific impulse gains with chamber pressure for the assumed film-cooled design illustrated are slightly less than for a regeneratively cooled LO_2/LH_2 design.

For contrast, Fig. 49 illustrates the loss in specific impulse anticipated with high chamber pressure LO_2/RP-1 designs which are film cooled. Because of the high molecular weight of the RP-1 constituent, little or no performance addition is assumed to be derived from the film coolant.

It is apparent that in the RP-1 designs, a combined regenerative- and film-cooled combustion zone design will be advantageous to avoid performance degradation. It appears additionally important to be able to

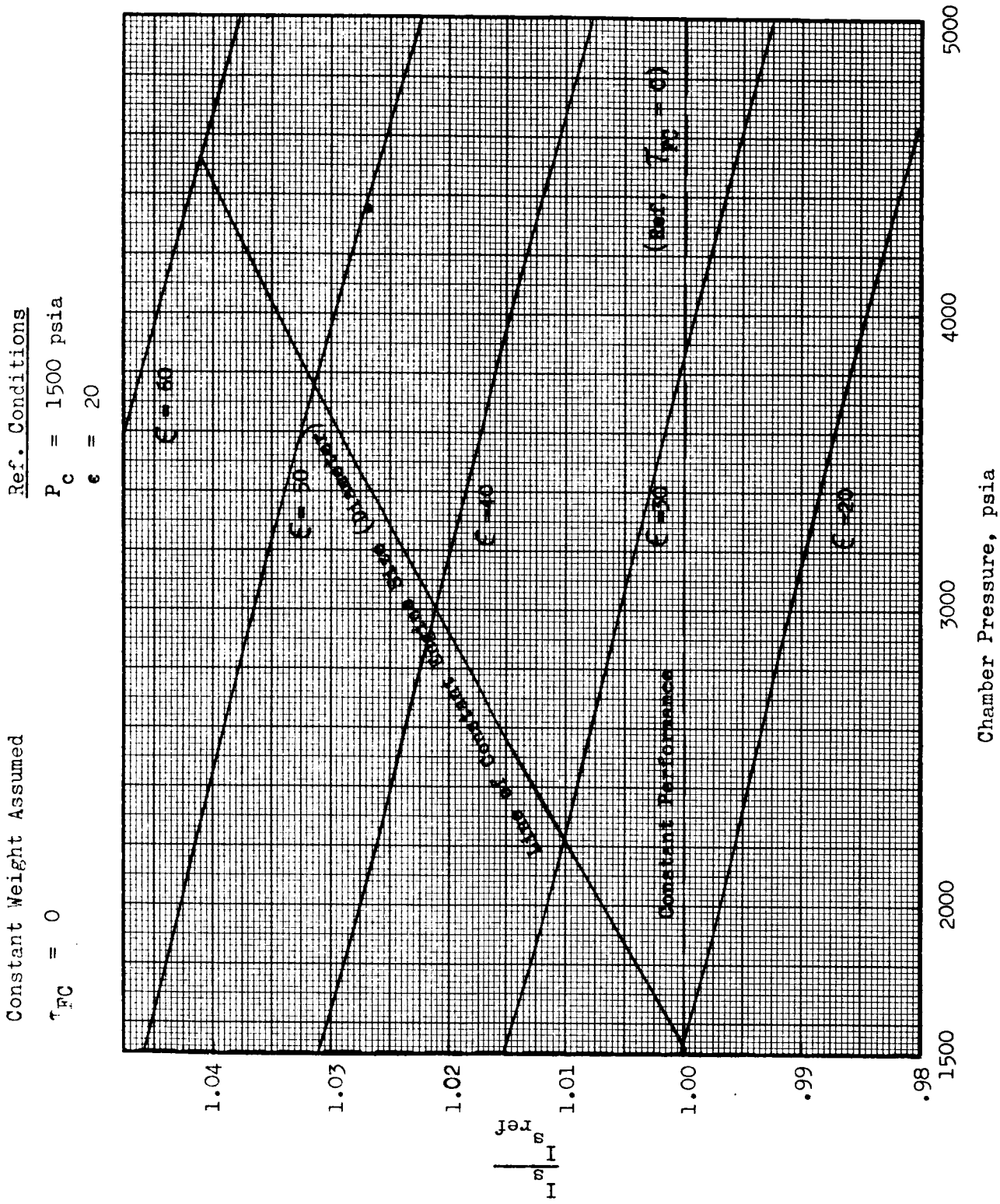

Figure 47. Engine Specific Impulse Comparison for Regeneratively Cooled LO_2/LH_2 Engines

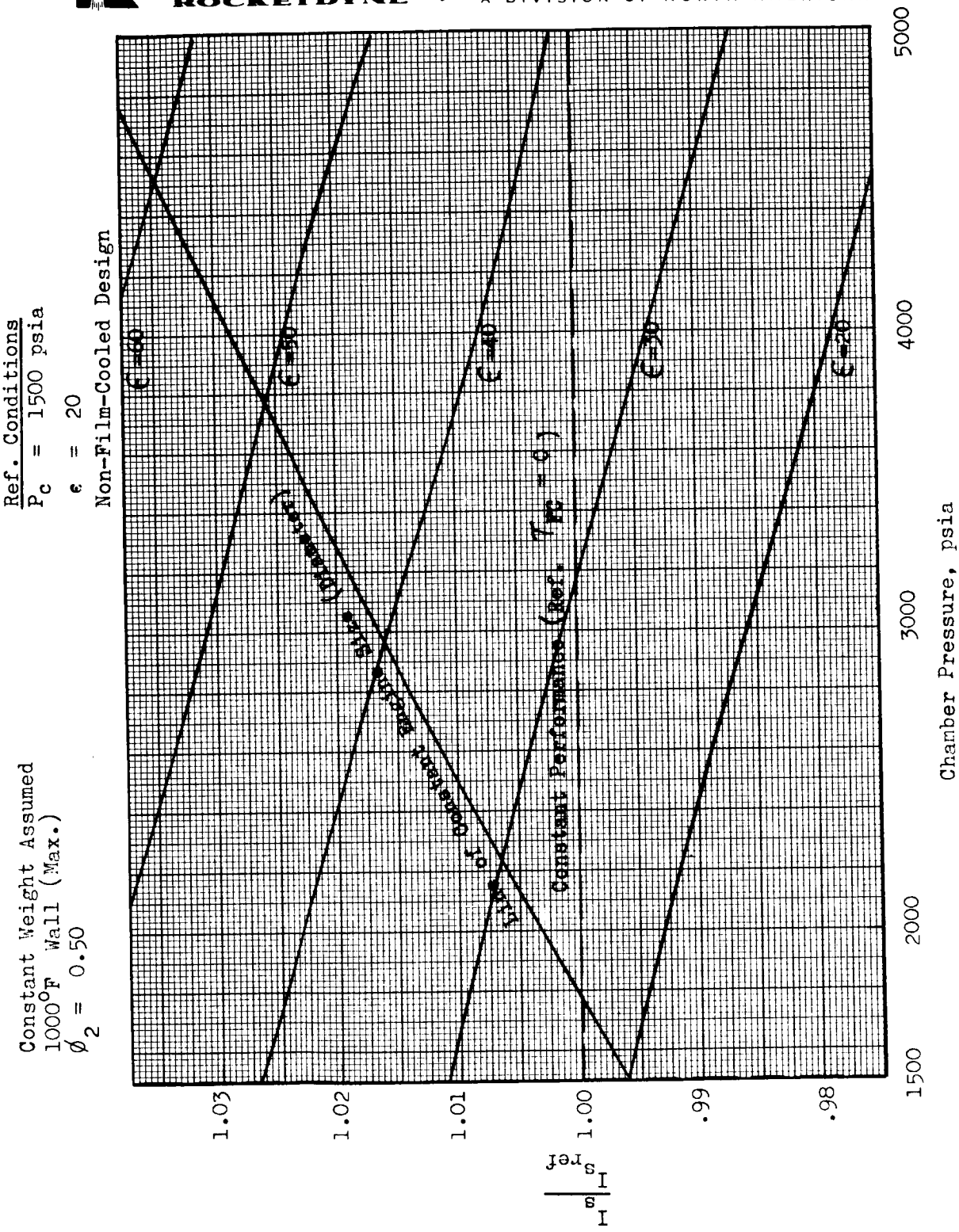

Figure 48. Engine Specific Impulse Comparison for Partially Film-Cooled LO_2/LH_2 Engines

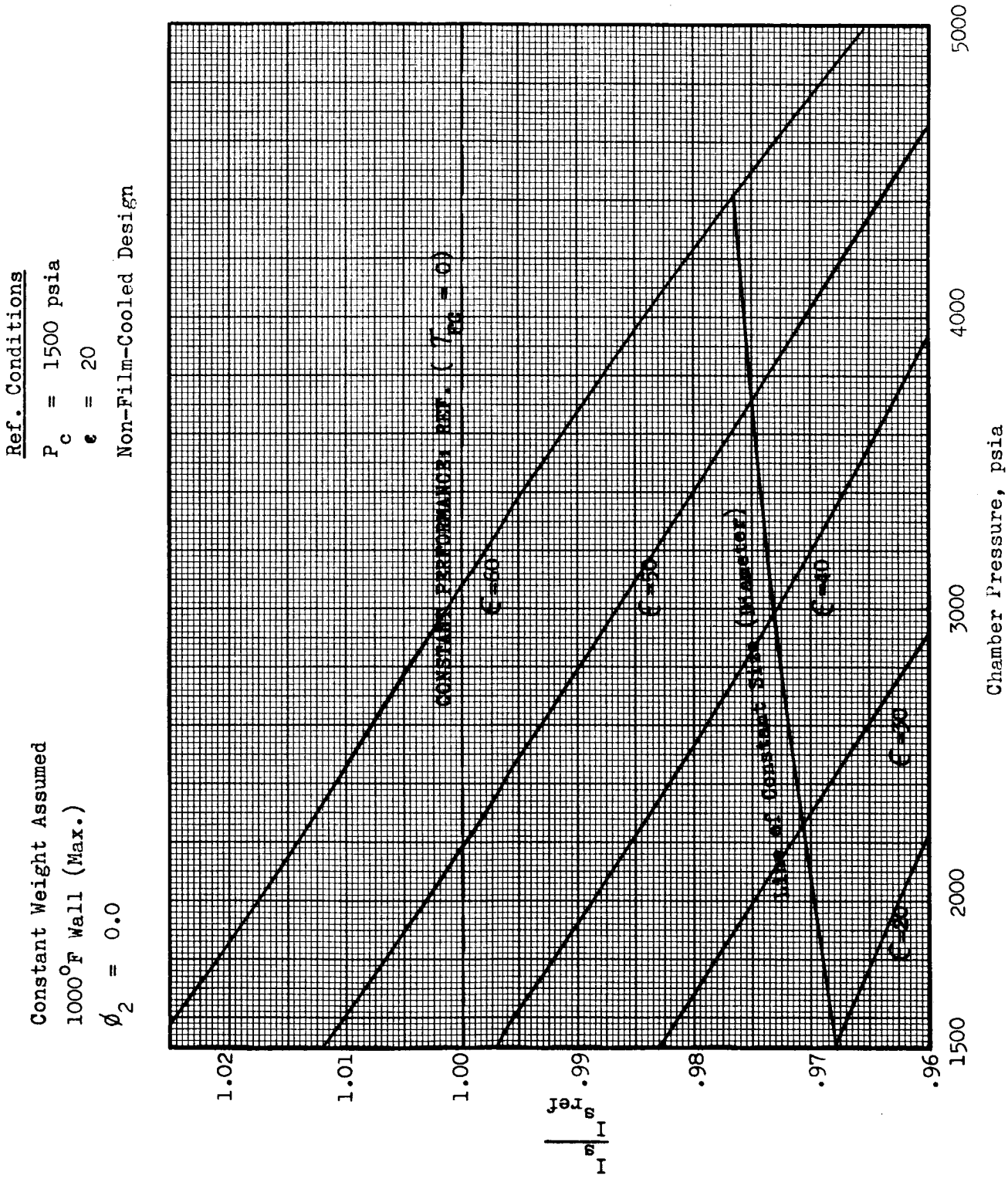

Figure 49. Engine Specific Impulse Comparison for Partially Film-Cooled LO_2/RP-1 Engines

RM 608-B-13 NEW 11-62

accurately define specific impulse losses resulting from film cooling and to diminish the losses imposed by the large turbine gas requirements at higher chamber pressures.

Performance Loss With Film Cooling

The percentage performance loss for each percent of film-coolant addition becomes important in the selection of the operating chamber pressure. With a film-cooled design, both the film coolant flow percentage requirement and the specific impulse performance increase with chamber pressure. As a result, the optimum chamber pressure for maximum specific impulse will be linked with obtaining a recovery of a good fraction of the film-coolant flow as specific impulse.

The considerations governing the regain of the film-coolant specific impulse are as follows:

1. Extent of film-coolant combustion with the mainstream
2. Axial location of combustion of film coolant
3. Thermal equilibrium of coolant with mainstream
4. Mixture ratio shift of the mainstream

If film cooling is limited to the subsonic combustion zone region and there is complete reaction of the film coolant with the excess mainstream oxidizer, the performance loss will be small and due principally to the pressure loss associated with the burning in a supersonic stream of the expansion nozzle. The percentage performance losses in LO_2/RP-1 and

LO_2/LH_2 engines with RP-1 and H_2 film coolants are shown in Fig. 50 and 51 for 0-, 50-, and 100-percent combustion and the additional assumption of no mixture ratio change losses.

Consideration of the maintenance of an overall thrust chamber mixture ratio at a value indicative of the highest specific impulse leads to the highest performance loss in the case of a film-cooled design where no interaction of the film coolant and the mainstream can be anticipated. This is a result of the mixture ratio shift of the mainstream core to a reduced specific impulse value and additionally to the assumed total loss of the film coolant. These losses were developed by considering the mixture ratio shift of the mainstream with film-coolant addition. Figures 52 and 53 show the shift for $LO_2/RP\text{-}1$ and LO_2/LH_2, respectively. The performance loss for the combined effect of the ratio of film coolant to total flow (φ) and the mainstream mixture ratio change from no film cooling (condition 1) to the film-cooled value may be derived as:

$$P.L. = 1 - (1 - \varphi) \frac{(I_s)_2}{(I_s)_1} \tag{258}$$

Figures 50 and 51 show that a significantly greater loss may occur under this condition.

An assumption of a thermal equilibrium condition between the film coolant and the mainstream prior to expansion may be developed from the dump-cooling energy balance equations. If the film coolant is assumed to be gaseous and infinite pressure ratio is assumed, the relationship

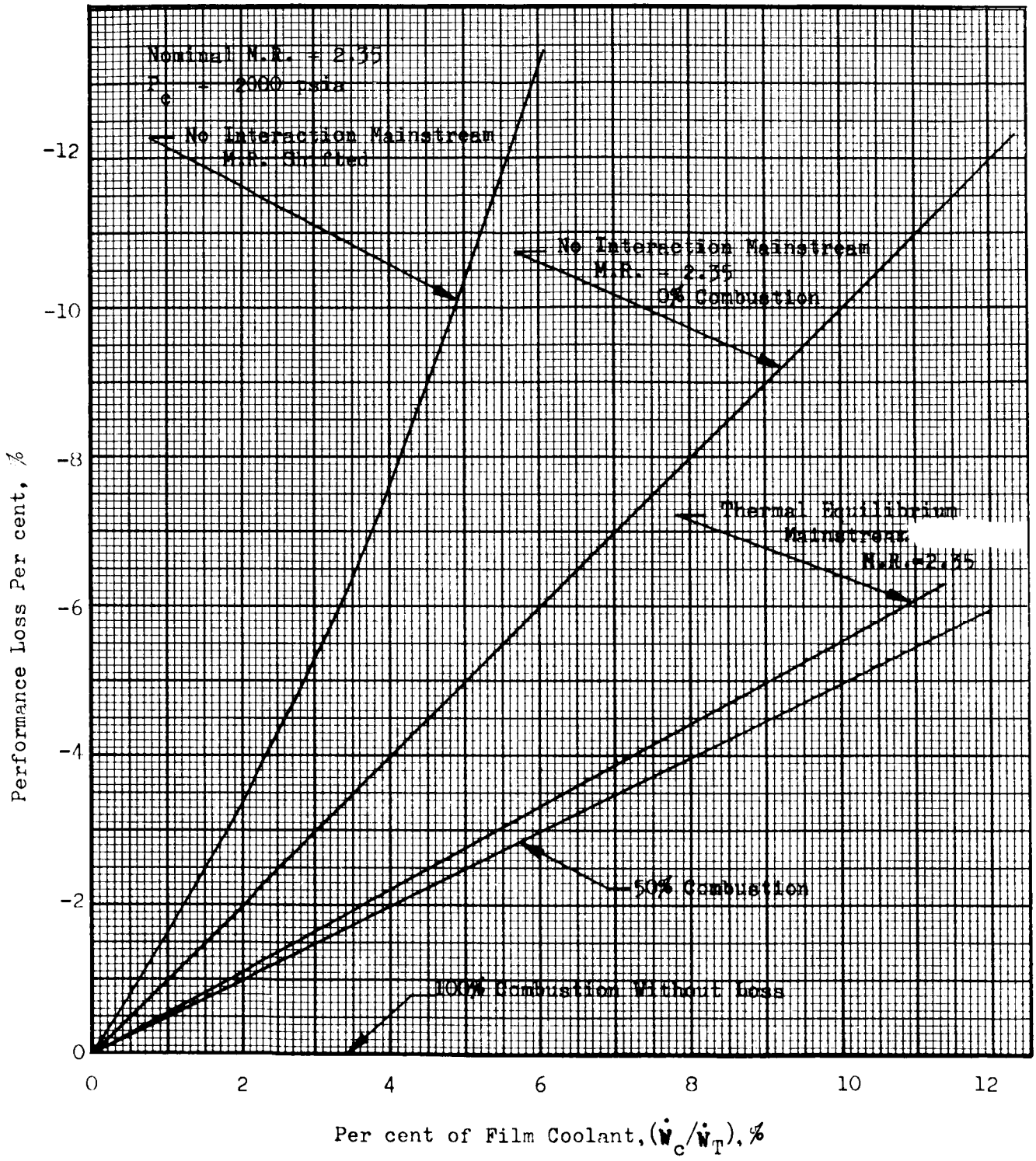

Figure 50. LO_2/RP-1 Film-Cooling Performance Loss

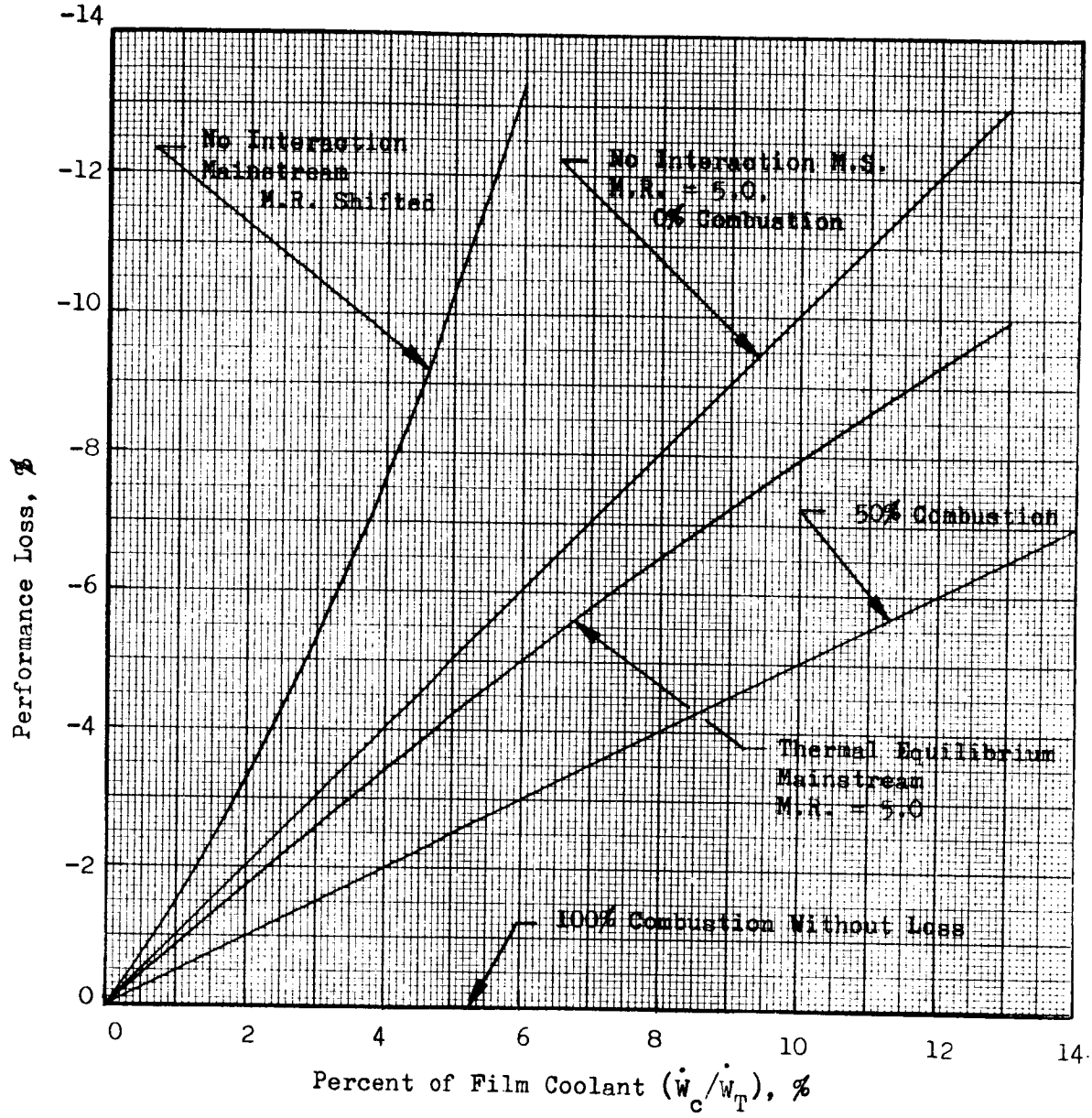

Figure 51. LO_2/LH_2 Film-Cooling Performance Loss

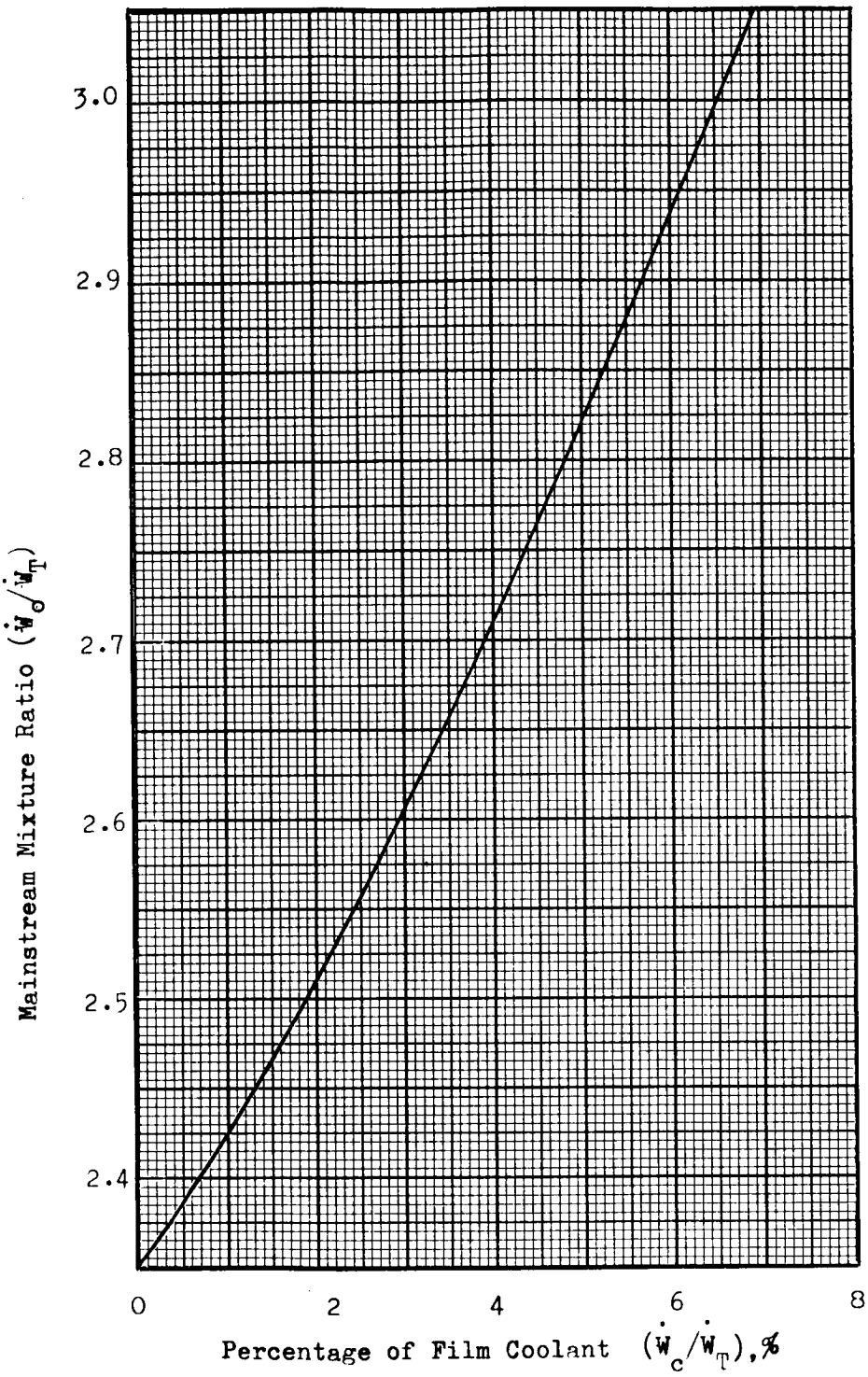

Figure 52. Effect of LO_2/RP-1 Mainstream Mixture Ratio Shift on Percent of Film Coolant for Nominal MR = 2.35

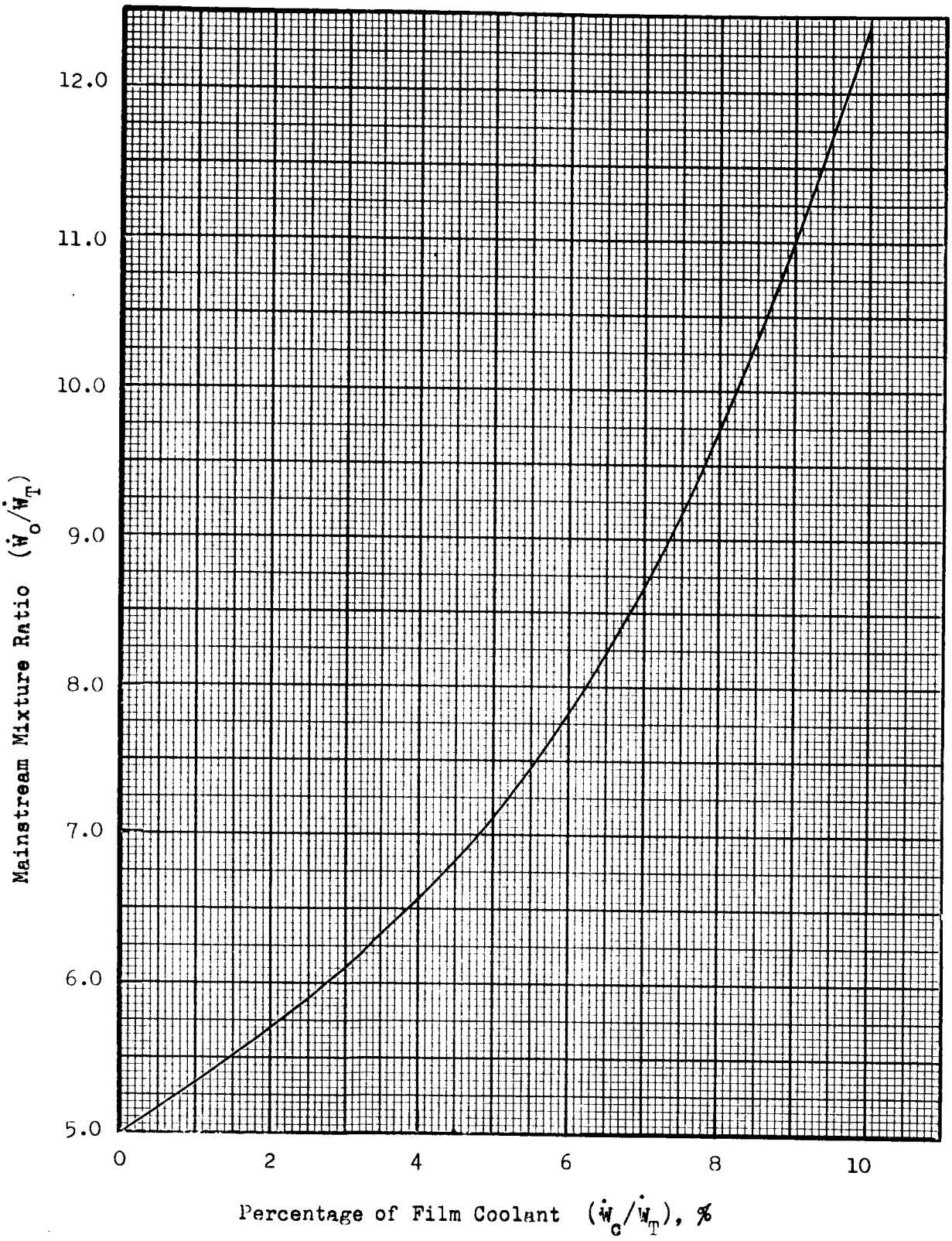

Figure 53. Effect of LO_2/LH_2 Mainstream Mixture Ratio Shift on Percent of Film Coolant at Nominal MR = 5.0

between the specific impulse with film cooling (condition 2) compared with none (condition 1) may be written as:

$$\frac{I_{s_2}}{I_{s_1}} = (\dot{W}_2/\dot{W}_1) \sqrt{\frac{T_{g2}}{T_{g1}}} + (\dot{W}_c/\dot{W}_1) \sqrt{\frac{C_{pc}}{C_{pg1}} \left(\frac{T_c}{T_{g1}}\right)} \tag{259}$$

where an assumption of a constant mainstream mixture ratio and specific heat is made.

Considering that the absorption of heat by the film coolant without combustion decreases the temperature of the mainstream, the appropriate heat balance may be written (assuming the initial film-coolant temperature is negligible) as:

$$\dot{W}_c \, C_{pc} \, (T_c) = \dot{W}_2 \, C_{pg} \, (T_{g1} - T_{g2}) \tag{260}$$

If $T_c = T_{g2}$

$$\frac{T_{g1}}{T_{g2}} = 1 + \left(\frac{\dot{W}_c}{\dot{W}_2}\right) \left(\frac{C_{pc}}{C_{pg}}\right) \tag{261}$$

If $\varphi = (\dot{W}_c/\dot{W}_1)$

$$\frac{I_{s2}}{I_{s1}} = \left[(1 - \varphi) + \varphi \sqrt{\frac{C_{pc}}{C_{pg}}}\right] \sqrt{\frac{1}{1 + \left(\frac{\varphi}{1 - \varphi}\right) \frac{C_{pc}}{C_{pg}}}} \tag{262}$$

Figures 50 and 51 include values of performance loss for thermal equilibrium. It is indicated that, assuming a gaseous constituent in both cases, the RP-1 provides a better performance on this percentage basis than the LH_2 film coolant. This is due principally to the film coolant to mainstream heat capacity ratio shown in the equation above.

The apparent minimization of performance loss that occurs when film cooling is used with hydrogen-based propellant combinations occurs as a result of the faster reaction rate of the hydrogen which results in an eventual higher fraction of the hydrogen film coolant combusting as well as achieving a higher temperature and, hence, contributing to an increased specific impulse.

It is evident from the above discussion that the mainstream core mixture ratio should be maintained at an on-mixture-ratio condition and similarly that the promotion of combustion for the fuel-rich film cooling gases near the wall is best. Figure 54 shows that the utilization of a nominal mixture ratio mainstream with a core rich in oxidizer adjacent to the film-coolant layer appears the most satisfactory in providing the minimum performance loss.

The extent of combustion of the film coolant is not calculable. However, a test program should follow the guidelines presented herein with initial testing at high coolant flows such that the performance loss is not masked by experimental error.

Such a program should, however, be conducted in a manner to indicate the performance loss at low percentage of film-coolant flows (as required in the actual case) by extrapolation down from a larger film-coolant flow condition. In such a manner, the error in small specific impulse differences obtained with the smaller actual film-coolant flowrates will not be within the "scatter" of the measurement.

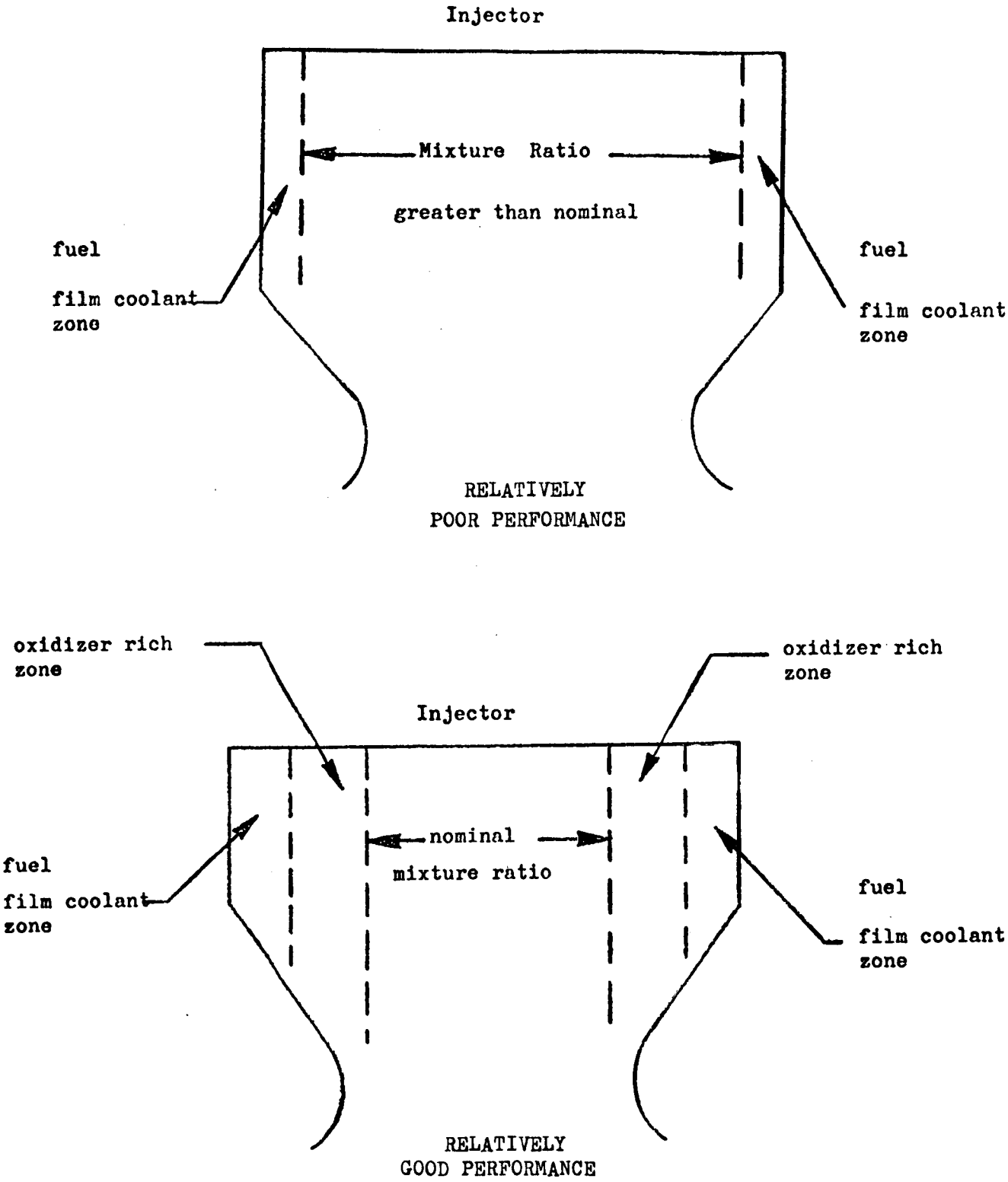

Figure 54. Effect of Mixture Ratio Variation on Performance With Film Cooling

Preliminary work was also performed on film-cooling performance losses using the Rocketdyne multielement performance digital computer program. The performance loss was considered under the assumptions: (1) the coolant mixes with part of the mainstream; (2) mixed streams and mainstream are expanded separately; and (3) the total specific impulse is obtained from a weighted average of the two separate streams. In considering the energy transfer between the two streams, the percentages of mixing, reaction, and heat transfer were varied.

Figures 55 and 56 illustrate typical cases for LO_2/LH_2 and LO_2/RP-1, respectively. It is shown that with hydrogen especially, a small degree of mixing with the mainstream materially reduces the performance loss. Further study with reaction at varying reaction mixture ratio conditions needs to be performed to establish losses under reaction conditions. Figure 55 shows that if any degree of mixing of the hydrogen film coolant can be expected with the mainstream, the decrease in specific impulse expected is small. This can be explained by examination of the high performance obtained with low-temperature heated hydrogen because of its low molecular weight. Preliminary analysis of a reaction condition with the mainstream gas indicates performance degradation levels about the same as for the mixing case.

Examination of analysis cases for RP-1 fuel indicates a marked difference in the predicted performance loss between the case where the coolant is assumed to mix and react with the mainstream and the case where the coolant is assumed to only mix with the mainstream. This is a result of the predominately endothermic reactions that occur when the coolant (RP-1) is allowed to react with the mainstream. For coolant flows greater than 5 percent, the 100-percent reaction curve indicates a higher performance loss than the 100-percent mixing curve. This is a result of the lower combustion temperature which is obtained when the coolant is allowed to

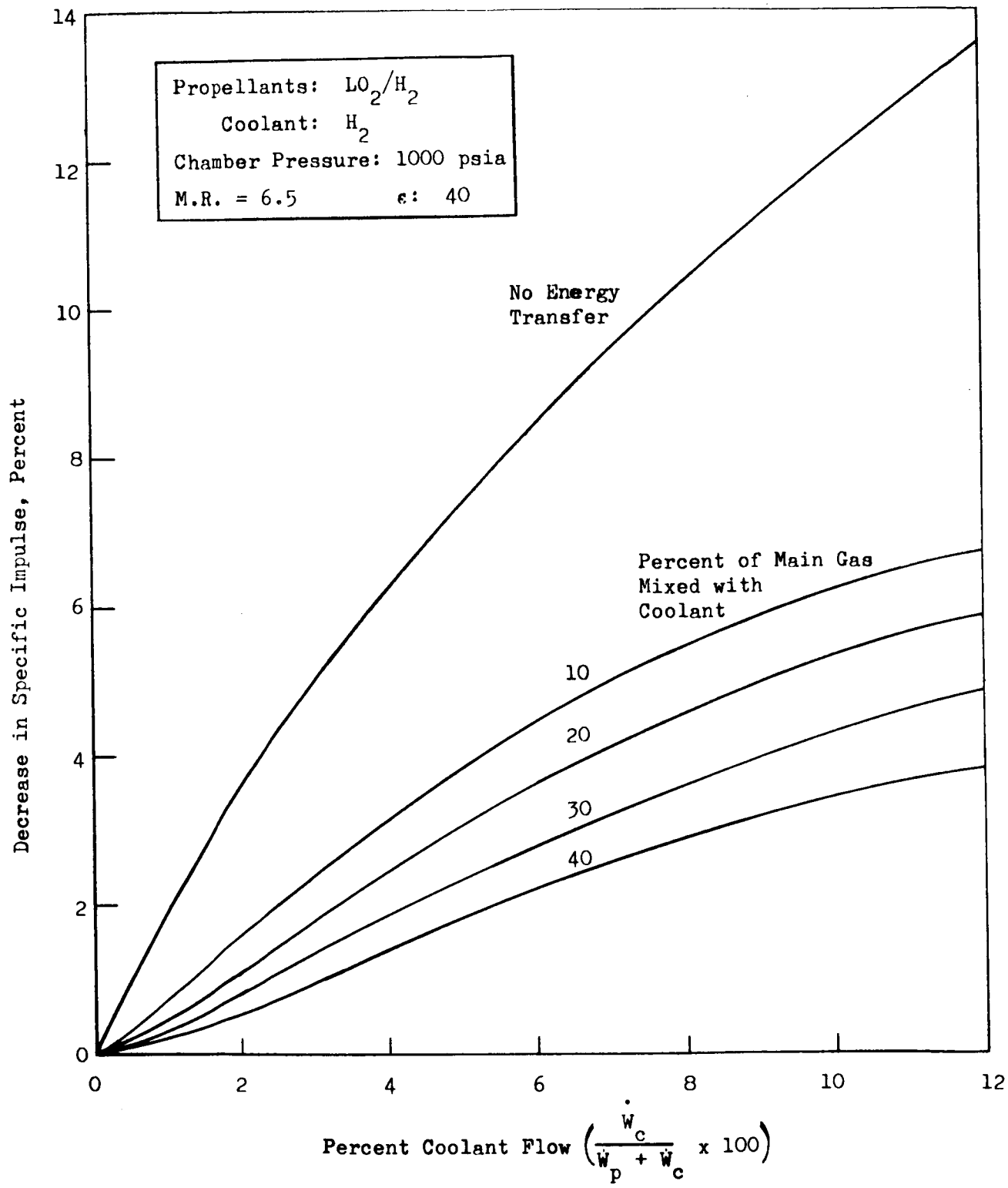

Figure 55. Loss in Specific Impulse with Film Cooling for LO_2/LH_2 (Based on 100-percent mixing)

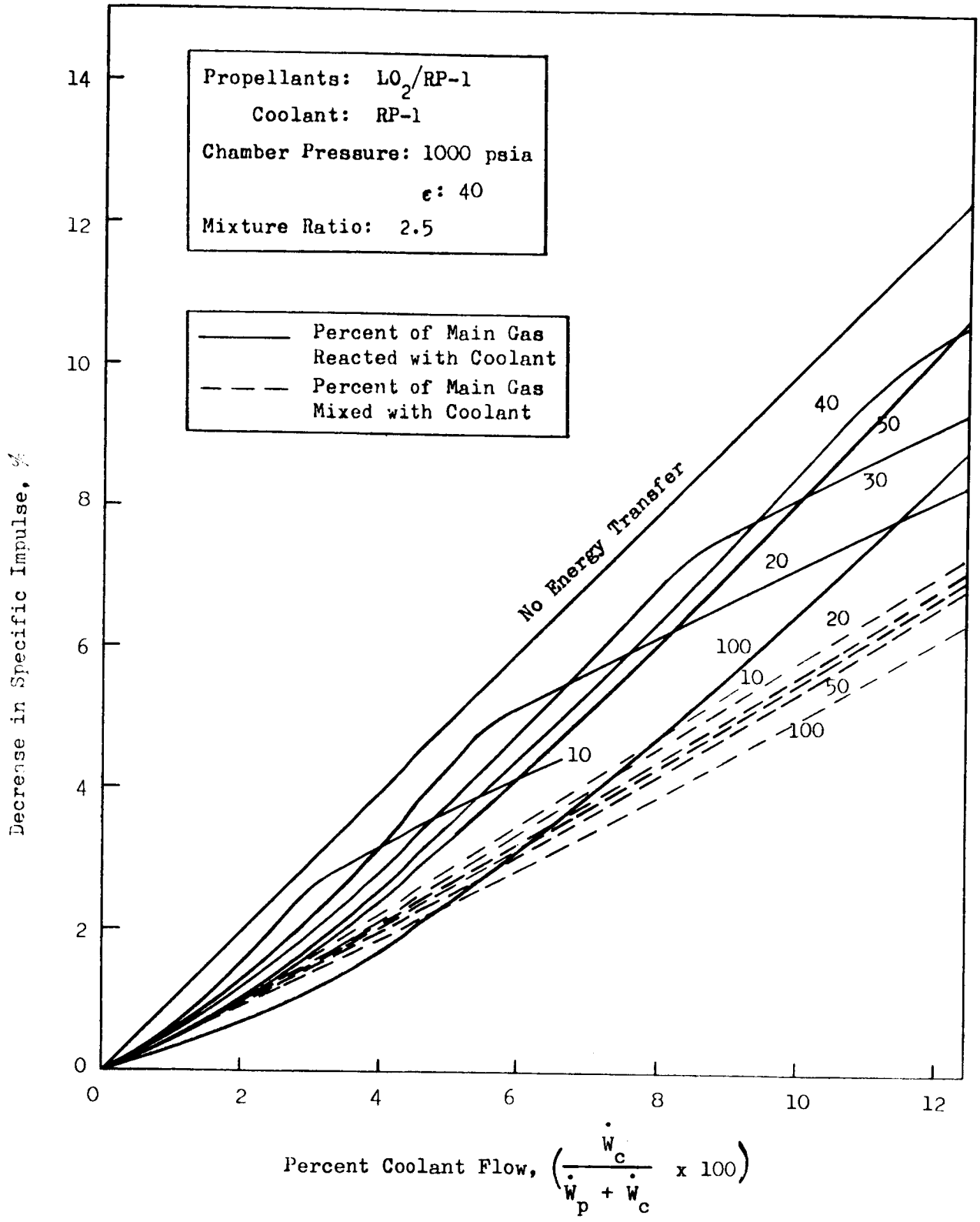

Figure 56. Loss in Specific Impulse with Film Cooling for LO_2/RP-1

react. For coolant flows lower than 5 percent, the mixing curve shows a higher performance loss. This is due to the fact that although the combustion temperature for the mixing case is slightly higher than for the reaction case, the molecular weight is also higher resulting in a lower specific impulse.

The percent reaction curves (Fig. 56) show an abrupt change in slope at certain values of coolant flow. This is primarily a result of the formulation of solid carbon at low mixture ratios (below approximately 1.0) which gives rise to a decrease in slope of the specific impulse vs mixture ratio curve. For example, the 10-percent reaction curve has an abrupt change in slope at a coolant flow of approximately 3 percent. At this point, the mixture ratio of the portion of the mainstream which is assumed to react with the coolant is approximately 1.0. The 100-percent reaction curve would have a change in slope at a coolant flow of approximately 24 percent, which corresponds to a mixture ratio of 1.0. Hence, this indicates that an increase in the amount of reaction between the two streams does not necessarily mean better performance. The performance loss is also a function of the amount of film coolant present.

In an overall design study, the payload increase may be typically visualized based on the impulse tradeoff as shown below:

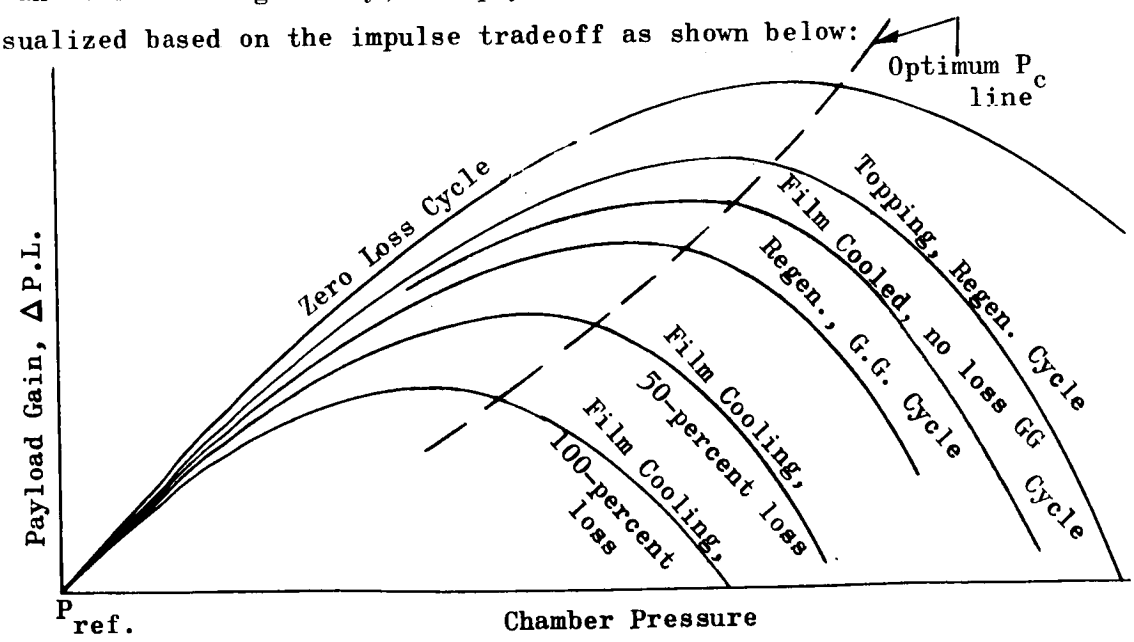

The zero-percent loss cycle where no pumping losses or mass transfer loss occurs is shown to give maximum payload gain. However, because of an increased engine weight with higher chamber pressure, an optimum chamber pressure will occur where the weight increase will negate the slightly increased specific impulse.

The topping regenerative cycle can be seen to optimize at the next higher engine performance point due to only a slight deficiency in the thermodynamic cycle. If a design is film cooled with zero-percent performance loss attributable to the film coolant, an optimum performance point is seen where the pumping losses and related turbine gas flows overshadow the specific impulse gain resulting from increased chamber pressure (gas generator cycle). The regenerative gas generator cycle is shown to be limited by the same influence with the large pumping pressure loss with increased chamber pressure quickly overtaking the payload gains.

Since overall gain in payload is small above a reference chamber pressure in the 1500- to 2000-psia range, if a film-cooled design is employed where a film-cooling performance loss occurs, the overall engine performance may be reduced below that of the regenerative cycle at a given chamber pressure. Under this circumstance, it is desirable to reduce chamber pressure where the required film-coolant rate is reduced or to choose the regenerative cycle.

As a result, it may be seen that the film or transpiration high-pressure design choice may be improper under an expected large mass transfer cooling loss circumstance.

Available data for film-cooling performance loss is questionable, either because of the overall poor performance of the injector tested or because

the film-coolant percentage used was not large and for the particular experiments within the scatter of the measurement accuracy. It is seen, however, that from the small gains in specific impulse shown with increased chamber pressure shown typically in Fig. 47 through 49 and from consideration of increased pumping and mass transfer cooling losses at high chamber pressure (>2000 psia), judicious care in optimizing the particular mission under consideration must be exercised. Reliability areas such as seals, overall stress levels, and failures to engine destruction at high operating pressures must also be compared.

Dump-Cooling Performance Degradation

Using the hydrogen dump cooling concept as a method for cooling the high area ratio portions of the nozzle skirt for a high chamber pressure design appears attractive with LO_2/LH_2 propellants. An allowable reduction in pump outlet pressure is provided by the parallel-flow cooling method with the dump-cooled design. Additionally, both a savings in tube and trapped propellant weight plus the allowance for skirt detachability from the main chamber resulting from parallel flow circuitry may be visualized. The minimum coolant weight flow for such a design was indicated in Ref. 1 as established by the maximum-allowable coolant temperature. This latter value may be only slightly less than the allowable wall temperature because of low heat flux values and large available coolant pressure.

Equating the heat input into the cooled wall surface with the hydrogen coolant bulk temperature rise for a minimum coolant flow:

$$q = \dot{W}_{c_{min}} (C_{p_c}) (T_{c_{max}} - T_{c_i}) \tag{263}$$

Consideration of coolant passage design and/or pressure drop restrictions may result in a design with a coolant flow greater than the specified minimum.

Since a performance degradation is anticipated with the dump-cooling process, an analysis was performed to determine it. The exhaust velocity of the dump coolant (V_c) and of the main thrust chamber gas (V_g) may be written considering the diminution of the exhaust pressure term as:

$$V_g = \sqrt{\frac{2g_c\ \chi}{\chi - 1}\ \frac{RT_g}{M_g}}\ (\Psi g) = \sqrt{2g_c\ Cp_g\ T_g}\ \Psi g \qquad (264)$$

$$V_c = \sqrt{\frac{2g\ \chi}{\chi - 1}\ \frac{RT_c}{M_c}}\ (\Psi c) = \sqrt{2g_c\ Cp_c\ T_c}\ \Psi c \qquad (265)$$

where

$$\Psi = \sqrt{1 - \frac{P_e}{P_o}\ \frac{\chi - 1}{\chi}} \qquad (266)$$

Considering the thrust ratio for the dump cooled case relative to the base case (condition 1):

$$\frac{F_2}{F_1} = \frac{\dot{W}_2 \sqrt{Cp_{g_2}\ T_{g_2}}\ \Psi g_2 + \dot{W}_c \sqrt{Cp_c\ T_c}\ \Psi_c}{\dot{W}_1 \sqrt{Cp_{g_1}\ T_{g_1}}\ \Psi g_1} \qquad (267)$$

If the flow reference value is stated as $\dot{W}$, the ratio of specific impulse values results as

$$\frac{I_{s_2}}{I_{s_1}} = \frac{\dot{W}_2}{\dot{W}_1} \sqrt{\frac{Cp_{g_2}\ T_{g_2}}{Cp_{g_1}\ T_{g_1}}}\ \frac{\Psi g_2}{\Psi g_1} + \frac{\dot{W}_c}{\dot{W}_1} \sqrt{\frac{Cp_c}{Cp_{g_1}}\ \frac{T_c}{Tg_1}}\ \frac{\Psi c}{\Psi g_1} \qquad (268)$$

If the dimensionless parameters are now defined:

$$\beta = \dot{W}_2/\dot{W}_1 \tag{269}$$

$$\Psi c_1 = \Psi c/\Psi g_1 \tag{270}$$

$$\varphi = \dot{W}_c/\dot{W}_1 \tag{271}$$

$$\Psi_{12} = \Psi g_2/\Psi g_1 \tag{272}$$

then Eq. 268 becomes:

$$\frac{I_{s_2}}{I_{s_1}} = \beta \Psi_{12} \sqrt{\frac{C_{pg_2}}{C_{pg_1}} \frac{Tg_2}{Tg_1}} + \varphi \Psi c_1 \sqrt{\frac{Cp_c}{Cp_{g_1}} \quad \frac{T_c}{T_{g_1}}} \tag{273}$$

Considering the gas temperature (T_{g_1}) to be the summative values of a state temperature condition (T_{g_o}) plus the quantity rejected into the thrust chamber jacket:

$$T_{g_1} = T_{g_o} + \frac{q_{rej}}{\dot{W}_{g_1} Cp_{g_1}} \tag{274}$$

In the dump-cooled case, the rejected heat rate is assumed transferred into the dump coolant instead of adding to the combustion temperature in the normal regenerative case. The effect of the changed fuel temperature upon the combustion efficiency has been assumed small; however,

consideration should be given to the vaporization rates of the fuel with and without the rejected heat contribution.

Defining:

$$f = \frac{q_{rej}}{\dot{W}_{g_1} \; Cp_{g_1} \; T_{g_o}} \tag{275}$$

and

$$\lambda = \sqrt{\frac{Cp_{g_2}}{Cp_{g_1}} \; \frac{T_{g_{2_M}}}{T_{g_{2_N}}}} \tag{276}$$

where the subscripts M and N refer to the chamber mixture ratio condition with and without dump cooling. The heat rejected may be written in terms of the coolant temperature rise as:

$$q_{rej} = \dot{W}_c \; Cp_c \; T_c \left[1 - \frac{T_i}{T_c} \right] \tag{277}$$

The ratio of specific impulse values with and without dump cooling becomes finally:

$$\frac{I_{s_2}}{I_{s_1}} = \beta \, \lambda \, \Psi_{12} \sqrt{\frac{1}{1 + f}} + \sqrt{\varphi} \; \Psi c_1 \sqrt{\frac{f}{1 + f} \left(\frac{1}{1 - \frac{T_i}{T_c}} \right)} \tag{278}$$

If a constant main gas mixture ratio is assumed for the regenerative- and the dump-cooled case, the total chamber flow is assumed constant,

and a high expansion pressure ratio of both the main chamber and dump-cooled gases is assumed, i.e.:

$$\Psi_{12} = 1.0$$

$$\Psi c_1 = 1.0$$

$$\lambda = 1.0$$

$$\beta = (1 - \varphi)$$

The specific impulse ratio for this specific case becomes:

$$\frac{I_{s_2}}{I_{s_1}} = (1 - \varphi) \sqrt{\frac{1}{1 + f}} + \varphi^{1/2} \sqrt{\frac{f}{1 + f} \left(\frac{1}{1 - \frac{T_i}{T_c}} \right)} \qquad (279)$$

These equations describing the performance loss with this cooling method were programmed for the digital computer. Sample checkout cases using hydrogen as a dump coolant illustrate first that only a small percentage of coolant flow is required (dependent upon the delta area ratio cooled), and secondly that the performance loss fraction of the dump coolant is similarly small. A qualitative conclusion is that from flow requirements, performance loss, and pressure drop standpoints this overboard H_2 cooling method appears excellent for use with LO_2/LH_2 propellants at high area ratio for high-chamber-pressure applications.

Figure 60 shows a typical construction method which would appear satisfactory for use. Buckling stiffnesses (pressure and thermal) cannot be provided by a double-wall design with a spiral cooling passage, and a tubular wall with multiple passes and with a large number of coolant tubes is unsatisfactory.

TURBINE EXHAUST GAS COOLING

FILM COOLING

The use of the available turbine exhaust gases for film cooling the nozzle wall surface was investigated using the film-cooling analysis equations discussed previously and in Ref. 1. Since the available turbine flow percentage increases with chamber pressure, whereas it will be shown that the percentage requirements of cooling flow do not change significantly, the method appears attractive for advanced nozzle, high-thrust designs particularly with high D_p/D_t ratios.

Film coolant provided by turbine exhaust gases is at approximately 1450 and 900 R stagnation temperatures for LO_2/RP-1 and LO_2/LH_2 gases, respectively. As a result, particularly in the case of LO_2/RP-1 propellants, a high wall temperature must be accepted with this cooling method. The inherent thermal expansion, thermal stress, and temperature problems must be examined for a satisfactory design feasibility study.

The film-coolant flowrate over a given surface area is inversely related to the accepted wall temperature; i.e., if a high wall temperature is allowed, the coolant flowrate for unit surface area may be minimized.

An analysis was performed to indicate the cooling limit requirement for a conventional material such as from the Inconel or stainless-steel family. A temperature limitation was specified at 1600 F. With the tangential-film-cooling method, wall surface temperatures will vary axially from the coolant injection temperature to the allowable value, at which point an additional injection slot is required.

Typical computer results of the study are indicated for the LO_2/LH_2 and LO_2/RP-1 propellant combinations in Tables 5 through 8. The study was conducted for D_p/D_t ratios of 3.5, 5, and 7 with advanced nozzle contours described in a later section of this report. A comparison of the D_p/D_t effect shows a considerable reduction in required turbine flow to maintain the limiting wall temperature with high D_p/D_t values. Coolant flow percentage values are seen to be approximately 6.5 percent of the flow for an LO_2/RP-1 nozzle of D_p/D_t = 3.5 and 1.5 percent for a nozzle D_p/D_t of 7. Comparable LO_2/LH_2 design requirements are 2.5 and 0.5 percent, respectively.

The low percentages of coolant requirement indicate that for the advanced nozzles, a large percentage of the cooling may be accomplished by using the turbine exhaust gases. In reality, turbine exhaust gas cooling may only be used in areas where the wall pressure becomes lower than the turbine exhaust pressure. For this analysis, ideal injection conditions for film cooling were assumed.

Coolant flow requirements would exponentially increase if the design wall temperature were reduced from the 1600 F maximum value because of a smaller allowable sensible heat pickup in the film coolant. However, the important conclusion to be considered is that with the advanced nozzle concepts the turbine exhaust gas method either singly or as augmentation will provide for a large fraction of the supersonic region heat removal if efficient injection means are used.

Turbine exhaust flow percentages available were found to be adequate for the LO_2/LH_2 designs for nozzle cooling. With the lower D_p/D_t design values for LO_2/RP-1 propellants, the turbine exhaust flow percentages were found to be inadequate because of a large nozzle surface area.

TABLE 5

LO_2/LH_2 TURBINE-EXHAUST-GAS COOLING REQUIREMENTS

FOR ADVANCED NOZZLE DESIGNS WITH $D_p/D_t = 3.5$

Thrust, million pounds	Chamber Pressure, psia	$\dot{W}_c/\dot{W}_T$ (throat to exit)	$\dot{W}_c/\dot{W}_T$ (ϵ = 20 to exit)
2	1500	0.025	0.0185
4	1500	0.023	0.0165
6	1500	0.022	0.0165
2	3000	0.024	0.0175
4	3000	0.022	0.0164
6	3000	0.021	0.0156
2	5000	0.022	0.0168
4	5000	0.021	0.0156
6	5000	0.020	0.015

T_c = 900 F

T_{wg} = 1600 F

ϵ (geometrical) = 36

TABLE 6

LO_2/LH_2 TURBINE-EXHAUST-GAS COOLING REQUIREMENTS

FOR ADVANCED NOZZLE DESIGNS WITH $D_p/D_t = 7.0$

Thrust, million pounds	Chamber Pressure, psia	$\dot{W}_c/\dot{W}_T$ (throat to exit)	$\dot{W}_c/\dot{W}_T$ (ϵ = 20 to exit)
2	1500	0.0056	0.00368
4	1500	0.00534	0.00355
6	1500	0.00515	0.00362
2	3000	0.0054	0.00358
4	3000	0.00495	0.00333
6	3000	0.00480	0.00315
2	5000	0.0051	0.0035
4	5000	0.00475	0.00315
6	5000	0.00455	0.00395

T_c = 900 R

T_{wg} = 1600 F

ϵ (geometrical) = 60

TABLE 7

LO_2/RP-1 TURBINE-EXHAUST-GAS COOLING REQUIREMENTS

FOR ADVANCED NOZZLE DESIGNS WITH $D_p/D_t = 3.5$

Thrust, million pounds	Chamber Pressure, psia	$\dot{W}_c/\dot{W}_T$ (throat to exit)	$\dot{W}_c/\dot{W}_T$ (ϵ = 20 to exit)
2	1500	0.069	0.045
4	1500	0.065	0.050
6	1500	0.062	0.047
2	3000	0.065	0.048
4	3000	0.060	0.045
6	3000	0.058	0.043
2	5000	0.062	0.047
4	5000	0.057	0.043
6	5000	0.055	0.042

T_c = 1450 F

T_{wg} = 1600 F

ϵ (geometrical) = 36

TABLE 8

LO_2/RP-1 TURBINE-EXHAUST-GAS COOLING REQUIREMENTS

FOR ADVANCED NOZZLE DESIGNS WITH $D_p/D_t = 7.0$

Thrust, million pounds	Chamber Pressure, psia	$\dot{W}_c/\dot{W}_T$ (throat to exit)	$\dot{W}_c/\dot{W}_T$ (ϵ = 55 to exit)
2	1500	0.016	0.0105
4	1500	0.014	0.011
6	1500	0.014	0.0087
2	3000	0.015	0.010
4	3000	0.014	0.0091
6	3000	0.013	0.0087
2	5000	0.014	0.0092
4	5000	0.013	0.0087
6	5000	0.0125	0.0084

T_c = 1450 R

T_{wg} = 1600 F

ϵ (geometrical) = 60

Design Considerations

From a design standpoint, certain pertinent considerations must be reviewed. The first of these is the necessary manifolding for the turbine gas coolant. To provide for a minimization of wall temperature, a number of turbine exhaust gas coolant manifolds must be positioned along the wall surface. If a tubular-wall or double-wall concept with compartmentizing is to be employed, gas passage is provided between injection stations. The rigidity and weight savings provided by the compartmentizing of the chamber wall circumference would indicate an advantage over the single-wall concept with exterior manifolding spaced longitudinally. Thermal growth and buckling problems are the most important for examination with such a design. Tangential flow direction and uniform circumferential distribution are imperative with turbine gas-cooled designs because the wall temperatures normally are at a high level and a large latitude in coolant flow or efficiency are not allowed.

Combined Turbine Gas and Regenerative Cooling

The combined concept for high-chamber-pressure designs where simultaneous turbine gas introduction and regenerative cooling are employed appears advantageous particularly with hydrogen fuel-based propellants because combustion efficiency and stability are significantly improved with an increased hydrogen injection temperature. The use of hydrogen as a coolant in the high area ratio portion of the nozzle combined with the turbine exhaust gas can allow the coolant to warm up and yet allow the hot gas-side wall temperatures and coolant pressure drop to be at minimal values. Figure 57 illustrates the combined concept. For a high D_p/D_t nozzle with a short length, turbine-gas introduction for film coolant may be made at one

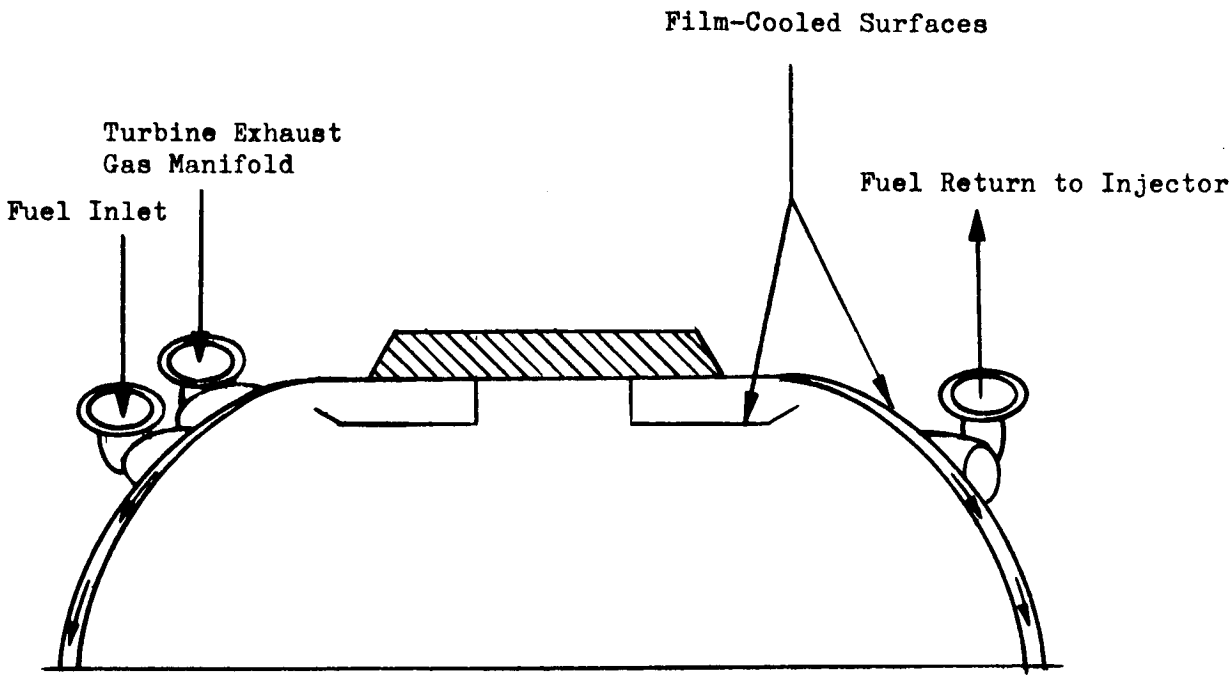

Figure 57. Typical Schematic of Advanced Nozzle High D_p/D_t Design with Film and Combined Turbine Gas Cooling

location at the juncture between the film-cooled high heat flux areas and the nozzle skirt attach point. To provide for tube number minimization and manifolding, a double coolant pass could be used with nearly circular coolant tubes.

Similarly, this combined cooling method appears attractive for LO_2/RP-1 propellants, especially if added carbon deposition on the wall surface may be anticipated from the fuel-rich turbine exhaust gases.

DUMP COOLING

A comparative study of the use of turbine exhaust gas for dump cooling was made. A comparison with the film-cooled case is shown in Table 9 where the advantages and disadvantages are outlined. A serious disadvantage is seen in the high wall temperature and consequent higher thermal stress condition for the dump-cooled case. This higher wall temperature value is necessitated by the required temperature differential between the coolant side wall and the bulk coolant. Designs for LO_2/LH_2 propellants at 3000 psia, considering cooling from an expansion area ratio of 20 to 30, indicated an 1800 F minimum wall temperature must be tolerated to maintain a reasonable pressure drop in the cooling passage without choking. Figures 58 and 59 show typical LO_2/LH_2 design case parameters for a conventional engine. The requirement for a lower wall temperature results in an extreme burden on the pump efficiency because of a reduction in pressure ratio caused by the higher cooling pressure requirement. A study of the maximum outlet pressures available at the turbine exit would be required.

TABLE 9

COMPARISON OF TURBINE EXHAUST GAS COOLING BY DUMP- AND FILM-COOLING METHODS

Factor	Film Cooled	Dump Cooled
Wall Temperature	Advantage	Disadvantage
Thermal Stress	Advantage	Disadvantage
Fabrication	Disadvantage	Advantage
Pressure Requirement	Advantage	Disadvantage
Weight	Advantage	Advantage
Performance	Unknown	Advantage
Carbon Coking (T_{wc})	-	Disadvantage
Carbon Coking (T_{wg})	Advantage	Advantage

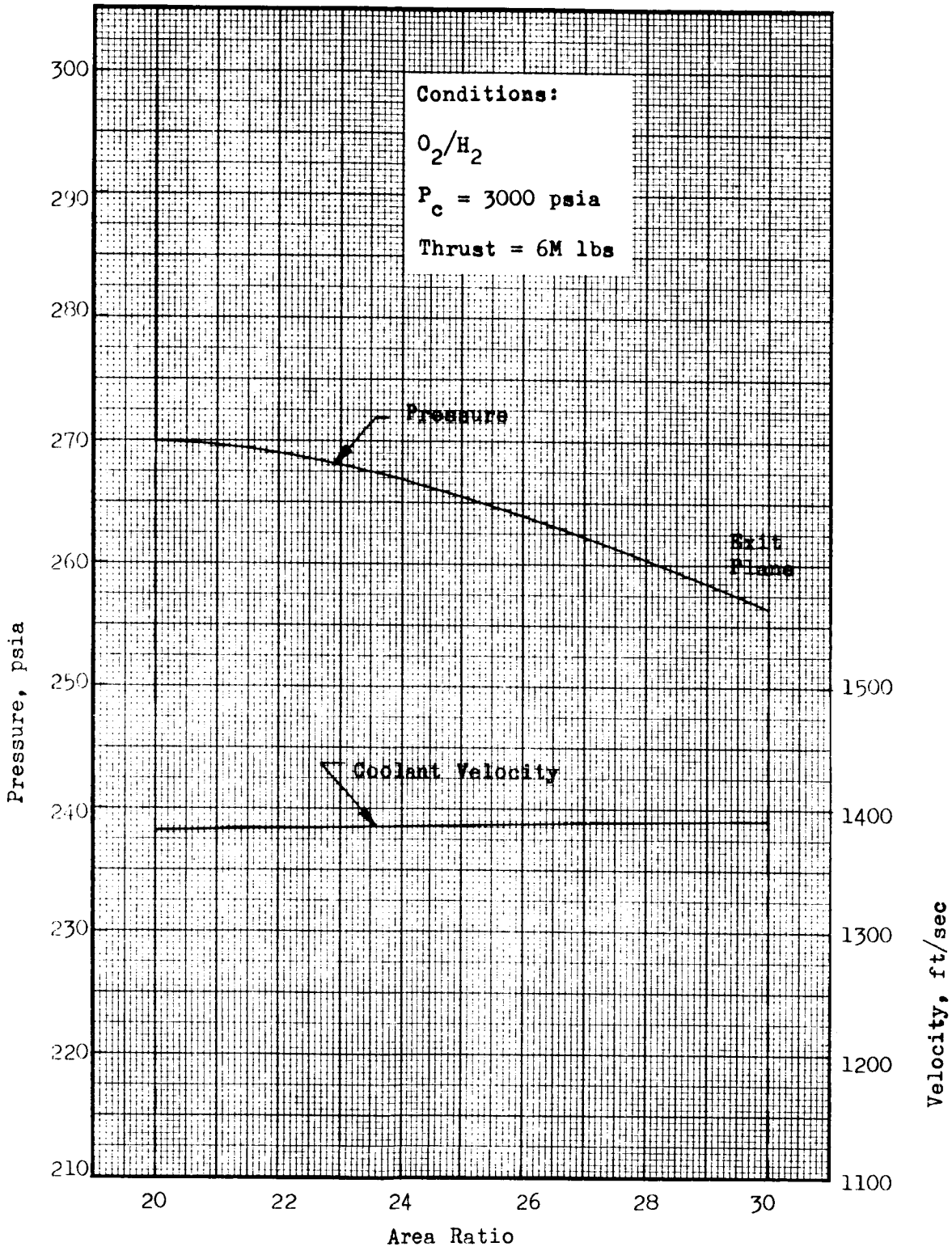

Figure 58. Coolant Velocity and Static Pressure Distribution for Turbine Gas Dump-Cooling Design

Conditions: O_2/H_2

P_c = 3000 psia

Thrust = 6M lbs

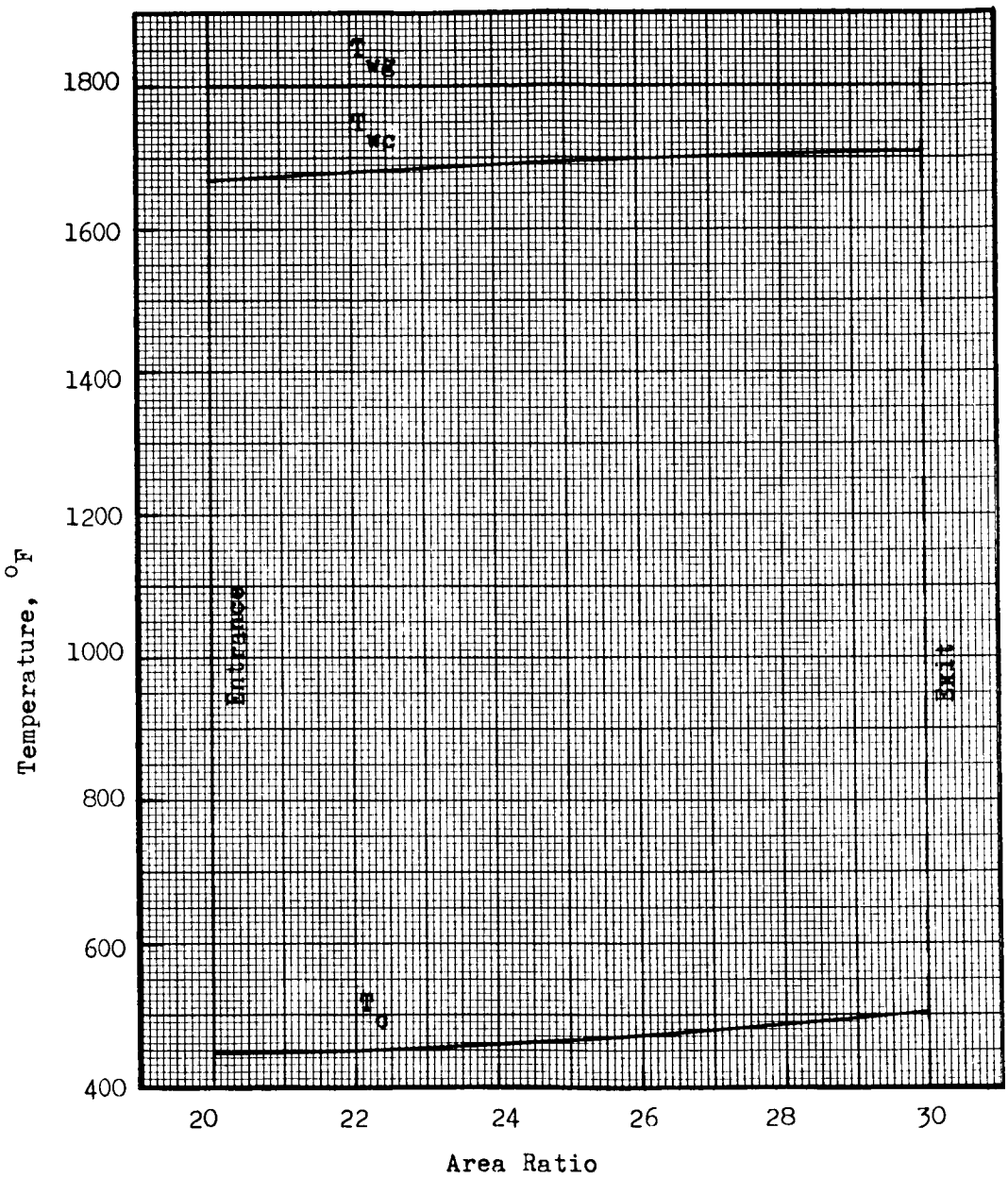

Figure 59. Coolant and Wall Temperatures for Dump-Cooling Design Employing Turbine Exhaust Gases

For the 3000-psia design case illustrated, the turbine outlet pressure was assumed to be 300 psia. Pressures of 200 psia and lower were found to result in choking in the coolant passages.

Materials of the 300-series stainless-steel and Inconel families are not suitable at the required high wall temperature values. More suitable choices are Hastelloy C and Rene 41 which have a better strength capability at the required higher temperatures. Figure 60 illustrates a possible overboard cooling method design approach.

The possibility of coke formation on the inside surface of the wall (coolant side) for a LO_2/RP-1 design would prove disasterous for a convectively cooled skirt. This carbon deposition caused by the fuel-rich turbine exhaust gases would provide an insulating effect against heat transfer, and as a result, the wall temperature would continue to rise with continued deposition until failure occurred.

During this analytical study, a sensitivity tradeoff between wall temperature and turbine exhaust outlet pressure was made. With the relatively low-pressure condition of the turbine exhaust gases combined with a high bulk temperature, coolant choking readily occurs if the wall temperature is reduced by only 100 F from the design value. As a result, the acceptance of high wall temperature values is mandatory.

The effect of the performance change with turbine-gas dump cooling was outlined above. Since the effects of combustion, of the shock introduction in the supersonic region, and of the momentum interchange between the film coolant and mainstream cannot be realistically analyzed for the film-cooling case, a comparison of the two methods cannot be made.

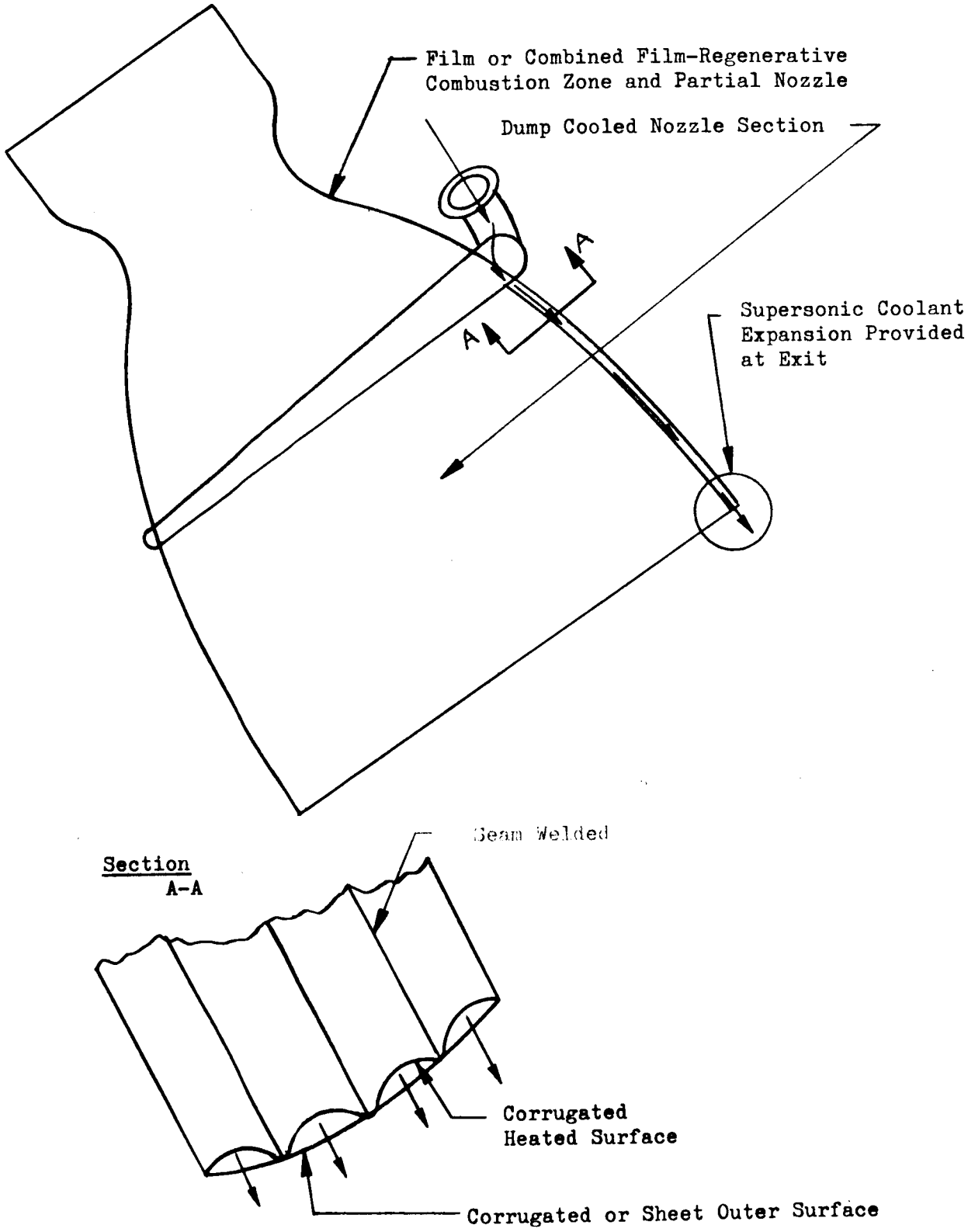

Figure 60. Typical Overboard Cooling Method for High Area Ratio

Consideration of all aspects (with the possible exception of performance) would consequently lead to the conclusion that, if the extremity of the nozzle is to be cooled by turbine exhaust gases, the most advantageous method is the multiple-slot film-cooling design. For a given maximum allowable heat transfer rate or wall temperature condition, a greater nozzle area may be effectively cooled. Alternately, because reliability is diminished with increased wall surface temperatures, the lower wall surface temperatures with the film-cooling method appears best.

COMBINED COOLING METHODS

The advantages of combining several cooling methods to tolerate high heat flux levels was investigated to develop the useful operating heat flux ranges. The combined cooling methods considered included the film-regenerative, film-ablative and film-radiative methods. Of these three, the film-regenerative combination appeared the most attractive.

FILM-REGENERATIVE COOLING

An exact differential equation solution for the codirectional case was presented in Ref. 1. A more approximate solution was made to allow graphical examination of the operating regimes where this cooling method can be used to advantage.

The total heat flux may be considered as the sum of the regenerative (R) and film-cooled (F) fractions as:

$$(q/A)_T = (q/A)_R + (q/A)_F \tag{280}$$

if the total heat input for the combined case is considered to remain the same.

This total heat input may be expressed as:

$$(q/A)_T = h_g \left(T_{aw} - \overline{T}_{wg}\right) = h_g \, T_{aw} \left(1 - \frac{\overline{T}_{wg}}{T_{aw}}\right) \tag{281}$$

which for a value of $\overline{T}_{wg}/T_{aw} < 1$ becomes less dependent on that factor.

The film-coolant heat absorption for a cylindrical film-cooled element is:

$$\frac{\dot{W}_{FC}\,\eta\,C_p\,\Delta T}{\pi\,\bar{D}\,L} = (q/A)_F = \frac{\dot{W}_{FC}\,C_p\,\eta\,(T_{wg} - T_i)}{\pi\,\bar{D}\,L} \tag{282}$$

in terms of the film cooling efficiency (η).

It was previously determined that the wall conduction limit, based on the differential temperature between the maximum allowable gas-side value and the coolant temperature, is the maximum heat flux limit for regenerative cooling as:

$$(q/A)_{CL} = \frac{k\,(T_{wg} - T_{rc})}{t} \tag{283}$$

Considering the ratio of the film-coolant heat absorption to the regenerative wall heat conduction limit assuming $T_i = T_{rc}$:

$$\frac{(q/A)_F}{(q/A)_{CL}} = \frac{\dot{W}_{FC}\,\eta\,C_p\,t}{\pi\,\bar{D}\,L\,k} \tag{284}$$

The relationship may also be expressed as:

$$\frac{(q/A)_F}{(q/A)_{CL}} = \frac{(q/A)_T - (q/A)_R}{(q/A)_{CL}} \tag{285}$$

Based upon coolant pressure drop considerations from previous work (Ref. 1), it appears that a reasonable upper limit for regenerative cooling as a fraction of the conduction limit value can be expressed as:

$$\frac{(q/A)_R}{(q/A)_{CL}} = K \tag{286}$$

where $K \approx 2/3$ at high heat flux conditions. Equation 285 may be expressed as:

$$\frac{(q/A)_F}{(q/A)_{CL}} = \frac{(q/A)_T - K\,(q/A)_{CL}}{(q/A)_{CL}} = \frac{(q/A)_T}{(q/A)_{CL}} - K \tag{287}$$

which results in:

$$\frac{\dot{W}_{FC}\,\eta\,C_p\,t}{\pi\,\bar{D}\,L\,k} = \frac{(q/A)_T}{(q/A)_{CL}} - K \equiv S \tag{288}$$

Figure 61 shows the above relationship for the film-cooled case alone ($K = 0$) and for a reasonable regenerative heat input condition ($K = 2/3$). A useful range for regenerative cooling singly is shown consequently to be 0 to 0.667 of the wall conduction limit. The combined film-regenerative method is useful from 0.667 to about 2.2 times the wall conduction limit. The latter upper limit developed from Fig. 62 shows the ratio of the combined film-regenerative cooling method to the singly film-cooled value. For $K = 0.667$, a near asymptotic behavior is shown at approximately 2.2 times the wall conduction limit, which represents only a 30-percent reduction in flow from the completely film-cooled case.

Based on the throat region of a high-chamber-pressure, large-thrust, element design, the regions for cooling operation for LO_2/LH_2 and LO_2/RP-1 propellants are given below.

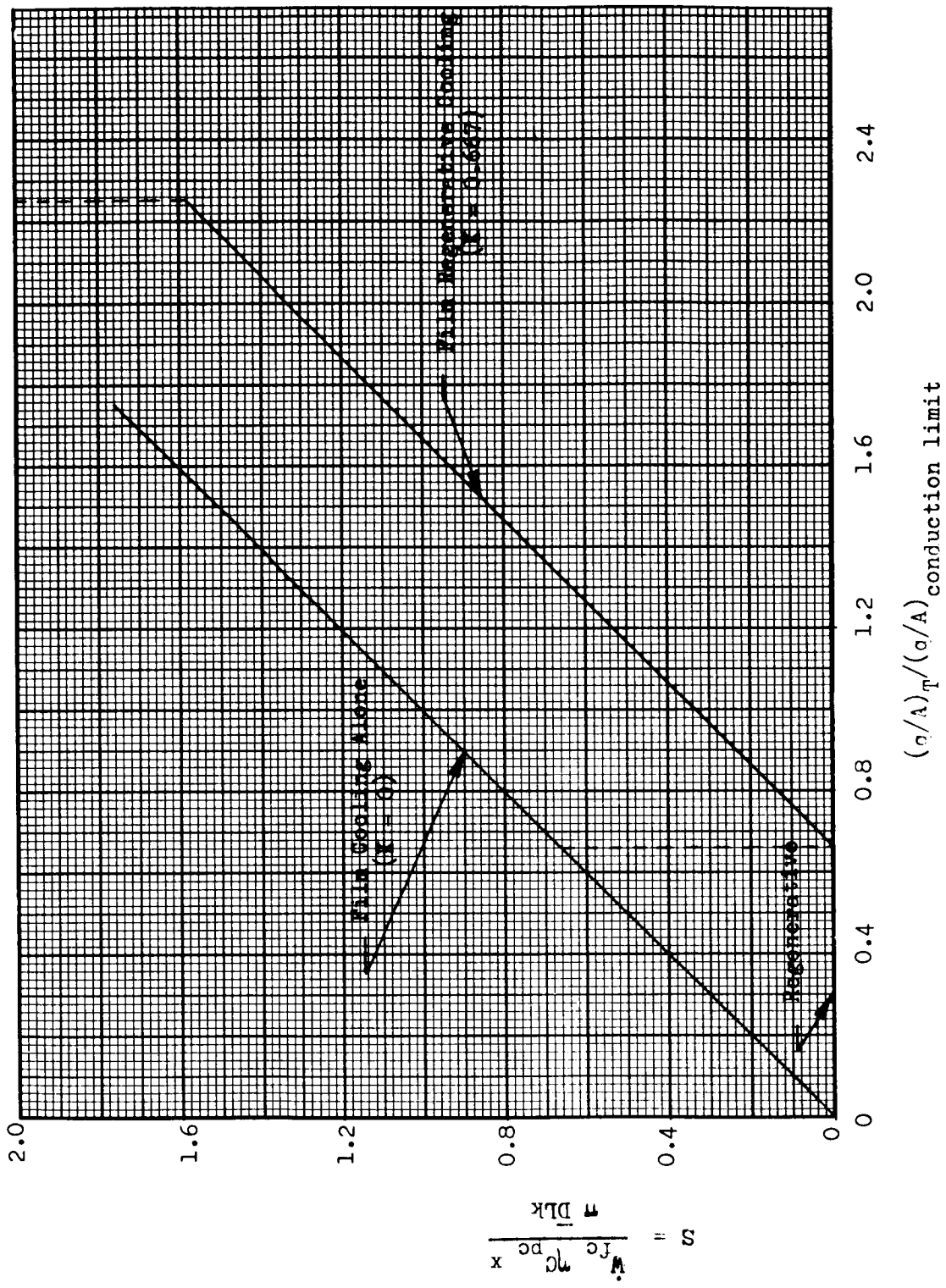

Figure 61. Approximate Combined Film-Regenerative Cooling Flow Requirement Diagram

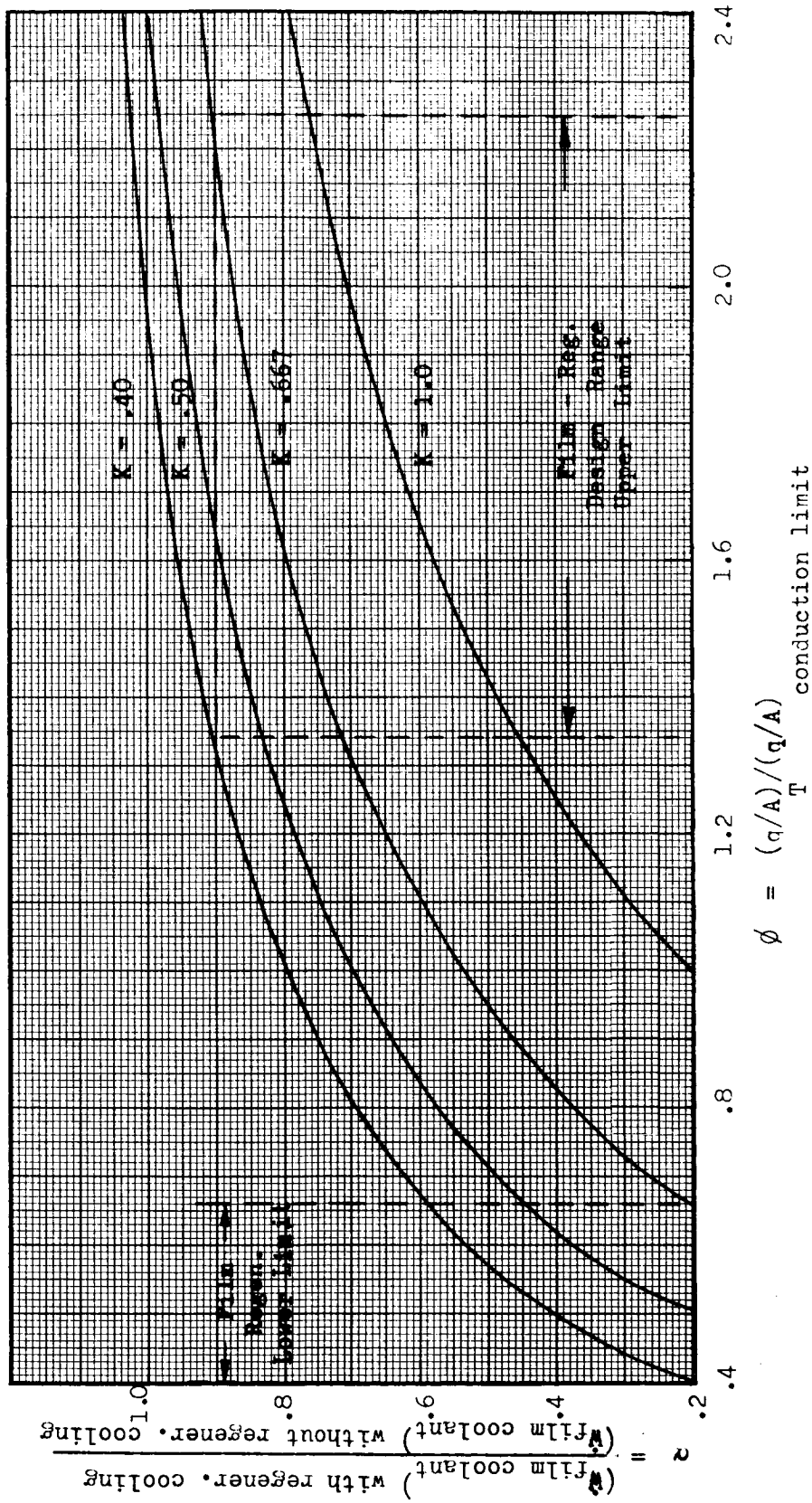

Figure 62. Ratio of Film-Coolant Requirements vs Heat Flux Ratio

Propellants	Chamber Pressure, psia $LO_2/RP-1$	LO_2/LH_2
Conduction Limit for 347 Stainless Steel or Inconel X (0.010-inch wall)	3200	2800
Upper Regenerative Limit (2/3 Conduction Limit)	2300	2030
Upper Film-Regenerative Limit (2.2 x Conduction Limit)	6000	5250
Upper Film Limit	> 6000	> 5250

The above table is based upon a throat heat flux condition. For combustion zone regions, the combined method may be used to much greater advantage at high chamber pressure because of the lower heat flux. The useful range of chamber pressures for the combined method listed above can consequently be further increased because of the large relative area in the combustion zone compared to the throat region. The practical upper limit for the combined film-regenerative or film-cooling methods is dependent upon additional considerations. The allowable performance loss based upon specific impulse changes must be weighed against the performance loss with increased fuel-film-coolant flowrates associated with increasing chamber pressure.

The parameter

$$S = \frac{\dot{W}_{FC}\, \eta\, C_p\, t}{D\, L\, \pi\, k} \tag{289}$$

may be written in terms of percent film coolant relative to the total flow (φ_{FC}) in a more useful dimensionless form:

$$(\eta/4)\ \varphi_{FC}\ (P_c g_c)\ c^*(t/\epsilon_c)(C_p/k)(\bar{D}/L) = S \tag{290}$$

For fixed-geometric dimensions, coolant, and wall properties, the functional relationship may be developed from Fig. 62 as:

$$\varphi_{FC} = f_1\ (P_c) \tag{291}$$

The total specific impulse (I_{s_T}) of the system as a function of the cooling method is:

$$I_{s_T} = (1 - \varphi_T - \varphi_{FC})\ I_{s_{chamber}} + \varphi_T\ I_{s_{turbine}} + \varphi_{FC}\ I_{s_{FC}} \tag{292}$$

The relationships:

$$\varphi_T = f_2\ (P_c) \tag{293}$$

$$I_{s_{turbine}} = f_3\ (P_c) \tag{294}$$

$$I_{s_{chamber}} = f_4\ (P_c) \tag{295}$$

$$I_{s_{FC}} = f_5\ (P_c) \tag{296}$$

may be combined to yield:

$$I_{s_T} = \left[\ 1 - f_2 - f_1\ \right] f_4 + f_2\ f_3 + f_1\ f_5 \tag{297}$$

The maximum performance point for the combined cooling method may then be optimized in terms of chamber pressure at the point:

$$\frac{\partial (I_{s_T})}{\partial (P_c)} = 0 \tag{298}$$

Preliminary work of this type was presented in Fig. 47 through 49 and on page 182 and should be considered in an engine optimization study where high-pressure designs are compared.

COMBINED FILM-ABLATIVE COOLING

The combined film-ablative method appears to offer considerable benefits over either method used singly. When fuel is used as a film coolant, the results are to: (1) reduce the effective combustion gas temperature, and (2) prevent surface oxidation and erosion of the char surface. A preliminary analysis was conducted from the closed-form ablation equation of Medford (Ref. 1). If it is assumed that effective heat of pyrolysis of the ablative resin is much greater than the heat gain of the pyrolysis gases in passing from the char-virgin interface to the char surface, then Medford's equation reduces to:

$$\Delta y_c = \left[\frac{2\, k_c\, \tau\, (T_{aw} - T_a)}{\rho\, Q_p^*} \right]^{1/2} \tag{299}$$

For a pyrolysis temperature (T_a) much lower than the adiabatic wall temperature, the char rate may be cut proportionally to the square root of the effective combustion gas temperature. From the relationship above, the char rate will be materially reduced as the adiabatic wall

temperature is decreased as will occur with film cooling. The effect is shown in the table below for the reduction in adiabatic wall temperature using phenolic-Refrasil material based on a pyrolysis temperature of 25 percent of the original adiabatic wall temperature.

Reduction in T_{aw} (T_{aw_1}/T_{aw_o})	Char Depth Ratio $\left[(\Delta y_c)_1/(\Delta y_c)_o\right]$
1.0	1.0
0.75	0.818
0.50	0.578
0.25	0

Thus, if the gas boundary temperature is reduced to near the pyrolysis temperature, a substantial reduction in char thickness can be achieved.

FILM-RADIATION COOLING

The combined film-radiation method was further reviewed from the background provided in Ref. 1. The conclusion was that the radiation method singly had a poor heat flux dissipation potential, but when combined with film cooling, it showed a substantial increase in allowable operating heat flux. The majority of the benefit is, however, derived from the film-coolant layer in such a combined system. The usefulness of the radiation-film method will still be limited to low-heat-flux applications. A probable application point in a high-pressure design would be in the high expansion ratio nozzle portion of a film-cooled or regenerative-film-cooled design where a residual film-coolant layer remains from the upstream section. Considering a new effective

film-cooled stagnation temperature as T_{aw}', the allowable radiation attach point area ratio ϵ_c may be decreased by the relationship:

$$(\epsilon'/\epsilon)_c = (T_{aw}' - T_r/T_{aw} - T_r)^{1.25} \tag{300}$$

If the gas boundary temperature approaches the radiation temperature, a substantial reduction in the radiation attach point may be made.

CONVENTIONAL ENGINE DESIGN LAYOUTS

Two design layouts of typical conventional engines in the 6-million-pound-thrust range were prepared, the first using LO_2/LH_2 propellants at a 3000-psia chamber pressure, and the second at a 2500-psia chamber pressure with the LO_2/RP-1 system. In particular, methods of film cooling the engines with liquid fuel and turbine exhaust gas were explored in addition to the current regenerative concepts.

Figures 63 and 64 show the LO_2/LH_2 and LO_2/RP-1 designs, respectively. A summary of the characteristic design parameters is included in Table 10. As no detailed investigation of the regenerative contribution to chamber wall cooling was conducted relative to the LO_2/RP-1 design, sufficient film coolant to absorb the full combustion chamber heat load was assumed in Table 10.

LO_2/LH_2 ENGINE

The most striking facet of this system is the physical size of the turbopumps, particularly the axial hydrogen pump. The pumps shown, adapted from Ref. 58, are quite firmly designed "green" pumps. Some reduction in hydrogen pump size might be realized by operation at the higher tip speeds possible with titanium impellers from the present design of 1000 ft/sec to perhaps 2000 ft/sec. The length and pump diameter as a result can be proportionately reduced. The use of multiple pump units, each of smaller thrust capability, provides a second alternative for overall size reduction. In addition, future designs may result in improvement of the head coefficient per stage, and as a result, the length may be reduced by a decreased number of stages.

TABLE 10

TYPICAL NOMINAL PERFORMANCE PARAMETERS-BELL CHAMBER DESIGN

Parameters	Propellants	
	LO_2/LH_2	$LO_2/RP-1$
Chamber		
Thrust, lbf	6×10^6	6×10^6
Specific Impulse (sea level), seconds	370	262
Engine Mixture Ratio	5.000	1.99
Thrust Chamber Mixture Ratio	6.28	2.40
Oxidizer Flowrate (pump inlet), lbm/sec	13,520	15,265
Oxidizer Flowrate (thrust chamber), lbm/sec	13,036	14,874
Fuel Flowrate (pump inlet), lbm/sec	2695	7671
Fuel Flowrate (thrust chamber), lbm/sec	2094	6200
Fuel Flowrate (film coolant), lbm/sec	61	526
Chamber Pressure, psia	3000	2500
Maximum Chamber Length, inches	24	27
Contraction Area Ratio	2	2
Throat Area, $in.^2$	1178	1459
Expansion Area Ratio	30	30
Nozzle Coefficient	1.694	1.647
Gas Generator and Turbine		
Oxidizer Flowrate, lbm/sec	484	391
Fuel Flowrate, lbm/sec	540	945
Mixture Ratio	0.900	0.415
Gas Temperature, F	1200	1500
Gas Pressure, psia	3000	2500
Turbine Outlet Temperature, R	900	1453
Turbine Outlet Pressure, psia	145	150

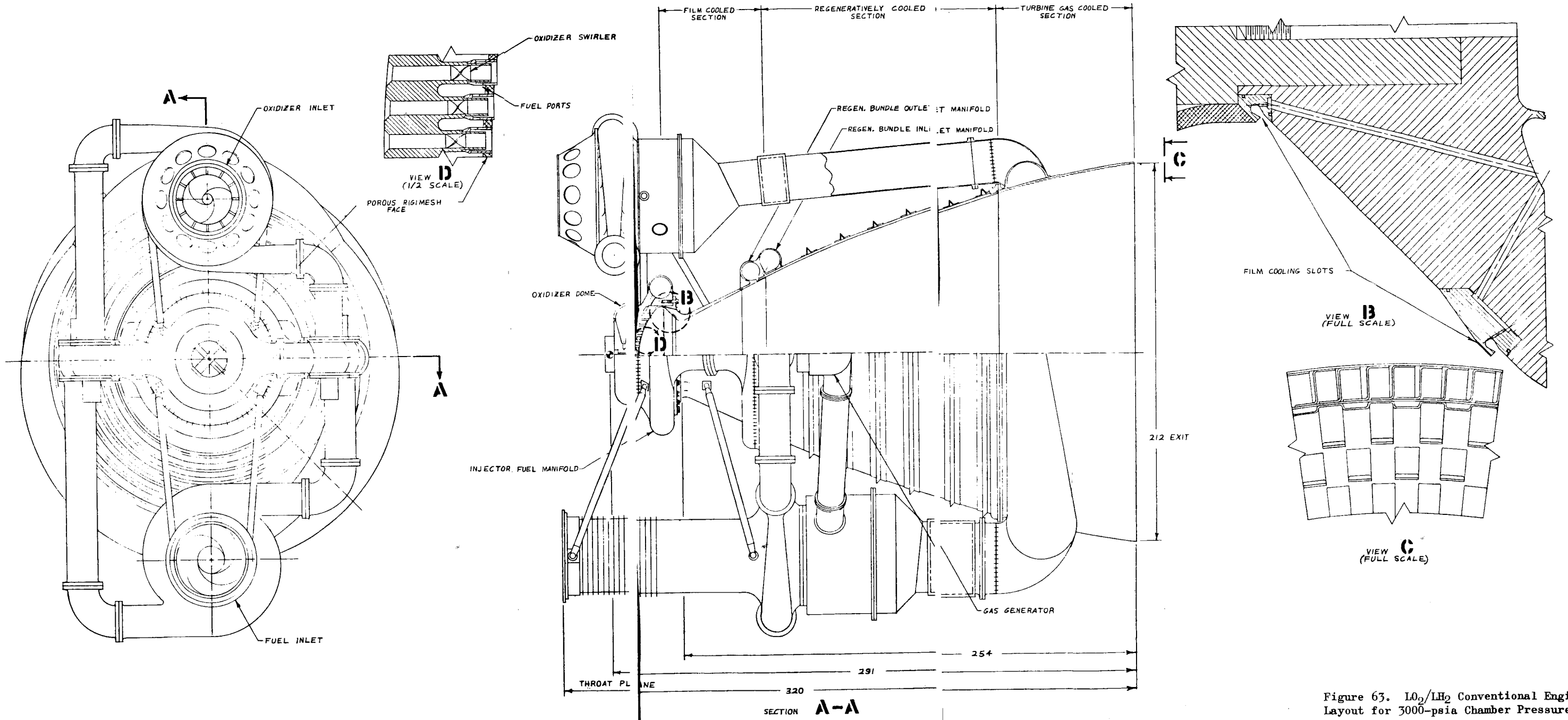

Figure 63. LO_2/LH_2 Conventional Engine Layout for 3000-psia Chamber Pressure

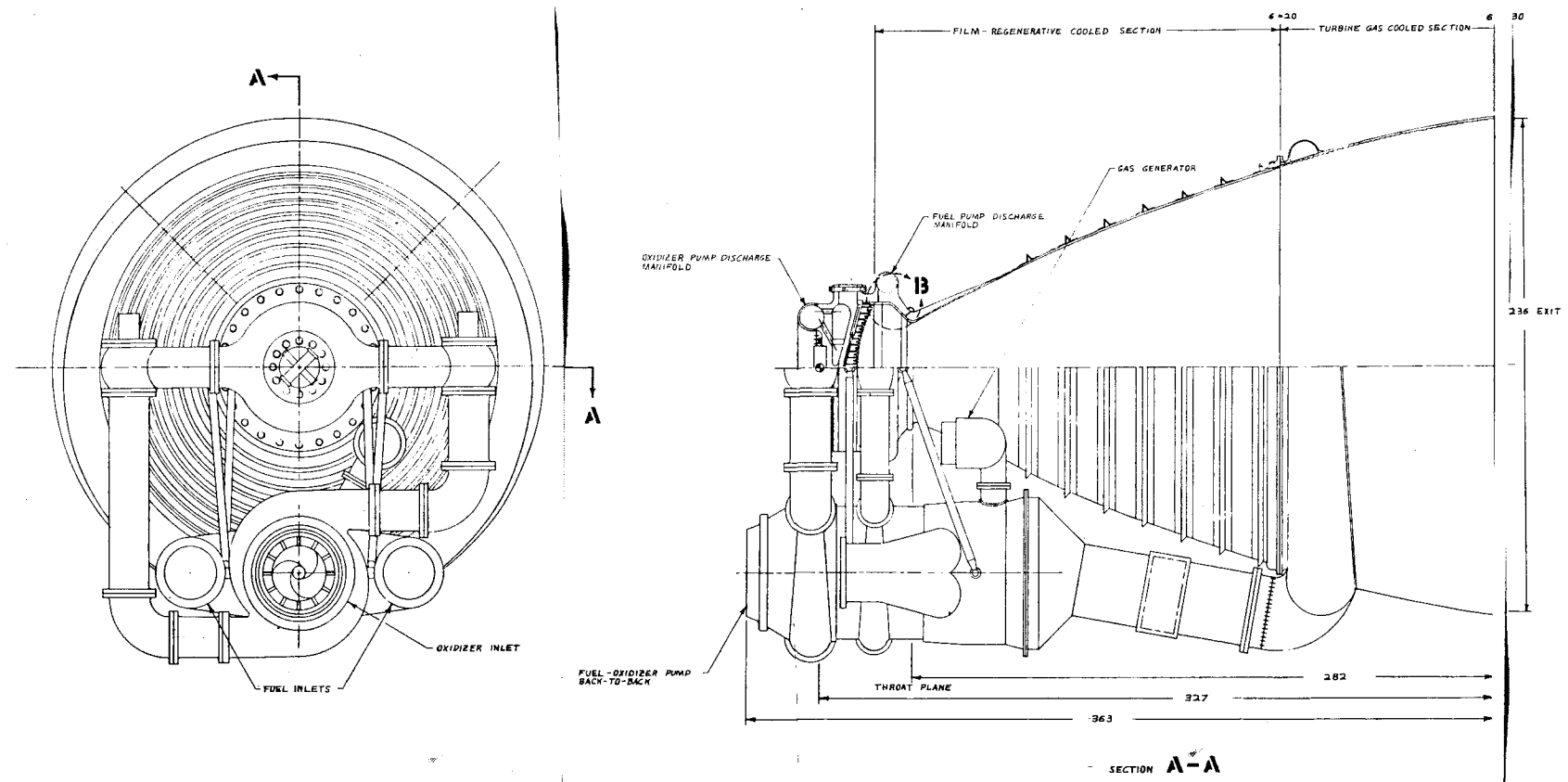

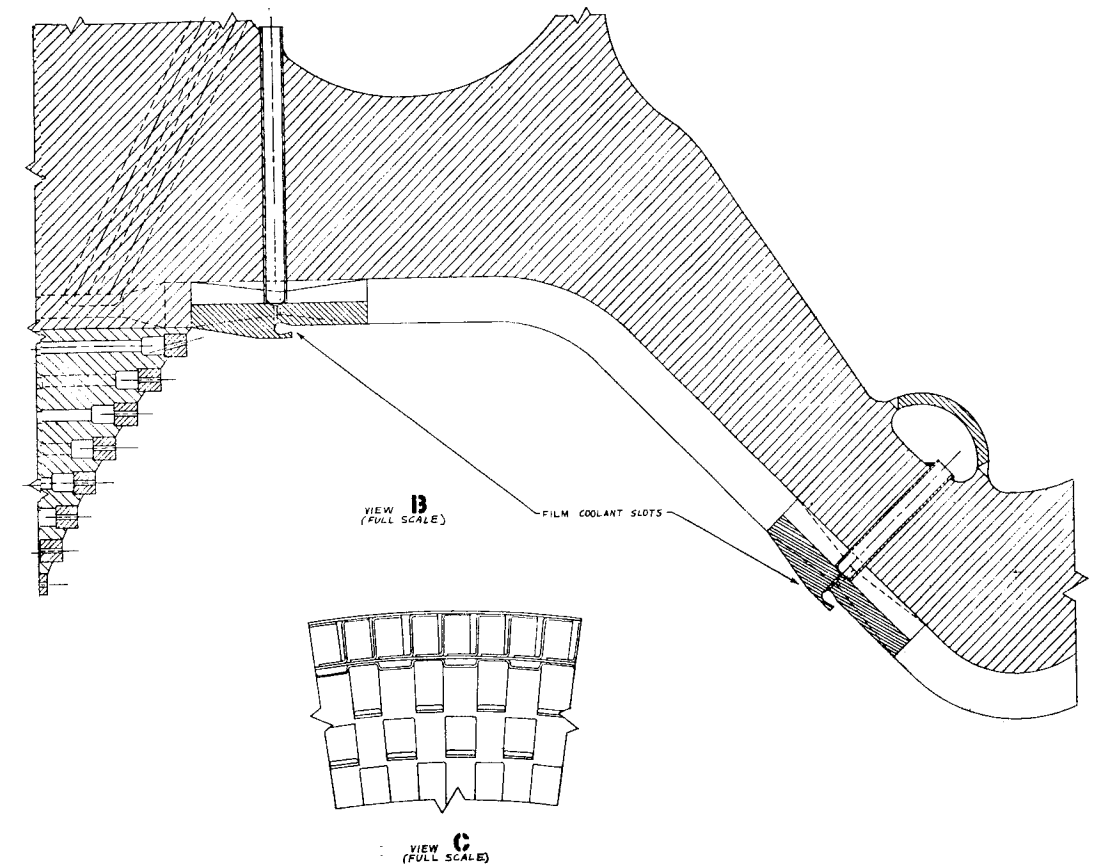

Figure 64. LO_2/RP-1 Conventional Engine Layout for 2500-psia Chamber Pressure

R-6199

It can be seen that the shape of the engine envelope is strongly influenced by turbopump arrangement. Projection of the pump inlets above the gimbal point produces a vehicle attachment problem in that any bellows placed on the inlets must be designed for considerable lateral excursion. Horizontal mounting of the hydrogen pump (i.e., mounting with axis of rotation perpendicular to vehicle centerline) was investigated, but the necessary addition of propellant inlet and turbine outlet elbows negated any significant envelope savings. The necessity of lengthening the turbine exhaust duct and enlarging the pump and/or increasing tank pressurization to offset the 1-psi pressure drop across the hydrogen inlet elbow influenced the selection of vertical mounting.

The thrust chamber contour was based on a contraction area ratio of 2 and an expansion area ratio of 30. A high contraction ratio was used to reduce heat transfer in the combustion chamber at the high operating pressure. An 80-percent bell contour was used for the nozzle. Combustion length was originally set at 14 inches, but adoption of a spherical injector face configuration required increasing the maximum distance from injector face to throat plane to 24 inches. This provides a characteristic length somewhat beyond the usual value of about 25 inches.

The small injector face radius is necessary to provide some radius on the forward surface of the injector hydrogen manifold, which experiences most of the pressure loading. Pressure drop across the more highly curved Rigimesh injector face is much less severe, and the requirement for a tapered hydrogen passage tends to reduce the curvature of the back plate over that of the face.

Other characteristics of the injector have been adapted from current injector concepts. Concentric-tube elements are used with a transpiration-

cooled Rigimesh face. Considerable machining time could be saved if the billet could be rough forged into a dished shape to reduce the amount of metal removal necessary. An integral LO_2 dome has been used.

The chamber is ignited by a single augmented spark igniter placed through the center of the injector face. The gimbal block is displaced a few inches from the top of the LO_2 dome to allow access to the igniter after the engine has been mounted in a vehicle or test stand.

The combustion chamber and throat are film cooled with a small amount of cold hydrogen (about 1.0 percent of total thrust chamber weight flow) diverted from the pump discharge. Cold hydrogen is used on the basis that it is a more effective film coolant. Estimates of orifice areas required to inject this small flowrate with an acceptable pressure drop indicate that it may be necessary to use warmer hydrogen from the tangential injector manifold to improve distribution with realistic hole sizes. The film cooling effect extends to a nozzle area ratio of about 5. Slightly upstream of this point, the solid-wall chamber section is welded to a manifold ring. This ring supports a double-pass, furnace-brazed, tube bundle which extends to an area ratio of 20. The remainder of the nozzle is film cooled with turbine exhaust introduced from a sheet-metal skirt structure (Fig. 63).

From the pump discharge, oxidizer passes through a twin outlet duct system similar to current large engines. Twin valves admit LO_2 directly to the oxidizer dome. The fuel is supplied in a similar manner to the inlet manifold of the regenerative tube bundle. It is collected in another manifold and transferred to the injector manifold in twin ducts, as shown.

Hydrogen film coolant is introduced at two planes in the combustion chamber, the first immediately below the injector, the second just upstream of the throat (Fig. 63). Coolant is supplied through drilled passages to two machined rings which have been brazed into grooves in the wall. The injector face Rigimesh has been extended to cover the upstream end of the first coolant ring, while it is assumed that the flow from the upstream ring is sufficient to protect the leading portion of the downstream ring. The ring geometry consists of a line of small holes drilled so as to tangent a milled slot. As the surface of the slot turns the streams through more than a right angle, it is expected that the initially circular streams will flatten and merge into a continuous, circumferential sheet of coolant, directed exactly parallel to the wall with a negligible radial component. The slot pictured actually directs the film 15 degrees into the wall, hopefully gaining a more stable film. If, in the course of analysis or testing, it is found that imparting a tangential component to the coolant velocity vector is in any way beneficial, the holes may be easily slanted tangentially. In addition, the juxtaposition of radial hole and axial machined slot provides accurate coolant metering through the holes, reasonable ease of fabrication, and the option of melting out, remachining or replacing, and rebrazing the rings during a development program.

The turbine-gas-cooled skirt (Fig. 63) follows current gas-film-cooled skirt design philosophy. Firings of past designs, in which distinct shingles spanning perhaps 10 inches of circumference apiece were welded to the Z-section stringers, showed tangential thermal buckling of the shingles and consequent dimensional variation of the gas metering slits formed by the shingle edges to be a serious problem. The suggested design uses staggered perforations in a sheet which is welded to the stringers. It is expected that tangential and longitudinal thermal strain over the span of a perforation will adjust without buckling.

LO_2/RP-1 ENGINE

Again in the LO_2/RP-1 design, the current state-of-the-art turbopump projects beyond the nominal thrust chamber envelope. Double outlets were used to obtain a more uniform distribution of propellants to the thrust chamber, with reasonably sized lines.

As in the LO_2/LH_2 design, the thrust chamber was sized for a contraction ratio of 2 and an 80-percent bell nozzle to an expansion area ratio of 30. An initial chamber length of 22 inches grew to a maximum of 27 inches when a dished injector face was added.

The injector concept (Fig. 64) is essentially a concentric-ring design, adapted to a spherical injector face. The injection pattern is drilled into copper rings which are brazed into grooves machined in the injector face. Oxidizer is distributed tangentially in a circumferential manifold before being distributed radially in the LO_2 dome. Fuel is distributed from large radial holes or doghouses. Smaller axial holes are drilled from the ring grooves into the dome and the doghouses to feed the rings. Ignition is accomplished by hypergol slug.

Optimization of film coolant introduction and flow is even more critical in this system than in the LO_2/LH_2 case because the film requirement without regenerative cooling comprises around 2.5 percent of the total flow. It is hoped that the maintenance of a regeneratively cooled wall will preserve the carbon layer observed at lower chamber pressures, yielding a significant reduction in film-coolant requirements. A two-pass bundle fed from the injector is shown. Film coolant is tapped directly from the fuel pump discharge manifold, on the basis that the regenerative contribution of this 2.5 percent is less important than its having a low bulk temperature upon injection.

Of the several methods of film-coolant introduction applicable to tube wall chambers, the most effective are believed to be those involving injection from a special manifold introduced into the brazed bundle. Concepts involving drilling, slotting, or louvering the actual tube bundle all suffer from problems of dimensional variations affecting coolant metering, diffuse streams from low L/D orifices, and uneven circumferential film distribution, to varying degrees.

The concept shown in Fig. 64 eliminates the possible leak paths and loss of strength inherent in cutting off the tubes on one side of the coolant introduction point and resuming them on the other by necking them locally and feeding coolant through the interstices. Machined ring segments are held against the necked tube walls by supply tubes inserted from the outside of the chamber shell. The junction between the supply tubes and ring segments could be by threaded joint with static seal or by braze ring, but an internal arc weld made with a programmed, rotating electrode is shown.

Turbine gas film cooling between the nozzle area ratios of 20 to 30 is accomplished in a manner similar to the LO_2/LH_2 design.

ADVANCED CHAMBER DESIGN

A companion study to the conventional engine design study was made to develop a comparison of conventional and advanced chamber cooling systems. Design considerations are discussed below for LO_2/LH_2 and LO_2/RP-1 propellant systems and typical design layouts are presented for LO_2/LH_2.

ADVANCED NOZZLE CONSIDERATIONS

The development of advanced nozzle contours was made under a number of imposed conditions. The study considered the following advanced nozzle-combustion chamber types:

1. Combustion chamber:
   a. Annular
   b. Multichamber
   c. Toroidal
2. Nozzle:
   a. External shroud (expansion deflection, reverse flow, horizontal flow)
   b. Internal shroud (spike)
   c. Aerodynamic shroud

An external shroud nozzle was selected from the above list in combination with an annular combustor design having a continuous surface. Additional designs where an impingement on the nozzle surface occurs due to a discontinuous combustion zone to nozzle surface were also briefly studied.

Chamber Contours

With an annular combustor design, large characteristic length values may be incorporated into short combustion lengths by the provision of readily obtained high contraction ratio values. The combustion zone length was consequently chosen as the limiting value for the annular designs. A 14-inch minimum length was selected for the LO_2/LH_2 designs, and a 20-inch length for the LO_2/RP-1 designs. Contraction ratio values of 2 and 4 were examined.

A review of previous work conducted by Rocketdyne in the study of advanced nozzle designs indicated that maximum and minimum "plug"-to-equivalent throat diameter ratios (D_p/D_t) could be established. A lower limit of 3.5 was established to allow for the inclusion of the turbomachinery unit within the nozzle center. An upper limit of D_p/D_t of 7.0 was determined by consideration of the base pressure drag losses. Above this value, an adequate turbine flow is not available for the increase in the base pressure value to an ambient condition.

A length selection for the nozzle was made by consideration of a reasonable performance. The use of available previously developed optimum thrust maps were employed for this purpose. Area ratio selections were made to correspond, approximately, to the previous bell nozzle analyses. The three chosen D_p/D_t values of 3.5, 5.0, and 7.0 had corresponding area ratios of 36, 36, and 60, respectively. The resulting dimensional values derived for two of these contours using reverse-flow nozzles are given in Tables 11 and 12 . These two nozzles are shown in Fig. 65 and 66.

TABLE 11

ADVANCED NOZZLE CONTOURS

($D_p/D_t = 3.5$, $\epsilon = 36$)

Configuration	Chamber Pressure, psia		
	1500	3000	5000
2-million-pound-thrust			
D_p	107	75.6	58.1
δ_T	2.17	1.54	1.18
L	67.6	48.1	36.9
D_e	173	123	95
4-million-pound-thrust			
D_p	151	107	82.7
δ_T	3.1	2.2	1.7
L	95.7	67.5	52.5
D_e	245	173	135
6-million-pound-thrust			
D_p	185	130	101
δ_T	3.8	2.7	2.1
L	117	82.6	64.0
D_e	301	212	164

All values in inches.

Symbols defined in Fig. 65.

TABLE 12

ADVANCED NOZZLE DIMENSIONS

($D_p/D_t = 7$, $\epsilon = 60$)

Configuration	Chamber Pressure, psia		
	1500	3000	5000
2-million-pound-thrust			
D_p	213	151	116
δ_T	1.08	0.77	0.59
L	24.3	17.3	9.4
D_e	219	156	120
4-million-pound-thrust			
D_p	301	213	165
δ_T	1.53	1.08	0.84
L	34.4	24.3	18.9
D_e	310	219	170
6-million-pound-thrust			
D_p	369	260	202
δ_T	1.89	1.33	1.03
L	42.2	29.8	23
D_e	380	268	207

All values in inches.

Symbols defined in Fig. 65 .

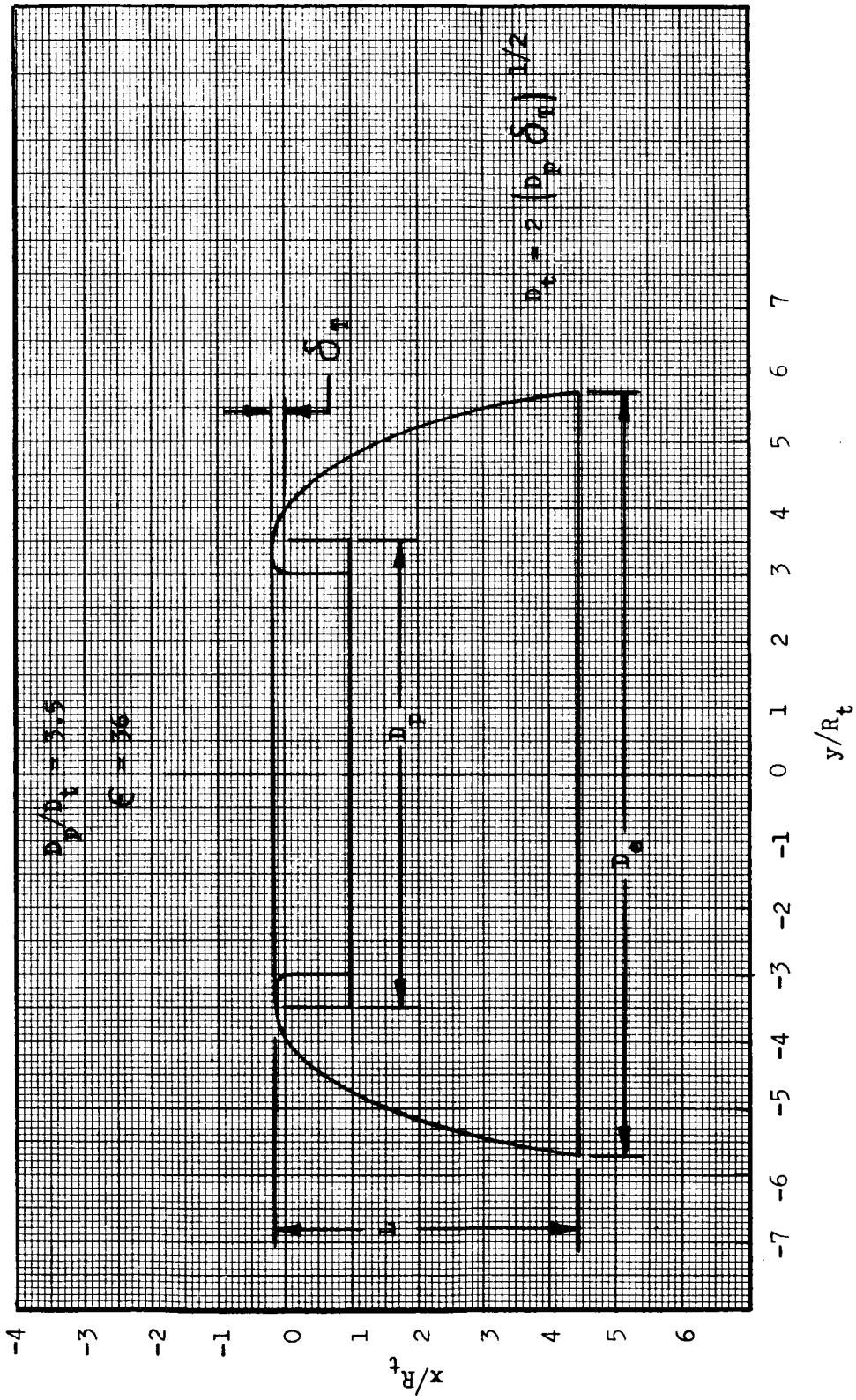

Figure 65. Annular Combustor Design Reverse-Flow Nozzle

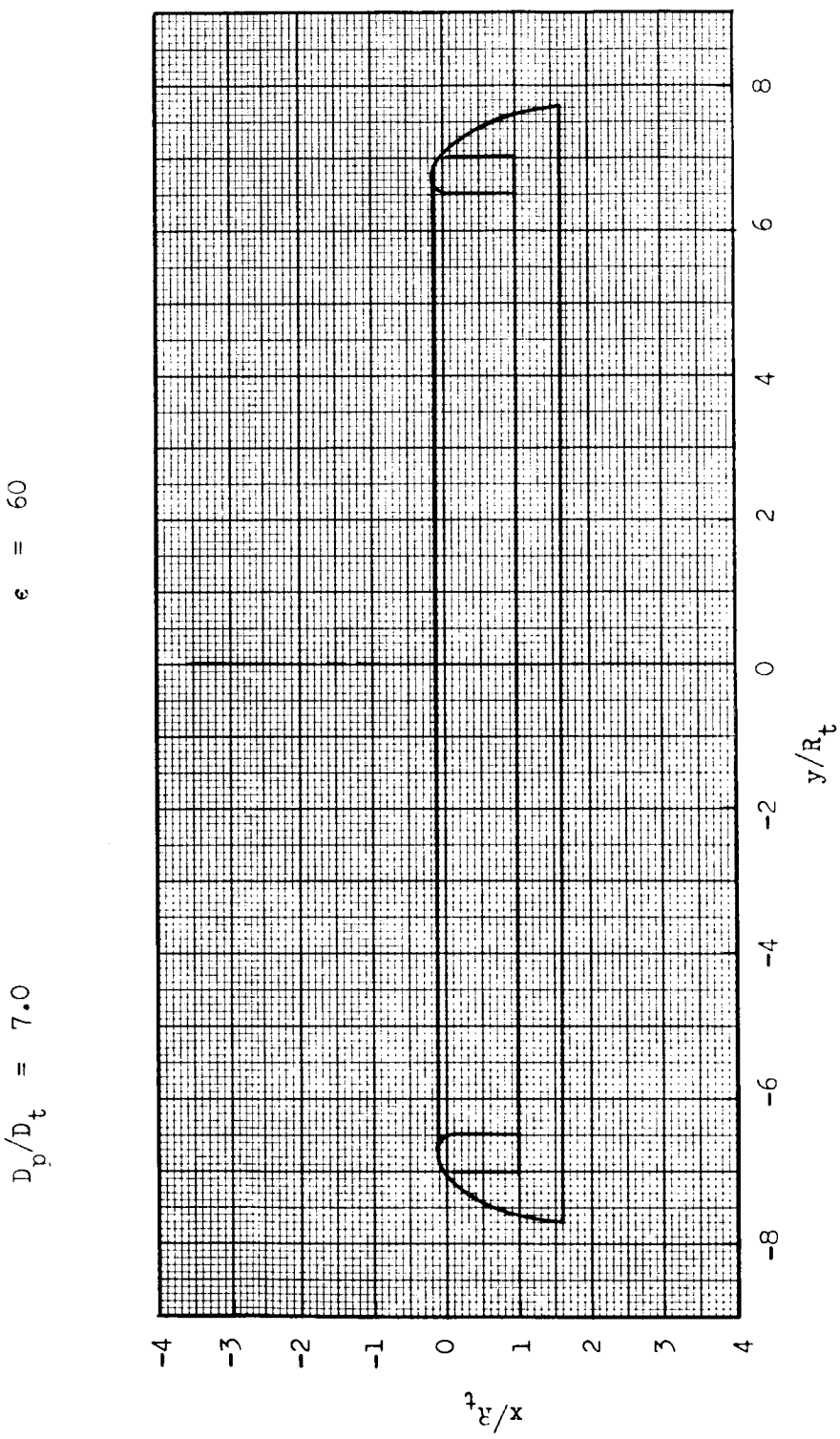

Figure 66. Annular Combustor Design Reverse-Flow Nozzle

608-B-13 NEW 11-62

Heat Transfer Coefficients

The heat transfer coefficients for the annular combustion zone and throat region were developed with the use of the transport property and temperature conditions reported in Ref. 1. Reference temperature conditions for the evaluation of boundary layer properties were based on the Eckert reference temperature method.

The finite difference method for boundary layer evaluation was employed, using the new equations and procedure outlined in the above section on the gas-side heat transfer coefficient. Table 13 gives the comparative heat flux values obtained for the combustion zone and throat regions.

Nozzle wall curvature effects upon the heat transfer coefficients for the advanced nozzles was neglected for this initial evaluation due to the uncertainty of the added effect. The apparent magnitude indicated in the section describing wall curvature effects indicated that an increase in the heat transfer rate can be imposed by the nozzle turn dependent upon the radius of curvature of the turning region.

COOLING STUDIES

Nozzle contours and gas-side film coefficient values discussed in the previous section were employed in detailed design analyses. The advanced nozzle designs investigated were examined first to see if regenerative cooling appeared sufficient for both the combustion chamber and nozzle. Secondly, a study of the film-cooling requirements for the high heat flux regions was made. A tradeoff for the combined regenerative-film case was subsequently investigated.

TABLE 13

SUMMARY OF HEAT TRANSFER VALUES FOR ANNULAR NOZZLE DESIGNS
(WITHOUT WALL CURVATURE EFFECTS)

Propellants	P_c, psia	ϵ_c	θ_o, inches	θ_o,* inches	Re_θ*	h_{gcz}, Btu/in.^{2}-sec-R	h_g,* Btu/in.^{2}-sec-R	(q/A)*, Btu/in.^{2}-sec
LO_2/LH_2								
Case								
1	1500	2	0.001	0.0145	15138	0.0071	0.0107	41.9
2	1500	4	0.0014	0.0121	12714	0.0038	0.0111	43.4
3	3000	4	0.0011	0.011	22949	0.0066	0.0198	79.2
4	3000	2	0.00071	0.0130	27068	0.0130	0.0191	76.5
5	5000	2	0.00055	0.0119	41133	0.0200	0.0292	107
LO_2/RP-1**								
Case								
1	1500	2	0.0012	0.0148	20276	0.0047	0.0069	31.2
2	1500	4	0.0017	0.0121	17229	0.0024	0.0071	32.2
3	3000	4	0.0012	0.0110	30591	0.0048	0.0126	58.8
4	3000	2	0.00085	0.0128	35627	0.0084	0.0122	57.1
5	5000	2	0.00066	0.0121	55012	0.0127	0.019	90

*Throat value
**Values without an assumed carbon layer

Values are independent of thrust level.

Combustion zone heat transfer coefficient values are average values.

Heat flux values evaluated at a 1600 F wall temperature.

ROCKETDYNE • A DIVISION OF NORTH AMERICAN AVIATION, INC.

LO_2/LH_2 Propellant System

Regeneratively-Cooled Nozzle. Design analysis was performed with the digital computer program previously described. A hand-check of the values of the heat transfer coefficient in the throat vicinity for these designs indicated that the upper chamber pressure limit for complete regenerative cooling with LO_2/LH_2 propellants based on a reasonable pressure drop requirement was slightly less than the lower value of 1500 psia selected for this program. To achieve a reasonable compromise for coolant pressure drop without necessitating an excessive film-coolant flow, a limit based upon the absolute upper limit of regenerative cooling in terms of the heat conduction limit for the wall material was used. A review of the results of the previous contract effort illustrated a reasonable heat flux value as:

$$(q/A)_{\substack{\text{maximum}\\ \text{regenerative}}} = (2/3)\ q/A_{\substack{\text{maximum wall}\\ \text{conduction limit}}} \qquad (301)$$

Regions with heat fluxes above this maximum prescribed design value were assumed to be film-cooled for the first analysis. Values of plug-to-equivalent circular throat diameter, D_p/D_t, from 3.5 to 7.0 were examined. Figures 67 and 68 illustrate the calculated heat flux distribution down the nozzle length for 1500 and 5000 psia chamber pressures.

Results of the analysis for the 2- to 6-million-pound thrust level illustrated a large tube number requirement in the nozzle because of the large nozzle diameter. To provide a limitation on the number of coolant tubes based upon heat transfer considerations rather than stress conditions, the use of a high-strength material such as Inconel X became evident. If the ductility of materials such as those of the stainless-

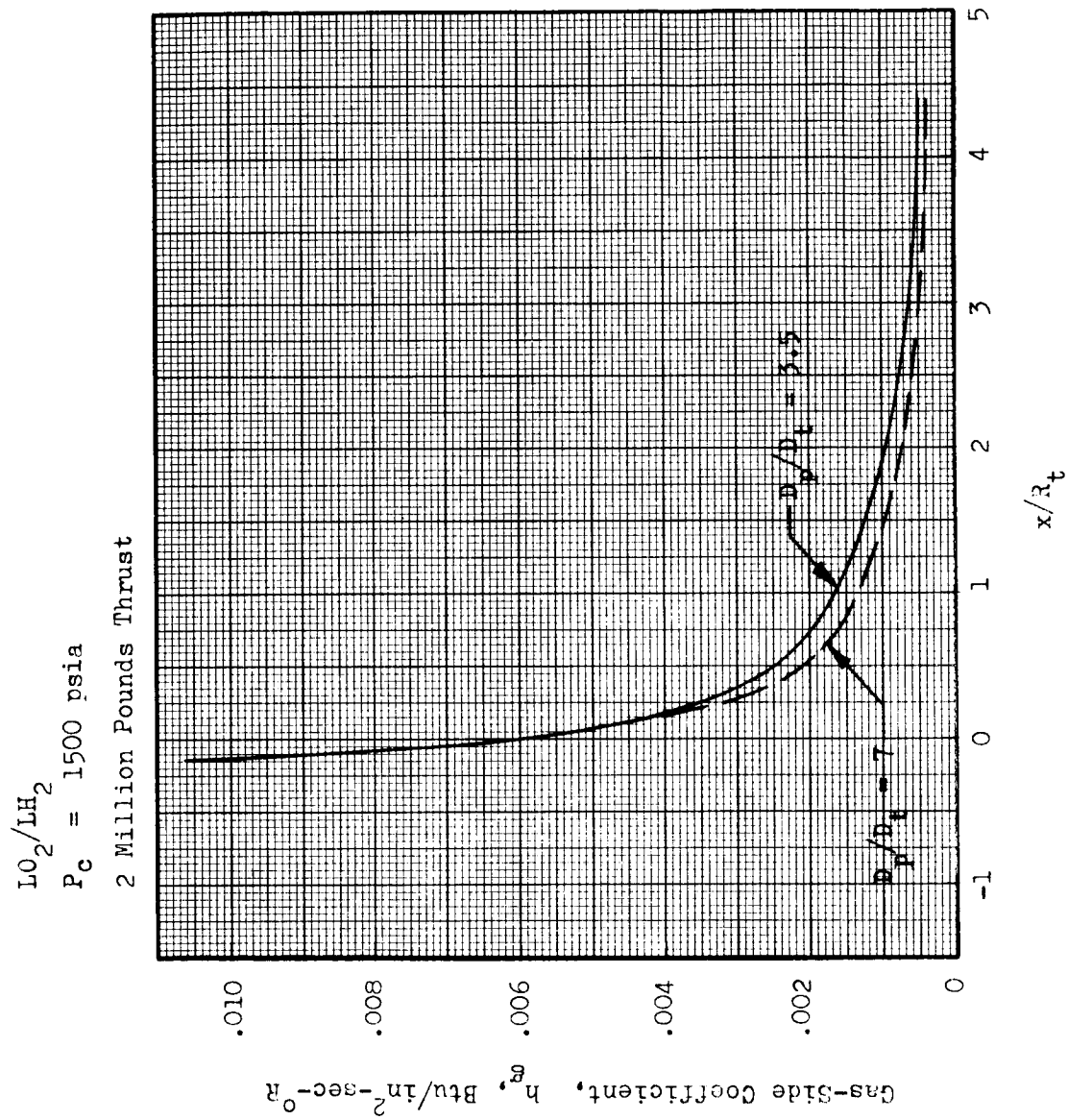

Figure 67. Advanced Nozzle Heat Transfer Coefficient Distribution

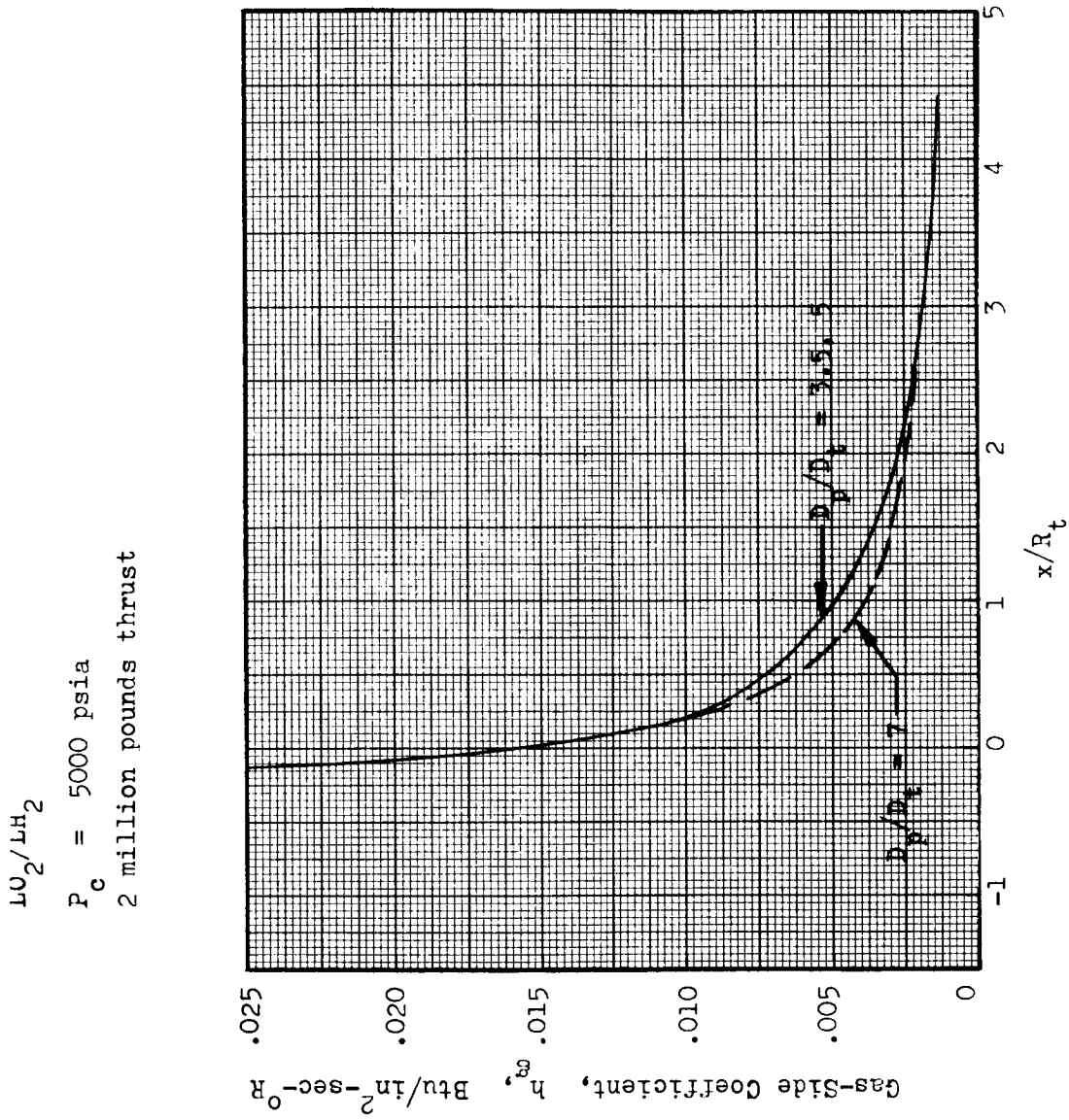

Figure 68. Advanced Nozzle Heat Transfer Coefficient Distribution

steel family should appear to be a more desirable feature from a standpoint of handling stress values imposed on the wall surface which are above the yield value, an even larger number of coolant tubes would be required. Some reduction of the tube-number requirement would be achieved with a reduction in the maximum heat flux in the regeneratively cooled section.

The calculated tube number requirements are given in Table 14 for a single uppass design which results in the lowest pressure drop choice. A compromise appears to be necessary to reduce the tube number to a more reasonable value. A double-tube-pass design with a fuel-coolant inlet manifold at the attach point between the nozzle and combustion chamber reduces the number of coolant tubes required by a substantial 40 percent. To achieve a reasonable pressure drop with the two-pass cooling circuit, a lower heat flux below the 2/3 wall conduction limit value may have to be tolerated.

Nozzle regenerative-coolant pressure drop values for the single-pass design at the 1500-, 3000-, and 5000-psia levels are approximately 400, 650, and 850 psi, respectively. For a two-pass design, comparable values are 560, 910, and 1200 psi, respectively. The sensitivity of the coolant pressure drop to the minimum nozzle area ratio point which is regeneratively cooled indicates that increases in film-cooled nozzle length values above those shown in Table 15 could substantially reduce the nozzle coolant pressure drop. Consideration must also be given to the addition of the combustion zone section pressure drop if this region is to employ partial regenerative cooling.

Coolant temperature rises in the supersonic nozzle portion were found to be small due to the employment of the entire fuel flowrate as regenerative coolant. The use of the entire fuel flow as coolant with an advanced

TABLE 14

APPROXIMATE COOLANT TUBE NUMBER REQUIREMENTS
FOR ADVANCED NOZZLE DESIGNS
BASED UPON COOLING REQUIREMENTS
FOR A SINGLE UP-PASS DESIGN
WITH LO_2/LH_2 PROPELLANTS

D_p/D_t	Chamber Pressure, psia	Number of Tubes		
		2-Million-Pound Thrust	4-Million-Pound Thrust	6-Million-Pound Thrust
3.5	1500	2000	2800	3500
5.0	1500	4000	5600	7000
7.0	1500	6000	8400	10,500
3.5	3000	2000	2800	3500
5.0	3000	4000	5600	7000
7.0	3000	6000	8400	10,500
3.5	5000	2000	2800	3500
5.0	5000	4000	5600	7000
7.0	5000	6000	8400	10,500

TABLE 15

SUPERSONIC REGION FILM-COOLED LENGTH REQUIRED FOR ADVANCED NOZZLE DESIGNS WITH LO_2/LH_2 PROPELLANTS

D_p/D_t	Chamber Pressure, psia	Film Cooled Length, inches		
		2-Million-Pound Thrust	4-Million-Pound Thrust	6-Million-Pound Thrust
3.5	1500	3.9	5.5	6.7
5.0	1500	2.6	3.6	4.5
7.0	1500	2.4	3.4	4.1
3.5	3000	6.2	8.7	10.7
5.0	3000	4.5	6.3	7.7
7.0	3000	3.6	5.1	6.2
3.5	5000	8.2	11.5	14.0
5.0	5000	5.7	8.0	9.9
7.0	5000	4.2	5.9	7.2

nozzle concept is necessitated by the large nozzle surface area compared to that for a conventional convergent-divergent nozzle. A limited temperature rise of the coolant could theoretically allow a lesser percentage of the fuel to be used as coolant, but an increased number of coolant tubes would be necessary and would correspondingly increase coolant pressure drop. Cost, pressure drop and stress, reliability and weight with an increased number of coolant tubes would have to be optimized. Typical coolant bulk temperature rises for a 2-million-pound thrust chamber nozzle section were 110, 80, and 50 R for chamber pressures of 1500, 3000, and 5000 psia, respectively. Added to this would be an almost equal rise for the combustion zone region if it is regeneratively cooled. At an even larger thrust level, a diminishment in coolant bulk temperature rise would occur because of a more favorable larger thrust-to-nozzle surface area ratio at the increased thrust values.

The large number of nearly circular tubes required is dictated by the throat region in a regenerative design. The use of large combustion zone contraction ratio designs and shallow entrance curvature from the subsonic section would appear to reduce the severity of the heat transfer rate in the throat vicinity. Because of an apparent higher heat transfer rate in the throat vicinity with the advanced nozzle designs with annular combustors, the regenerative-cooling heat conduction feasibility limits become reduced below that for a conventional bell nozzle chamber.

Regeneratively Cooled Annular Combustion Zone. The intense heat flux values in the throat region which occur at high chamber pressures in the advanced thrust chamber designs necessitate film cooling of the nozzle supersonic section to the extent indicated in Table 15. In addition, depending upon the rapidity of contraction of the combustion zone annulus in the subsonic section, it may also be necessary to supply fuel film

coolant there. The majority of the combustion zone may, however, be regeneratively cooled even at high chamber pressures, if necessary. The contrast with a conventional cylindrical combustion chamber is brought about as the result of a considerably greater combustion zone area contraction ratio allowed by the narrow throat width positioned at a large diameter. This is achieved without a significant increase in weight.

An analysis was performed to examine the limits for regenerative cooling in the combustion zone region in terms of a variable required contraction ratio with chamber pressure. Employing the previous assumption for the nozzle regenerative cutoff point based on a compromise for reasonable pressure drop and the wall conduction limit as:

$$(q/A)_{design} = (2/3)\ (q/A)_{wall\ conduction\ limit} \qquad (302)$$

Figure 69 was developed.

Superimposed onto the curves for combustion zone heat transfer convective coefficient vs contraction area ratio for varying chamber pressure are the wall heat conduction limit line and the appropriate design limit value. The resulting solution for the minimum combustion zone contraction ratio is approximately 1.5, 3.0, and 4.5 for chamber pressures of 1500, 3000, and 5000 psia, respectively. Pressure drops were not evaluated but could be maintained at reasonable levels dependent upon the combustion region contraction ratio specified. Because of the high level of heat transfer coefficient maintained over an assumed 14-inch combustion length, a more practical design might employ a lower maximum heat flux by an increased contraction ratio value.

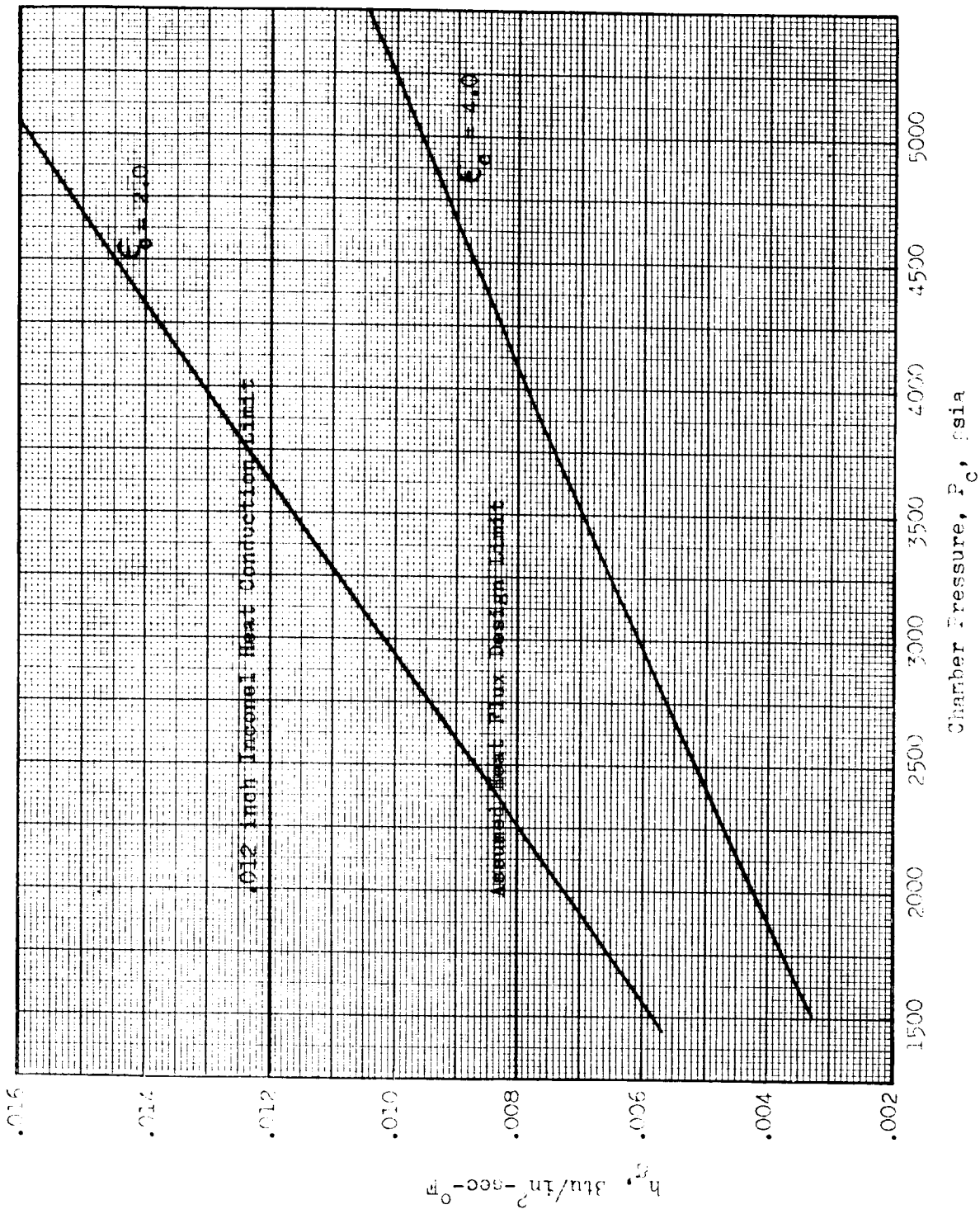

Figure 69. Regenerative Design Limits for the Combustion Zone of an Annular Design Using LO_2/LH_2

At all except the required high contraction ratios at high chamber pressures approaching 5000 psia, the regenerative means of cooling an annular combustion zone appear possible. Due to somewhat higher heat transfer coefficients (above those listed in Table 13) in the vicinity of the injector face because of local recirculation and minimized boundary layer thickness at this point, some film-cooling supplementation from the injector may appear desirable.

Figure 70 shows a typical cooling method for a 3000-psia chamber pressure, 6-million-pound-thrust advanced nozzle design with an annular combustor. The application of the previous remarks hold generally for combustors of advanced nozzle designs.

Film-Cooled, Annular Combustion Zone. Due to the complexity apparent with the annular design for a tube wall combustor, an investigation into the film-cooling benefit derived by using varying percentages of film coolant relative to the total flow was conducted. Manifolding pressure drop and thermal stress considerations, etc. would indicate a more advantageous avenue of choice to be a completely film-cooled combustor design. The larger integral value of surface area and heat flux for the combustion zone, as compared with the required film-cooled portion of the nozzle indicated previously, results in the largest fraction of film-coolant requirement in the combustion zone.

Table 16 summarizes calculated film-coolant requirements for a D_p/D_t ratio of 3.5 and a maximum wall surface temperature of 2000 R (1540 F). Typical values lie between 1 to 4 percent of the total chamber propellant flow for the thrust and chamber pressure range of interest. Low thrust and high chamber pressure contribute to increased film-coolant flow

Note: Not to scale

Arrows indicate flow direction of regenerative coolant

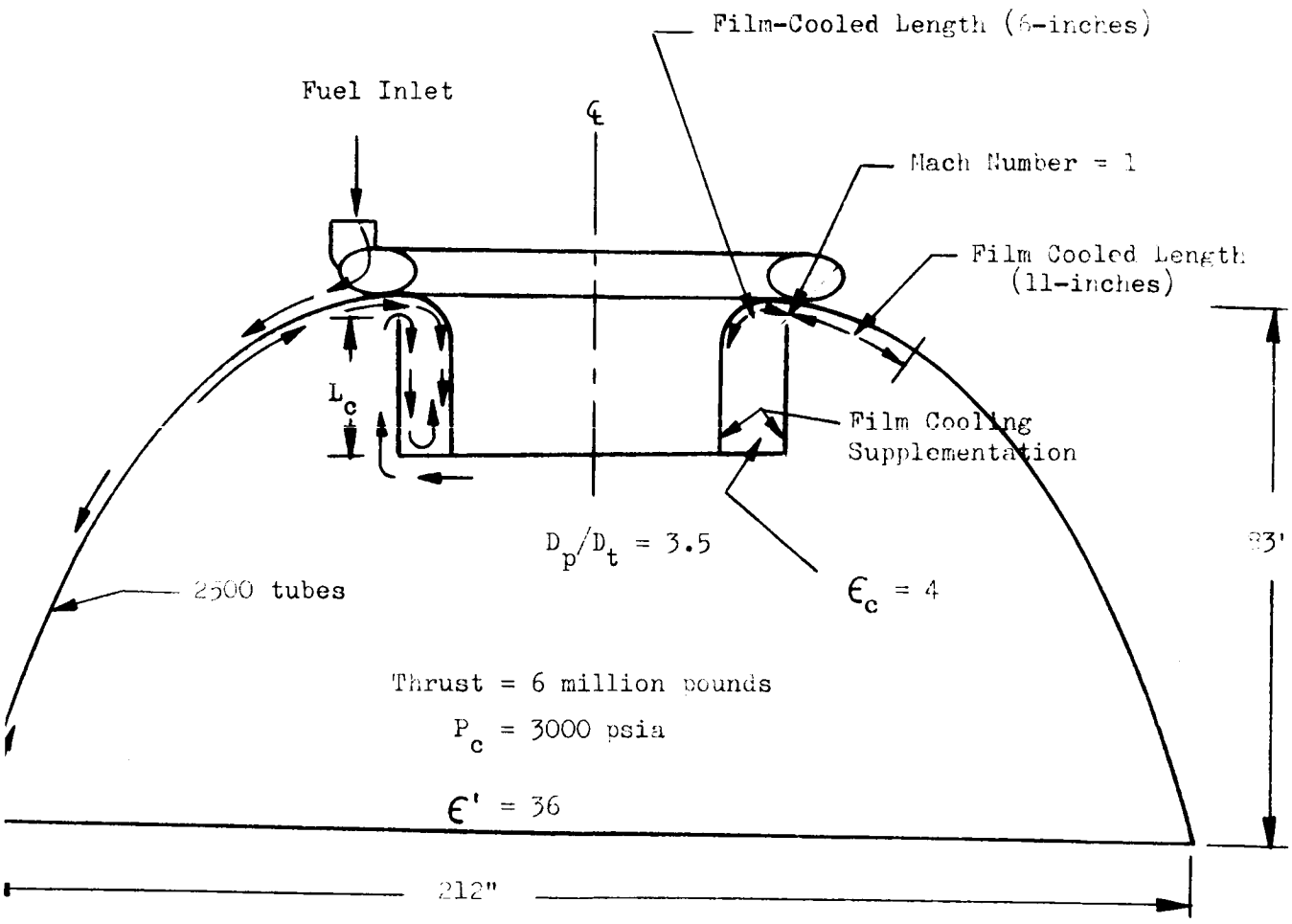

Figure 70. Typical Advanced Nozzle Design Configuration with Annular Combustion Chamber for LO_2/LH_2 Propellants

TABLE 16

SUMMARY OF APPROXIMATE FILM COOLING REQUIREMENTS FOR AN ANNULAR COMBUSTOR WITH $D_p/D_t = 3.5$ AT A MAXIMUM WALL TEMPERATURE OF 2000 R WITH LO_2/LH_2 PROPELLANTS

Chamber Pressure, psia	$\dot{W}_c/\dot{W}_t$, percent			
	2-Million-Pound Thrust $\epsilon_c = 2$	6-Million-Pound Thrust $\epsilon_c = 2$	2-Million-Pound Thrust $\epsilon_c = 4$	6-Million-Pound Thrust $\epsilon_c = 4$
1500	2.7	1.8	1.6	1.0
3000	3.3	2.0	1.9	1.1
5000	3.8	2.4	2.2	1.4

requirements. A 4 percent value of $\dot{W}_c/\dot{W}_t$ is equivalent to 24 percent of the total fuel at a mixture ratio of 5:1. Increased contraction ratio values will decrease the film coolant flow almost proportionally. On the other hand, an increased D_p/D_t value will increase the film-coolant flow values because of a proportionally increased surface area for a fixed combustion length. A D_p/D_t value of 7.0, for example, would double the requirements listed in Table 16 for a fixed contraction rate.

The film-cooling equation of Hatch and Papell (Ref. 31) modified as described in Ref. 1 was used for the above analysis with an assumed cooling efficiency of η = 25 percent. The equation employed was:

$$\left(\frac{T_{aw} - T_{wg}}{T_{aw} - T_c}\right) = e^{-h_g A/\dot{W}_c \; C_{p_c} \; \eta_f} \tag{303}$$

where the required coolant flow $(\dot{W}_c)$ was computed for a maximum allowable wall temperature (T_{wg}).

Combined Film-Regenerative Cooling. The film-regenerative cooling trade-off requirements for LO_2/LH_2 engine designs were evaluated with the combined regenerative-film cooling digital computer program derived previously and described in Ref. 1. The analysis of the requirements for the annular combustors was based upon a film cooling efficiency of 25 percent, 0.012-inch Inconel-X wall thickness, an assumed infinite conductance between the film coolant and the wall surface and a coolant-side heat transfer coefficient fixed at a 0.005 Btu/in.^{2}-sec-F value. In actuality, this latter coefficient would vary depending upon the heat flux distribution desired between the film and regenerative coolants. Typical

film-coolant flow reductions of 5 percent to 20 percent are found possible with the smaller reduction at the higher chamber pressure values. Improvement in this percentage reduction of the coolant flowrates could be accomplished with a higher coolant-side heat transfer coefficient value at the expense of added pressure drop. For combustion chamber designs at large D_p/D_t ratios, the desirability of the combined method becomes apparent to reduce a possible otherwise prohibitive film-coolant flow percentage.

Combined film-regenerative cooling along the wall in the first portion of the supersonic nozzle region is the best approach for cooling because tubular wall construction employed at the higher area ratios may be extended into the throat vicinity without difficulty. A fuel-film-coolant manifold located in the subsonic section just upstream of the throat may be used to combine the film-cooled technique with the regenerative-cooling method. Film coolant in the supersonic portion of the flow may contribute to a greater performance loss than for that employed to cool the wall in the subsonic combustion zone region, hence, the desirability of minimizing the nozzle film-coolant flow.

The above film-cooling analysis and combined film-regenerative cooling analysis may be somewhat conservative in that a higher-than-actual required film-cooling flow is predicted. Further study of injection techniques to improve film-cooling efficiencies may be anticipated. Similarly, with further experimental study the far downstream effects of the film-cooling techniques will become better defined.

LO_2/RP-1 Propellant System

Computer methods were employed as previously described for LO_2/LH_2 to design and analyze the cooling methods for nozzles with D_p/D_t ratios of 3.5, 5, and 7.0 at thrust levels of 2, 4, and 6 million pounds with LO_2/RP-1 propellants from 1500- to 5000-psia chamber pressures. Chamber designs were examined for regenerative, film, and combined methods.

Regenerative Cooling. In the design analysis, the assumption was made that a carbon layer would be deposited on the gas-side wall surface according to the relation

$$\frac{\Delta x}{k} = e^{9-0.51G}, \quad \frac{\text{in.}^2\text{-sec-F}}{\text{Btu}} \tag{304}$$

where

$$G = \text{lbm/in.}^2\text{-sec}$$

based on a conservative estimate of the data examined for conventional chambers (Ref. 1). The stability of the carbon layer adherence and the magnitude of its value as a function of wall temperature and chamber pressure for advanced nozzle designs is in question. At high chamber pressures (> 1500 psi), a considerable reduction in effectiveness of the carbon layer on the control of the heat flux is predicted by Eq. 304.

Throat Region. The throat region heat flux vs chamber pressure is shown in Fig. 71 for a 6-million-pound thrust level. Representative values with the inclusion of the carbon layer effect are 15, 42, and

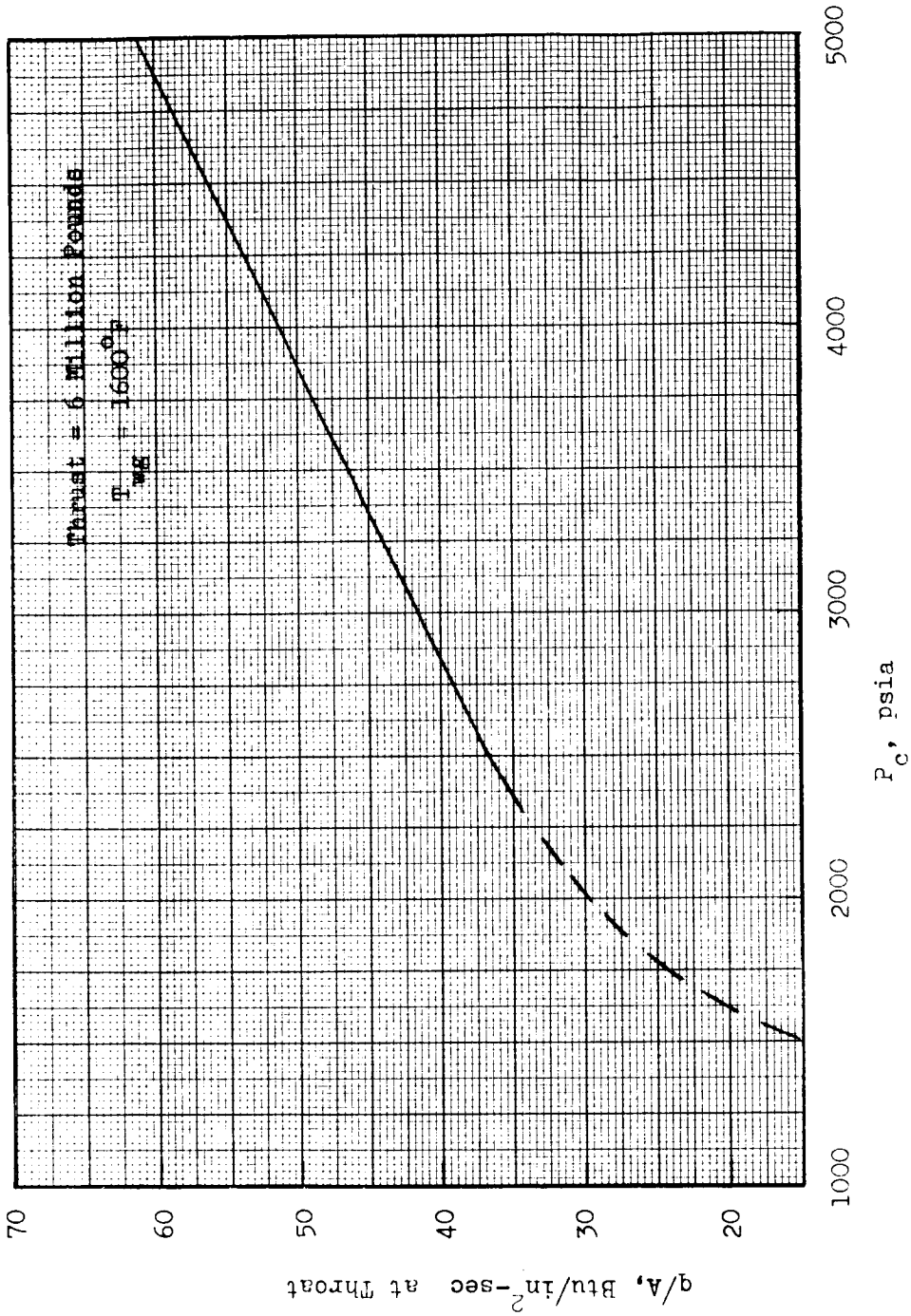

Figure 71. Throat Heat Flux for LO_2/RP-1 Propellants Advanced Nozzle Design

61 Btu/in.^{2}-sec for chamber pressure values of 1500, 3000, and 5000 psia, respectively.

Throat gas-side heat transfer coefficients will not change significantly with a thrust level change from 2 to 6 million pounds for an advanced combustion chamber concept if the combustion zone length remains constant. Similarly, for a constant-area contraction ratio, the combustion zone heat fluxes remain essentially independent of thrust. If the length or contraction ratio of the combustion zone is changed, correction to the throat convective coefficient can be made by the approximation:

$$h_g \propto \frac{1}{\left[\int_0^x \overline{Re}_g\right]^{0.2}} \tag{305}$$

where the integral quantity represents an average Reynolds number throughout the combustion length to account for boundary layer growth effects.

The wall heat conduction limit for a typical design case is shown in Fig. 72. From a design standpoint, assuming as before that the maximum pressure drop limit corresponds to a heat flux of about 2/3 of the conduction limit, the limiting chamber pressure is about 2250 psi. A more detailed computer analysis shows a more practical design limit would be something less than 2000-psia chamber pressure. If a large adhering carbon layer could be promoted, the limit of this method for the cooling of the throat region could be raised from the above stated value.

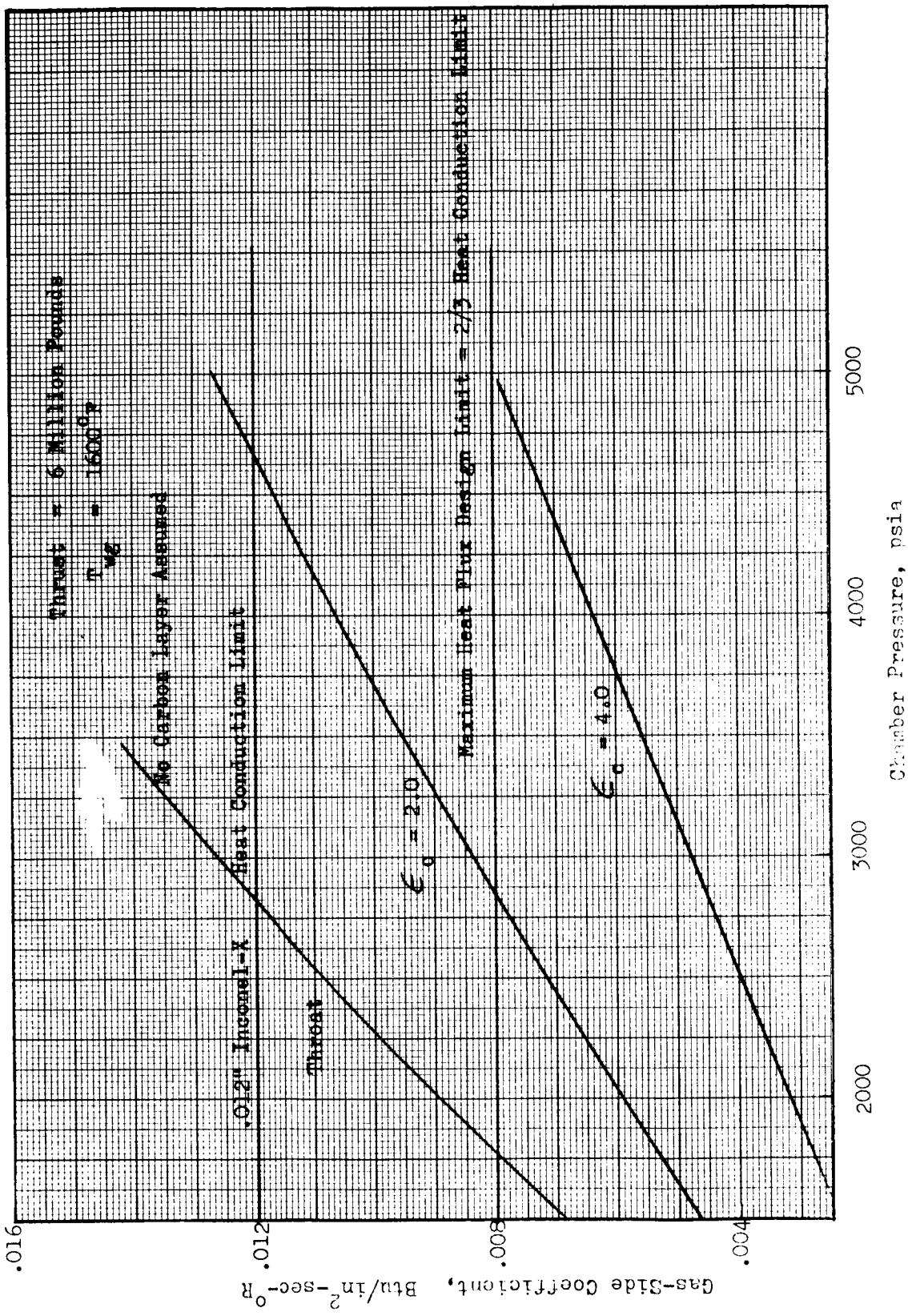

Figure 72. Regenerative Design Upper Chamber Pressure Limits for Combustion Zone of an Annular Nozzle Design Using LO_2/RP-1 Propellants

Combustion Region. The carbon layer deposition is assumed by Eq. 304 to be significantly higher under an increased contraction area ratio condition which corresponds to a mass velocity. In addition, the combined effect of a high combustion zone area contraction ratio results in lower gas-side convective film coefficients. Due to these combined effects on the reduction of heat transfer into the wall surface, the regenerative concept can be employed in the combustion zone to high chamber pressure values. The extension of the regenerative feasibility regime (combustion zone) is shown in Fig. 73. A contraction area ratio of 2 is seen to allow regenerative-cooling feasibility in the combustion zone to a chamber pressure exceeding 5000 psia. The coolant pressure drop and tube number in the combustion zone becomes dependent upon the specific design chosen.

Nozzle Regenerative Cooling Limit Analysis. An analysis was performed to determine coolant pressure drops, tube number, coolant bulk temperature rise, and heat flux variation for the advanced nozzles with LO_2/RP-1 propellants. The nozzle D_p/D_t values closely examined were 3.5 and 7.0. Coolant pass arrangement was assumed as a single uppass for convenience of design analysis. A two-pass arrangement would reduce the required tube number by 40 percent at the expense of an increased pressure drop.

Analysis indicated that a large fraction of the length could be regeneratively cooled even at high chamber pressures. The length of the possible regeneratively cooled portion is given by the difference between the total length given in Tables 11 and 12 and the film-cooled length values indicated in Table 17. Regenerative cooling cutoff points were found to correspond to heat fluxes approximately 2/3 of the conduction limit. At higher values, the coolant pressure drop was seen to markedly increase.

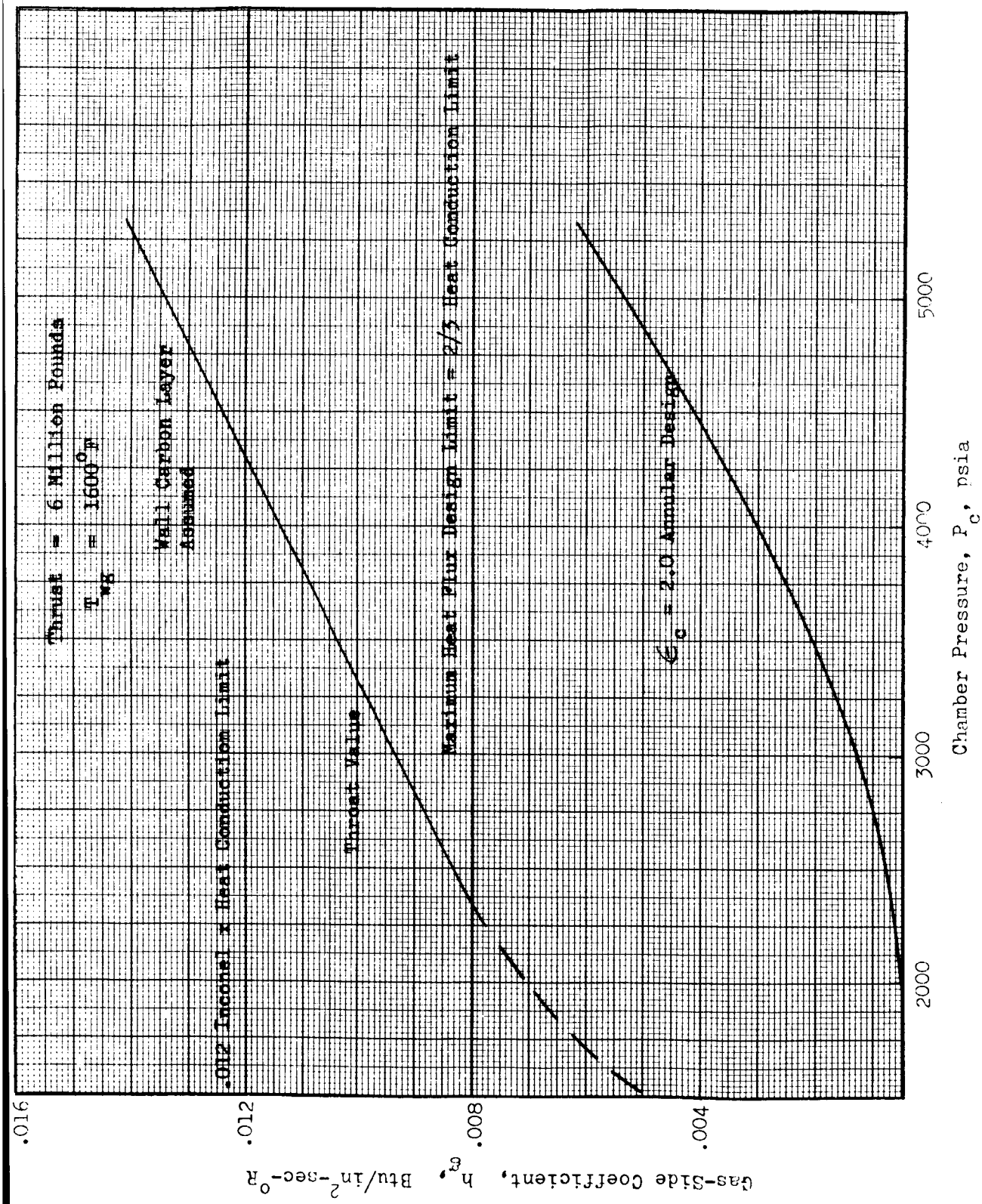

Figure 73. Regenerative Design Limits for the Combustion Zone of an Annular Design Using LO_2/RP-1 Propellants

TABLE 17

MINIMUM SUPERSONIC REGION FILM-COOLED LENGTHS
FOR NOZZLE SKIRT WITH FILM-COOLING AUGMENTATION
ADVANCED NOZZLES WITH LO_2/RP-1

Thrust, million pounds	D_p/D_t	Minimum Film-Cooled Length, inches	
		3000-psia Chamber Pressure Design	5000-psia Chamber Pressure Design
2	3.5	3.6	4.6
4	3.5	5.0	6.5
6	3.5	6.1	7.9
2	7.0	2.4	2.3
4	7.0	3.2	3.3
6	7.0	4.0	3.9

The only designs where it appeared to be possible to cool the nozzle skirt completely were at the 1500-psia chamber pressure level. A further investigation indicates a slightly higher chamber pressure could be tolerated in terms of coolant pressure drop. A reasonable design limit for this cooling method may be bracketed between a 1500- to 2000-psia chamber pressure. Coolant pressure drop at 1500-psia chamber pressure was 216 psi for the $D_p/D_t = 3.5$ and 232 psi for the $D_p/D_t = 7.0$ design. Thrust level within the range examined shows little sensitivity to pressure drop. A limiting coolant-side wall temperature of 800 F was used.

The large-nozzle tube number requirement is indicated in Table 18. This is necessitated by the large chamber circumference. Reduction in tube number for an increased pressure drop could be accomplished by a two-pass arrangement or by cooling assistance with additional film or turbine gas augmentation. The limiting lower tube number will be determined by an internal pressure stress and allowable wall thickness for heat conduction into the regenerative propellant.

Combined Film-Regenerative Cooling. This combined method appears very attractive for high-chamber-pressure designs in the high heat flux regions since due to the large surface area of the combustion zone, complete cooling of the combustion zone and throat by film cooling approaches would lead to an anticipated large performance penalty.

The combustion chamber with the advanced nozzle design is located at a large diameter such that the inherent geometry allows the use of comparatively high combustion zone area contraction ratios. This is beneficial from two standpoints. The first is the reduction of the convective gas-side heat transfer coefficient due to a lower effective gas mass velocity. The relationship provided by Eq.304 similarly indicates a larger effective carbon deposition resistance with a reduced mass velocity.

TABLE 18

APPROXIMATE COOLANT TUBE NUMBER REQUIREMENTS FOR ADVANCED NOZZLE DESIGNS BASED UPON REGENERATIVE COOLING WITH A SINGLE UP-PASS DESIGN WITH LO_2/RP-1 PROPELLANTS

D_p/D_t	Chamber Pressure, psia	Number of Tubes		
		2-Million-Pound Thrust	4-Million-Pound Thrust	6-Million-Pound Thrust
3.5	1500	1700	2400	3000
5.0	1500	3500	4800	6000
7.0	1500	5100	7200	9000
3.5	3000	1700	2400	3000
5.0	3000	3500	4800	6000
7.0	3000	5100	7200	9000
3.5	5000	1700	2400	3000
5.0	5000	3500	4800	6000
7.0	5000	5100	7200	9000

Film-cooling augmentation in the combustion region at high chamber pressure can be beneficially coupled with a large combustion zone since with the high contraction ratio the surface area is not materially changed. Hence, the film-cooling requirements may be reduced proportionally. The film-cooling augmentation, if the wall temperature is high enough to promote cracking of the fuel film coolant, will contribute to an artificial deposition of surface carbon and correspondingly significantly lower the regenerative cooling requirements for a defined metal gas-side wall temperature. The carbon deposition thickness which can be promoted under these circumstances can be verified only by experiment.

Film Cooling

The combustion zone film-cooling requirements for the LO_2/RP-1 design cases were determined for a range of contraction ratios and chamber pressures. The qualitative results indicate that unless the fabrication simplicity for the film-cooling method overshadows the performance degradation expected, the combined film-regenerative method appears the more attractive. In the throat region at chamber pressures approaching 5000 psia, the heat flux condition is such that complete film cooling is the only apparent practical method because the allowable percentage of heat flux absorption by regenerative means would be small.

The combustion region for typical advanced nozzles lends itself to high area contraction ratios as pointed out previously. As a result, film-cooling requirements may be proportionately decreased.

In the nozzle expansion region downstream of the throat, a region exists where the heat flux is not low enough for complete regenerative cooling.

In this region, the surface may be film cooled at the expense of a performance loss almost proportional to the amount of injected coolant. For the moderate chamber pressure range, the combined film-regenerative means is the more attractive.

Table 17 shows the film-cooled lengths required downstream of the throat for various advanced nozzle designs with differing thrust and chamber pressure conditions. These lengths are short enough to require only single-slot injection.

RP-1 film-cooling flowrate computed values depend on the effectiveness of the injection technique and conceivably upon the stability of the film-coolant layer as indicated in a previous discussion. The layer stability effectiveness will have to be explored experimentally to provide exact conditions for injection length and flow tradeoff for maximum flow utilization efficiency. Due to the hydrocarbon nature of the RP-1, cracking of the fuel to lower molecular weight species is expected. The effective heat capacity as a coolant can only be explored under pressure and temperature conditions which will promote cracking of the RP-1 film coolant as would be representative of the high temperature combustion conditions. Due to the high molecular weight of the RP-1 film coolant in contrast to hydrogen, a severe performance penalty would be anticipated with excessive use of RP-1 film coolant. Hence, the use of film cooling should be restricted to the local throat region.

The foregoing remarks illustrate that the combined method would be advantageous wherever film cooling is considered for use. The emphasis would change from the hydrogen case to the RP-1 case because for the latter a high degree of regenerative cooling combined with a small fraction of film cooling is of paramount importance to diminish performance losses.

ADVANCED CHAMBER DESIGN LAYOUTS

Typical design layouts of 6-million-pound-thrust, 3000-psia chamber pressure LO_2/LH_2 advanced engines are shown in Fig. 74 and 75. Propellant ducts have been omitted on these drawings due to their complexity. The nozzle dimensions have been sized for D_p/D_t ratios of 3.5 and 5.0, respectively, and an expansion area ratio of 36. The rough layout at a D_p/D_t ratio of 3.5 showed that it was impossible to fit the axial hydrogen pump into the plug. Excessive envelope length prompted the second layout at $D_p/D_t = 5.0$, which shows the lower portion of the hydrogen pump enclosed in the plug.

The extent to which advanced nozzles offer shorter engine lengths than conventional nozzles is dictated primarily by the ground rules of the study. For example, if thrust vector control methods not requiring engine movement (e.g., side-gas injection, segment throttling, segment rotation) and complex vehicle-engine interconnects are allowed, some length can usually be saved by integration of pumps and tank bottom. The pumps can conceptually be put inside the tank and the tank bottom can be used for a centerbody.

In the present situation, the most practical avenue for length reduction is probably the use of more than two pumps. For two fuel and two oxidizer pumps, the fuel pump length would decrease by about 37 inches.

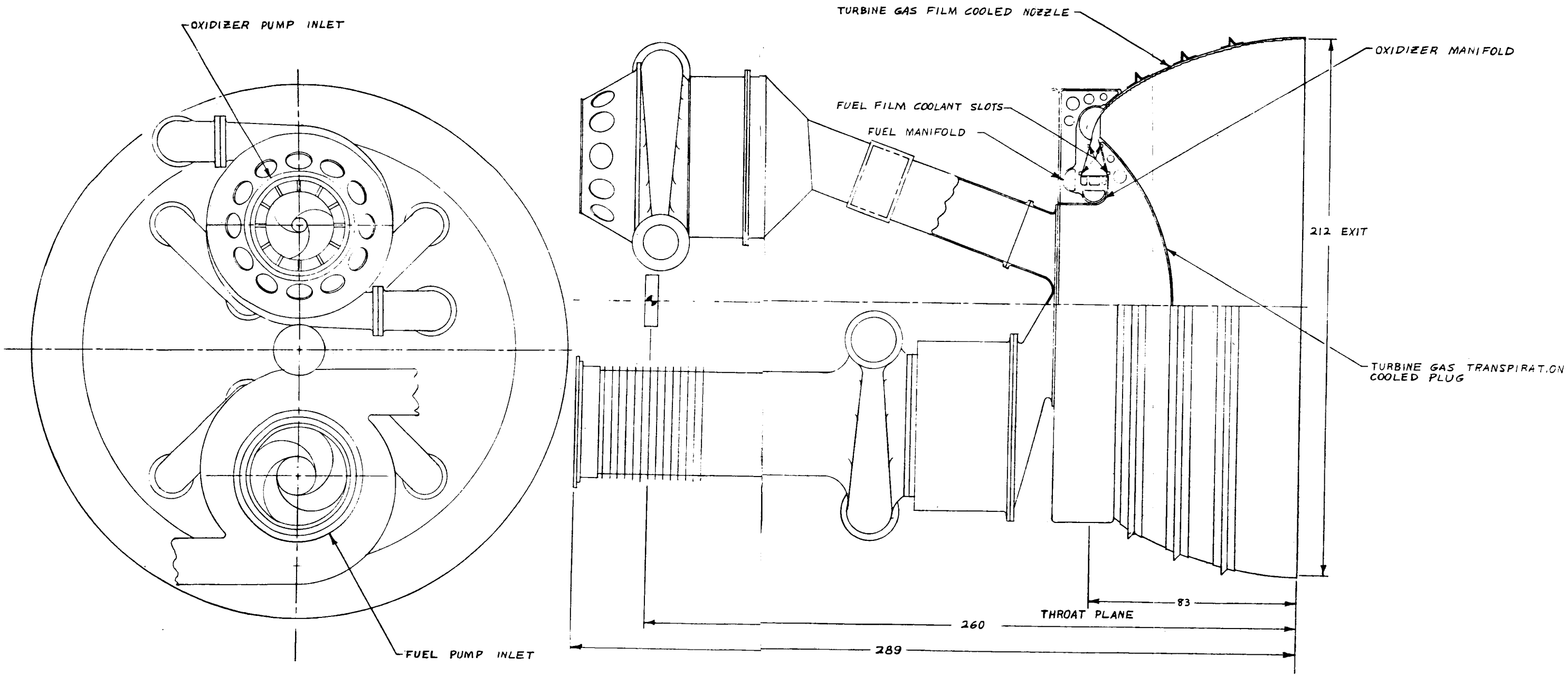

Figure 74. LO_2/LH_2 Advanced Engine Design Layout for 3000-psia Chamber Pressure and D_p/D_t = 3.5, Thrust = 6 million pounds

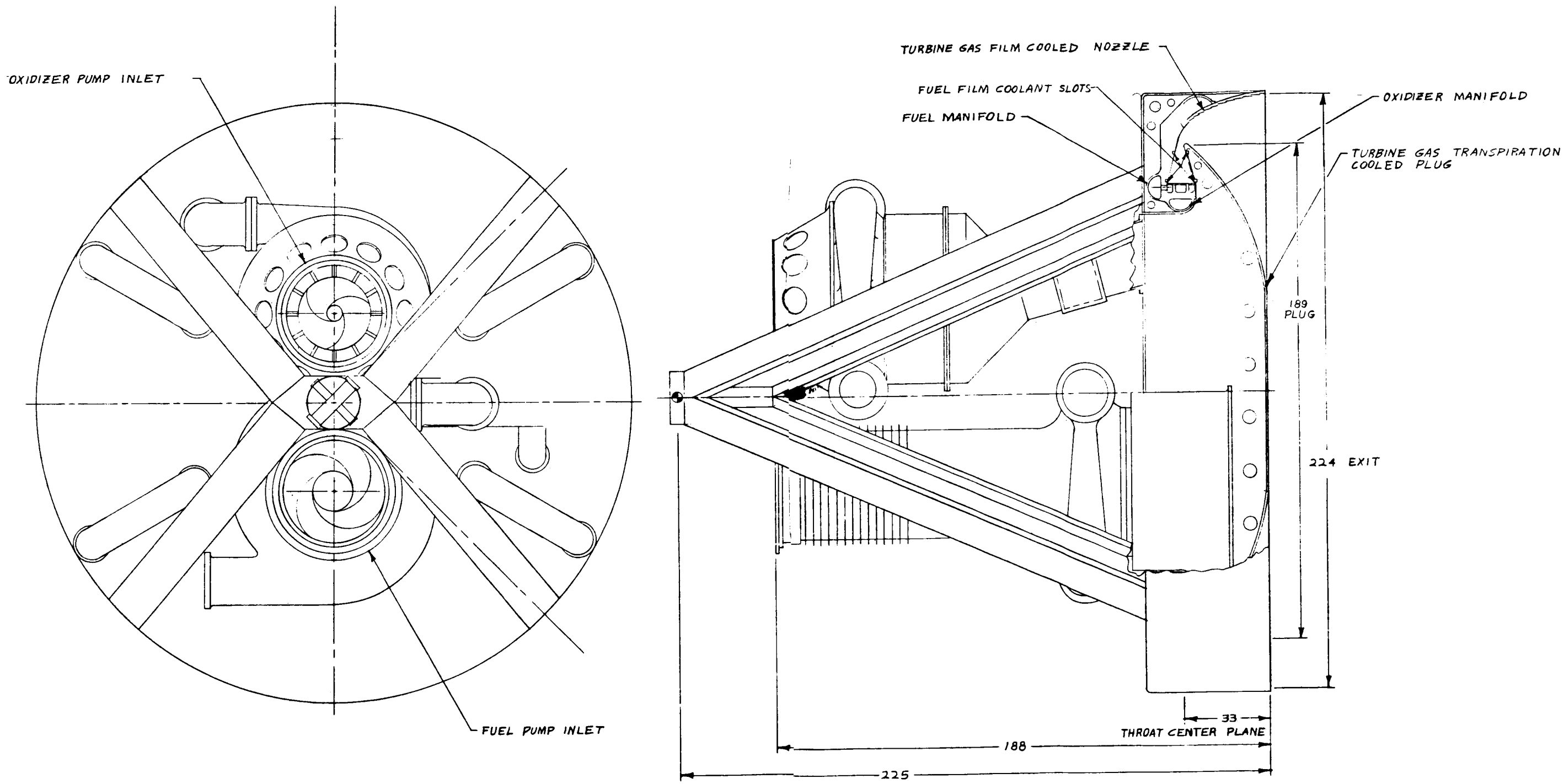

Figure 75. LO_2/LH_2 Advanced Engine Design Layout for 3000-psia Chamber Pressure and D_p/D_t = 5.0, Thrust = 6 million pounds

R-6199

If engine length is based on the length from exit plane to the pump inlet for all designs, then the following comparative values are obtained:

Nozzle	Number of Pumps	Length to Pump Inlets, inches	Percent Length
Bell	2	320	100.0
H-F (D_p/D_t = 3.5)	2	289	90.4
H-F (D_p/D_t = 5.0)	2	188	58.7
H-F (D_p/D_t = 3.5)	4	252	78.8
H-F (D_p/D_t = 5.0)	4	151	47.2

As in the LO_2/LH_2 bell design layouts, the combustion chamber has a film-cooled solid wall. Two hydrogen film-coolant introduction planes are used. The combustion region is sized to a contraction area ratio of 4:1 and a minimum combustion length of 14 inches. The lower portion of the combustion chamber is supported by a continuation of the plug honeycomb box structure.

Little room is available to start and end a regenerative tube bundle, as was done in the bell engine, so it is fortunate that the nozzle can be cooled with 2.5 percent of the total flow as turbine exhaust gas. Since the turbine exhaust comprises 6.8 percent of total flow, the remaining 4.3 percent is used to cool the nozzle plug. Corresponding length fractions of the bell designs could not be cooled by this method, as heat flow per unit length drops off much more rapidly in point-deflection nozzles than in conventional nozzles.

The plug is reinforced by radial honeycomb shear webs, around and through which turbine gas circulates. Skirt flow is tapped from the centerbody with radial ducts.

I-beams are shown for the thrust structure, although a honeycomb thrust cone might be lighter. A closed cone would decrease access to the engine, and would require reinforcement where the pumps pierced the shell.

NOVEL COOLING METHODS

CONTACT RESISTANCE LINER

The use of a thin-walled refractory metal liner to provide a semi-insulating surface which may be operated at high wall temperatures presents a novel approach for heat flux reduction in a regenerative-cooling design. Examination of the governing heat flux input equation

$$q/A = h_g \ (T_{aw} - T_{wg}) \tag{306}$$

as the wall temperature is elevated to near the adiabatic wall temperature shows that the wall heat input approaches zero regardless of the chamber pressure condition. If, in addition, the adiabatic wall temperature is slightly reduced by a fuel-rich region near the wall, the heat flux is further minimized. Table 19 compares the relative heat inputs for various refractory metals held at a T_{wg} equal to either their respective melting temperatures or the adiabatic wall temperature to a reference regenerative wall temperature of 2000 R. It is seen that in most instances the heat input is reduced to nearly zero. The melting point of a refractory metal is not an attainable design point. Because the refractory metals are normally subject to very rapid oxidation at elevated temperatures, a practical design-limiting wall temperature would probably be set by the allowable temperatures for oxidation-resistant coatings which range from about 3300 to 3800 R depending upon the coating, the refractory metal, and the desired lifetime. Even with this restriction, Table 19 shows that a substantial reduction in wall heat flux can be made at a nominal wall temperature of 3400 R. If a relatively nonoxidizing atmosphere can be provided by a highly fuel-rich boundary layer near

TABLE 19

HEAT FLUX REDUCTIONS WITH CONTACT RESISTANCE LINERS

Material	Ultimate T_{wg}, R	*Relative Heat Input at T_{aw} = 6200 R	*Relative Heat Input at T_{aw} = 5500 R
Conventional	2000	1	0.83
Tungsten	6630	0	0
Molybdenum	5190	0.241	0.07
Tantalum	5885	0.075	0
Columbium	4807	0.332	0.165
Rhenium	6216	0	0
Hafnium	4326	0.446	0.28
Coated Refractories	3400	0.67	0.50
Film-Protected Refractories	4000	0.525	0.355

*Neglecting shield radiation

heat transfer coefficients at high interface temperatures and high interface ΔT cover the same range of values as those obtained at moderate conditions and that the coefficients are controllable to a degree by adjustment of fitting tolerances and surface conditions. Analytical studies also indicated that with proper design allowances, the contact heat transfer coefficients might vary locally over a factor of 4 or 5 about the nominal design value without producing a failure condition.

With refractory metal usage in a LO_2/LH_2 design, some problems arising due to brittleness and hydrogen absorption are foreseen; the magnitude of this problem is reduced by the fact that little strength is required for the liner. A molybdenum-alloy liner would perhaps be the best material choice for these propellants. With LO_2/RP-1 propellants, carburizing at high temperatures is a problem. Tantalum is a better choice and it has good ductility. For the LO_2/RP-1 design, if a carbon layer is deposited on the refractory liner, the heat flux rate will be even further reduced.

The most promising application for the contact resistance liner appears to be with combined regenerative and film cooling. Film-cooling heat absorption is most effective when the contacting wall (adiabatic or nonadiabatic) is allowed to rise to high temperatures. The refractory sleeve can rise to about twice the absolute temperature of a stainless steel wall; moreover, the insulating effect of the contact resistance permits a lower film efficiency. At the same time, a fuel-film-coolant layer protects the liner from oxidation by the hot combustion gas, as mentioned above.

FILM COOLING WITH SPIRAL TANGENTIAL INJECTION

Design concepts have been described in the literature employing film-cooled designs where the film coolant is injected tangentially to the wall surface but normal to the flow direction. These designs provide a centrifugal component to the film coolant to develop a better film stability with less entrainment loss without cooling benefit. Three drawbacks to such designs can be noted. The first is the manufacturing problem of numerous long L/D orifices or spiral slots at a very shallow angle to the surface requiring a thick wall construction. In addition, when the film coolant is injected in a noncoaxial manner, the efficiency of usage is degraded by the velocity difference effect; i.e., the shear between the mainstream and film-coolant layer is for the two methods

$$\tau_{gc} \propto V_g\left(1 - \frac{V_c}{V_g}\right), \quad \text{coaxial tangential film} \tag{307}$$

$$\tau_{gc} \propto V_g \quad , \quad \text{spiral tangential film} \tag{308}$$

indicating a higher gas-to-coolant layer shear and heat input for the spiral-film-cooling case. Lastly, these concepts cannot be used in combination with regenerative cooling to reduce the film-coolant requirement.

One of these new design concepts has been developed by Marquardt wherein a ribbon of metal is grooved on one side to permit the film coolant to pass from the outside to the inside of the chamber. The ribbon is then spiral wound onto a mandrel to form the desired chamber nozzle contour (Fig. 76). The distribution of coolant and the wall porosity are controlled by the groove size, the groove spacing along the ribbon, and the groove angle. Various bonding techniques have been tried. Aluminum was successfully diffusion bonded using 40- and 6-mil aluminum. Strong bonds

were formed with no clogging of coolant passages. Similarly, copper was diffusion welded and diffusion bonded using a thin sheet of aluminum to form strong bonds and clear passages. Work was also done on bonding stainless steel and tantalum.

The Marquardt concept is somewhat similar to the Pratt and Whitney wafer spiral cooling concept shown in Fig. 76. The two concepts are compared as follows:

	Marquardt	Pratt and Whitney
Construction	Continuous ribbon (wound edgewise)	Individual wafers
Thickness (axial)	0.02 to 0.04 inch	1/8 inch
Passages	One side only (parallel channels)	Both sides (cross channels)

The Pratt and Whitney design has the advantage that each wafer can be individually calibrated before being included in the hardware. The use of a cross-passage type of design reduces the problem of nonuniform flow distribution due to passage clogging.

The Marquardt design may be easier to build, and the slots can be cut to give the desired flow distribution. Even though a cross-passage type of flow pattern is not utilized, many more slots can be introduced due to the thinner walls, resulting in a close approach to transpiration cooling. However, because of the larger number of slots, they are obviously smaller and thus more prone to clogging for a given coolant flowrate.

Further cooling efficiency evaluations based on data currently being obtained and reported by Marquardt and Pratt and Whitney, as well as a comparison of the slot size manufacturing problem and a weight examination and comparison to the conventional shingle approach is necessary before additional design recommendations can be made.

FLOX SUBSTITUTION

The substitution of a fluorinated oxidizer (FLOX) for oxygen appears to be attractive from a specific impulse performance gain standpoint. This is shown in Table 20 where specific impulse results are compared for O_2, F_2-O_2 (30-70), and F_2-O_2 (70-30) by weight with RP-1 and H_2. The values were calculated by the Rocketdyne N-element theoretical rocket performance computer program. Chamber pressures of 1500 and 5000 psia were considered. Full-shifting and frozen-equilibrium values are included in Table 20 for an area expansion ratio of 30. The mixture ratios given for the FLOX cases are essentially optimum. It is anticipated that due to the relatively high flame temperature conditions, the full shifting case would be most representative of the theoretical maximum performance. A specific impulse gain of up to almost 15 seconds can be achieved with H_2 fuel, while up to about 45 seconds can be achieved with RP-1 for the range of FLOX concentration covered (Table 20).

Combustion gas physical properties and combustion chamber parameters are summarized in Table 21 for FLOX/H_2 and in Table 22 for FLOX/RP-1. Previously obtained values for LOX systems from Ref. 1 are also included for comparison. It is significant that combustion gas specific heat values for the FLOX cases are lower than those for LOX with both H_2 and RP-1 fuels.

EFFECT ON CHAMBER HEAT FLUX

The effect of fluorine substitution on the heat transfer rate was investigated by considering the variations in the gas-side heat transfer

TABLE 20

PERFORMANCE COMPARISON OF F_2/O_2 WITH O_2 OXIDIZER

Fuel	Oxidizer	P_c, psia	Shifting		Frozen	
			MR	I_{s_s}, lbf-sec/lbm	MR	I_{s_f}, lbf-sec/lbm
H_2	O_2	1500	5.0	451.8	5.0	439.5
	O_2	5000	5.0	452.2	5.0	443.9
	F_2/O_2 (30-70)	1500	5.8	455.8	4.6	449.7
	F_2/O_2 (30-70)	5000	5.8	456.6	4.6	446.4
	F_2/O_2 (70-30)	1500	7.0	464.6	---	---
	F_2/O_2 (70-30)	5000	7.0	465.4	---	---
RP-1	O_2	1500	2.35	349.3	2.35	331.6
	O_2	5000	2.35	350.4	2.35	337.2
	F_2/O_2 (30-70)	1500	3.2	372.5	---	---
	F_2/O_2 (30-70)	5000	3.2	375.0	---	---
	F_2/O_2 (70-30)	1500	3.8	394.0	3.8	362.0
	F_2/O_2 (70-30)	5000	3.8	394.5	---	---

ϵ = 30 (vacuum)

TABLE 21

FLOX/HYDROGEN COMBUSTION GAS PHYSICAL PROPERTIES AND CHAMBER PARAMETERS

Oxidizer F_2/O_2	MR	P_c, psia	MW	C_p, Btu/lbm-R	γ_f	γ_s	c*, ft/sec	T_g, R	Pr	μ, lbm/in.-sec x 10^6
0-100	5.0	5000	11.92	0.977	1.206	1.172	7801	6160	0.824	6.02
0-100	5.0	1500	11.83	0.974	1.209	1.162	7733	6029	0.822	5.97
30-70	5.0	1500	11.01	0.967	1.230	1.182	7927	5965	0.810	5.34
30-70	5.8	1500	12.16	0.893	1.224	1.166	7793	6345	0.814	5.70
30-70	5.0	5000	11.08	0.970	1.227	1.194	7991	6085	0.814	——
30-70	5.8	5000	12.28	0.896	1.220	1.177	7829	6536	0.814	——
70-30	5.0	1500	10.05	0.947	1.264	1.211	8178	5917	0.795	4.72
70-30	7.0	1500	12.24	0.787	1.260	1.181	7970	6823	0.795	5.38
70-30	5.0	5000	10.108	0.949	1.261	1.225	8319	6026	0.795	——
70-30	7.0	5000	12.392	0.791	1.254	1.193	8236	7084	0.797	——

ROCKETDYNE • A DIVISION OF NORTH AMERICAN AVIATION, INC.

TABLE 22

FLOX/RP-1 COMBUSTION GAS PHYSICAL PROPERTIES AND CHAMBER PARAMETERS

Oxidizer F_2/O_2	MR	P_c, psia	MW	C_p, Btu/lbm-R	γ_f	γ_s	c*, ft/sec	T_g, R	Pr	μ, lbm/in.-sec x 10^6
0-100	2.35	1500	22.59	0.492	1.218	1.149	5834	6589	0.817	5.82
0-100	2.35	5000	22.89	0.494	1.213	1.159	5912	6845	0.820	5.97
30-70	2.5	1500	20.83	0.471	1.254	1.175	6304	6897	0.798	——
30-70	3.1	1500	22.42	0.446	1.248	1.196	6265	7229	0.802	5.93
30-70	2.5	5000	21.08	0.472	1.250	1.188	6357	7157	0.800	——
30-70	3.1	5000	22.81	0.448	1.241	1.163	6355	7607	0.804	——
70-30	3.1	5000	20.99	0.429	1.283	1.184	6675	7846	0.788	——
70-30	3.1	5000	21.28	0.431	1.277	1.192	6738	8170	0.788	——

coefficient and the variation in the heat flux. Using the modified Stanton relationship:

$$\frac{St}{Pr^{-2/3}} = \frac{C}{Re^{0.2}} \tag{309}$$

and assuming a combustion length-based Reynolds number, this reduces at the throat to:

$$\frac{h_g}{G^* \, C_p \, Pr^{-2/3}} = \frac{C}{Re_x^{0.2}} \tag{310}$$

For the same combustion zone geometry (x = constant)

$$h_g \propto \frac{C_p \, (G^*)^{0.8} \mu^{0.2}}{Pr^{2/3}} \tag{311}$$

Based on the definition:

$$\frac{P_c \, g_c}{G^*} = c^* \tag{312}$$

Equation 311, for a given chamber pressure, reduces to:

$$h_g \propto \frac{C_p \, \mu^{0.2}}{(c^*)^{0.8} \, Pr^{2/3}} \tag{313}$$

A comparison of the gas-side film coefficients for the FLOX combinations as calculated from Eq.313 shows that in all cases the heat transfer coefficient value is below that for LOX-based systems at the same chamber pressure. FLOX heat transfer coefficients range from 75 to 96 percent of the LOX-based values for hydrogen fuel, and from 70 to 92 percent with RP-1 fuel.

A more realistic comparison is the heat flux. On this basis the equation for heat flux comparison becomes:

$$q/A \propto \frac{C_p \, \mu^{0.2}}{(c^*)^{0.8} \, (Pr)^{2/3}} \, (T_g - T_{wg}) \tag{314}$$

Initially, the wall surface was set at 2000 R for the H_2 and RP-1 designs. This assumes the absence of a carbon layer on the gas-side wall surface for RP-1. For this condition, the heat fluxes are not significantly different. The heat fluxes for FLOX are from 87 to 99 percent of the LOX values with hydrogen as the fuel and from 98 to 103 percent with RP-1 fuel.

EFFECT OF GAS-SIDE CARBON DEPOSITION

The higher operating mixture ratio for the FLOX combinations with RP-1 (3.1 to 3.8) would appear to provide a lesser amount of carbon for wall deposition than with oxygen as the oxidizer (MR = 2.35). For the oxygen and FLOX cases, the performance printouts show little or no free carbon available in the exhaust products. But carbon is well known to deposit with LO_2/RP-1 at least for chamber pressures below 2000 psia.

If the deposition of carbon on the wall surface is materially less for the FLOX case, the heat transfer rate to the wall surface could become prohibitively high. Available Rocketdyne operating data with FLOX systems from model motor and Atlas vernier tests as well as some limited data with large engine testing indicates that heat flux values with FLOX are not significantly higher than with LOX at low percentages of F_2, but do appear to be higher for large percentages of F_2. Current Atlas large-thrust engine testing at low fluorine percentages (30 percent) shows engine coolant bulk temperature rises identical to the 100-percent oxygen case indicating retention of the hypothesized carbon layer. More quantitative confirmation at high fluorine percentages and high mixture ratio values is necessary.

At chamber pressures above the 2000-psia value, film cooling is required and, consequently, on an equivalent basis, the heat fluxes for FLOX and LOX would be comparable as would be the film-cooling flowrates. For lower chamber pressures where the carbon layer deposition may be a predominating factor or where subsequently high gas-side wall surface temperatures are attained, the higher flame temperature associated with the FLOX combinations results in a higher heat transfer rate, especially as the wall surface temperature approaches the flame temperature. A comparison was made under the assumption of a fixed wall resistance and "coating" combination such that the surface temperature reached levels from 2000 to 5000 R. Figure 77 illustrates the resultant effect. As much as a 40 percent greater heat transfer rate can occur due to the higher FLOX flame temperature for the higher percentage FLOX combination at the higher mixture ratio.

Under the condition that the same carbon layer resistance is present for the FLOX substitution case as with LOX, the allowable maximum regeneratively-cooled limit for FLOX will be that value which gives the same heat flux

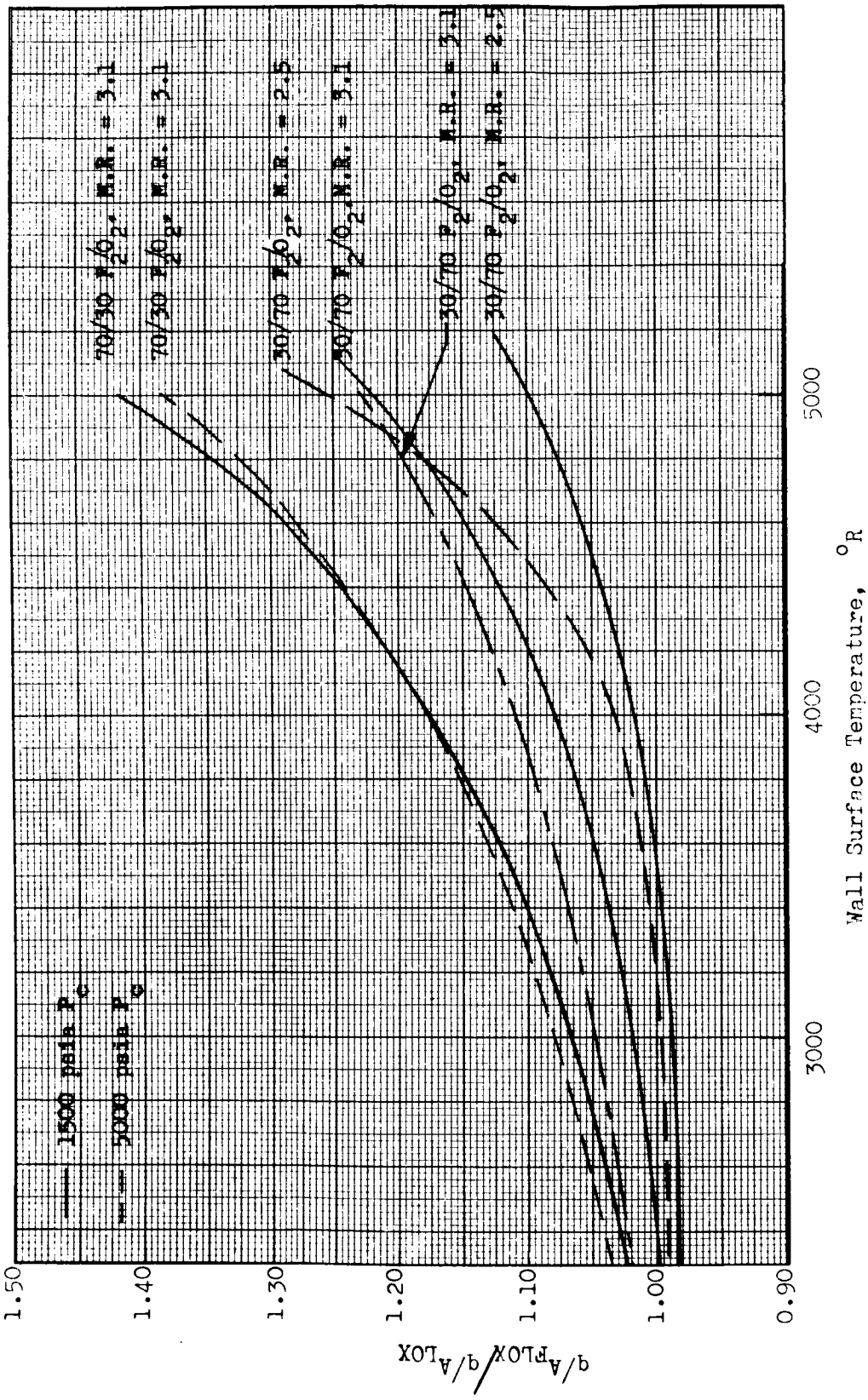

Figure 77. Effect Upon Heat Transfer Rate of Varying Gas-Side Surface Temperature with RP-1 Fuel

at the maximum chamber pressure for LOX. This may be estimated from the expression:

$$\left[\frac{P_{c_{FLOX}}}{P_{c_{LOX}}}\right]_{\substack{\text{upper}\\ \text{limit}}} = \left[\frac{(q/A)_{FLOX}}{(q/A)_{LOX}}\right]^{-1.25}_{P_{c_{LOX}}} \tag{315}$$

This relation is plotted in Fig. 78. Its use may be illustrated by the following example. If a 2000-psia upper limit is visualized for an RP-1 regeneratively cooled case with LOX, a 20-percent increase in heat flux for the same chamber pressure due to the use of FLOX translates to an upper chamber pressure limit reduction to 1600 psia. Equation 315 and Fig. 78 assume that the heat flux change percentage is uniform along the chamber length.

MIXTURE RATIO SHIFT EFFECTS

The mixture ratio shift to a higher value, which is indicated for fluorine addition to the oxidizer, results in a lesser amount of fuel available to provide cooling either of the mass-transfer type for high-chamber-pressure conditions or regenerative cooling for moderate heat fluxes. For film or transpiration cooling, the result is that an increased percentage of the available fuel is required for the coolant. Under the assumption of equivalent heat fluxes, the mass transfer coolant flow percentage remains a constant percent of the total. Accordingly, the effect of a change in mixture ratio on the percent of the total fuel required for film cooling is derived to be:

$$\frac{(\dot{W}_{FC}/\dot{W}_F)_2}{(\dot{W}_{FC}/\dot{W}_F)_1} = \frac{(1 + MR)_2}{(1 + MR)_1} \tag{316}$$

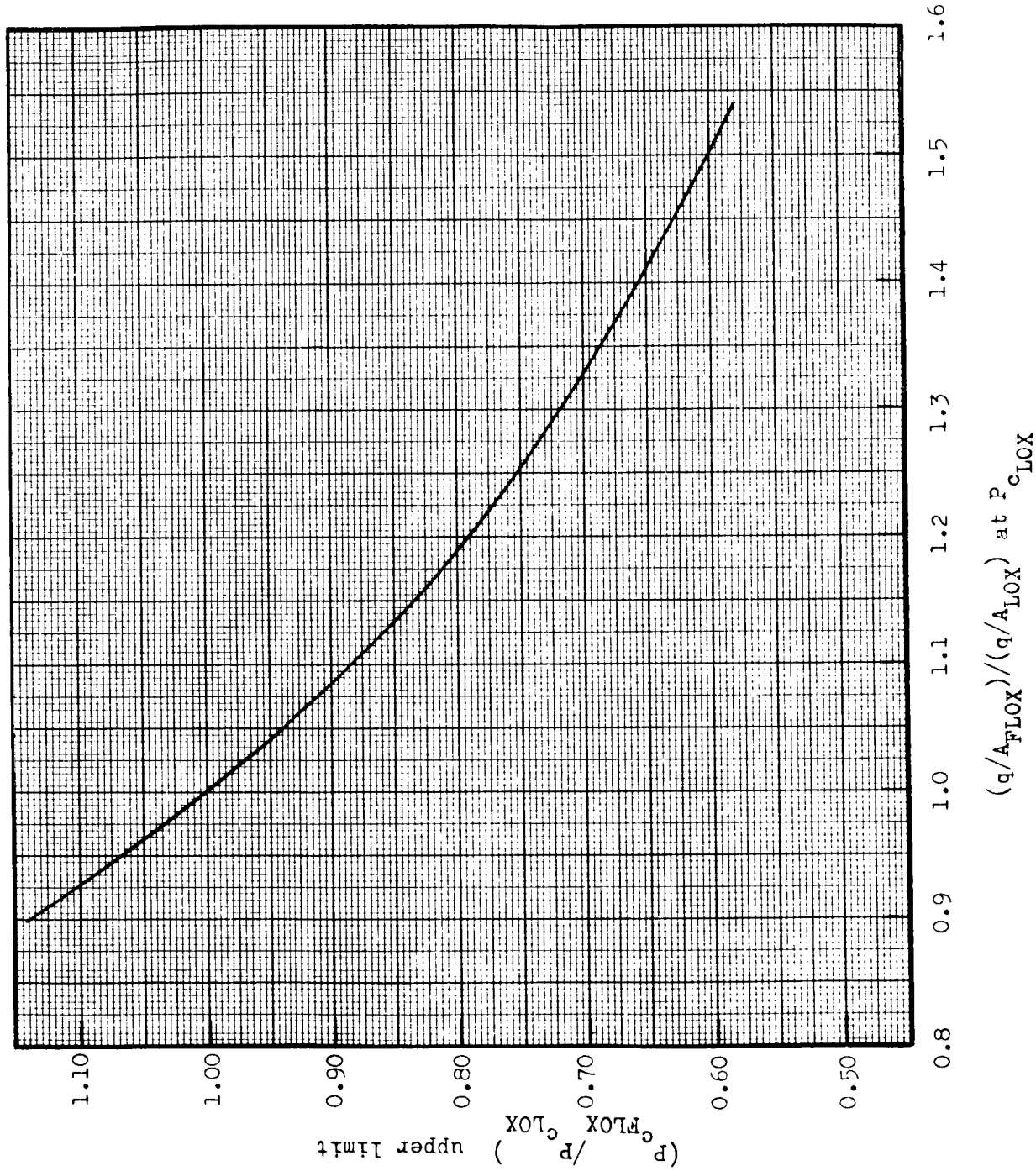

Figure 78. Regenerative-Cooling Upper Limit Change with Heat Flux Change

For a typical mixture ratio of 3.8 for 70-30 FLOX as compared to 2.35 for O_2 with RP-1 fuel, Eq.316 gives a ratio of 1.43. Thus, if 6 percent of the fuel were required for the O_2 case, then 8.6 percent would be necessary for the FLOX design. This change in fuel flow percentage will be even further increased if higher mixture ratios are chosen based on a bulk density optimum or other considerations. With the increased percentage of fuel flow, the main chamber mixture ratio will be increased to a value further from the optimum point. As a result, a performance loss due to the shift in the mainstream mixture ratio and the possible incomplete combustion of the fuel mass transfer coolant at the wall may occur. For cases where the film coolant flow is a small fraction of the total fuel as with hydrogen film coolant, the expected performance-loss percentage is small and this consideration is minor.

For a regeneratively cooled portion of a chamber design, the shift to a higher mixture ratio results in a smaller quantity of fuel available as a coolant. For the conventional and advanced single nozzle, large thrust designs this presents no problem to provide a design for the optimum pressure drop. For a multichamber or multielement combustion zone, however, where the surface area exposed to high heat fluxes is large, a reduction in the coolant passage hydraulic diameter is required causing an increase in the pressure drop for a required coolant passage velocity.

Consideration of the effect of mixture ratio shift, for a given chamber pressure, on coolant pressure drop from the standpoint of a change in passage hydraulic diameter may be examined on the assumption of a constant heat flux during the mixture ratio change. This leads to a requirement of an almost constant coolant mass velocity (G) for RP-1 to maintain the

required coolant-side heat transfer coefficient. If circular coolant passages are assumed, consideration of the variation of the number of circular passages and the diameter leads to the solution (for nearly constant specific impulse):

$$\frac{(d_h)_2}{(d_h)_1} = \frac{(1 + MR)_1}{(1 + MR)_2} \tag{317}$$

Assuming the coolant flow as incompressible and the coolant passage lengths as fixed, then the pressure drop relation becomes:

$$\Delta P \propto \frac{1}{d_h^{0.2}} \quad \frac{1}{d_h} = \frac{1}{d_h^{1.2}} \tag{318}$$

(For high Reynolds number conditions, the 0.2 exponent on the diameter factor for the friction coefficient expressed above approaches zero and $\Delta P \propto d_h^{-1.0}$). By combining Eq. 317 and 318, the coolant pressure drop relation becomes:

$$\frac{\Delta P_2}{\Delta P_1} = \left[\frac{(1 + MR_2)}{(1 + MR_1)}\right]^{1.2} \quad \text{(incompressible flow with circular passages } h_c \propto G) \tag{319}$$

If the coolant-side heat transfer coefficient is proportional to $G^{0.8}/d_h^{0.2}$, then the exponent on the right side of Eq. 319 is reduced to 0.60, and the pressure drop becomes less dependent on the mixture ratio. For high-chamber-pressure thrust chambers with RP-1 coolant, an exponent of almost 1.2 is probably the most realistic value. Thus, for an increase

in mixture ratio from 2.35 to 3.8, a 54-percent increase in pressure drop will occur.

For a compressible coolant such as hydrogen, if the momentum losses are assumed to be small relative to the frictional losses then:

$$\Delta P \propto \frac{1}{d_h^{1.2}} \left(\frac{1}{\rho}\right) \tag{320}$$

If the total heat input into the coolant remains at a constant value (which implies a fixed heat flux) and if the coolant-side heat transfer coefficient is dependent only on $G^{1.0}$, then:

$$\bar{\rho} \propto \frac{1}{\bar{T}_c} \propto (\dot{W}_F) \propto \frac{1}{(1 + MR)} \tag{321}$$

Combining Eq. 317, 320, and 321 gives:

$$\frac{\Delta P_2}{\Delta P_1} = \left[\frac{1 + MR_2}{1 + MR_1}\right]^{2.2} \qquad \text{(compressible flow, circular passages, } h_c \propto G) \tag{322}$$

In reality, the effect of coolant property changes and the coolant wall temperature-to-bulk temperature relationship and the hydraulic diameter effect on the heat transfer coefficient can affect the relationship given by Eq. 322. For hydrogen, as an example, assuming $(T_{wc} \gg T_c)$, a constant wall temperature, and a constant coolant-side film coefficient such that:

$$G^{0.8} \propto \frac{d_h^{0.2}}{(\bar{T}_c)^{0.55}} \tag{323}$$

results in:

$$\frac{\Delta P_2}{\Delta P_1} = \left[\frac{1 + MR_2}{1 + MR_1}\right]^{0.94} \quad \text{(compressible flow with circular passages and constant coolant film coefficient)} \tag{324}$$

Thus, it appears that in this case the mixture ratio exercises a lesser effect on the pressure drop.

If the coolant passages depart radically from a circular cross-section such that the passage hydraulic diameter is not affected by changes in mixture ratio, Eq. 319 and 324 become:

$$\frac{\Delta P_2}{\Delta P_1} = 1.0 \quad \text{(elongated passages with incompressible flow and } h_c \propto G\text{)} \tag{325}$$

$$\frac{\Delta P_2}{\Delta P_1} = \left[\frac{1 + MR_2}{1 + MR_1}\right]^{-0.24} \quad \text{(elongated passages with compressible flow and constant film coefficient)} \tag{326}$$

It is seen that for this case an increase in mixture ratio would be beneficial with compressible flow to reduce coolant pressure drop. However, for the actual designs of large-scale engines, the coolant temperature would be at an optimum average value as provided by a bypassed coolant flow. As a result, an increased mixture ratio would result in a lesser amount of flow bypass.

With a multichamber or multielement combustion zone design, the surface area is large and the coolant bulk temperature may not be at an

optimum condition as allowed in a design with bypassed flow. Under these circumstances Eq.326 would be valid and small mixture ratio increases could be very desirable.

CONCLUSIONS

On the basis of the analytical effort presented, definite limitations of regenerative cooling with conventional materials such as stainless steel and Inconel X occur in the 1500- to 2000-psi chamber pressure range. With curvature and roughness effects, the limit may be extended slightly, but unless high-conductivity wall materials or high-temperature materials such as refractories, or under certain circumstances copper metal tubes may be employed, definite limits have been established for the regenerative methods.

Reliability of high-pressure regeneratively cooled designs was shown to be greatly influenced by thermal fatigue and stress factors with higher wall temperature conditions associated with the upper limits of regenerative cooling contributing to a shortened number of cycles to tube failure.

Gains in specific impulse and consequently payload are small above a reference condition of about 1500-psia chamber pressure. As a result, if mass transfer cooling methods such as film, film-regenerative, or transpiration cooling are used, gains in specific impulse could be negated if 1- to 2-percent performance loss occurs with film or transpiration cooling. Under a high-cooling performance-loss circumstance, conceivably a lower chamber pressure regeneratively cooled design could be a better mission optimization choice. The performance loss for mass-transfer-cooled designs remains a critical area with only a small amount of data available. However, limits of film-cooling performance loss were provided analytically for O_2/RP-1 and O_2/H_2 propellant combinations.

An extended analysis of the film-cooling approach was shown with a view toward gaining a fundamental understanding of this cooling approach as well as for determining methods for minimization of flow requirements. It was indicated that further data would be required to determine film-coolant layer temperature and velocity profiles under simulated rocket engine flow and heat flux conditions before the mass transfer cooling concept is complete.

For high-pressure engines using a gas generator cycle and large expansion ratio skirts, alternative cooling methods become useful to improve impulse performance and reduce regenerative pressure losses. Using the turbine exhaust as film coolant results in a large allowable fraction of the nozzle surface area to be cooled by this means.

Cooling limits and requirements for advanced and multichamber nozzles were also established during the completed work and were shown to be not substantially different than for the bell nozzle engines, but with flow and coolant circuit manifolding problems peculiar to the particular design.

At the high thrust levels (2 to 6 million pounds) with advanced nozzle configurations it was apparent that large pump sizes need to be reduced either through small pump unit clustering or increased speeds.

Study of novel methods which included preliminary reviews of contact-resistance liners and film cooling with spiral injection may possibly provide unique designs if manufacturing problems can be overcome.

Studies of substitution of F_2-O_2 combinations for the high-pressure designs indicated at moderate FLOX concentrations that heat transfer rates were within 10 percent of those using oxygen alone. Hence, within the foreseeable mixture ratio and concentration range, direct substitution from a cooling standpoint appears practical.

EXPERIMENTAL STUDIES

The main objective of the experimental studies was to determine the gas-side heat transfer at high heat flux conditions existing in high-pressure high-thrust rocket engines under condition of mass transfer cooling and under base conditions of no mass transfer cooling. This information was required to develop the necessary engineering technology to design cooling systems for liquid rocket engines operating at chamber pressures from 1500 to 5000 psia and thrust levels to 6 million pounds.

The entire investigation of gas-side heat transfer was conducted in a small workhorse motor with a rectangular cross-sectioned throat. The two-dimensional nozzle simulated the heat flux conditions existing in the nozzles of large rocket engines operating at high chamber pressures. Because of the reduced dimensions of the experimental system, these heat loads occurred at lower chamber pressures. The generated heat was absorbed by coolant water flowing at high velocities through drilled cooling passages in the copper walls of the nozzle. This method of absorbing gas heat fluxes permitted the calorimetric measurement of nozzle heat flux during steady-state conditions. The nozzle heat load calibration thus obtained was used to evaluate several supplemental nozzle cooling techniques, including film (radial and tangential) and transpiration.

Twelve successful hot-firing tests were conducted; seven were utilized to define the steady-state calorimetric nozzle heat flux profile under base conditions of no mass transfer cooling. The remaining tests were conducted to determine the relative effectiveness and efficiency of the supplemental cooling techniques.

TEST HARDWARE

The original design concept for the experimental test motor consisted of a chamber containing 34 water-cooled copper tubes which were brazed together to form the chamber walls. This design provided for maximum heat absorption. The calculated maximum throat heat flux for water cooling occurred at about 1000 psia, although adequate cooling was provided in the combustion zone and flow development sections for 2000-psia chamber pressure operation. Because of problems encountered with this initial concept, as discussed below, the design finally utilized for the test program consisted of a solid copper chamber assembly containing drilled coolant passages. The later design provided adequate cooling to about 850 psia, but had advantages in the areas of improved sealing, thermal shock, and structural strength. The operating chamber pressure range of this motor was extended by the utilization of supplemental cooling techniques.

TUBE BUNDLE COMBUSTION CHAMBER

The original combustion chamber was composed of 34 copper tubes of 0.250-inch OD and 0.030-inch wall thickness. The tubular construction permitted a smooth transformation from a 2.50-inch-diameter circular cross section at the injector face to a 2.0- by 1.0-inch-rectangular cross section for development of a two-dimensional flow pattern in the nozzle.

The tubes were individually swedged in hand dies and then formed into shape on a steel mandrel. The general shape of the tubular wall structure is shown in Fig. 79, which shows the tube bundle on the mandrel.

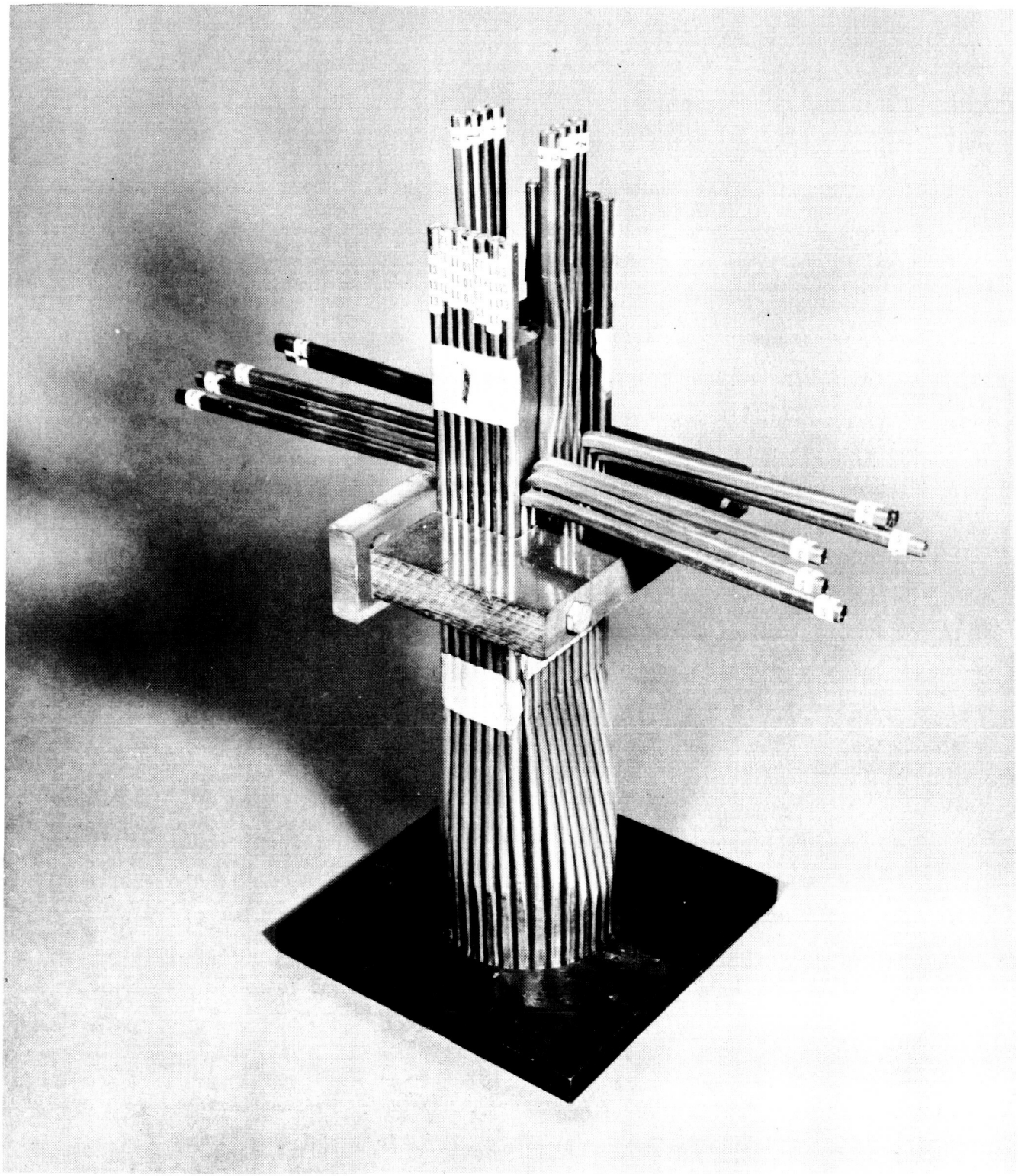

5AE25-12/17/63 SIC

Figure 79. Tube Bundle Combustion Chamber on Mandrel

The tubular structure buildup was to be completed by a two-step brazing process. First, the tubes were brazed together with a high-temperature alloy while fastened in a graphite mandrel and jig arrangement similar to that shown in Fig. 79. The tubes were then brazed with a lower-temperature alloy to a stainless-steel ring manifold at the injector and to stainless-steel tubular manifolds at the two-dimensional nozzle end.

The straight walls of the nozzle were composed of the tube wall structure extending from the combustion chamber, while the opposite tapering walls of the throat region were composed of a pair of copper spacer bar inserts between stainless-steel backup plates bolted together. Transverse water-coolant passages milled in the inserts permitted water cooling of the throat and calorimetric measurement of the throat heat fluxes.

The desire to utilize water cooling for the injector resulted in a novel design consisting of four stainless-steel parts and one copper part brazed back-to-back to permit seven coaxial propellant passages, a hydrogen manifold, an inlet water manifold, an exit water manifold, and six radial water-coolant passages in the copper face. All components of the injector were machined and brazed into the two major injector assemblies by vendors. However, during the final assembly brazing operation, unexpected difficulty was experienced by the vendor in eliminating leaks. This brazing required the use of a special high-temperature braze furnace which was not available at Rocketdyne except at an exorbitant cost. Because of the unanticipated brazing problem, some design changes were required which finally resulted in a leak-proof injector.

To evaluate the injector and ignition sequence, four shakedown firings with LO_2/GH_2 each programmed for a 3-second mainstage, were performed employing the water-cooled injector in conjunction with ablative chamber

walls. The first three firings employed a simple cylindrical shape, while the fourth test employed the two-dimensional rectangular contour of the water-cooled hardware. Smooth and stable ignition was achieved in each firing. However, in the fourth test, a severe fire occurred which destroyed the injector, the chamber and two-dimensional nozzle backup structures, the hypergolic ignition flow system, and more than half of the instrumentation and control wiring to the hardware. The cause of the fire was believed due to the breaking loose of the 85-15 TEAB hypergolic igniter line and subsequent spraying of hypergol over the hardware and test pit area. Fabrication of a new injector and backup structures was necessary.

Subsequent brazing attempts with the new injector were unsuccessful in sealing the tube bundle chamber to the manifold and nozzle end. Leakage problems also persisted in the injector braze joints. Because of these fabrication problems with the tube bundle chamber and water-cooled injector, an alternate assembly was designed.

MACHINED-PASSAGE THRUST CHAMBER

This new hardware assembly consisted of five major components and was used exclusively during the experimental hot firings. The components were: a transpiration-cooled coaxial jet injector, a combustion chamber section, a flow development section, a nozzle section, and a flanged backup structure to support the assembly. Several different supplemental cooling sections were fabricated for installation immediately upstream of the nozzle. An assembly view of the research motor is shown in Fig. 80 and 81.

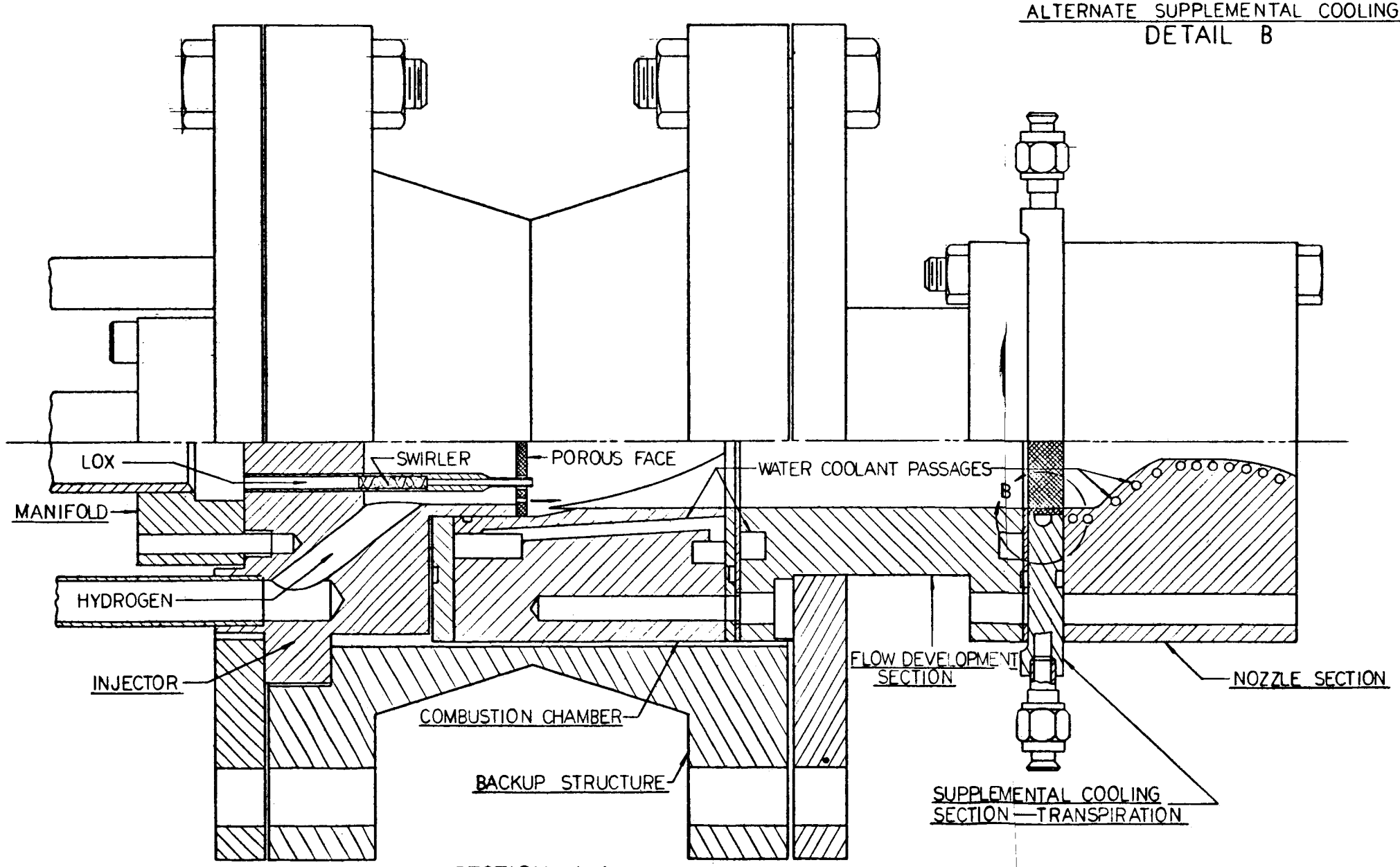

SECTION A-A

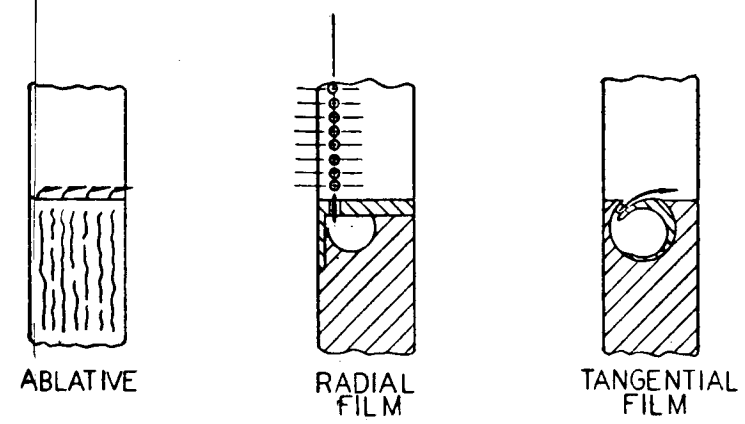

ALTERNATE SUPPLEMENTAL COOLING SECTIONS
DETAIL B

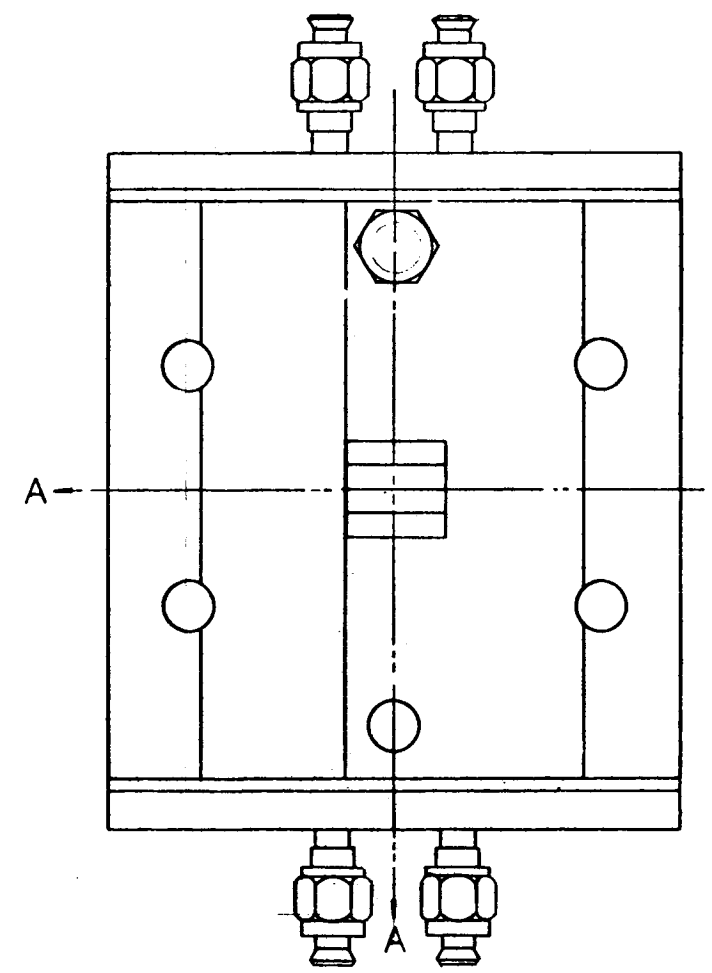

Figure 80. Machined-Passage Thrust Chamber Assembly

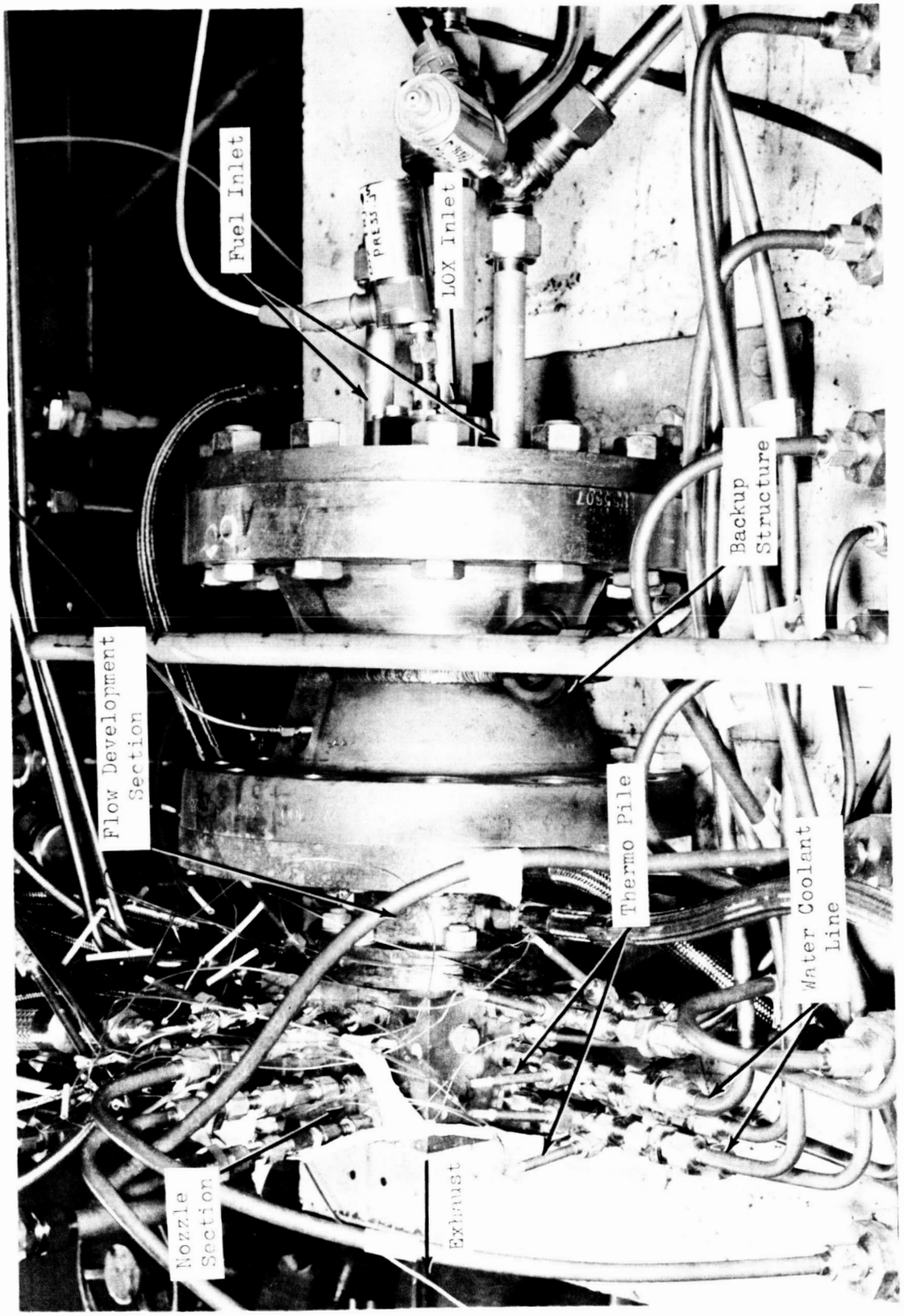

Figure 81. Machined-Passage Thrust Chamber Assembly

A seven-element coaxial jet injector with a transpiration-cooled face was designed and fabricated for use with LO_2/GH_2. The injector assembly, is shown in Fig. 82 and 83. The geometrical relationships of the injector elements were patterned after the J-2 engine design. Preliminary calculations indicated approximately 15 percent of the total gaseous hydrogen fuel flow would be injected through the 0.150-inch-thick porous face to provide adequate cooling for the injector and additional film cooling for the combustion chamber and flow development sections. The remaining hydrogen was injected through the fuel annuli. Liquid oxygen was injected through seven injector tubes containing twisted swirler elements. The swirlers accelerated the liquid oxygen atomization process and thus ensured uniform combustion gas composition at the chamber throat. The design allowed simple replacement of the injector elements to permit variations of the system pressure drop so that a range of flowrates and chamber pressures could be accommodated. The complex water-coolant passages required for the original injector were thus eliminated in the transpiration-cooled design.

Because of the fabrication problems that arose with the tube bundle combustion chamber and nozzle, an alternate chamber was designed, as mentioned above. The first section formed the converging combustion chamber and tapered from a 2.25-inch diameter round cross section at the injector end to a 2.0- x 1.0-inch rectangular cross section over a 3.0-inch length. It was machined from 6-inch-diameter Chromalloy round stock and had a double-pass water-cooling system consisting of sixteen 3/16-inch-diameter drilled passages ending in ring manifolds at either end. An assembly drawing of this component is shown in Fig. 84. Photographs of the two end views prior to final brazing are presented in Fig. 85 and 86.

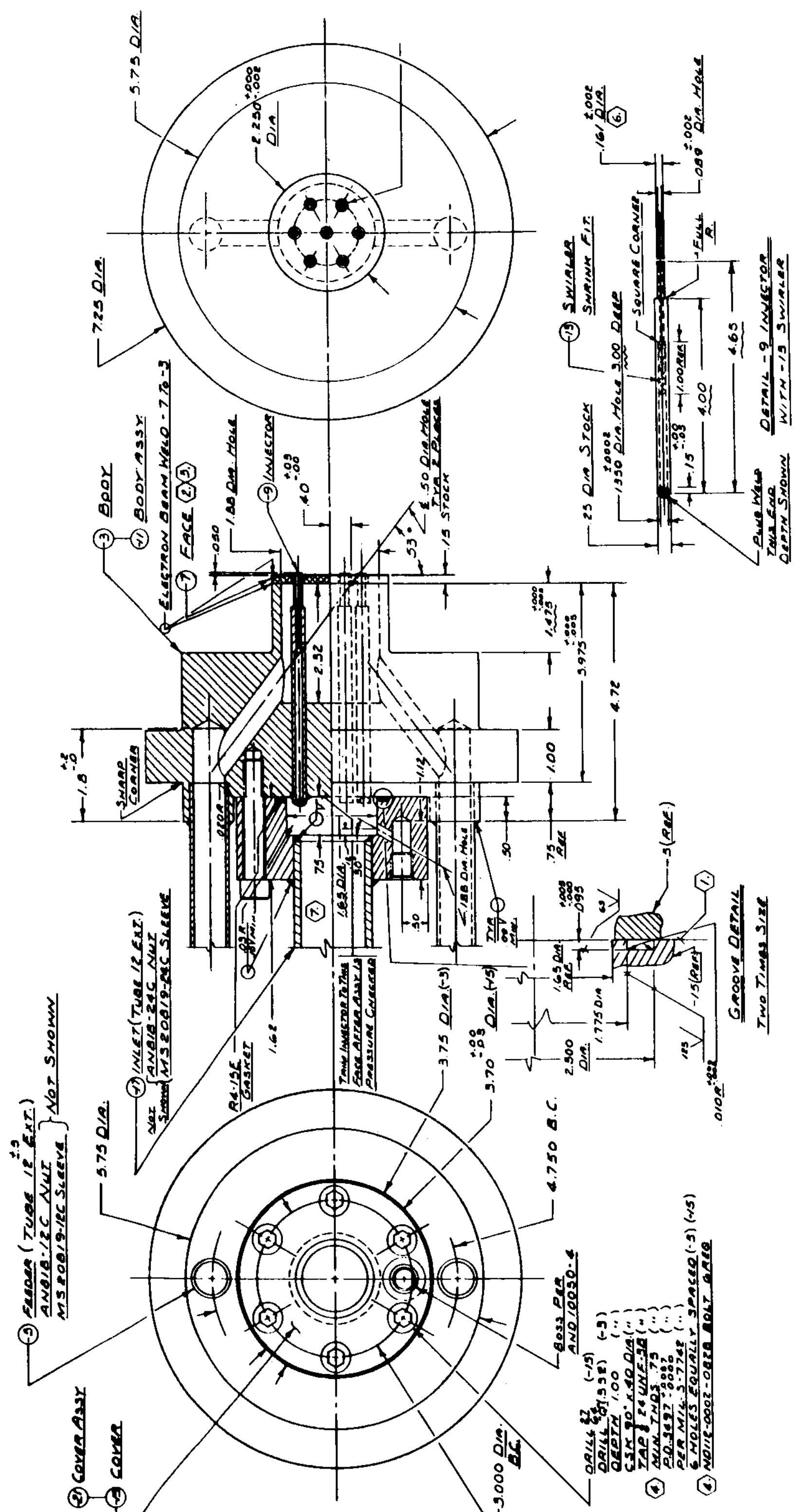

Figure 82. Transpiration-Cooled Coaxial Injector Assembly

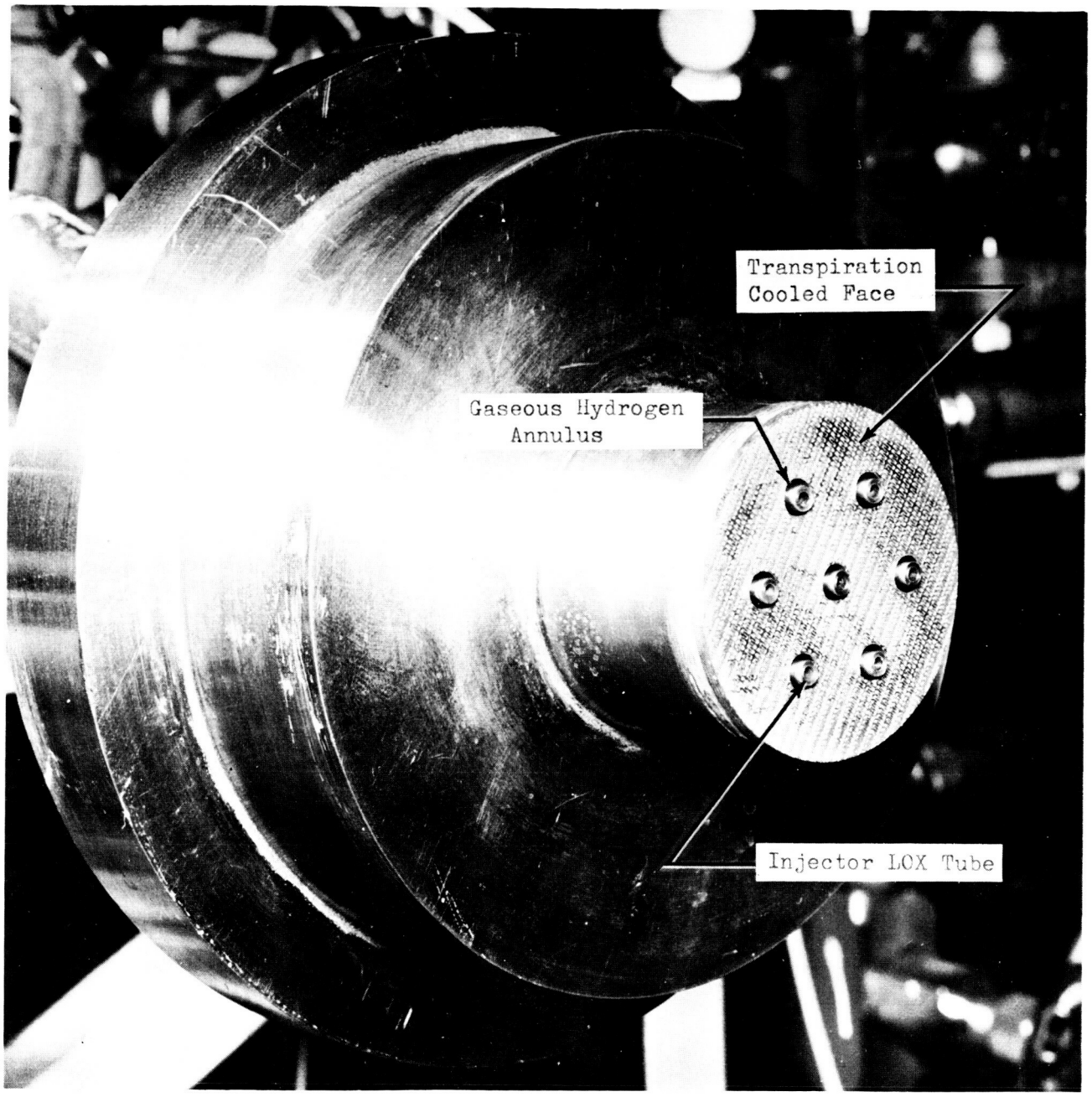

SAE34-11/25/64-S1A

Figure 83. Transpiration-Cooled Coaxial Injector

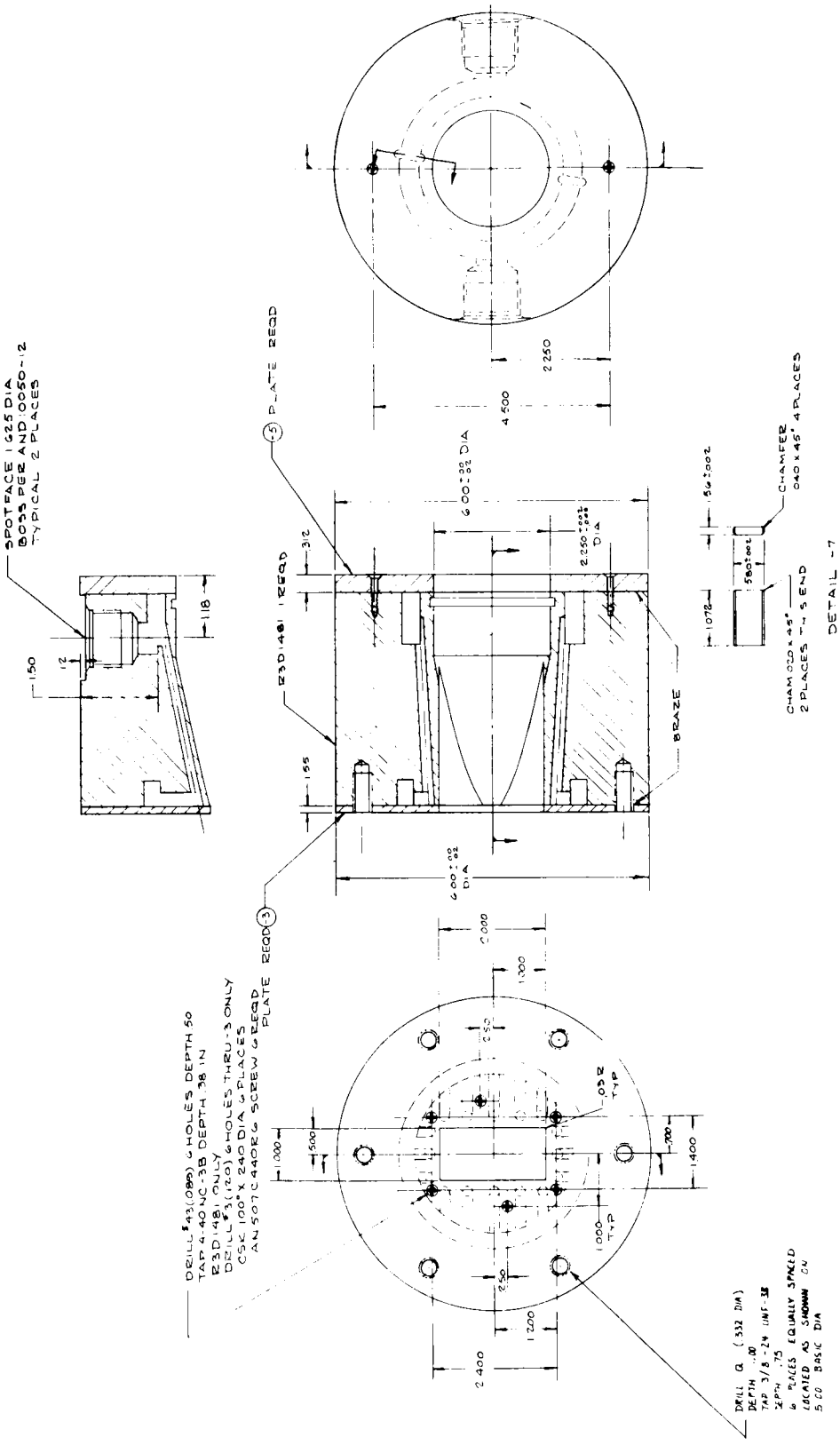

Figure 84. Machined-Passage Combustion Chamber Assembly

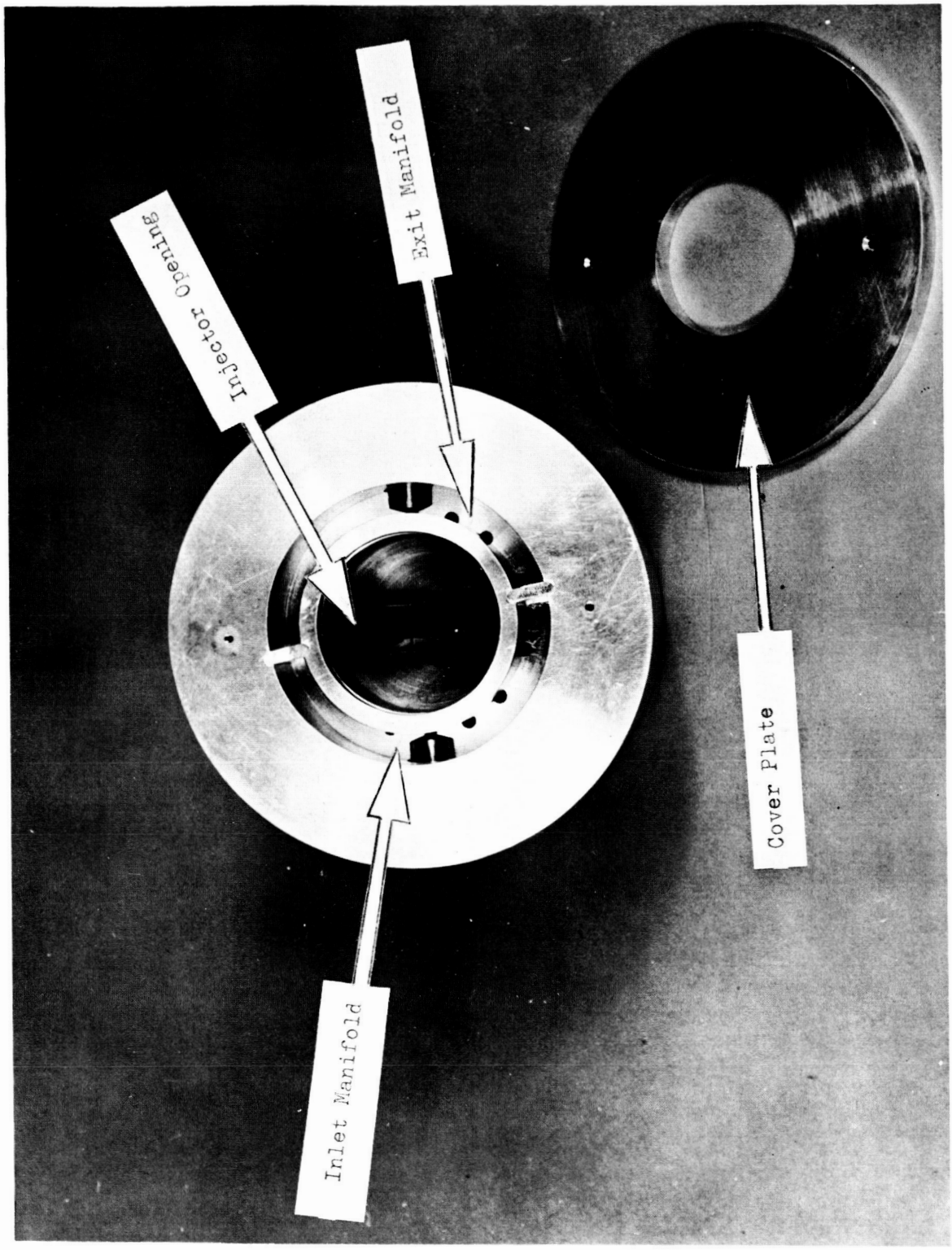

1XW31-3/27/64-S1A

Figure 85. View of Machined-Passage Combustion Chamber Before Brazing of Manifold Covers (Injector End)

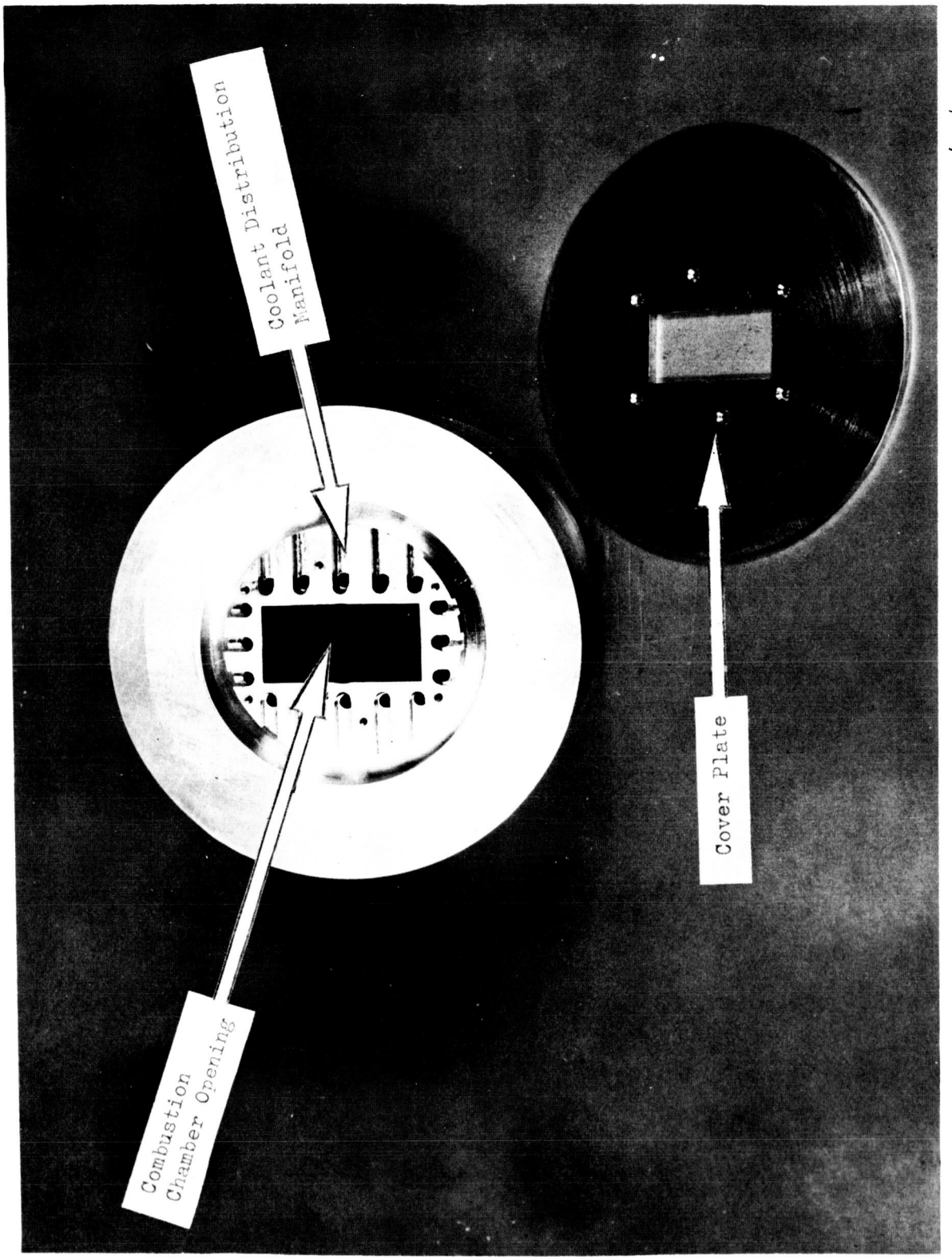

1XW31-3/27/64-S1B

Figure 86. View of Machined-Passage Combustion Chamber Before Brazing of Manifold Covers (2-D End)

Figures 87 and 88 are views of the machined two-dimensional flow development section. The overall length of this chamber component was 4.42 inches, including the manifold-covering end plates brazed to either end. The flow development section was cooled by twenty-four 1/8-inch-diameter drilled water passages located on centers 0.125 inch from the gas-heated walls.

The two-dimensional nozzle was intended to simulate the heat flux conditions existing in the nozzles of large rocket engines operating at chamber pressures of 2000 to 5000 psia (from approximately 20 to 100 Btu/in.^{2}-sec). Because the dimensions of the experimental motor were smaller, these heat loads occurred at much lower chamber pressures. The required experimental chamber pressures were calculated according to the simplified Bartz equation (Ref. 60)

$$h_g = \frac{0.026}{D^{0.2}} \left(\frac{\mu^{0.2} C_p}{Pr^{0.6}} \right)_o \left(\frac{P_c g_c}{c^*} \right)^{0.8} \left(\frac{A^*}{A} \right)^{0.8} \sigma \tag{327}$$

and

$$\frac{q}{A} = h_g \left(T_{rg} - T_{wg} \right) \tag{328}$$

where

$$\sigma = \frac{1}{\left\{ \frac{1}{2} \frac{T_{wg}}{T_{rg}} \left[1 + \left(\frac{\chi - 1}{2} \right) Ma^2 \right] + \frac{1}{2} \right\}^{0.68} \left[1 + \left(\frac{\chi - 1}{2} \right) Ma^2 \right]^{0.12}} \tag{329}$$

and

$$D = D_E = \frac{4 \text{ (cross-sectional area)}}{\text{(wetted perimeter)}} \tag{330}$$

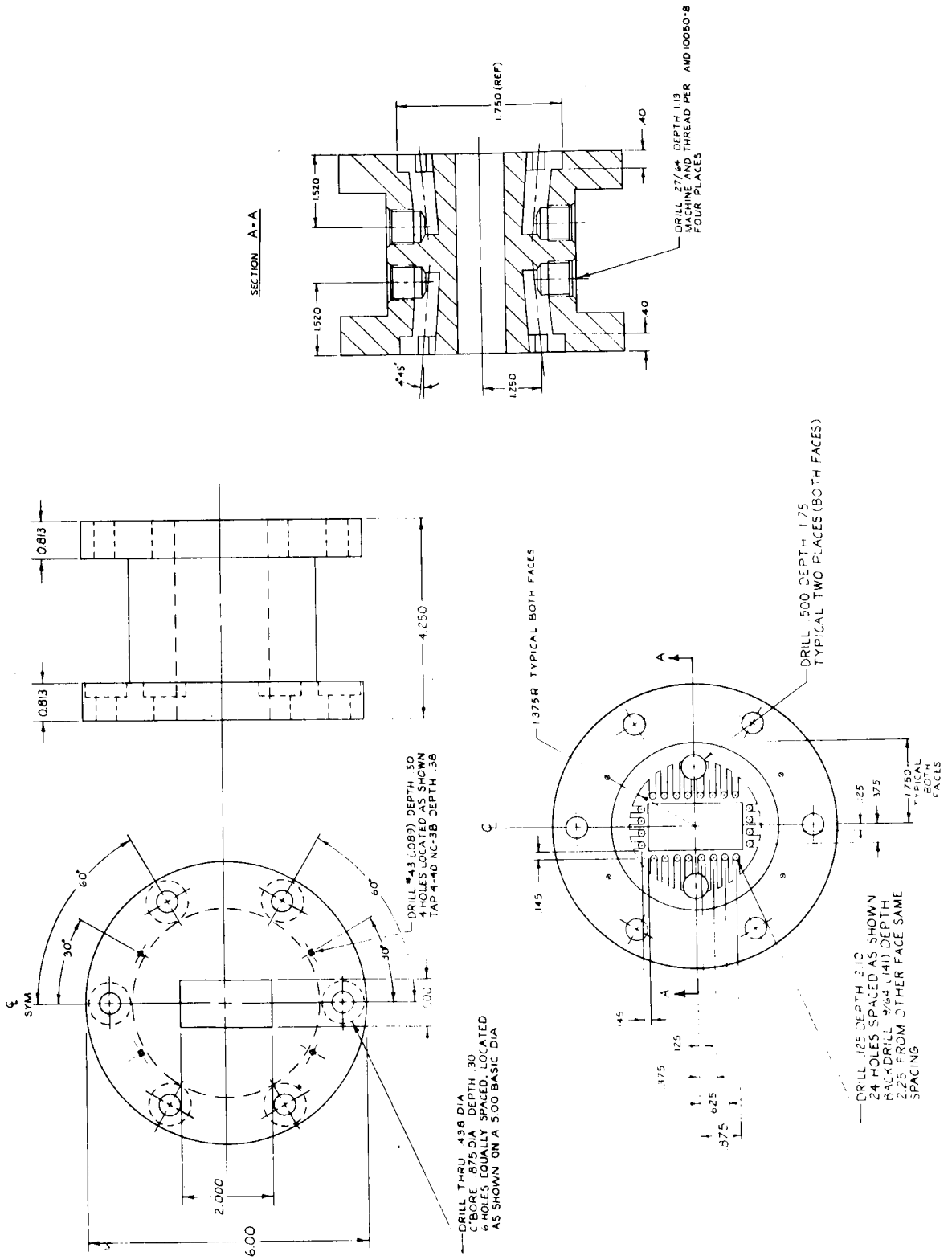

Figure 87. Machined-Passage 2-D Flow Development Section

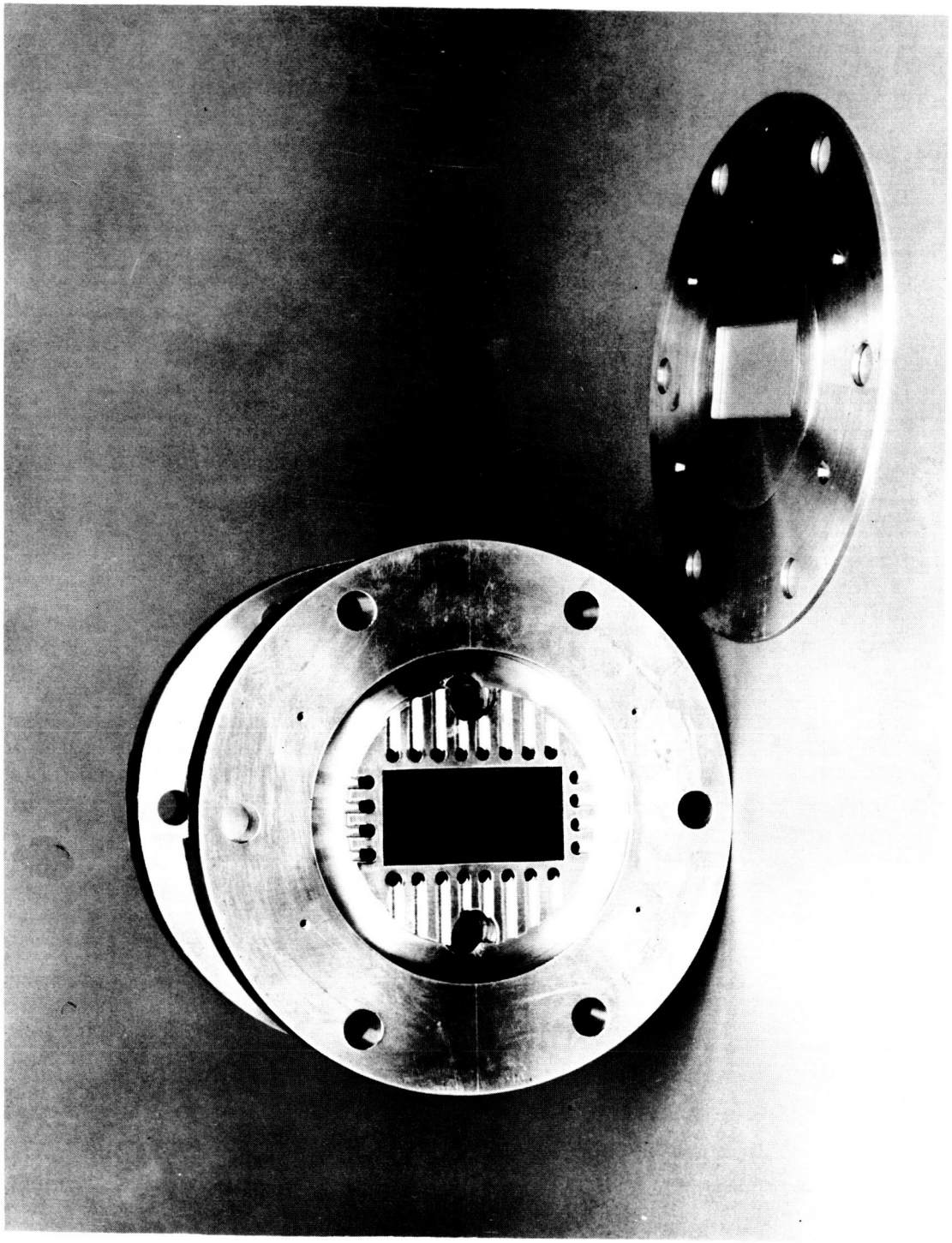

1XW32-4/13/64-S1A

Figure 88. Machined-Passage 2-D Flow Development Section

using the Bartz simplified expressions for Pr and μ along with values for c* and T_g from the Rocketdyne performance computer program. The curves of Fig. 89 indicate that, at the higher pressures, the expected nozzle heat loads in the experimental motor were about as high or higher than any of the heat loads encountered at the throat of present engines and, therefore, presented a formidable design problem.

The required water flowrates were calculated by the correlation scheme of Gambill (Ref. 61) for subcooled nucleate boiling which assumes:

$$q_{ul} = q_{NB} + q_{conv} = q_{NB} + h_c (T_{wc} - T_c) A \qquad (331)$$

For water at pressures near 1000 psia at bulk temperatures near 100 F at high liquid velocities, Eq. 331 became:

$$q_{ul}/A = 2.5 + 0.028 (T_s - T_c) + 0.00097 u_c^{0.9} (T_s + 30 - T_c) \qquad (332)$$

which fitted a limited amount of high-pressure water burnout data obtained at Rocketdyne. The calculated minimum coolant velocities in the nozzle section at three discrete locations are shown in Fig. 90 for LO_2/GH_2 at various chamber pressures. When the water velocities (and resultant pressure drops) were given a safety factor and the requirements of wall conduction also considered, the maximum heat flux for water cooling occurred at about 50 Btu/in.^{2}-sec. For the experimental motor, this occurred in the throat at a chamber pressure of slightly less than 1000 psia.

The nozzle section was fabricated from four machined OFHC copper parts brazed together into one unit. The 1.0- by 2.0-inch inlet area converged

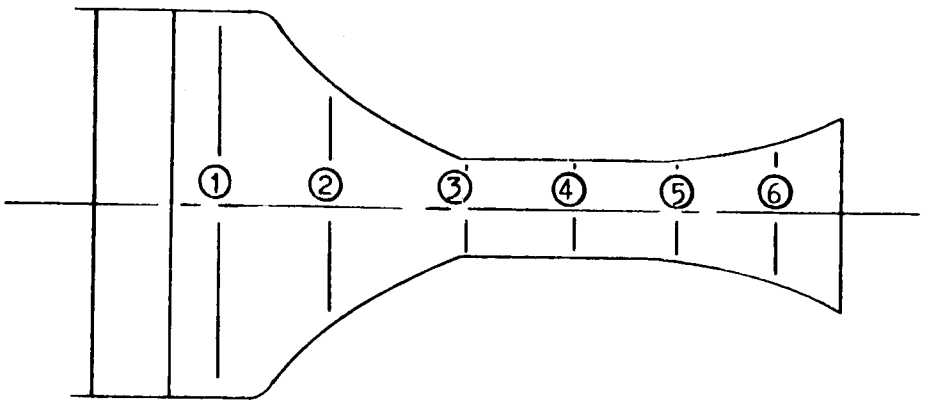

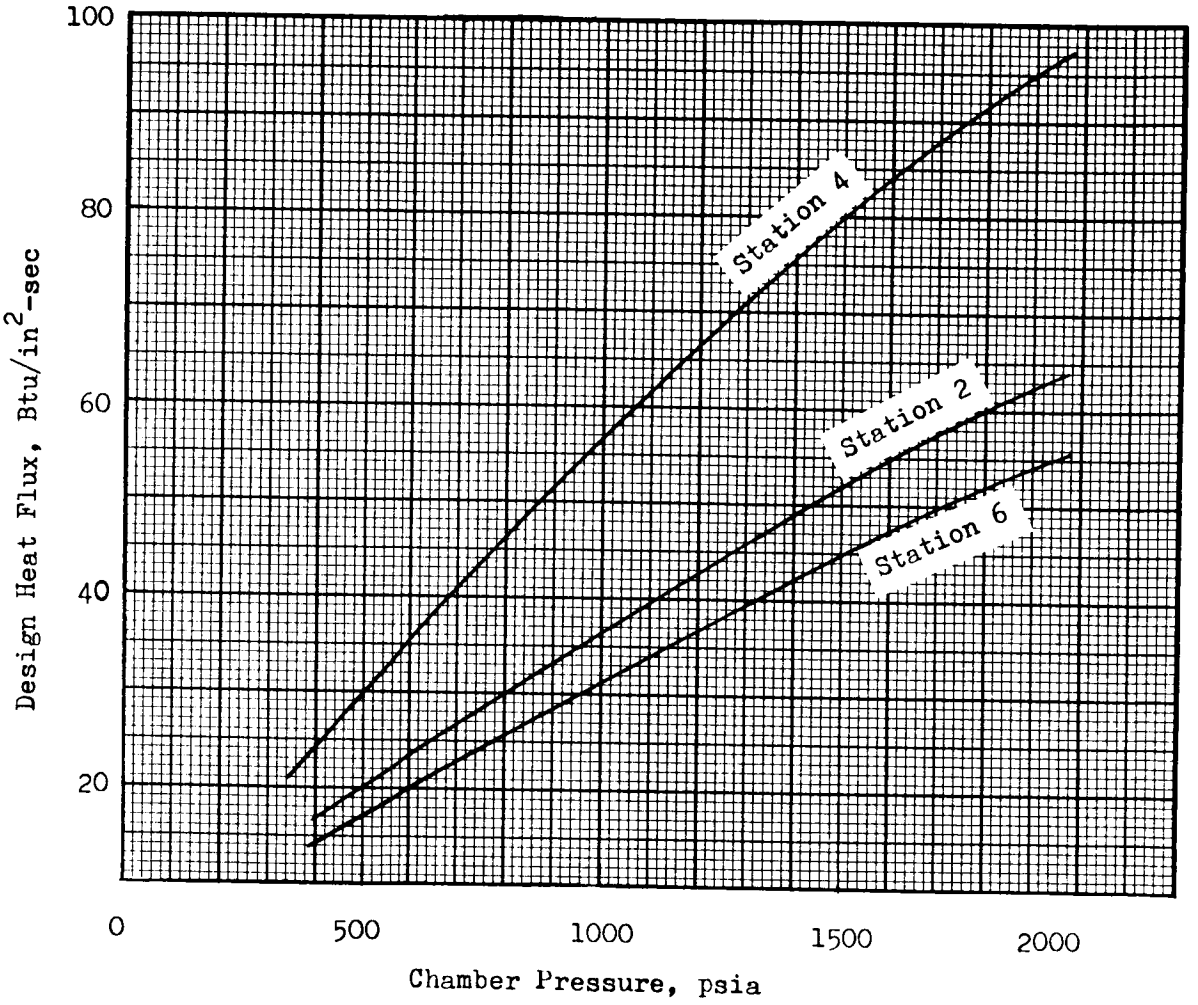

Figure 89. Nozzle Heat Flux Distribution as a Function of Chamber Pressure

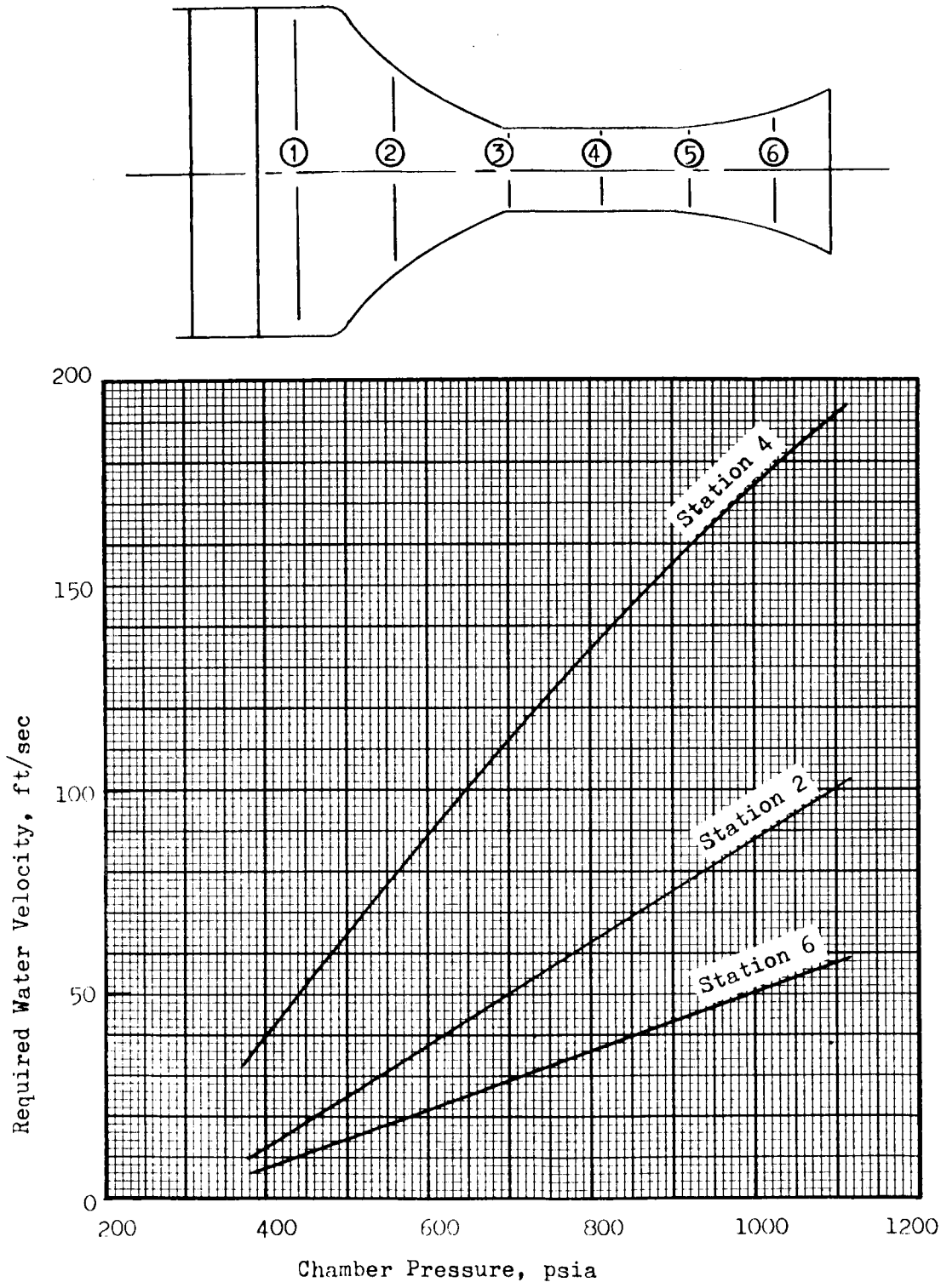

Figure 90. Minimum Required Water Coolant Velocities as a Function of Chamber Pressure in the Nozzle

to a 1.0- by 0.5-inch rectangular throat to provide a 4:1 contraction ratio nozzle. The resulting nozzle contour is shown in Fig. 91. The upper and lower nozzle surfaces were cooled by flowing high-velocity water through the 24 drilled passages (Fig. 92). The individual coolant passages were manifolded together as shown. The sides of the nozzle were cooled with the transverse-drilled passages. The heat flux measurements were determined only on the upper and lower surfaces. The nozzle assembly was completed by brazing on the two outer side plates (Fig. 93) to form the assembly shown in Fig. 94.

The four major chamber components were bolted together and supported within a flanged steel backup structure. Flexitallic seals were used at each interconnection to prevent hot-gas leakage. Access holes were drilled through the backup structure to permit connection to the hypergol and chamber pressure instrumentation taps.

SUPPLEMENTAL COOLING INJECTION SYSTEMS

The advantages of combining several cooling methods simultaneously to tolerate higher heat flux levels was investigated to increase the operating range of the motor. The supplemental cooling techniques used were in addition to normal water cooling.

Four types of supplemental cooling systems were considered for the experimental test program: film cooling with continuous-slot tangential injection, film cooling with radial hole injection, transpiration cooling, and ablative cooling. The three systems actually evaluated are shown in Fig. 95 through 99 ; the latter was not accomplished for reasons discussed below. Ambient gaseous hydrogen was used as the coolant in the mass addition experiments.

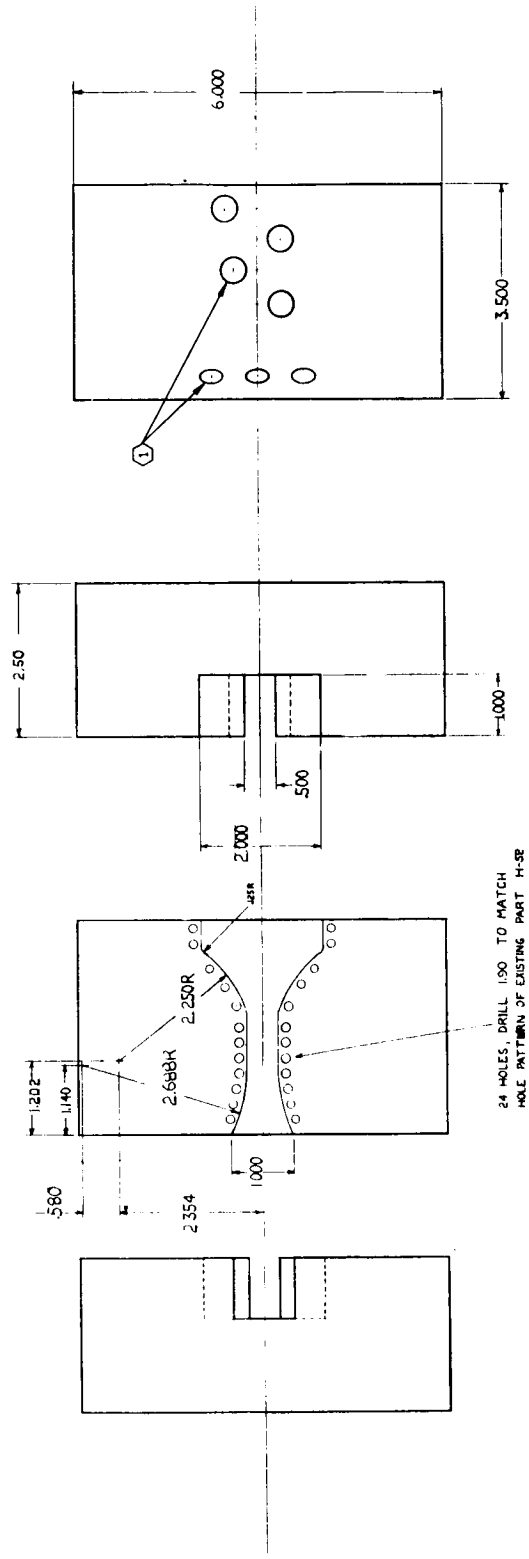

Figure 91. Machined-Passage Nozzle Spacer Bar and Sideplate Unit

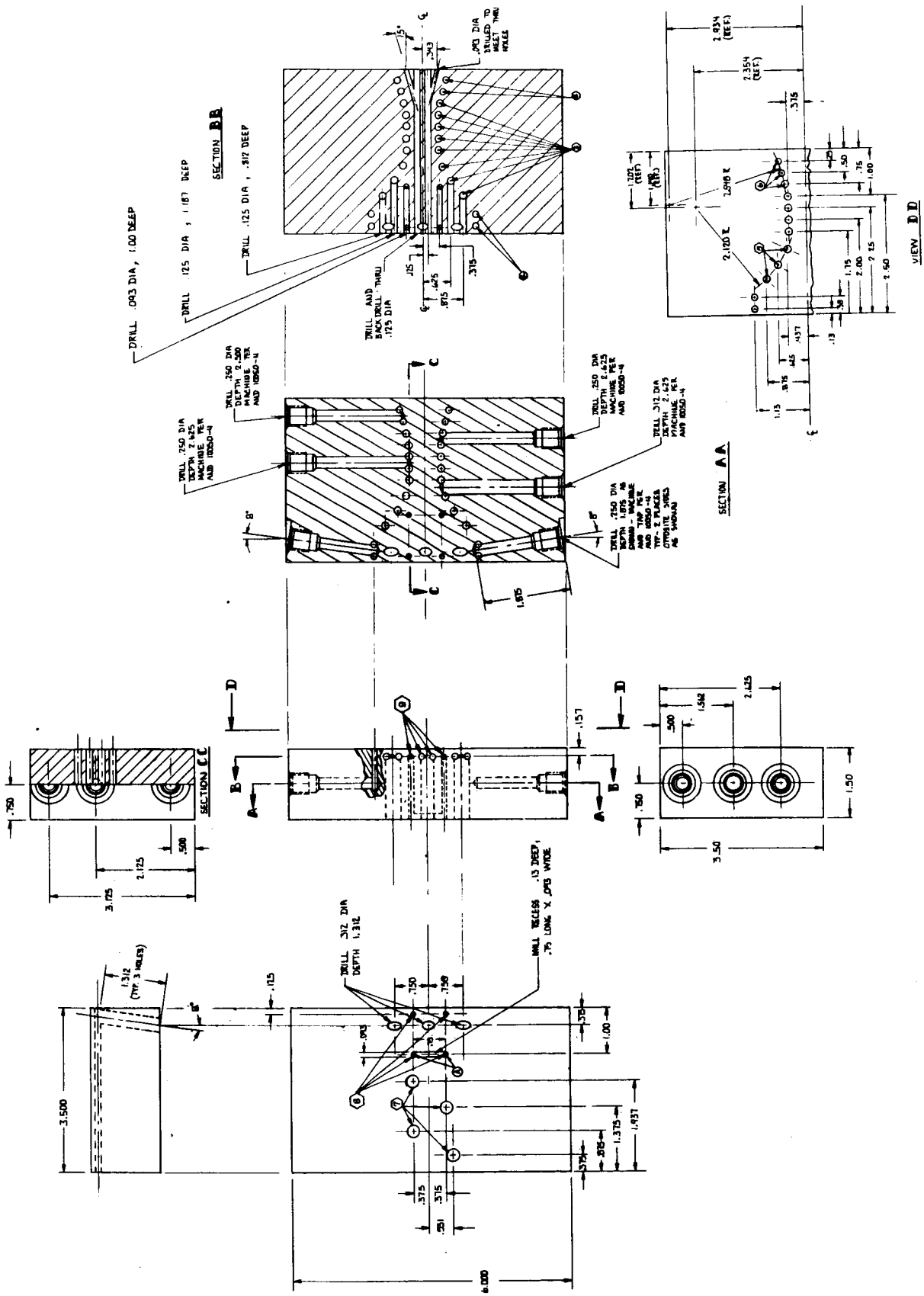

Figure 92. Machined-Passage Nozzle Sideplate

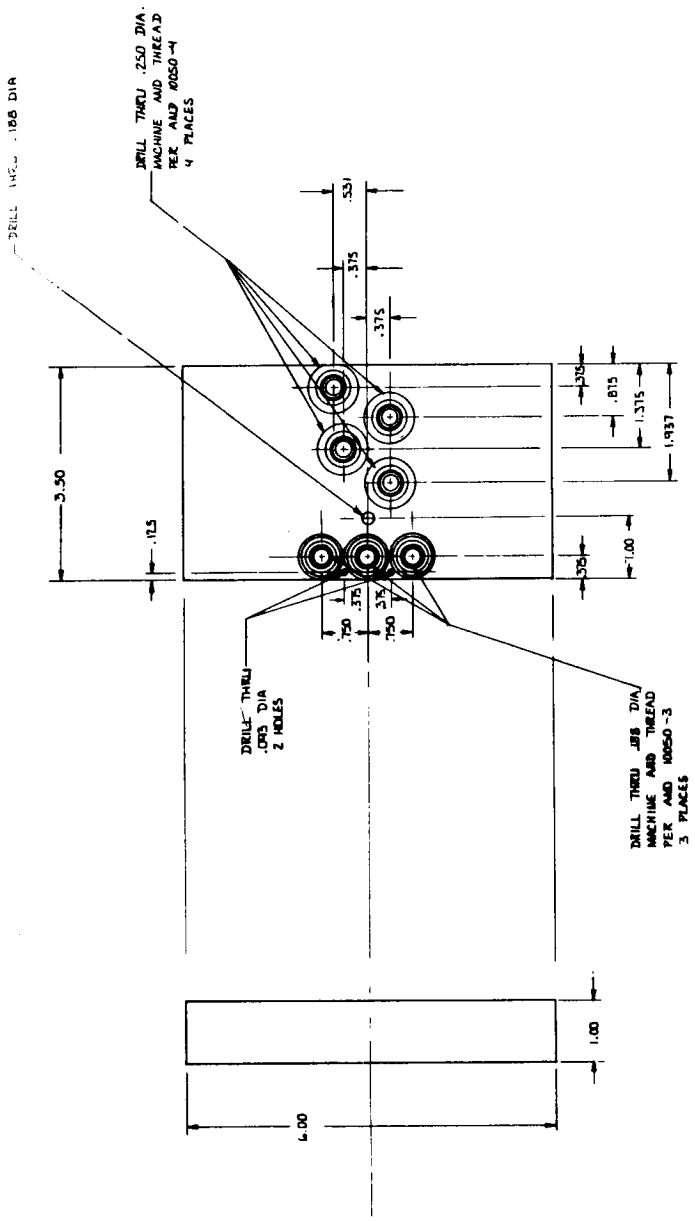

Figure 93. Machined-Passage Nozzle Outer Sideplate

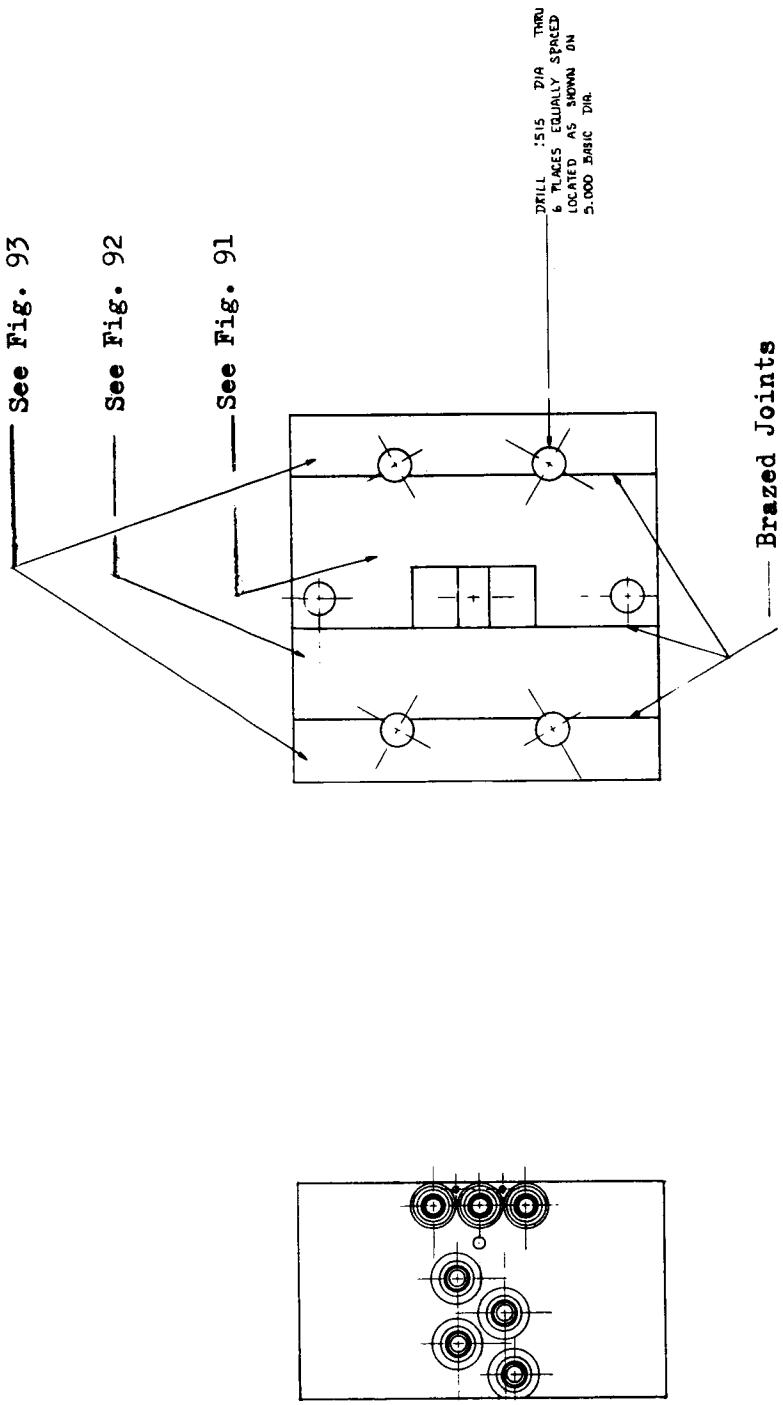

Figure 94. Machined-Passage Nozzle Assembly

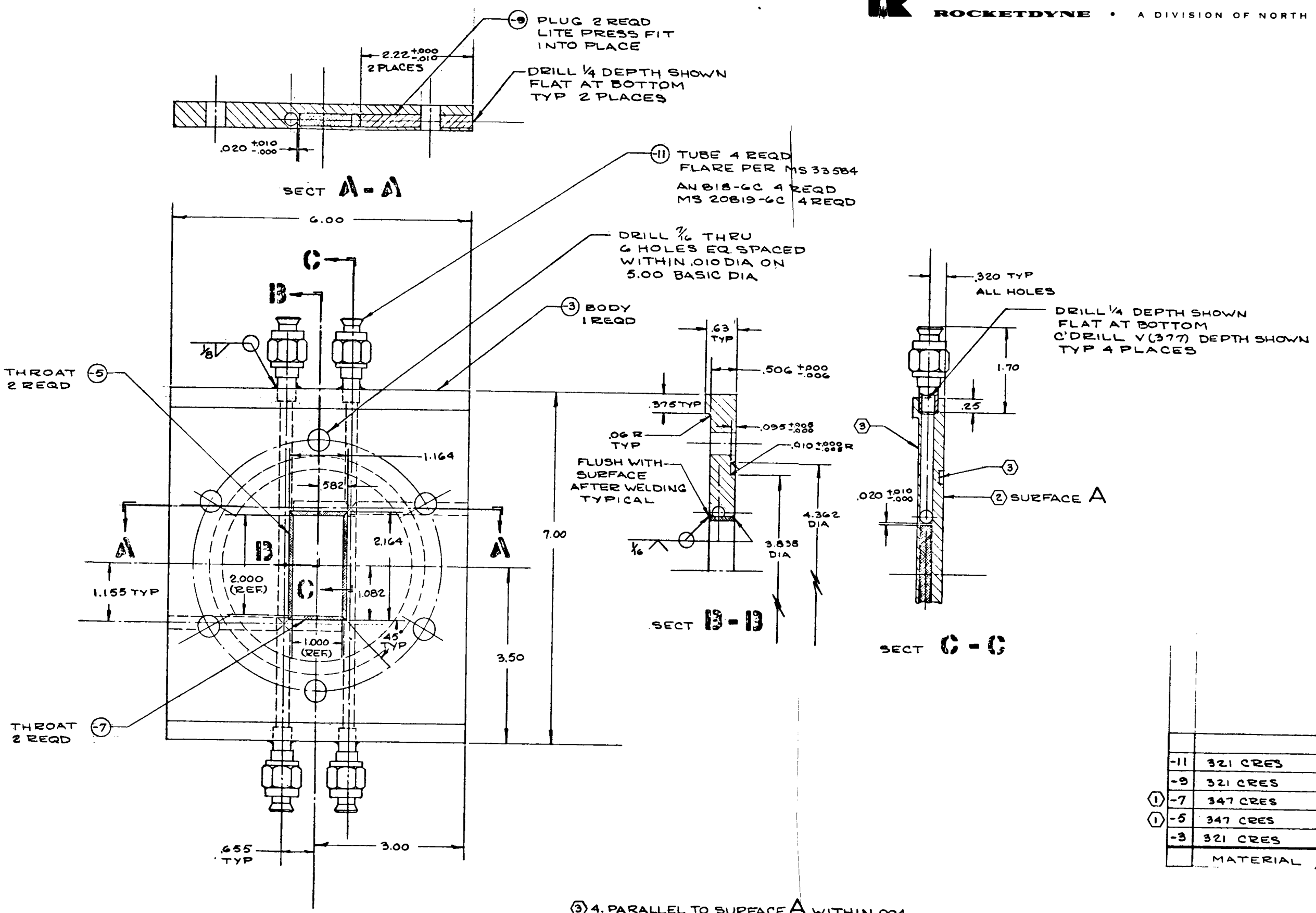

-11	321 CRES	.375 DIA X .065 WALL X 2.00	
-9	321 CRES	.312 DIA X 2.25	
(1) -7	347 CRES	.082 X .50 X 1.25	REGIMESH
(1) -5	347 CRES	.082 X .50 X 2.25	REGIMESH
-3	321 CRES	.75 X 6.00 X 7.00	
	MATERIAL	SIZE	

(3) 4. PARALLEL TO SURFACE A WITHIN .004 TOTAL
(2) 3. FLAT WITHIN .004 TOTAL
2. WELD PER RA0107-027
(1) 1. POROSITY RATING: 300 CFM / FT² WITH A 20" ΔP USING STD. AIR TO ATMOS.

NOTE: UNLESS OTHERWISE SPECIFIED

Figure 95. Transpiration-Cooling Section
R-6199

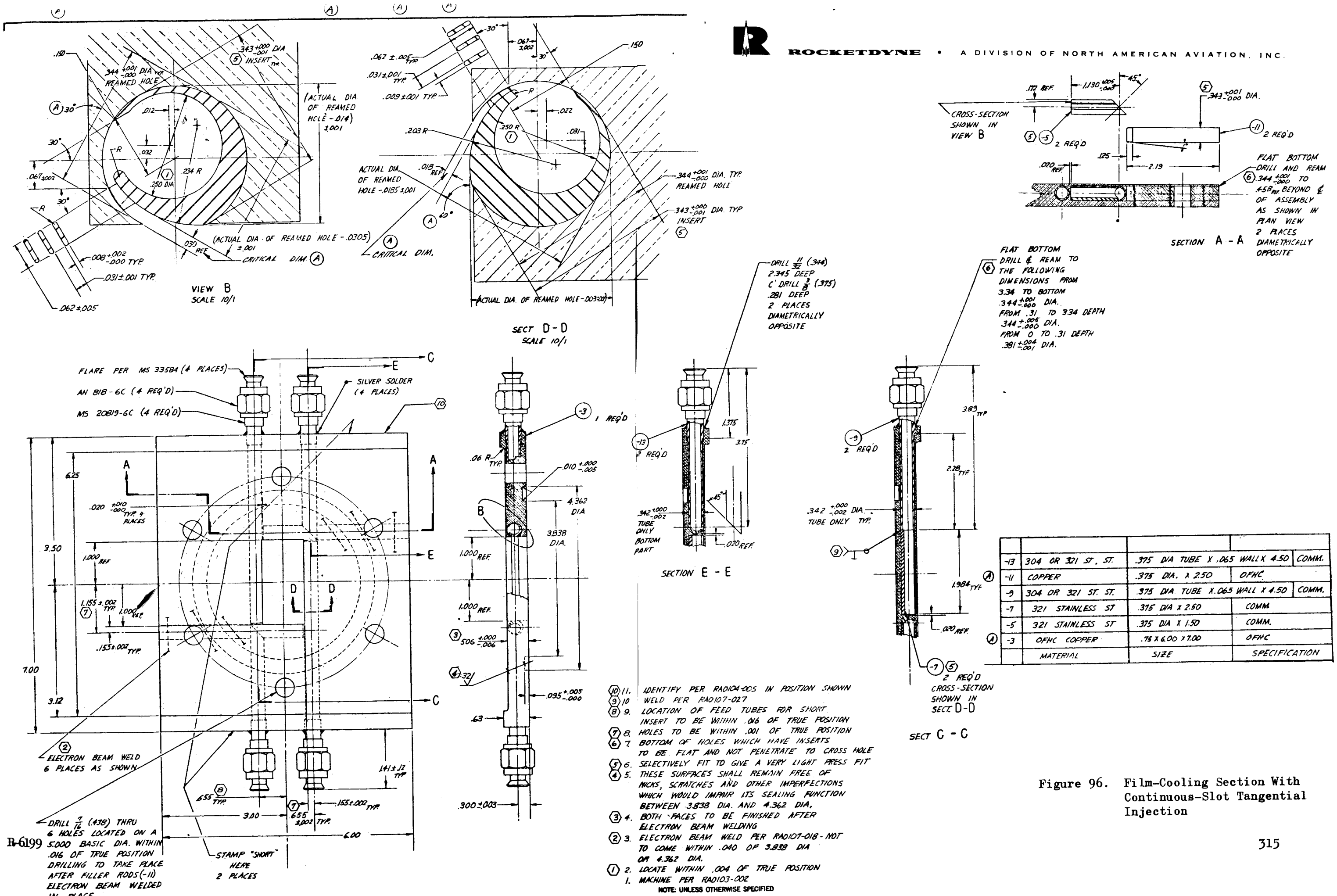

-13	304 OR 321 ST. ST.	.375 DIA TUBE X .065 WALL X 4.50		COMM.
(A) -11	COPPER	.375 DIA. X 2.50	OFHC	
-9	304 OR 321 ST. ST.	.375 DIA. TUBE X .065 WALL X 4.50		COMM.
-7	321 STAINLESS ST	.375 DIA X 2.50	COMM.	
-5	321 STAINLESS ST	.375 DIA X 1.50	COMM.	
(A) -3	OFHC COPPER	.75 X 6.00 X 7.00	OFHC	
	MATERIAL	SIZE	SPECIFICATION	

(10) 11. IDENTIFY PER RA0104-005 IN POSITION SHOWN
(9) 10 WELD PER RA0107-027
(8) 9. LOCATION OF FEED TUBES FOR SHORT INSERT TO BE WITHIN .016 OF TRUE POSITION
(7) 8. HOLES TO BE WITHIN .001 OF TRUE POSITION
(6) 7. BOTTOM OF HOLES WHICH HAVE INSERTS TO BE FLAT AND NOT PENETRATE TO CROSS HOLE
(5) 6. SELECTIVELY FIT TO GIVE A VERY LIGHT PRESS FIT
(4) 5. THESE SURFACES SHALL REMAIN FREE OF NICKS, SCRATCHES AND OTHER IMPERFECTIONS WHICH WOULD IMPAIR ITS SEALING FUNCTION BETWEEN 3.838 DIA. AND 4.362 DIA.
(3) 4. BOTH FACES TO BE FINISHED AFTER ELECTRON BEAM WELDING
(2) 3. ELECTRON BEAM WELD PER RA0107-018 - NOT TO COME WITHIN .040 OF 3.838 DIA OR 4.362 DIA.
(1) 2. LOCATE WITHIN .004 OF TRUE POSITION
1. MACHINE PER RA0103-002

NOTE: UNLESS OTHERWISE SPECIFIED

Figure 96. Film-Cooling Section With Continuous-Slot Tangential Injection

R-6199

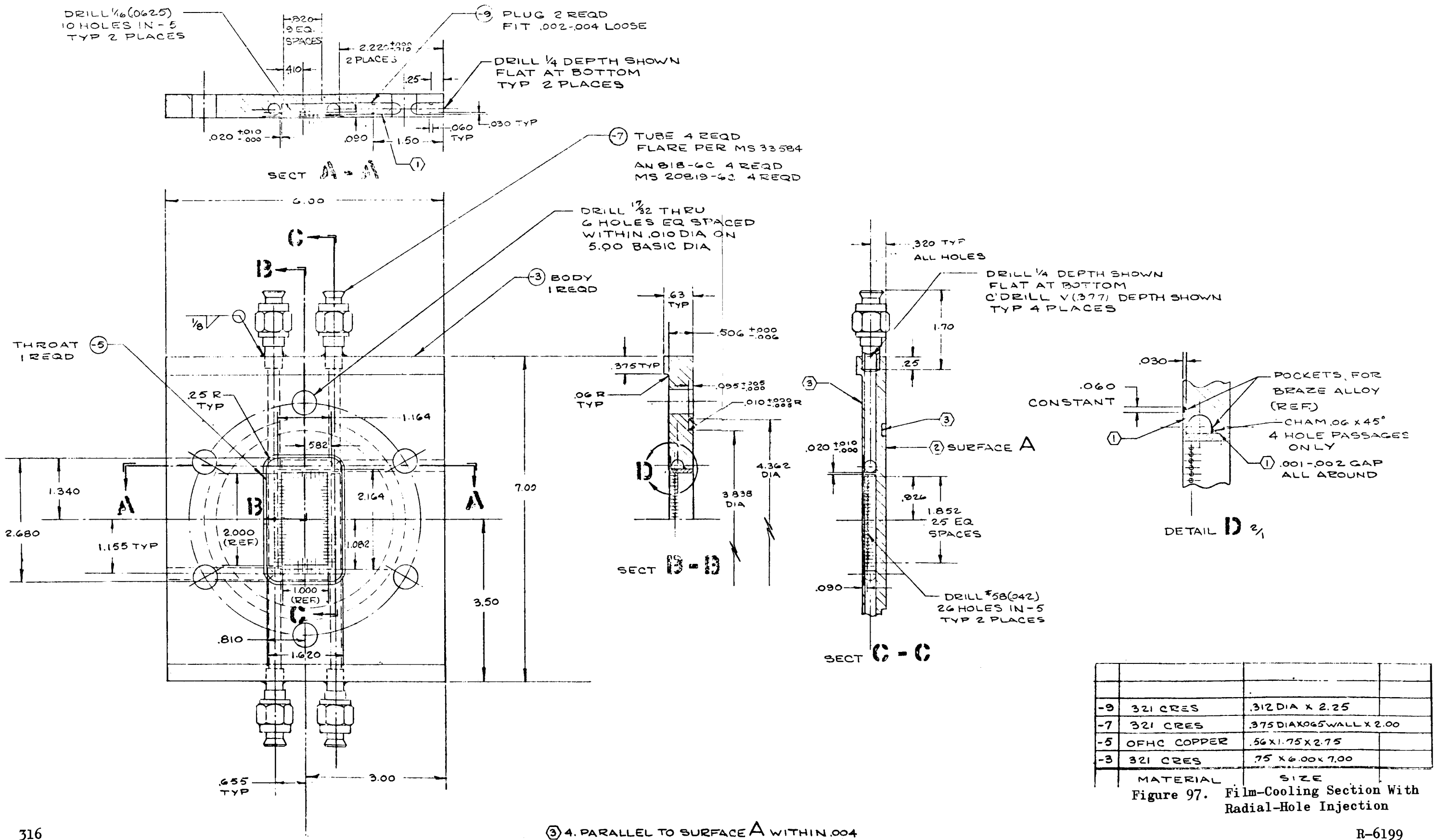

-9	321 CRES	.312 DIA x 2.25	
-7	321 CRES	.375 DIA x .065 WALL x 2.00	
-5	OFHC COPPER	.56 x 1.75 x 2.75	
-3	321 CRES	.75 x 6.00 x 7.00	
	MATERIAL	SIZE	

Figure 97. Film-Cooling Section With Radial-Hole Injection

3. 4. PARALLEL TO SURFACE A WITHIN .004 TOTAL
2. 3. FLAT WITHIN .004 TOTAL
2. WELD PER RA0107-027
1. 1. FURNACE BRAZE PER RA0107-010

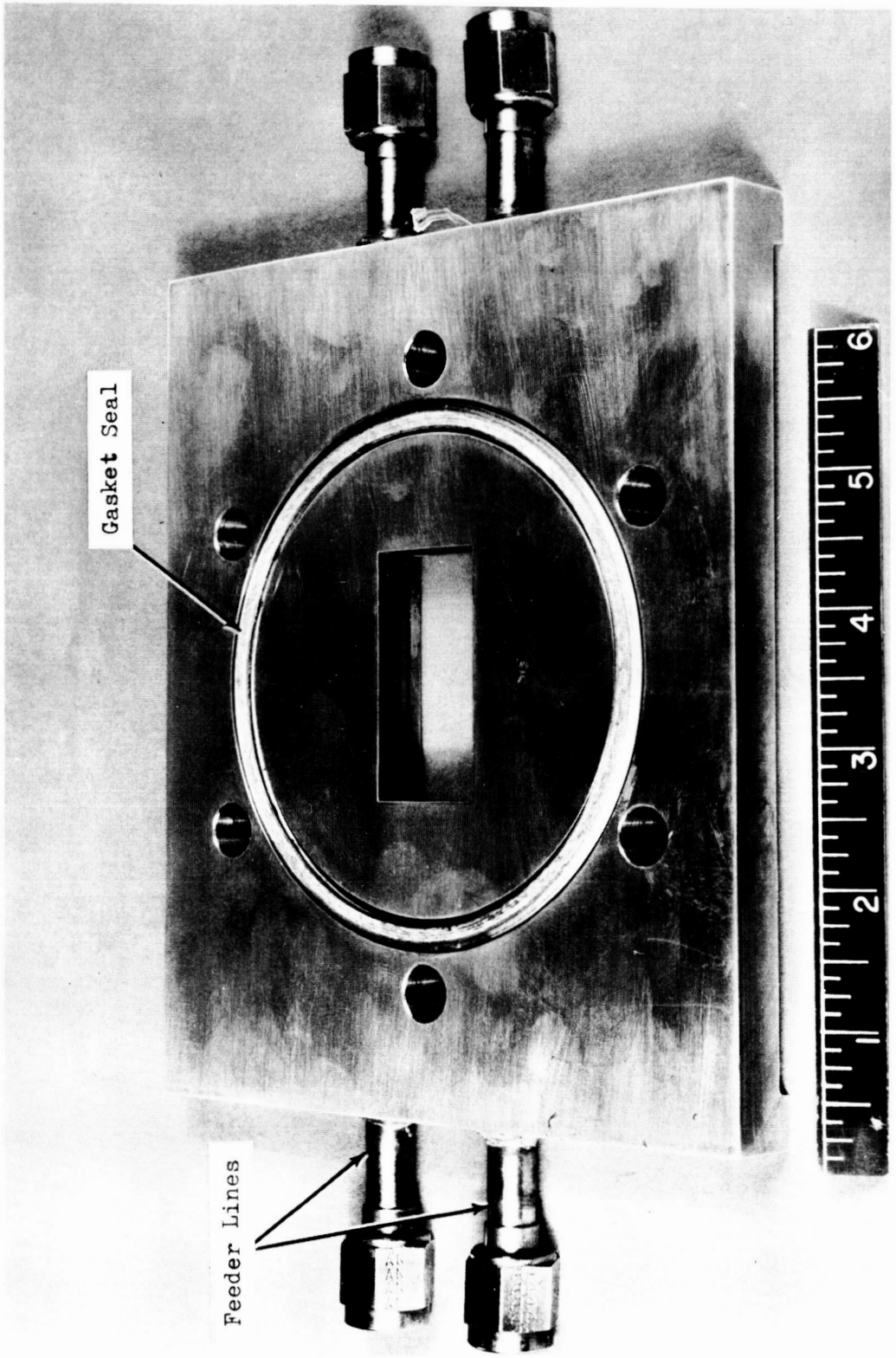

Figure 98. Overall View of Typical Supplemental Cooling Section

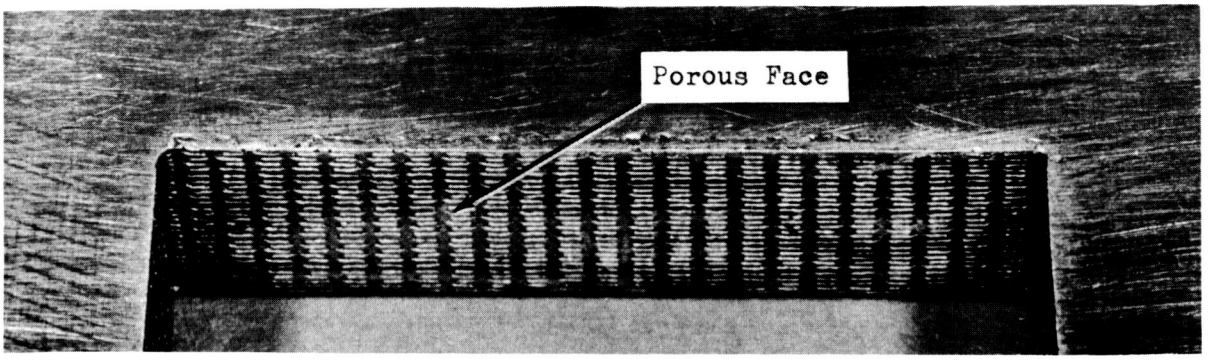

a. Transpiration Cooling

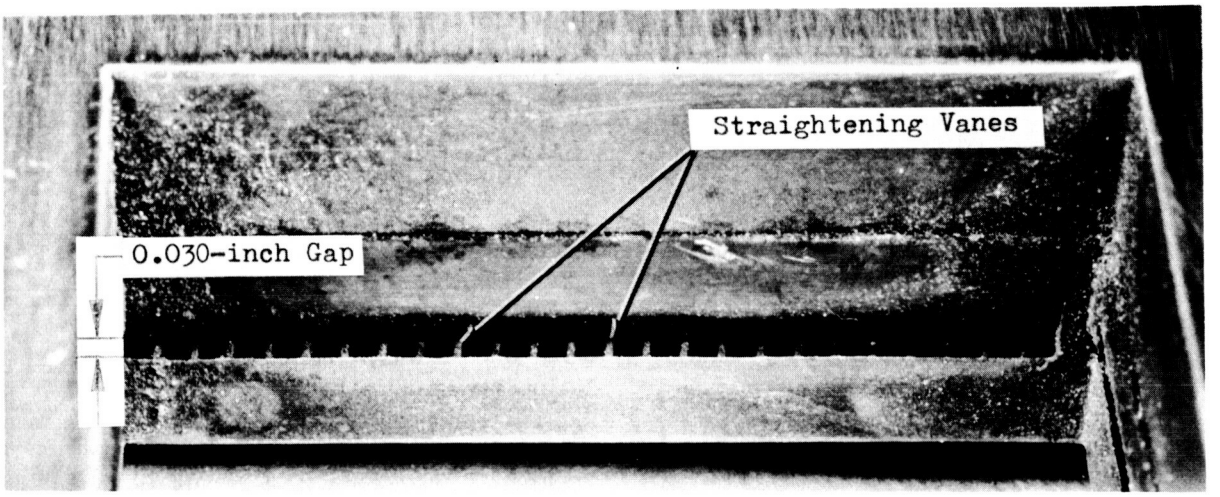

b. Tangential Slot Film Cooling

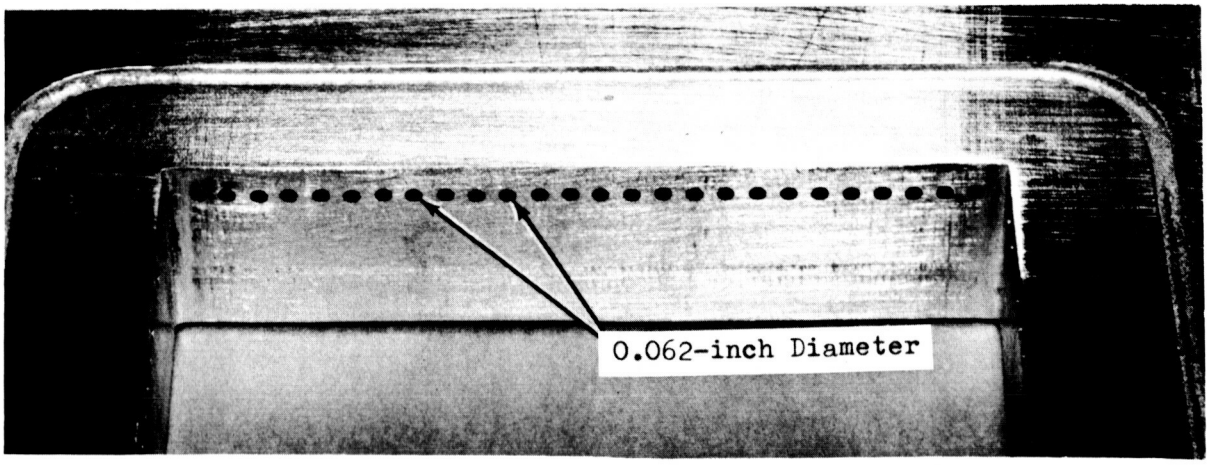

c. Radial Hole Film Cooling

Figure 99. Enlarged Views of Supplemental Cooling Sections

The film-coolant injection area was sized to give coolant injection velocities equal to an 850-ft/sec combustion gas velocity corresponding to a 2000-psia chamber pressure. The resulting injection velocities were correspondingly lower at reduced chamber pressure conditions due to the reduced film-coolant flowrate requirements. A primary design consideration for the supplemental film-coolant sections was to provide a uniform velocity across each coolant face. The frictional pressure drop across the continuous slot was calculated by the following equation:

$$\Delta h_s = (f\ \ell/4\ R_h)\ \frac{\alpha\ V_s^2}{2\ g_c} \tag{333}$$

According to Perry (Ref. 62), the ratio of the friction loss in the feeder line to the pressure drop across the coolant slot should be equal to or less than 10 percent. Assuming a constant orifice coefficient, the percentage of flow maldistribution across the slot was given by:

$$\text{Percent maldistribution} = 100\left[1 - \sqrt{\frac{\Delta h_s - \Delta h_f}{\Delta h_s}}\right] \tag{334}$$

With a 5-percent maldistribution factor, the head loss across the feeder pipe was calculated. The feeder pipe diameter was determined by equating the head loss in terms of the friction factor and kinetic energy of the inlet hydrogen coolant gas.

$$\Delta h_f = f\left(\frac{\ell}{D}\right)\frac{\alpha\ V_f^2}{2\ g_c} \tag{335}$$

As indicated by Fig. 96 and 99, several design innovations were incorporated to ensure good coolant distribution across the length of the

slot at each coolant face. The slot thicknesses were lengthened to maximize the pressure drop by frictional losses. Also, 150 parallel-spaced vanes, each 0.008 inch thick and spaced on 0.039-inch centers, were positioned within the slots to reduce the transverse component of film-coolant velocity and thus ensure tangential coolant injection with respect to the combustion gas flow. The design provided for the injection of hydrogen through a 0.030-inch slot gap for the top and bottom instrumented walls. The slot angularity was 30 degrees with respect to the combustion gas stream.

An additional design consideration for the film-cooling injectors was the assurance of adequate cooling for the copper leading edge adjacent to the slot. The following equation was used to calculate the maximum expected gas-side wall temperature of this surface during testing with supplemental film cooling:

$$\frac{q}{A} = \frac{k}{\Delta x} (T_{wg} - T_{wc}) = h_c (T_{wc} - T_c) \tag{336}$$

The coolant-side heat transfer coefficient (h_c) was determined by a correlation of the form (Ref. 63):

$$h_c = K G_b^{0.8} D^{-0.2} (T_b/T_w)^{0.5} \tag{337}$$

Under the most severe chamber operating conditions, the calculated conduction limit of the thin OFHC copper section was not exceeded. This conclusion was later verified during the hot-firing program.

The basic body design for the radial hole (Fig. 97 and 99) configuration and the transpiration-cooled section (Fig. 95 and 99) were similar to

the slotted configuration. The transpiration-cooled section was fabricated first and consisted of a stainless-steel body with a 0.082-inch-thick porous face welded around the inside periphery. The specifications of the face material provided for a 20-psi pressure drop with a 300-scfm/ft^2 air flow when exhausting to the atmosphere. The high-pressure-drop characteristics of this material assured good flow distribution of the injected gas coolant.

The radial hole configuration was made by modifying the transpiration section. The porous face material was removed from the body and replaced with an OFHC copper insert. The insert, brazed to the stainless-steel body, contained 72 radially drilled holes equally spaced around the chamber periphery. The holes were 0.062 inch in diameter on the top and bottom instrumented walls. The total flow area was identical to the section containing the continuous slot.

Each supplemental cooling hardware section was fed by two feed lines; opposite chamber surfaces were fed from the same source. The coolant flowrates were controlled by calibrated sonic flow restrictors. In this manner, the flowrates were dependent only upon the upstream pressure, independent of chamber pressure, for subcritical values. The total heat flux with supplemental cooling was considered as the sum of the water cooled flux (c) and the film cooled flux (fc) fractions as:

$$(q/A)_T = (q/A)_c + (q/A)_{fc} \tag{338}$$

if the total heat input for the combined case was considered to be the same as with no film cooling. The portion absorbed by film cooling was

$$(q/A)_{fc} = \frac{\dot{W}_{fc}\ \eta\ C_p\ \Delta T_{fc}}{x\ z} \tag{339}$$

in terms of the film cooling efficiency (η). An efficiency factor of 20 percent was assumed during the design of the hardware. A maximum-allowable ΔT of 1000 F was permitted for the film-coolant temperature increase.

The portion absorbed by the water coolant was calculated by

$$\left(\frac{q}{A}\right)_c = \dot{W}_c \, C_p \, \Delta T_c / A_c \tag{340}$$

SUPPORTING TEST EQUIPMENT

PROPELLANT FLOW SYSTEMS

The propellant and coolant flow systems are shown schematically in Fig. 100. Mixture ratio and chamber pressure control for the research test motor was established by regulation of the fuel and oxidizer feed system supply pressures. A photograph of the completed test facility is shown in Fig. 101.

The gaseous hydrogen fuel was stored in a bank of 24 high-pressure bottles rated at 3000 psig (Fig. 102). The total system capacity was 600 ft^3. Filtered gas from the bottles was distributed through a set of manifolds. The hydrogen injection pressure was controlled by a dome-type pressure regulator located downstream of a venturi meter used for flow measurements. Parallel hydrogen flow was supplied to the motor for film-cooling purposes. The film-coolant and main injector flows were controlled with sonic orifice restrictors.

LOX was supplied from a 40-gallon tank. Gaseous helium was supplied through a dome regulator and provided pressurization for the system.

The hypergolic igniter system consisted of a helium-pressurized triethylboron feed tank with the necessary shutoff valves. The hypergol was injected through an orifice located in the combustion chamber.

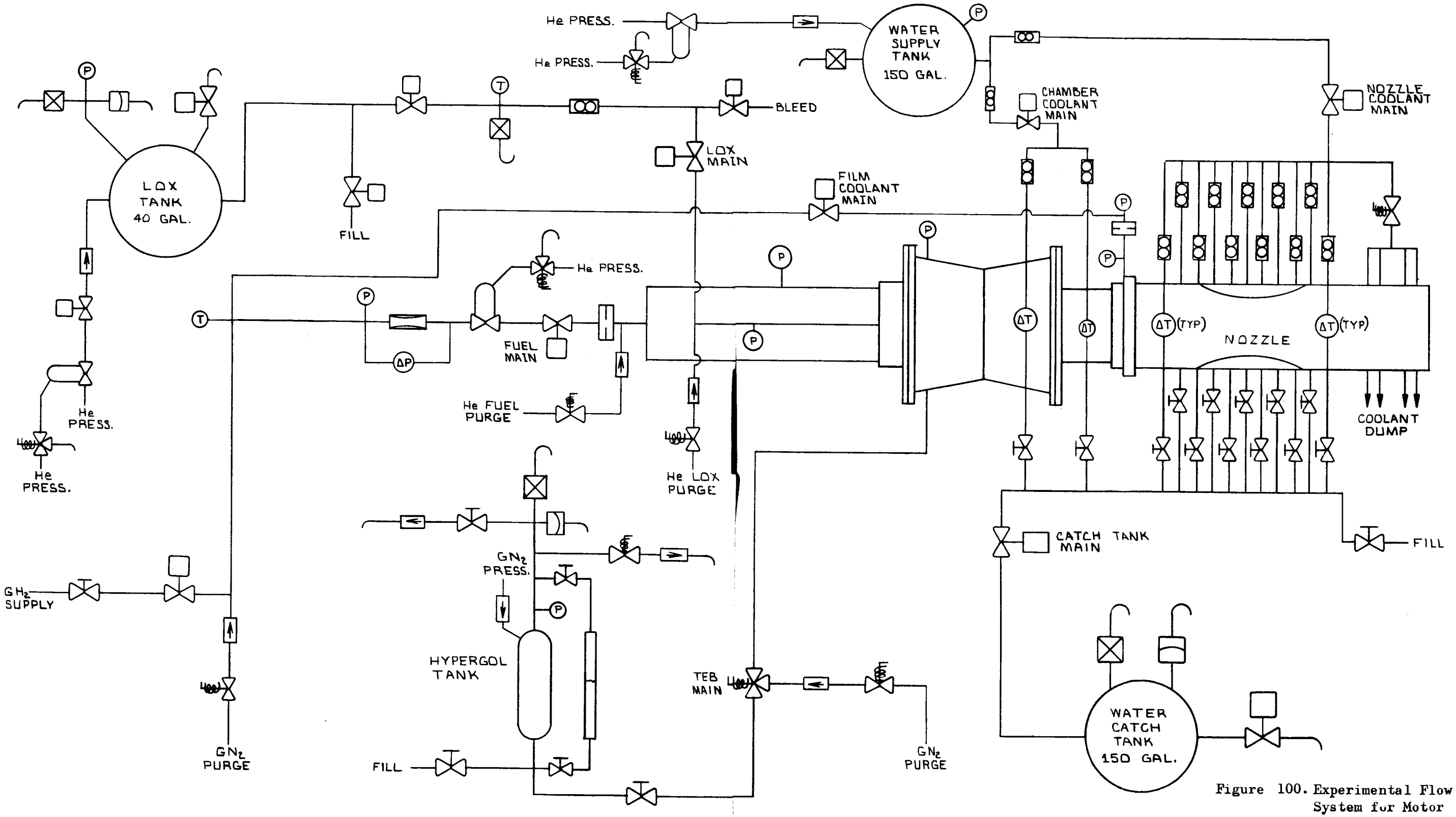

Figure 100. Experimental Flow System for Motor Firings

R-6199

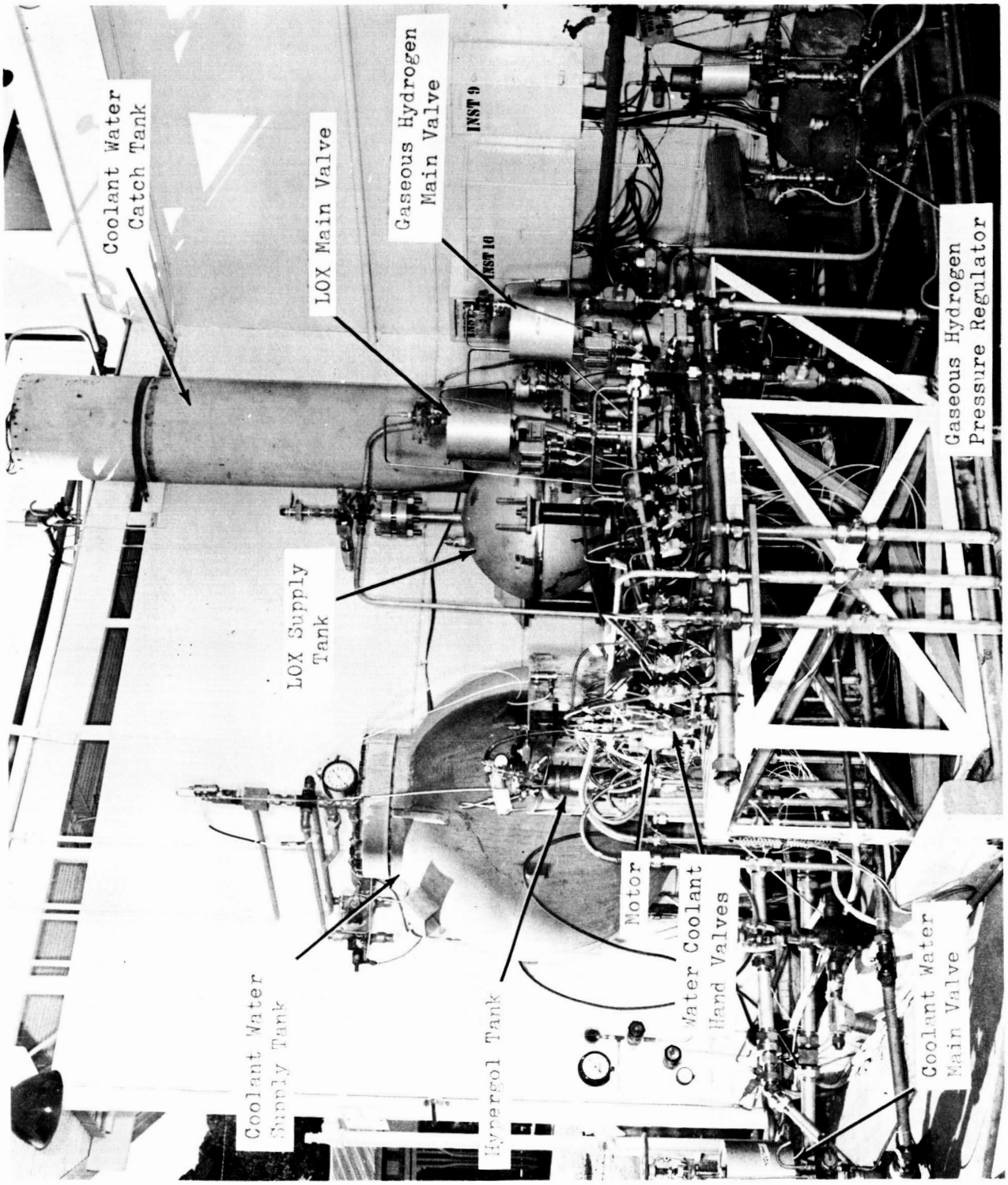

5AE21-12/14/64-S1B

Figure 101. High Pressure Test Stand Facility

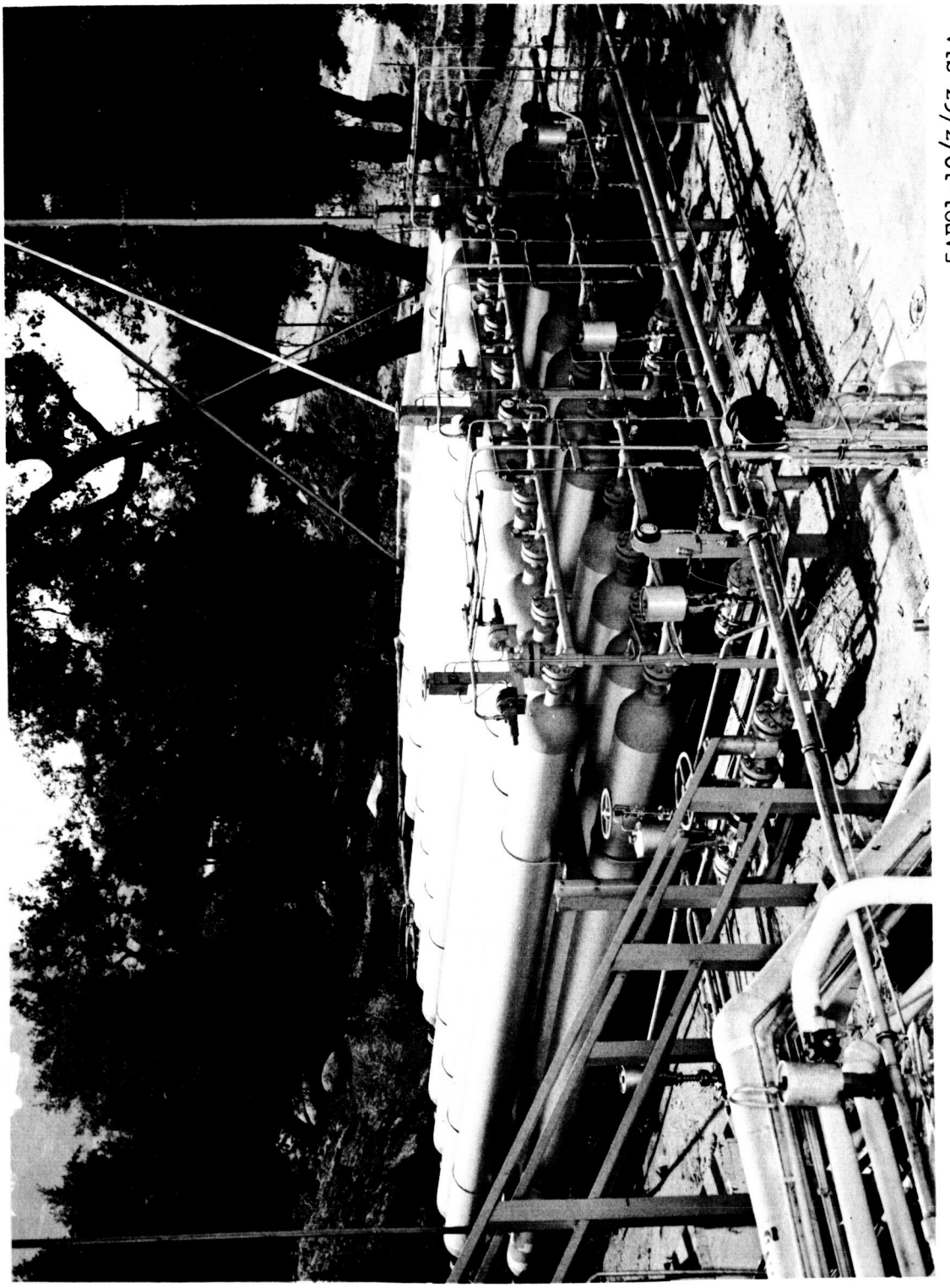

5AE91-10/3/63-S1A

Figure 102. High Pressure Hydrogen Supply System

The water coolant was supplied from a 150-gallon, 2000-psig spherical supply tank. Gaseous nitrogen was used initially as a pressurant, but was replaced with helium during the program to provide increased water flowrates. The system branched immediately downstream of the supply tank into two separate systems; one for supplying coolant to the chamber nozzle, and the other for supplying water to the combustion chamber and flow development sections. After cooling the test hardware, approximately 95 percent of the coolant was collected in a receiving tank. The remaining 5 percent was dumped overboard. The supply and receiving tanks were equipped with the necessary valving and pressure relief devices. The supply tank was provided with a fill valve to permit recycling of the coolant from the receiving tank back to the supply tank. Deionized water was used as a coolant to minimize corrosion and scale deposition in the hardware coolant passages.

The propellant and hypergol systems were initially purged with gaseous nitrogen. However, early in the program, the nitrogen was replaced with helium because nitrogen was suspected to contain moisture contamination.

The machined-passage thrust chamber assembly is shown installed in the flow system in Fig. 81.

SEQUENCE CONTROL SYSTEM

The sequential operation of the test motor was controlled remotely by preset switch contacts in an Eagle timer. The following main valves were signaled by the timer: LOX, fuel, hypergol, nozzle coolant, chamber coolant, catch tank coolant, and the film-coolant main valve. The main fuel and oxidizer valve positions were monitored by microswitches and recorded on an Esterline-Angus recorder. The power signals from the Eagle timer for the other valves were also recorded. A typical Esterline-Angus graph is shown in Fig. 103.

Prior to each hot firing test, 1000-psig water pressure was locked up between the catch tank and the coolant supply valves. This was done to prevent subsequent ramming of the test hardware during the programmed sequence operation. The water supply tank was normally pressurized to 1800 psig. The first sequenced event was the opening of the coolant main valves, immediately followed by the catch tank main valve. Liquid oxygen was the first propellant sequenced to reach the chamber. Ignition was accomplished by injecting 100-percent triethylboron directly into the established LOX flow. Triethylboron was hypergolic with liquid oxygen and burned cleanly without leaving chamber deposits which would have adversely effected the heat transfer results. The step to mainstage operation was accomplished by opening the main hydrogen fuel valve. As soon as the chamber pressure exceeded 150 psig, the hypergol flow was checked off. For the tests with supplemental cooling, the film-coolant flow preceded the main hydrogen flow by approximately 0.8 second. Mainstage combustion continued until the main LOX valve was closed. Fuel-rich conditions were maintained during the shutdown transient to prevent posttest oxidation of the hardware. The water-coolant flow was terminated last.

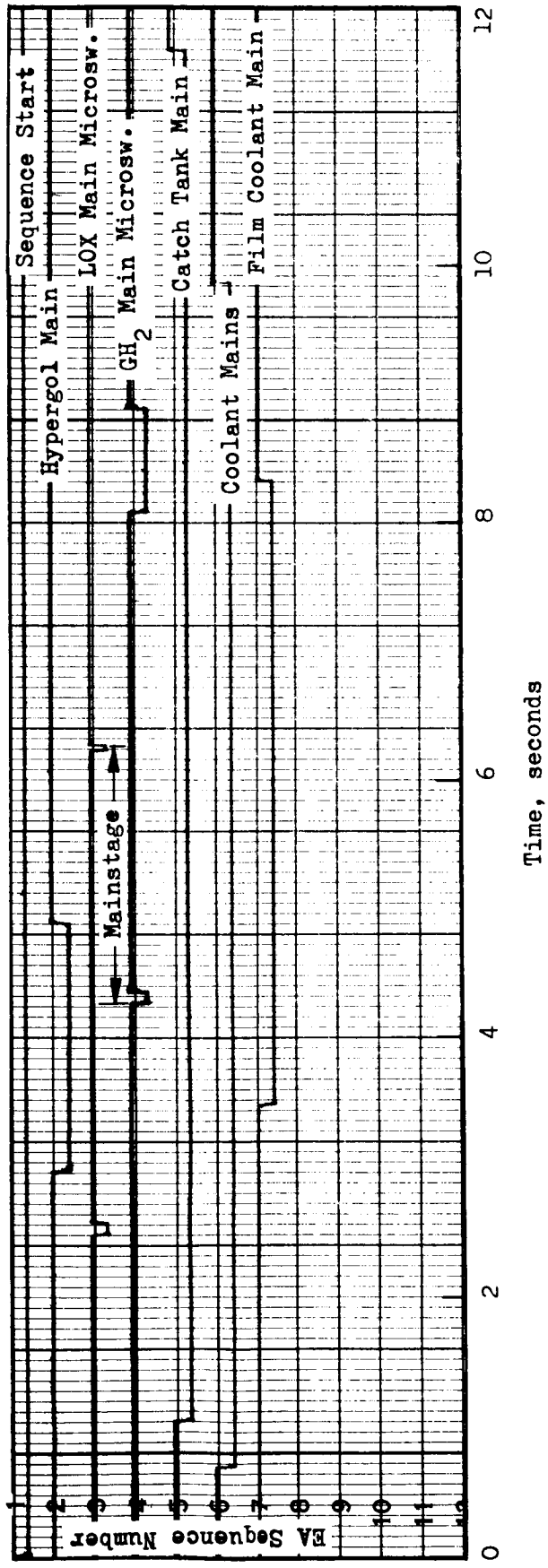

Figure 103. Typical Firing Sequence with Film Cooling

INSTRUMENTATION

The instrumentation consisted of 15 temperature, 11 pressure, and 16 flow measurements. Eleven simultaneous measurements of coolant water ΔT were made to define the heat flux distribution in the nozzle throat region. Difference chromel-constantan thermopiles were employed to obtain the necessary emf. These signals were converted from analog to digital with a Beckman 210 digital acquisition system. The digital data from the Beckman were recorded on IBM 729 tape. Selected digitized data were converted to analog signals, and a Brush recording was simultaneously made. Upon completion of each test firing, the Brush recording and magnetic tape were available for further processing. The IBM 7094 converted the raw digitized data to a graphical output. Typical CRT outputs are shown in Fig. 104 and 105. These data will be discussed in a later section of this report.

The digital system full-scale accuracy was listed as 0.11 percent for 24 hours and 0.129 percent for 6 months, with 0.065-percent precision. These values were with 3.29 sigma limits at the 99.9-percent confidence level.

All water coolant and liquid oxygen flow measurements were obtained with calibrated turbine flowmeters and recorded on an oscillograph. The gaseous hydrogen flowrate was obtained from a calibrated venturi meter. The actual flow was calculated according to the following equation (Ref. 64):

$$\dot{W}_f = Y\ A\ C_D \sqrt{\frac{2\ g_c\ \rho_1\ (P_1 - P_2)}{1 - \beta^4}} \qquad (341)$$

A value of 0.972 for the discharge coefficient (C_D) in the above equation was experimentally obtained on a water flow bench.

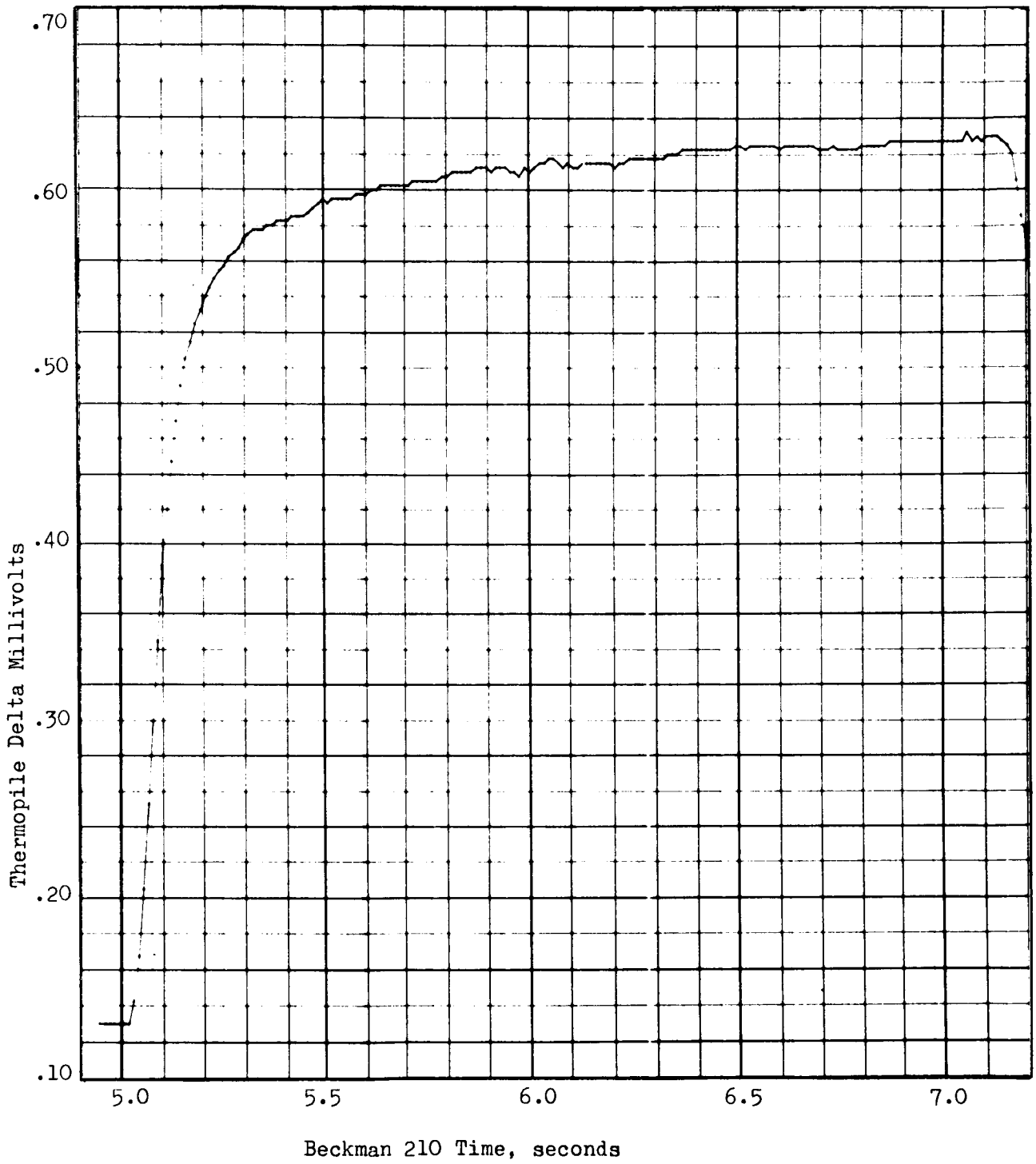

Figure 104. Typical Nozzle Water Coolant Temperature Rise Curve for Calorimetric Test Firing, Test No. 006, Station 4

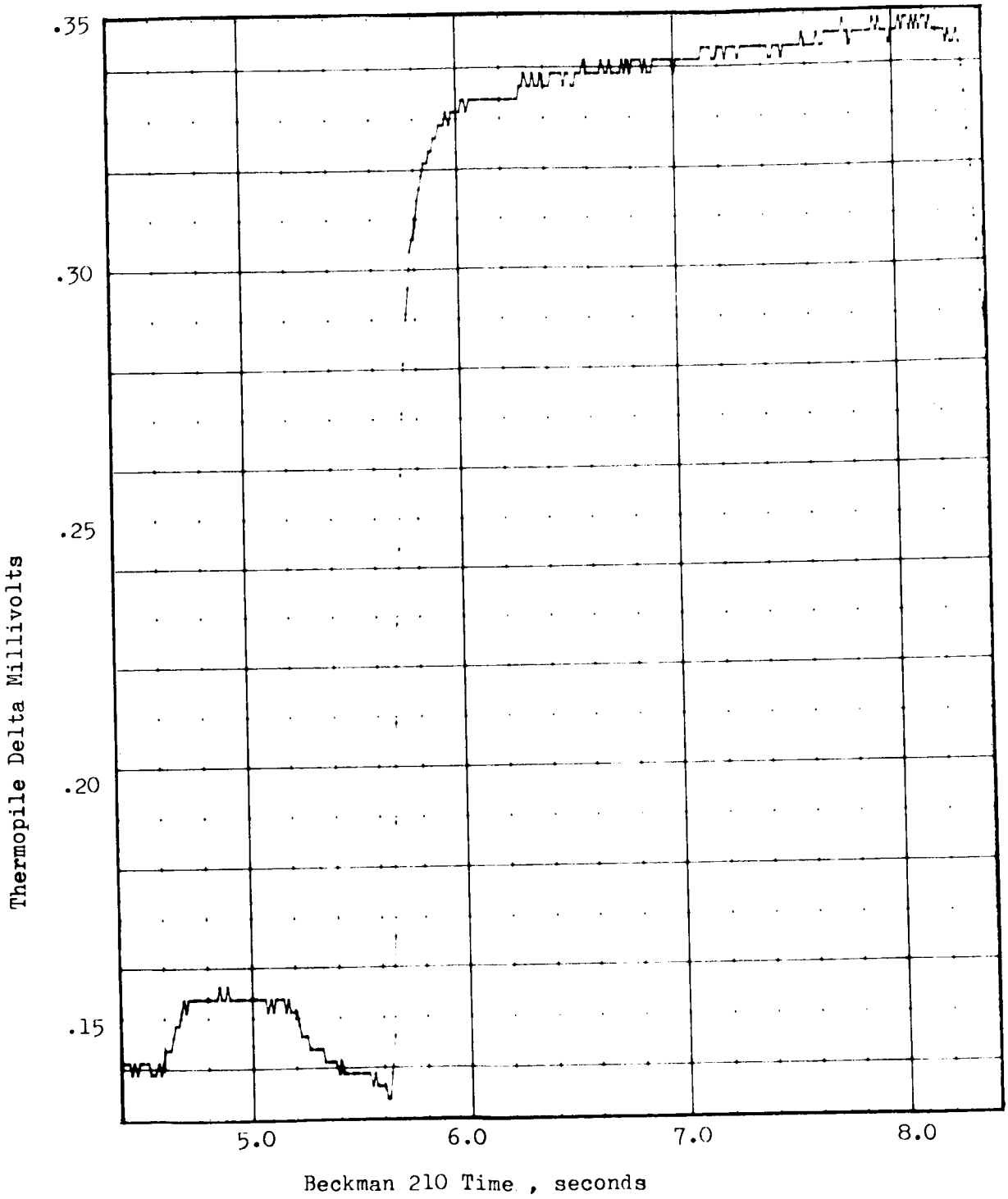

Figure 105. Typical Nozzle Water Coolant Temperature Rise for Test Firing with Supplemental Cooling, Test No. 010, Station 4

EXPERIMENTAL TEST RESULTS

COLD-FLOW STUDIES

The transpiration-cooled section, the oxidizer propellant feed system, and the coolant passages of the thrust chamber hardware assembly were cold-flow tested prior to hot firing.

The injector flows were made with water discharging to atmospheric pressure to permit visual inspection of the LOX injector swirler effectiveness. Gaseous nitrogen was used to simulate the fuel flow. Figure 106 shows a typical flow spray pattern simulating an injector ΔP corresponding to a 1000-psia chamber pressure. The discharge coefficient (C_D) for the injector oxidizer side was experimentally determined to be 0.64 which compared favorably with the preliminary design value of 0.60. This value was also verified later during the hot-firing tests (Fig. 107).

Several oxidizer tank blowdowns were made with liquid nitrogen to determine the flow characteristics of the feed system. These data were then adjusted for the corresponding liquid oxygen flows.

For the cold-flow studies in the chamber coolant passages, the individual coolant flowrates were adjusted to provide the desired water velocities for adequate cooling. Approximately 1600-psia maximum water pressure was available at the test hardware, providing a range of 110 to 180 ft/sec in water velocity in the nozzle coolant passages.

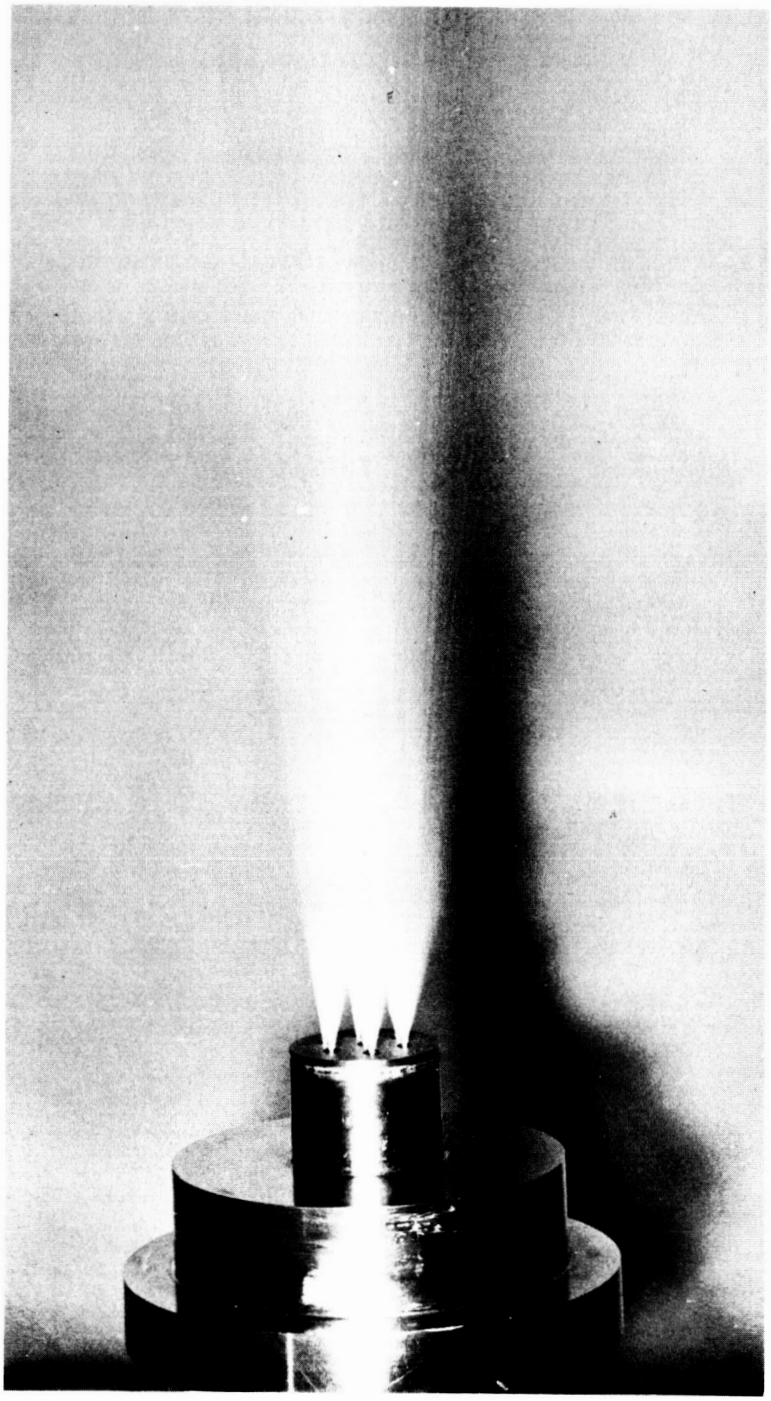

5AE34-11/25/64-S1B

Figure 106. Water Flow Test with Transpiration-Cooled Coaxial Injector

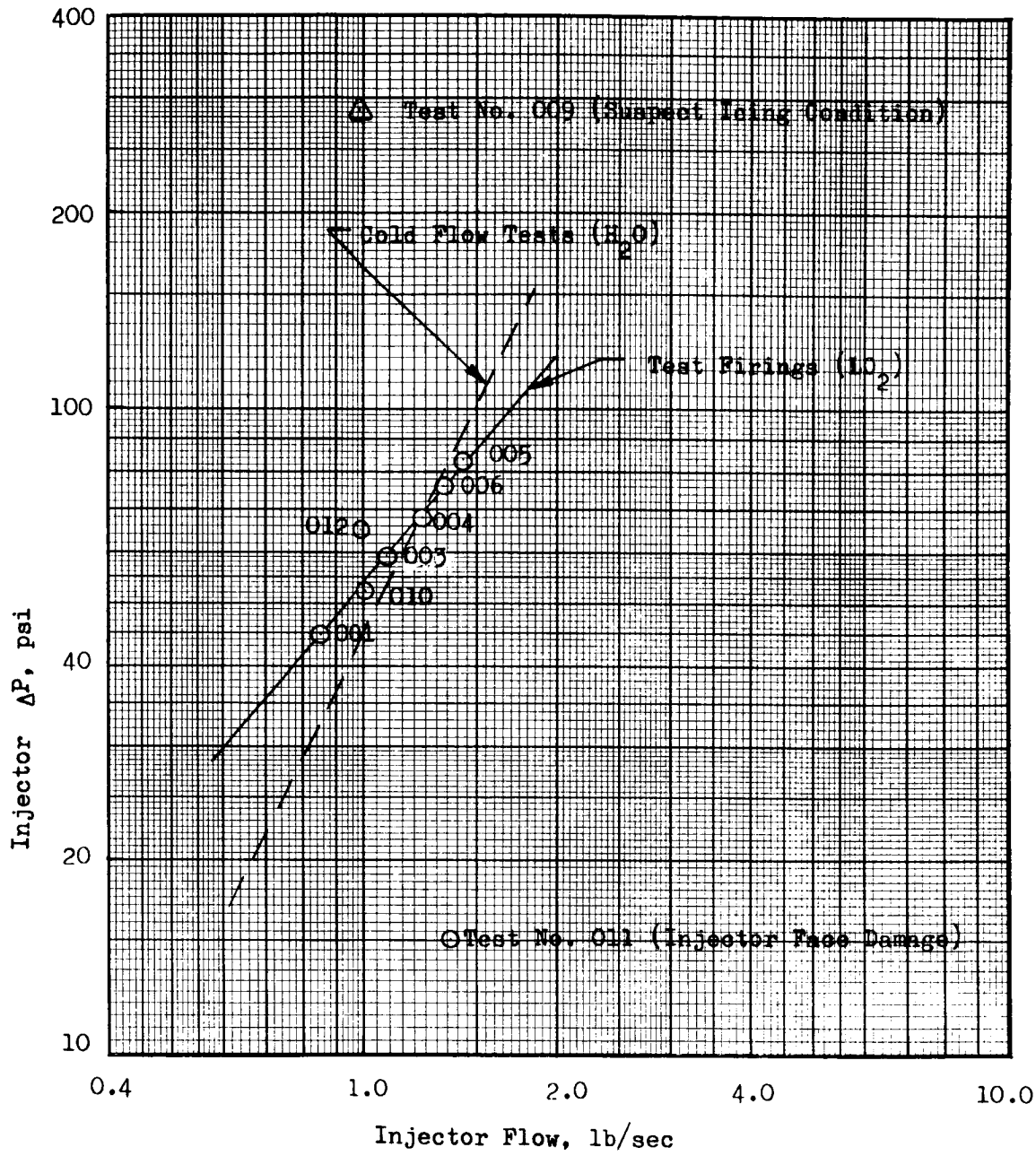

Figure 107. Oxidizer-Side Injector ΔP Results

CALORIMETRIC TEST FIRINGS

The first phase of the experimental firings was the basic determination of gas-side heat fluxes in the nozzle of the research test motor under conditions of no mass transfer cooling. The small size of the rectangular cross-sectioned throat, together with the high contraction ratio nozzle, permitted a maximum of 35 Btu/in.^{2}-sec heat flux to be absorbed by using water coolant flowing at high velocities in drilled cooling passages in the copper walls. This method of absorbing heat fluxes permitted a calorimetric measurement of heat flux at five discrete nozzle stations under steady-state conditions. The primary purpose of these measurements was to calibrate the nozzle heat load as a function of chamber pressure. This calibration was necessary for the evaluation of supplemental cooling techniques studied in the later phases. These correlations permitted extrapolation to higher heat fluxes at chamber pressures beyond the limits of water cooling. At these higher heat flux conditions, the supplemental cooling methods were required to protect the nozzle walls.

Seven calorimetric hot-firing tests were conducted over a chamber pressure range of 512 to 792 psia. A nominal injector mixture ratio of 5.0 was used with LO_2/GH_2 propellants. Ninety percent of the stabilized chamber pressure was generally achieved within 50 milliseconds after hydrogen ignition. Steady-state heat flux conditions were obtained in 3 seconds or less of mainstage combustion time.

A brief summary of the performance results is shown in Table 23. A test-by-test description of each motor firing follows.

TABLE 23

EXPERIMENTAL PROGRAM TEST RESULTS

	Test No.											
	001	002	003	004	005	006	007	008	009	010	011	012
Chamber Pressure, psia	554	512	618	692	792	790	695	574	664	703	832	689
LOX Flow, lb/sec	0.841	0.896	1.082	1.232	1.361	1.330	1.191	0.961	0.981	1.007	1.385	0.997
GH_2 Flow, lb/sec	0.242	0.162	0.198	0.232	0.266	0.268	0.224	0.199	0.280	0.234	0.282	0.235
Injector Mixture Ratio	3.48	5.53	5.46	5.31	5.12	4.96	5.32	4.83	3.51	4.30	4.91	4.24
Supplemental Coolant Flow, lb/sec	0	0	0	0	0	0	0	0.137		0.182	0.153	0.191
Characteristic Velocity, ft/sec		7352	7330	7246	7400	7486	7437					
Combustion Efficiency, percent c^* frozen		95.8	95.4	93.6	95.3	96.6	96.1					
Experimental Heat Flux, Btu/in.^{2}/sec												
Combustion Chamber									4.16	6.00	4.27	9.88
Flow Development Section									4.28	6.78	8.00	4.68
*Nozzle Station 1		10.95	11.60	11.33	12.50	11.75	11.25	6.74		2.89	4.58	5.40
Nozzle Station 3		21.07	23.46	25.96	27.67	28.70	26.26	19.71		8.75	18.98	16.43
Nozzle Station 4		25.65	29.14	31.20	32.88	33.21	30.64	25.10		13.97	20.71	21.10
Nozzle Station 5		22.06	25.07	25.95	27.16	26.03	26.71	20.92		13.58	22.67	18.13
Nozzle Station 6		11.77	13.24	14.10	14.94	14.27	15.77	10.24		6.51	11.24	9.07

*See Fig. 89 for nozzle station locations.

ROCKETDYNE • A DIVISION OF NORTH AMERICAN AVIATION, INC.

Test No. 001

An ignition test utilizing 100-percent triethylboron hypergolic fluid was conducted prior to test 001. Satisfactory ignition characteristics were demonstrated. Subsequently, the first hot firing achieved a chamber pressure of 554 psia for the 1.3-second programmed mainstage duration. The experimental heat flux was lower than the predicted value because a steady-state condition was not reached during the short test duration. However, a definite trend, as shown by the nozzle throat coolant water thermopile output chart of Fig. 108, was indicated toward a steady-state condition. Figure 108 also shows the motor start sequence as reflected by temperature changes in the nozzle coolant water. No hardware damage was sustained, and no leakage was observed during the test.

Test No. 002

Steady-state heat flux conditions were achieved during this 3.1-second mainstage duration firing after approximately 2.0 seconds of mainstage combustion. The chamber pressure during this test was 512 ±30 psia. An intermittent 105-cps chugging instability was experienced during the second half of mainstage. Chug is defined as an interaction between feed system and chamber relaxation. It is caused by an interaction between the chamber pressure and the injection flowrate. Chugging can usually be damped by using a sufficiently high value of injector pressure drop. Past experience has shown that a ratio of injector pressure drop to chamber pressure of 15 percent is usually adequate. The coaxial jet injector used for this program was designed to provide a 15-percent injector pressure drop at an 850-psia chamber pressure. The actual chamber pressures achieved during the program varied from 512 to 832 psia

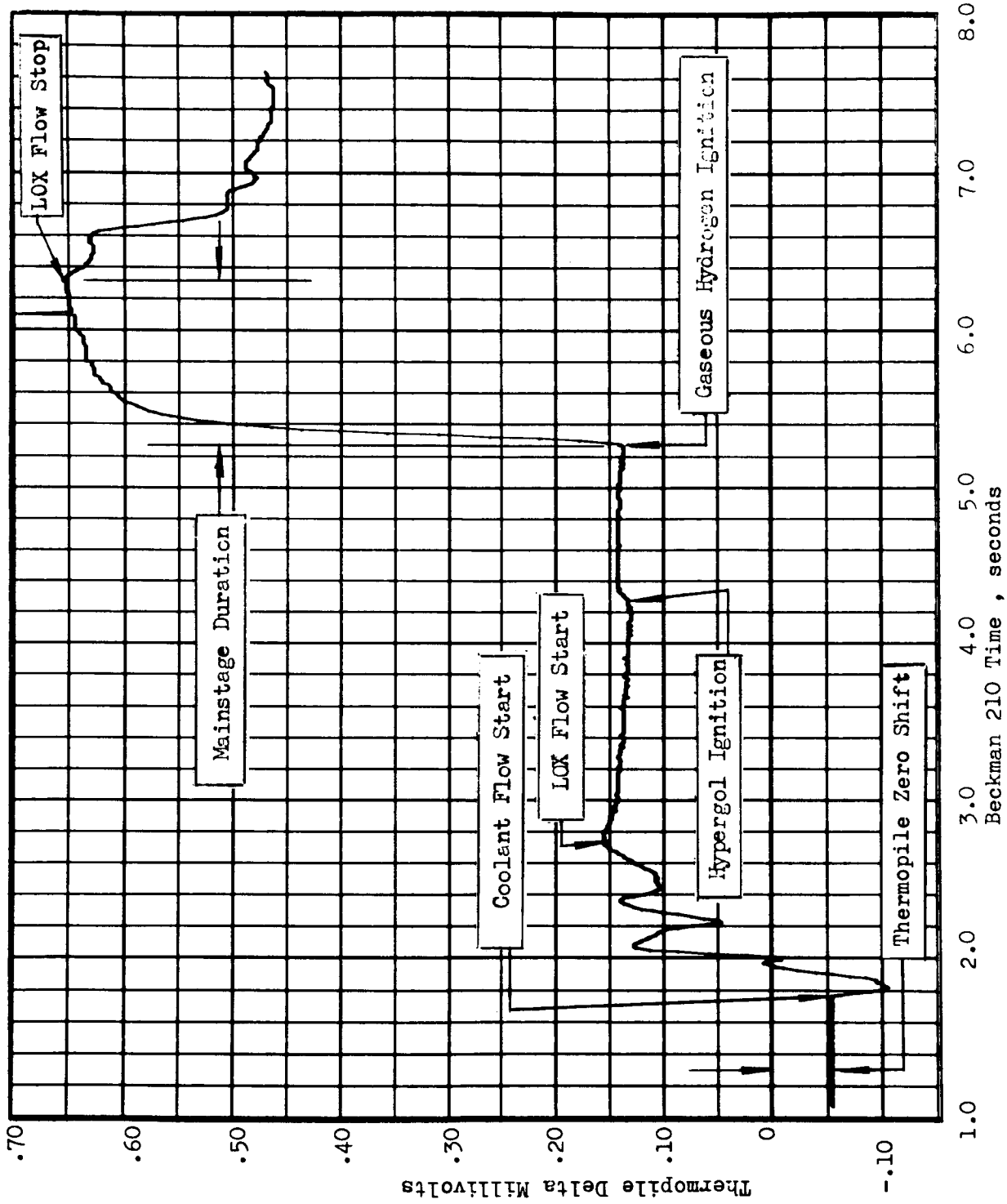

Figure 108. Transient Thermopile MV Output at Station 4 for Test No. 001

with corresponding critical injector pressure drop ratios of 7.4 to 10.5 percent. The chugging obtained was generally of low-pressure amplitude and frequency such that the heat transfer results should not be affected.

Test No. 003

Steady-state heat flux conditions were achieved during this 3.1-second test firing. The chamber pressure was 618 ±25 psia with a slight intermitten chug at 114 cps. Posttest inspection revealed slight coolant-water leakage into the chamber from the nozzle and flow development chamber sections. Repairs were made and the hardware reassembled for further testing.

Test No. 004

A gaseous hydrogen leak developed at the venturi meter before test 004. The meter was replaced with a section of straight-run tubing for the firing. The fuel flow was calculated for sonic flow conditions through the No. 13 drill orifice located upstream of the hydrogen injector manifold. The chamber pressure was 692 ±34 psia with a slight intermitten chug at 126 cps. Steady-state heat flux measurements were obtained. Posttest leakage was again observed from the flow development section coolant water. The leakage was subsequently repaired.

Test No. 005

The repaired fuel venturi meter was reinstalled for this test. A chamber pressure of 792 ±20 psia was achieved, the highest obtained during the program without supplemental cooling. Quasi-steady-state measurements

were recorded during the programmed 1.6-second mainstage firing. No hardware damage was sustained.

Test No. 006

This firing was essentially a repeat of the previous test except with an extended 2.1-second duration to obtain steady-state heat flux measurements. The chamber pressure was 790 psia. Slight coolant-water leakage was observed posttest from the flow development section. The output from the water-coolant thermopile located at nozzle station 4 (throat) is shown in Fig. 104. Steady-state conditions were attained.

Test No. 007

This test was a repeat of Test 004 to gain confidence in the fuel flow measurement. It was the last test in this series for the calorimetric determination of the nozzle heat flux distribution without mass addition cooling. The chamber pressure was 695 psia for a duration of 3.1 seconds.

SUPPLEMENTAL COOLING TEST FIRINGS

Considering the available water-coolant supply pressure and the conduction-cooling limit of the drilled-passage copper walls, a maximum throat heat flux of about 35 Btu/in.^{2}-sec could be absorbed by water cooling. This limit occurred at a chamber pressure of 850 psia. Corresponding calculations for the flow development section and combustion chamber indicated a similar upper limit.

For operations at higher chamber pressures, the additional nozzle heat flux was removed by supplemental cooling methods. The three types of supplemental cooling methods evaluated are shown in Fig. 95 through 97.

The 0.506-inch wide supplemental cooling sections were designed for installation upstream of the nozzle section as shown in Fig. 80. The ablative high-silica phenolic-laminated insert was fabricated but never test fired for reasons discussed below. The calorimetric heat flux distribution in the nozzle was obtained for each supplemental cooling test to determine the relative effectiveness of each method. The difference between the measured heat flux during these test firings with mass transfer cooling and the extrapolated calorimetric values for no mass transfer cooling represent the respective cooling effectiveness at each nozzle station. The relative effectiveness for each method evaluated is discussed later.

Test No. 008--Transpiration Cooled

The supplemental coolant flow system contained two No. 41 drill orifices for expected sonic flowrate control. The pressure drop across the porous transpiration face (Fig. 99a), however, was considerably higher than anticipated. The back pressure on the orifices prevented sonic flow, and the resulting coolant flowrate was less than the desired value. The coolant flowrate, as measured by the venturi meter, represented 11.8 percent of the total main coaxial injector propellant flowrate. The chamber pressure for this 3.1-second test was 574 ±45 psia. Moderately heavy 112-cps chugging was sustained.

Test No. 009--Transpiration Cooled

Target chamber pressure for this test was 850 psia. An overshoot in chamber pressure to 1050 psia occurred at main propellant ignition, followed by 350 milliseconds of pressure fluctuations to a stable value of 664 psia. Again, the pressure drop across the supplemental cooling injector face was excessive; also, an extremely high pressure drop occurred in the LOX injection system of the coaxial jet injector (Fig. 107). The high injector pressure drops were attributed to icing conditions in the main propellant and supplemental coolant propellant feed systems. The GN_2 source used for purging was common to both systems. The purge flow was activated immediately prior to each run start sequence. For this reason, the nitrogen purge gas was analyzed posttest for water impurity. A dew-point analysis revealed approximately 510 ppm by volume of water contamination which was considered excessive and probably accounted for temporary restriction in the motor injection systems. The purge gas was replaced with dry helium prior to the next test.

The hard start caused a permanent deformation in the originally flat porous coaxial injector face. A 0.020-inch deflection occurred at the center of the 2.25-inch-diameter face. This deformation was not considered a detriment to further testing.

The measurement of supplemental cooling flowrate was not obtained due to a transducer failure; the heat flux data were therefore not reduced.

Test No. 010--Slot Injection, Film Cooled

The continuous slot film injector section (Fig. 99b) was installed upstream of the nozzle section for three firings. The chamber pressure for Test 010 was 703 psia. Steady-state heat flux conditions were obtained within the 2.5-second mainstage firing as indicated by Fig. 105. The relatively low slot injector pressure drop allowed sonic film-coolant flowrate control at the two upstream orifices. Intermittent 110-cps chugging was noted. Injection system icing was not observed with the new gaseous helium purge system. No damage was sustained to either the chamber or film coolant hardware.

Test No. 011--Slot Injection, Film Cooled

The hard-start characteristics of a previous test were repeated for Test 011. This phenomenon was probably associated with the start sequence used for the film-cooling tests. The film-coolant flow was ignited at the chamber nozzle inlet approximately 500 milliseconds ahead of the main fuel injection through the coaxial jet injector. The chamber pressure increase due to the combusted film-coolant flowrate and main LOX flow was sufficiently high to check off the hypergol flow. Thus, the main fuel propellant ignition may have been delayed several milliseconds, causing a hard ignition of the accumulated propellants.

Posttest inspection of the test hardware revealed that the porous injector face had separated from the body. Further investigation indicated the failure occurred in the Regimesh material adjacent to the circumferential electron-beam weld. A portion of the face material became lodged in the nozzle throat. The mainstage performance test data appeared normal.

Because the chamber pressure was near the 850-psia target value, it was concluded that the face probably was lost during the shutdown sequence, the time of maximum pressure differential. The failure was caused by progressive test-to-test deformation of the porous mesh face with subsequent catastrophic yielding. Since no other damage was sustained to the coaxial jet injector, repairs were made by attaching a new porous face.

Coolant-water leakage was observed from the downstream flange of the two-dimensional flow development section. A replacement part was installed prior to the next test firing.

Test No. 012--Radial Hole Injection, Film Cooled

The radial-hole film-coolant injector (Fig. 99c) was evaluated at a chamber pressure of 689 psia. A smooth starting transient was obtained. No hardware damage was sustained and no leakage was observed.

Test No. 013--Slot Injection, Film Cooled

The tangential slot configuration (Fig.99b) was reinstalled upstream of the nozzle to provide supplemental cooling for a planned 1000-psia chamber pressure operation prior to an ultimate 1500- to 2000-psia test. The film-coolant flowrate was sonically orificed to provide a flow equal to 15 percent of the total propellant flowrate. The programmed mainstage duration was 2.0 seconds.

The test was terminated by an observer after a 760-millisecond duration due to excessive combustion gas leakage at several chamber locations.

Posttest examination of the motor hardware revealed severe burning of the copper combustion chamber, flow development and the adjacent film-cooling sections as shown in Fig. 109 and 110. Only minor damage appeared to be sustained by the nozzle. No significant damage was done to the propellant feed systems or associated facility support systems. A discharge water-coolant line was separated from the flow development section at the threaded pipe connection. The transpiration face of the coaxial jet injector was separated from the injector body, approximately 25 percent of the original Regimesh material was lodged in the nozzle throat. The damaged coaxial jet injector is shown in Fig. 111.

The output from the chamber pressure transducer was recorded on oscillograph (Fig. 112). All other pressure recordings were made on relatively slow-response (0.25 sec/in.) Brown strip charts. The failure analysis, therefore, was difficult due to the relatively slow instrumentation response characteristics.

The relatively high film-coolant flowrate caused a gradual increase in chamber pressure to 1170 psig (Fig. 112). This pressure was considerably in excess of the GH_2 manifold purge and hypergol injection tank pressures, and undoubtedly caused: (1) an oxidizer-rich pocket of uncombusted gases to accumulate behind the porous injector face, and (2) stoppage of the hypergol flow into the chamber. Simultaneously, with the opening of the main hydrogen fuel valve, a detonation occurred in the hydrogen manifold, blasting off the transpiration-cooled main injector face. An instantaneous rise in chamber pressure to 1900 psig is noted on the oscillograph record, with similar pressure spikes observed in the injection system pressure recordings. Further evidence of a detonation is suggested by the deformed LOX tube (Fig. 111). At this same time, the coolant turbine flowmeter

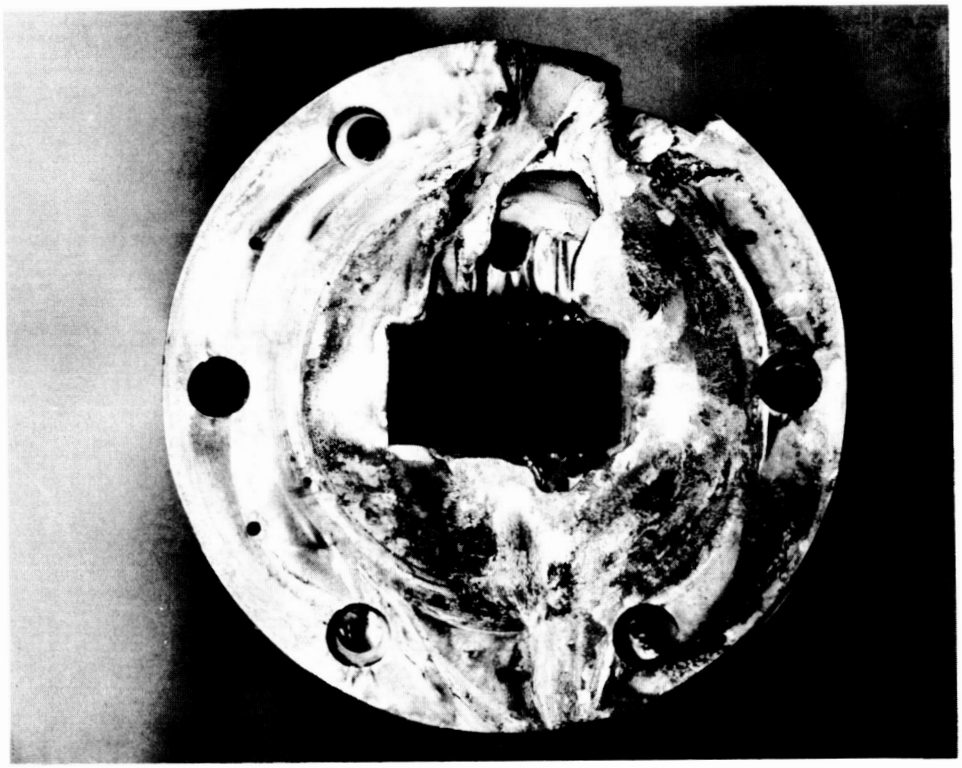

b. Flow Development Section

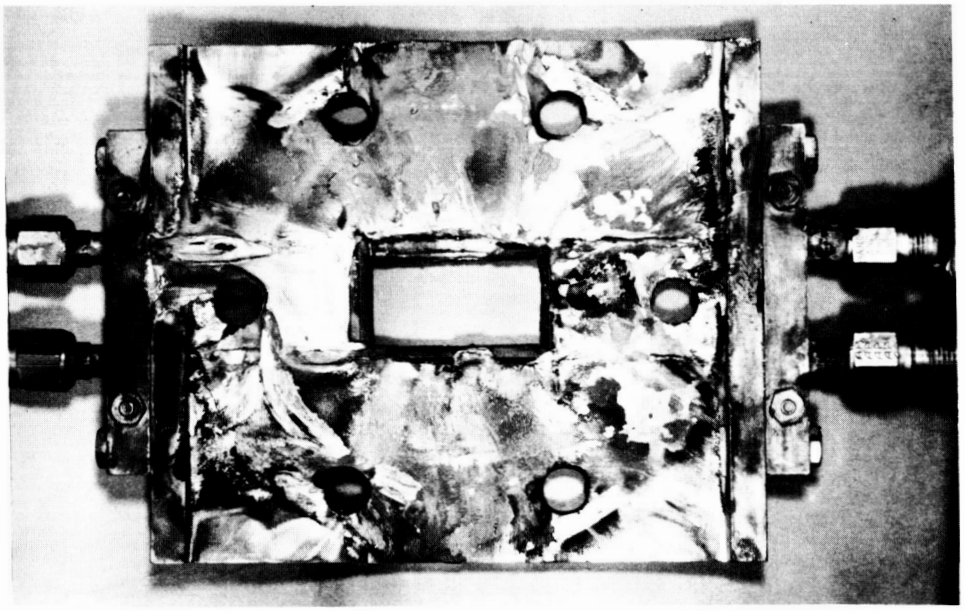

a. Film Cooling Section

Figure 109. Hardware Damage, Posttest 013

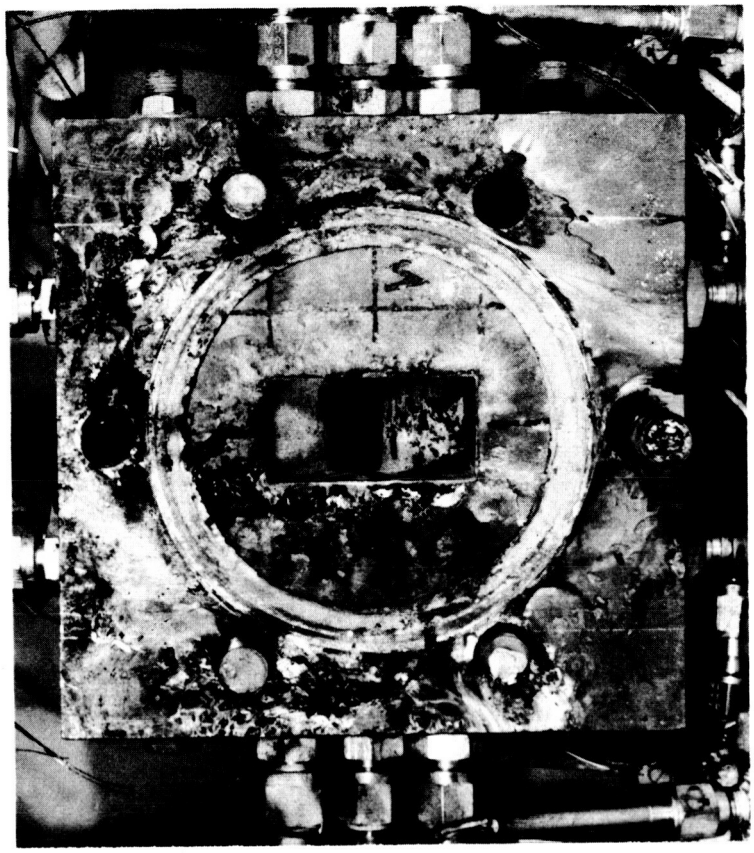

b. Nozzle Section

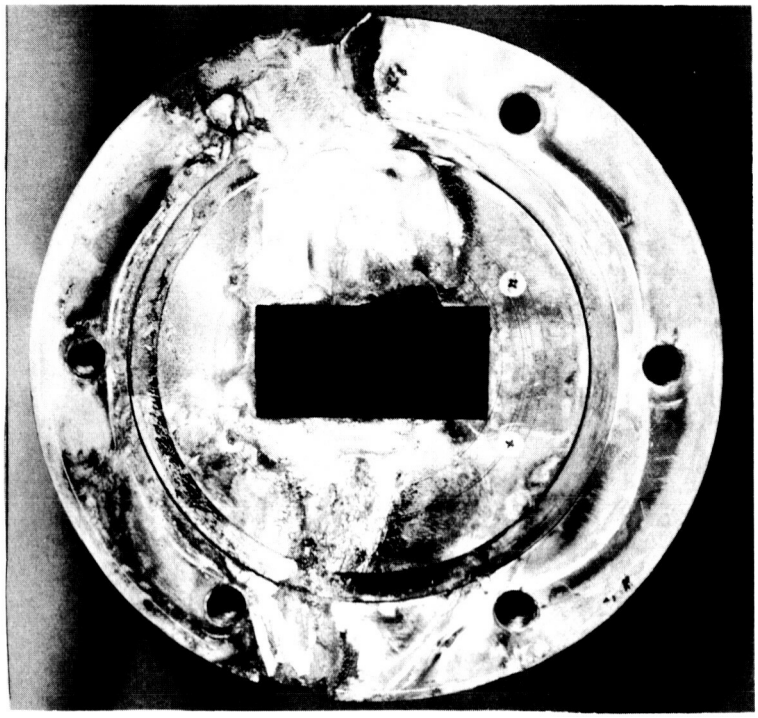

a. Combustion Chamber Section

Figure 110. Hardware Damage, Posttest 013

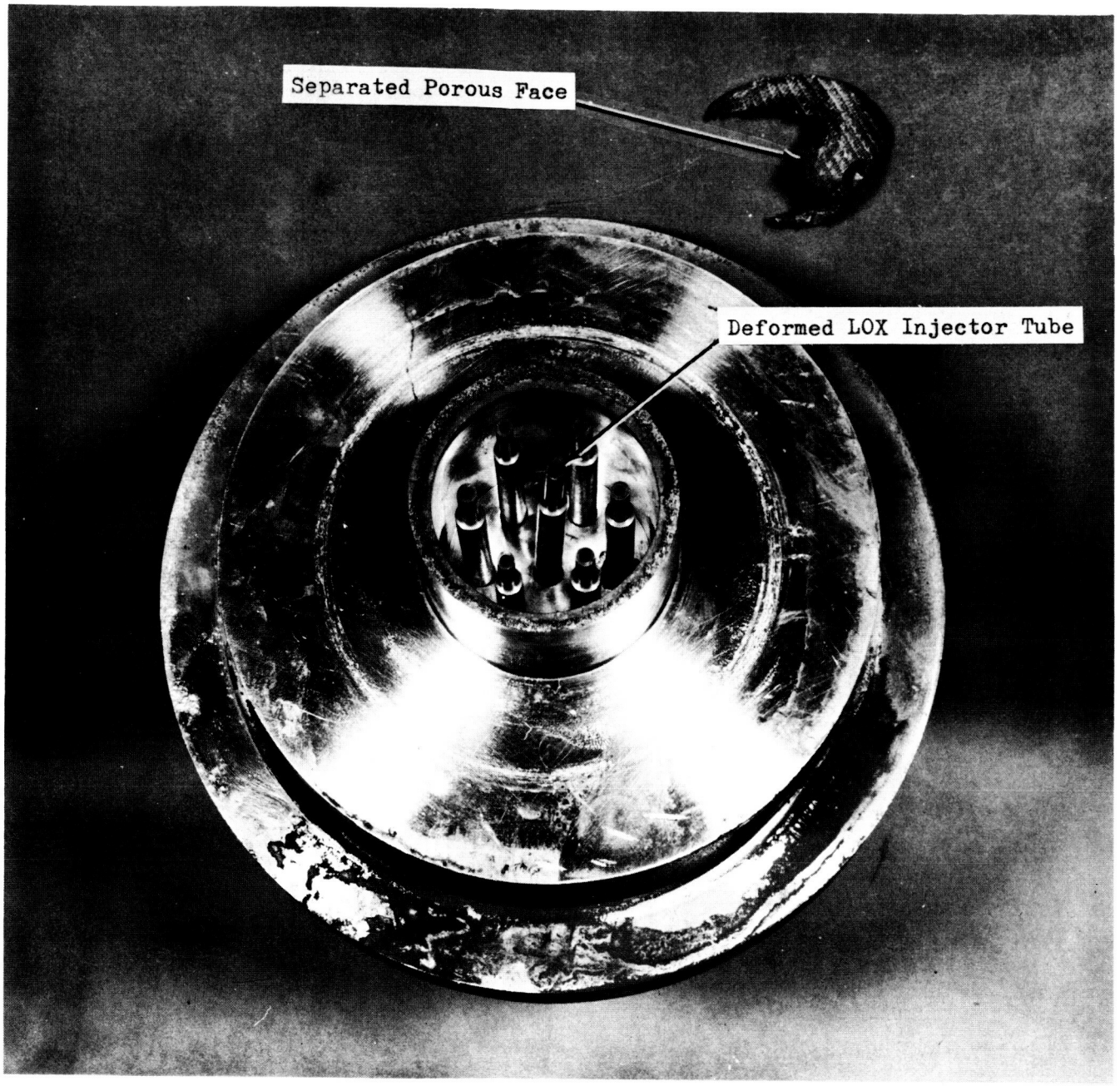

Figure 111. Coaxial Jet Injector Damage, Posttest 013

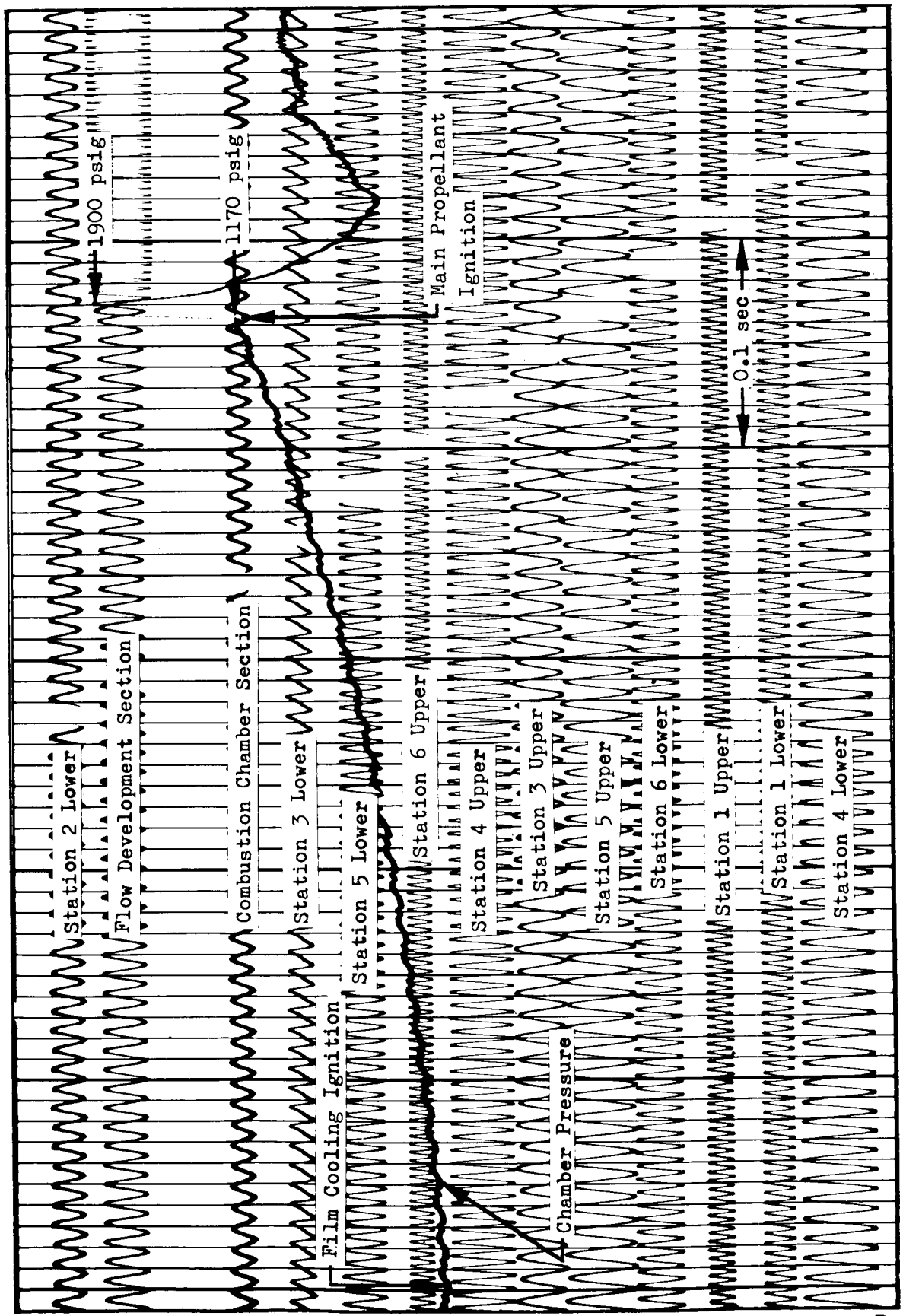

Figure 112. Oscillograph Record of Test No. 013

supplying water to the flow development section overspun, corresponding to the separation of the coolant discharge line from the chamber. The female threads in this section were slightly oversized and apparently the shock loading imposed by the detonation was sufficient to dislodge the tube fitting. The coolant-water flow unbalance caused by the ambient pressure discharge of this one line caused localized overheating and eventual failure of the copper chamber. Following the detonation, the chamber pressure dropped to 940 psig, and gradually decayed to 600 psig for the remaining 650 milliseconds of combustion.

The chamber assembly had experienced previous hard starts during Tests 009 and 011 without serious consequence. It was concluded that the catastrophic failure during Test 013 was due primarily to the loss of coolant water.

The extensive loss of hardware during Test 013 prevented completion of the remaining two high chamber pressure firings planned for 1000 and 1500 to 2000 psia.

EXPERIMENTAL DATA ANALYSIS

CALORIMETRIC RESULTS

The experimentally obtained calorimetric nozzle heat flux distributions (tests 002 through 007) are plotted in Fig. 113 through 118. Each water-cooled nozzle segment contained four instrumented water passages for cooling a discrete increment of the inner wall. Heat transfer data were not obtained at station 2 because the water was also required to flow axially to provide coolant to a portion of the side walls. Calorimetry was used to determine the rate of heat transfer to each cooling segment. As discussed previously, the individual coolant flowrates were measured by individual turbine flowmeters, and the coolant temperature rises were indicated by thermopiles immersed in the inlet and outlet streams. The heat flux absorbed by the coolant was calculated at each station by Eq. 340.

Also shown in Fig. 113 through 118 are the heat flux values estimated from the simplified Bartz equation (Ref. 60) corrected for the heat loss to the coolant water. The wall surface area of each cooled segment was determined to calculate the local heat flux using Eq. 327 through 330. By neglecting the small axial changes in the combustion gas molecular weight and specific heat ratio, the local combustion gas recovery temperature was calculated by the following equation:

$$(T_{rg})_x = T_g \left(\frac{c^*_{actual}}{c^*_{theoretical}} \right)^{2.0} \pm \frac{\left[(q/A)_{measured} (A_g) \right]_x}{\dot{W}_g \, C_p} \qquad (342)$$

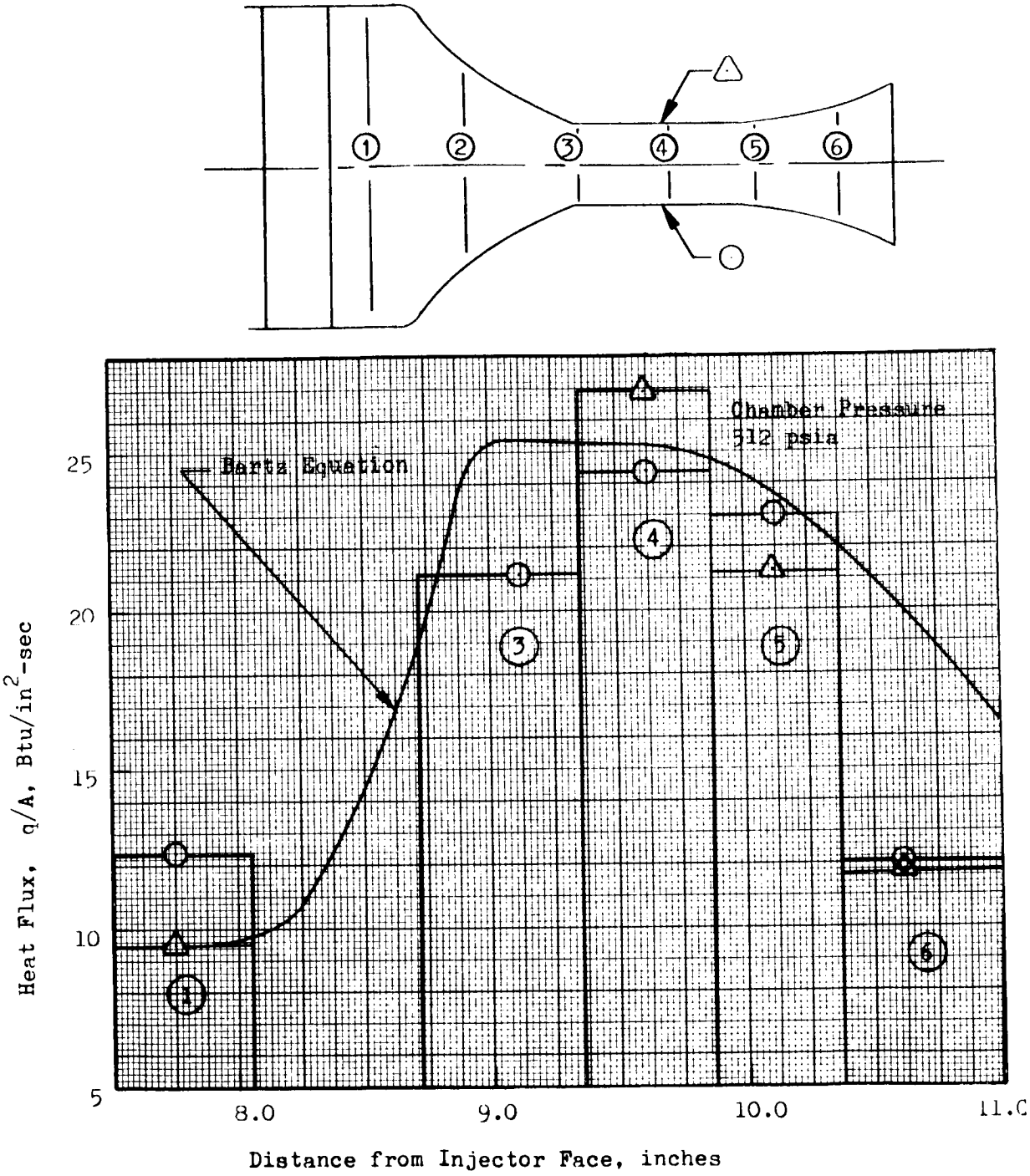

Figure 113. Nozzle Heat Flux Distribution for Test No. 002

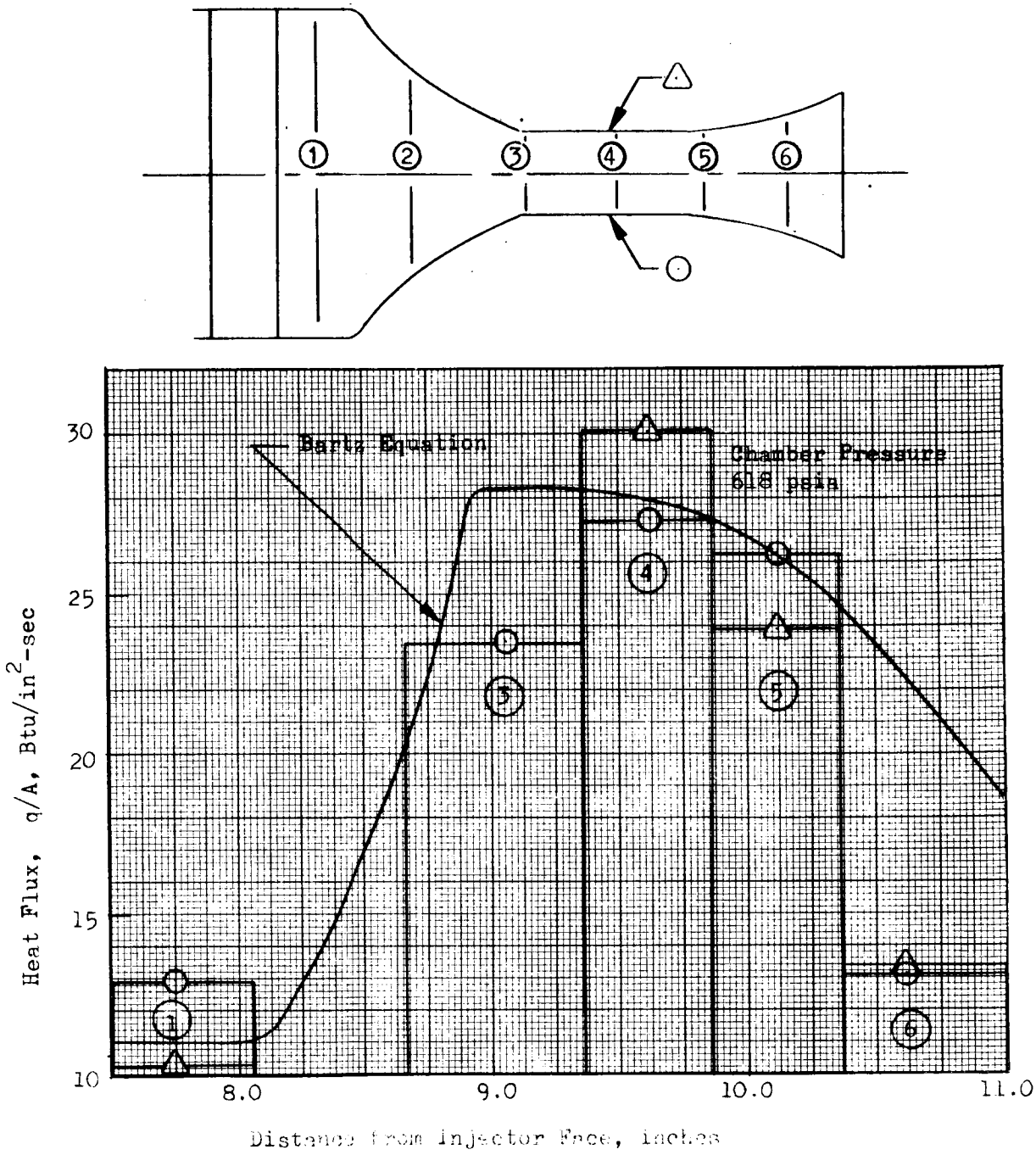

Figure 114. Nozzle Heat Flux Distribution for Test No. 003

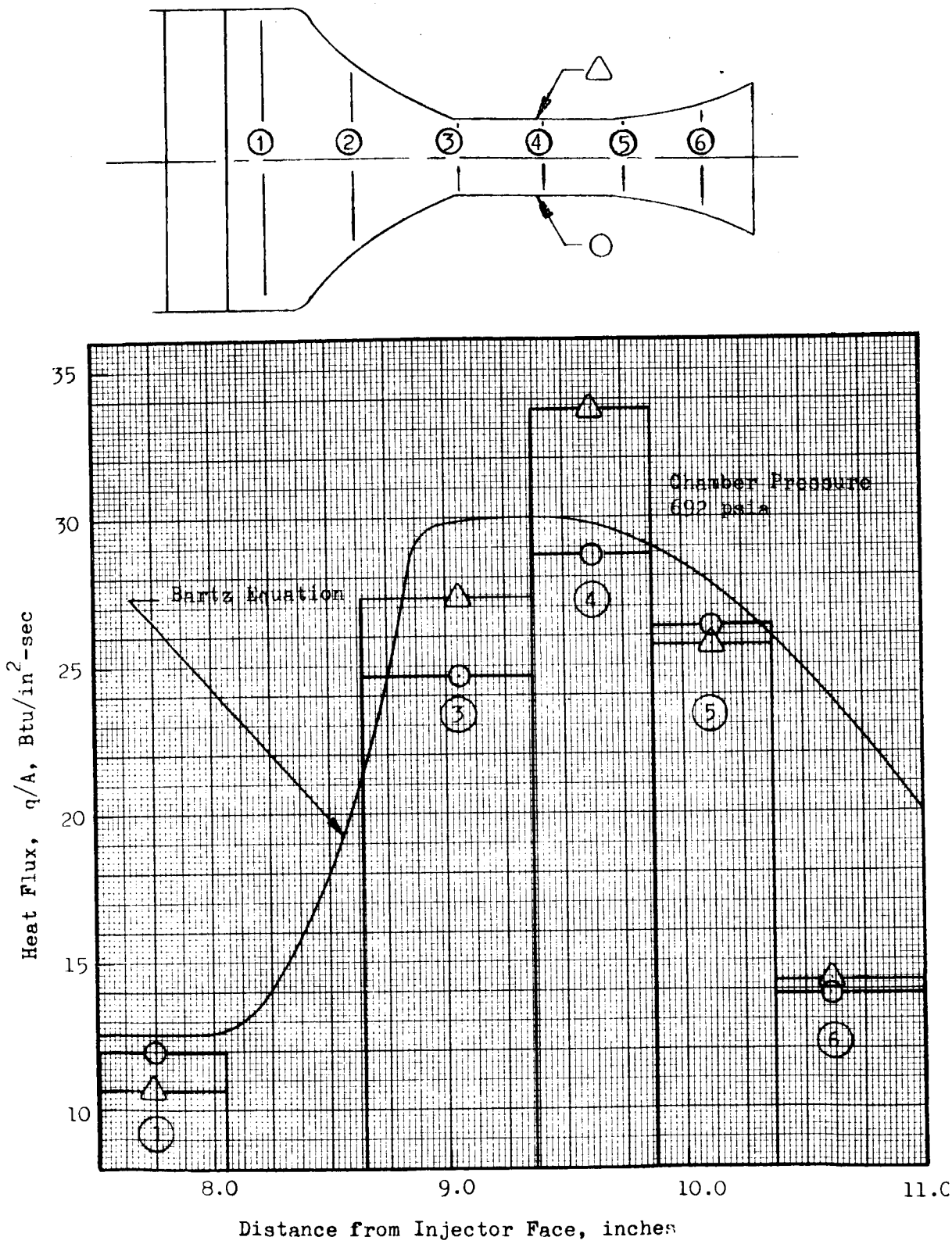

Figure 115. Nozzle Heat Flux Distribution for Test No. 004

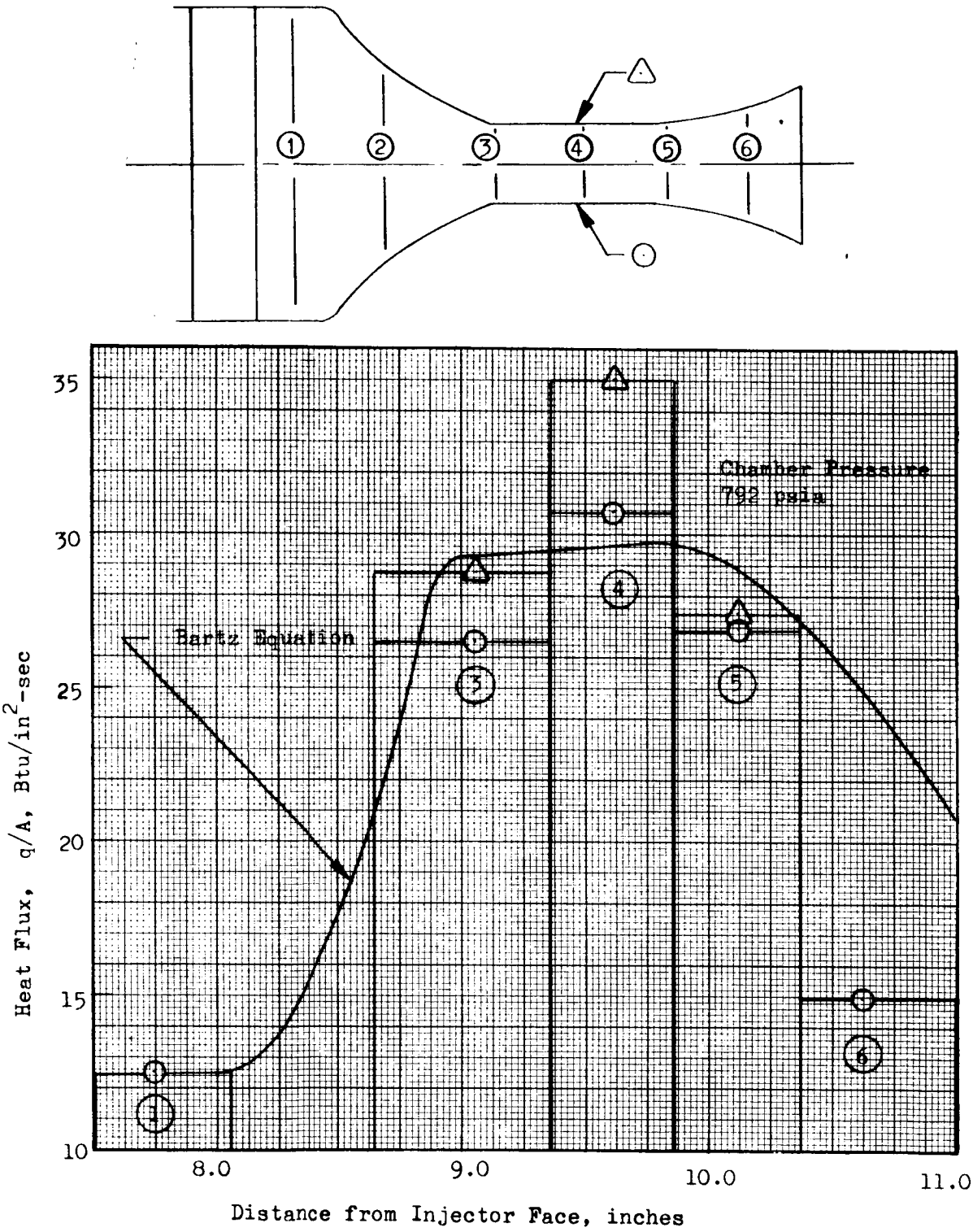

Figure 116. Nozzle Heat Flux Distribution for Test No. 005

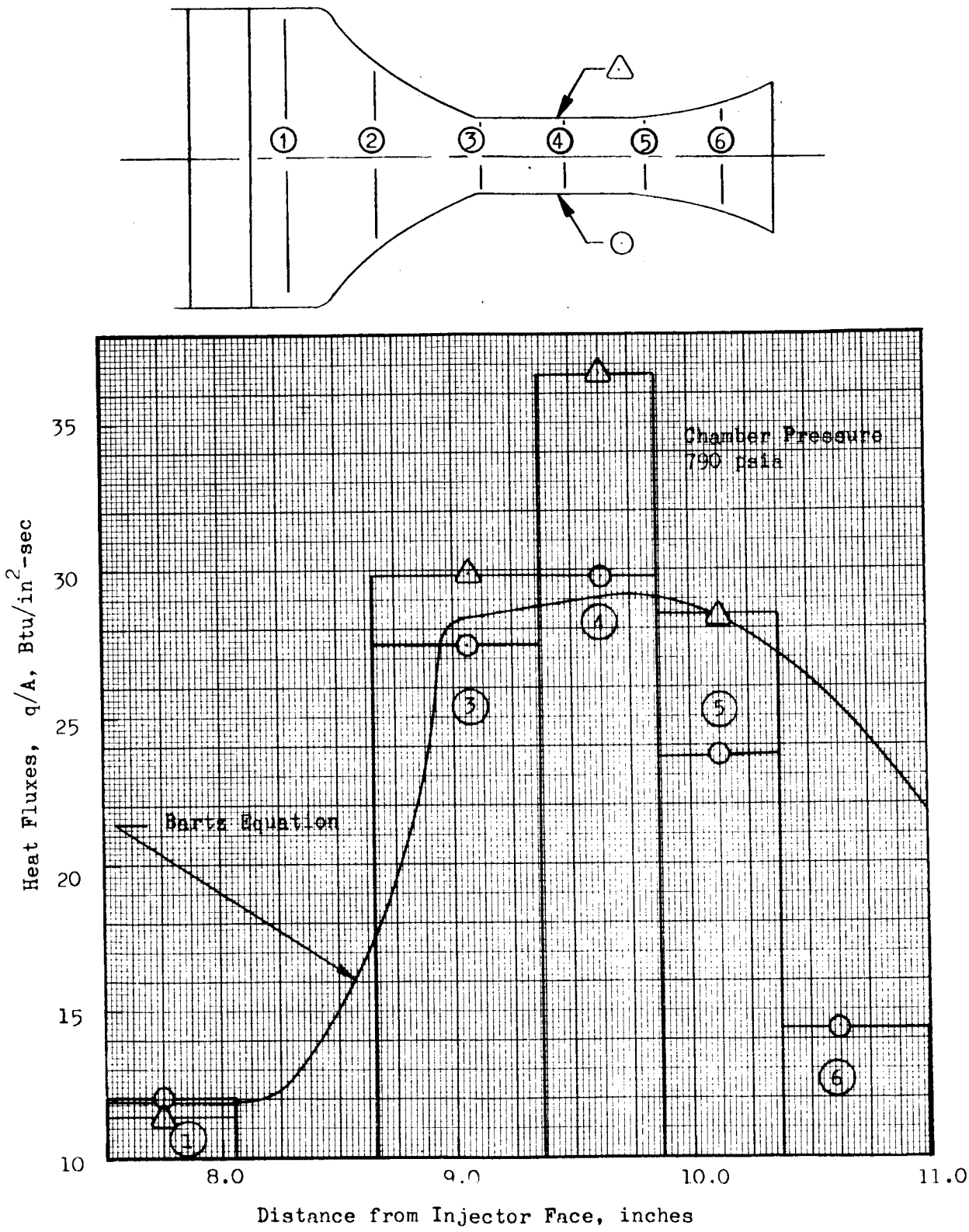

Figure 117. Nozzle Heat Flux Distribution for Test No. 006

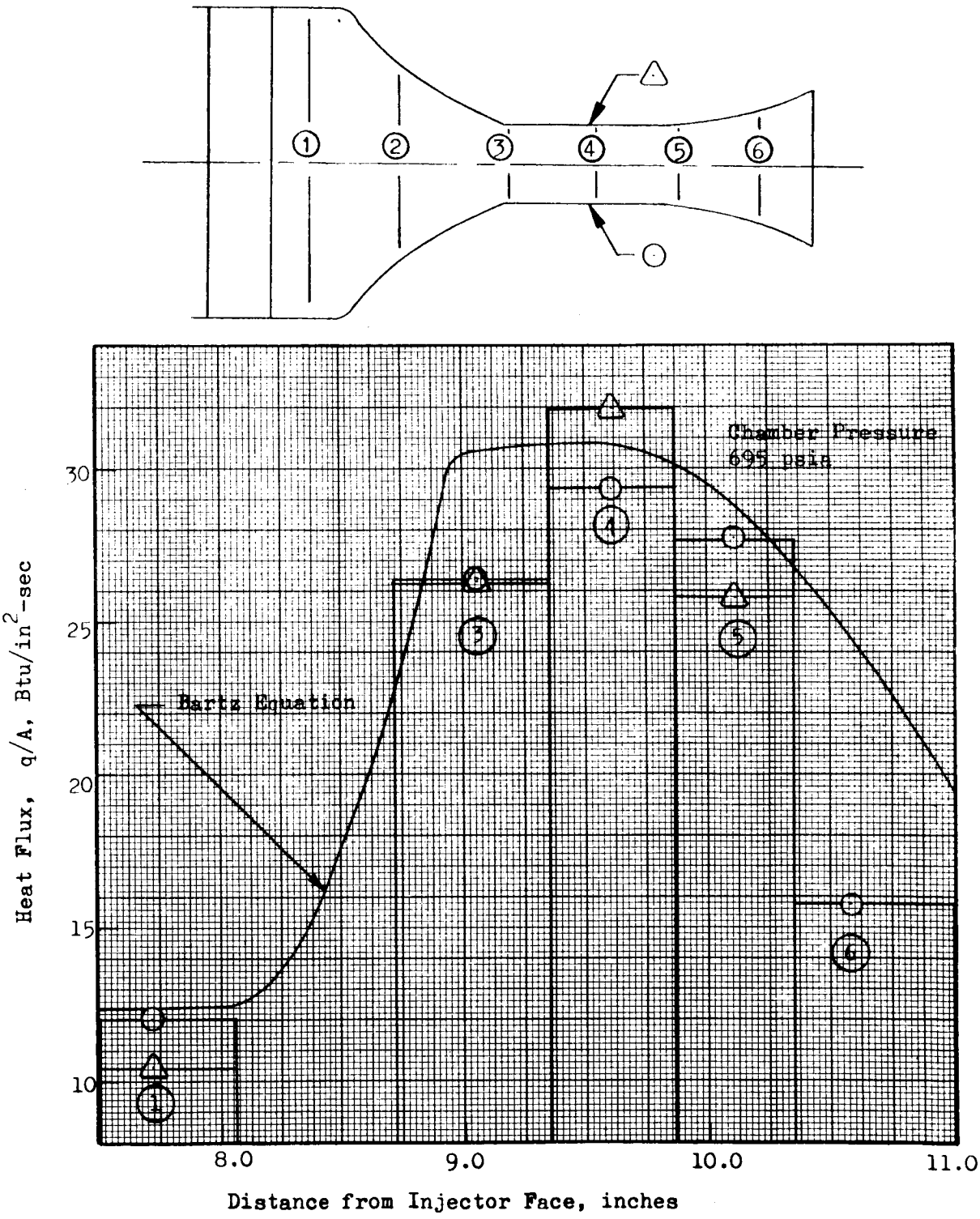

Figure 118. Nozzle Heat Flux Distribution for Test No. 007

Values of theoretical frozen characteristic velocity and the combustion gas stagnation temperatures were obtained from the Rocketdyne performance computer program. The experimental characteristic velocity value for each test was obtained by the following expressions which assumed isentropic flow in the nozzle:

$$c^*_{actual} = \frac{\left[(P_c)_{o \text{ at station } 1}\right] A_t \, g_c}{W_g} \tag{343}$$

The nozzle inlet stagnation chamber pressure was calculated in terms of the measured injector-end static pressure by the following relationship (Ref. 65)

$$(P_c)_o = \frac{\left[1 + \left(\frac{\varkappa-1}{2}\right)Ma^2\right]^{\frac{\varkappa}{\varkappa-1}}}{1 + \varkappa (Ma)^2} \, (P_{inj})_{static} \tag{344}$$

Using the appropriate heat balance equations, the gas-side wall temperatures were calculated at each nozzle station by:

$$(T_{wg})_x = \frac{\left[(q/A)_{measured} \, (t)\right]_x}{k} + (T_{wc})_x \tag{345}$$

where

$$(T_{wc})_x = \frac{\left[(q/A)_{measured} \, (A_g)\right]_x}{A_c \, h_c} + T_c \tag{346}$$

The coolant-side heat transfer coefficient (h_c) was calculated by the Rocketdyne correlation:

$$Nu = \frac{h_c \, D}{k} = 0.005 \, Re^{0.95} \, Pr^{0.4} \tag{347}$$

In several instances, the calculated value for the coolant-side wall temperature (T_{wc}) exceeded the water saturation temperature at the existing pressure. In these cases, a value of T_{wc} equal to the saturation temperature plus 30 F was used to determine the gas-side wall temperature (T_{wg}). Values for T_{wc} varied from 300 to 600 F during the calorimetric test firing series. Similarly, the calculated values for T_{wg} ranged from 1150 to 1375 F at the nozzle throat. The throat area remained constant throughout the experimental test program without evidence of copper wall melting.

Excellent agreement was obtained between the experimental heat flux data and the Bartz calculations at nozzle station 1 indicating that the hot-gas flow was probably fairly well developed. Station 2 test data were not obtained as mentioned previously. The experimental data for station 3 were generally lower than the predicted Bartz values. This discrepancy may have been due to the nozzle geometry in this region. The station 3 water passages cooled a portion of the converging nozzle section as well as a portion of the constant area throat section. These varying nozzle dimensions were accounted for in the calculation of the Bartz gas-side heat transfer coefficient by the A^*/A and D terms. The calorimetric heat flux calculation, however, considered only the measured wall surface area, independent of the nozzle contraction ratio. The experimental values obtained at this particular location represent, therefore, an average value for the true local heat flux.

As expected, the maximum heat flux occurred at station 4, the nozzle throat location. With the exception of tests No. 005 and 006, good agreement was obtained between the Bartz predictions and the actual recorded heat flux data. The maximum heat flux obtained during the

program, without supplemental mass addition cooling, was 33.2 Btu/in.^{2}-sec. This was the average station 4 value obtained at a chamber pressure of 790 psia. A typical high-thrust rocket engine using a LO_2/LH_2 propellant combination would experience similar nozzle heat fluxes at approximately 1750-psia chamber pressure (Ref. 1), the established feasibility limit for complete regenerative cooling with this propellant system.

The station 5 test results, compared with the theoretical predictions, are similar to the station 3 results. The water-coolant passages were common to both the constant throat area region of the nozzle and the beginning of flow divergence.

The greatest discrepancy between the Bartz analytical predictions and the experimental results occurred at station 6; the test values were consistently 60 to 70 percent lower than the predictions. A similar trend was reported by Welsh (Ref. 66) with a small motor burning 80-percent aniline/20-percent furfuryl alcohol fuel and red fuming nitric acid oxidizer. Most of the discrepancy noted was ascribed to the insulating carbon deposition. This could not be the present case with LO_2/GH_2 propellants. Further, the triethylboron hypergolic fluid used during all tests burned cleanly without residue deposition.

Combustion gas flow separation from the nozzle walls upstream of station 6 would cause a reduction in the measured heat flux. The nozzle pressure required to cause the hypothesized separation was calculated by the following empirical correlation (Ref. 67)

$$P_{sep} = 0.3\, P_a + 12\, \frac{P_a^{2.9}}{P_o^{1.9}} - 8 \times 10^{-4}\, P_o \qquad (348)$$

The calculated pressure suggests that flow separation could not occur in the existing nozzle contour. If the nozzle area at station 6 were approximately 10 times larger than actual, flow separation would occur.

Another cause for the observed phenomena might be that the combustion reactions were not completed in the relatively short chamber. However, since the calculated combustion efficiencies were consistently high, this does not appear likely

Another consideration was that the gas-side nozzle wall surface area at station 6 was large with respect to the water-coolant surface area. Therefore, a proportionately larger heat sink was available for conductive heat transfer to the copper nozzle block with a corresponding reduction in measured heat transfer to the cooling water.

Perhaps the most plausible explanation for the observed deviation in heat flux from the Bartz predictions is that the test nozzle cross section was rectangular in shape. As indicated by Eq. 330, the hydraulic diameter was used in calculating the gas-side heat transfer coefficients. According to Schlichting (Ref. 7) the applicability of the hydraulic diameter concept has been verified experimentally only up to Mach 1. This suggests that possibly another correlation relating the boundary layer and combustion gas velocity profiles should be used in noncircular nozzles for supersonic flow.

There was also a difference in the heat flux measurements between the upper and lower nozzle wall surfaces. This trend was consistent between tests for the same station location. Adjacent stations on the same surface, however, were not consistently higher or lower. These relatively

small differences were attributed to instrumentation discrepancies. The data shown in Table 23 represent the average heat flux values obtained at each axial station.

The experimental heat flux data from all of the calorimetric test firings are plotted in Fig. 119 through 123 for each discrete nozzle station. A least-squares linear correlation was obtained and drawn through each set of data. It is obvious from these data that the rate of change in measured heat flux with respect to changes in chamber pressure vary along the nozzle length. The observed slope $[\Delta(q/A)/\Delta P_c]$ is shown for each discrete nozzle location in Fig. 124.

SUPPLEMENTAL COOLING RESULTS

The calorimetric heat flux distribution in the nozzle was obtained for each supplemental cooling test to determine the relative effectiveness of each individual method. The difference between the measured calorimetric heat flux $[(q/A)_{water}]$ during the test firings with mass transfer addition and the extrapolated values of Fig. 119 through 123 for no mass transfer cooling $[(q/A)_{total}]$ was related to the respective cooling effectiveness at each nozzle station. The heat transfer effectiveness was defined as the percent reduction in the total heat flux by the utilization of supplemental cooling techniques.

$$\text{Percent Effectiveness} = 100 \left[\frac{(q/A)_{total} - (q/A)_{water\ coolant}}{(q/A)_{total}} \right] \tag{349}$$

$$\text{Percent Effectiveness} = 100 \left[\frac{(q/A)_{film\ coolant}}{(q/A)_{total}} \right] \tag{350}$$

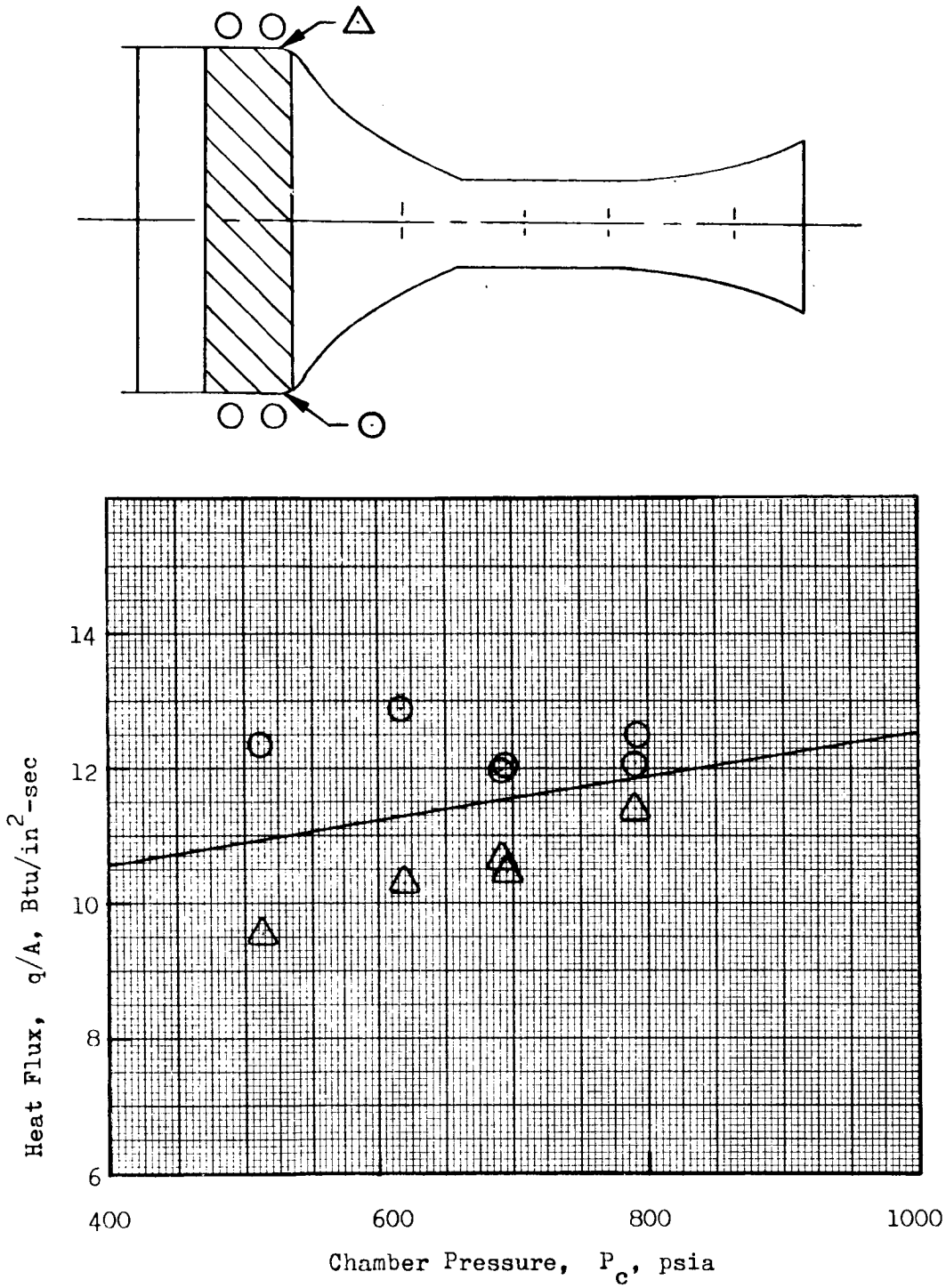

Figure 119. Calorimetric Nozzle Heat Flux at Station 1

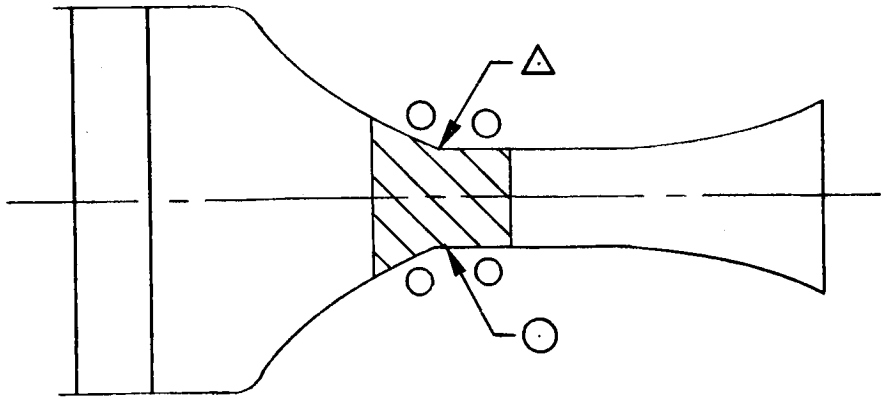

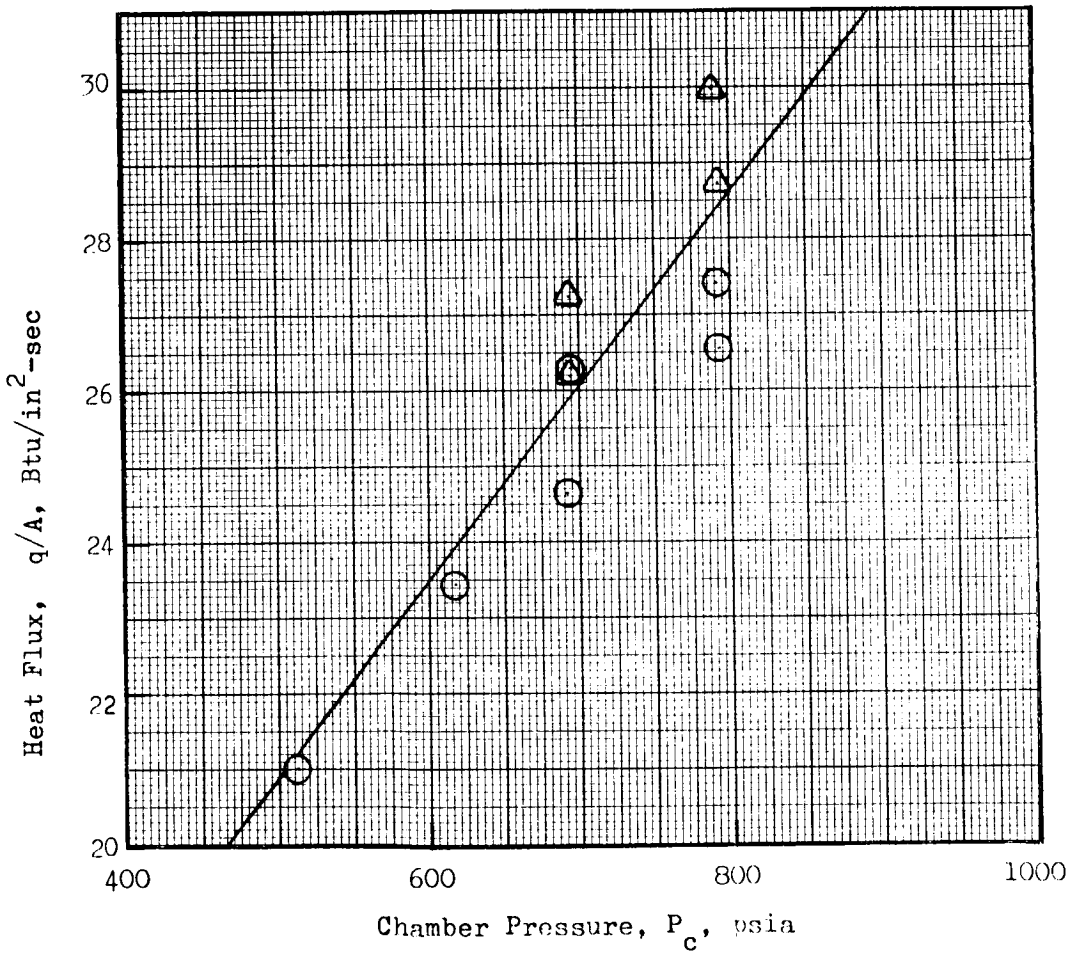

Figure 120. Calorimetric Nozzle Heat Flux at Station 3

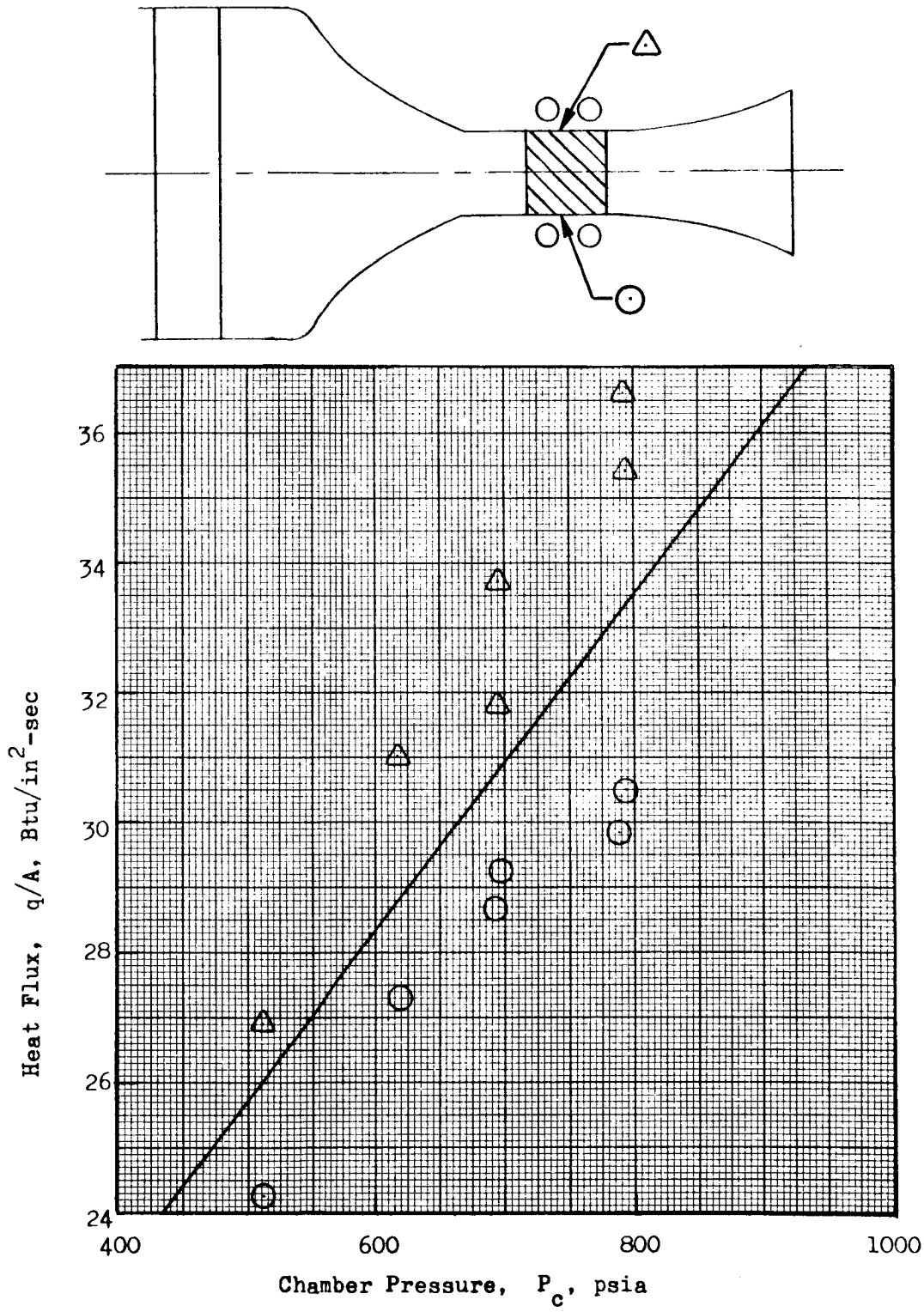

Figure 121. Calorimetric Nozzle Heat Flux at Station 4

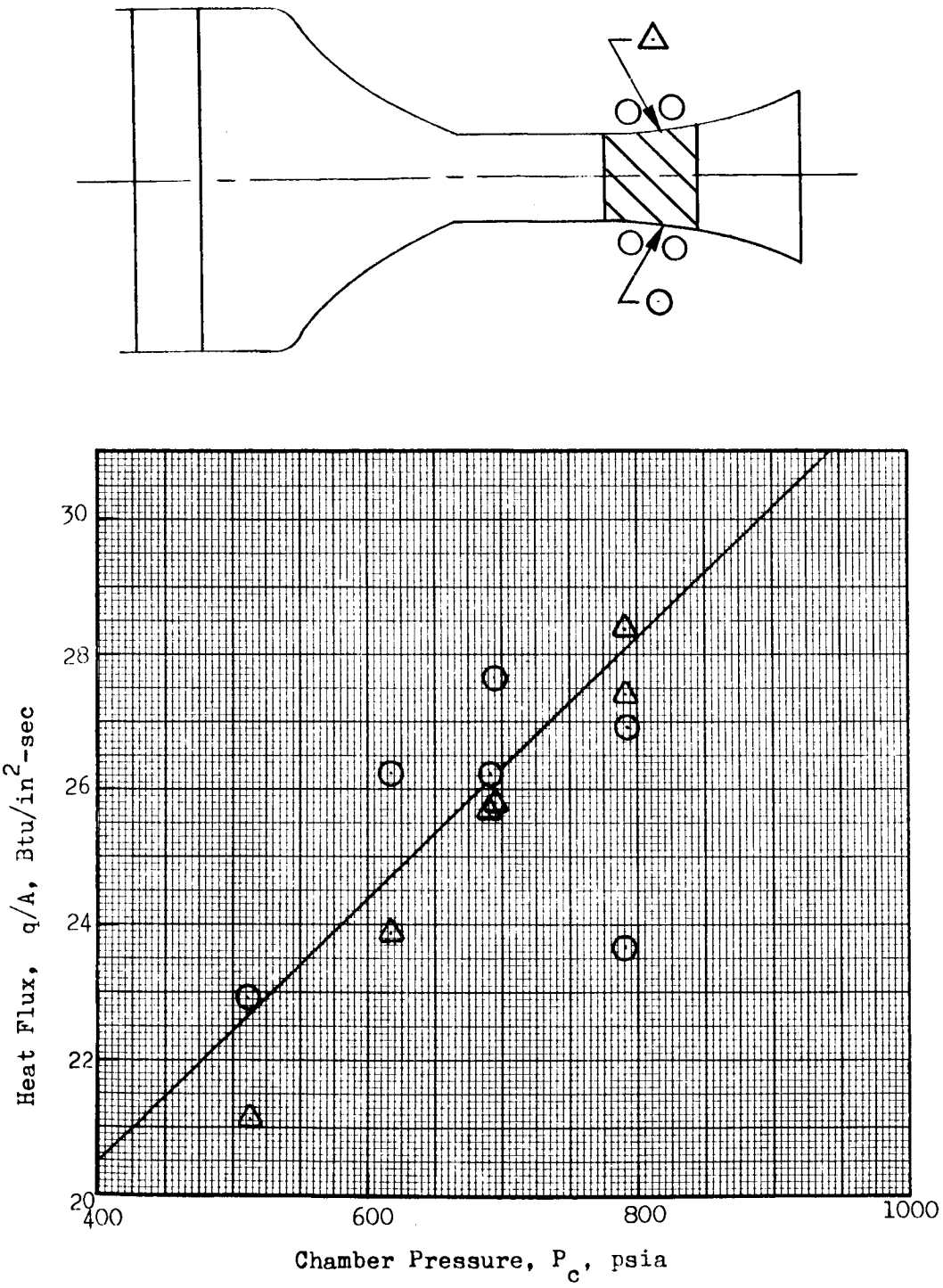

Figure 122. Calorimetric Nozzle Heat Flux at Station 5

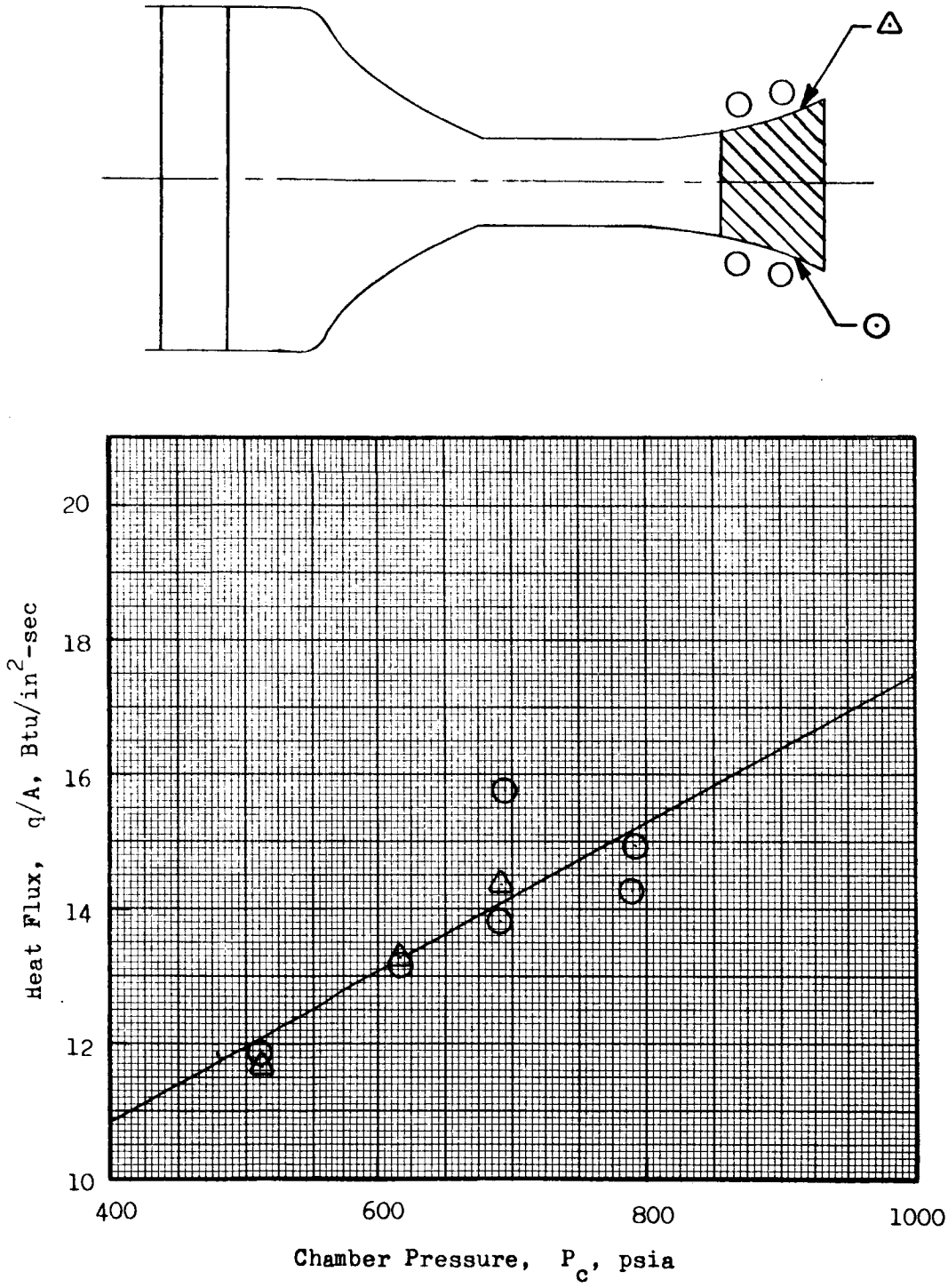

Figure 123. Calorimetric Nozzle Heat Flux at Station 6

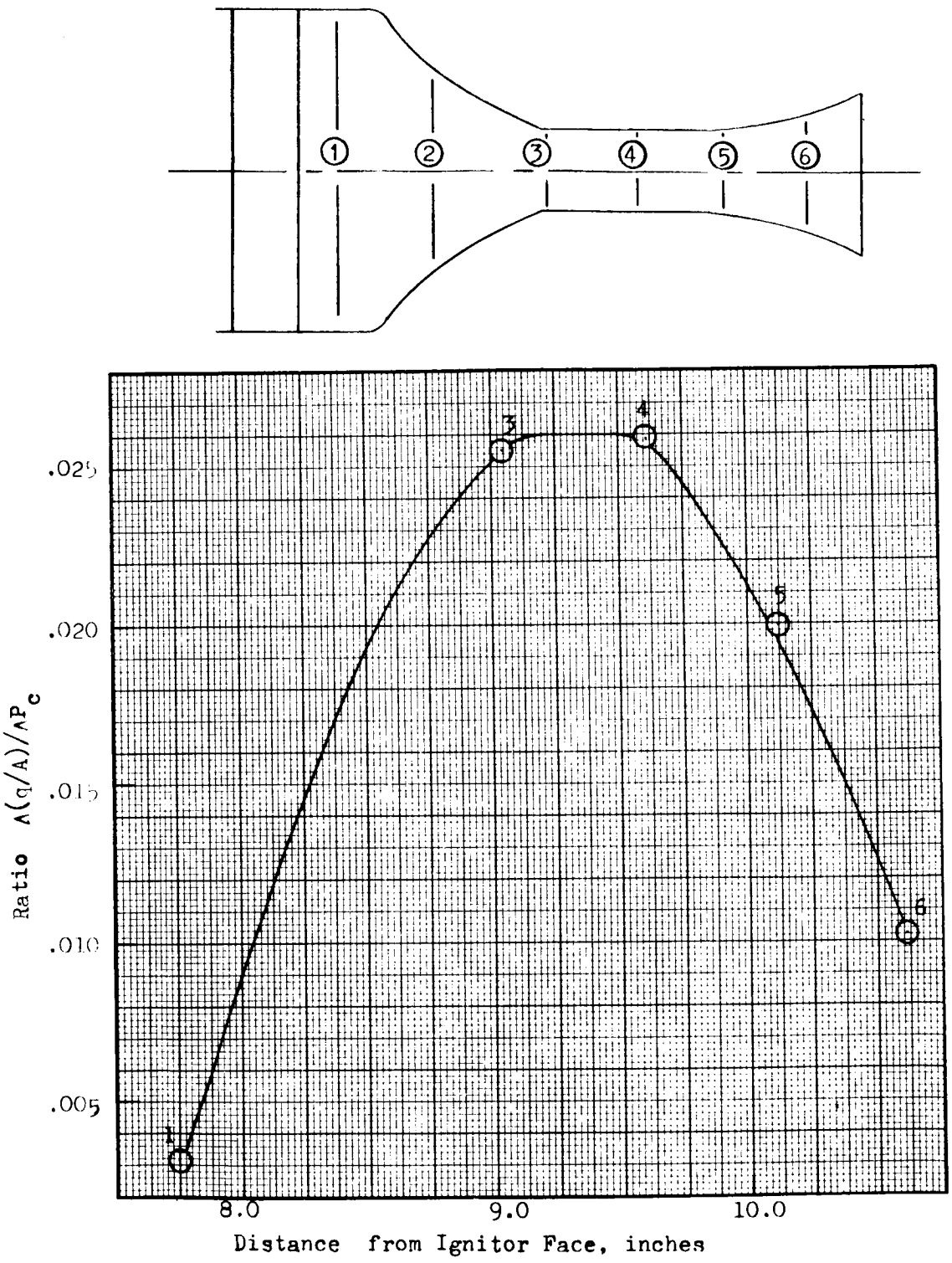

Figure 124. Effect of Chamber Pressure on Heat Flux

The effectiveness of the three supplemental cooling methods evaluated are shown in Fig. 125. Tests No. 008 and 011 were made with similar film-coolant flowrates in terms of the percent of total propellant flowrate through the coaxial injector. On this comparison basis, the film-cooled tangential slot method was more effective in reducing nozzle heat flux than the transpiration-cooling technique. Comparing tests No. 011 and 012, approximately the same effectiveness was obtained for both runs. However, the film-coolant percent flowrate for test 012 was 15.48 percent, compared to only 10.69 percent for test 011. Therefore, the effectiveness of the film-cooled section with tangential slot injection was greater than the radial-hole method. This conclusion is strengthened by the results of tests No. 012 and 010, which were made at approximately the same percent film-coolant flowrates.

As discussed previously, inspection of the motor hardware after test 011 revealed that a portion of the porous coaxial jet injector face had become lodged in the chamber nozzle throat. The effectiveness curve of Fig. 125 for test 011 is unique and contains a double point of inflection. A probable reason for the indicated reduction in throat heat flux was that the displaced injector face shielded the nozzle walls from the main combustion gas flow.

Calculations were made to verify that the indicated reductions in nozzle heat fluxes were caused by film-cooling phenomena and not by reductions in the combustion gas temperature due to lower chamber mixture ratios. Assuming the gaseous hydrogen film coolant mixed intimately with the main combustion gas stream and reacted completely to reduce the overall chamber mixture ratio, the corresponding recovery temperature (T_{rc}) would be reduced approximately 1000 F. However, an increase in the chamber

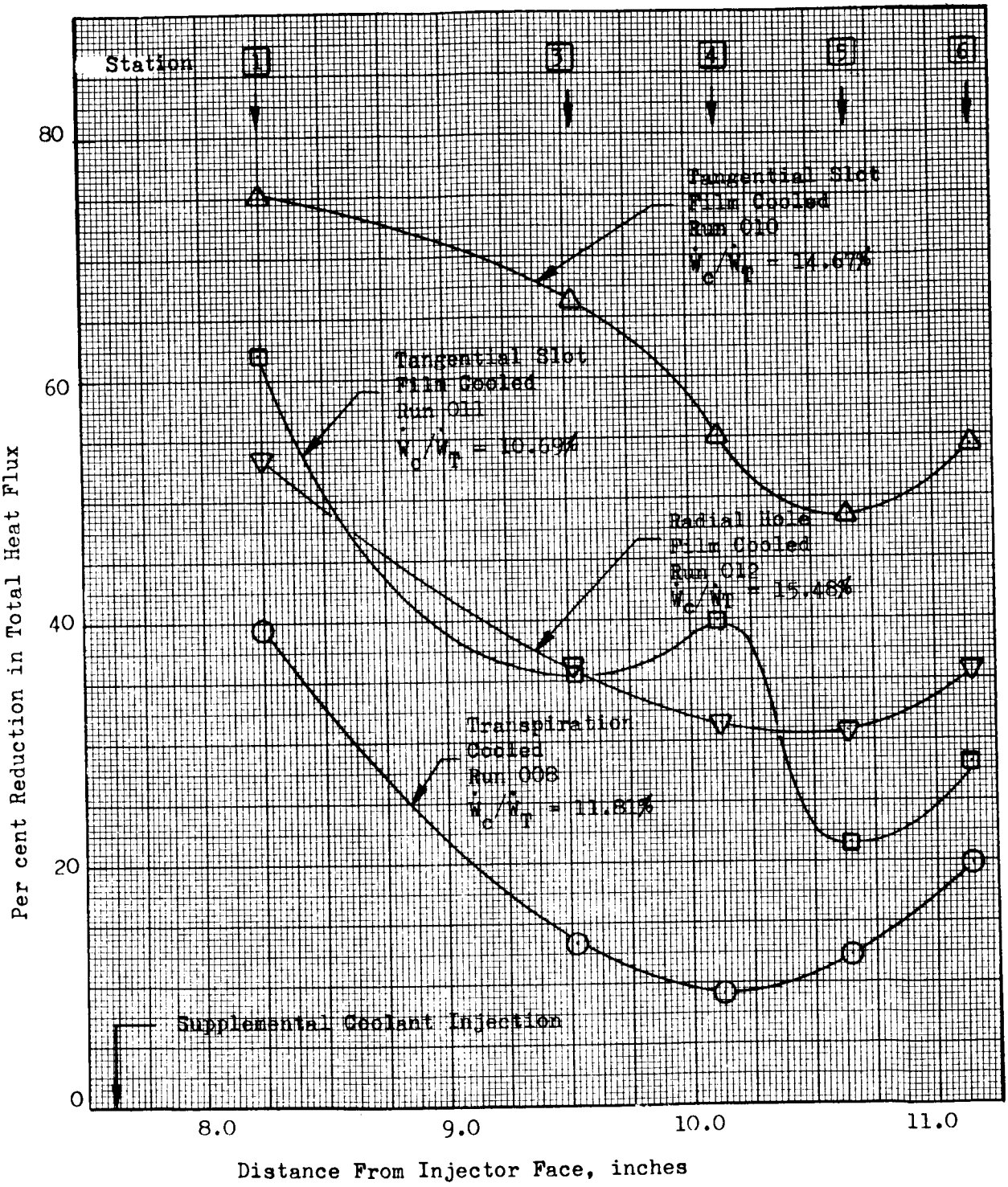

Figure 125. Relative Effectiveness of the Supplemental Cooling Method

mass flowrate would similarly be expected to increase the gas-side heat transfer coefficient. The combined consideration indicates that the total effect would be to maintain approximately similar gas-side heat flux conditions. Therefore, the measured reduction of nozzle heat flux was attributed to the film-cooling effectiveness.

The experimental gas-side wall temperatures were calculated by Eq. 345 and plotted in Fig. 126 through 129. The average wall temperatures at stations 1 and 4 were approximately 300 to 600 F lower, respectively, than those without film cooling.

As postulated in Ref. 1, an infinite conductance was assumed for the film-cooling layer so that the calculated gas-side wall temperature (T_{wg}) was equal to the local film-coolant temperature. The supplemental cooling efficiency for each test was then calculated by performing the following step-wise integration along the gas-side nozzle wall surface:

$$\int dT = \frac{z}{\dot{W}_{fc}\, C_p\, \eta} \int (q/A)_x \, dx \qquad (351)$$

For various assumed constant efficiency (η) values, the incremental change in the gas-side wall temperature was calculated for the corresponding experimental supplemental cooling heat flux. The lines of constant efficiency (η) for each supplemental cooling test are shown in Fig. 126 through 129. The highest efficiencies were obtained for the tangential-slot film-coolant tests. The transpiration method resulted in the lowest efficiency, with the radial-hole film-coolant design intermediate. Equation 351 was also integrated by equating the temperature change to the experimental values and solving for the average coolant efficiency for each nozzle station. These data are given in Table 24.

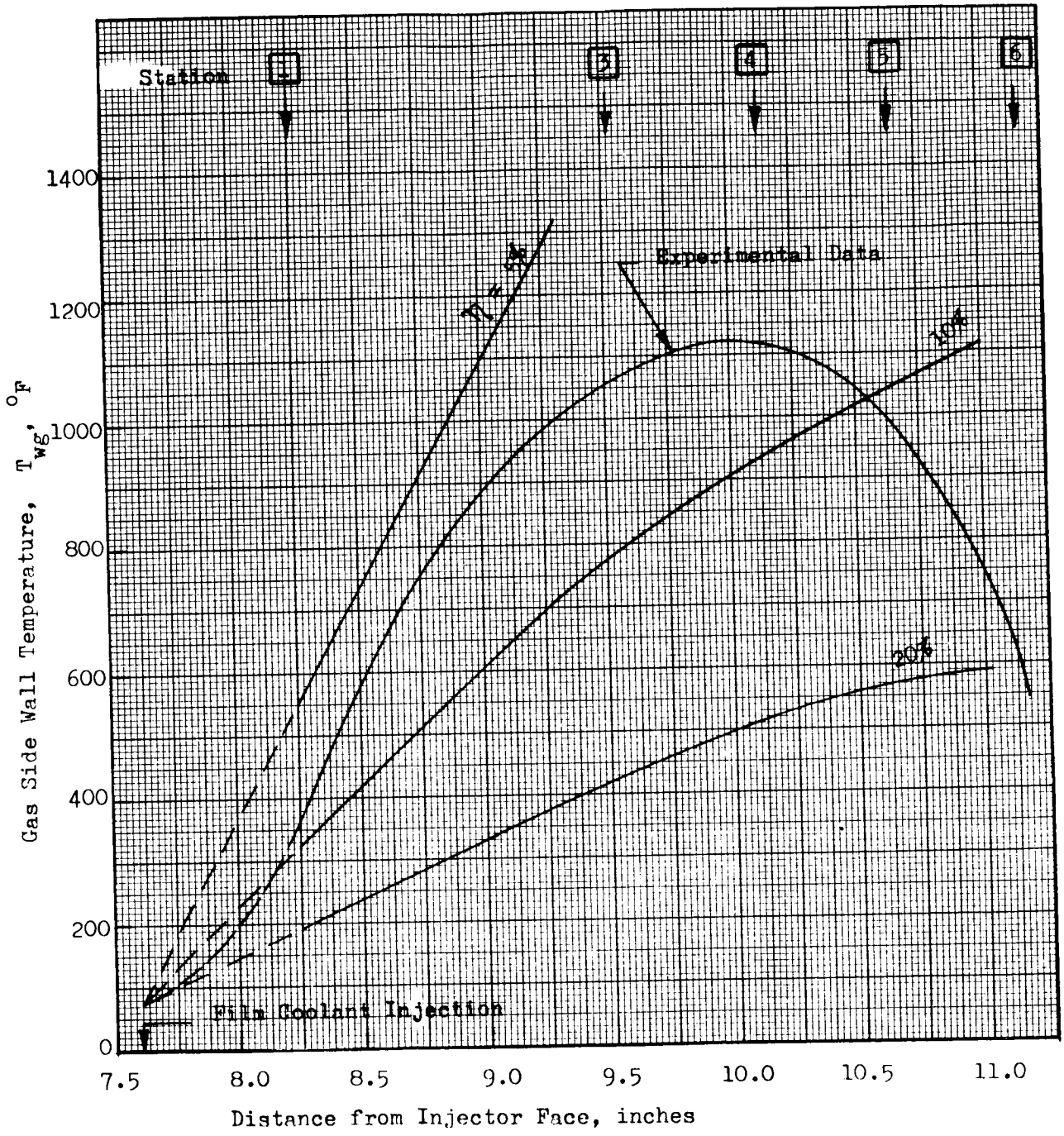

Figure 126. Transpiration-Cooling Efficiency, Test No. 008

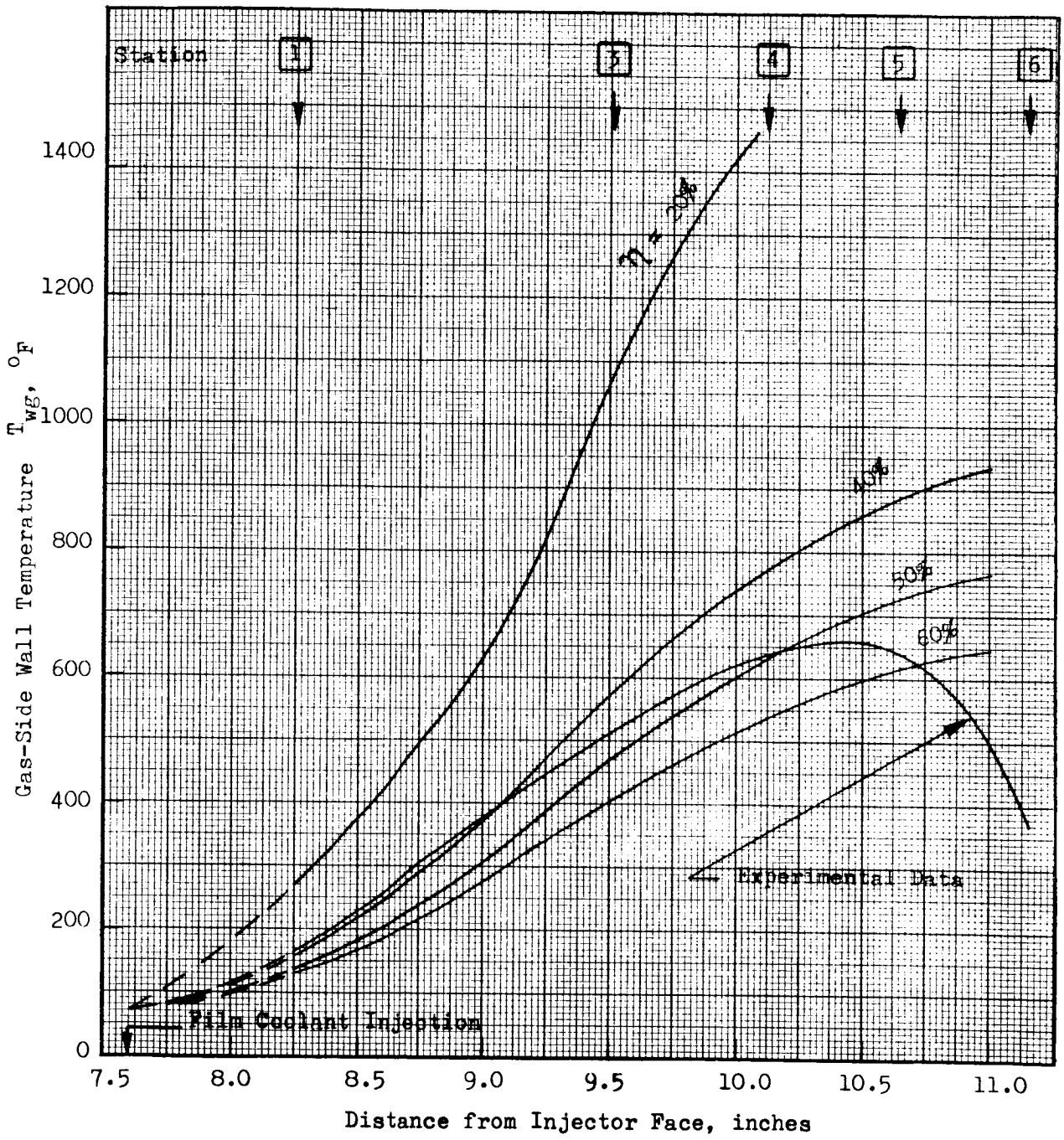

Figure 127. Film-Cooling Efficiency with Continuous-Slot Tangential Injection, Test No. 010

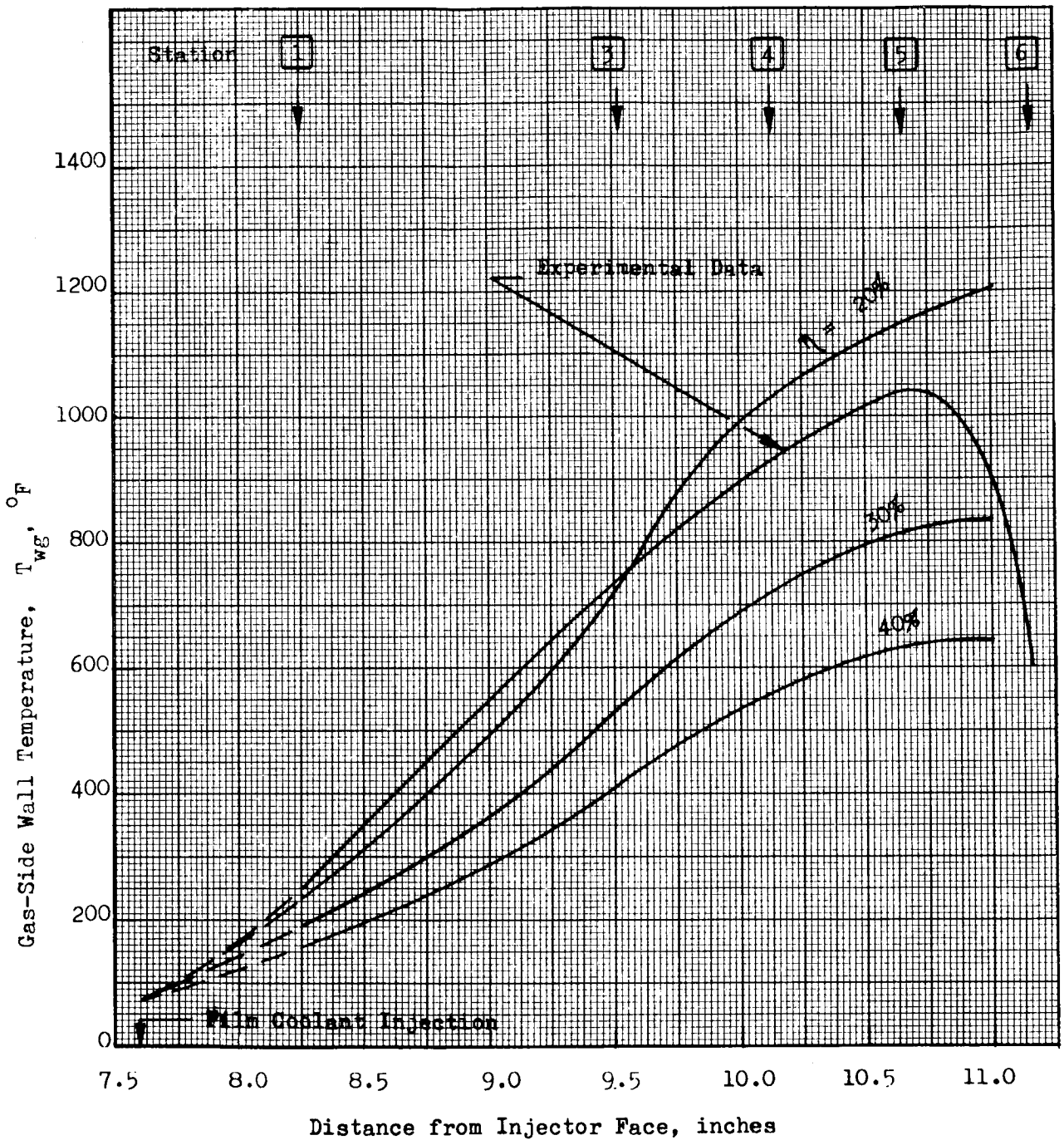

Figure 128. Film-Cooling Efficiency with Continuous-Slot Tangential Injection, Test No. 011

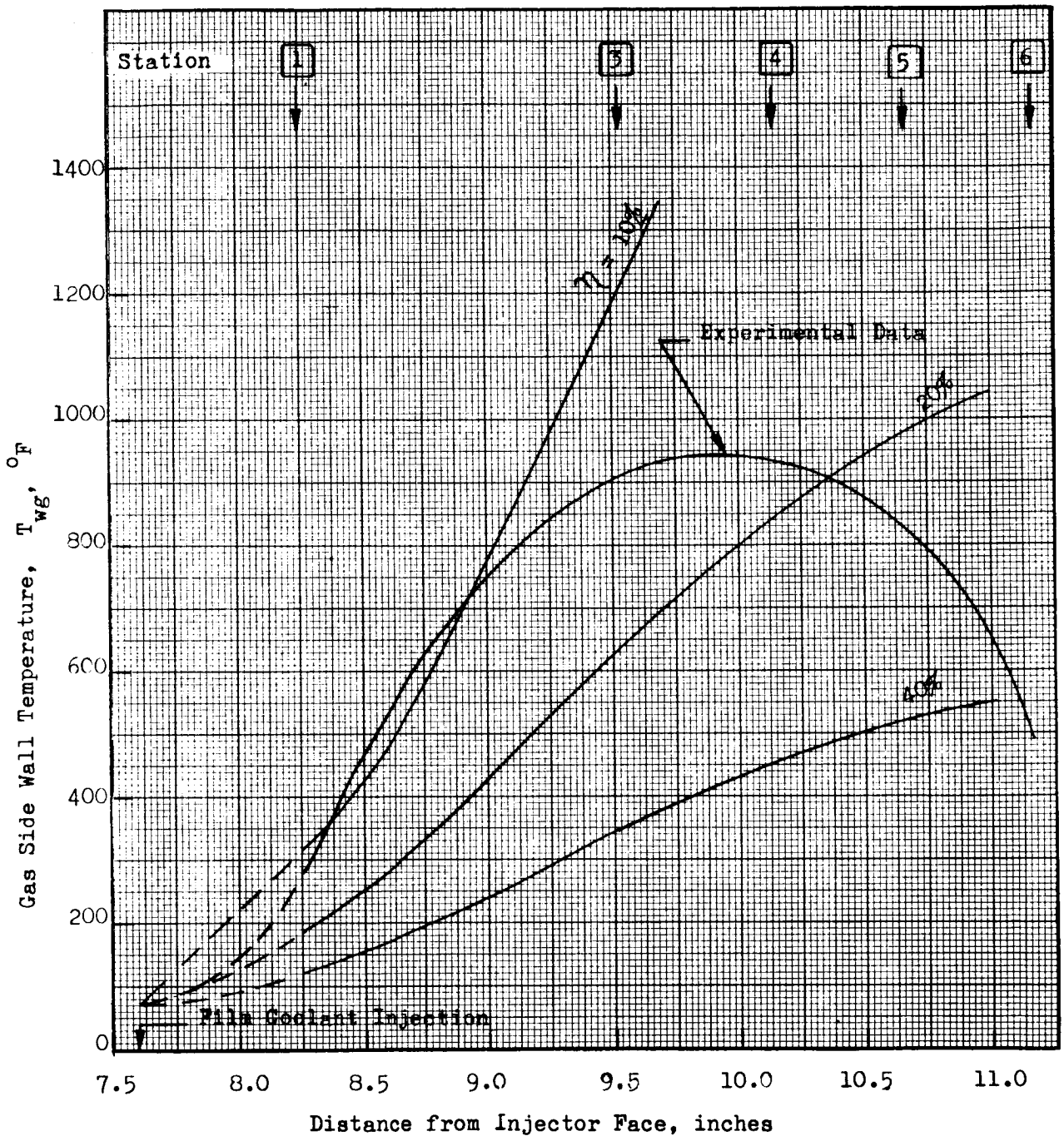

Figure 129. Film-Cooling Efficiency with Radial-Hole Injection, Test No. 012

TABLE 24

SUPPLEMENTAL COOLING EFFICIENCIES

Test Number	Cooling Type	Nozzle Station Cooling Efficiency, percent			
		1	2	3	4
008	Transpiration	7.3	6.9	10.3	20.2
010	Film-Slot	37.9	42.6	63.5	60.3
011	Film-Slot	19.6	16.9	25.9	31.7
012	Film-Radial	12.7	11.3	26.0	----

The cooling efficiencies for test 011 were considerably lower than those for the previous test. The lower efficiencies were probably associated with the separated porous injector face which lodged in the nozzle throat sometime during test 011.

The measured film-cooling efficiencies obtained with the continuous-slot tangential injection technique, especially in test 010, were considerably higher than the predicted values based on the correlation shown in Fig. 28 of Ref. 1. For example, for test 010, the average measured film-cooling efficiency from the nozzle entrance region to the throat area was about 60 percent. For this test, $C_{pc}\ G_c/C_{pg}\ G_g$ was on the order of 0.01, for which Fig. 28 of Ref. 1 predicts a film-cooling efficiency of only about 25 percent.

Therefore, a brief examination of general film-cooling calculational procedures was made to obtain an explanation for the higher experimental film-cooling efficiency.

The basis for thrust chamber film cooling in Ref. 1 was the method of Hatch and Papell (Ref. 31). Their method is based upon the incremental heat balance:

$$C_{pc} \dot{W}_c \frac{d T_c}{d x} = h_g z (T_g - T_c) \tag{352}$$

which integrates to

$$\frac{(T_g - T_c)_x}{(T_g - T_c)_{x_o}} = e^{\frac{-h_g x}{C_{pc}(\dot{W}_c/z)}} \tag{353}$$

The Hatch and Papell general method is fundamentally sound and is simple to apply; however, in the form of Eq. 353, it did not correlate the available data (Ref. 32). To bring data and theory into agreement, Papell had to define x_o as some diffusion distance x' downstream from the coolant slot and introduce a coolant efficiency factor (η_f) which was an empirical function of coolant and mainstream flowrates. Presumably it corrected for "mixing losses" of coolant.

In the early analytical studies of this program, another efficiency factor was defined which combined the diffusion length and relative flowrate corrections of Papell. However, the extrapolation of empirical correction factors to conditions other than those for which the factor has been determined is always uncertain. A short theoretical derivation of a new efficiency factor is presented here that shows that such a factor is fundamentally necessary. Of most importance is the fact that this derivation can be applied both to the adiabatic wall case as considered by Papell and to the combined film and regenerative cooling case which was the subject of the experimental studies described above.

Briefly, the basis for this derivation is the argument that the heat transfer coefficient between a main hot-gas stream and a film of cold gas along a wall should be higher than from a hot-gas stream to a cold wall. The reason is that in the first case the heat does not have to be carried across a laminar film where the resistance is higher. Therefore, η_f defined by:

$$h_g = \frac{h_g'}{\eta_f} \quad \text{or} \quad h_g\Big|_{\text{film cooling}} = \frac{h_g'\Big|_{\text{no film cooling}}}{\eta_f} \tag{354}$$

is the correction factor to be applied to the usual forced convection h_g' in Eq. 353. To derive η_f, reference is made to the following schematic representation of the flows.

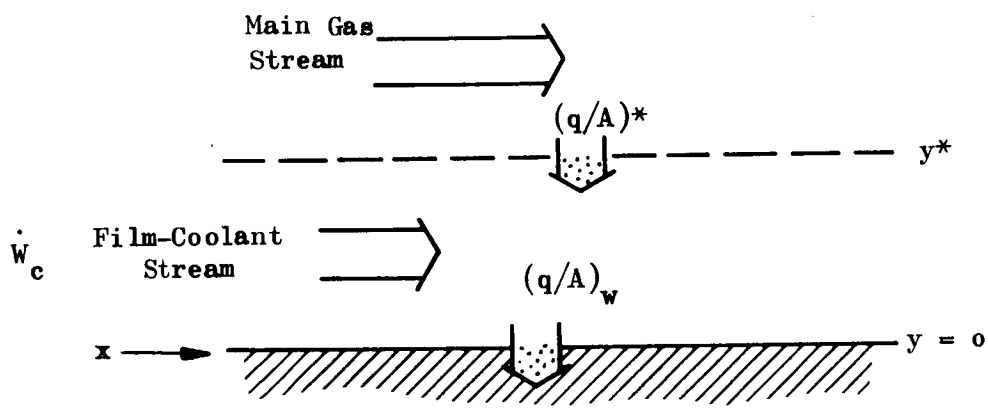

A film-coolant layer of thickness y* is flowing along the wall, receiving a heat flux (q/A)* from the main gas stream. For simplicity, film-coolant properties are assumed to be the same as the main stream. Then at any point y_1 in the main gas stream, the gas temperature is given by:

$$T_1 - T_w = \int_o^{y^*} \frac{dT}{dy}\, dy + \int_{y^*}^{y_1} \frac{dT}{dy}\, dy \tag{355}$$

assuming that a fully developed flow profile exists from the wall through the hot-gas stream.

Now a basic relation for turbulent forced convection is:

$$q/A = (k + \rho C_p \epsilon) \frac{dT}{dy} \tag{356}$$

so that Eq. 355 can be written

$$T_1 - T_w = \int_o^{y*} \frac{q/A}{k + \rho C_p \epsilon} dy + \int_{y*}^{y_1} \frac{q/A}{k + \rho C_p \epsilon} dy \tag{357}$$

For the film cooling model as shown above, Eq. 357 becomes

$$T_1 - T_w = \int_o^{y*} \frac{\left[(q/A)_w + \int_o^y \rho C_p u \frac{\partial T}{\partial x} dy\right] dy}{k + \rho C_p \epsilon} + \int_{y*}^{y_1} \frac{(q/A)*}{\rho C_p \epsilon} dy \tag{358}$$

where the heat flux in the film-coolant layer is separated into components due to film cooling (and to wall heat flux) and where the molecular conductivity term has been dropped in the mainstream where conditions are highly turbulent. Equation 358 is first rewritten as:

$$T_1 - T_w = \frac{(q/A)_w}{(q/A)*} \int_o^{y*} \frac{(q/A)^*}{k + \rho C_p \epsilon} dy + \int_o^{y*} \frac{\left[\int_o^y \rho C_p u (\frac{\partial T}{\partial x}) dy\right] dy}{k + \rho C_p \epsilon} + \int_{y*}^{y_1} \frac{(q/A)*}{\rho C_p \epsilon} dy \tag{359}$$

and then converted to dimensionless form:

$$T_1^+ = \frac{(q/A)_w}{(q/A)^*} \int_0^{y^{*+}} \frac{dy^+}{\frac{1}{Pr} + \epsilon^+} + \left(\frac{\partial T^+}{\partial x^+}\right) \int_0^{y^{*+}} \frac{\left[\int_0^{y^+} u^+ dy^+\right] dy^+}{\frac{1}{Pr} + \epsilon^+} + \int_{y^{*+}}^{y_1^+} \frac{dy^+}{\epsilon^+} \tag{360}$$

where

$$T^+ = \frac{(T - T_w)\, C_p \sqrt{\tau \rho}}{(q/A)^*}, \quad u^+ = \frac{u}{\sqrt{\tau/\rho}}, \quad y^+ = \frac{\sqrt{\tau/\rho}\, y}{\mu/\rho}$$

$$\epsilon^+ = 0.012\, u^+ y^+ \quad \text{for } y^+ < 26 \quad \text{and } \epsilon^+ = 0.36\, y^+ \text{ for } y^+ > 26$$

The expressions for eddy diffusivity are those of Deissler (Ref. 68). If the Prandtl number for gases is assumed 1.0, then the first integral is equal to u^+ for no film cooling at $y = y^{*+}$ and the third integral can be evaluated as the usual logarithmic turbulent core relationship. Equation 360 becomes

$$T_1^+ = \frac{(q/A)_w}{(q/A)^*} u^+_{y^{*+}} + \frac{\partial T^+}{\partial x^+} F(y^{*+}) + \frac{1}{0.36} \ln (y_1^+/y^{*+}) \tag{361}$$

where

$$F(y^{*+}) = \int_0^{y^{*+}} \frac{\left[\int_0^{y^+} u^+ dy^+\right] dy^+}{1 + \epsilon^+} \quad \text{is numerically evaluated} \tag{362}$$

From the energy balance:

$$\rho C_p \frac{\partial T}{\partial x} \int_0^{y*} u \, dy = (q/A)* - (q/A)_w = (q/A)* \left[1 - \frac{(q/A)_w}{(q/A)*} \right] \tag{363}$$

$$\frac{\partial T^+}{\partial x^+} = \frac{1 - (q/A)_w/(q/A)*}{\dot{W}^+} \quad \text{for } \dot{W}^+ = \int_0^{y*^+} u^+ \, dy^+ \tag{364}$$

so that the equation basic to film cooling is given by:

$$T^+ = \frac{(q/A)_w}{(q/A)*} u^+_{y*^+} + \left[1 - \frac{(q/A)_w}{(q/A)*} \right] \frac{F\left(y*^+\right)}{\dot{W}^+} + \frac{1}{0.36} \ln \left(y^+/y*^+\right) \tag{365}$$

Equation 365 is plotted in Fig. 130 for a range of $y*^+$ with $(q/A)_w = 0$ (complete film cooling) and in Fig. 131 for $(q/A)_w = 0.5 \cdot (q/A)*$ (combined film and regenerative cooling). For comparison, T^+ is also shown for no film cooling ($y*^+ = 0$). It is seen that T^+ is lower with film cooling. Application of Eq. 365 is made from the basic convection relationship

$$\frac{h_g}{h_g'} = \frac{St}{St'} = \frac{h_g/\rho C_p u_b}{h_g'/\rho C_p u_b} \tag{366}$$

which applies for practical film-cooling situations where the percentage film coolant is sufficiently low so that $(T_g - T_w)$ and u are not appreciably affected. Now

$$St = \frac{1}{T^+_{avg}} = \frac{1}{\int_0^A \frac{T^+ u^+}{A} \, dA} \tag{367}$$

so that

$$\frac{h_g'}{h_g} = \frac{T^+_{avg}}{T^{+\prime}_{avg}} = \eta_f \tag{368}$$

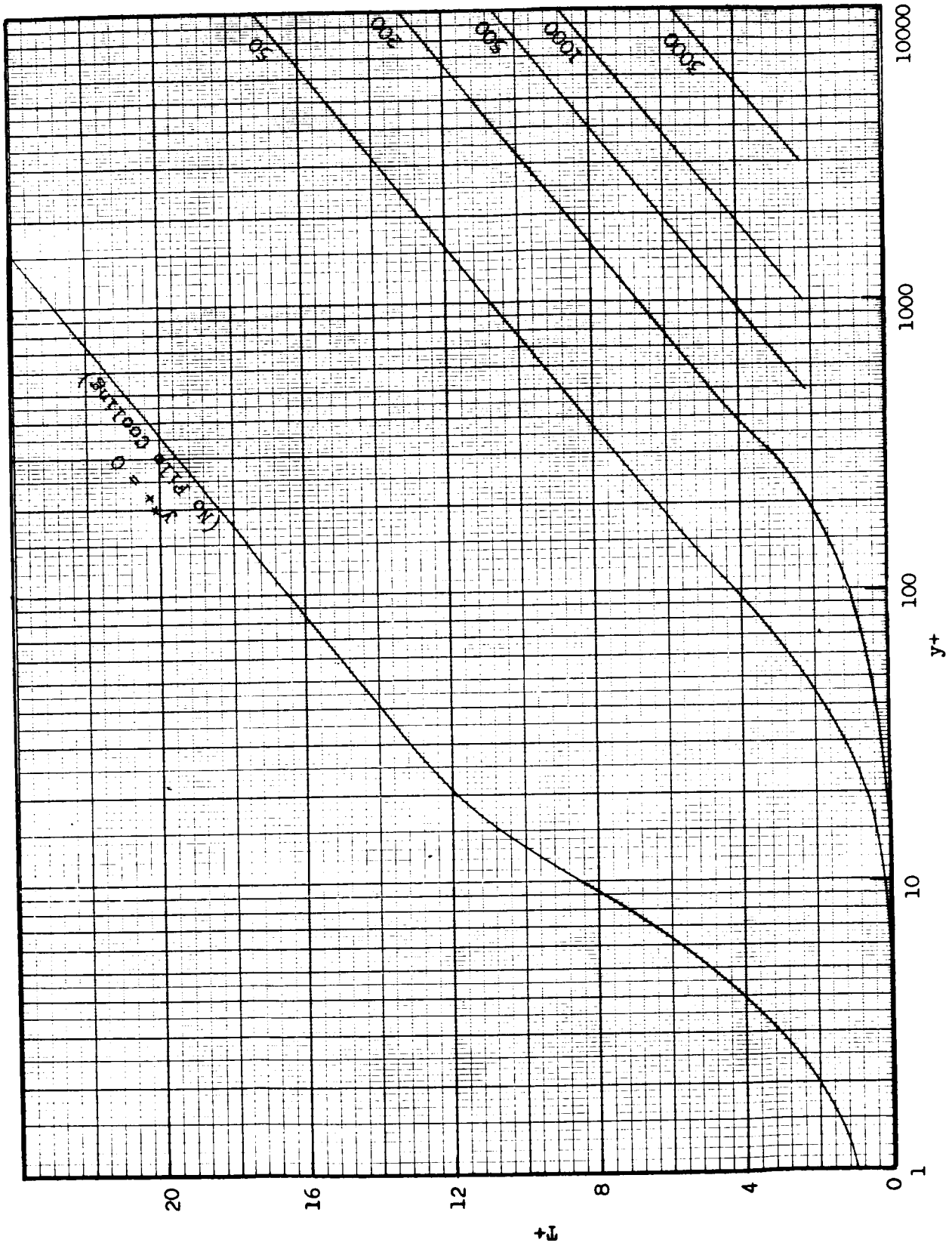

Figure 130. Variation of T^+ for Adiabatic Wall Conditions

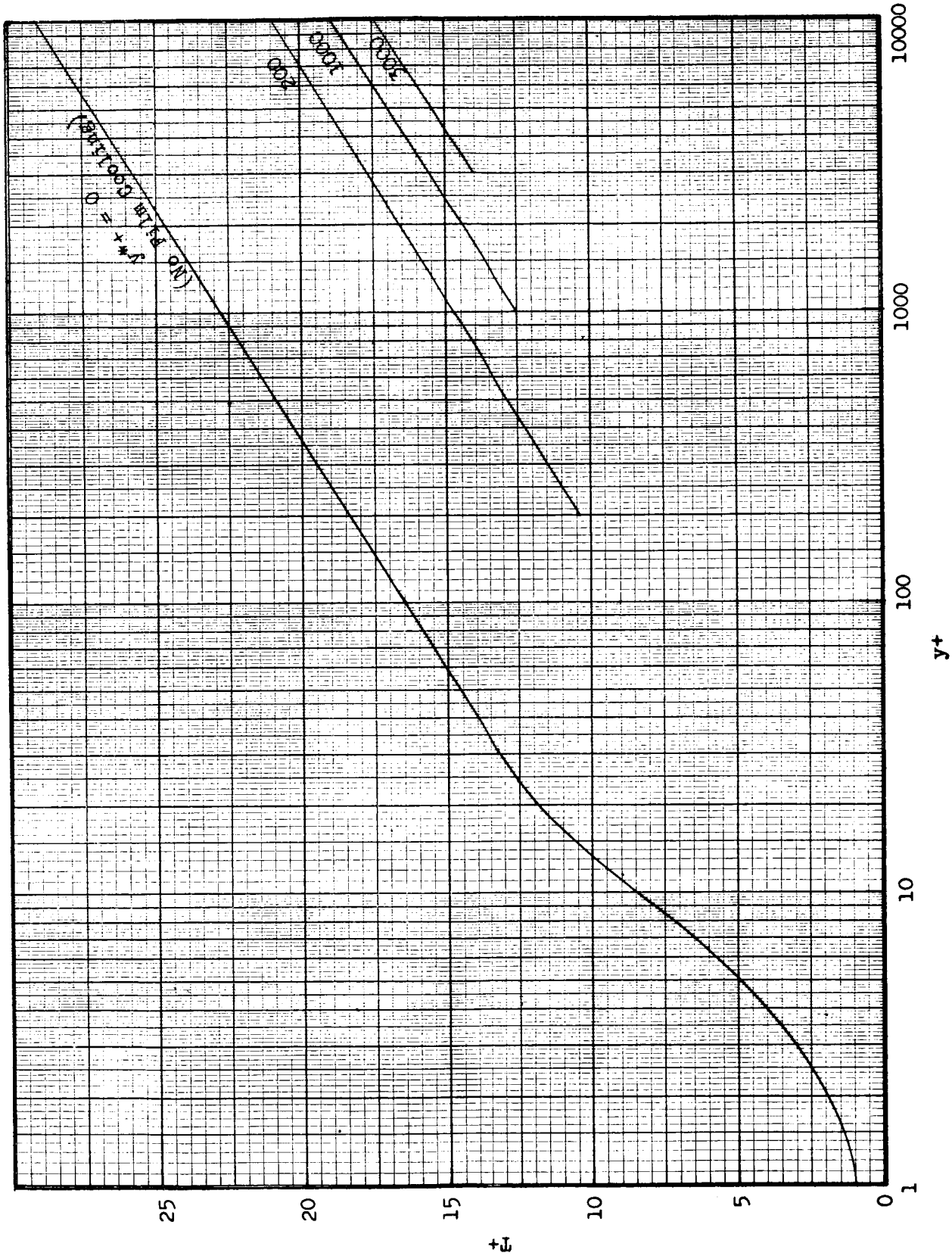

Figure 131. Variation of T^+ with 50 Percent of Total Heat Flux Absorbed by Regenerative Cooling

Therefore, η_f is obtained by integration of the dimensionless temperature profiles of the type shown in Fig. 130 and 131 in accordance with Eq. 367. An example of calculated η_f for main gas Reynolds numbers of 1 and 5 million and for complete and 50-percent film cooling is shown in Fig. 132. The values of η_f by this analysis are seen to be the same range of magnitude as the empirical η_f. The significant feature of Fig. 132 is that it shows film-cooling efficiency should be greatest when combined with regenerative cooling, a fact not established by the empirically obtained η_f but observed in the experiments discussed above.

COMBUSTION CHAMBER AND FLOW DEVELOPMENT SECTION HEAT FLUX

Average heat flux measurements were also obtained in the combustion chamber and flow development sections for tests 009 through 012. These data (Table 23) were obtained upstream of the supplemental coolant chamber injection location. As expected, the flow development gas-side heat flux increased with increasing chamber pressure. The opposite trend was indicated in the combustion chamber section, which suggested that the turbulent flame front may have moved further from the injector face with the increased injection velocities associated with the higher chamber pressures.

CONCLUSIONS

The results of calorimetric firing tests with LO_2/GH_2 indicated that the gas-side heat transfer can be accurately predicted for the high heat flux conditions of high-chamber-pressure operation, particularly for

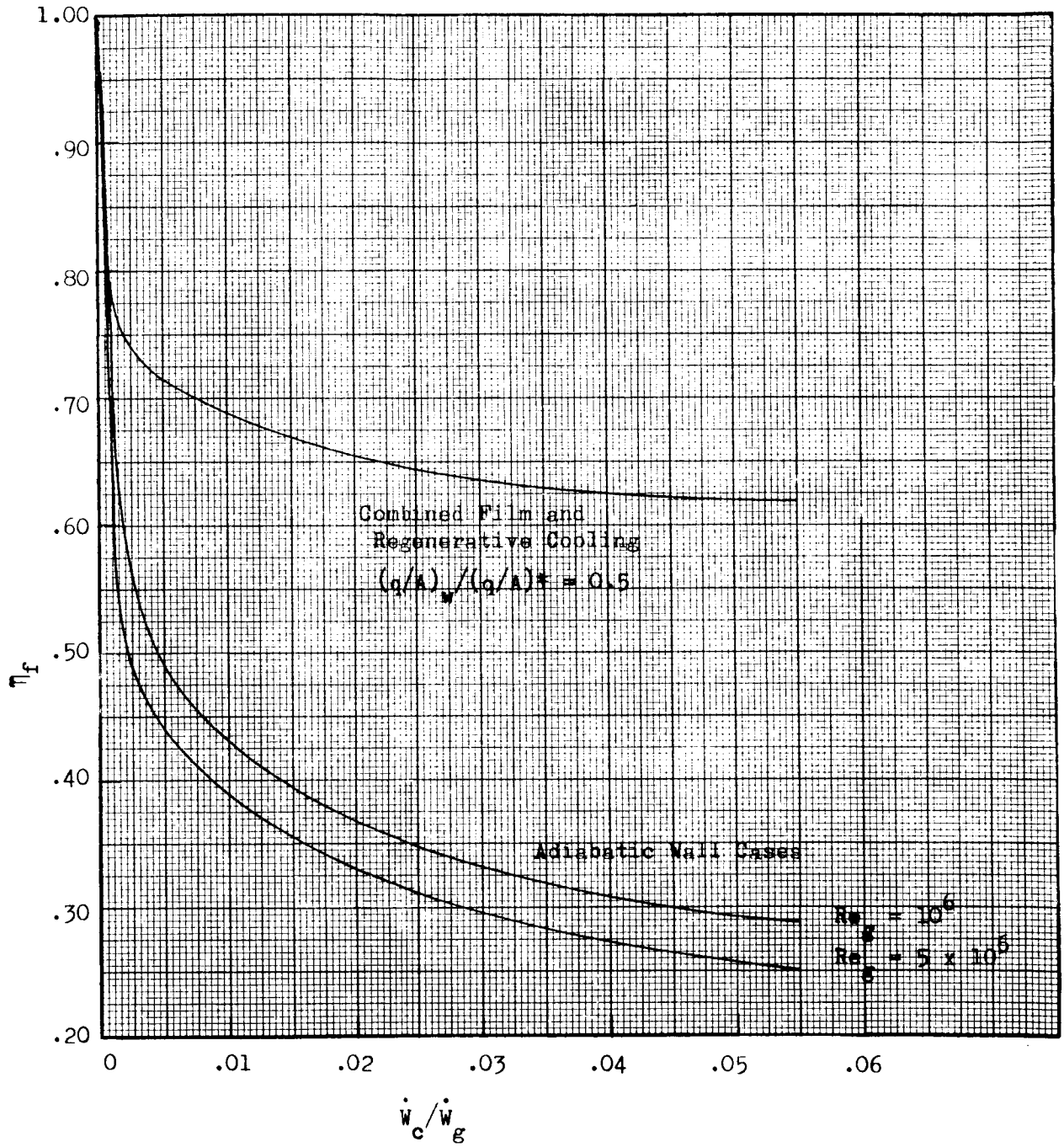

Figure 132. Effect of Partial Regenerative Cooling on Film Cooling Efficiency

the throat region. These results are in contrast to results previously obtained at Rocketdyne (Ref. 69 and 70) during firings with LO_2/RP-1 in a small motor with a 7.35-in.^{2} throat at chamber pressures of 1100 and 2000 psia. For this latter propellant system (Ref. 1) much lower heat fluxes are obtained compared to either the O_2/H_2 system or as predicted by equations such as that of Bartz. For example, in the throat region, the ratio of the measured heat flux to the predicted heat flux for LO_2/RP-1 is about 0.3 at 1100-psia chamber pressure and 0.6 at 2000 psia. The deviations are due to the existence of a gas-side carbon layer thermal resistance. An equation for predicting this resistance is included in Ref. 1.

The use of supplementary mass transfer cooling for the LO_2/LH_2 system appears to be very attractive for extending the feasibility limits of regenerative cooling above the approximate 1750-psia chamber pressure limit. By combining tangential-slot injection film cooling with regenerative cooling, high film-coolant utilization efficiencies can be achieved, which for large-thrust engine applications will result in minimal performance loss. Because of the large effect of gas-side carbon layer resistance with the LO_2/RP-1 system for small-model motors experimental verification of the efficiency of RP-1 mass transfer cooling techniques would be best carried out in relatively large-thrust, high-chamber-pressure engines, where the carbon layer resistance would probably not be present.

THERMAL BUCKLING EXPERIMENTS

Analytical investigations of the operating characteristics of high-chamber-pressure engines indicated that thermal stresses in the nozzle coolant tube bundle may be a limiting factor in engine design. These stresses are of sufficient magnitude so that loading past the tube metal yield point occurs, and inelastic conditions prevail in portions of the tube wall.

Two types of stresses occur in the nozzle coolant tubes. The first of these, inelastic tangential stress, will be described briefly for purposes of orientation. The second type of stress, longitudinal inelastic thermal buckling, comprises the subject of this study.

When a tube is subjected to internal pressure, the wall is placed in tension. Under the correct conditions of temperature and pressure, the tensile stress may be above the yield point, in the plastic region. If, at the same time, a temperature gradient is present across the tube wall, due to conduction of the cooling heat load, the outer surface attempts to expand relative to the inner surface, placing the outer surface in compression. Thus, the condition may exist wherein the inner surface of the coolant tube wall is in the plastic condition in tension, and the outer surface is stressed into the plastic region under compression. Under these conditions, an elastic core remains, but the tube may fail under repeated cycling dependent upon the amount of plasticity induced.

A longitudinal thermal stress is produced in the nozzle coolant tube by the asymmetric heating condition. The hot-gas side of the tube tends to expand relative to the cold side and back walls. The constraint to

this growth imposed by the tube bundle produces an axial or longitudinal thermal stress which may, under severe conditions, cause an inelastic buckling failure. Typical buckling failures are shown in Fig. 34.

Inelastic buckling is differentiated from elastic, or Eulerian buckling by the fact that the failure occurs locally as a ripple on the surface of the tube instead of the entire tube forming a bow. The material will not recover from an inelastic buckle, but assumes a permanent deformed shape because the stress imposed is greater than the yield point.

The present inelastic buckling study described herein was undertaken to investigate some of the parameters that influence inelastic buckling failures. Studies of this nature with tube-wall to tube-radius ratio values of interest in nozzle cooling tubes are nonexistent in the published literature.

EXPERIMENTAL APPARATUS

The apparatus used is shown in Fig.133 and 134. The two copper end plates served as bus bars for electrical power connection and as rigid constraints to axial growth of the tube. Thus, as the tube was electrically heated, a longitudinal thermal stress was imposed. The spacer blocks were made from an electrical insulating material and prevented axial movement of the test section.

A typical single-tube test section is shown in Fig.135 and 136. In all cases, the heated length was 2 inches and the tubes were 0.50-inch OD, type 321 stainless steel. Eight chromel-alumel thermocouples were clamped onto the test section in four pairs, giving the temperature

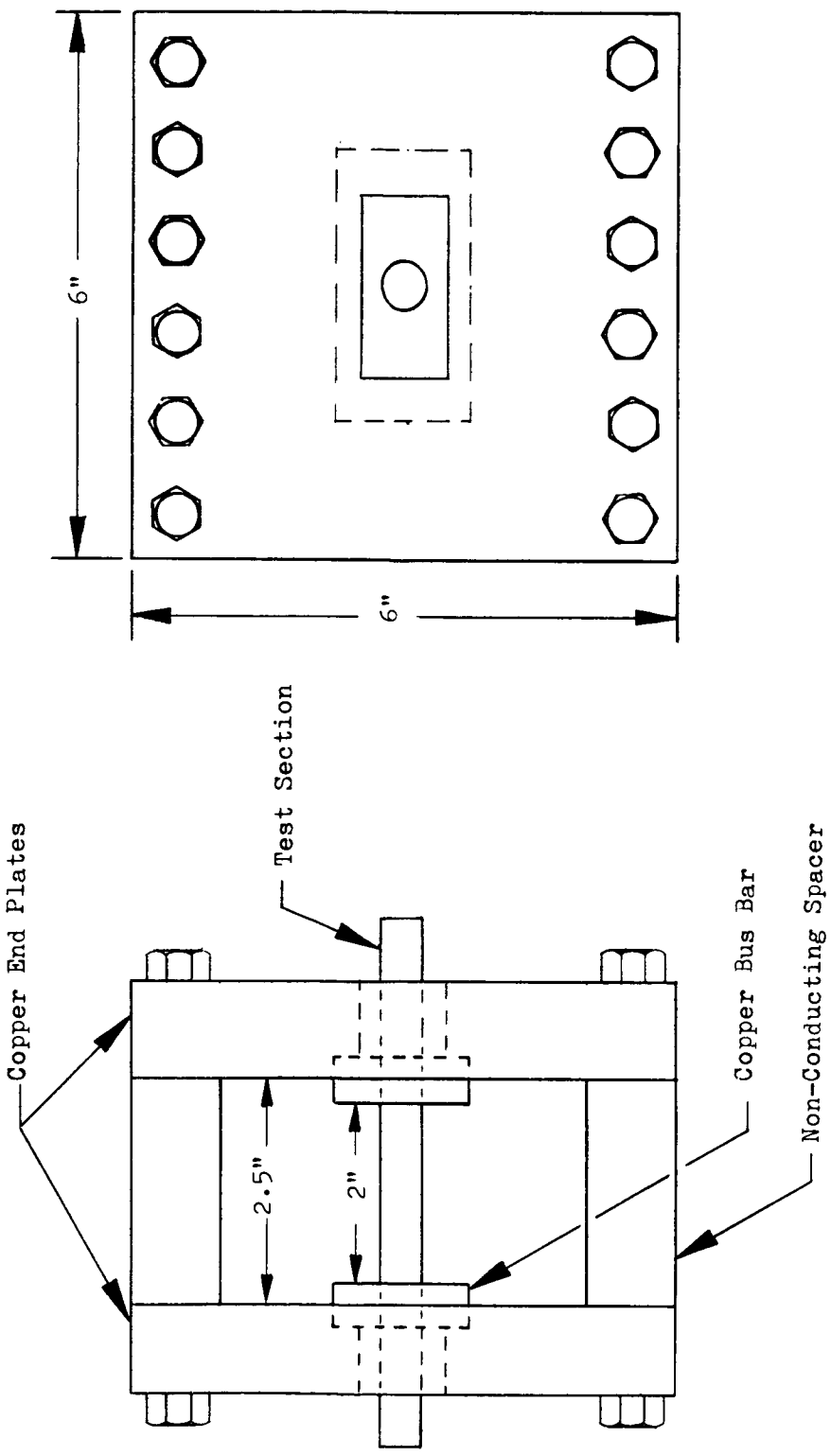

Figure 133. Schematic of Thermal Buckling Test Apparatus

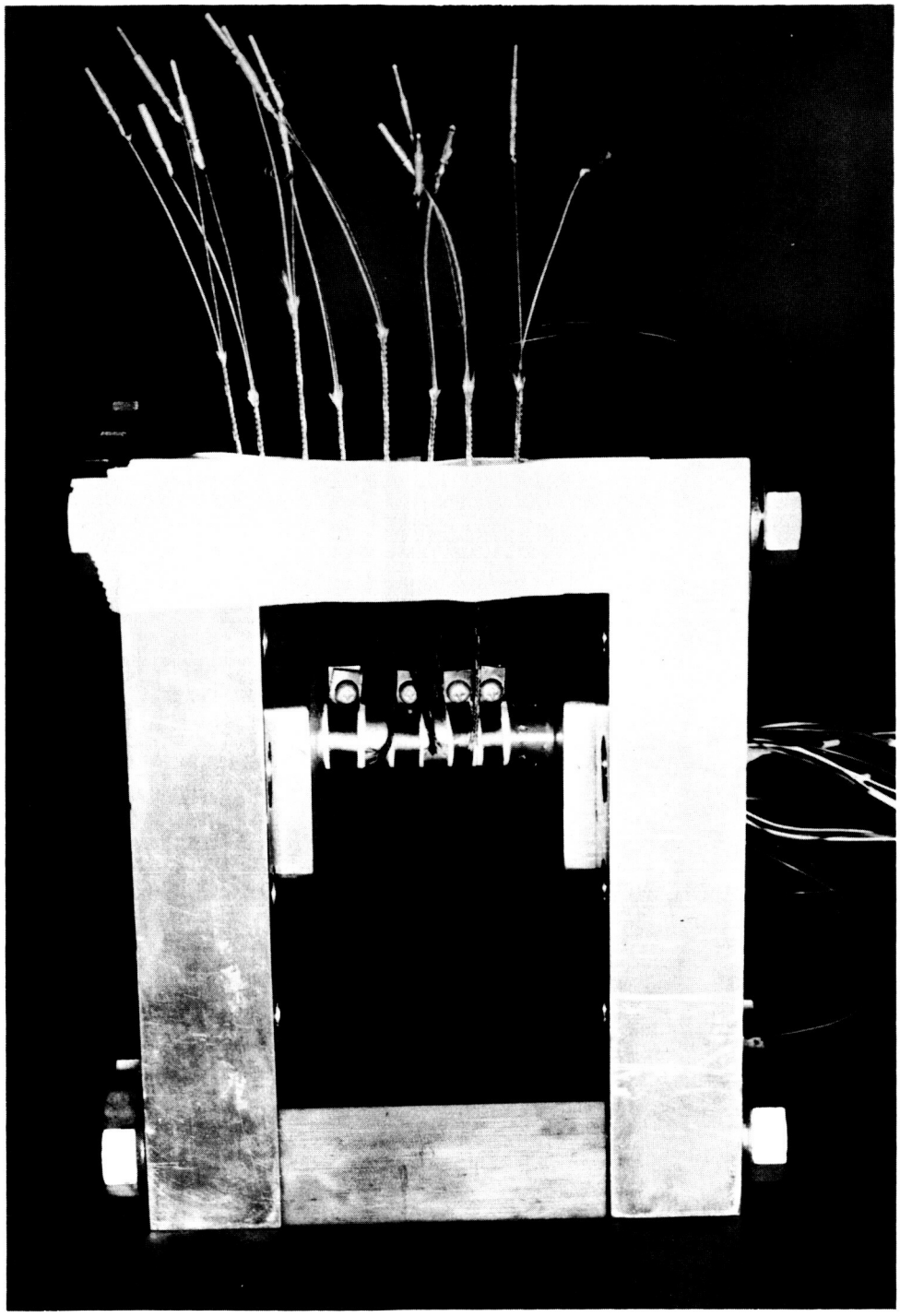

5AE21-1/20/65-S1B

Figure 134. Thermal Buckling Test Apparatus

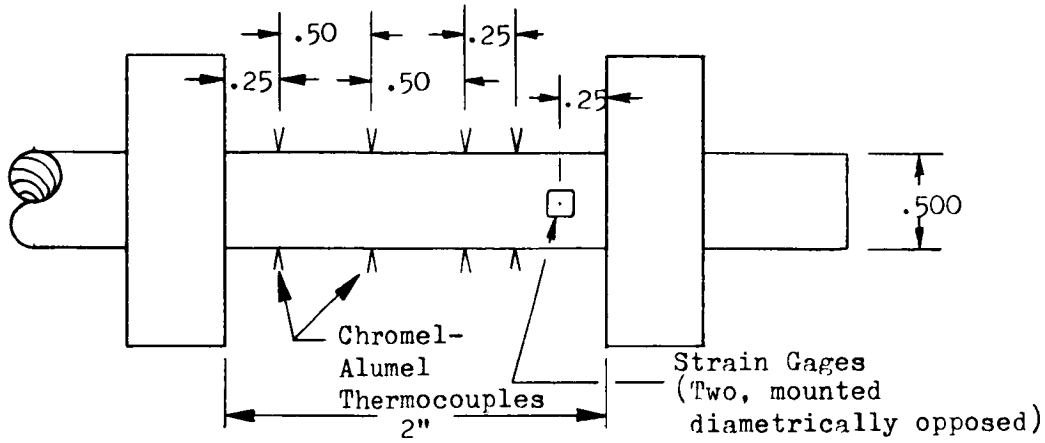

Test Sections No. 1 thru 4

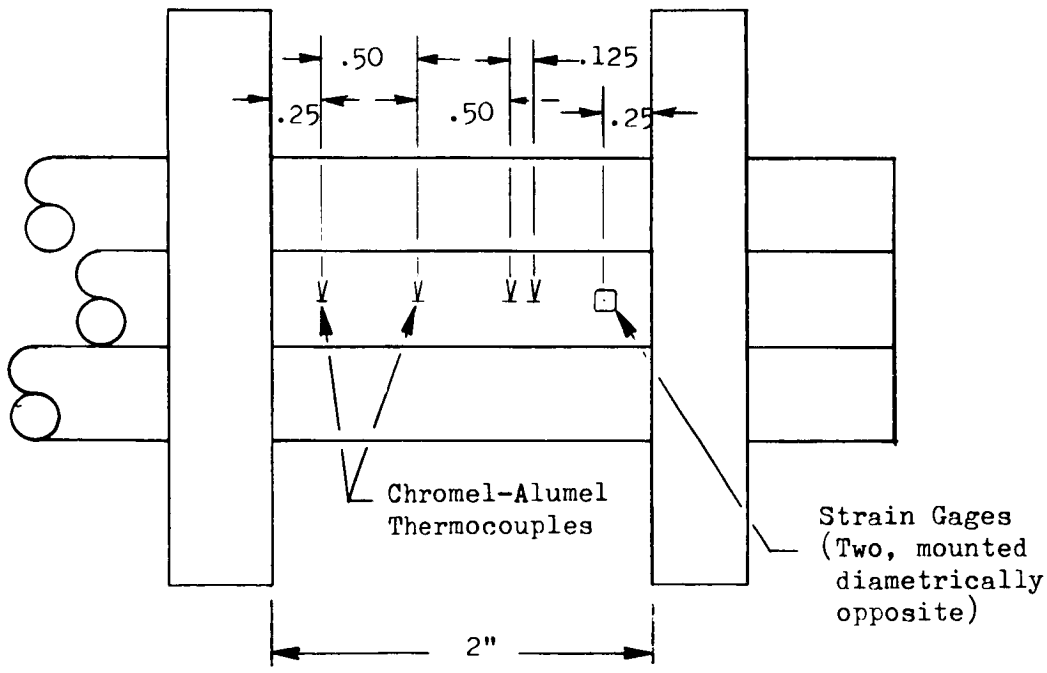

Test Section #5

Figure 135. Schematic of Test Section

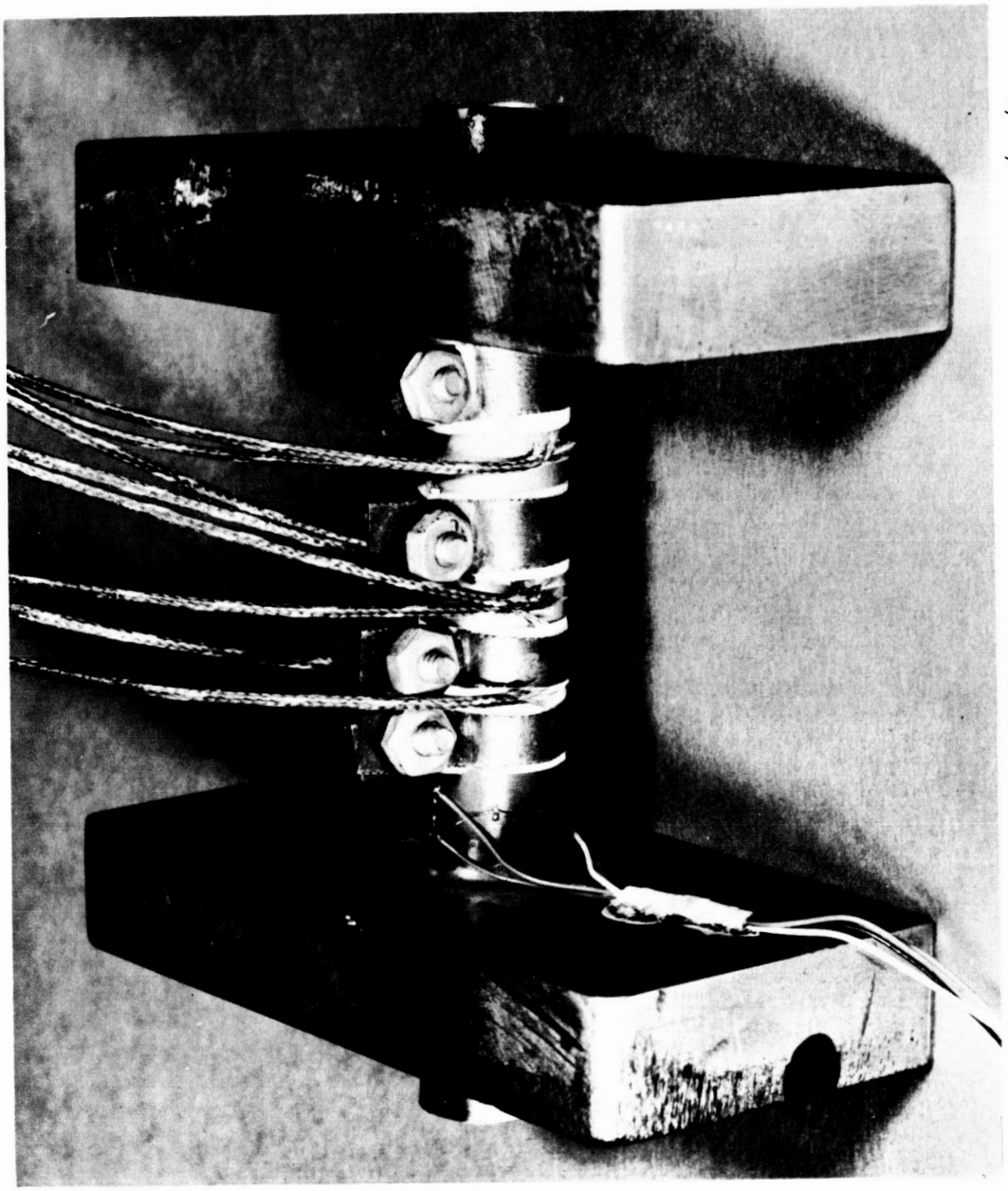

Figure 136. Single-Tube Test Section

profile along the tube. The thermocouples were electrically insulated from the tube by small sections of mica approximately 0.001 inch thick. Micro-Systems Model P05-16-121 silicon semiconductor strain gages were mounted at one end of the test section to measure the axial preload imposed on the tube upon tightening the copper-end support plates. Table 25 summarizes the test sections employed.

TABLE 25

THERMAL BUCKLING TEST SECTIONS

Test Section Number	Number of Tubes	Wall Thickness, inches	Comments
1	1	0.010	Heated to failure
2	1	0.006	Heated to failure
3	1	0.012	Heated to failure
4	1	0.010	Cycled
5	3	0.010	Heated to failure

EXPERIMENTAL PROCEDURE

The test sections were instrumented with thermocouples and strain gages as described above. The apparatus was assembled except for one of the copper end plates. Weights were placed on the free end of the test section to calibrate the strain gages in place. The remaining end plate was then assembled to the apparatus and the bolts tightened until a

10,000-psi preload stress was placed on the tube. The bolts were tightened so that the two strain gages, spaced 180 degrees apart, gave identical readings to ensure that no bending stress was placed on the test section.

The electrical power leads were then connected, and d-c power applied in small increments. The temperatures were recorded and sufficient time allowed between each power increase for the temperatures to reach a steady-state condition. The power was increased until visual observation of buckling was observed except for test No. 4. Test section No. 4 (identical to test section No. 1) was temperature-cycled to a level below the previously determined failure point 10 times with no indication of buckling. The temperature was then increased until failure occurred.

RESULTS

Types of Failure

Two different types of buckling failure were apparent in the tests conducted. Test sections No. 1, 4, and 5 (0.010 and 0.012-inch wall thickness) buckled with a fairly uniform ripple around the periphery of the tube. Figure 137 shows the failure of test section No. 1. The deep dimple was caused by additional heating past the failure point. The symmetric ripple around the periphery was typical of the failures experienced by the other heavier wall tube. The appearance of this type of failure is typical of those experienced with engine cooling jacket tubes.

Test section No. 2(0.006-inch wall) failed in a different manner. The buckling consisted of a series of diamond-shaped dimples in a spiral pattern on the tube (Fig. 138). This type of failure is characteristic of the elastic buckling failure experienced by large-diameter, thin-wall cylinders.

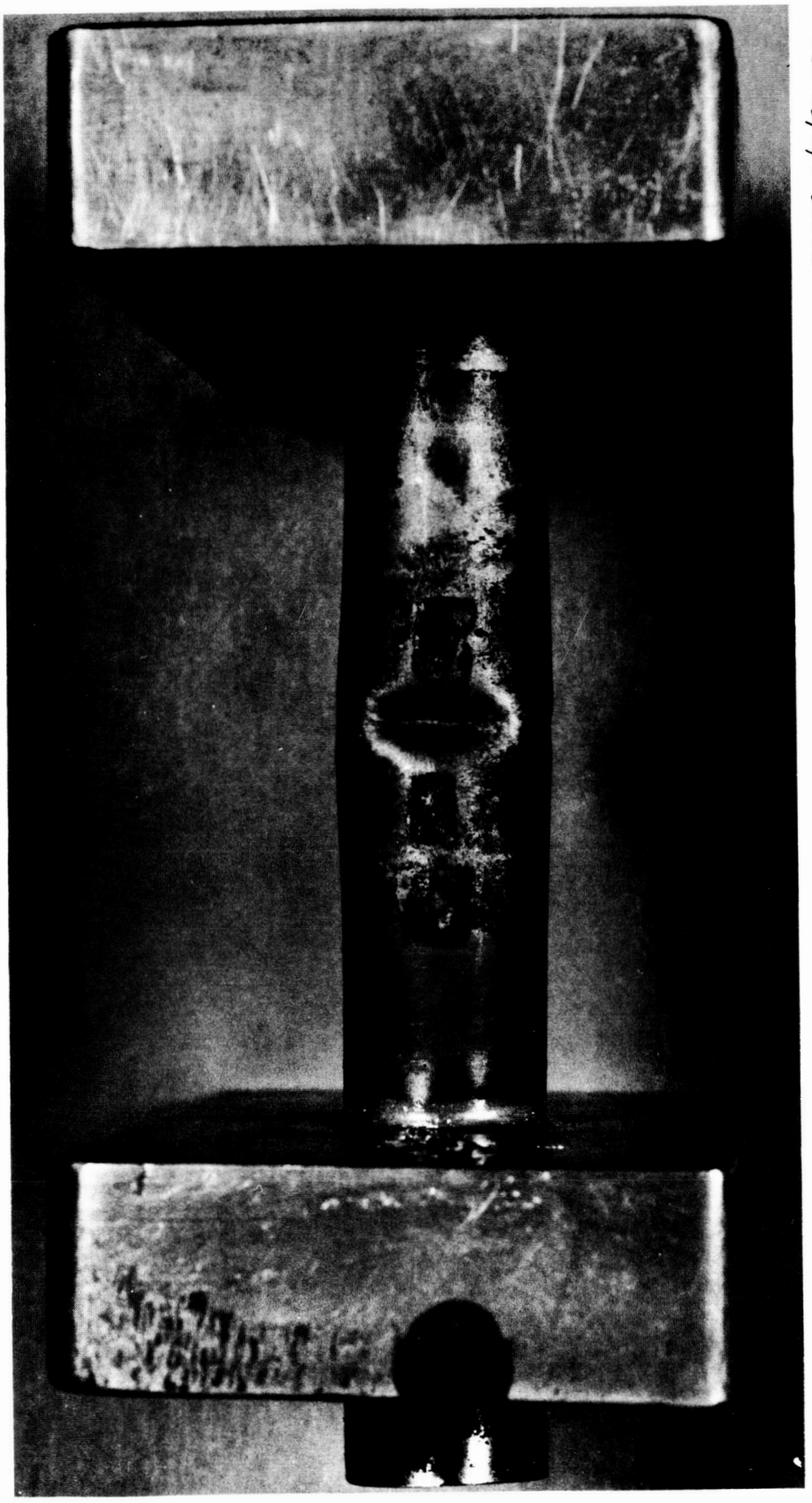

5AE26-2/2/65-S1A

Figure 137. Ripple Type Failure

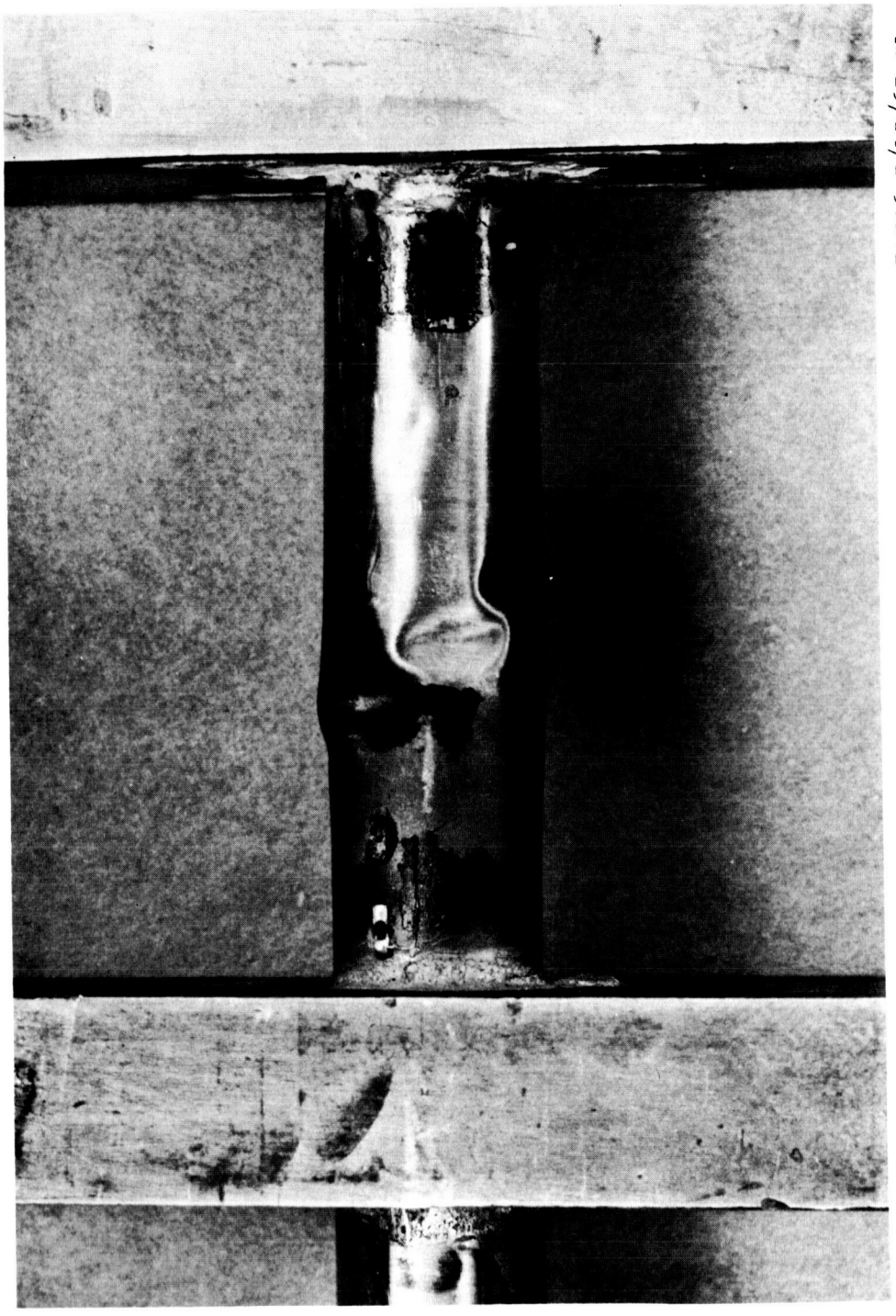

5AE46-5/18/65-S1

Figure 138. Diamond Type Failure

The triple-tube test section (No. 5) illustrated the effect of side constraint on buckling behavior. This test section was heated until the silver braze between the tubes began to melt. The two outer tubes failed in a manner similar to the circumferential ripple observed for the single-tube, relatively thick-wall test sections. However, it was not possible to buckle the center tube without destroying the braze joint between the tubes. Figure 139 illustrates the failure of the multiple-tube test section.

Effect of Cycling

It was desired to determine the effect of temperature cycling below the thermal buckling failure point on a typical single-tube test section. Therefore, test section No. 4 was constructed identical with test section No. 1. The test specimen was temperature cycled to a point somewhat below the failure temperature of test section No. 1. After 10 cycles failed to produce evidence of tube failure, the specimen was heated until buckling occurred. As will be discussed below, the failure occurred at a higher temperature and calculated strain than the test section that was not cycled.

However, it was observed that after the first temperature cycle, the tube preload was relieved during cool down. Since the apparatus employed was characterized by a constant length rather than constant preload, it was not possible to again place the same preload on the test section after the first cycle. The strain gages used to measure the initial preload were burned off after heating to approximately 500 F. It was believed more meaningful to retain the original constrained length than to impose an unknown preload on the section after the unloading relief of the first

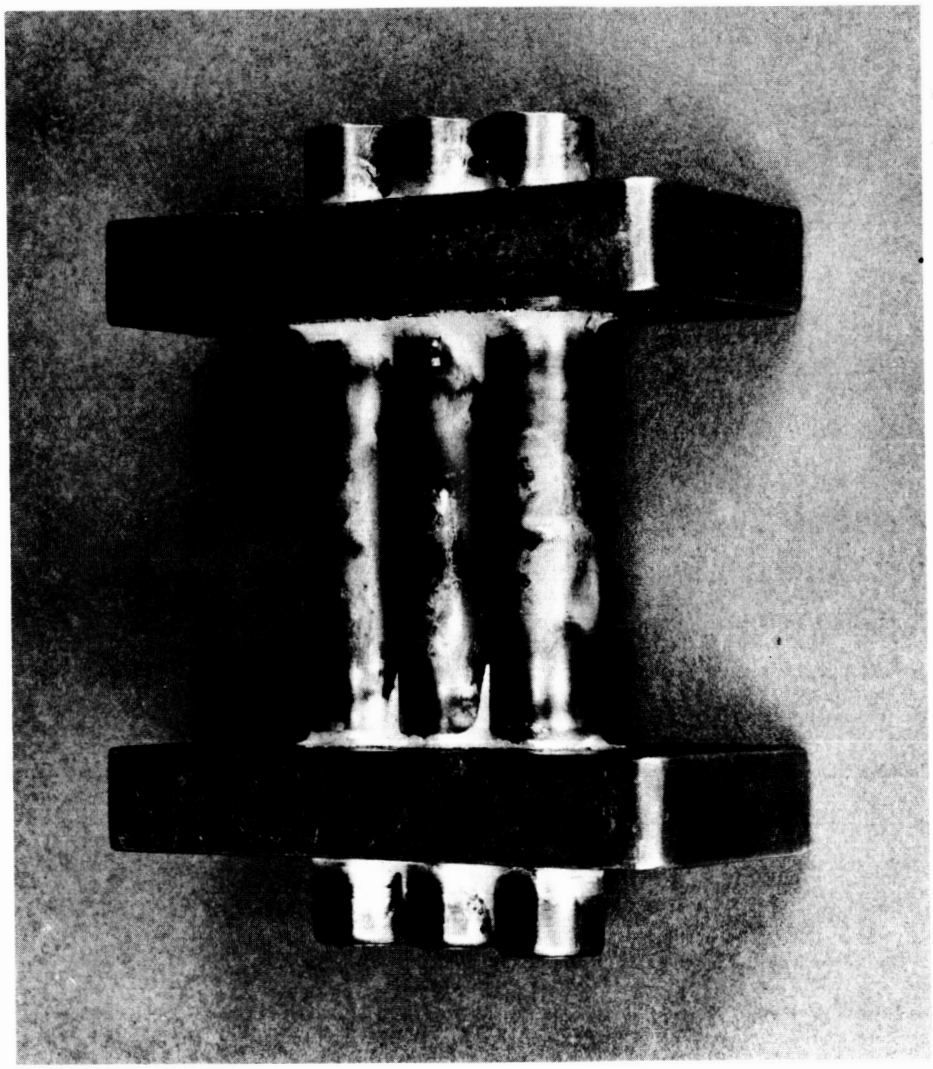

5AE46-5/14/65-S1

Figure 139. Multiple Tube Failure

cycle. Thus, an unknown portion of the calculated strain at failure was not actually strain, but expansion to reach the initial test section length. The strain values will be discussed more fully below.

Strain at Failure

The buckling strain at failure was calculated from the measured temperature profile along the test specimens. As discussed above, eight thermocouples were placed in four diametrically opposite pairs along the heated length. The temperatures from the two thermocouples at any one axial location on the tube were averaged to minimize the effects of heat generation variation with wall thickness discrepancies around the tube circumference.

Two temperature measurements on either side of the axial midpoint were obtained for each test section. This enabled the graphical construction of axial temperature profiles, assuming the generated heat was lost mainly by conduction to the bus bars, a linear temperature profile, and constant physical properties. The profiles obtained for the five test specimens are shown in Fig. 140. The right side of the profile for test section No. 2 presents an impossible situation; i.e., heat conduction from the bus bar to the center of the tube. Therefore, the left portion of the temperature profile was assumed to be correct to the geometrical center of the tube, and its intersection with the $x = 1.0$ and the temperature point at $x = 1.25$ were utilized to construct the curve labeled 2', which was used to calculate the strain for test section No. 2. The strain calculated from curves 2 and 2' differed by less than 15 percent.

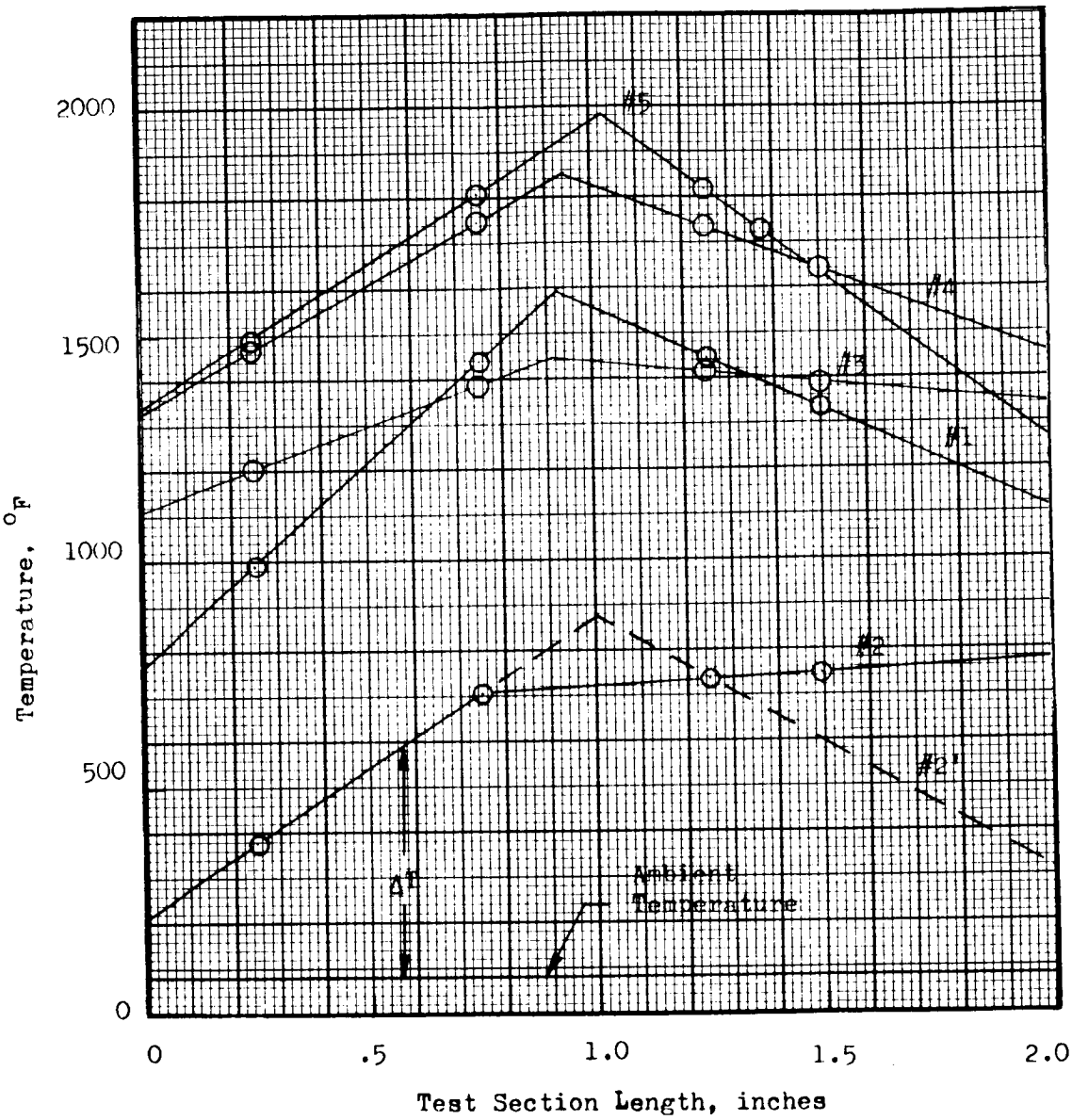

Figure 140. Linearized Test Section Temperature Profiles Prior to Failure

The assumption of linear temperature profiles and constant physical properties does not represent the true case. The temperature profile for a fin with uniform heat generation and insulated surfaces was calculated and compared to the temperature profile for test section No. 1. The comparison is shown in Fig. 141 . The difference in strain for the two curves was negligible, although the value of maximum temperature, or failure temperature is affected somewhat. The strain was calculated from the equation of thermal expansion:

$$\epsilon = \frac{\Delta L}{L} = \frac{L - L_o}{L_o} = \frac{[1 + \alpha \Delta T]\, L_o - L_o}{L_o} \qquad (369)$$

The test sections were divided into 1/8-inch segments for the calculation of L, and the local temperature at each increment was used. Thus, the temperature profiles were numerically integrated for the determination of the total strain. The calculated values at failure are listed in Table 26. In general, the strain values were much greater than the corresponding yield point values of about 0.003 in./in. Therefore, inelastic conditions were achieved.

TABLE 26

STRAIN AT FAILURE FOR THERMAL BUCKLING EXPERIMENTS

Test Section	1	2	3	4	5
ϵ, in./in.	0.0144	0.00586	0.0151	0.0185	0.0168
$\sim T_{max}$, F	1500	800	1410	1800	1975

The strain at failure for test sections 1, 2, and 3 is shown in Fig. 142 as a function of D/t. It should be noted that the term D/t has been found to be of significance in the elastic buckling of thin-wall cylinders. From Fig. 142, it appears that this term is also of importance in inelastic buckling.

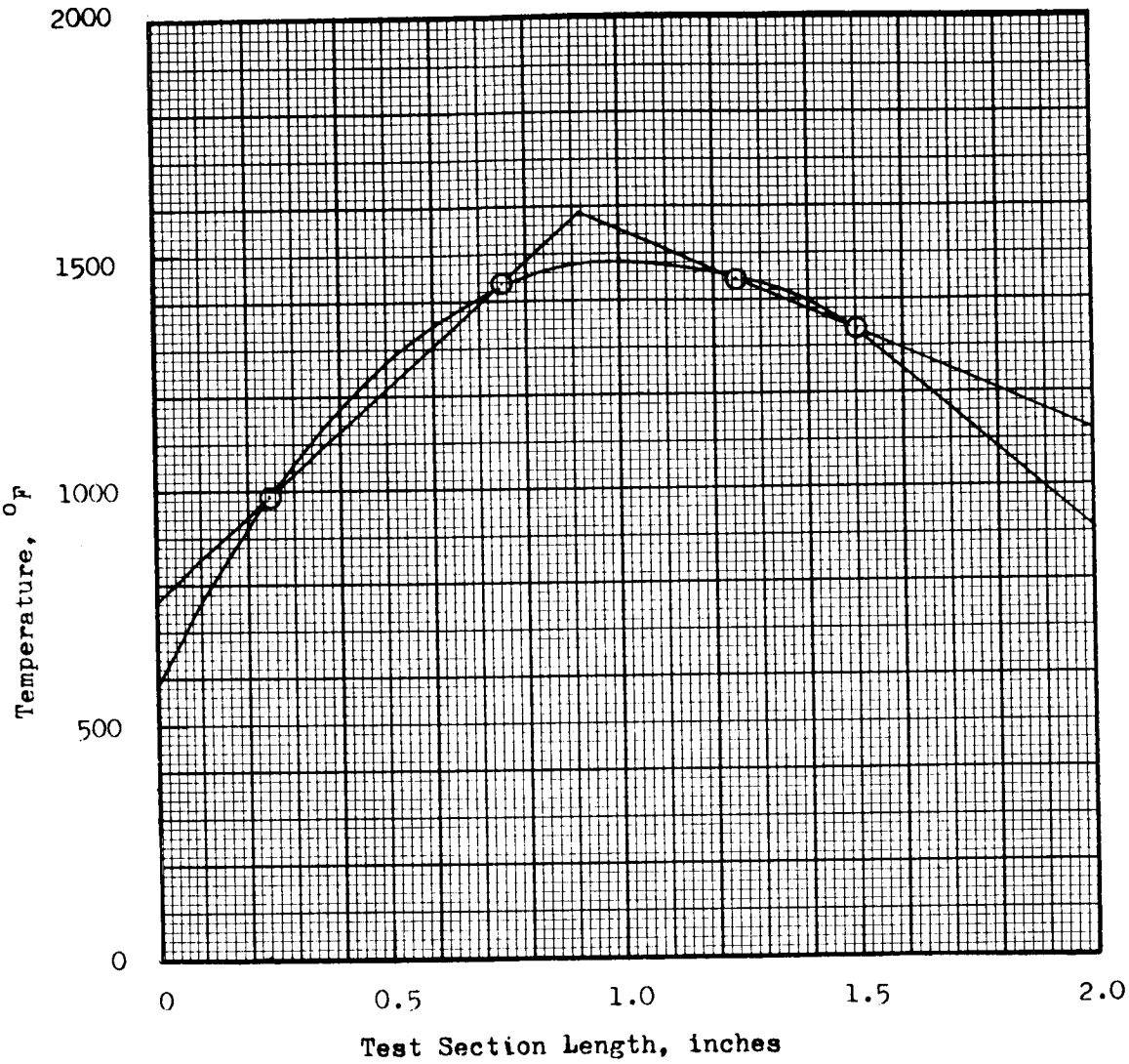

Figure 141. Comparison of Linearized and Heat Generation Temperature Profiles for Test No. 1

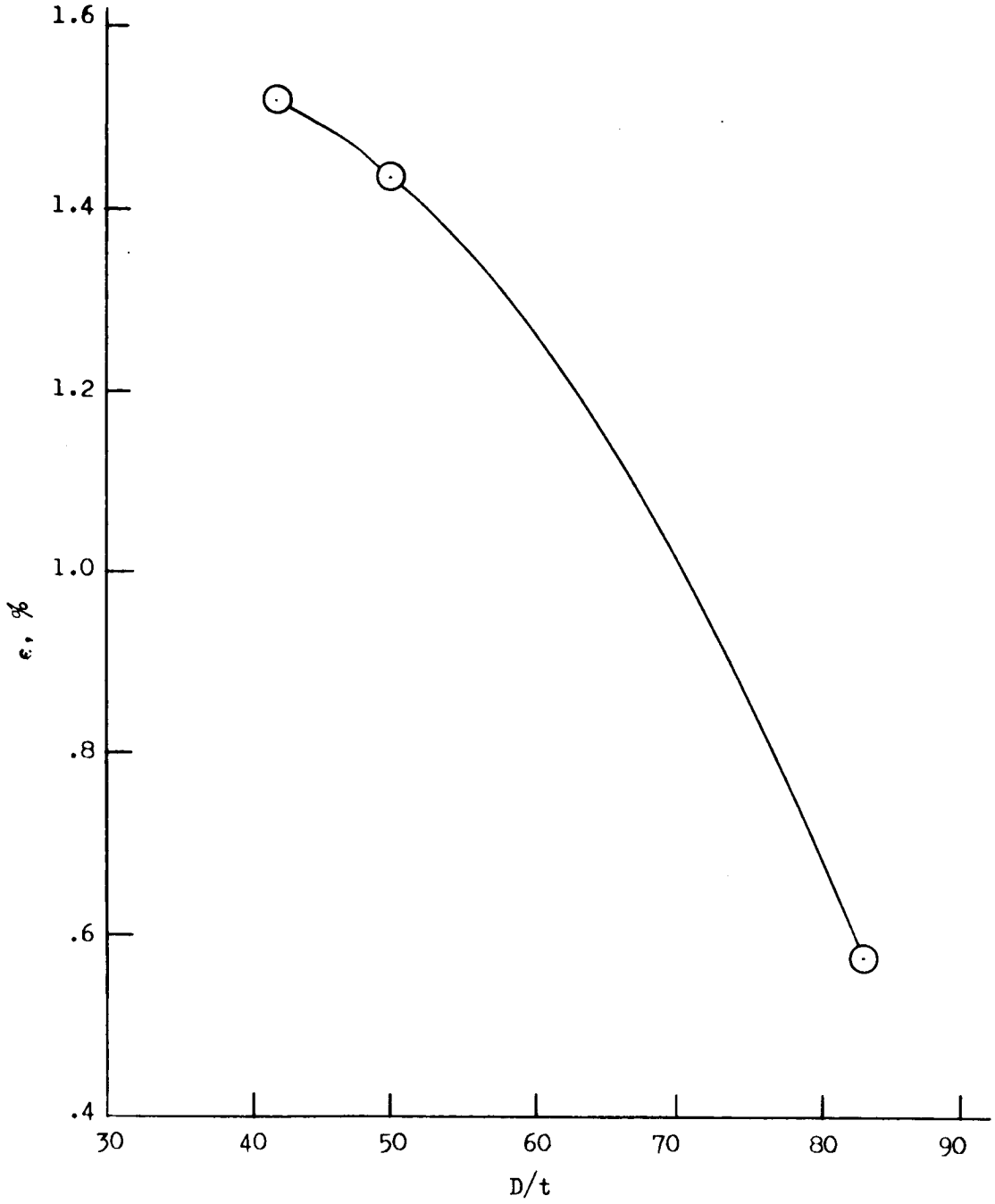

Figure 142. Effect of Tube Diameter to Wall Thickness Ratio on Strain at Failure

Multiple buckles were observed spaced axially along the test sections. However, all but the center portion of the tubes were influenced by the presence of thermocouple clamps. Therefore, no valid conclusions regarding the buckling wavelength-to-diameter ratio may be drawn from the present work.

Test section No. 2 was the only one which exhibited multiple distinct buckles around the periphery of the tube. These failures were distributed spirally around the circumference, and were, therefore, subject to the thermocouple clamp influence described above. Therefore, no conclusions may be drawn concerning the effect of the number of circumferential buckling waves on the buckling strain.

As mentioned above, test section No. 4 was thermally cycled before heating to failure. The preload was relieved after the first cycle, a permanent deformation being sustained upon unloading. A gap was produced between the end support plate and the bus bar, so that external pressure had to be applied to the end support plate to make electrical contact upon the initiation of subsequent temperature cycles. Thus, in the calculation of strain in Eq. 369, a portion of the measured ΔT was utilized to thermally expand the tube until the original length was attained. The actual buckling strain is lower than the calculated value from Table 26.

The strain at failure for the triple-tube, 0.010-inch-wall test section (No. 5) is higher than the failure strain for test section No. 3 with a single tube of 0.012-inch wall thickness. This illustrates the effect of additional support on increasing the buckling strain. The failure with this test section occurred in the two outer tubes, which were constrained on one side only. It was not possible to buckle the center

tube without melting the silver braze joining the tubes, and thus destroying the constraint of the multiple-tube configuration. Thus, the allowable strain is significantly increased with multiple tubes.

CONCLUSIONS

The following conclusions may be drawn from the experimental results:

1. Two different types of inelastic buckling occur: individual buckling waves, and a ripple completely encircling the tube, dependent upon tube wall thickness. For tube wall thicknesses of interest in high-chamber-pressure engines, the ripple-type failure is the most likely to occur.
2. The term D/t appears to have significance in inelastic buckling in correlating buckling strain and determining the type of buckling failure.
3. The thermal cycling experiment was not directly applicable to engine cooling conditions, as the nozzle tubes are not free to sustain a permanent deformation, as was the case in the subject experiment.
4. Buckling strain is significantly increased with the additional constraint obtained from multiple-tube configurations. The temperature at failure was increased approximately 500 F with the triple-tube test section.

The following recommendation is made based on the results of the present study. Future inelastic buckling tests should be made with closer control of the experimental variables to obtain the effect of D/t on buckling

strain. These tests should be conducted with a temperature environmental chamber mounted on a tensile-compressive testing machine. Tests should also be conducted to determine the effects of thermal cycling on buckling strain, utilizing this type of apparatus.

NOMENCLATURE

A	=	area
a	=	velocity ratio; exponent in Eq. 8; constant in Eq. 46
B	=	constant in Eq. 49
Ca	=	Crocco number
C_D	=	discharge coefficient
C_f	=	skin friction coefficient
C_p	=	specific heat at constant pressure
c^*	=	characteristic exhaust velocity
D	=	diameter; ductility
De	=	Dean number
D_p/D_t	=	plug diameter-to-equivalent circular throat diameter
d	=	dissipation
d_h	=	hydraulic diameter
E	=	elasticity
F	=	thrust
f	=	friction factor; function of
G	=	mass velocity
g_c	=	universal constant = 32.17 lbm-ft/lbf-sec^2
H	=	compressible shape factor, enthalpy
$\overline{H}$	=	incompressible shape factor
h	=	convective heat transfer coefficient; depth; friction head
h_c	=	coolant-side heat transfer coefficient

h_g = gas-side heat transfer coefficient

h_g' = gas-side heat transfer coefficient without film cooling

h_L = liquid-side heat transfer coefficient

I_s = specific impulse

K = constant in Eq. 17, 63, 85, and 99

k = thermal conductivity

k_c = char thermal conductivity

L = film-cooled length; combustion zone length; length

L* = characteristic chamber length

ℓ = mixing length; friction length

Ma = Mach number

MR = mixture ratio

MW = molecular weight

m = circumferential wavelength function

N = number of chambers in multichamber configuration

N_f = number of cycles to failure

Nu = Nusselt number

n = velocity profile exponent; exponent in Eq. 46

P = pressure

ΔP = pressure differential

P_c = chamber pressure

P.L. = performance loss

Pr = Prandtl number

p = internal pressure

Q_p^* = heat of pyrolysis

q = external pressure; heat transfer rate

q/A = heat flux

R = tube inside radius; chamber radius; gas constant

RA = reduced area

Re = Reynolds number

Re* = Reynolds number based on friction velocity

R_t = nozzle throat radius

r = radius

r_c = radius of curvature

S = integration variable

St = Stanton number

s = distance along surface

T^+ = dimensionless temperature = $(T - T_w)\, C_p \sqrt{\tau\rho}/(q/A)^*$

T = temperature; surface tension

T^* = temperature at film-coolant interface

t = energy parameter; thickness

U = velocity

u = velocity

u^* = friction velocity

u^+ = dimensionless velocity = $u/\sqrt{\tau\rho}$

V = velocity

v = velocity

v^* = friction velocity

$\dot{W}$ = flowrate

$\dot{W}^+$ = dimensionless flowrate = $\int_0^{y^*} u^+ \, dy^+$

We = Weber number

x = distance

x^+ = dimensionless distance = $x \sqrt{\tau\rho}/(\mu/\rho)$

Δx = wall thickness

Y = expansion factor

y = distance from wall; normal distance

y^+ = dimensionless distance = $y\sqrt{\tau\rho}/(\mu/\rho)$

Δy = char depth

z = distance

z^+ = dimensionless distance = $z\sqrt{\tau\rho}/(\mu/\rho)$

GREEK LETTERS:

α = shear stress constant in Eq. 2; Reynolds number exponent; thermal coefficient of expansion; kinetic energy coefficient

β = ratio of constriction cross section to pipe cross section

γ = variable in Eq. 2

δ = boundary layer velocity thickness, film-coolant depth; thermal strain parameter; film-coolant shear parameter

δ^* = boundary layer displacement thickness

δ_T = annular nozzle throat depth

ϵ = expansion area ratio; strain; eddy viscosity; roughness height

$\Delta\epsilon$ = total strain

ϵ' = emissivity

ϵ^* = generalized roughness parameter defined by Eq. 78

ϵ_c = contraction area ratio

ζ = constant in Eq. 49

η = dimensionless mixing parameter; efficiency; modulus ratio

θ = momentum thickness

Λ = incompressible laminar flow pressure gradient function

λ = wavelength

μ = Poisson's ratio, viscosity

ν = kinematic viscosity

ρ = density

σ = free jet mixing parameter; stress; exponential growth function; Stefan-Boltzmann constant

τ = time; shear stress

τ_o, τ_w = shear stress at the wall

τ_{FC} = film cooling flow fraction

τ_T = turbine gas flow fraction

φ = energy thickness

φ_1 = turbine gas efficiency of utilization; function in Eq. 84

φ_2 = film cooling efficiency of utilization; function in Eq. 84

φ_3 = reference chamber I_s efficiency; function in Eq. 84

φ_4 = chamber I_s efficiency; function in Eq. 84

$\varphi_{\epsilon T}$ = elastic tangential strain fraction

φ_{LT}' = coolant-side longitudinal thermal strain to tangential strain

φ_{max_T} = maximum tangential surface strain

φ_{min_T} = minimum tangential surface strain

φ_{PT} = plastic tangential strain fraction

φ_P = performance ratio

$\varkappa$ = specific heat ratio

ψ = surface stability parameter

ω = constant in Eq. 38

SUBSCRIPTS:

a = inside wall; char formation; ambient

aw = adiabatic wall

BL = boundary layer

b = bulk

C = thrust chamber

CL = conduction limit

c = curvature; coolant; combustion stagnation; char

conv = convection

D = diameter

E = energy thickness; equivalent

e = exit; endurance limit; elastic

F = free jet; film cooled

FC = film coolant

f	=	effective value; uncurved; fracture; final; film cooling; frozen; feeder line
fc	=	film coolant
g	=	gas
h	=	hydraulic
i	=	inside; initial
L	=	laminar; longitudinal; liquid
M	=	main gas stream
NB	=	nucleate boiling
o	=	uncurved; stagnation
p	=	pressure; propellant
pp	=	plastic
R	=	regenerative
r	=	radial; reference condition
rg	=	gas recovery
s	=	surface length; shifting; surface; slot
sep	=	separation
T	=	total; thermal; tangential; turbine; turbulent
t	=	tangent value; tangential, throat
ul	=	upper limit
w	=	wall
wc	=	coolant-side wall
wg	=	gas-side wall
y	=	yield

θ = momentum thickness basis

φ = energy thickness basis

∞ = free stream

SUPERSCRIPTS

$\overline{}$ = average; effective

$*$ = throat condition; at coolant interface

REFERENCES

1. R-3999, Investigation of Cooling Problems at High Chamber Pressures, Final Report for period 9 April 1962 to 8 January 1963, Contract NAS8-4011, Rocketdyne, a Division of North American Aviation, Inc., Canoga Park, California, May 1963.

2. Elliott, D. G., D. R. Bartz, and S. Silver: "Calculation of Turbulent Boundary-Layer Growth and Heat Transfer in Axi-Symmetric Nozzles," JPL Technical Report No. 32-387, 15 February 1963.

3. Tromblay, J. E.: "Calculation of Friction Drag in Rocket Nozzles and Demonstration of the Effect Upon Specific Impulse," ADM 61-13, Rocketdyne, a Division of North American Aviation, Inc., Canoga Park, California, 25 January 1961.

4. Mayer, E.: "Analysis of Convective Heat Transfer in Rocket Nozzles," ARS Journal, 31, 1961, 911-917.

5. Culik, F. and J. Hill: "A Turbulent Analog of the Stewartson-Illingworth Transformation," J. Aero-Sciences, 25, 1958, 259.

6. Launder, B. E.: "An Improved Pohlhausen-Type Method of Calculating the Two-Dimensional Laminar Boundary Layer in a Pressure Gradient," Trans. ASME, August 1964, 360-364.

7. Schlichting, H.: Boundary Layer Theory, Fourth Edition, McGraw-Hill Book Co., Inc., New York, 1960.

8. Truckenbrodt, E.: "Ein Quadraturverfahren zur Berechnung der Laminaren und Turbulanten Reibungsschicht bei Ebener und Rotationssymmetrischer Strömung," Ing. Arch. 20, 1952, 211-228.

9. Wieghardt, K. and W. Tillmann: "Zur Turbulenten Reibungsschicht bei Druckanstieg," UM 6617, 1941.

10. Rotta, J.: "Beitrag Zur Berechnung der Turbulenten Grenzschichten," Ing. Arch. 19, 1951, 31-41.

11. Eckert, E. R. G.: "Engineering Relations for Heat Transfer and Friction," Trans. ASME, 78, 1956, 1273-1283.

12. Johnson, H. A. and M. W. Rubesin: "Aerodynamic Heating and Convective Heat Transfer," Trans. ASME, 71, 1949, 447-456.

13. Rayleigh: "Dynamics of Revolving Fluids," Proc. Roy. Soc. London, V6A, 1916, 148-154.

14. Kassner, R. and E. Knoernschild: "Friction Laws and Energy Transfer in Circular Flow," WAFB#78, 1948.

15. Smithberg, E. and F. Landis: "Friction and Forced Convection Heat Transfer in Tubes with Twisted Tape Swirl Generators," Jour. of Heat Trans., Trans. ASME, February 1964, 40-49.

16. Eskinazi, and M. Yeh: "An Investigation of Fully Developed Turbulent Flows in Curved Channels," J.A.S. 23, 1956, 23-25.

17. Wattendorf, F. L.: "Study of Curvature on Fully Developed Turbulent Flow," Proc. Royal Soc. London, 148, 1935, 565-598.

18. Dean, W. R.: "The Streamline Motion of a Fluid in a Curved Pipe," Phil. Mag. (7), 4, 208 (1927) and 5, 673 (1928).

19. Ito, H.: "Friction Factors in Turbulent Flow in Curved Pipes," Journal Basic Engr., Trans. ASME D 81, 1959, 123.

20. White, C.: "Fluid Friction and Its Relation to Heat Transfer," Trans. Inst. Chem. Engineers, 10, 1932, 66.

21. Dipprey, D. F. and R. H. Sabersky: "Heat and Momentum Transfer in Smooth and Rough Tubes at Various Prandtl Numbers," Int. J. Heat Mass Transfer, 6, 1963, 329-353.

22. R-6010, Multichamber Engine Investigation, Volume 2, Rocketdyne, a Division of North American Aviation, Inc., Canoga Park, California, 30 December 1964, CONFIDENTIAL.

23. Unpublished data obtained through private communication with R. W. Graham, NASA Lewis Research Center, Cleveland, Ohio.

24. R-6129, Supercritical Pressure Liquid Hydrogen Heat Transfer Data Compilation, W. S. Miller, J. D. Seader, and D. M. Trebes, Rocketdyne, a Division of North American Aviation, Inc., Canoga Park, California, 21 April 1965.

25. Adler, M.: "Strömung in Gekrünmten Rohren," ZAMM 14, 1934, 257.

26. McAdams, W. H.: Heat Transmission, 3rd Edition, McGraw-Hill Book Co., Inc., New York, 1954, 228.

27. Seban, R. and E. McLaughlin: "Heat Transfer in Tube Coils with Laminar and Turbulent Flow," Int. Journal of Heat and Mass Transfer, 6, 1963, 387-395.

28. R-5652-4P, Final Program Progress Report for Product Engineering, Vol. 2, Heat Transfer Studies, Rocketdyne, a Division of North American Aviation, Inc., Canoga Park, California, 1 April 1965.

29. Hendricks, R. C. and F. Simon: "Heat Transfer to Hydrogen Flowing in a Curved Tube," ASME Meeting Paper Philadelphia, November 1963, NASA Lewis Research Center, Cleveland, Ohio.

30. Krieth, F.: "Influence of Curvature on Heat Transfer to Incompressible Fluids," Trans. ASME, 77, 1955, 1247-1256.

31. Hatch, J. and S. Papell: "Use of a Theoretical Flow Model to Correlate Data for Film Cooling or Heating an Adiabatic Wall by Tangential Injection of Gases of Different Fluid Properties," NASA TND 130, 1959.

32. Papell, S. and A. Trout: "Experimental Investigation of Air Film Cooling Applied to an Adiabatic Wall by Means of an Axially Discharging Slot," NASA TND-9, 1959.

33. Carslaw, H. S. and J. C. Jaeger: "Conduction of Heat in Solids," Oxford, 1959, 54.

34. Ambramovich, G. N.: "The Theory of Turbulent Jets," Translation by M.I.T., M.I.T. Press, Cambridge, Massachusetts, 1963.

35. Seban, R. and L. Back: "Velocity and Temperature Profiles in Turbulent Boundary Layers with Tangential Injection," Journal of Heat Transfer, February 1962, 45-54.

36. Korst, H. and W. Chow: "Compressible Non-Isoenergetic Two-Dimensional Turbulent Jet Mixing, etc." University of Illinois MFTN 392-4 OSR TN 59-30.

37. Lamb, H.: "Hydrodynamics," Dover, N. Y., 1945.

38. CEM 920-7708, "Theoretical Potential Flow Analysis of Plane Two-Dimensional Liquid Jet Neglecting Viscous Effects," W. Wagner, Rocketdyne, a Division of North American Aviation, Inc., Canoga Park, California, 1959.

39. CEM 720-7709, "Theoretical Examination of Liquid Viscosity Effects on Showerhead Stream Breakup," W. Wagner, Rocketdyne, a Division of North American Aviation, Inc., Canoga Park, California, 1959.

40. Kinney, G., et al.: "Internal Liquid Film Cooling Experiments with Air Stream Temperatures to 2000^{0}F in 2-inch and 4-inch Diameter Horizontal Tubes," NACA R1087, 1952.

41. Graham, A. R.: "Film Cooling of Rocket Motors," Ph.D. Thesis, Purdue University, Mechanical Engineering, January 1958.

42. Sellers, J. P.: Personal Communication, Rocketdyne, a Division of North American Aviation, Inc., Canoga Park, California.

43. Smith, R. W.: "Fatigue Behavior of Materials under Strain Cycling in Low and Intermediate Life Range," NASA TND 1574, April 1963.

44. Shanley, F. R.: Strength of Materials, McGraw-Hill Book Co., Inc., New York, 1957, 671-705.

45. Bland, D. R.: "Elastoplastic Thick Walled Tubes of Work Hardening Material Subject to Internal and External Pressures and to Temperature Gradients," Journ. of Mech. and Phys. of Solids, 4, Pergammon Press, London, 1956, 209-229.

46. Flugge, W.: "Stresses in Shells," Springer-Verlag, Berlin, 1960.

47. Shanley, F. R.: Strength of Materials, McGraw-Hill Book Co., Inc., New York, 1957, 601-608.

48. Timoshenko, S.: "Theory of Elastic Stability," McGraw-Hill Book Co. Inc., New York, 1936.

49. Lee, L. H. N.: "Inelastic Buckling of Cylindrical Shells Under Axial Compression and Internal Pressure," Development in Mechanics, Vol. 1, Proceed. of Seventh Midwestern Mech. Conf., Plenum Press, N. Y., 1961, 190-202.

50. Lee, L. H. N.: "Inelastic Buckling of Cylindrical Shells under Axial Compression and External Pressure," Proceed. of Fourth National Cong. of Applied Mech., 1962, 989-998.

51. Lee, L. H. N.: "Inelastic Buckling of Initially Imperfect Cylindrical Shells Subject to Axial Compression, JAS,29, 1962, 87-95.

52. Kammash, T. B. et al.: "The Elastic Plastic Cylinder Subjected to Radially Distributed Heat Source," Journal of Mech. and Phys. of Solids, 8, No. 1, 1960.

53. Timoshenko, S.: Theory of Elasticity, 2nd Ed. McGraw-Hill Book Co., Inc., New York, 1951.

54. Batterman, S. C.: "Plastic Buckling of Axially Compressed Cylindrical Shells," AIAA Paper 65-141, 25 January 1965.

55. Manson, S.: "Thermal Stresses, Part 2, Comparative Suitability of Materials," Machine Design, November 1961, 165-168.

56. Coffin, L.: "A Study of the Effects of Cyclic Thermal Stresses on a Ductile Material," ASME Trans. 76, 1954.

57. Lu, S., M. Trubert, and W. Nash: "Elevated Temperature Characteristics of Type 347 Stainless Steel," ASTM Proceedings, 61, 1961, 108.

58. R-5155, High-Pressure Pumping Technology, Interim Report, G. S. Wong, Rocketdyne, a Division of North American Aviation, Inc., Canoga Park, California, May 1963, CONFIDENTIAL

59. RR 64-28, Experimental Study of Contact Resistance Liner Concept for High-Pressure Thrust Chamber Applications, W. S. Hines, Rocketdyne, a Division of North American Aviation, Inc., Canoga Park, California, August 1964.

60. Bartz, D. R.: "A Simple Equation for Rapid Estimation of Rocket Nozzle Convective Heat Transfer Coefficients," Jet Propulsion, 27, 1957, 49-51.

61. Gambill, W. R.: "Generalized Prediction of Burnout Heat Flux for Flowing, Subcooled, Wetting Liquids," Chem. Eng. Progress Symposium Series, No. 41, 59, 1963, 71-87.

62. Chemical Engineers' Handbook, Fourth edition, McGraw-Hill Book Co., Inc., New York, 1963.

63. Simoneau, R. J. and R. E. Hendricks: "A Simple Equation for Correlating Turbulent Heat Transfer to a Gas," ASME Paper No. 64-HT-36 presented at Seventh National Heat Transfer Conference, Cleveland, Ohio, 9-12 August 1964.

64. "Fluid Meters - Their Theory and Application," Report of ASME Research Committee on Fluid Meters, Fifth Edition, 1959.

65. Sutton, G. P.: Rocket Propulsion Elements, Third Edition, John Wiley and Sons, Inc., 1963, 73.

66. Welsh, W. E.: "Review of Results of an Early Rocket Engine Film-Cooling Investigation at the Jet Propulsion Laboratory," JPL Technical Report No. 32-58, March 1961.

67. Nall, K. L.: "Compressible Fluid Flow," Aerojet Training Manual.

68. Deissler, R. G.: "Heat Transfer and Fluid Friction for Fully Developed Turbulent Flow of Air and Supercritical Water With Variable Properties," Trans. ASME, 76, 1954, 73-85.

69. CER 921-1005, "Experimental Gas-Side Heat Transfer Coefficients; P_c = 1125 psia, LOX:RP-1 Propellants," J. P. Sellers, Rocketdyne, a Division of North American Aviation, Inc., Canoga Park, California, 16 February 1959.

70. CER 0122-2026, "Experimental Gas-Side Heat Transfer Coefficients; P_c = 2000 psia and LOX:RP-1 Propellants," J. P. Sellers, Rocketdyne, a Division of North American Aviation, Inc., Canoga Park, California, 27 April 1960.

71. Miller, W. S., J. D. Seader, and D. M. Trebes: "Forced Convection Heat Transfer to Liquid Hydrogen at Supercritical Pressures," paper presented at The International Institute of Refrigeration, Commission I, Grenoble, France, 9-11 June 1965.